THE UNIVERSITY OF CHICAGO

MULTIFUNCTIONAL SULFUR-BASED COORDINATION COMPLEXES AND POLYMERS

A DISSERTATION SUBMITTED TO

THE FACULTY OF THE DIVISION OF THE PHYSICAL SCIENCES

IN CANDIDACY FOR THE DEGREE OF

DOCTOR OF PHILOSOPHY

DEPARTMENT OF CHEMISTRY

BY

JIAZE XIE

CHICAGO, ILLINOIS

JUNE 2022

Table of Contents

List of Figures

List of Schemes

List of Tables

List of Equations

List of Abbreviations

$\{^1H\}$	Proton decoupled
°	degree
°C	degree Celcius
^{119}Sn	Tin-119
^{11}B	Boron-11
^{13}C	Carbon-13
^{19}F	Fluorine-19
^1H	Hydrogen-1
^2H	Hydrogen-2 or deuterium
^{31}P	Phosphorus-31
^7Li	Lithium-7
A	absorbance
AcO	acetyl
AFM	atomic force microscopy
Anal. calc.	analysis calculated
Avg	average
B.M.	Bohr magnetons
BAr^F_4	tetrakis(3,5-bis(trifluoromethyl)phenyl)borate
BDT	1,4-benzenedithiolate
BHT	benzenehexathiolate
Bu	n-butyl
BzO	benzoyl
CASSCF	complete active space self-consistent field
CIF	crystallographic information
cm	centimeter
cm^{-1}	wavenumber
CP	coordination polymer
Cp	cyclopentadienyl
C_p	specific heat capacity
Cp^*	pentamethylcyclopentadienyl
CSD	Cambridge Structural Database
CV	cyclic voltammetry
d	deuterium or doublet
D	crystalline domain size
$D(E_F)$	density of states at Fermi level
DCM	dichloromethane

DFT	density functional theory
DMA	dimethylacetamide
DMBDT	2,5-dimethyl-1,4-benzenedithiol
DME	1,2-dimethyloxyethane
DMF	N,N-dimethylformamide
dmit	1,3-dithiole-2-thione-4,5-dithiolate
DMSO	dimethylsulfoxide
DOS	density of states
dppe	1,2-bis(diphenylphosphino)ethane
dppf	1,1'-bis(diphenylphosphino)ferrocene
dppp	1,3-bis(diphenylphosphino)propane
DPV	differential pulse voltammetry
DSC	differential scanning calorimetry
e	electron, electron charge
$E_{1/2}$	reduction potential of a compound under any conditions
EA	elementary analysis
EPR	electron paramagnetic resonance
Et_2O	diethyl ether
ett	ethylenetetrathiolate
eV	electronvolt
EXAFS	extended X-ray absorption fine structure
Fc	ferrocene
Fc^+	ferrocenium
FTIR	Fourier transform infrared
FWHM	full width at half maximum
g	gram
g	electron g-factor
G	conductance
GHz	gigahertz
H	enthalpy
h	the heat transfer coefficient
HDPE	high-density polyethylene
High resolution	high-resolution
HOMO	highest occupied molecular orbital
HONO	highest occupied natural orbital
H-R	Hagen-Rubens approximation
HS	high-spin
Hz	Hertz
I	intensity, laser power, current
ICP-MS	inductively-coupled plasma mass spectrometry
ICP-OES	inductively-coupled plasma optical emission spectroscopy

IR	Infrared
J	Joule
K	Kelvin
k_B	Boltzmann constant
kcal	kilocalorie
KK	Kramers-Kronig transmission
LAXS	large angle X-ray scattering
LIESST	light-induced excited spin state trapping
LS	low-spin
LUMO	lowest unoccupied molecular orbital
LUNO	lowest unoccupied natural orbital
m	multiplet, mass, mild, meter
m^*	effective mass
Me	methyl
m_e	electron's mass
MeCN	acetonitrile
MeOH	methol
meV	millielectrovolt
mg	milligram
MHz	megahertz
mL	milliliter
mM	millimolar
mm	millimeter
mmol	millimole
MOF	metal-organic framework
mol	mole
m_s	spin quantum number
mV	millivolt
mW	milliwatt
N	coordination number
n	charge density
NIR	near -infrared
nm	nanometer
NMP	N-methylpyrrolidone
NMR	nuclear magnetic resonance
NO	natural orbital
NON	natural occupation number
P_{abs}	the laser power absorbed by the sample
para	parallel
PDF	pairwise distribution function
PE	petroleum ether

PEDOS	poly(3,4-ethylenedioxyselenophene)
perp	perpendicular
Ph	phenyl
PT	photo-thermal
PTE	photo-thermal electric
PV	photovoltaic
PVDF	polyvinylidene fluoride
q	quartet
q	the magnitude of the scattering momentum transfer
QCP	Quantum Chemistry Package
Q_{ext}	external heat lost
Q_L	absorbed light energy
R	resistance, interatomic distances, Gaussian spot radius, reflectance
R_H	Hall coefficient
R_{sheet}	sheet resistance
RT/rt	room temperature
s	second, strong, singlet, separation distance between neighboring electrical probes
S	spin, Seebeck coeffient, siemens, surface area of the system
S	entropy
S(q)	properly corrected and normalized powder diffraction intensity
S_0^2	amplitude reduction factor
SAXS	small-angle X-ray scattering
SBU	secondary building units
SCO	spin crossover
SEM	scanning electron microscopy
sh	shoulder
STEG	solar thermoelectric
SXRD	single crystal X-ray diffraction
t	time, triplet, thickness
T	temperature, triplet
T_0	characteristic temperature used in VRH model
$T_{1/2}$	transition temperature of spin crossover-temperature of half high-spin
TBA	tetra-n-butylammonium
TCNQ	tetracyanoquinodimethane
TD-DFT	time-dependent density functional theory
TE	thermal electric
TEA	tetraethylammonium
TGA	thermogravimetric analysis
THF	tetrafuran
TMA	tetramethylammonium

TMBDT	2,3,5,6-tetramethyl-1,4-benzenedithiol
tmdt	trimethylene-tetrathiafulvalene-dithiolate
TMTSF	tetramethyl-tetraselenafulvalene
TOF	turnover frequency
TPA	tris(2-pyridylmethyl)amine
TTF	tetrathiafulvalene
TTFtt	tetrathiafulvalene-2,3,6,7-tetrathiolate
TTFtt$(C_2H_4CN)_4$	2,3,6,7-tetrakis(2'-cyanoethylthio)tetrathiafulvalene
UPS	ultraviolet photoelectron spectroscopy
UV	ultraviolet
V	voltage, volt
V2RDM	variational 2-electron reduced density matrix
vis	visible
VRH	variable-range hopping
VT	variable temperature
w	weak
W	watt
WAXS	wide angle X-ray scattering
XAS	X-ray absorption spectroscopy
XPS	X-ray photoelectron spectroscopy
XRD	X-ray diffraction
XRF	X-ray fluorescence
XRPD/PXRD	X-ray powder diffraction
ZT	dimensionless figure of merit (thermal electrics)
β	width of the peak at half of its height
δ	isomer shift, chemical shift
ΔE_0	change in the photoelectron energy
ΔE_Q	quadrupole splitting
ϵ	absorption extinction coefficient
η	efficiency
θ	diffraction angle, dimensionless temperature
κ	thermal conductivity, Scherrer constant
λ	wavelength
μA	microamp
μ_{eff}	effective magnetic moment
μL	microliter
μM	micromolar
μV	microvolt
μΩ	microOhm
ν	frequency
ρ	correlation, resistivity

σ	electrical conductivity
σ^2	Debye-Waller factors
τ	the cooling time coefficient
χ	magnetic susceptibility
Ω	Ohm
ω	frequency

Acknowledgement

First and foremost, I would like to thank my advisor, Prof. John Anderson, for all of his support and guidance over the years. Without his faith and trust, I could never finish my PhD studies, literally speaking. While a lot of physics and material science are discussed in this thesis, I was not qualified for such research in the beginning of my graduate program. More awfully, poor language ability made my life and study once further helpless. As being suffering Chicago's winter, I thought of quit more than once, but John is the person who did not give up me and encouraged me to learn anything, from whatever English classes or Physics textbooks. Thank John for giving me time to grow up. Years later, I may not remember any publications but will recall the band structure that I drew on John's board.

Next, I would like to thank my committee members, Prof. Dmitri Talapin and Prof. Jiwoong Park, for their role in my defense and for their support and instruction for our collaboration projects. I also thank group members from both labs, especially Baorui Cheng and Dr. Yu Zhong from Park group and Jia-Ahn Pan, Di Wang and Dr Chengkun Zhou from Talapin group. With their help, I was able to finish a lot of physical characterization in their labs.

I would also like to thank the Anderson lab as a whole for their friendly helps about science or non-science. In particular, I need to thank Dr. Noah Horwitz. Noah is my second PhD mentor who taught me how to do chemistry and how to be a researcher. He is smart but humble; funny in the life but meticulous about science. He is a good friend and teacher.

Thank Dr. Alex Filatov for his help and lessons about all X-ray techniques. All the structural and composition characterizations of my materials are largely dependent on X-ray techniques and Alex participates almost all my projects. He is one of most reliable collaborators. Similarly, I want

to thank Prof. David Mazziotti, Jan-Niklas Boyn and Simon Ewing for the help with theoretical calculations and thank Prof. Shrayesh Patel and Dr. Tengzhou Ma for assistance of Seebeck measurements.

Last but not least, I would like to thank my family and friends who have supported me outsides of my academic career. Due to visa status and COVID 19, I have only gone back home twice in six years. I really appreciate the understanding and unconditional supports from my family, which allows me to focus on studying mainly. It is a pity that they could not attend my defense that they were expecting for years, and I swear I will send photos and videos instead. Finally, a special thank is given to my love, Xiaotong Sun. Thanks for your companion, patience and encouragement. Every time I feel upset and frustrated, I miss your laugh, which is impressive and inspiring as the same as the “pig head” you drew on my desk. Mua, Dr. Xiaotong Sun.

Abstract

Coordination polymers, especially metal-organic frameworks, have been one of the fastest developing areas in materials science. Despite the myriad applications of these materials, the development of physical properties such as conductivity and magnetism, has been comparatively slower due to the insulating nature of both diamagnetic metals and organic linkers. One successful strategy to address these shortcomings has been to use sulfur-based linkers and metal-sulfur clusters. This approach has led to materials with "state of the art" physical properties, but is surprisingly limited to only a few systems and morphologies. The main limitation is challenging synthesis including the isolation of sulfur-based linkers and clusters and the controlled growth of targeted materials. In the course of this thesis, I have discovered design principles which enable the synthesis of a modular family of these materials. Furthermore, based on these well-defined materials, physical characterization demonstrates their interesting conductive, magnetic, optical and thermal properties, which show promising applications ranging from spintronics to energy applications.

Chapter 2 outlines that well-studied Fe_4S_4 clusters can be connected with 1,4-benzenedithiolate to generate highly crystalline and soluble 1D-chains. Further electrochemical studies suggest that the reversible redox behavior of Fe_4S_4 clusters, known in biological systems, is retained in the polymers. Correspondingly, the conductivity can be tuned over a 10^4-fold range by redox control. Later, we were also able to isolate new Fe_4S_4-based polymers with either 2,3,5,6-tetramethyl-1,4-benzenedithiolate and 2,5-benzene-1,4-benzenedithiolate, the work of which is introduced in Chapter 3. Methylation results in the general trend of increasing electron-richness in the series, but the tetramethyl version exhibits unexpected properties arising from steric constraints, such as a UV-visible absorption blue-shift and enhanced solubility with larger counterions. All these results

highlight how substitutions on organic linkers can modulate electronic factors to fine-tune the electronic structures of metal-organic materials. Overall, these works demonstrate the feasibility of using sulfur-containing nodes and linkers to synthesize crystalline extended metal chalcogenides to develop novel functional materials. Such synthetic strategies provide access to materials based on molecular metal-chalcogenide clusters that can be thought of as mimics of solid-state chalcogenides that are "expanded" by longer organic linkers.

In addition to using well-developed sulfur-based nodes and linkers, a lot of my efforts have been devoted to developing new redox-active sulfur-linkers. A derivative of the well-known TTF core, tetrathiafulvalene-2,3,6,7-tetrathiolate ($TTFtt^{4-}$), is an attractive target. However, due to the inherent sensitivity of the $TTFtt^{4-}$ species, there has been relatively little well-defined application of this linker. For this reason, I have developed new TTFtt transmetalating reagents and Chapter 4 illustrates the detailed synthesis and metalation of a new tin derivative of $TTFtt^{4-}$. The highly reversible redox behavior of the bis-dibutyltin derivative, $TTFtt(SnBu_2)_2$, allows for isolation of the radical cation and dication forms of this linker for the first time. These serve as convenient precursors for the synthesis of other $TTFtt^{4-}$ metal complexes of varying charge states without the need for additional post-synthetic oxidation. Followingly, Chapter 5 demonstrates that instead of group 10 metals, a diiron complex bridged by the doubly-oxidized $TTFtt^{2-}$ undergoes a thermally induced Fe-centered spin-crossover which yields significant diradical character on $TTFtt^{2-}$. The molecular studies in Chapter 4 and 5 shed insights on new TTFtt chemistry and the interesting properties found in these complexes motivates us to further explore the physics of extended materials based on TTFtt.

The first target was previously synthesized NiTTFtt materials. Although reported, their structure, purity, composition, and hence properties are ill-defined due to synthetic challenges. Chapter 6

shows that using the doubly-oxidized TTFtt($SnBu_2$)$_2^{2+}$ precursor, I have been able to generate neutral NiTTFtt chains with a precise composition. Surprisingly, these completely amorphous polymers exhibit record conductivity as pressed pellets (1280 S/cm) and detailed characterization suggests metallic behaviors. Theory suggests that molecular overlap that is robust to structural distortions is the origin of high conductivity. This unusual set of structural and electronic features results in remarkably stable conductivity which is maintained in air for weeks and at temperatures up to 140 °C. This is the first example of an intrinsic organic metal without any crystalline ordering and thus raises fundamental questions about electron transport in amorphous organic metals. Beyond metallics, Chapter 7 demonstrates that instead of using dicationic precursors, using neutral TTFtt($SnBu_2$)$_2$ leads to reduced NiTTFt chains and they are typical p-type semiconductors with about 0.3 eV bandgaps. This result suggests a metal-to-semiconductor transition enabled by pre-synthetic redox control. Furthermore, we also discovered high-performance photo-thermal electric conversion based on these polymers and investigated these properties in detail. Compared to conventional multi-component hybrid devices, single-component NiTTFtt polymers show fast and efficient NIR-Seebeck voltage production with high durability. These properties make NiTTFtt materials promising for potential applications such as solar energy harvesting, NIR-photosensors, and night cameras.

Last but not least, recently, 2D sheets of MoS_2 have attracted attention for their unique physical properties, such as high charge mobility. Incorporating MoS-based clusters as nodes with conjugated, redox-active linkers will allow for the synthesis of porous structures with tunable electronic properties with potential applications in energy or ion storage. Chapter 8 summarizes some initial results about the synthesis of MoS_2-like coordination frameworks built with TTFtt and Mo_3S_7 clusters. Upon *in situ* oxidation during the synthesis, the conductivity of the resulting

neutral framework can be increased to 0.2 S/cm, 100 times higher than that of unoxidized materials. X-ray absorption spectroscopy studies of both the dianionic and neutral materials indicate that the oxidation state of Mo does not change upon oxidation and that the Mo-S and Mo-Mo distances are close to nano-MoS_2 in both cases. In addition, we have also begun work on the synthesis of thin films of these Mo-based materials. Based on the exciting properties shown in previous TTFtt-based materials, we believe such extended-MoS_2 organic frameworks could enable exciting new physical phenomena.

In short, this thesis presents two series of sulfur-based coordination materials, Fe_4S_4-based and TTFtt-based ones. With new synthesis strategies and ration designs, all reported materials display high compositional purity and, in many cases, crystallinity. These well-defined systems allow us to explore new chemistry and physics such as organic diradicals, metallics, photo-thermal electrical conversions. These multifunctional sulfur-based coordination materials show the possibility to impact applications ranging from spintronics to detectors.

Preface

All chapter parts have an independent compound numbering system. Characterization spectra are provided in the corresponding appendix for each chapter.

Chapter 1: Introduction

1.1 Electrically Conducting Sulfur-Based Coordination Polymers

Hybrid inorganic-organic materials are an attractive area of research as they can exhibit a wide array of physical and chemical properties that can be tuned through substitution of their components. Recent interest in these types of materials is exemplified by coordination polymers (CPs)[1] and hybrid perovskites.[2] The variety of nodes and linkers leads to a limitless array of materials with control over composition, functionality, and morphology. By the virtue of such structural and chemical flexibility, CPs, typified by porous metal-organic frameworks (MOFs), are widely applied in areas such as gas separation,[3] storage,[4] catalysis,[5] and medicine.[6] However, the majority of these materials rely on hard O and N-based linkers and diamagnetic metal ions such as Zn^{2+} or Zr^{4+} which are inherently electrically insulating, limiting their utility in applications such as advanced electronics.[7]

In the last decade, a few synthetic strategies have been proposed to improve the electrical conductivity of CPs.[8] Among most efficient methods, two main themes are improving metal-ligand conjugation and harnessing π-stacking interaction between organic moieties. While the majority of conductive CPs still reply upon hard O- and N-based linkers, such as quinones, detailed studies have shown that energetic matching and orbital overlap between transition metals and less-electronegative sulfur atoms enhance electronic couplings and delocalization leading to improvements in conductivity.[9] Indeed, several new materials with remarkable properties, such as highly electrically conductive and magnetic semiconductors, have been made of dithiolene-based ligands.[10] Furthermore, sulfur-containing ligands are commonly redox-active, which provides another dimension to control the electronic properties via redox chemistry. In addition to the sulfur-based linkers, the use of multi-metallic nodes with heavier chalcogenides should offer

similarly exciting advantages in redox activity and conductivity. Heavy chalcogenide-based clusters are in some ways atomic level units of solid-state transition metal chalcogenides.[11] As such, CPs built with these clusters as SBUs may be thought of as inorganic-organic mimics of minerals with the added benefits of tunability and porosity.

Although the sulfur-based CPs are pursued for many reasons, research on sulfur-based CPs is dramatically more limited than that on "classic" CPs. This dearth is likely motivated by two factors: 1) Sulfur-based precursors and ligands are typically more sensitive to ambient conditions than O- and N- based linkers, and 2) While reliable synthetic protocols for O- and N-based CPs exist, similar protocols for chalcogenide systems have not been well-studied, such as usage of templating agents, which leads to relatively poor crystallinity of final materials.

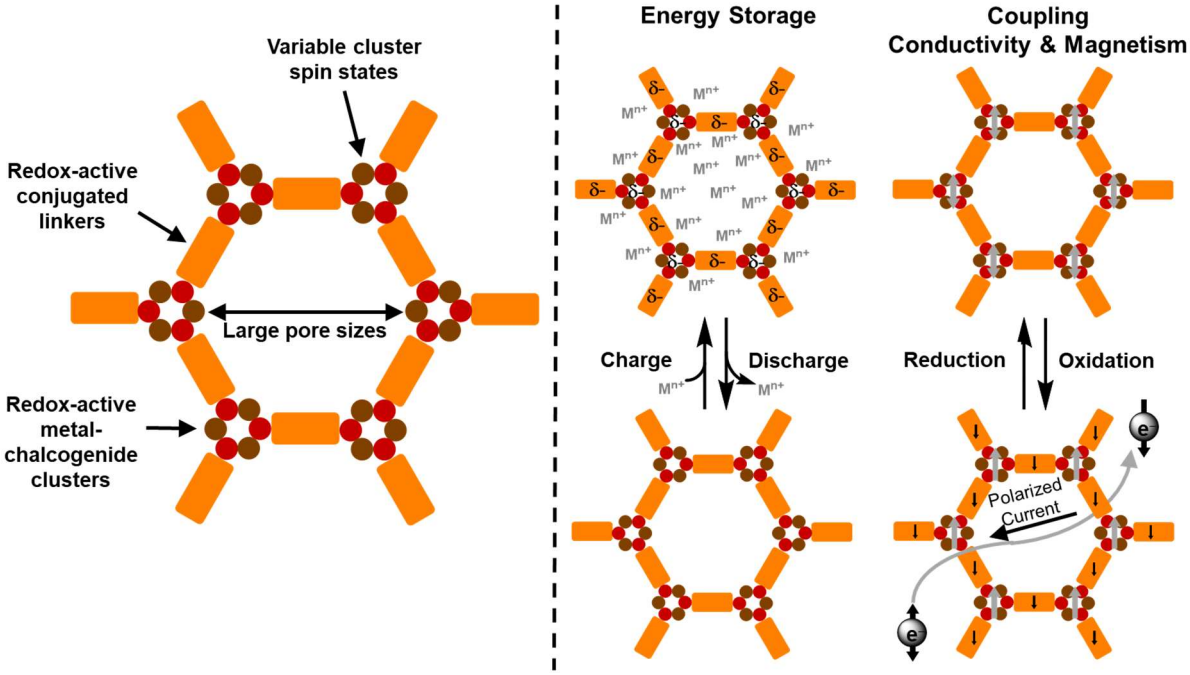

Figure 1.1. Redox-active sulfur-based coordination polymers and its proposed applications in electrochemical energy storage and coupling conductivity and magnetism.

Therefore, in pursue of new material physics and application performance, my PhD research has focused on developing new synthetic methodologies to create well-defined sulfur-based coordination materials and study their physical and chemical properties (**Figure 1.1**). Specifically,

two families of sulfur-based coordination materials are targeted: 1) A series of 1D CPs composed of Fe_4S_4 clusters and the bridging linkers, 1,4-benzendithiolate and its derivatives (Chapter 2 and 3); 2) molecular complexes (Chapter 4 and 5) and CPs (Chapter 6, 7 and 8) based on redox-active tetrathiafulvalene-2,3,6,7-tetrathiolate (TTFtt) linkers.

1.2 Metal-Sulfur Clusters as Coordination Polymer Nodes

Since Robson's seminal discovery of diamondoid Cu frameworks in the 1990's,[12] tens of thousands of MOFs have been reported as an emergent class of porous materials. Much of the seminal work in this area has relied upon metal oxygen bonds to form nodes or secondary building units (SBUs) as exemplified by carboxylate linkers and metal oxide clusters found in MOF-5 and UiO-66.[13] While metal-oxygen clusters are widely used as secondary building units in the construction of coordination polymers or metal-organic frameworks, multimetallic nodes with heavier chalcogenide atoms (S, Se, and Te) are comparatively untapped. The lower electronegativity of heavy chalcogenides means that transition metal clusters of these elements generally exhibit enhanced coupling, delocalization, and redox-flexibility. Leveraging these features in coordination polymers provides these materials with extraordinary properties in catalysis, conductivity, magnetism, and photoactivity. In a recent perspective,[14] I and my colleagues summarized common transition metal heavy chalcogenide building blocks used in coordination polymers and their properties. Based on recent discoveries, we also outline potential challenges and opportunities for applications in this field.

While the strategy of using organosulfur ligands to generate metal-thiolate SBUs directly in the construction of CPs has been remarkably successful, preformed transition metal sulfide/selenide clusters are also attractive SBUs for new materials. Transition metal-chalcogenide clusters have been investigated for some time as mimics or molecular analogues of chalcogenide minerals.[15]

These clusters are potentially useful building blocks in the construction of functional materials because of their tunable structural diversity, catalytic activity, multiple accessible redox states, and magnetic properties.

In Chapter 2, I demonstrated that the most thoroughly studied Fe_4S_4 clusters can be connected with 1,4-benzenedithiolate (BDT) through solvothermal reactions between $BDTH_2$ and $[NR_4]_2[Fe_4S_4](SPh)_4$ (R = methyl or n-butyl groups, Ph = phenyl) to generate highly crystalline 1D-chain polymers (**Figure 1.2**).[16] The crystallinity of these chains is possibly due to slow or reversible ligand substitution processes between BDT and benzenethiolate. Furthermore, it was found that anionic chains exhibited counterion dependent solubility. The tetramethylammonium (TMA) salt is soluble in dimethylformamide (DMF) and small-angle X-ray scattering (SAXS) confirms that the anionic chains exist as swollen polymer coils in solution. Besides the solubility, further studies show that the redox-activity of the Fe_4S_4 clusters can be accessed with chemical reagents as post-synthetic reduction increases the electrical conductivity of the materials by up to 4 orders of magnitude from $5(3) \times 10^{-10}$ to $5(2) \times 10^{-6}$ Scm^{-1}.

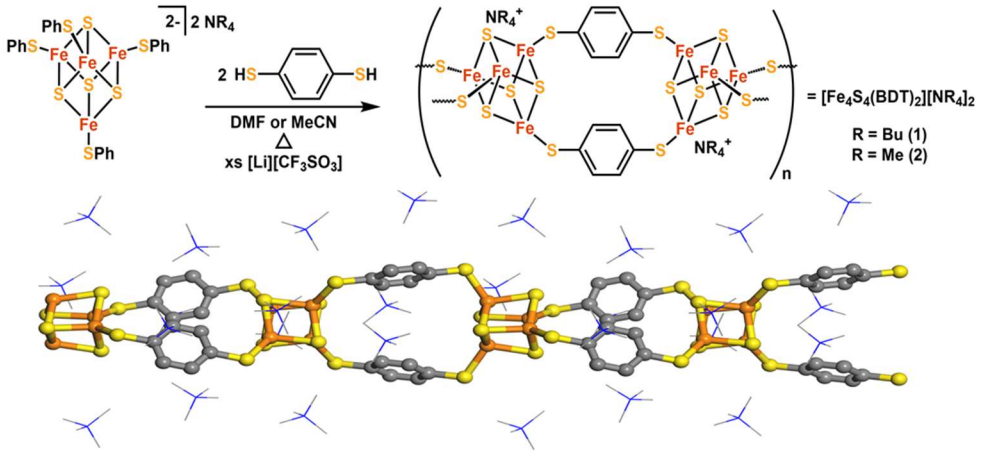

Figure 1.2. Synthesis scheme of Fe_4S_4-BDT chains and the structure of $[TMA]_2[Fe_4S_4(BDT)_2]$.

One of the notable advantages of molecular materials is the ability to precisely tune structure, properties, and function via molecular substitutions. While many studies have demonstrated this

principle with classic carboxylate-based coordination polymers, there are comparatively fewer examples where systematic changes to sulfur-based coordination polymers have been investigated. As a follow-up work of Chapter 2, Chapter 3 presents such a study on 1D coordination chains of redox-active Fe_4S_4 clusters linked by methylated 1,4-benzene-dithiolates. A series of new Fe_4S_4-based CPs were synthesized with either 2,5-dimethyl-1,4-benzenedithiol (DMBDT) or 2,3,5,6-tetramethyl-1,4-benzenedithiol (TMBDT) (**Figure 1.3**). The structures of these compounds have been characterized based on synchrotron X-ray powder diffraction while their chemical and physical properties have been characterized by techniques including X-ray photoelectron spectroscopy (XPS), cyclic voltammetry (CV) and UV–visible spectroscopy. Methylation results in the general trend of increasing electron-richness in the series, but the tetramethyl version exhibits unexpected properties arising from steric constraints. All these results highlight how substitutions on organic linkers can modulate electronic factors to fine-tune the electronic structures of metal-organic materials.

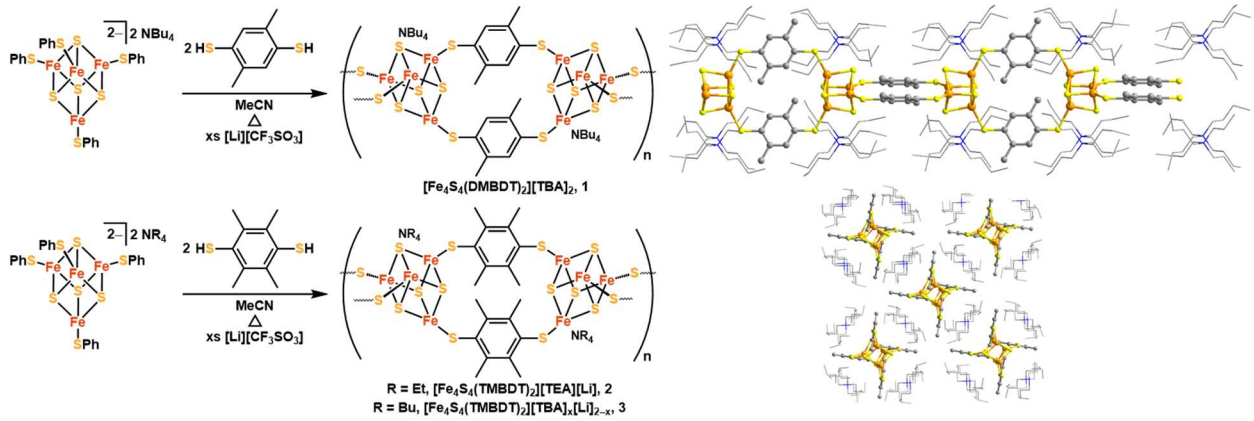

Figure 1.3. Synthesis scheme of Fe_4S_4-DMBDT/TMBDT chains and the structure of $[TBA]_2[Fe_4S_4(DMBDT)_2]$. TBA = tetra-n-butylammonium.

In short, while clusters formed from transition metals and heavy chalcogenides have been known for many years with some examples of CPs reported nearly 40 years ago, these building blocks have still received far less attention than their oxide counterparts in MOF chemistry. This is despite

the fact that these clusters have features such as unique geometries, redox and magnetic properties, and hard-soft matching which make them attractive for many applications. My recent work, summarized in Chapter 2, and 3, illustrates that these promising building blocks can be reliably incorporated into new CP materials with appropriate synthesis protocols. This area therefore offers exciting potential for emerging areas in CP and MOF materials and applications.

1.3 Isolation of Redox-Active TTFtt and Studies from Molecular Level

Conjugated coordination polymers have attracted recent attention due to promising applications in superconductivity,[17] energy storage,[18] thermoelectrics,[19] spintronics,[20] and other fields.[21, 22,23] However, delocalized metal-organic systems are still rare and most coordination polymers are limited to architectures constructed with nitrogen and oxygen based ligands.[23, 24] Some of the most conductive materials[25] in this area have instead used sulfur based linkers which are perhaps best exemplified by dithiolene units that leverage both a better energy match between sulfur atoms and metal centers and ligand-based redox activity.[26] Nevertheless, stability and controllable synthetic conditions are still significant challenges associated with the incorporation of dithiolene based linkers. Molecular dithiolene complexes have great utility in addressing these challenges as they allow for a detailed understanding of the properties and reactivity of dithiolene units. Furthermore, molecular dithiolene complexes can be used as transmetalating agents to generate materials in a controlled manner.[21f, 26c] Of possible dithiolene ligands, TTFtt (**Figure 1.4**) is attractive as it combines the above mentioned properties of dithiolenes with the favorable electronic properties of tetrathiafulvalene (TTF).[27] Organic radical salts of TTF and its derivatives are well-known for outstanding electronic properties, such as being components in organic conductors such as TTF-TCNQ (TCNQ = tetracyanoquinodimethane) and organic superconductors such as $[TMTSF]_2[PF_6]$ (TMTSF: tetramethyl-tetraselenafulvalene).[28] While TTF has been incorporated

into coordination polymers to improve conductivity[29] and enable switching of porosity[30] or magnetism,[31] TTFtt has much less precedent in well-defined complexes or materials. Some conductive TTFtt-transition metal chains were reported by IBM Research Laboratory in 1979 with limited characterization data.[32a] In 1995, McCullough and coworkers crystalized the first homobimetallic TTFtt complex and the TTFtt unit was proposed as a promising building block for new magnetic, electronic and optical materials.[33a, b] However, there has been little progress towards this end over the following decades. Only one report of installing TTFtt between fullerene supported Co centers using a decarbonylative process at high temperature has been structurally characterized and limited characterization has been reported on molybdocene fragments bridged by TTFtt.[34]

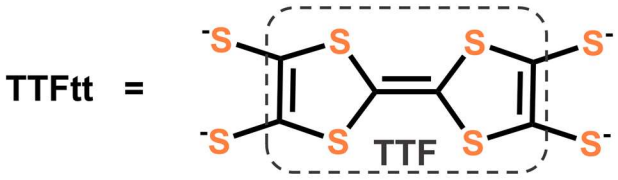

Figure 1.4. The structure of TTFtt with the TTF core indicated.

The primary challenge with the incorporation of TTFtt into molecules or materials is the sensitivity of this moiety and its synthons. Unprotected $TTFttH_4$ has not been isolated and characterized, although $TTFttLi_4$ can be generated transiently as a highly reactive and sensitive solid for metalations as reported in McCullough's work.[33] The conventional synthetic technique for the incorporation of TTFtt involves the *in-situ* deprotection of derivatives such as 2,3,6,7-tetrakis(2'-cyanoethylthio)tetrathiafulvalene, $TTFtt(C_2H_4CN)_4$.[35] This deprotection typically requires the use of an excess of strong base which limits the choice of solvent and also leads to undesirable side reactions due to the highly basic, nucleophilic, and reducing properties of the $TTFtt^{4-}$ tetra-anion. Furthermore, the required excess base may also introduce side-reactions. These issues have directly limited the investigation and incorporation of TTFtt.

To alleviate these issues and enable the facile and controlled installation of TTFtt between transition metals, we were inspired by previous work by Donahue and coworkers that demonstrated that capping of dithiolene units such as 1,2,4,5-benzenetetrathiolate with dialkyltin groups enables smooth transmetalation to transition metals.[36, 37] Chapter 4 outlines that capping the molecule TTFtt with dialkyl tin groups enables the isolation of a stable series of redox congeners and facile transmetalation to Ni and Pd (**Figure 1.5**). A comprehensive characterization of these molecular complexes provides a new and deep understanding about TTFtt chemistry, which is also a key reference library used for more complicated systems in the following studies.

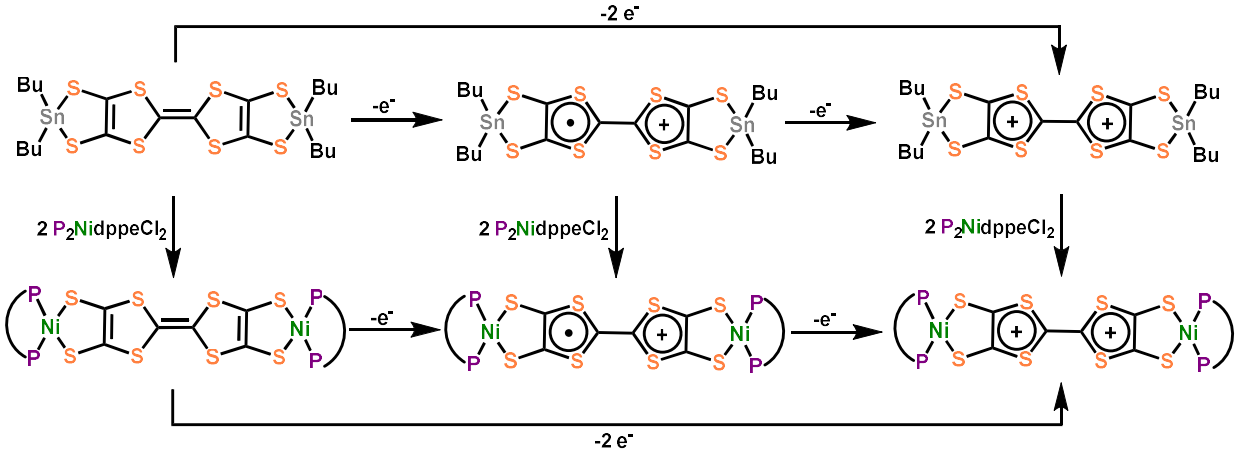

Figure 1.5. Demonstration of redox and transmetallation of TTFtt-Sn precursors.

In addition, we have also metalated $TTFtt^{4-}$ with paramagnetic Fe (II) centers. Surprisingly, the bis-iron complex bridged by the doubly-oxidized $TTFtt^{2-}$ ligand undergoes a thermally gated organic spin change. In this process, two $S = 2$ Fe centers exhibit spin-crossover behavior that is coupled to a significant decrease in the singlet-triplet gap of the TTFtt core (**Figure 1.6**). Typically, observing significant diradical character at low temperature in organic compounds is relatively rare and is unknown in the well-studied TTF moiety. Further theoretical calculations showed that the ground state of this complex has significant diradical character. This work is discussed in Chapter 5 in detail.

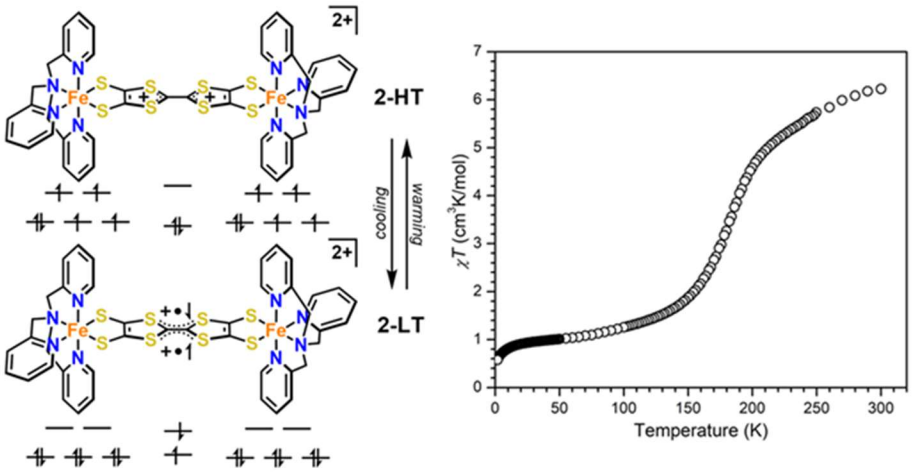

Figure 1.6. Demonstration of iron's spin crossover triggering TTF core's diradical character and its corresponding temperature-dependent magnetic susceptibility.

In summary, Chapter 4 and 5 discuss that molecular dithiolene complexes, specifically TTFtt-Sn compounds, can be used as efficient transmetalating agents to generate materials in a controlled manner. Taking advantages of crystallography and solubility, characterization on resulting molecular dithiolene complexes allows for a detailed understanding of the properties and reactivity of TTFtt, which provides insights for the design of related solid-state materials.

1.4 Multifunctional CPs Based on TTFtt Building Blocks

Due to synthetic challenges, only few ill-defined MTTFtt materials have been reported and amorphousness and impurities generally limits the characterization to simple conductivity measurements.[32] Since the geometry of Nickel-bisdithiolenes is known to be square-planar, the complexity of structural predictions for NiTTFtt polymers is dramatically simplified. Thus, having characterized bimetallic molecular $TTFtt^{4-}$ complexes, my focus shifted towards the synthesis of conjugated, redox-active NiTTFtt CPs and these studies are included in Chapter 6 and 7.

Using the doubly-oxidized $TTFtt(SnBu_2)_2^{2+}$ precursor, I have been able to generate neutral NiTTFtt chains with a precise composition (**Figure 1.7**). Chapter 6 outlines that despite its disordered structure, NiTTFtt exhibits remarkably high electronic conductivity (~10^3 S/cm) and

intrinsically glassy metallic behavior. Analysis with advanced theory shows that these properties are enabled by strong molecular overlap and correlation that are robust to structural perturbations. This unusual set of structural and electronic features results in remarkably stable organic conductivity which is maintained in air for weeks and at temperatures up to 140 °C. Our results demonstrate that molecular design can enable metallic conductivity even in heavily disordered materials. This both raises fundamental questions about how band-like transport can exist in the absence of periodic structure as well as suggests exciting new applications for these materials.

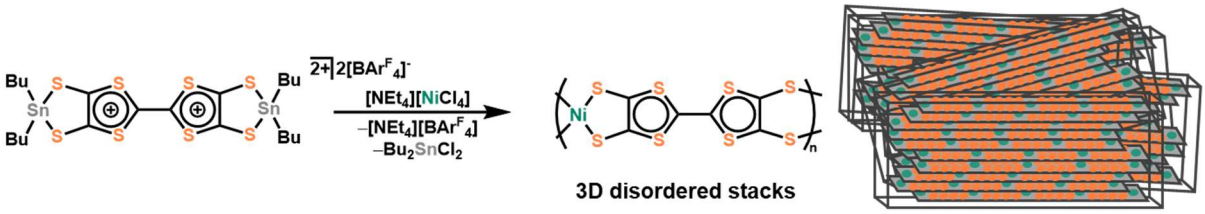

Figure 1.7. Depiction of the synthesis and proposed structure of amorphous NiTTFtt.

Furthermore, instead of using dicationic precursors, using neutral TTFtt$(SnBu_2)_2$ leads to fully reduced NiTTFt chains, namely, $Li_{1.2}Ni_{0.4}$[NiTTFtt] and $[Li(THF)_{1.5}]_{1.2}Ni_{0.4}$[NiTTFtt] (**Figure 1.8**). Interestingly, unlike n-type metallic NiTTFtt, physical characterization suggests reduced NiTTFtt materials are typical p-type semiconductors. In addition to the metal-to-semiconductor transition via pre-synthetic redox control, physical characterization also demonstrates that the broad spectral absorption and electrically conducting nature of both oxidized and reduced TTFtt-based materials enables highly efficient NIR-thermal conversion and good photo-thermal electric (PTE) performance. The NiTTFtt materials reported here represent the best single-component organic PTE materials for both p-type and n-type applications, and the tunable photo-thermal (PT) properties, thermal electric (TE) properties, and carrier character suggests that using synthetic strategies to rationally change the redox-states of coordination polymer materials is a powerful strategy for generating new PTE candidates. Detailed characterizations on PTE properties of the NiTTFtt redox series are included in Chapter 7.

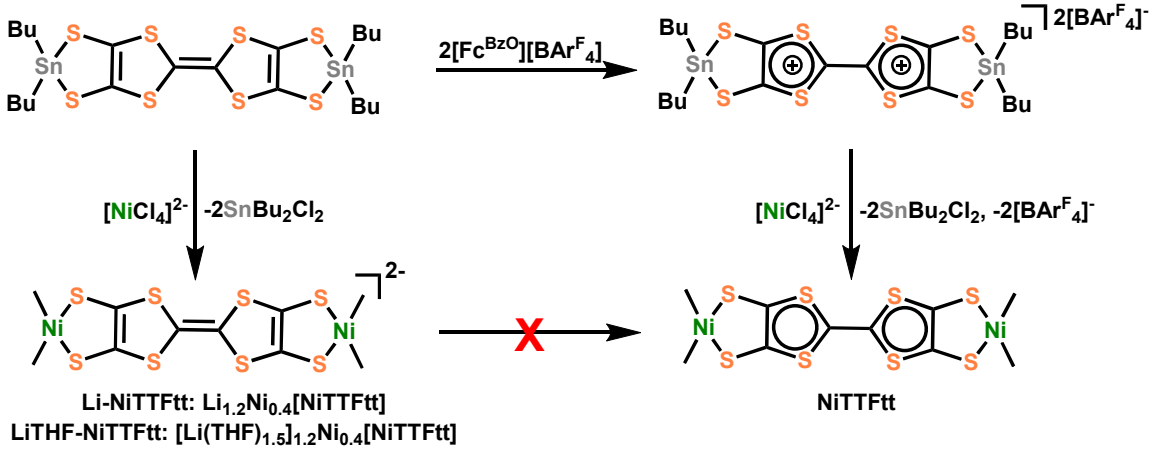

Figure 1.8. Depiction of synthesis of NiTTFtt chains at different oxidation states via pre-synthetic redox control.

In addition to iron-sulfur clusters, recently, discrete MoS-based clusters have also attracted attention, as they are atomic islands of functional MoS_2 materials. In 2018, Ji et al. have successfully linked Mo_3S_7 clusters with BDT to form dimers, cages, and 1D chains (**Figure 1.9**).[38] The highly crystalline chains of MOS-3 display dramatically improved catalytic activity for HER with a 40-fold enhancement in turnover frequency (TOF) over molecular Mo_3S_7-cluster complexes. However, unlike inorganic congeners, these materials are poorly conductive due to weak conjugation between clusters and linkers. Plus, in the view of the structure dimension, these polymer chains are not comparable to inorganic MoS_2, which is a classic 2D materials.

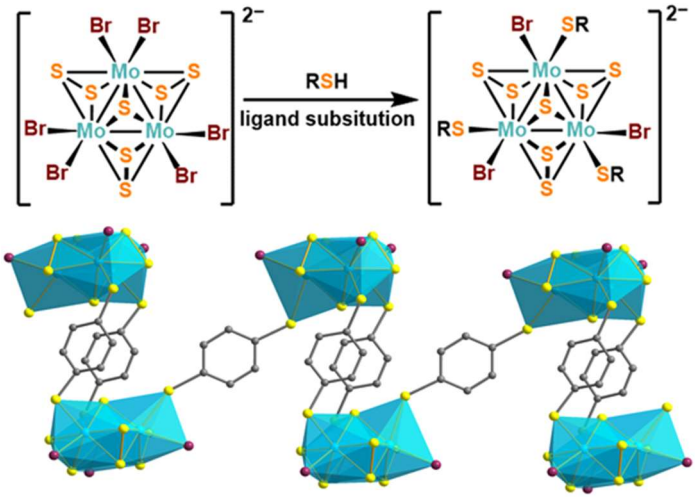

Figure 1.9. Mo_3S_7 clusters connected by BDT into a chain structure (MOS-3).

In Chapter 8, my current work demonstrates that incorporating MoS-based clusters as nodes with TTFtt, which is a conjugated redox-active linker, will lead to a more delocalized and conductive MoS_2-like extended framework (**Figure 1.10**). The conductivity of these materials can be tuned by ligand-based redox events. What's more, we have also begun work on the synthesis of thin films of these Mo-based materials. Based on the exciting properties shown in TTFtt-based materials, we expect such extended-MoS_2 organic frameworks could enable exciting new physical phenomena.

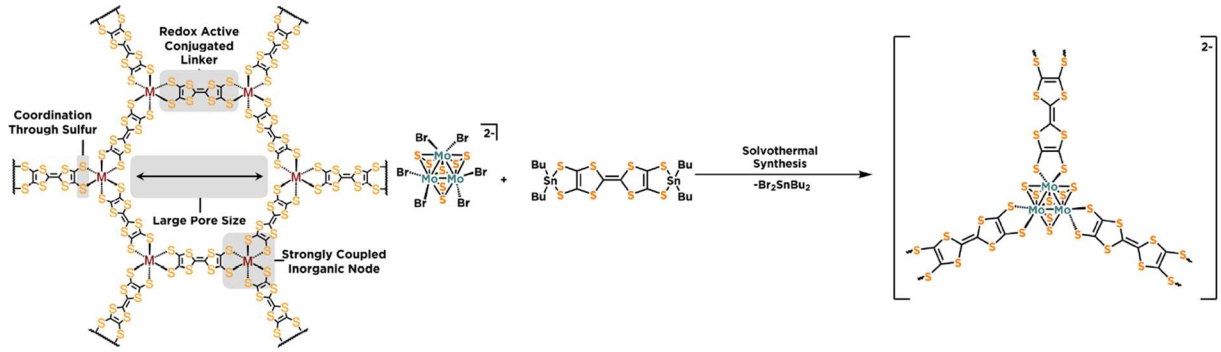

Figure 1.10. Depiction of proposed 2D/3D TTFtt-based frameworks and synthesis of MoS_2-like coordination polymers.

1.5 References

[1] (a) Li, J. R.; Kuppler, R. J.; Zhou, H. C. Selective Gas Adsorption And Separation In Metal-Organic Frameworks. *Chem. Soc. Rev.* **2009**, *38* (5), 1477–1504. (b) Lee, J.; Farha, O. K.; Roberts, J.; Scheidt, K. A.; Nguyen, S. T.; Hupp, J. T. Metal-Organic Framework Materials As Catalysts. *Chem. Soc. Rev.* **2009**, *38* (5), 1450–1459. (c) Ma, L.; Abney, C.; Lin, W. Enantioselective Catalysis With Homochiral Metal–Organic Frameworks. *Chem. Soc. Rev.* **2009**, *38* (5), 1248. (d) Sumida, K.; Rogow, D. L.; Mason, J. A.; Mcdonald, T. M.; Bloch, E. D.; Herm, Z. R.; Bae, T.-H.; Long, J. R. Carbon Dioxide Capture In Metal–Organic Frameworks. *Chem. Rev.* **2012**, *112* (2), 724–781. (e) Furukawa, H.; Cordova, K. E.; O'Keeffe, M.; Yaghi, O. M. The Chemistry And Applications Of Metal-Organic Frameworks. *Science (80).* **2013**, *341* (6149), 1230444–1230444. (f) Zhang, Y.; Feng, X.; Yuan, S.; Zhou, J.; Wang, B. Challenges And Recent Advances In MOF–Polymer Composite Membranes For Gas Separation. *Inorg. Chem. Front.* **2016**, *3* (7), 896–909. (g) Maurin, G.; Serre, C.; Cooper, A.; Férey, G. The New Age Of Mofs And Of Their Porous-Related Solids. *Chem. Soc. Rev.* **2017**, *46* (11), 3104–3107. (h) Trickett, C. A.; Helal, A.; Al-Maythalony, B. A.; Yamani, Z. H.; Cordova, K. E.; Yaghi, O. M. The Chemistry Of Metal–Organic Frameworks For CO_2 Capture, Regeneration And Conversion. *Nat. Rev. Mater.* **2017**, *2* (8), 17045.

[2] (a) Kojima, A.; Teshima, K.; Shirai, Y.; Miyasaka, T., Organometal Halide Perovskites as Visible-Light Sensitizers for Photovoltaic Cells. *J. Am. Chem. Soc.* **2009,** *131* (17), 6050-6051. (b)

Hao, F.; Stoumpos, C. C.; Cao, D. H.; Chang, R. P. H.; Kanatzidis, M. G., Lead-Free Solid-State Organic–Inorganic Halide Perovskite Solar Cells. *Nat. Photonics* **2014,** *8*, 489. (c) Zhao, Y.; Zhu, K., Organic-Inorganic Hybrid Lead Halide Perovskites for Optoelectronic and Electronic Applications. *Chem. Soc. Rev.* **2016,** *45* (3), 655-689.

[3] (a) J.-R. Li, R. J. Kuppler and H.-C. Zhou, Selective Gas Adsorption and Separation in Metal–Organic Frameworks, *Chem. Soc. Rev.*, 2009, **38**, 1477. (b) H. Furukawa, K. E. Cordova, M. O'Keeffe and O. M. Yaghi, The Chemistry and Applications of Metal-Organic Frameworks, *Science*, 2013, **341**, 1230444–1230444. (c) Y. Zhang, X. Feng, S. Yuan, J. Zhou and B. Wang, Challenges and Recent Advances in MOF–Polymer Composite Membranes for Gas Separation, *Inorg. Chem. Front.*, 2016, **3**, 896–909. (d) G. Maurin, C. Serre, A. Cooper and G. Férey, The New Age of MOFs and of Their Porous-Related Solids, *Chem. Soc. Rev.*, 2017, **46**, 3104–3107.

[4] (a) K. Sumida, D. L. Rogow, J. A. Mason, T. M. McDonald, E. D. Bloch, Z. R. Herm, T.-H. Bae and J. R. Long, Carbon Dioxide Capture in Metal–Organic Frameworks, *Chem. Rev.*, 2012, **112**, 724–781. (b) C. A. Trickett, A. Helal, B. A. Al-Maythalony, Z. H. Yamani, K. E. Cordova and O. M. Yaghi, The Chemistry of Metal–Organic Frameworks for CO_2 Capture, Regeneration and Conversion, *Nat. Rev. Mater.*, 2017, **2**, 17045.

[5] (a) L. Ma, C. Abney and W. Lin, Enantioselective Catalysis with Homochiral Metal–Organic Frameworks, *Chem. Soc. Rev.*, 2009, **38**, 1248. (b) J. Lee, O. K. Farha, J. Roberts, K. A. Scheidt, S. T. Nguyen and J. T. Hupp, Metal–Organic Framework Materials as Catalysts, *Chem. Soc. Rev.*, 2009, **38**, 1450.

[6] (a) P. Horcajada, R. Gref, T. Baati, P. K. Allan, G. Maurin, P. Couvreur, G. Férey, R. E. Morris and C. Serre, Metal–Organic Frameworks in Biomedicine, *Chem. Rev.*, 2012, **112**, 1232–1268. (b) W. Cai, J. Wang, C. Chu, W. Chen, C. Wu and G. Liu, Metal-Organic Framework-Based Stimuli-Responsive Systems for Drug Delivery, *Adv. Sci.*, 2019, **6**, 1801526.

[7] a) Du, D. Y.; Qin, J. S.; Li, S. L.; Su, Z. M.; Lan, Y. Q. Recent Advances in Porous Polyoxometalate-Based Metal-Organic Framework Materials. *Chem. Soc. Rev.* **2014**, *43*, 4615-4632. b) Li, B.; Leng, K.; Zhang, Y.; Dynes, J. J.; Wang, J.; Hu, Y.; Ma, D.; Shi, Z.; Zhu, L.; Zhang, D.; Sun, Y.; Chrzanowski, M.; Ma, S. Metal–Organic Framework Based Upon the Synergy of a Brønsted Acid Framework and Lewis Acid Centers as a Highly Efficient Heterogeneous Catalyst for Fixed-Bed Reactions. *J. Am. Chem. Soc.* **2015**, *137*, 4243-4248. c) Wang, B.; Lv, X. L.; Feng, D. W.; Xie, L. H.; Zhang, J.; Li, M.; Xie, Y. B.; Li, J. R.; Zhou, H. C. Highly Stable Zr(IV)-Based Metal-Organic Frameworks for the Detection and Removal of Antibiotics and Organic Explosives in Water. *J. Am. Chem. Soc.* **2016**, *138*, 6204-6216.c) Bai, Y.; Dou, Y. B.; Xie, L. H.; Rutledge, W.; Li, J. R.; Zhou, H. C. Zr-Based Metal-Organic Frameworks: Design, Synthesis, Structure, and Applications. *Chem. Soc. Rev.* **2016**, *45*, 2327-2367.

[8] (a) Sun, L.; Campbell, M. G.; Dincă, M. Electrically Conductive Porous Metal-Organic Frameworks. *Angew. Chemie Int. Ed.* **2016**, *55* (11), 3566–3579. (b) Xie, L. S.; Skorupskii, G.; Dincă, M. Electrically Conductive Metal–Organic Frameworks. *Chem. Rev.* **2020**, *120* (16), 8536–8580.

[9] (a) Sun, Y.; Sheng, P.; Di, C.; Jiao, F.; Xu, W.; Qiu, D.; Zhu, D. Organic Thermoelectric Materials and Devices Based on p- snd n-Type poly(Metal-1,1,2,2-ethenetetrathiolate)s. *Adv. Mater.* **2012**, *24* (7), 932–937. (b) Givaja, G.; Amo-Ochoa, P.; Gómez-García, C. J.; Zamora, F. Electrical Conductive Coordination Polymers. *Chem. Soc. Rev.* **2012**, *41* (1), 115–147. (c) Sun, L.; Miyakai, T.; Seki, S.; Dincă, M. Mn_2(2,5-disulfhydrylbenzene-1,4-dicarboxylate): A Microporous Metal–

Organic Framework with Infinite (−Mn–S−)$_\infty$ Chains and High Intrinsic Charge Mobility. *J. Am. Chem. Soc.* **2013**, *135* (22), 8185–8188. (d) Sun, L.; Hendon, C. H.; Minier, M. A.; Walsh, A.; Dincă, M. Million-Fold Electrical Conductivity Enhancement in Fe_2(DEBDC) Versus Mn_2(DEBDC) (E = S, O). *J. Am. Chem. Soc.* **2015**, *137* (19), 6164–6167. (e) Sun, Y.; Qiu, L.; Tang, L.; Geng, H.; Wang, H.; Zhang, F.; Huang, D.; Xu, W.; Yue, P.; Guan, Y. S.; Et Al. Flexible n-Type High-Performance Thermoelectric Thin Films of poly(Nickel-ethylenetetrathiolate) Prepared by An Electrochemical Method. *Adv. Mater.* **2016**, *28* (17), 3351–3358. (f) Electrically Conductive Porous Metal-Organic Frameworks. *Angew. Chemie Int. Ed.* **2016**, *55* (11), 3566–3579.

[10] T. Kusamoto and H. Nishihara, Zero-, One- and Two-Dimensional Bis(Dithiolato)Metal Complexes with Unique Physical and Chemical Properties, *Coord. Chem. Rev.*, 2019, **380**, 419–439.

[11] R. Llusar and C. Vicent, Trinuclear Molybdenum Cluster Sulfides Coordinated to Dithiolene Ligands and Their Use in the Development of Molecular Conductors, *Coord. Chem. Rev.,* 2010, **254**, 1534–1548.

[12] B. F. Hoskins and R. Robson, Design and Construction of a New Class of Scaffolding-like Materials Comprising Infinite Polymeric Frameworks of 3D-Linked Molecular Rods. A Reappraisal of the Zinc Cyanide and Cadmium Cyanide Structures and the Synthesis and Structure of the Diamond-Rela, *J. Am. Chem. Soc.*, 1990, **112**, 1546–1554.

[13] (a) H. Li, M. Eddaoudi, M. O'Keeffe and O. M. Yaghi, Design and Synthesis of an Exceptionally Stable and Highly Porous Metal-Organic Framework, *Nature*, 1999, **402**, 276–279. (b) J. H. Cavka, S. Jakobsen, U. Olsbye, N. Guillou, C. Lamberti, S. Bordiga and K. P. Lillerud, A New Zirconium Inorganic Building Brick Forming Metal Organic Frameworks with Exceptional Stability, *J. Am. Chem. Soc.*, 2008, **130**, 13850–13851.

[14] J. Xie, L. Wang, and J.S. Anderson, Heavy Chalcogenide-Transition Metal Clusters as Coordination Polymer Nodes. *Chem. Sci.*, 2020, **11**, 8350-8372.

[15] (a) H. D. Selby, B. K. Roland and Z. Zheng, Ligand-Bridged Oligomeric and Supramolecular Arrays of the Hexanuclear Rhenium Selenide Clusters−Exploratory Synthesis, Structural Characterization, and Property Investigation, *Acc. Chem. Res.*, 2003, **36**, 933–944. (b) S. C. Lee, W. Lo and R. H. Holm, Developments in the Biomimetic Chemistry of Cubane-Type and Higher Nuclearity Iron–Sulfur Clusters, *Chem. Rev.*, 2014, **114**, 3579–3600. (d) W. H. Zhang, Z. G. Ren and J. P. Lang, Rational Construction of Functional Molybdenum (Tungsten)-Copper-Sulfur Coordination Oligomers and Polymers from Preformed Cluster Precursors, *Chem. Soc. Rev.*, 2016, **45**, 4995–5019.

[16] N. E. Horwitz, J. Xie, A. S. Filatov, R. J. Papoular, W. E. Shepard, D. Z. Zee, M. P. Grahn, C. Gilder and J. S. Anderson, Redox-Active 1D Coordination Polymers of Iron–Sulfur Clusters, *J. Am. Chem. Soc.*, 2019, **141**, 3940–3951.

[17] Huang, X.; Zhang, S.; Liu, L.; Yu, L.; Chen, G.; Xu, W.; Zhu, D. Superconductivity in a Copper(II)-Based Coordination Polymer with Perfect Kagome Structure. *Angew. Chemie Int. Ed.* **2018**, *57* (1), 146–150.

[18] (a)Wang, L.; Han, Y.; Feng, X.; Zhou, J.; Qi, P.; Wang, B. Metal–Organic Frameworks for Energy Storage: Batteries and Supercapacitors. *Coord. Chem. Rev.* **2016**, *307*, 361–381. (b)Sheberla, D.; Bachman, J. C.; Elias, J. S.; Sun, C.-J.; Shao-Horn, Y.; Dincă, M. Conductive

MOF Electrodes for Stable Supercapacitors with High Areal Capacitance. *Nat. Mater.* **2017**, *16* (2), 220–224. (c)Wada, K.; Sakaushi, K.; Sasaki, S.; Nishihara, H. Multielectron-Transfer-Based Rechargeable Energy Storage of Two-Dimensional Coordination Frameworks with Non-Innocent Ligands. *Angew. Chemie Int. Ed.* **2018**, *57* (29), 8886–8890. (d)Feng, D.; Lei, T.; Lukatskaya, M. R.; Park, J.; Huang, Z.; Lee, M.; Shaw, L.; Chen, S.; Yakovenko, A. A.; Kulkarni, A.; et al. Robust and Conductive Two-Dimensional Metal−organic Frameworks with Exceptionally High Volumetric and Areal Capacitance. *Nat. Energy* **2018**, *3* (1), 30–36. (e)Park, J.; Lee, M.; Feng, D.; Huang, Z.; Hinckley, A. C.; Yakovenko, A.; Zou, X.; Cui, Y.; Bao, Z. Stabilization of Hexaaminobenzene in a 2D Conductive Metal–Organic Framework for High Power Sodium Storage. *J. Am. Chem. Soc.* **2018**, *140* (32), 10315–10323.

[19] (a)Sun, Y.; Sheng, P.; Di, C.; Jiao, F.; Xu, W.; Qiu, D.; Zhu, D. Organic Thermoelectric Materials and Devices Based on P- and n-Type Poly(Metal 1,1,2,2-Ethenetetrathiolate)S. *Adv. Mater.* **2012**, *24* (7), 932–937. (b)Jiao, F.; Di, C.; Sun, Y.; Sheng, P.; Xu, W.; Zhu, D. Inkjet-Printed Flexible Organic Thin-Film Thermoelectric Devices Based on p- and n-Type Poly(Metal 1,1,2,2-Ethenetetrathiolate)s/Polymer Composites through Ball-Milling. *Philos. Trans. R. Soc. A Math. Phys. Eng. Sci.* **2014**, *372* (2013), 20130008. (c)Sun, Y.; Qiu, L.; Tang, L.; Geng, H.; Wang, H.; Zhang, F.; Huang, D.; Xu, W.; Yue, P.; Guan, Y.; et al. Flexible N-Type High-Performance Thermoelectric Thin Films of Poly(Nickel-Ethylenetetrathiolate) Prepared by an Electrochemical Method. *Adv. Mater.* **2016**, *28* (17), 3351–3358. (d)Sun, L.; Liao, B.; Sheberla, D.; Kraemer, D.; Zhou, J.; Stach, E. A.; Zakharov, D.; Stavila, V.; Talin, A. A.; Ge, Y.; et al. A Microporous and Naturally Nanostructured Thermoelectric Metal-Organic Framework with Ultralow Thermal Conductivity. *Joule* **2017**, *1* (1), 168–177.

[20] (a)Wang, Z. F.; Su, N.; Liu, F. Prediction of a Two-Dimensional Organic Topological Insulator. *Nano Lett.* **2013**, *13* (6), 2842–2845. (b)Kambe, T.; Sakamoto, R.; Kusamoto, T.; Pal, T.; Fukui, N.; Hoshiko, K.; Shimojima, T.; Wang, Z.; Hirahara, T.; Ishizaka, K.; et al. Redox Control and High Conductivity of Nickel Bis(Dithiolene) Complex π-Nanosheet: A Potential Organic Two-Dimensional Topological Insulator. *J. Am. Chem. Soc.* **2014**, *136* (41), 14357–14360. (c)Chakravarty, C.; Mandal, B.; Sarkar, P. Bis(Dithioline)-Based Metal–Organic Frameworks with Superior Electronic and Magnetic Properties: Spin Frustration to Spintronics and Gas Sensing. *J. Phys. Chem. C* **2016**, *120* (49), 28307–28319. (d)Liu, L.; DeGayner, J. A.; Sun, L.; Zee, D. Z.; Harris, T. D. Reversible Redox Switching of Magnetic Order and Electrical Conductivity in a 2D Manganese Benzoquinoid Framework. *Chem. Sci.* **2019**, *10* (17), 4652–4661. (e)Yang, L.; He, X.; Dincă, M. Triphenylene-Bridged Trinuclear Complexes of Cu: Models for Spin Interactions in Two-Dimensional Electrically Conductive Metal–Organic Frameworks. *J. Am. Chem. Soc.* **2019**, *141* (26), 10475–10480.

[21] (a)Clough, A. J.; Yoo, J. W.; Mecklenburg, M. H.; Marinescu, S. C. Two-Dimensional Metal–Organic Surfaces for Efficient Hydrogen Evolution from Water. *J. Am. Chem. Soc.* **2015**, *137* (1), 118–121. (b)Dong, R.; Pfeffermann, M.; Liang, H.; Zheng, Z.; Zhu, X.; Zhang, J.; Feng, X. Large-Area, Free-Standing, Two-Dimensional Supramolecular Polymer Single-Layer Sheets for Highly Efficient Electrocatalytic Hydrogen Evolution. *Angew. Chemie Int. Ed.* **2015**, *54* (41), 12058–12063. (c)Miner, E. M.; Fukushima, T.; Sheberla, D.; Sun, L.; Surendranath, Y.; Dincă, M. Electrochemical Oxygen Reduction Catalysed by Ni_3(Hexaiminotriphenylene)$_2$. *Nat. Commun.* **2016**, *7* (1), 10942. (d)Huang, X.; Yao, H.; Cui, Y.; Hao, W.; Zhu, J.; Xu, W.; Zhu, D. Conductive Copper Benzenehexathiol Coordination Polymer as a Hydrogen Evolution Catalyst. *ACS Appl. Mater. Interfaces* **2017**, *9* (46), 40752–40759. (e)Miner, E. M.; Wang, L.; Dincă, M. Modular O2 Electroreduction Activity in Triphenylene-Based Metal–Organic Frameworks. *Chem. Sci.* **2018**, *9*

(29), 6286–6291. (f) Ji, Z.; Trickett, C.; Pei, X.; Yaghi, O. M. Linking Molybdenum–Sulfur Clusters for Electrocatalytic Hydrogen Evolution. *J. Am. Chem. Soc.* **2018**, *140* (42), 13618–13622.

[22] (a)Tang, Q.; Zhou, Z. Electronic Properties of π-Conjugated Nickel Bis(Dithiolene) Network and Its Addition Reactivity with Ethylene. *J. Phys. Chem. C* **2013**, *117* (27), 14125–14129. (b)Campbell, M. G.; Sheberla, D.; Liu, S. F.; Swager, T. M.; Dincă, M. Cu 3 (Hexaiminotriphenylene) 2 : An Electrically Conductive 2D Metal-Organic Framework for Chemiresistive Sensing. *Angew. Chemie Int. Ed.* **2015**, *54* (14), 4349–4352. (c)Hendon, C. H.; Rieth, A. J.; Korzynski, M. D.; Dinca, M. Grand Challenges and Future Opportunities for Metal-Organic Frameworks. *ACS Cent Sci*. **2017**, pp 554–563. (d)Liu, L.; Li, L.; DeGayner, J. A.; Winegar, P. H.; Fang, Y.; Harris, T. D. Harnessing Structural Dynamics in a 2D Manganese–Benzoquinoid Framework To Dramatically Accelerate Metal Transport in Diffusion-Limited Metal Exchange Reactions. *J. Am. Chem. Soc.* **2018**, *140* (36), 11444–11453. (e)Hoppe, B.; Hindricks, K. D. J.; Warwas, D. P.; Schulze, H. A.; Mohmeyer, A.; Pinkvos, T. J.; Zailskas, S.; Krey, M. R.; Belke, C.; König, S.; et al. Graphene-like Metal–Organic Frameworks: Morphology Control, Optimization of Thin Film Electrical Conductivity and Fast Sensing Applications. *CrystEngComm* **2018**, *20* (41), 6458–6471.

[23] (a)Darago, L. E.; Aubrey, M. L.; Yu, C. J.; Gonzalez, M. I.; Long, J. R. Electronic Conductivity, Ferrimagnetic Ordering, and Reductive Insertion Mediated by Organic Mixed-Valence in a Ferric Semiquinoid Metal–Organic Framework. *J. Am. Chem. Soc.* **2015**, 137 (50), 15703–15711. (b)Jeon, I.-R.; Negru, B.; Van Duyne, R. P.; Harris, T. D. A 2D Semiquinone Radical-Containing Microporous Magnet with Solvent-Induced Switching from T_c = 26 to 80 K. *J. Am. Chem. Soc.* **2015**, *137* (50), 15699–15702. (c)Jeon, I.-R.; Sun, L.; Negru, B.; Van Duyne, R. P.; Dincă, M.; Harris, T. D. Solid-State Redox Switching of Magnetic Exchange and Electronic Conductivity in a Benzoquinoid-Bridged MnII Chain Compound. *J. Am. Chem. Soc.* **2016**, *138* (20), 6583–6590. (d)DeGayner, J. A.; Jeon, I.-R.; Sun, L.; Dincă, M.; Harris, T. D. 2D Conductive Iron-Quinoid Magnets Ordering up to T_c = 105 K via Heterogenous Redox Chemistry. *J. Am. Chem. Soc.* **2017**, *139* (11), 4175–4184. (e)Ziebel, M. E.; Darago, L. E.; Long, J. R. Control of Electronic Structure and Conductivity in Two-Dimensional Metal-Semiquinoid Frameworks of Titanium, Vanadium, and Chromium. *J. Am. Chem. Soc.* **2018**, *140* (8), 3040–3051. (f)DeGayner, J. A.; Wang, K.; Harris, T. D. A Ferric Semiquinoid Single-Chain Magnet via Thermally-Switchable Metal–Ligand Electron Transfer. *J. Am. Chem. Soc.* **2018**, *140* (21), 6550–6553.

[24] (a)Sheberla, D.; Sun, L.; Blood-Forsythe, M. a; Er, S.; Wade, C. R.; Brozek, C. K.; Aspuru-Guzik, A.; Dincă, M. High Electrical Conductivity in Ni_3(2,3,6,7,10,11-Hexaiminotriphenylene)$_2$, a Semiconducting Metal–Organic Graphene Analogue. *J. Am. Chem. Soc.* **2014**, *136* (25), 8859–8862. (b)Dou, J. H.; Sun, L.; Ge, Y.; Li, W.; Hendon, C. H.; Li, J.; Gul, S.; Yano, J.; Stach, E. A.; Dincă, M. Signature of Metallic Behavior in the Metal-Organic Frameworks M_3(Hexaiminobenzene)$_2$ (M = Ni, Cu). *J. Am. Chem. Soc.* **2017**, *139* (39), 13608–13611.

[25] (a)Kambe, T.; Sakamoto, R.; Hoshiko, K.; Takada, K.; Miyachi, M.; Ryu, J. H.; Sasaki, S.; Kim, J.; Nakazato, K.; Takata, M.; et al. π-Conjugated Nickel Bis(Dithiolene) Complex Nanosheet. *J. Am. Chem. Soc.* **2013**, *135* (7), 2462–2465. (b)Huang, X.; Sheng, P.; Tu, Z.; Zhang, F.; Wang, J.; Geng, H.; Zou, Y.; Di, C.; Yi, Y.; Sun, Y.; et al. A Two-Dimensional π–d Conjugated Coordination Polymer with Extremely High Electrical Conductivity and Ambipolar Transport Behaviour. *Nat. Commun.* **2015**, *6* (1), 7408. (c)Maeda, H.; Sakamoto, R.; Nishihara, H. Coordination Programming of Two-Dimensional Metal Complex Frameworks. *Langmuir* **2016**, *32* (11), 2527–2538. (d)Huang, X.; Li, H.; Tu, Z.; Liu, L.; Wu, X.; Chen, J.; Liang, Y.; Zou, Y.; Yi, Y.; Sun, J.;

et al. Highly Conducting Neutral Coordination Polymer with Infinite Two-Dimensional Silver–Sulfur Networks. *J. Am. Chem. Soc.* **2018**, *140* (45), 15153–15156. (e)Dong, R.; Han, P.; Arora, H.; Ballabio, M.; Karakus, M.; Zhang, Z.; Shekhar, C.; Adler, P.; Petkov, P. S.; Erbe, A.; et al. High-Mobility Band-like Charge Transport in a Semiconducting Two-Dimensional Metal–Organic Framework. *Nat. Mater.* **2018**, *17* (11), 1027–1032. (f)Cui, Y.; Yan, J.; Chen, Z.; Zhang, J.; Zou, Y.; Sun, Y.; Xu, W.; Zhu, D. $[Cu_3(C_6Se_6)]_n$: The First Highly Conductive 2D π–d Conjugated Coordination Polymer Based on Benzenehexaselenolate. *Adv. Sci.* **2019**, *6* (9), 1802235.

[26] (a)Sun, L.; Miyakai, T.; Seki, S.; Dincă, M. Mn 2 (2,5-Disulfhydrylbenzene-1,4-Dicarboxylate): A Microporous Metal–Organic Framework with Infinite $(-Mn-S-)_\infty$ Chains and High Intrinsic Charge Mobility. *J. Am. Chem. Soc.* **2013**, *135* (22), 8185–8188. (b)Sun, L.; Campbell, M. G.; Dincă, M. Electrically Conductive Porous Metal-Organic Frameworks. *Angew. Chemie Int. Ed.* **2016**, *55* (11), 3566–3579. (c)Horwitz, N. E.; Xie, J.; Filatov, A. S.; Papoular, R. J.; Shepard, W. E.; Zee, D. Z.; Grahn, M. P.; Gilder, C.; Anderson, J. S. Redox-Active 1D Coordination Polymers of Iron–Sulfur Clusters. *J. Am. Chem. Soc.* **2019**, *141* (9), 3940–3951.

[27](a)Segura, J. L.; Martn, N. New Concepts in Tetrathiafulvalene Chemistry. *Angew. Chemie Int. Ed.* **2001**, 40(8),1372–1409. (b)Wang, H.; Cui, L.; Xie, J.; Leong, C. F.; D'Alessandro, D. M.; Zuo, J. Functional Coordination Polymers Based on Redox-Active Tetrathiafulvalene and Its Derivatives. *Coord. Chem. Rev.* **2017**, *345*, 342–361.

[28] Bryce, M. R. Recent Progress on Conducting Organic Charge-Transfer Salts. *Chem. Soc. Rev.* **1991**, *20* (3), 355.

[29] (a)Narayan, T. C.; Miyakai, T.; Seki, S.; Dincă, M. High Charge Mobility in a Tetrathiafulvalene-Based Microporous Metal–Organic Framework. *J. Am. Chem. Soc.* **2012**, *134* (31), 12932–12935. (b)Sun, L.; Park, S. S.; Sheberla, D.; Dincă, M. Measuring and Reporting Electrical Conductivity in Metal-Organic Frameworks: Cd_2(TTFTB) as a Case Study. *J. Am. Chem. Soc.* **2016**, *138* (44), 14772–14782. (c)Xie, L. S.; Dincă, M. Novel Topology in Semiconducting Tetrathiafulvalene Lanthanide Metal-Organic Frameworks. *Isr. J. Chem.* **2018**, *58* (9–10), 1119–1122. (d) Xie, L. S.; Alexandrov, E. V.; Skorupskii, G.; Proserpio, D. M.; Dincă, M. Diverse π – π Stacking Motifs Modulate Electrical Conductivity in Tetrathiafulvalene-Based Metal–Organic Frameworks. *Chem. Sci.* **2019**, 10, 8558-8565.

[30] (a)Su, J.; Yuan, S.; Wang, H.-Y.; Huang, L.; Ge, J.-Y.; Joseph, E.; Qin, J.; Cagin, T.; Zuo, J.-L.; Zhou, H.-C. Redox-Switchable Breathing Behavior in Tetrathiafulvalene-Based Metal–Organic Frameworks. *Nat. Commun.* **2017**, *8* (1), 2008. (b)Souto, M.; Romero, J.; Calbo, J.; Vitórica-Yrezábal, I. J.; Zafra, J. L.; Casado, J.; Ortí, E.; Walsh, A.; Mínguez Espallargas, G. Breathing-Dependent Redox Activity in a Tetrathiafulvalene-Based Metal–Organic Framework. *J. Am. Chem. Soc.* **2018**, *140* (33), 10562–10569.

[31] (a)Wang, H.-Y.; Ge, J.-Y.; Hua, C.; Jiao, C.-Q.; Wu, Y.; Leong, C. F.; D'Alessandro, D. M.; Liu, T.; Zuo, J.-L. Photo- and Electronically Switchable Spin-Crossover Iron(II) Metal-Organic Frameworks Based on a Tetrathiafulvalene Ligand. *Angew. Chemie Int. Ed.* **2017**, *56* (20), 5465–5470. (b)Su, J.; Hu, T.-H.; Murase, R.; Wang, H.-Y.; D'Alessandro, D. M.; Kurmoo, M.; Zuo, J.-L. Redox Activities of Metal–Organic Frameworks Incorporating Rare-Earth Metal Chains and Tetrathiafulvalene Linkers. *Inorg. Chem.* **2019**, *58* (6), 3698–3706.

[32] (a)Rivera, N. M.; Engler, E. M.; Schumaker, R. R. Synthesis and Properties of Tetrathiafulvalene–Metal Bisdithiolene Macromolecules. *J. Chem. Soc., Chem. Commun.* **1979**, 4,

184–185. (b)Yoshioka, N.; Nishide, H.; Inagaki, K.; Inagaki, K.; Tsuchida, E. Electrical Conductive and Magnetic Properties of Conjugated Tetrathiolate Nickel Polymers. *Polym. Bull.* **1990**, *23* (6), 631–636. (c)Dahm, S.; Strunz, W.; Keller, H. J.; Schweitzer, D. Preparation and Physical Properties of Highly Conducting Metal (M = Ni, Co, Cu) Coordination Polymers. *Synth. Met.* **1993**, *55* (2–3), 884–889.

[33] (a)McCullough, R. D.; Belot, J. A. Toward New Magnetic, Electronic, and Optical Materials: Synthesis and Characterization of New Bimetallic Tetrathiafulvalene Tetrathiolate Building Blocks. *Chem. Mater.* **1994**, *6* (8), 1396–1403. (b)McCullough, R. D.; Belot, J. A. Toward New Magnetic, Electronic, and Optical Materials: Synthesis and Characterization of New Bimetallic Tetrathiafulvalene Tetrathiolate Building Blocks. *Chem. Mater.* **1994**, *6* (8), 1396–1403. (c)McCullough, R. D.; Belot, J. A.; Seth, J.; Rheingold, A. L.; Yap, G. P. A.; Cowan, D. O. Building Block Ligands for New Molecular Conductors: Homobimetallic Tetrathiafulvalene Tetrathiolates and Metal Diselenolenes and Ditellurolenes. *J. Mater. Chem.* **1995**, *5* (10), 1581.

[34] Bellec, N.; Vacher, A.; Barrière, F.; Xu, Z.; Roisnel, T.; Lorcy, D. Interplay between Organic–Organometallic Electrophores within Bis(Cyclopentadienyl)Molybdenum Dithiolene Tetrathiafulvalene Complexes. *Inorg. Chem.* **2015**, *54* (10), 5013–5020.

[35] Svenstrup, N.; Rasmussen, K. M.; Hansen, T. K.; Becher, J. The Chemistry of TTFTT; 1: New Efficient Synthesis and Reactions of Tetrathiafulvalene-2,3,6,7-Tetrathiolate (TTFTT): An Important Building Block in TTF-Syntheses. *Synthesis.* **1994**, 809–812.

[36] (a)Cerrada, E.; Fernandez, E. J.; Jones, P. G.; Laguna, A.; Laguna, M.; Terroba, R. Synthesis and Reactivity of Trinuclear Gold(III) Dithiolate Complexes. X-Ray Structure of $[Au(C_6F_5)(S_2C_6H_4)]_3$ and $[Au(C_6F_5)(S_2C_6H_4)(SC_6H_4SPPh_3)]$. *Organometallics* **1995**, *14* (12), 5537–5543. (b)Doidge-Harrison, S. M. S. V.; Irvine, J. T. S.; Khan, A.; Spencer, G. M.; Wardell, J. L.; Aupers, J. H. Diorganotin 1,3-Dithiole-2-Thione-4,5-Dithiolate Compounds, $R_2Sn(dmit)$: The Crystal Structure of MePhSn(dmit). *J. Organomet. Chem.* **1996**, *516* (1–2), 199–205. (c)Aupers, J. H.; Chohan, Z. H.; Cox, P. J.; Doidge-Harrison, S. M. S. V.; Howie, A.; Khan, A.; Spencer, G. M.; Wardell, J. L. Syntheses and Structures of Diorgano(Halo- Orpseudohalo-)(1,3-Dithiole-2-Thione-4,5-Dithiolato)-Stannates (1-), $[Q][R_2SnX(dmit)]$ (Q=onium Cation; X=halide Orpseudohalide). *Polyhedron* **1998**, *17* (25–26), 4475–4486. (d)Cerrada, E.; Elipe, S.; Laguna, M.; Lahoz, F.; Moreno, A. Dithiolate and Diselenolate Tin Complexes as Ligands Transfer Reagent towards Other Metals. *Synth. Met.* **1999**, *102* (1–3), 1759–1760. (e)Adams, C. J.; Fey, N.; Parfitt, M.; Pope, S. J. A.; Weinstein, J. A. Synthesis, Structures and Properties of a New Series of Platinum–Diimine–Dithiolate Complexes. *Dalt. Trans.* **2007**, 39, 4446. (f)Shin, K. S.; Jung, Y. J.; Lee, S. K.; Fourmigué, M.; Barrière, F.; Bergamini, J. F.; Noh, D. Y. Redox Bifunctionality in a Pt(Ii) Dithiolene Complex of a Tetrathiafulvalene Diphosphine Ligand. *J. Chem. Soc. Dalt. Trans.* **2008**, *96* (43), 5869–5871. (g)Llusar, R.; Triguero, S.; Polo, V.; Vicent, C.; Gómez-García, C. J.; Jeannin, O.; Fourmigué, M. Trinuclear Mo_3S_7 Clusters Coordinated to Dithiolate or Diselenolate Ligands and Their Use in the Preparation of Magnetic Single Component Molecular Conductors. *Inorg. Chem.* **2008**, *47* (20), 9400–9409. (h)Cerrada, E.; Moreno, A.; Laguna, M. S,C- and S,S-Coupling via Dithiolate Transfer Reactions from Tin to Nickel Complexes. *Dalt. Trans.* **2009**, No. 34, 6825. (i)Ogawa, T.; Sakamoto, M.; Honda, H.; Matsumoto, T.; Kobayashi, A.; Kato, M.; Chang, H. Self-Association and Columnar Liquid Crystalline Phase of Cationic Alkyl-Substituted-Bipyridine Benzenedithiolato Gold(III) Complexes. *Dalt. Trans.* **2013**, *42* (45), 15995.

[37] (a)Nomura, M.; Fourmigué, M. Dinuclear Cp* Cobalt Complexes of the 1,2,4,5-Benzenetetrathiolate Bischelating Ligand. *Inorg. Chem.* **2008**, *47* (4), 1301–1312. (b)Arumugam,

K.; Shaw, M. C.; Chandrasekaran, P.; Villagrán, D.; Gray, T. G.; Mague, J. T.; Donahue, J. P. Synthesis, Structures, and Properties of 1,2,4,5-Benzenetetrathiolate Linked Group 10 Metal Complexes. *Inorg. Chem.* **2009**, *48* (22), 10591–10607.

[38] Z. Ji, C. Trickett, X. Pei and O. M. Yaghi, Linking Molybdenum–Sulfur Clusters for Electrocatalytic Hydrogen Evolution, *J. Am. Chem. Soc.*, 2018, **140**, 13618–13622.

Chapter 2: Redox-Active 1D Coordination Polymers of Iron-Sulfur Clusters

2.1 Introduction

There has been a surge of interest in coordination polymers exhibiting intrinsic magnetic and conductive properties as these materials show potential for applications in energy storage and electronics.[1] It is crucial to carefully match the properties, particularly the electronic properties, of the metal and linker in these materials to optimize their performance. Detailed studies have shown that moving from O-based linkers to less electronegative and consequently more donating N-based linkers improves coupling and delocalization.[1] By the same rationale, further work has shown that using heavier chalcogenide-based linkers (S-based in particular) in place of more common O- or N-based ligands can enhance electronic coupling leading to improvement in conductivity.[2]

These studies have generated several examples of materials which highlight that the combination of organosulfur ligands with transition metal ions leads to coordination polymers with desirable properties such as high electrical conductivity.[3, 4] The majority of these materials, however, are based on monometallic nodes. Comparatively, the use of metal-chalcogenide clusters as building blocks has been underexplored. The use of metal-chalcogenide clusters to rationally impart desired properties to materials is well demonstrated by recent work in which hydrogen evolution catalysts can be prepared from Mo-S clusters linked by organosulfur ligands.[5] Among possible metal chalcogenide clusters, the cubane-type Fe_4S_4 cluster stands out as an attractive building block due to its redox-activity, stability, electronic delocalization, and complex magnetic features – properties also exploited by nature in ubiquitous iron-sulfur proteins.[6] Of particular relevance are proteins containing chains of Fe_4S_4 clusters that facilitate electron transport over long distances.[7]

Several synthetic examples further demonstrate the utility of Fe_4S_4 clusters towards building materials with unusual physical and chemical properties. For instance, Kanatzidis and coworkers have prepared a crystalline framework[8] and a family of amorphous chalcogels with Fe_4S_4 units connected by inorganic chalcogenide linkers. The Fe_4S_4 clusters retain their redox-activity in the chalcogels, enabling redox catalysis by these materials.[9] Additionally, Pickett and coworkers have studied the synthesis and conductivity of a series of materials in which Fe_4S_4 clusters are bound to substituted polypyrroles through electrostatic interactions or pendant thiolates.[10] These examples illustrate the potential of materials synthesized with Fe_4S_4 clusters.

In this Chapter, we report the preparation of coordination polymers containing 1D chains of Fe_4S_4 clusters linked by an organochalcogenide ligand, 1,4-benzenedithiolate (BDT, **Scheme 2.1**). This represents a highly unusual example where Fe_4S_4 clusters can be combined with organic linkers to form crystalline coordination polymers. The choice of counterion and solvent controls the packing and solubility of the anionic chains, allowing isolation and characterization of two distinct crystalline solids. The redox-activity of the Fe_4S_4 clusters is maintained in the polymer, manifesting as redox-dependent electrical conductivity in the solid materials. These results show the promise of using redox-active metal-chalcogenide clusters as building blocks for coordination polymers with tunable physical properties.

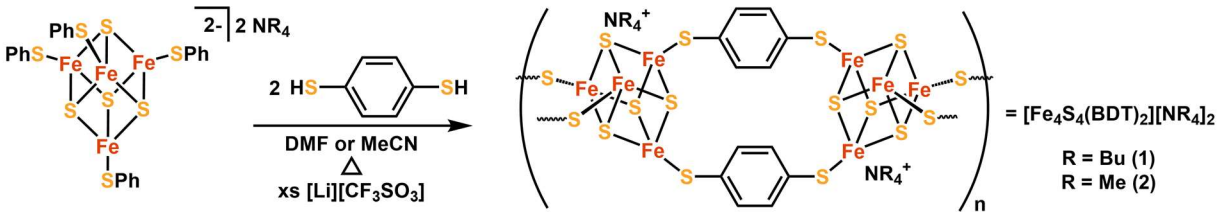

Scheme 2.1. Synthesis of $[Fe_4S_4(BDT)_2][NR_4]_2$ coordination polymers.

2.2 Results and Discussion

2.2.1 Synthesis and Composition

Heating $[Fe_4S_4(SPh)_4][TBA]_2$ (TBA = tetra-n-butylammonium) with 2 equivalents of 1,4-benzenedithiol ($BDTH_2$) in N,N-dimethylformamide (DMF) leads to the precipitation of $[(Fe_4S_4)(BDT)_2][TBA]_2$ (**1**) as a dark purple to black solid. Similarly, $[(Fe_4S_4)(BDT)_2][TMA]_2$ (**2**) is obtained by heating in MeCN when TBA is replaced by tetramethylammonium (TMA) as the counterion. X-ray powder diffraction (XRPD) analysis demonstrates that both of these materials are crystalline. Furthermore, we have observed that the crystallinity of both **1** and **2** can be increased by addition of excess $[Li][CF_3SO_3]$ to the reaction mixture. We speculate that this effect may be attributed to ionic screening as discussed below.

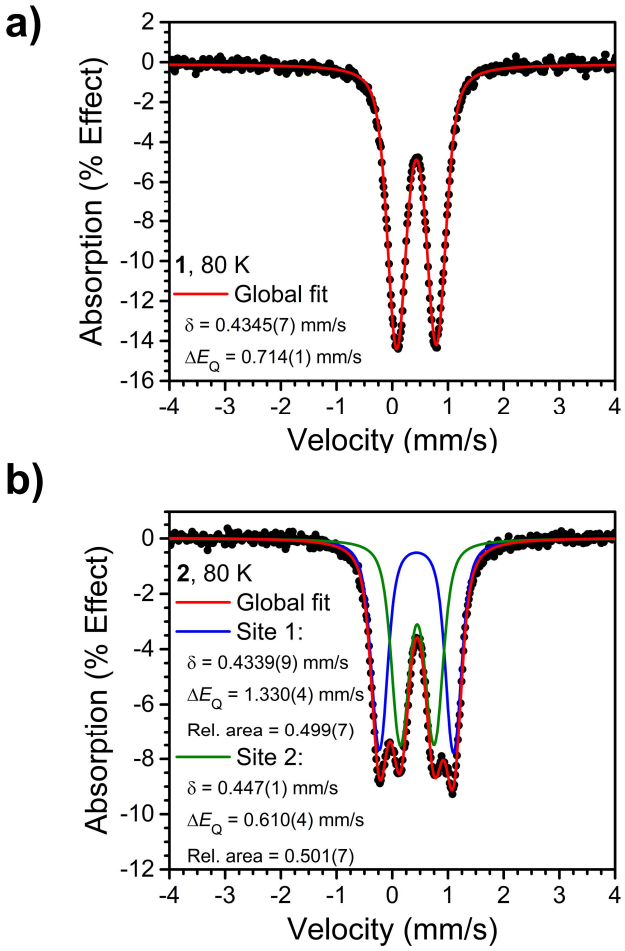

Figure 2.1. ^{57}Fe Mössbauer spectrum of (a) 1 and (b) 2 recorded at 80 K.

We have performed several experiments to validate the proposed compositions of **1** and **2**. Digestion of **1** and **2** in 12 M hydrochloric acid followed by extraction with C_6D_6 or CD_2Cl_2 and ^{1}H NMR analysis supports the presence of BDT in the structures (**Figure A.4** and **Figure A**.6). No thiophenol from the $[Fe_4S_4(SPh)_4]^{2-}$ starting material is observed, which is also consistent with complete ligand substitution in the precipitated material. The infrared spectra of **1** and **2** do not show any features attributable to S-H stretching modes near 2500 cm^{-1}, further demonstrating that BDT is fully deprotonated in **1** and **2** (**Figure A.39** and **Figure A**.40). Additionally, digestion in D_2SO_4 followed by dilution with $(CD_3)_2SO$ and ^{1}H NMR analysis confirms the presence of TBA in **1** and TMA in **2** (**Error! Reference source not found.** and **Error! Reference source not found.**). The presence of intact Fe_4S_4 clusters is more difficult to confirm with the same method, as these clusters are not stable to acid digestion. Mössbauer spectroscopy, however, provides strong evidence for the presence of intact Fe_4S_4 clusters in **1** and **2**. The 80 K ^{57}Fe Mössbauer spectrum (**Figure 2.1**a) of **1** consists of a quadrupole doublet with isomer shift (δ) of 0.4345(7) mm/s and quadrupole splitting (ΔE_Q) of 0.714(1) mm/s. These values are similar to those reported for other $[Fe_4S_4]^{2+}$ cluster materials and to $[Fe_4S_4(SPh)_4]^{2-}$,[6, 8, 9b] suggesting that the cluster is present in **1** in the same oxidation state as the $[Fe_4S_4(SPh)_4][TBA]_2$ precursor. The spectrum (**Figure 2.1**b) of **2** can be fitted by two quadrupole doublets with δ of 0.4339(9) and 0.447(1) mm/s and ΔE_Q of 1.330(4) and 0.610(4) mm/s, suggesting that two distinct $[Fe_4S_4]$ sites are present in the structure of **2**. All spectra are fit with Voigt line profiles, potentially reflecting a distribution of Mössbauer parameters due to structural disorder.[11] Spectra of **1** and **2** at 25 K and 4.2 K are similar to those at 80 K, showing increases in quadrupole splittings upon cooling (**Figure A.34** and **Figure A**.35).

Additional experiments were performed to verify the empirical formulas of **1** and **2**. X-ray photoelectron spectroscopy (XPS) gives an Fe:S atomic ratio of 1:1.96 and 1:1.95, as expected for **1** and **2** respectively. In addition, inductively-coupled plasma mass spectrometry (ICP-MS) measurements on nitric acid digests of **1** and **2** indicate that little Li^+ (1.4% and 7% relative to TBA or TMA respectively) is incorporated into the materials (see below, **Table 2.1**). Finally, the results from combustion analysis are also consistent for these materials. All of this data supports the assigned formulas of $[(Fe_4S_4)(BDT)_2][TBA]_2$ and $[(Fe_4S_4)(BDT)_2][TMA]_2$ for **1** and **2** respectively.

2.2.2 Structural Determination

The crystal structures of **1** and **2** were solved ab initio using simulated annealing and then further refined with the Rietveld method from synchrotron XRPD data with input from the experimentally determined formulas (**Figure 2.2** and **Figure** 2.3). The structure of **1** consists of chains of Fe_4S_4 clusters connected by pairs of BDT groups surrounded by TBA cations. Each Fe_4S_4 cluster is equidistant from four TBA cations 5.97 Å from the Fe_4S_4 centroid. The axis-to-axis separation between adjacent chains is 11.93 Å, and the separation between Fe_4S_4 clusters within the chain is 9.92 Å (centroid to centroid). The rings of the BDT linkers in each pair and the Fe atoms to which they are coordinated are coplanar. In the structure of **2**, similar Fe_4S_4-BDT chains are present. In the absence of the bulky TBA cations, the separation between chains decreases to 8.59 Å with the TMA cations confined to channels between the chains. Two Fe_4S_4 sites alternate along each chain, with distances of 5.77 and 6.77 Å respectively to each of the nearest four TMA cations.

In contrast to **1**, the ring formed by the pair of BDT groups and the Fe_4S_4 clusters in **2** is buckled, with a Fe-S-C_6H_4-S-Fe dihedral angle of 43.5°. The closest separation between Fe_4S_4 clusters is

10.24 Å within each chain and 10.00 Å between chains. The presence of two distinct sites for the Fe_4S_4 clusters is consistent with the Mössbauer spectrum of **2**.

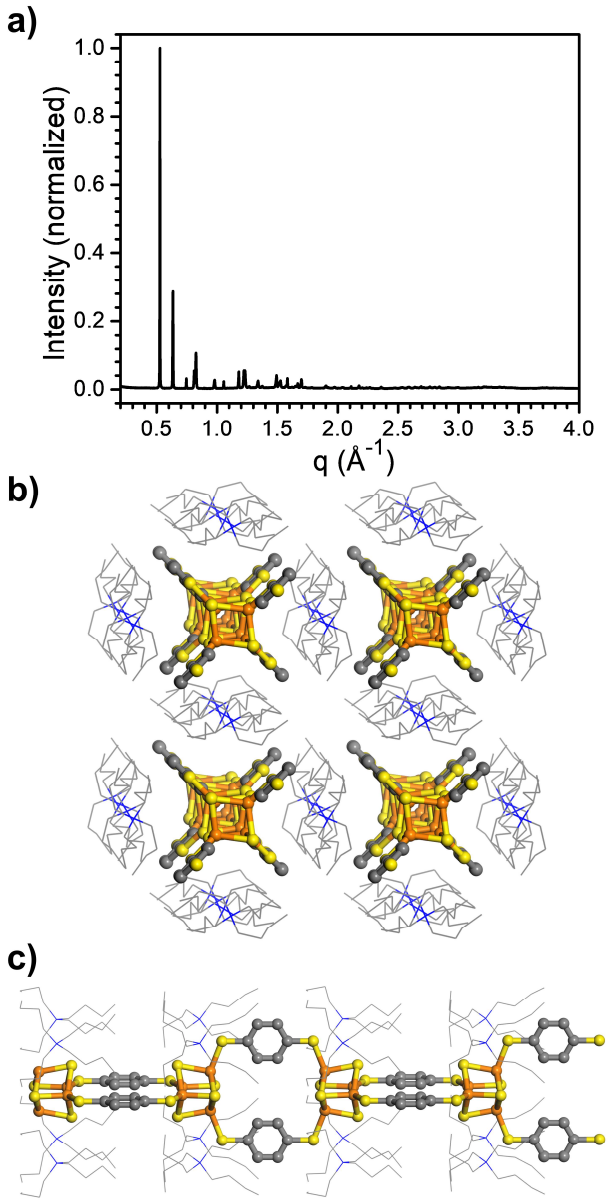

Figure 2.2. X-ray powder diffraction pattern (a) and structure of 1 solved from synchrotron X-ray powder diffraction data viewed (b) parallel to the Fe_4S_4-BDT chain and (c) perpendicular to the chain. Atoms shown as balls and sticks with Fe = orange, S = yellow, C = gray, N = blue; H atoms omitted for clarity; tetrabutylammonium ions are rendered as sticks to highlight the Fe_4S_4-BDT chain.

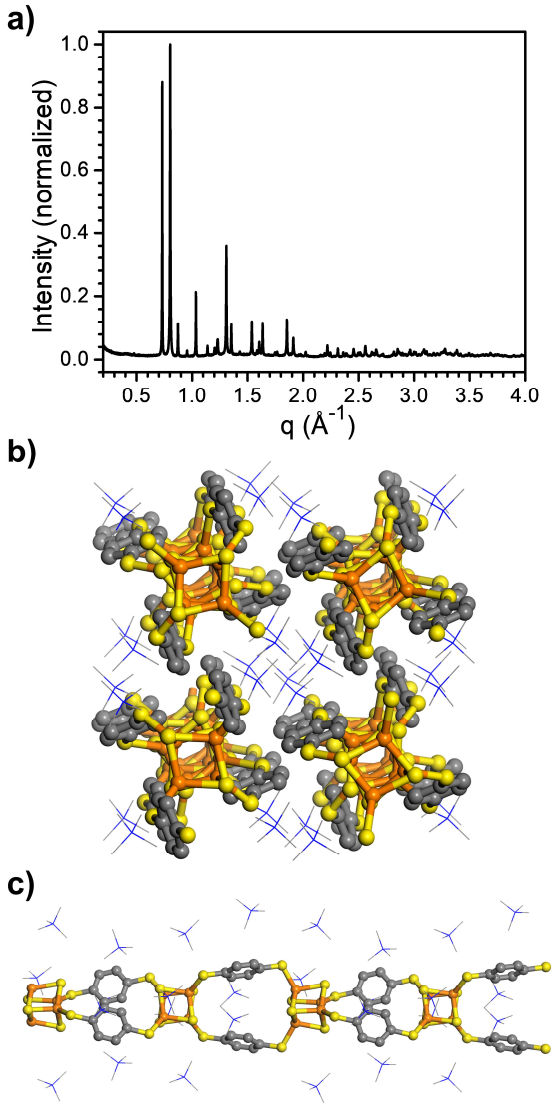

Figure 2.3. X-ray powder diffraction pattern (a) and structure of 2 solved from synchrotron X-ray powder diffraction data viewed (b) parallel to the Fe_4S_4-BDT chain and (c) perpendicular to the chain. Atoms shown as balls and sticks with Fe = orange, S = yellow, C = gray, N = blue; H atoms omitted for clarity; tetramethylammonium ions are rendered as sticks to highlight the Fe_4S_4-BDT chain.

We had initially hypothesized that the combination of Fe_4S_4 clusters and BDT could produce an extended 3D framework, but the observed 1D structures suggest that other conformations of these materials are accessible. We hypothesize that the choice of cation may be an important point of modulation to control morphology. In **1**, the Fe_4S_4-BDT chains are separated by TBA cations, but in **2**, the smaller TMA cations allow closer contact between the chains. Additionally, the size of

the cation is found to affect the conformation of the chains, which highlights that the coordination of BDT to Fe is flexible. The different structures imbued by these cations, as well as the different synthetic conditions required to isolate **2**, prompted us to investigate the solution phase behavior of these materials.

2.2.3 Solution Behavior of Fe_4S_4-BDT Chains

The observation that addition of Li^+ during synthesis of **1** and **2** slows the rate of precipitation and improves crystallinity led us to hypothesize that the Fe_4S_4-BDT chains might form in solution prior to packing with TBA or TMA and subsequent precipitation. We note that initial attempts to synthesize **2** by heating of $BDTH_2$ with $[Fe_4S_4(SPh)_4][TMA]_2$ in DMF resulted in negligible formation of a precipitate (in some cases, a small amount of an amorphous solid degradation product formed and was filtered out). Furthermore, addition of 5 equivalents of $[TBA][PF_6]$ to this solution after cooling to room temperature resulted in rapid precipitation of poorly-crystalline **1**. This suggests that chains of **2** may be forming in solution but are sufficiently soluble in DMF to avoid precipitation. Addition of $[TBA][PF_6]$ then putatively triggers rapid packing of the chains which forces the observed precipitation.

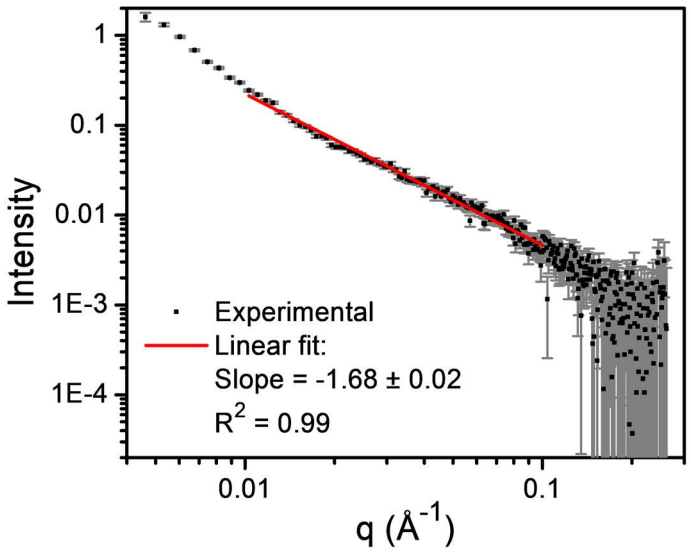

Figure 2.4. Small angle X-ray scattering (SAXS) from a DMF solution of 2.

To test this hypothesis the solubility of isolated **2** was also investigated. Isolated crystalline **2** is soluble in DMF, and addition of [TBA][PF_6] to this solution also results in the immediate precipitation of poorly-crystalline **1**. This precipitation can be slowed by the addition of excess [Li][CF_3SO_3], suggesting that ionic strength likely plays a role in ion packing and hence in controlling the rate of crystallization (**Figure A.47**). In this way, the [Li][CF_3SO_3] may act similarly to the competing ligands often used as modulators in syntheses of MOFs.[12] The use of noncoordinating salts as modulators is less explored, but ionic strength has been invoked as a factor affecting the dynamics of other soluble coordination polymers.[13] To further examine the solution structure of these chains, small angle X-ray scattering (SAXS) experiments were carried out on a near-saturated DMF solution of **2** (**Figure 2.4**). The SAXS data are best fit to a power-law behavior at higher q, with a slope on a log-log plot near $-5/3$ that is indicative of a swollen polymer coil structure.[14] The full range of data can also be fit well by the unified exponential/power-law model described by Beaucage,[14] yielding a similar result (**Figure A.23**). This type of scattering has been reported for other charged polymers such as DNA.[15] Taken together, these results indicate that the Fe_4S_4-BDT chain persists in solution, and it seems that the identity of the counterion plays an important role in solubility and crystallization.

The Fe_4S_4-BDT chains found in both **1** and **2** contain Fe_4S_4 clusters with a similar separation to those in biological electron transport chains.[7, 16] This raises the possibility that electrical conductivity could occur along these chains. Furthermore, we hypothesized that the shorter chain-chain contacts in **2** might also facilitate enhanced electronic coupling. As such, we next investigated the electronic structure and conductivity of these materials.

2.2.4 Electronic Properties of Fe_4S_4-BDT Chains

The diffuse reflectance UV-visible spectra of **1** and **2** (**Figure 2.5**) show a broad band near 560 nm, along with a shoulder near 820 nm and additional absorption in the UV region. Solutions of **2** in DMF show similar features, providing further evidence that the Fe_4S_4-BDT chains persist in solution. The 560 nm feature is red-shifted from the 450 nm absorption observed for monomeric $[Fe_4S_4(SPh)_4]^{2-}$ in solution (**Figure A.26**). This band has been attributed to a ligand-to-metal charge transfer transition involving the thiolate ligand.[17] The more electron rich nature of the BDT ligand in **1** versus the thiophenolate ligand in the monomer may explain this shift.

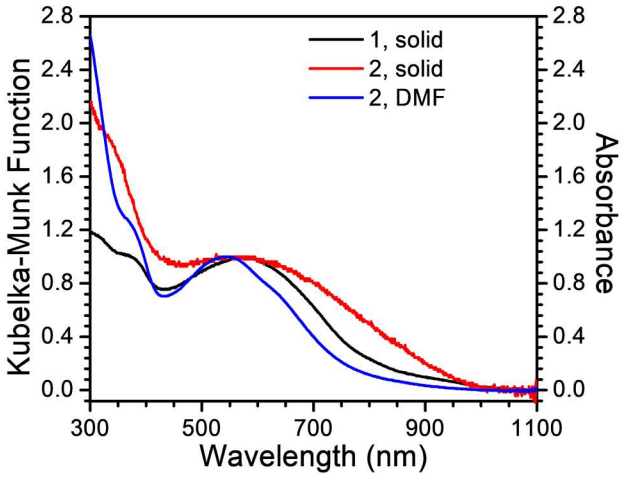

Figure 2.5. Normalized UV-visible diffuse reflectance spectra of 1 and 2 in a [Mg][SO_4] matrix plotted as a Kubelka-Munk function and absorbance spectrum of 2 in DMF solution.

The electron transfer series of biologically relevant cubane-type Fe_4S_4 clusters has been studied extensively. Of these, the $[Fe_4S_4]^{2+}$ and $[Fe_4S_4]^{+}$ cores are the most stable and thoroughly characterized oxidation states.[18] The redox behavior of these Fe_4S_4-BDT chains was investigated by cyclic voltammetry (CV) on DMF solutions of **2** (**Figure 2.6**). These measurements are complicated by the dependence of solubility on counterion as noted above. When 0.1 M [TMA][PF_6] is used as the electrolyte, the Fe_4S_4-BDT chains partially precipitate as an amorphous

solid, forming a fine suspension. We suspect that this precipitation is due to a much higher concentration of TMA as compared with the conditions for the synthesis of **2**. When 0.1 M $[Li][CF_3SO_3]$ is used instead, no precipitation is observed. With $[TMA][PF_6]$ as the electrolyte, the CV response of this suspension is similar to that of the $[Fe_4S_4(SPh)_4][TMA]_2$ monomer in solution (**Figure A.43**), showing quasi-reversible reductions at -1.43 and -2.13 V vs. $FeCp_2^+/FeCp_2$ (**Figure A.44**). With $[Li][CF_3SO_3]$ as the electrolyte, reductive features are similarly observed at -1.6 and -2.2 V vs. $FeCp_2^+/FeCp_2$ (**Figure 2.6**). By comparison to the monomer, these features correspond to the $[Fe_4S_4]^{2+}/[Fe_4S_4]^+$ and $[Fe_4S_4]^+/[Fe_4S_4]^0$ redox couples. Upon scanning past the first reductive feature in $[Li][CF_3SO_3]$ electrolyte, a deposit is observed on the working electrode which re-dissolves at more oxidizing potentials. This suggests that the Fe_4S_4-BDT chain containing $[Fe_4S_4]^+$ clusters is less soluble, and may explain the non-ideal shape of the CV features and changes upon repeated scans (**Figure A.46**). Despite this complexity, the electrochemistry results demonstrate that the redox-activity of the Fe_4S_4 clusters is preserved in the Fe_4S_4-BDT chains present in **2** and likely in 1 as well.

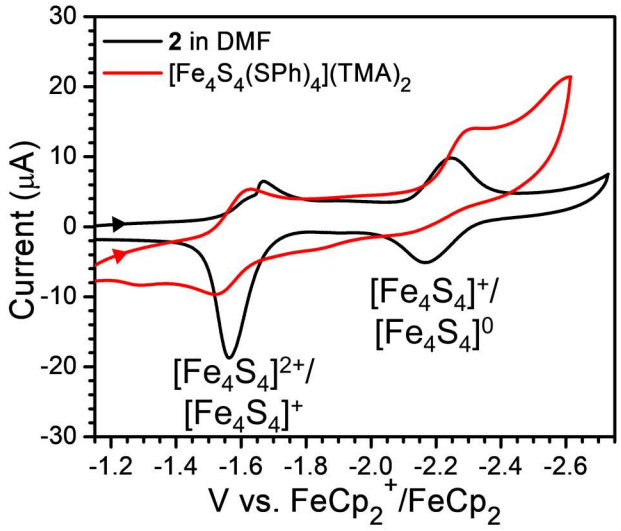

Figure 2.6. Cyclic voltammograms of 2 and monomeric $[Fe_4S_4(SPh)_4][TMA]_2$. Arrow denotes scan direction. Conditions: DMF, 0.1 M $[Li][CF_3SO_3]$, 0.1 V/s.

In addition to these reductive features, an irreversible oxidation was observed at approximately -0.3 V vs. $FeCp_2^+/FeCp_2$ with both electrolytes. Because bulky ligands have been shown to improve the stability of the $[Fe_4S_4]^{3+}$ oxidation state,[19] we had hypothesized that this state might be stabilized in a coordination polymer. However, the irreversible oxidation near the potential observed in the monomer suggests that this is not the case for the Fe_4S_4-BDT chains in solution or suspension.

As-synthesized **1** and **2** are both poor electrical conductors, with room temperature pressed pellet conductivities of $\sigma = 3(3) \times 10^{-11}$ S/cm and $5(3) \times 10^{-10}$ S/cm respectively. For comparison, the conductivities of the monomeric starting materials ($[Fe_4S_4(SPh)_4][TBA]_2$ and $[Fe_4S_4(SPh)_4][TMA]_2$) are both below 10^{-12} S/cm. The similarity in values for **1** and **2** suggests that insulation of the Fe_4S_4-BDT chains by the large TBA cation is not the only factor leading to low conductivity. Instead, we propose that these insulating behaviors may be ascribed to two factors. Firstly, there is likely a low concentration of charge carriers along the chain due to the $S = 0$ ground state of $[Fe_4S_4]^{2+}$. Secondly, we note the observed bulk conductivity of pressed pellet samples is a weighted average of the conductivity in each crystallographic direction plus grain boundary resistance. Both of these factors will lower the measured conductivity.[20]

Doping experiments were carried out to introduce additional charge carriers and improve the conductivities of these materials. Solid **1** and **2** were soaked in a THF solution containing 0.5 equivalents of bis(pentamethylcyclopentadienyl)cobalt(II) ($CoCp^*_2$) per Fe_4S_4 unit and excess $[Li][CF_3SO_3]$. The reductively-doped analogues of **1** and **2** exhibited enhanced conductivities of $6(2) \times 10^{-9}$ S/cm and $5(2) \times 10^{-6}$ S/cm respectively. In contrast, similar doping experiments with an oxidizing agent, ferrocenium tetrafluoroborate ($[Fc][BF_4]$), in the presence of excess [TMA][Br] resulted in no measurable enhancement ($7(5) \times 10^{-12}$ S/cm and $7(1) \times 10^{-10}$ S/cm for **1**

and **2** respectively). The crystallinity of all doped materials was maintained as verified by their XRPD patterns (**Figure A.15** - **Figure A**.18).

Reduction of the $[Fe_4S_4]^{2+}$ cluster requires incorporation of an additional cation for charge balance, either Li^+ or $CoCp^*_2{}^+$. ICP-MS was therefore used to assess the degree of reduction in **1** and **2** (**Table 2.1**). For analysis of the ICP-MS data, it is assumed that exchange of TBA or TMA with Li^+ or $CoCp^*_2{}^+$ does not occur. This assertion is supported by the observation that the Li^+ content in **1** and **2** does not increase upon soaking in a THF solution of $[Li][CF_3SO_3]$ without reductant. The increase in Li and Co content upon treatment indicates reduction by 0.07(2) and 0.24(6) electrons per formula unit for **1** and **2** respectively. The lower degree of reduction in **1** is consistent with the smaller increase in conductivity upon treatment and may be due to difficulty incorporating the additional cations into the densely packed structure. Mössbauer spectroscopy was used to further characterize the reduced materials (**Figure A.33** - **Figure A**.37). For both **1** and **2**, the spectra of the reduced materials show no additional signals attributable to free Fe^{2+} or Fe^{3+},[21] indicating that the Fe_4S_4 clusters remain intact. Mössbauer spectra of monomeric Fe_4S_4 clusters show small increases in isomer shift and quadrupole splitting upon reduction from $[Fe_4S_4]^{2+}$ to $[Fe_4S_4]^+$.[21,22] With **1**, no significant changes are seen in the Mössbauer spectra, consistent with the small degree of reduction estimated from ICP-MS. In contrast, the spectrum of **2** shows small changes in shape (**Figure A.37**). This suggests an additional, unresolved contribution from a species with higher isomer shift than the as-synthesized **2**. Subtraction of the spectra of the as-synthesized and reduced materials reveals a broad additional signal in the same region as literature spectra of $[Fe_4S_4]^+$ compounds (**Figure A.38**).[21] This contribution can be approximated in fits to the spectrum of reduced **2** by addition of a third site with similar δ and ΔE_Q to literature $[Fe_4S_4]^+$ spectra (full treatment of the $[Fe_4S_4]^+$ species with two Fe sites was not

possible given the low intensity of this feature and overlap with signals from $[Fe_4S_4]^{2+}$ sites). These changes are reversible by brief exposure to dry air, further supporting their attribution to reduced $[Fe_4S_4]^{+}$ clusters. While interpretation of the Mössbauer spectra is complicated by the presence of overlapping signals, these data support that the reversible redox-activity of the Fe_4S_4 clusters is preserved.

Table 2.1. Li and Co content of 1 and 2 before and after reduction in the solid state.

Molar ratio	Compound **Reduced 1**	Compound **Reduced 2**
Li/Fe_4S_4		
Before reduction	3(1)%	14(5)%
After reduction	9(1)%	28(4)%
Increase amount	6(2)%	15(6)%
Co/Fe_4S_4		
Before reduction	0.14(4)%	0.08(2)%
After reduction	1.2(3)%	9.0(6)%
Increase amount	1.1(3)%	9.0(6)%
Reduction degree	7(2)%	24(6)%

Finally, we have also investigated chemical reduction of **2** in the solution phase. Upon treatment with approximately 0.5 equivalents of sodium acenaphthylene ($[Na][C_{12}H_8]$), DMF solutions of **2** show changes in their UV-visible absorption spectra consistent with partial reduction of the Fe_4S_4 clusters from $[Fe_4S_4]^{2+}$ to $[Fe_4S_4]^{+}$ (**Figure A.27**).[23] A small amount of precipitate was observed, consistent with the lower solubility of the reduced polymer observed during cyclic voltammetry

experiments. SAXS and IR measurements support the persistence of the polymer structure in the reduced solution (**Figure A.24**, **Figure A**.25, **Figure A**.41 and **Figure A**.42). Following precipitation of the partially reduced solution by addition of Et_2O, an amorphous solid was obtained with conductivity of $1.5(5) \times 10^{-5}$ S/cm. In contrast, material precipitated from a DMF solution of **2** without added reductant showed a conductivity of $3(4) \times 10^{-9}$ S/cm. ICP-MS measurements of the Na/Fe ratio were used to assess the degree of reduction between these two materials. These data indicate that the material was reduced by 0.6(4) electrons per cluster. This result further supports that the introduction of charge carriers by accessing the $[Fe_4S_4]^+$ oxidation state is advantageous for preparing materials with enhanced electrical conductivity.

2.3 Conclusion

We have synthesized and characterized two new materials incorporating redox-active Fe_4S_4 clusters with an organochalcogenide ligand, BDT. Synchrotron X-ray powder diffraction data analysis revealed that the materials feature 1D chains of Fe_4S_4 clusters connected by pairs of BDT ligands. Small angle X-ray scattering measurements and precipitation experiments proved the persistence of these chains in solution. The choice of counterion is important in determining the packing and solubility of these anionic chains. Mössbauer spectroscopy and cyclic voltammetry demonstrate that the redox-activity of the Fe_4S_4 cluster is preserved in these materials, and chemical reduction is shown to impart enhanced electrical conductivity. These results lay the groundwork for a new class of materials based on metal-sulfur clusters with organosulfur ligands.

2.4 Experimental Section

General Methods

All manipulations were performed under an inert atmosphere of dry N_2 using a Schlenk line or MBraun UNIlab glovebox unless otherwise noted. ^{1}H NMR measurements were performed on Bruker DRX 400 or 500 spectrometers. Elemental analyses (C, H, N) were performed by Midwest Microlabs. Inductively coupled plasma mass spectrometry (ICP-MS) data was obtained with an Agilent 7700x ICP-MS and analyzed using ICP-MS Mass Hunter version B01.03. The samples were diluted in 2% HNO_3 matrix and analyzed with a ^{159}Tb internal standard against a 12-point standard curve over the range from 0.1 ppb to 500 ppb. The correlation was > 0.9997 for all analyses of interest. Data collection was performed in Spectrum Mode with five replicates per sample and 100 sweeps per replicate. Dimethylformamide (DMF), tetrahydrofuran (THF), and acetonitrile (MeCN) used in preparing the coordination polymers were initially dried and purged with Ar on a solvent purification system from Pure Process Technology. DMF was then passed through activated alumina before use. THF was stirred with liquid NaK alloy and then filtered through activated alumina and stored over 4Å molecular sieves. MeCN was stored over 4Å molecular sieves. Dimethylacetamide (DMA) was sparged with N_2, transferred into the glovebox, passed through activated alumina and stored over 4Å molecular sieves. [TMA][PF_6] was recrystallized from H_2O and dried at 160 °C before use.[24] All other chemicals were purchased from commercial sources and used as received. [$Fe_4S_4(SPh)_4$][TBA]$_2$ was prepared as previously described.[25]

1,4-Bis(isopropylthio)benzene

1,4-Bis(isopropylthio)benzene was synthesized following a reported procedure,[26] but the synthetic method and purification have been modified as follows:

A dispersion of 60% NaH in mineral oil (19.2 g, 480 mmol) was added to a 500 mL three-neck flask and then washed with hexane twice and DMA once under a N_2 atmosphere. After adding DMA (100 mL), 2-propanethiol (52 mL, 480 mmol) was injected slowly and in portions to avoid excessive foaming (if necessary, use of ice bath and drop funnel is helpful). Subsequently, DMA (100 mL) and a solution of 1,4-dibromobenzene (28.3 g. 120 mmol) in DMA (150 mL) were injected, and the mixture was heated for 17 h to 100 °C. The mixture was cooled, poured into 100 mL saturated NaCl solution and extracted with Et_2O (3×100 mL). The organic layer was washed with H_2O (5×50 mL), dried with [Mg][SO_4], and evaporated. The yellowish oil was further purified by vacuum distillation. Yield: 22 g (82%). Ref. b.p. 168-169 °C. ^{1}H NMR (400 MHz, $CDCl_3$): δ 7.31 (4 H, s), 3.36 (2 H, spt, J = 3.4 Hz), 1.28 (12 H, d, J = 1.3 Hz) ppm.

1,4-Benzenedithiol

Safety note: In our experience any excess Na was consumed by side reactions with the solvent and was not present after heating. However, care should be taken to ensure that no Na metal is present before adding the HCl solution. Addition of a few drops of the acid solution first is recommended to check for bubbling that would indicate the presence of Na metal.

Sodium (1.8 g, 80 mmol), dry DMA (40 mL) from the glovebox, and 1,4-Bis(isopropylthio)benzene (4.5 g, 20 mmol) were added in sequence to a 125 mL three-neck flask under N_2 atmosphere and the mixture was heated to 100 °C for 8 h. During this time the reaction mixture became thick with precipitate. The reaction solution was quenched with diluted HCl solution (concentrated HCl solution (34-37% w/w, 10 mL) + H_2O (50 mL)) in an ice bath and stirred for another 0.5 h under an inert atmosphere. The mixture was extracted with Et_2O (2×75 mL). The organic layer was washed with H_2O (5×30 mL), dried with [Mg][SO_4], and evaporated. A white powder was obtained by washing with hexanes (20 mL). More product can be recovered

by storing the hexane washes in a freezer (-35 °C) overnight, resulting in a pale yellow to white powder. Overall yield: 1.9 g (67%). ^{1}H NMR (400 MHz, $CDCl_3$): δ 7.16 (4 H, s) and 3.41 (2 H, s) ppm.

$[Fe_4S_4(SPh)_4][TMA]_2$

The synthesis of this compound has been reported previously,[27] but details of the synthetic method and purification had not been published.

MeOH (80 mL) was added to a 250 mL Schlenk flask with a stir bar and deoxygenated by four pump-purge cycles with N_2. The flask was then cooled in an ice/water bath. Sodium (1.8 g, 80 mmol) was added with stirring and continued cooling and allowed to dissolve fully before returning the flask to room temperature. PhSH (8.2 mL, 80 mmol) was then injected into the reaction mixture. In a separate 250 mL Schlenk flask, anhydrous $FeCl_3$ (3.2 g, 20 mmol) and MeOH (50 mL) were deoxygenated by four pump-purge cycles with N_2 and transferred via cannula to the flask containing the [Na][PhS] solution. Sulfur (0.64 g, 20 mmol) was added and the reaction mixture stirred overnight at room temperature. This mixture was then filtered into a solution of [TMA][Br] (2.3 g, 15 mmol) in methanol (45 mL), resulting in precipitation of the crude product as a black solid. This suspension was filtered and the resulting solid dried under vacuum. The crude solid was dissolved in ~70 °C deoxygenated MeCN (40 mL) and passed through a glass frit before deoxygenated MeOH (130 mL) was added via slow cannula transfer while heating to ~60 °C. Slow cooling of this solution to −35 °C resulted in the formation of large black crystals that were collected by filtration, washed with MeOH, and dried under vacuum (4.0 g, 85%). ^{1}H NMR (400 MHz, CD_3CN): δ 8.19 (8 H, d, J = 5.7 Hz), 5.91 (8 H, br. s), 5.30 (4 H, t, J = 5.6 Hz), 3.07 (24 H, s) ppm.

[$Fe_4S_4(BDT)_2$][TBA]$_2$ (1)

[$Fe_4S_4(SPh)_4$][TBA]$_2$ (192 mg, 0.15 mmol) and [Li][CF_3SO_3] (117 mg, 0.75 mmol) were added to a 24 mL vial and dissolved in DMF (12 mL). A solution of 1,4-benzenedithiol (43 mg, 0.30 mmol) in DMF (3 mL) was added and the vial was sealed and placed in a heating block on a 140 °C hot plate. The reaction mixture was heated for 2 days, after which **1** was separated by centrifugation, washed with DMF (4x2 mL) and THF (3x2 mL), and dried under vacuum. Compound **1** was obtained as a black powder (102 mg, 61%). Anal. calc. for $Fe_4S_8C_{44}H_{80}N_2$: C 47.31%, H 7.22%, N 2.51%; found: C 44.61%, H 6.62%, N 2.18%. The combustion analysis for this material is improved upon soaking with excess TBA (see below).

[$Fe_4S_4(BDT)_2$][TMA]$_2$ (2)

[$Fe_4S_4(SPh)_4$][TMA]$_2$ (140 mg, 0.15 mmol) and [Li][CF_3SO_3] (936 mg, 6.0 mmol) were added to a 24 mL vial and dissolved in MeCN (9 mL). A solution of 1,4-benzenedithiol (43 mg, 0.30 mmol) in MeCN (6 mL) was added and the vial was sealed and placed in a heating block on a 100 °C hot plate. The reaction mixture was heated for 2 days, after which **2** was separated by centrifugation, washed with MeCN (4x2 mL), and dried under vacuum. **2** was obtained as a black powder (68 mg, 58%). Anal. calc. for $Fe_4S_8C_{20}H_{32}N_2$: C 30.78%, H 4.13%, N 3.59%; found: C 30.46%, H 4.11%, N 3.62%.

Reductive doping experiments of solid state 1 and 2

1 (0.05 mmol, 56 mg) or **2** (0.05 mmol, 39 mg) was soaked in a solution of $CoCp^*_2$ (0.5 equivalents, 0.025 mmol, 8 mg) and excess [Li][CF_3SO_3] (5 equivalents, 0.25 mmol, 39 mg) in THF (5 mL) and then stirred at room temperature overnight. The reduced product was isolated by centrifugation, washed with THF (typically 4x2 mL) until the wash solvent was colorless, and

dried under vacuum. Crystallinity was maintained as verified by XRPD (Figure A.15 and Figure A.17). The degree of reduction was analyzed by ICP-MS (**Table 2.1**).

Oxidative doping experiments of solid state 1 and 2

1 (0.05 mmol, 56 mg) or **2** (0.05 mmol, 39 mg) was soaked in a solution of [Fc][BF_4] (0.5 equivalents, 0.025 mmol, 7 mg) and excess [TMA][Br] (5 equivalents, 0.25 mmol, 38 mg) in MeCN (4 mL) and MeOH (1 mL) and then stirred at room temperature overnight. The oxidized product was isolated by centrifugation, washed with MeCN (typically 4x2 mL) until the wash solvent was colorless, and dried under vacuum. Crystallinity was maintained as verified by XRPD (Figure A.16 and Figure A.18).

Chemical reduction of 2 in solution

The concentration of **2** in DMF was determined by inductively-coupled plasma optical emission spectroscopy (ICP-OES). Three aliquots of each solution batch were dried, digested in HNO_3, and the Fe content was measured versus a Cu internal standard.

A solution of [Na][$C_{12}H_8$] was prepared in THF (2.5 mL) by stirring sodium (10 mg, 0.43 mmol) and excess acenaphthylene (80 mg, 0.53 mmol) at room temperature overnight. This solution was passed through a glass microfiber filter and diluted 10-fold with DMF prior to use.

The [Na][$C_{12}H_8$] solution (0.5 equivalents, 1.24 mL, 0.022 mmol) was added dropwise to a stirred solution of **2** in DMF (27 mL, 34 mg, 0.043 mmol) and then stirred overnight. The reduced solid was precipitated by addition of an equal volume Et_2O and then separated by centrifugation, washed with THF (4x2 mL), and dried under vacuum. The material was amorphous as checked by XRPD.

Treatment with [R_4N][PF_6]

A mixture of **1** or **2** (0.05 mmol, 55 mg or 39 mg) and a solution of [TBA][PF_6] or [TMA][PF_6] respectively (0.25 mmol, 67 mg or 55 mg) in DMF/MeCN (5 mL) was stirred overnight at 100 °C in the glovebox. In the next morning, the solid was isolated by centrifugation and washed with fresh DMF/MeCN (3×2 mL) and THF (3×2 mL). After drying for hours under vacuum, the crystallinity was still maintained, as examined by XRPD (Figure A.13 and Figure A.14). Further ICP-MS analysis suggested that the Li content decreases (Table A.1). The C, H, N analysis results of as-synthesized **1** with [Li][CF_3SO_3] deviate from the theoretical values slightly but by washing with [TBA][PF_6], the C, H, N analysis matches with the assigned formula. Anal. calc. for **1**, $Fe_4S_8C_{44}H_{80}N_2$: C 47.31%, H 7.22%, N 2.51%; found: C 47.40%, H 7.33%, N 2.36%.

2.5 References

[1] (a) Bhattacharya, B.; Layek, A.; Mehboob Alam, M.; Maity, D. K.; Chakrabarti, S.; Ray, P. P.; Ghoshal, D. Cd(II) Based Metal–Organic Framework Behaving As A Schottky Barrier Diode. *Chem. Commun.* **2014**, *50* (58), 7858. (b) Sheberla, D.; Sun, L.; Blood-Forsythe, M. A; Er, S.; Wade, C. R.; Brozek, C. K.; Aspuru-Guzik, A.; Dincă, M. High Electrical Conductivity In Ni 3 (2,3,6,7,10,11-Hexaiminotriphenylene) 2 , A Semiconducting Metal–Organic Graphene Analogue. *J. Am. Chem. Soc.* **2014**, *136* (25), 8859–8862. (c) Campbell, M. G.; Sheberla, D.; Liu, S. F.; Swager, T. M.; Dincă, M. Cu_3(Hexaiminotriphenylene)$_2$: An Electrically Conductive 2D Metal-Organic Framework For Chemiresistive Sensing. *Angew. Chemie Int. Ed.* **2015**, *54* (14), 4349–4352. (d) Darago, L. E.; Aubrey, M. L.; Yu, C. J.; Gonzalez, M. I.; Long, J. R. Electronic Conductivity, Ferrimagnetic Ordering, And Reductive Insertion Mediated By Organic Mixed-Valence In A Ferric Semiquinoid Metal–Organic Framework. *J. Am. Chem. Soc.* **2015**, *137* (50), 15703–15711. (e) Jeon, I.-R.; Negru, B.; Van Duyne, R. P.; Harris, T. D. A 2D Semiquinone Radical-Containing Microporous Magnet With Solvent-Induced Switching From T_C = 26 to 80 K. *J. Am. Chem. Soc.* **2015**, *137* (50), 15699–15702. (f) Wang, L.; Han, Y.; Feng, X.; Zhou, J.; Qi, P.; Wang, B. Metal–Organic Frameworks For Energy Storage: Batteries And Supercapacitors. *Coord. Chem. Rev.* **2016**, *307*, 361–381. (g) Shi, C.; Xia, Q.; Xue, X.; Liu, Q.; Liu, H. J. Synthesis Of Cobalt-Based Layered Coordination Polymer Nanosheets And Their Application In Lithium-Ion Batteries As Anode Materials. *RSC Adv.* **2016**, *6* (6), 4442–4447. (h) Liu, W.; Yin, X.-B. Metal–Organic Frameworks For Electrochemical Applications. *Trac Trends Anal. Chem.* **2016**, *75*, 86–96. (i) Jeon, I.-R.; Sun, L.; Negru, B.; Van Duyne, R. P.; Dincă, M.; Harris, T. D. Solid-State Redox Switching Of Magnetic Exchange And Electronic Conductivity In A Benzoquinoid-Bridged Mn II Chain Compound. *J. Am. Chem. Soc.* **2016**, *138* (20), 6583–6590. (j) Degayner, J. A.; Jeon, I. R.; Sun, L.; Dincă, M.; Harris, T. D. 2D Conductive Iron-Quinoid Magnets Ordering Up to T_c = 105 K Via Heterogenous Redox Chemistry. *J. Am. Chem. Soc.* **2017**, *139* (11), 4175–

4184. (k) Dou, J.-H.; Sun, L.; Ge, Y.; Li, W.; Hendon, C. H.; Li, J.; Gul, S.; Yano, J.; Stach, E. A.; Dincă, M. Signature Of Metallic Behavior In The Metal–Organic Frameworks M_3(Hexaiminobenzene)$_2$ (M = Ni, Cu). *J. Am. Chem. Soc.* **2017**, *139* (39), 13608–13611. (l) Sheberla, D.; Bachman, J. C.; Elias, J. S.; Sun, C.-J.; Shao-Horn, Y.; Dincă, M. Conductive MOF Electrodes For Stable Supercapacitors With High Areal Capacitance. *Nat. Mater.* **2017**, *16* (2), 220–224. (m) Sun, L.; Liao, B.; Sheberla, D.; Kraemer, D.; Zhou, J.; Stach, E. A.; Zakharov, D.; Stavila, V.; Talin, A. A.; Ge, Y.; Et Al. A Microporous And Naturally Nanostructured Thermoelectric Metal-Organic Framework With Ultralow Thermal Conductivity. *Joule* **2017**, *1* (1), 168–177. (n) Wada, K.; Sakaushi, K.; Sasaki, S.; Nishihara, H. Multielectron-Transfer-Based Rechargeable Energy Storage Of Two-Dimensional Coordination Frameworks With Non-Innocent Ligands. *Angew. Chemie Int. Ed.* **2018**, *57* (29), 8886–8890. (o) Park, J.; Lee, M.; Feng, D.; Huang, Z.; Hinckley, A. C.; Yakovenko, A.; Zou, X.; Cui, Y.; Bao, Z. Stabilization Of Hexaaminobenzene In A 2D Conductive Metal–Organic Framework For High Power Sodium Storage. *J. Am. Chem. Soc.* **2018**, *140* (32), 10315–10323. (p) Feng, D.; Lei, T.; Lukatskaya, M. R.; Park, J.; Huang, Z.; Lee, M.; Shaw, L.; Chen, S.; Yakovenko, A. A.; Kulkarni, A.; Et Al. Robust And Conductive Two-Dimensional Metal−Organic Frameworks With Exceptionally High Volumetric And Areal Capacitance. *Nat. Energy* **2018**, *3* (1), 30–36. (q) Ziebel, M. E.; Darago, L. E.; Long, J. R. Control Of Electronic Structure And Conductivity In Two-Dimensional Metal-Semiquinoid Frameworks Of Titanium, Vanadium, And Chromium. *J. Am. Chem. Soc.* **2018**, *140* (8), 3040–3051. (r) Aubrey, M. L.; Wiers, B. M.; Andrews, S. C.; Sakurai, T.; Reyes-Lillo, S. E.; Hamed, S. M.; Yu, C.; Darago, L. E.; Mason, J. A.; Baeg, J.; Et Al. Electron Delocalization And Charge Mobility As A Function Of Reduction In A Metal–Organic Framework. *Nat. Mater.* **2018**, *17* (7), 625–632. (s) Xie, L. S.; Sun, L.; Wan, R.; Park, S. S.; Degayner, J. A.; Hendon, C. H.; Dincă, M. Tunable Mixed-Valence Doping Toward Record Electrical Conductivity In A Three-Dimensional Metal–Organic Framework. *J. Am. Chem. Soc.* **2018**, *140* (24), 7411–7414.

[2] (a) Sun, Y.; Sheng, P.; Di, C.; Jiao, F.; Xu, W.; Qiu, D.; Zhu, D. Organic Thermoelectric Materials And Devices Based On P- And N-Type Poly(Metal 1,1,2,2-Ethenetetrathiolate)S. *Adv. Mater.* **2012**, *24* (7), 932–937. (b) Givaja, G.; Amo-Ochoa, P.; Gómez-García, C. J.; Zamora, F. Electrical Conductive Coordination Polymers. *Chem. Soc. Rev.* **2012**, *41* (1), 115–147. (c) Sun, L.; Miyakai, T.; Seki, S.; Dincă, M. Mn 2 (2,5-Disulfhydrylbenzene-1,4-Dicarboxylate): A Microporous Metal–Organic Framework With Infinite (−Mn–S−)$_\infty$ Chains And High Intrinsic Charge Mobility. *J. Am. Chem. Soc.* **2013**, *135* (22), 8185–8188. (d) Sun, L.; Hendon, C. H.; Minier, M. A.; Walsh, A.; Dincă, M. Million-Fold Electrical Conductivity Enhancement In Fe_2(DEBDC) Versus Mn_2(DEBDC) (E = S, O). *J. Am. Chem. Soc.* **2015**, *137* (19), 6164–6167. (e) Sun, Y.; Qiu, L.; Tang, L.; Geng, H.; Wang, H.; Zhang, F.; Huang, D.; Xu, W.; Yue, P.; Guan, Y. S.; Et Al. Flexible N-Type High-Performance Thermoelectric Thin Films Of Poly(Nickel-ethylenetetrathiolate) Prepared By An Electrochemical Method. *Adv. Mater.* **2016**, *28* (17), 3351–3358. (f) Electrically Conductive Porous Metal-Organic Frameworks. *Angew. Chemie Int. Ed.* **2016**, *55* (11), 3566–3579.

[3] (a) Rivera, N. M.; Engler, E. M.; Schumaker, R. R. Synthesis And Properties Of Tetrathiafulvalene–Metal Bisdithiolene Macromolecules. *J. Chem. Soc., Chem. Commun.* **1979**, 4, 184–185. (b) Dirk, C. W.; Bousseau, M.; Barrett, P. H.; Moraes, F.; Wudl, F.; Heeger, A. J. Metal Poly(Benzodithiolenes). *Macromolecules* **1986**, *19* (2), 266–269. (c) Vicente, R.; Ribas, J.; Cassoux, P.; Valade, L. Synthesis, Characterization And Properties Of Highly Conducting

Organometallic Polymers Derived From The Ethylene Tetrathiolate Anion. *Synth. Met.* **1986**, *13* (4), 265–280. (d) Szczepura, L. F.; Galloway, C. P.; Zheng, Y.; Han, P.; Wilson, S. R.; Rauchfuss, T. B.; Rheingold, A. L. $C_4S_6^{2-}$: A Bridging Bis(Dithiolato) Ligand For The Preparation Of Semiconducting Inorganic Polymers. *Angew. Chemie Int. Ed.* **1995**, *34* (17), 1890–1892. (e) Cerrada, E.; Diaz, M. C.; Diaz, C.; Laguna, M.; Sabater, A. New Conducting Coordination Polymers Containing $M(dmit)_2$ Links. *Synth. Met.* **2001**, *119* (1–3), 91–92. (f) Mitsumi, M.; Murase, T.; Kishida, H.; Yoshinari, T.; Ozawa, Y.; Toriumi, K.; Sonoyama, T.; Kitagawa, H.; Mitani, T. Metallic Behavior And Periodical Valence Ordering In A MMX Chain Compound, $Pt_2(etcs_2)_4I$. *J. Am. Chem. Soc.* **2001**, *123* (45), 11179–11192. (g) Kanehama, R.; Umemiya, M.; Iwahori, F.; Miyasaka, H.; Sugiura, K.; Yamashita, M.; Yokochi, Y.; Ito, H.; Kuroda, S.; Kishida, H.; Et Al. Novel ET-Coordinated Copper(I) Complexes: Syntheses, Structures, And Physical Properties (ET = BEDT-TTF = Bis(Ethylenedithio)Tetrathiafulvalene). *Inorg. Chem.* **2003**, *42* (22), 7173–7181.

[4] (a) Kambe, T.; Sakamoto, R.; Hoshiko, K.; Takada, K.; Miyachi, M.; Ryu, J. H.; Sasaki, S.; Kim, J.; Nakazato, K.; Takata, M.; Et Al. A Π-Conjugated Nickel Bis(Dithiolene) Complex Nanosheet. *J. Am. Chem. Soc.* **2013**, *135* (7), 2462–2465. (b) Kambe, T.; Sakamoto, R.; Kusamoto, T.; Pal, T.; Fukui, N.; Hoshiko, K.; Shimojima, T.; Wang, Z.; Hirahara, T.; Ishizaka, K.; Et Al. Redox Control And High Conductivity Of Nickel Bis(Dithiolene) Complex Π-Nanosheet: A Potential Organic Two-Dimensional Topological Insulator. *J. Am. Chem. Soc.* **2014**, *136* (41), 14357–14360. (c) Huang, X.; Sheng, P.; Tu, Z.; Zhang, F.; Wang, J.; Geng, H.; Zou, Y.; Di, C.; Yi, Y.; Sun, Y.; Et Al. A Two-Dimensional Π-d Conjugated Coordination Polymer With Extremely High Electrical Conductivity And Ambipolar Transport Behaviour. *Nat. Commun.* **2015**, *6* (1), 7408. (d) Dong, R.; Pfeffermann, M.; Liang, H.; Zheng, Z.; Zhu, X.; Zhang, J.; Feng, X. Large-Area, Free-Standing, Two-Dimensional Supramolecular Polymer Single-Layer Sheets For Highly Efficient Electrocatalytic Hydrogen Evolution. *Angew. Chemie Int. Ed.* **2015**, *54* (41), 12058–12063. (e) Pal, T.; Kambe, T.; Kusamoto, T.; Foo, M. L.; Matsuoka, R.; Sakamoto, R.; Nishihara, H. Interfacial Synthesis Of Electrically Conducting Palladium Bis(Dithiolene) Complex Nanosheet. *Chempluschem* **2015**, *80* (8), 1255–1258. (f) Clough, A. J.; Yoo, J. W.; Mecklenburg, M. H.; Marinescu, S. C. Two-Dimensional Metal–Organic Surfaces For Efficient Hydrogen Evolution From Water. *J. Am. Chem. Soc.* **2015**, *137* (1), 118–121. (g) Maeda, H.; Sakamoto, R.; Nishihara, H. Coordination Programming Of Two-Dimensional Metal Complex Frameworks. *Langmuir* **2016**, *32* (11), 2527–2538. (h) Huang, X.; Yao, H.; Cui, Y.; Hao, W.; Zhu, J.; Xu, W.; Zhu, D. Conductive Copper Benzenehexathiol Coordination Polymer As A Hydrogen Evolution Catalyst. *ACS Appl. Mater. Interfaces* **2017**, *9* (46), 40752–40759. (i) Huang, X.; Zhang, S.; Liu, L.; Yu, L.; Chen, G.; Xu, W.; Zhu, D. Superconductivity In A Copper(II)-Based Coordination Polymer With Perfect Kagome Structure. *Angew. Chemie Int. Ed.* **2018**, *57* (1), 146–150.

[5] Ji, Z.; Trickett, C.; Pei, X.; Yaghi, O. M., Linking Molybdenum–Sulfur Clusters for Electrocatalytic Hydrogen Evolution. *J. Am. Chem. Soc.* **2018,** *140* (42), 13618-13622.

[6] (a) Beinert, H.; Holm, R. H.; Münck, E., Iron-Sulfur Clusters: Nature's Modular, Multipurpose Structures. *Science* **1997**, *277* (5326), 653-659. (b) Venkateswara Rao, P.; Holm, R. H., Synthetic Analogues of The Active Sites of Iron−Sulfur Proteins. *Chem. Rev.* **2004,** *104* (2), 527-560.

[7] (a) Jormakka, M.; Törnroth, S.; Byrne, B.; Iwata, S., Molecular Basis of Proton Motive Force Generation: Structure of Formate Dehydrogenase-N. *Science* **2002,** *295* (5561), 1863-1868. (b) Jormakka, M.; Richardson, D.; Byrne, B.; Iwata, S., Architecture of NarGH Reveals a Structural Classification of Mo-bisMGD Enzymes. *Structure* **2004,** *12* (1), 95-104. (c) Sazanov, L. A.; Hinchliffe, P., Structure of the Hydrophilic Domain of Respiratory Complex I from Thermus thermophilus. *Science* **2006,** *311* (5766), 1430-1436. (d) Jormakka, M.; Yokoyama, K.; Yano, T.; Tamakoshi, M.; Akimoto, S.; Shimamura, T.; Curmi, P.; Iwata, S., Molecular mechanism of energy conservation in polysulfide respiration. *Nat. Struct. Mol. Biol.* **2008,** *15*, 730. (e) Hayashi, T.; Stuchebrukhov, A. A., Electron tunneling in respiratory complex I. *Proc. Natl. Acad. Sci. U.S.A.* **2010,** *107* (45), 19157-19162. (f) Weinert, T.; Huwiler, S. G.; Kung, J. W.; Weidenweber, S.; Hellwig, P.; Stärk, H.-J.; Biskup, T.; Weber, S.; Cotelesage, J. J. H.; George, G. N.; Ermler, U.; Boll, M., Structural basis of enzymatic benzene ring reduction. *Nat. Chem. Biol.* **2015,** *11*, 586. (g) Youngblut, M. D.; Tsai, C.-L.; Clark, I. C.; Carlson, H. K.; Maglaqui, A. P.; Gau-Pan, P. S.; Redford, S. A.; Wong, A.; Tainer, J. A.; Coates, J. D., Perchlorate Reductase Is Distinguished by Active Site Aromatic Gate Residues. *J. Biol. Chem.* **2016,** *291* (17), 9190-9202. (h) Wagner, T.; Ermler, U.; Shima, S., The methanogenic CO_2 reducing-and-fixing enzyme is bifunctional and contains 46 [4Fe-4S] clusters. *Science* **2016,** *354* (6308), 114-117. (i) Glasser, N. R.; Oyala, P. H.; Osborne, T. H.; Santini, J. M.; Newman, D. K., Structural and mechanistic analysis of the arsenate respiratory reductase provides insight into environmental arsenic transformations. *Proc. Natl. Acad. Sci. U.S.A.* **2018,** published ahead of print August 13, 2018 https://doi.org/10.1073/pnas.1807984115.

[8] Trikalitis, P. N.; Bakas, T.; Papaefthymiou, V.; Kanatzidis, M. G., Supramolecular Assembly of Hexagonal Mesostructured Germanium Sulfide and Selenide Nanocomposites Incorporating the Biologically Relevant Fe4S4 Cluster. *Angew. Chemie Int. Ed.* **2000,** *39* (24), 4558-4562.

[9] (a)Yuhas, B. D.; Prasittichai, C.; Hupp, J. T.; Kanatzidis, M. G., Enhanced Electrocatalytic Reduction of CO_2 With Ternary Ni-Fe_4S_4 And Co-Fe_4S_4-Based Biomimetic Chalcogels. *J. Am. Chem. Soc.* **2011,** *133* (40), 15854-15857. (b) Shim, Y.; Yuhas, B. D.; Dyar, S. M.; Smeigh, A. L.; Douvalis, A. P.; Wasielewski, M. R.; Kanatzidis, M. G., Tunable Biomimetic Chalcogels With Fe_4S_4 Cores And $[Sn_nS_{2n+2}]^{4-}$ (N = 1, 2, 4) Building Blocks for Solar Fuel Catalysis. *J. Am. Chem. Soc.* **2013,** *135* (6), 2330-2337.

[10] (a) Moutet, J.-C.; Pickett, C. J., Iron–sulphur clusters in ionic polymers on electrodes. *J. Chem. Soc., Chem. Commun.* **1989,** 3, 188-190. (b) Pickett, C. J.; Ryder, K. S.; Moutet, J.-C., Synthesis and anodic polymerisation of an L-cystine derivatised pyrrole; copolymerisation with a tetraalkylammonium pyrrole allows reduction of the cystinyl film to a cysteinyl state that binds electroactive $[Fe_4S_4]^{2+}$ centres. *J. Chem. Soc., Chem. Commun.* **1992,** 9, 694-697. (c) Pickett, C. J.; Ryder, K. S.; Moutet, J.-c., Iron–sulfur clusters in ionic polymers on electrodes. *J. Chem. Soc., Dalton Trans.* **1993,** 24, 3695-3703. (d) Pickett, C. J.; Ryder, K. S., Bioinorganic reaction centres on electrodes. Modified electrodes possessing amino acid, peptide and ferredoxin-type groups on a poly(pyrrole) backbone. *J. Chem. Soc., Dalton Trans.* **1994,** 14, 2181-2189.

[11] Rancourt, D. G.; Ping, J. Y., Voigt-based methods for arbitrary-shape static hyperfine parameter distributions in Mössbauer spectroscopy. *Nucl. Instrum. Methods Phys. Res.* **1991**, *58* (1), 85-97.

[12] (a) Morris, W.; Wang, S.; Cho D.; Auyeung, E.; Li, P.; Farha, O. K.; Mirkin, C. A. Role of Modulators in Controlling the Colloidal Stability and Polydispersity of the UiO-66 Metal−Organic Framework. *ACS Appl. Mater. Interfaces* 2017, *9*, 33413-33418; (b) Schaate, A.; Roy, P.; Godt, A.; Lippke, J.; Waltz, F.; Wiebcke, M.; Behrens, P. Modulated Synthesis of Zr-Based Metal–Organic Frameworks: From Nano to Single Crystals *Chem. Eur. J.* 2011, *17*, 6643 – 6651

[13] Friese, V. A. and Kurth, D. G. Soluble dynamic coordination polymers as a paradigm for materials science. *Coord. Chem. Rev.* 2008, *252*, 199–211

[14] (a) Beaucage, G., Approximations Leading to a Unified Exponential/Power-Law Approach to Small-Angle Scattering. *J. Appl. Crystallogr.* **1995,** *28* (6), 717-728. (b) Beaucage, G., Small-Angle Scattering from Polymeric Mass Fractals of Arbitrary Mass-Fractal Dimension. *J. Appl. Crystallogr.***1996,** *29* (2), 134-146. (c) Ilavsky, J.; Jemian, P. R., Irena: tool suite for modeling and analysis of small-angle scattering. *J. Appl. Crystallogr.* **2009,** *42* (2), 347-353.

[15] Hammouda, B.; Worcester, D., The Denaturation Transition of DNA In Mixed Solvents. *Biophys. J.* **2006,** *91* (6), 2237-2242.

[16] Page, C. C.; Moser, C. C.; Chen, X.; Dutton, P. L., Natural engineering principles of electron tunnelling in biological oxidation–reduction. *Nature* **1999,** *402*, 47.

[17] Depamphilis, B. V.; Averill, B. A.; Herskovitz, T.; Que, L.; Holm, R. H., Synthetic Analogs of The Active Sites of Iron-Sulfur Proteins. VI. Spectral and Redox Characteristics of The Tetranuclear Clusters $[Fe_4S_4(SR)_4]^{2-}$. *J. Am. Chem. Soc.* **1974,** *96* (13), 4159-4167.

[18] Venkateswara Rao, P.; Holm, R. H., Synthetic Analogues of The Active Sites of Iron−Sulfur Proteins. *Chem. Rev.* **2004**, *104* (2), 527-560.

[19] O'Sullivan, T.; Millar, M. M., Synthesis and Study of An Analog for the $[Fe_4S_4]^{3+}$ Center of Oxidized High Potential Iron-Sulfur Proteins. *J. Am. Chem. Soc.* **1985,** *107* (13), 4096-4097.

[20] Sun, L.; Park, S. S.; Sheberla, D.; Dincă, M. Measuring And Reporting Electrical Conductivity In Metal-Organic Frameworks: Cd_2(TTFTB) as A Case Study. *J. Am. Chem. Soc.* **2016**, *138* (44), 14772–14782.

[21] Laskowski, E. J.; Frankel, R. B.; Gillum, W. O.; Papaefthymiou, G. C.; Renaud, J.; Ibers, J. A.; Holm, R. H., Synthetic analogs of the 4-Fe active sites of reduced ferredoxins. Electronic properties of the tetranuclear trianions $[Fe_4S_4(SR)_4]^{3-}$ and the structure of $[(C_2H_5)_3(CH_3)N]_3[Fe_4S_4(SC_6H_5)_4]$. *J. Am. Chem. Soc.* **1978,** *100* (17), 5322-5337.

[22] Kanatzidis, M. G.; Baenziger, N. C.; Coucouvanis, D.; Simopoulos, A.; Kostikas, A., Synthesis, structural characterization, and electronic structures of the mixed terminal ligand iron-sulfur cubanes $[Fe_4S_4Cl_2(XPh)_2]^{2-}$ (X = S, O) and $[Fe_4S_4(SPh)_2(OC_6H_4Me\text{-}p)_2]^{2-}$. The first examples of $[Fe_4S_4]^{2+}$ cores with a noncompressed D2d idealized geometry. *J. Am. Chem. Soc.* **1984,** *106* (16), 4500-4511.

[23] Cambray, J.; Lane, R. W.; Wedd, A. G.; Johnson, R. W.; Holm, R. H., Chemical and Electrochemical Interrelationships of the 1-Fe, 2-Fe, And 4-Fe Analogs of The Active Sites of Iron-Sulfur Proteins. *Inorg. Chem.* **1977,** *16* (10), 2565-2571.

[24] Willy, L.; Emil, M., Über Die Salze Der Phosphor-Hexafluorwasserstoffsäure, HPF_6. *Ber. Dtsch. Chem. Ges. (A And B Series)* **1930,** *63* (5), 1058-1070.

[25] Christou, G.; Garner, C. D.; Balasubramaniam, A.; Ridge, B.; Rydon, H. N.; Stiefel, E. I.; Pan, W.-H., Tetranuclear Iron-Sulfur and Iron-Selenium Clusters. In *Inorg. Synth.*, Fackler, J. P. J., Ed. 1982; Vol. 21.

[26] Maiolo, F.; Testaferri, L.; Tiecco, M.; Tingoli, M., Fragmentation of Aryl Alkyl Sulfides. A Simple, One-Pot Synthesis of Polymercaptobenzenes From Polychlorobenzenes. *J. Org. Chem.* **1981,** *46* (15), 3070-3073.

[27] Que, L.; Bobrik, M. A.; Ibers, J. A.; Holm, R. H., Synthetic Analogs of The Active Sites Of Iron-Sulfur Proteins. VII. Ligand Substitution Reactions Of The Tetranuclear Clusters $[Fe_4S_4(SR)]^{2-}$ And The Structure Of Bis(Tetramethylammonium) [tetra-μ-Sulfide-Tetrakis(Benzenethiolato)Tetrairon]. *J. Am. Chem. Soc.* **1974,** *96* (13), 4168-4178.

Chapter 3: Steric and Electronic Effects of Ligand Substitution on Fe_4S_4-based CPs

3.1 Introduction

A large fraction of coordination polymers rely on oxygen rich nodes or secondary building units (SBUs) with bridging linkers that generally bind through O or N.[1] These design principles enable the synthesis of a broad array of materials, and in many cases the functionality of these materials can be tuned by molecular modifications to the organic linkers.[2] Indeed, this synthetic modularity is one of the key strengths of coordination polymer materials.

There are several examples where S-based coordination polymers exhibit exceptional properties, but materials composed of metal-heavy chalcogenide clusters and S-based ligands are still comparatively understudied.[3] The dramatically different synthetic procedures, M-S bond strengths, and stabilities of sulfur-rich coordination polymers raise the question of whether the molecular tunability that is a hallmark of classic coordination polymers is preserved with heavier chalcogenide analogues.

Iron-sulfur clusters, which are key cofactors in biology,[4] are particularly appealing candidates for MOF nodes. Despite this, there have been relatively few examples of materials designed around these units.[5] Previously, our group demonstrated that one of the most thoroughly studied molecular sulfide clusters, Fe_4S_4 clusters, can be linked with 1,4-benzenditiolate (BDT) through solvothermal reactions to generate charged highly crystalline 1D-chain polymers.[6] The physical properties of these materials can be tuned via cluster-based redox events and are also sensitive to the choice of counterions. The comparatively simple composition and structure of these materials prompted us

to examine whether molecular tuning of the dithiolate linker to modulate physical properties would be possible.

Herein, we report new Fe_4S_4-based chains synthesized using two methylated linker variants, 2,5-dimethyl-1,4-benzenedithiol (DMBDT) and 2,3,5,6-tetramethyl-1,4-benzenedithiol (TMBDT). The dimethylated compound $[Fe_4S_4(DMBDT)_2][TBA]_2$ (TBA = NBu_4^+) was generated with the DMBDT ligand and TBA cations (**1**, **Scheme 3.1**). Two permethylated compounds, $[Fe_4S_4(TMBDT)_2][TEA][Li]$ (TEA = NEt_4^+, **2**) and $[Fe_4S_4(TMBDT)_2][TBA]_x[Li]_{2-x}$ (**3**), were made with the TMBDT ligand using either TEA or TBA cations. X-ray powder diffraction (XRPD) data were collected on this group of materials, and the structure of **1** was elucidated via rigorous and detailed *ab initio* structure solution and Rietveld refinement based on synchrotron XRPD data. Cyclic voltammetry (CV) reveals the redox activity of the Fe_4S_4 clusters is maintained, and shows that the degree of methylation of the linker influences the redox potential of these polymers. These results demonstrate that iron-sulfur cluster-based coordination polymers can be tuned by linker functionalization, but that permethylation results in additional changes to packing and properties. This study shows that the properties of S-based coordination polymers can be tuned in an analogous manner to that observed in MOFs supporting that the molecular design principles that are a strength of coordination polymers are also applicable in heavier chalcogenide analogues.

3.2 Results and Discussion

3.2.1 Synthesis and Composition

Solvothermal reaction conditions similar to those previously reported were followed and modified to obtain the desired materials (**Scheme 3.1**).[6] In the case of **1**, $[Fe_4S_4(SPh)_4][TBA]_2$ was

heated with 5 equivalents of DMBDT in acetonitrile (MeCN) resulting in the formation of a dark purple solid. Similarly, the syntheses of **2** and **3** were performed by heating Fe_4S_4 precursors with the appropriate cation with 2 equivalents of TMBDT in MeCN. Consistent with our previous report, the addition of excess $[Li][CF_3SO_3]$ was used to increase crystallinity. During optimization of the synthesis conditions, we also noted that the yield of **3** was increased with the addition of $[TBA][PF_6]$. The influence of these additives underscores the importance that ion concentrations have in the packing and crystallinity of these charged 1D structures.

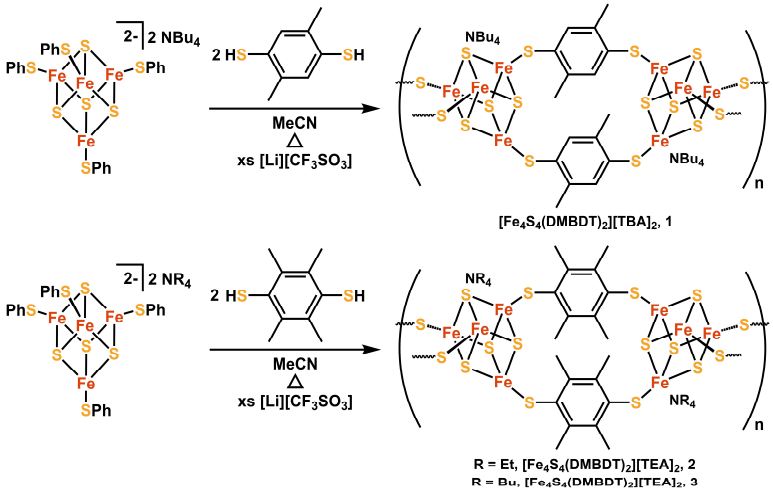

Scheme 3.1. Synthesis of Fe_4S_4 chain compounds 1-3 with differentially methylated 1,4-benzenedithiol ligands.

After isolating **1-3** as solids, we then performed several experiments to examine the chemical composition of these materials. Digestion of **1-3** in 12 M hydrochloric acid followed by extraction in CD_2Cl_2 or C_6D_6 and ^1H NMR analysis confirmed the incorporation of the methylated ligands in the structures (**Figure B.7**, **Figure B**.9 and **Figure B**.11). The complete substitution of the thiophenolate ligands was further established by Infrared spectroscopy (IR) which shows that no thiophenol (-SH) stretches are observed which would be present if residual protonated linkers were present (**Figure B.15**, **Figure B**.16 and **Figure B**.17). This is also confirmed by the absence of thiophenol features in the digestion experiments. Alternatively, digestion in D_2SO_4 diluted with

DMSO-d_6 followed by ^{1}H NMR analysis confirms the incorporation of the counterions, TEA and TBA, in all three corresponding materials (**Figure B.8**, **Figure B**.10 and **Figure B**.12).

X-ray fluorescence (XRF) and X-ray photoelectron spectroscopy (XPS) data were also collected on 1-3 to further corroborate the assigned compositions and ascertain any differences arising from methylation of the linkers. XRF analysis shows Fe:S ratios of 0.5 for **1**, **2**, and **3**, consistent with the expectation of two S-based linkers per Fe_4S_4 cluster (Table A.1). However, while the Fe:S ratio is similar to the previously synthesized unmethylated materials by XRF, XPS data shows a Fe:N ratio for the TMBDT materials higher than expected. In addition, Inductively-Coupled Plasma Mass Spectrometry and Optical Emission Spectroscopy (ICP-MS and ICP-OES) data also shows a significant amount of Li in these materials. These data suggest that the cation composition in the TMBDT materials may be different with some Li^+ replacing the alkyl ammonium cations.

Elemental analysis confirms a more complicated composition for the TMBDT materials. Compound **1** passes combustion analysis for the formula $[Fe_4S_4(DMBDT)_2][TBA]_2$. Conversely, combustion analysis on **2** is more consistent with a formula of $[Fe_4S_4(TMBDT)_2][TEA][Li]$. Notably, this composition is also consistent with both XPS and ICP-MS analysis. We have been unable to obtain combustion analysis on **3** which is consistent with a simple formula and thus we propose the ambiguous formula $[Fe_4S_4(TMBDT)_2][TBA]_x[Li]_{2-x}$. ICP-OES and XPS data on **3** support a comparatively higher Li content ($x \sim 1.3$), and we suspect that variable cations and solvation may make the exact composition of this compound somewhat ill-defined. Nevertheless, the XRF analysis and structural analysis (see below) supports a chain structure in this material as well.

The sum of these composition analyses suggests that the cluster to linker ratio of these materials can be preserved with methylation of the dithiolate linker, but that permethylation of the

benzenedithiolate linker results in a different preferential composition, likely as a result from steric constraints on packing between the comparatively bulky methyl groups with large alkyl ammonium cations.

3.2.2 Structural Determination

The impact of the methyl groups on the packing of compounds **2** and **3** can also be inferred from the crystallinity of these compounds compared with the previous materials $[Fe_4S_4(BDT)_2][NR_4]_2$ as well as **1**. While compound **1** is highly crystalline (see below), similar to the BDT based compounds, both **2** and **3** have limited or no crystallinity. This makes confidently assigning the structure of these materials challenging. While the compositional data supports the possibility of a chain structure, we also worked to obtain structural data to support this assignment. As such, SAXS data were acquired on **3** (**Figure B.28**). Fitting the data provides a power-law slope of −2. Notably, the previous chain materials with BDT show a −5/3 power law. The larger value observed in **3** could in principle be due to the formation of a 2D sheet, but it could also arise from an expanded swollen coil.[7] Such an expanded swollen coil would be expected if the steric requirements of the linker were larger, precisely as is the case in **3**. As such, SAXS data support a similar chain structure in the TMBDT materials even though we do not have an atomically resolved structure for these compounds due to the poor crystalline packing induced by the permethylation of the linkers.

In contrast, the dimethylated material **1** is highly crystalline enabling structure solution from powder data (**Figure 3.1**A).[8] The crystal structure of **1** was solved *ab initio* using chemical crystallographic knowledge from the compound with unmethylated BDT ligands, simulating annealing, and then refined with the Rietveld method from high-resolution (HR) synchrotron XRPD data (**Figure 3.1**). The X-ray data were first collected at the CRISTAL HR XRPD beamline

of the SOLEIL synchrotron [l = 0.72800 Å] on a first sample (**Figure B.23**), and then at the 11-BM HR beamline [λ = 0.45793 Å] of the APS synchrotron on a second subsequently synthesized purer sample. The indexing process (using PREDICT/DICVOL) carried out independently on the data collected at both synchrotrons revealed a tetragonal unit cell with a very large volume of about 12000 Å, approximately four times larger than the tetragonal unit cell of $[Fe_4S_4(BDT)_2][TBA]_2$ (a' = 2a , c' = c).[9] This substantially complicated the solution of this structure, but via a careful analysis a successful solution was obtained.

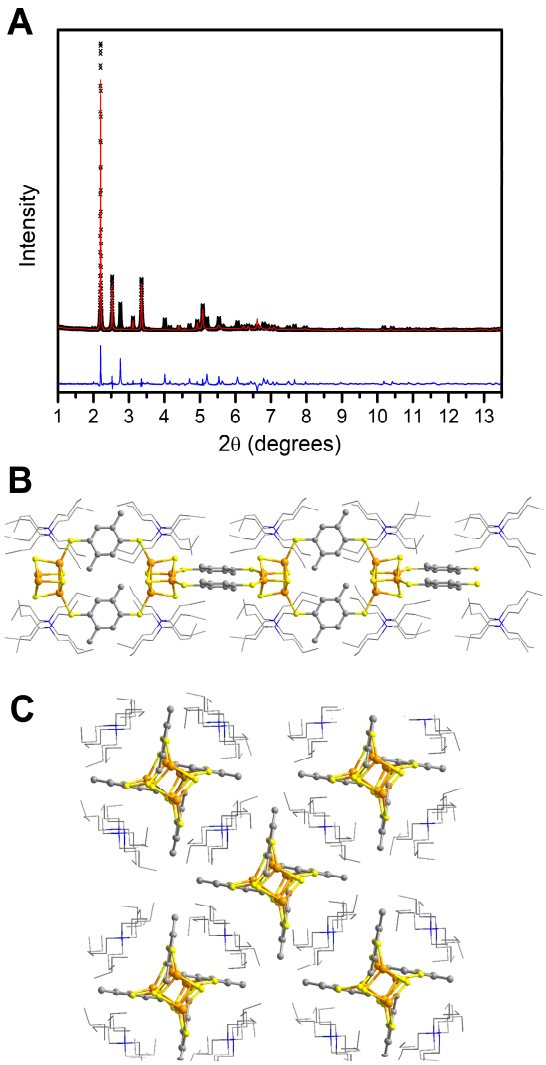

Figure 3.1. Structural determination of compound 1. (A) XRPD pattern (black) with Rietveld fit (red) and residual (blue). (B) Side view of chains with a ball-and-stick model. (C) End view of chains

We initially assumed, based on our previous compounds, that the structure consisted of $Fe_4S_4(DMBDT)_2$ chains running along the *c*-axis, with TBA cations located at about the mid-distance between the Fe_4S_4 clusters and neighboring chains. The unit cell content as well as the symmetry of the two distinct moieties in **1** puts a limit on the overall symmetry of the unit cell, thus restricting Z to a maximum value of 8 and yielding a large volume of about 1500 Å for the asymmetric unit.

A high symmetry space group $P4_2/ncm$ (#138) with Z = 16 accounts for all of the X-ray 11-BM data reflections and absences, whereas the CRISTAL data were marred with a few weak impurity lines. As the polymeric $Fe_4S_4(DMBDT)_2$ chains are incompatible with diagonal mirror symmetry, the $P4_2/n$ (#86) with Z = 8 tetragonal space group, which is a maximal subspace group of $P4_2/ncm$, was chosen instead. The validity of a chemically sensible packing of the components of **1** using the $P\ 4_2/n$ space group was established using FOX simulations with Simulated Annealing and Rigid Bodies.[10] As mentioned, the large volume of the unit cell and the large number of independent atoms (150) in **1** presents a significant challenge for structure solution. To alleviate this issue, we started with the most symmetric models that involve the smallest number of free parameters.

In the present case, the crystal structure comprises two distinct building blocks of $Fe_4S_4(DMBDT)_2$ and TBA. The initial Fe_4S_4 cluster was modeled using literature-based bond lengths of Fe–S = 2.272 Å and Fe–Fe = 2.735 Å in the cuboidal core which yields a S–S distance of 3.610 Å if one assumes perfectly regular S and Fe tetrahedra in the cluster.[11] For the DMBDT molecules, the C–C bond lengths were taken as 1.4 Å, 1.506 Å for the C–S bonds, and 1.0 Å for the C–H bonds. The TBA molecule was built using C–N and C–C bond lengths both equal to 1.51 Å, as well as a C–H bond distance of 1.0 Å.

The model of the polymeric $Fe_4S_4(DMBDT)_2$ chain was built using the previously reported structure of $[Fe_4S_4(BDT)_2][TBA]_2$.[6] To reduce the number of variables, an initial starting extended model was built with coplanar DMBDT rings to make them related through an inversion center. Further distortion of the 1D chain is carried out to maintain the maximum symmetry to allow chemically sensible H···H interatomic distances. This procedure results in a rotation of the two DMBDT sides by 19° with respect to the main chain. For further details on the structural manipulations and the Python code written to perform them, see Appendix B. The rotation of the independent DMBDT rings requires that the whole 1D polymeric chain be counter-rotated by 8° in order to leave as much space as possible for the TBA cations. Alternative rotations of the chains and ligands were also considered but were rejected based on the quality of their Rietveld refinements (see Appendix B).

For symmetry reasons, the N atoms of the TBA cations were placed at midpoints between the centers of neighboring Fe_4S_4 clusters. This choice leads to the (0 1/4 1/4) and (0 3/4 1/4) independent positions in the unit cell. The positioning of the whole TBA cations (in spite of a deceptive two-fold indetermination) was chosen unequivocally to produce the largest S···C interatomic contacts resulting in a good agreement with the associated van der Waals distance (3.5 Å). The outer $-CH_2-CH_3$ tails of the butyl substituents were also adjusted in compliance with the molecular bond distances and bond angles in order to further minimize a number of other very short interatomic contacts such as C···H and H···H interactions between neighboring TBA cations or TBA cations and an adjacent polymeric chain.

The obtained model was then 'frozen' and used for the Rietveld refinement using the GSAS software package producing a final Rp value of approximately 15% (**Figure 3.1**A).[12] Further Rietveld refinement attempts using numerous alternatives and often conflicting structural restraints

led to unsolvable problems with respect to the least-squares convergence. While the rigid-body approach is certainly an acceptable structure solution in this case, a less than ideal fit (which is typically considered to be less than 15% for the Rp factor of merit) is obtained due to the need to use a higher symmetry than is likely for the molecular subunits in order to describe this large crystal structure (1200 atoms in the unit cell). With this in mind, only the intermolecular contacts and general packing can be reliably interpreted.

The crystal structure of **1** consists of chains of Fe_4S_4 clusters connected by pairs of DMBDT groups surrounded by TBA cations. Another way to look at the suggested crystal structure is in terms of TBA-built tubes or TBA-sheaths surrounding each 1D $Fe_4S_4(DMBDT)_2$ polymeric chain (**Figure 3.1**B and C and **Figure B**.27). This is overall similar to the previously reported complex $[Fe_4S_4(BDT)_2][TBA]_2$.[6] The separation between Fe_4S_4 clusters within the polymeric chains is now 10.38 Å, which is slightly more than the previously observed value of 9.92 Å. This expanded value is consistent with the larger steric constraints imposed by the methylation of the linker. Furthermore, while the sheathed structure of **1** is similar to that observed in $[Fe_4S_4(BDT)_2][TBA]_2$ the overall packing of the chains and countercations is quite different, as is clearly illustrated by an end-on view of the structure (**Figure 3.1**C).

Overall, this challenging structural analysis verifies that the chain structure of these compounds is preserved in **1**. Furthermore, the packing and inter-cluster distances observed in **1** support that the steric constraints of the organic linker, even with the substitution of two comparatively small methyl groups, can have a large perturbative effect on the structure. This is consistent with the poorer crystallinity and alternative cation incorporation observed in **2** and **3**. With a firmer picture of the structural ramifications of linker methylation we then turned to examining what electronic effects this substitution had.

3.2.3 Electronic Properties

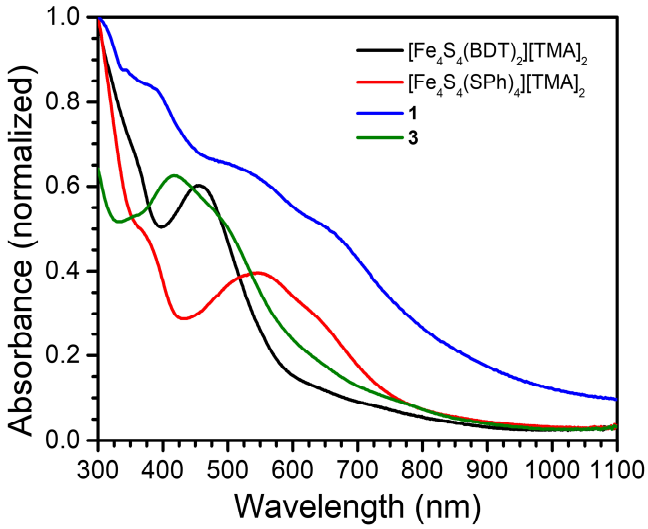

Figure 3.2. Normalized UV-visible spectra of 1, 3, and reference compounds in DMF solution.

UV-visible spectroscopy (UV-vis) was initially employed to investigate the electronic properties of **1** and **3** (**Figure 3.2**). Unfortunately, **2** was insoluble in all solvents we examined, precluding more detailed characterization of its properties. In our previous work we used shifts in features at around 450 nm from the monomeric clusters, assigned as ligand-to-metal charge transfer transitions, as markers for how electron-rich the chains were. Given this hypothesis, we expected to observe more significant red-shifts in the methylated materials arising from an increased inductive donation. A shift in comparison to monomeric iron-sulfur clusters is observed as expected, however, a comparison to the unmethylated BDT derivative is convoluted by broadening and splitting of the features. Nevertheless, there appears to be little to no shift in the energies of the features between **1** and $[Fe_4S_4(BDT)_2][TMA]_2$ with the main features in **1** coming at ~530 and ~660 nm. Furthermore, compound **3** doesn't show similarly red-shifted features, but instead shows one blue shifted feature at ~420 nm and another shoulder at ~500 nm when compared with $[Fe_4S_4BDT_2][[TMA]_2$ and the monomeric thiophenolate capped cluster.

These results are inconsistent with our initial hypothesis, but are actually expected based on prior literature studies on the effect of methylation of thiophenolate donors on Fe_4S_4 clusters.[13] The enhanced steric requirements imposed by methylation can influence both the Fe–S distance as well as the Fe–S–C angle, causing differential red- or blue-shifts based on different donation from S as a result of these structural changes. Indeed, the structure of **1** shows different orientations of the linker due to methylation, supporting this conclusion. We propose that there is competition between enhanced donation from the methyl groups and steric constraints in **1**, resulting in no significant shift from the features in $[Fe_4S_4BDT_2][TMA]_2$, but that steric effects dominate in **3** resulting in the observed blue-shift. As a final point, the observed solution absorbances of **1** and **3** are also seen in solid state diffuse reflectance data which further supports that similar structures are maintained between solution and solid phases (Figure B.18 and Figure B.19).

We also performed electrochemical analysis to further investigate how methylation affects the electronic structure of these chains. Two iron-sulfur cluster reductive features were observed previously, corresponding to the $[Fe_4S_4]^{2+}/[Fe_4S_4]^{+}$ and $[Fe_4S_4]^{+}/[Fe_4S_4]^{0}$ couples. As before, the redox activity of **1** and **3** was examined by cyclic voltammetry in a solution of Dimethylformamide (DMF) with $[Li][CF_3SO_3]$ as the electrolyte (**Figure 3.3**). The reductive features for the unmethylated material were observed at −1.6 and −2.2 V vs $FeCp_2^{+}/FeCp_2$. Slight shifts to more negative potentials are observed for **1**, with similar features observed at −1.8 and −2.3 V vs $FeCp_2^{+}/FeCp_2$, confirming the hypothesis that more electron-donating methyl-substituted linkers results in more electron-rich chains. These results also demonstrate that the redox activity of the Fe_4S_4 clusters is preserved even with methylation on the ligand. The first reductive feature, assigned as the $[Fe_4S_4]^{2+}/[Fe_4S_4]^{+}$ couple is reversible upon cycling but the second feature is only quasi-reversible (**Figure B.20**).

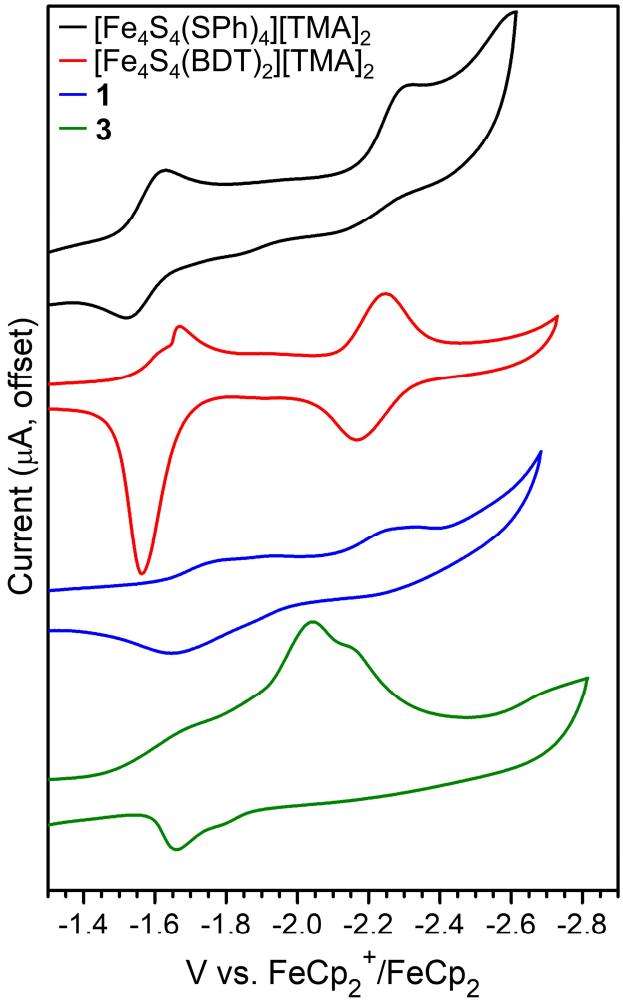

Figure 3.3. Cyclic voltammograms of 1, 3, unmethylated $[Fe_4S_4(BD\text{-}T)_2][TMA]_2$, and monomeric $[Fe_4S_4(SPh)_4][TMA]_2$. Conditions: DMF, 0.2 M $[Li][CF_3SO_3]$, 0.1 V/s.

While the voltammogram of **1** displays a similar pattern to that of $[Fe_4S_4(BDT)_2][[TMA]_2$, the voltammogram of **3** is significantly different. The first reductive feature of **3** shifts to more negative potentials but the second reductive feature shifts to more positive potentials. This observation is consistent with the UV-vis data suggesting that the steric constraints in **3** lead to a more complicated effect on electronic structure than would be expected from a simple enhancement of donation from methylation. Finally, we also collected electrical conductivity data for **1**-**3** which were generally consistent with the unmethylated material (**Table B.2**). This is consistent with the

hypothesis that bulk electrical conductivity is more limited by the insulating alkylammonium cations than the inherent electronic structure of the chains.

3.3 Conclusion

In this work we have examined how linker methylation affects the physical properties of coordination polymer chains composed of Fe_4S_4 clusters. Solvothermal synthesis enabled the generation of three new chain materials. The structure of the dimethylated DMBDT variant **1** was determined by *ab initio* structure solution and Rietveld refinement. Further methylation, however, led to Li incorporation and more complicated structures, compositions, and solubility. The electronic structures of these new materials were investigated by UV-vis spectroscopy and electrochemistry. These analyses show parallels between how methylation affects the electronic structure of molecular and extended materials composed of Fe_4S_4 clusters. Overall, this work describes a systematic approach in exploring the effects of methylation on the ligand component of S-based coordination polymers. Importantly, the molecular design principles that make coordination polymers attractive classes of materials for many applications are preserved in heavier chalcogenide analogues, paving the way to expanding families of these promising materials.

3.4 Experimental Section

General Methods

All manipulations were performed under an inert atmosphere of dry nitrogen gas using a Schlenk line or N_2-filled MBraun UNILab glovebox unless otherwise noted. ^{1}H NMR measurements were performed on Bruker DRX 400 or 500 spectrometers. Elemental analyses (C, H, N) were performed by Midwest Microlabs. Dimethylformamide (DMF) and acetonitrile (MeCN) were initially dried and purged with N_2 on a solvent purification system from Pure Process Technology. DMF and MeCN were then passed through activated alumina and stored over 4Å molecular sieves. Dimethylacetamide (DMA) was sparged with N_2, transferred into the glovebox, passed through activated alumina and stored over 4Å molecular sieves. [TBA][PF_6] was recrystallized from H_2O and dried at 160 °C before use. [$Fe_4S_4(SPh)_4$][TEA]$_2$, [$Fe_4S_4(SPh)_4$][TBA]$_2$ were prepared as previously described.[14] 1,4-dibromo-tetramethylbenzene was prepared following literature procedure.[15] The synthesis of 1,4-bis(isopropylthio)-2,3,5,6-tetramethylbenzene and 1,4-bis(isopropylthio)-2,5-dimethylbenzene were performed via modification of a related synthesis.[6] 2,5-dimethyl-1,4-benzenedithiol and 2,3,5,6- tetramethyl-1,4-benzenedithiol have been previously reported,[16] but were synthesized using an alternate procedure as shown below.[6] All synthesis of **1-3** were conducted in a N_2-filled glovebox. All other chemicals were purchased through commercial means unless noted.

1,4-Bis(isopropylthio)-2,5-dimethylbenzene

A dispersion of 60% NaH in mineral oil (6.4 g, 160 mmol) was added to a 500 mL three-neck flask and then washed with hexane twice and DMA once under a N_2 atmosphere. After adding DMA (33 mL), 2-propanethiol (17.3 mL, 160 mmol) was injected slowly and in portions to avoid excessive foaming (if necessary, use of an ice bath and drop funnel is helpful). Subsequently, DMA

(33 mL) and a solution of 2,5-dimethyl-1,4-dibromobenzene (10.56 g. 40 mmol) in DMA (50 mL) were injected, and the mixture was heated for 17 h to 100 °C. The mixture was cooled, poured into 33 mL saturated NaCl solution and extracted with Et_2O (3 × 33 mL). The organic layer was washed with H_2O (5 × 50 mL), dried with [Mg][SO_4], and evaporated. The yellowish solid was further purified by vacuum distillation. Yield: 9.9 g (97%).^{1}H NMR (400 MHz, $CDCl_3$) δ 7.19 (1 H, s), 3.33 (2 H, spt, J = 8.0 Hz), 2.35 (12 H, s), 1.30 (12 H, d, J = 4 Hz) ppm. ^{13}C NMR (400 MHz, $CDCl_3$) δ 20.36, 23.25, 37.81, 133.21, 133.27, 137.24. Anal. Calc. for $C_{14}H_{22}S_2$: C 66.09%, H 8.72%. Found: C 66.24%, H 8.84%.

2,5-dimethyl-1,4-benzenedithiol

Sodium (4.0 g, 180 mmol), dry DMA (100 mL) from the glovebox, and 1,4-Bis(isopropylthio)benzene (4.5 g, 18 mmol) were added in sequence to a 250 mL three-necked flask under N_2 atmosphere and the mixture was heated to 100 °C for 8 h. During this time the reaction mixture became yellow with thick precipitate. The reaction solution was quenched with diluted HCl solution (concentrated HCl solution (34−37% w/w, 20 mL) + H_2O (105 mL)) in an ice bath and stirred for another 0.5 h under an inert atmosphere. The mixture was then extracted with Et_2O (2 × 75 mL). The organic layer was washed with H_2O (5 × 30 mL), dried with [Mg][SO_4], and evaporated. A white powder was obtained by washing with hexanes (20 mL). More product can be recovered by storing the hexane washes in a freezer (−35 °C) overnight, resulting in a pale yellow powder. Overall yield: 2.4 g (80%). ^{1}H NMR (400 MHz, $CDCl_3$) δ 7.09 (2 H, s), 3.20 (2 H, s), 2.25 (2 H, s) ppm. Other spectroscopic characterization was identical to that previously reported.[16a]

1,4-bis(isopropylthio)-2,3,5,6-tetramethylbenzene

A dispersion of 60% NaH in mineral oil (6.4 g, 160 mmol) was added to a 500 mL three-neck flask and then washed with hexane twice and DMA once under a N_2 atmosphere. After adding DMA (40 mL), 2-propanethiol (17.4 mL, 160 mmol) was injected slowly and in portions to avoid excessive foaming. Subsequently, DMA (40 mL) and a solution of 1,4-dibromo-tetramethylbenzene in DMA (40 mL) were injected, and the mixture was heated for 17 h to 100 ºC. The mixture was cooled, poured into 40 mL saturated brine solution and extracted with Et_2O (3 × 50 mL). The organic layer was washed with H_2O (4 × 30 mL), dried with [Mg][SO_4] and evaporated. The final product was white powders. Yield: 11.5 g (99%). ^{1}H NMR (400 MHz, $CDCl_3$) δ 3.01 (2 H, spt, J = 3.0 Hz), 2.58 (12 H, s), 1.18 (12 H, d, J = 1.2 Hz) ppm. ^{13}C NMR (400 MHz, $CDCl_3$) δ 20.56, 23.25, 39.69, 134.84, 139.47. Anal. Calc. for $C_{16}H_{26}S_2$: C 68.03%, H 9.28%. Found: C 68.85%, H 9.51%.

2,3,5,6-tetramethyl-1,4-benzenedithiol

Sodium (1.8 g, 80 mmol), dry DMA (40 mL) from the glovebox, and 1,4-bis(isopropylthio)-2,3,5,6-tetramethylbenzene (5.6 g, 20 mmol) were added in sequence to a 125 mL three-neck flask under N_2 atmosphere and the mixture was heated to 100 C for 8h. The reaction solution was quenched with diluted HCl (concentrated HCl solution (34-37% w/w, 10 mL) + H_2O (50 mL)) in an ice bath and stirred for another 0.5 h under an inert atmosphere. The mixture was extracted with Et_2O (3 × 50 mL). The organic layer was then washed with H_2O (5 × 30 mL), dried with [Mg][SO_4] and evaporated. A white powder was obtained by washing with cold hexanes (20 mL) and dried. The product was stored in the glovebox for the usage. Yield: 2.7 g (69%). ^{1}H NMR (400 MHz, $CDCl_3$) δ 3.19 (2 H, s), 2.40 (12 H, s) ppm. Other spectroscopic characterization was identical to that previously reported.[16b]

[$Fe_4S_4(DMBDT)_2$][TBA]$_2$ (1)

[$Fe_4S_4(SPh)_4$][TBA]$_2$ (190 mg, 0.15 mmol) and [Li][CF_3SO_3] (117 mg, 0.75 mmol) were added to a 24 mL vial and dissolved in MeCN (4 mL). A solution of 2,5-dimethyl-1,4- benzenedithiol (130 mg, 0.75 mmol) in MeCN (3 mL) was added and the vial was sealed and placed in a heating block on a 100 °C hot plate. The reaction mixture was heated for 2 days and the solid was separated by centrifugation, washed with MeCN (4 × 4 mL), and dried under vacuum. A dark-purple solid was obtained (53 mg, 30%). Anal. Calc. for $Fe_4S_8C_{48}H_{88}N_2$: C 49.15%, H 7.56%, N 2.39%. Found: C 49.98%, H 7.44%, N 2.55%.

[$Fe_4S_4(TMBDT)_2$][TEA][Li] (2)

[$Fe_4S_4(SPh)_4$][TEA]$_2$ (105 mg, 0.10 mmol) and [Li][CF_3SO_3] (300 mg, 2.0 mmol) were added to a 24 mL vial and dissolved in MeCN (6 mL). A solution of 2,3,5,6-tetramethyl-1,4-benzenedithiol (40 mg, 0.20 mmol) in MeCN (4 mL) was added and the vial was sealed and placed in a heating block on a 100 °C hot plate. The reaction mixture was heated for 2 days and further separated by centrifugation, washed with MeCN (4 × 4 mL), and dried under vacuum. A dark-brown solid was obtained (46 mg, 45%). Anal. Calc. for $Fe_4S_8C_{28}H_{44}NLi$: C 38.15%, H 5.03%, N 1.59%. Found: C 36.83%, H 5.38%, N 1.64%.

[$Fe_4S_4(TMBDT)_2$][TBA]$_x$[Li]$_{2-x}$ (3)

[$Fe_4S_4(SPh)_4$][TBA]$_2$ (130 mg 0.10 mmol), [Li][CF_3SO_3] (620 mg, 4.0 mmol), and [TBA][PF_6] (38 mg, 0.10 mmol) were added to a 24 mL vial and dissolved in MeCN (6 mL). A solution of 2,3,5,6-tetramethyl-1,4- benzenedithiol (40 mg, 0.20 mmol) in MeCN (4 mL) was added and the vial was sealed and placed in a heating block on a 100 °C hot plate. The reaction mixture was heated for 2 days and further separated by centrifugation, washed with MeCN (4 × 4 mL), and

dried under vacuum. A dark-brown solid was obtained (38 mg, 31%). We were unable to obtain a combustion analysis consistent with a simple molecular formula.

3.5 References

[1] a) H. Deng, S. Grunder, K. E. Cordova, C. Valente, H. Furukawa, M. Hmadeh, F. Gandara, A. C. Whalley, Z. Liu, S. Asahina, H. Kazumori, M. O'Keeffe, O. Terasaki, J. F. Stoddart and O. M. Yaghi, *Science*, 2012, **336**, 1018–1023. b) X. Zhang, Z. J. Chen, X. Y. Liu, S. L. Hanna, X. J. Wang, R. Taheri-Ledari, A. Maleki, P. Li and O. K. Farha, *Chem. Soc. Rev.*, 2020, **49**, 7406-7427. c) H. Ghasempour, K. Y. Wang, J. A. Powell, F. ZareKarizi, X. L. Lv, A. Morsali and H. C. Zhou, *Coord. Chem. Rev.*, 2021, **426**.

[2] a) O. M. Yaghi, M. O'Keeffe, N. W. Ockwig, H. K. Chae, M. Eddaoudi and J. Kim, *Nature*, 2003, **423**, 705-714. b) X. Kong, H. Deng, F. Yan, J. Kim, J. A. Swisher, B. Smit, O. M. Yaghi and J. A. Reimer, *Science*, 2013, **341**, 882-885. c) W. Lu, Z. Wei, Z.-Y. Gu, T.-F. Liu, J. Park, J. Park, J. Tian, M. Zhang, Q. Zhang, T. Gentle Iii, M. Bosch and H.-C. Zhou, *Chem. Soc. Rev.*, 2014, **43**, 5561-5593. d) T. Islamoglu, S. Goswami, Z. Y. Li, A. J. Howarth, O. K. Farha and J. T. Hupp, *Acc. Chem. Res.*, 2017, **50**, 805-813. e) O. M. Yaghi, *ACS Central Science*, 2019, **5**, 1295-1300.

[3] a) Z. Ji, C. Trickett, X. Pei and O. M. Yaghi, *J. Am. Chem. Soc.*, 2018, **140**, 13618-13622. b) J. Xie, L. Wang, and J. S. Anderson, *Chem. Sci.*, 2020, **11**, 8350−8372. c) J. A. Kephart, C. G. Romero, C.-C. Tseng, K. J. Anderton, M. Yankowitz, W. Kaminsky and A. Velian, *Chemical Science*, 2020, **11**, 10744-10751. d) Y. Kamakura and D. Tanaka, *Chem. Lett.*, 2021, **50**, 523-533.

[4] a) H. Beinert, R. H. Holm and E. Münck, *Science*, 1997, **277**, 653-659. b) P. Venkateswara Rao and R. H. Holm, *Chem. Rev.*, 2004, **104**, 527-560. c) W. E. Broderick, B. M. Hoffman and J. B. Broderick, *Acc. Chem. Res.*, 2018, **51**, 2611-2619. d) R. D. Britt, G. Rao and L. Tao, *Nature Reviews Chemistry*, 2020, **4**, 542-549. e) Brown, A.C.; Suess, D. L. M.; in *Comprehensive Coordination Chemistry 3* (2021).

[5] a) J.-C. Moutet and C. J. Pickett, *J. Chem. Soc., Chem. Commun.*, 1989, **3**, 188-190. b) C. J. Pickett, K. S. Ryder and J.-C. Moutet, *J. Chem. Soc., Chem. Commun.*, 1992, **9**, 694-697. c) C. J. Pickett, K. S. Ryder and J. C. Moutet, *J. Chem. Soc. Dalton*, 1993, **24**, 3695-3703. d) C. J. Pickett and K. S. Ryder, *J. Chem. Soc. Dalton*, 1994, **14**, 2181-2189. e) C. J. Pickett, S. K. Ibrahim and D. L. Hughes, *Faraday Discuss.*, 2000, **116**, 235-244. f) T. P. N., B. Thomas, P. Vasilios and K. M. G., *Angew. Chem. Int. Ed.*, 2000, **39**, 4558-4562. g) B. D. Yuhas, C. Prasittichai, J. T. Hupp and M. G. Kanatzidis, *J. Am. Chem. Soc.*, 2011, **133**, 15854-15857. h) Y. Shim, B. D. Yuhas, S. M. Dyar, A. L. Smeigh, A. P. Douvalis, M. R. Wasielewski and M. G. Kanatzidis, *J. Am. Chem. Soc.*, 2013, **135**, 2330-2337. i) J. Liu, M. S. Kelley, W. Wu, A. Banerjee, A. P. Douvalis, J. Wu, Y. Zhang, G. C. Schatz and M. G. Kanatzidis, *Proc. Natl. Acad. Sci.*, 2016, **113**, 5530-5535. j) Y. Shim, R. M. Young, A. P. Douvalis, S. M. Dyar, B. D. Yuhas, T. Bakas, M. R. Wasielewski and M. G. Kanatzidis, *J. Am. Chem. Soc.*, 2014, **136**, 13371-13380.

[6] N. E. Horwitz, J. Xie, A. S. Filatov, R. J. Papoular, W. E. Shepard, D. Z. Zee, M. P. Grahn, C. Glider, and J. S. Anderson, *J. Am. Chem. Soc.,* 2019, **141**, 3940–3951.

[7] a) G. Beaucage, *J. Appl. Crystallogr.*, 1995, **28**, 717-728. b) G. Beaucage, *J. Appl. Crystallogr.*, 1996, **29**, 134-146.

[8] David, W.I.F., K. Shankland, L.B. McCusker, and C. Bärlocher, eds. *Structure Determination from Powder Diffraction Data*. Oxford: Oxford University Press, **2006**. Oxford Scholarship Online, **2010**.

[9] a) D. Louër and A. Boultif, *Powder Diffr.*, 2014, **29**, S7-S12. b) J. R. Blanton, R. J. Papoular and D. Louër, *Powder Diffr.*, 2019, **34**, 233-241.

[10] V. Favre-Nicolin and R. Cerny, *J. Appl. Crystallogr.*, 2002, **35**, 734-743.

[11] a) L. Que, M. A. Bobrik, J. A. Ibers and R. H. Holm, *J. Am. Chem. Soc.*, 1974, **96**, 4168-4178. b) T. O'Sullivan and M. M. Millar, *J. Am. Chem. Soc.*, 1985, **107**, 4096-4097. c) T. J. Ollerenshaw, C. D. Garner, B. Odell and W. Clegg, *J. Chem. Soc. Dalton*, 1985, **10**, 2161-2165.

[12] A.C. Larson and R.B. Von Dreele, "General Structure Analysis System (GSAS)", (Report No. 86-748), Los Alamos National Laboratory, Los Alamos, NM.

[13] N. Ueyama, T. Sugawara, M. Fuji, A. Nakamura, and N. Yasuoka, *Chem. Lett.*, 1985, **14**, 175-178.

[14] G. Christou, C. D. Garner, A. Balasubramaniam, B. Ridge, H. N. Rydon, E. I. Stiefel,and W. H. Pan. *Inorg. Synth.,* 1982, **21**, 33.

[15] I. Kaur, M. Jazdzyk, N. N. Stein, P. Prusevich, and G. P. Miller, *J. Am. Chem. Soc.,* 2010, **132**, 1261-1263.

[16] a) P. Beimling and G. Koßmehl, *Chem. Ber.* 1986, **119**, 3198-3203. b) M. S. Raasch, *J. Org. Chem.* 1979, **44**, 2629–2632.

Chapter 4: Tin Dithiolene Transmetalating Agents and Resulted Complexes

4.1 Introduction

As discussed in the introduction chapter, TTFtt has been proposed as an attractive building block for molecular materials for two decades as it combines the redox chemistry of TTF and dithiolene units.[1] $TTFttH_4$, however, is inherently unstable and the incorporation of TTFtt units into complexes or materials typically proceeds through the *in-situ* generation of the tetraanion $TTFtt^{4-}$. Capping of $TTFtt^{4-}$ with Bu_2Sn^{2+} units dramatically improves the stability of the TTFtt moiety and furthermore enables the isolation of a redox series where the TTF core carries the formal charges of 0, +1, and +2. All of these redox congeners show efficient and clean transmetalation to Ni and Pd resulting in an analogous series of bimetallic complexes capped by 1,2-bis(diphenylphosphino)ethane (dppe) ligands. Furthermore, by using the same transmetalation method, we synthesized analogous palladium complexes capped by 1,1'-bis(diphenylphosphino)ferrocene (dppf) which had been previously reported. All of these species have been thoroughly characterized through a systematic survey of chemical and electronic properties by techniques including cyclic voltammetry (CV), ultraviolet-visible-near infrared spectroscopy (UV-vis-NIR), electron paramagnetic resonance spectroscopy (EPR), nuclear magnetic resonance spectroscopy (NMR) and X-ray diffraction (XRD). These detailed synthetic and spectroscopic studies highlight important differences between the transmetalation strategy presented here and previously reported synthetic methods for the installation of TTFtt.

In addition, the utility of this stabilization strategy can be illustrated by the observation of unusual TTF radical-radical packing in the solid state and dimerization in the solution state.

Theoretical calculations based on variational 2-electron reduced density matrix methods have been used to investigate these unusual interactions and illustrate fundamentally different levels of covalency and overlap depending on the orientations of the TTF cores. Taken together, this work demonstrates that tin-capped TTFtt units are ideal reagents for the installation of redox-tunable TTFtt ligands enabling the generation of entirely new geometric and electronic structures.

4.2 Results and Discussion

4.2.1 Synthesis of Sn and Ni Capped TTFtt Redox Congeners

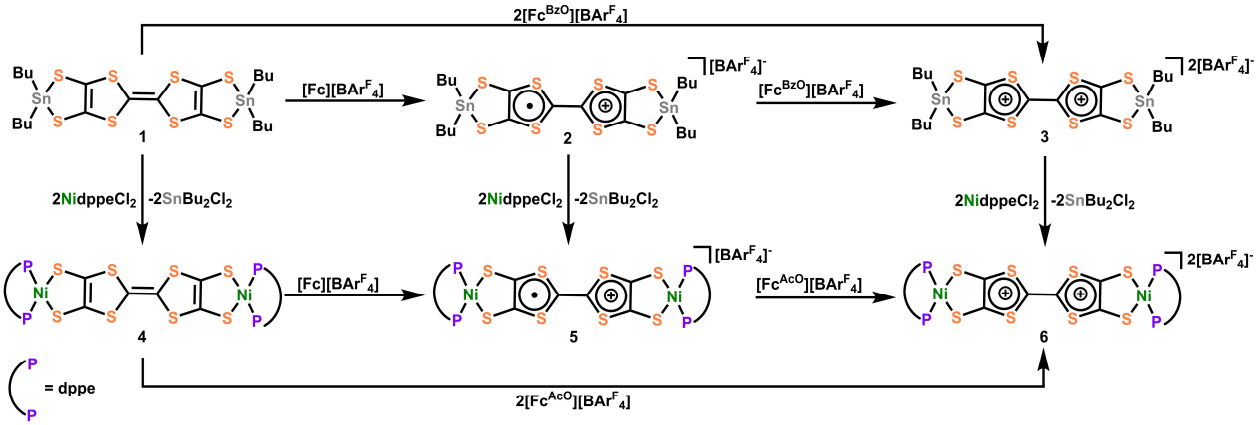

Scheme 4.1. The synthesis of Sn and Ni complexes with TTFtt as a bridging ligand.

All of the reactions involved with Sn and Ni complexes are summarized in **Scheme 4.1**. Compound **1** was synthesized via deprotection of TTFtt$(C_2H_4CN)_4$ with excess sodium methoxide and subsequent reaction with excess Bu_2SnCl_2 in MeOH. In contrast to the high reactivity of the $TTFtt^{4-}$ tetra-anion, **1** was indefinitely stable as a solid at room temperature and red crystals can be obtained via recrystallization from boiling acetonitrile at 80 °C. The stability of **1** under these conditions suggests that the use of common solvothermal synthetic conditions for coordination polymers should be viable. The CV of neutral **1** shows two quasi-reversible features, suggesting

that two oxidized species are chemically accessible (**Figure 4.1**A). The reagents [Fc][BAr^F_4] and [Fc^{BzO}][BAr^F_4] (Fc^+ = ferrocenium, Fc^{BzO} = benzoyl ferrocenium) were therefore used to chemically access the singly and doubly oxidized redox congeners, **2** and **3**. While brown crystals of **2** were obtained which verified the proposed structure of this compound, the oxidation reaction of **1** with 2 equivalents of [Fc^{BzO}][BAr^F_4] under the same conditions led to the formation of **3•2Fc^{BzO}** where each Sn center is coordinated by an additional Fc^{BzO} molecule (**Figure C.53**). To avoid the formation of these adducts, the reaction and crystallization were both conducted in THF solvent which enabled the isolation of green crystals of **3•2THF**.

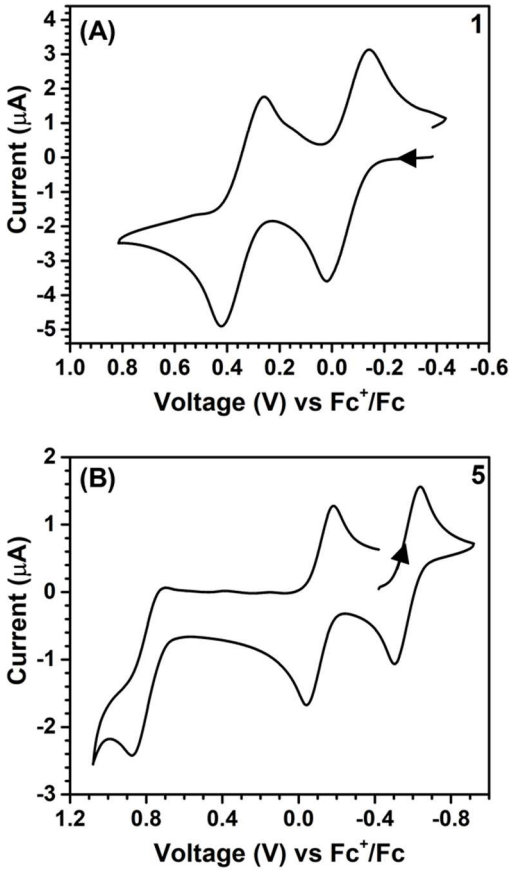

Figure 4.1. Cyclic voltammograms of 1 (a) and 5 (b). Arrow denotes scan direction.
Conditions: DCM, 0.1 M [TBA][PF6], 0.1 V/s.

The ability of these stannylated species for ligand transmetalation was tested by reactions with 2 equivalents of dppe$NiCl_2$ in DCM or Et_2O at room temperature. All metalation processes proceed smoothly and provide the three corresponding dinickel complexes, **4**-**6**, in good yield. Complex **4** with a formally neutral TTF core was obtained as an insoluble orange-yellow powder. Compounds **5** and **6**, however, were much more soluble enabling crystallization as dark brown and purple crystals respectively. The Ni complexes are also redox-active as indicated by their CV's which show two quasi-reversible oxidations shifted ~0.4 V more negative than those observed in **1** (**Figure 4.1**B). Compounds **5** and **6** could also be generated by oxidizing **4** with $[Fc][BAr^F{}_4]$ and $[Fc^{AcO}][BAr^F{}_4]$ (Fc^{AcO} = acetyl ferrocenium) respectively as verified by NMR spectroscopy.

These compounds demonstrate that the stannylation of the reactive and unstable $TTFtt^{4-}$ anion is an effective strategy to both stabilize unusual redox series as well as to enable facile transmetalation to transition metals. These tin agents are much more stable than conventional *in-situ* formed $TTFtt^{4-}$ anions, allowing for purification, long-term storage, and convenient utility under a wide range of conditions with various solvents. In addition to these advantages, complexes **2** and **3** provide additional synthetic flexibility via controlled redox "doping." For instance, complex **2**, with a TTF radical cation core, enables direct insertion of radical linkers between metal centers. Furthermore, **3** is one of only a few examples of isolable dicationic TTF motifs.[2, 3] The facile redox and transmetalation chemistry of **1**-**3** paves the way for the synthesis of new materials with precisely tuned redox states.

4.2.2 Solid State Structures

Compounds **1**-**3**, **5**, and **6** have been crystallographically characterized and their single crystal X-ray diffraction (SXRD) structures are shown in **Figure 4.2**. Their packing patterns are shown in

Figure C.48 - Figure C.52. Compounds **1**, **3**, and **5** crystallize in the triclinic space group P-1, compounds **2** and **6** crystallize in the monoclinic space groups $P2_1/c$ and C2/c, respectively. The geometrical parameters of the TTF cores such as bond lengths and dihedral angles are typically sensitive to the redox state of the TTF unit.[2f] Interestingly, in the present Sn capped redox series some of these changes are muted. For instance, planarization of the TTF core is typically observed only upon oxidation, but in **1** the neutral TTF rings are nearly coplanar (**Figure C.46**). The trends in the C–C and C–S bond lengths are more informative and are shown in **Table 4.1**. As the molecular charge increases, the C–C bond distances in the TTF cores also increase, while the C–S bond lengths generally decrease. These trends are consistent for both the Sn series in **1**-**3** and the Ni series from **5** to **6**. These changes are consistent with previous studies showing similar geometric trends upon oxidation of TTF molecules.[2f] Conversely, there is little change or trend in the M–S distances for either the Sn or the Ni complexes, supporting the assignment of primarily TTF-centered redox events.

Most of these compounds also display intermolecular TTF-TTF packing interactions in their SXRD structures, as has been observed extensively in other TTF based systems.[4] Compounds **1**, **5** and **6** show extended one-dimensional chains via weak side-to-side sulfur-sulfur interactions, although another unusual additional polymorph of **5** was found which will be discussed more thoroughly below. Compound **2** forms dimers in the solid-state via π-stacking. Finally, dicationic **3** shows no significant intermolecular interaction as the TTF core is effectively shielded by the large $[BAr^F{}_4]$ anions.

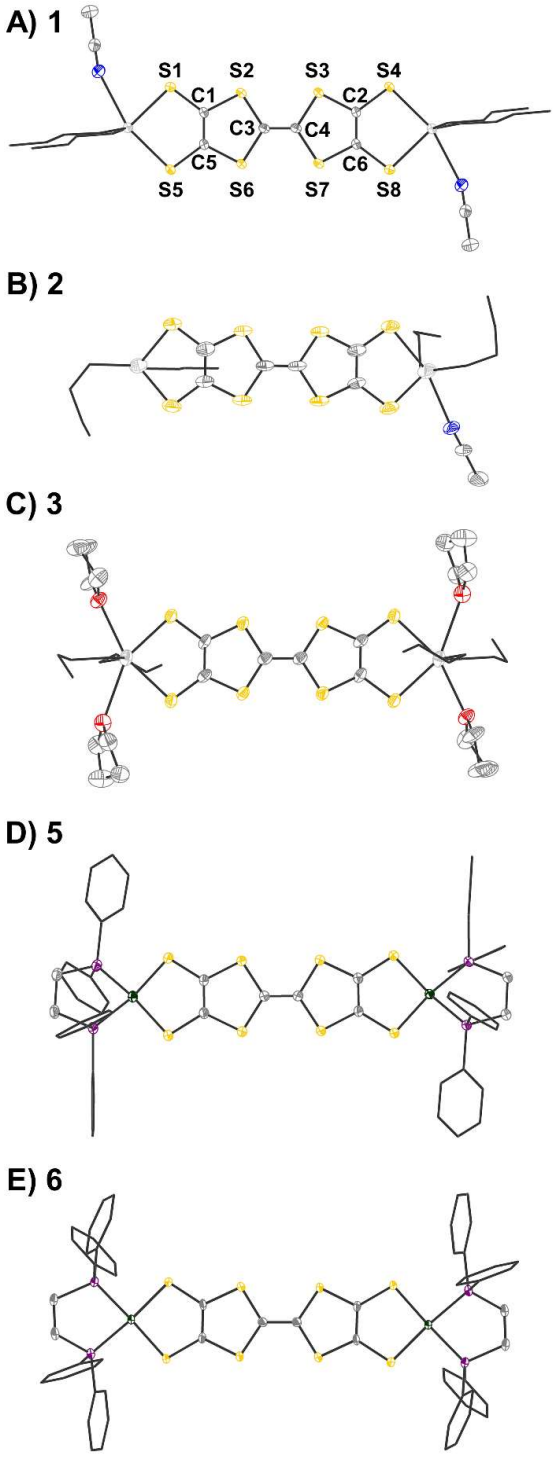

Figure 4.2. Single crystal X-ray diffraction (SXRD) structures of A) 1•2MeCN, B) 2•0.5THF•0.5MeCN, C) 3•4THF, D) 5, and E) 6. [BAr^{F}_{4}] anions, solvent, H atoms, and disorder are omitted and n-butyl and phenyl groups are shown in wireframe for clarity. The labeling scheme shown for 1 applies for all compounds. Ellipsoids are shown at 50% probability. Selected bond lengths are included in Table 4.1. Sn is shown in light grey; Ni, green; S, yellow; P, purple; O, red; N, blue; C, dark grey.

Table 4.1. SXRD metrical parameters for 1-3, 5, and 6.

	C_3-C_4 (Å)	$C_{1,2}$-$C_{5,6}$ (Å)	C-S (Å)[a]	M-S (Å)	M-S' (Å)
1	1.333(5)	1.338(4)	1.746(3)-1.760(3)	2.4579(7)	2.5050(7)
2[b]	1.351(16)	1.37(2)	1.72(1)-1.76(1)	2.455(4)	2.446(3)-2.563(3)
3	1.436(18)	1.402(12)	1.681(9)-1.732(8)	2.535(2)	2.502(3)
5	1.385(2)	1.361(2)	1.726(2)-1.740(1)	2.1616(5)	2.1750(8)
6	1.412(5)	1.379(3)	1.704(2)-1.726(2)	2.1684(7)	2.1790(7)

a: C-S bonds includes all C-S bonds in the TTFtt linker.

b: The two five-membered rings of 2's TTF core are not symmetric.

4.2.3 Electronic Properties of Sn and Ni Complexes

The synthetic ease of accessing these series of redox congeners motivates examination of their electronic structure. As discussed above, CV shows two oxidation peaks for **1** at −0.14 V and 0.28 V vs. Fc^+/Fc. In **5,** these features shift to −0.58 V and −0.11 V respectively. The Ni species display an additional irreversible peak at 0.79 V vs Fc^+/Fc which is tentatively assigned as a Ni^{II} to Ni^{III} oxidation. Redox events at similar potentials were seen for the preliminary study of the complex $(dpppNi)_2TTFtt$ (dppp = 1,3-bis(diphenylphosphino)propane) although limited characterization of this complex is reported.[1c, d] It is worth noting that appreciable film deposition at the working electrode surface was observed on repeated scans in our CV studies. We anticipate that this arises from reaction of the oxidized congeners with the $[PF_6]^-$ electrolyte anions as has been previously proposed.[5] The CV of **5** with $[Na][BAr^F{}_4]$ as the electrolyte medium was performed and no obvious degradation was observed over multiple scans. This enhanced stability from fluorinated aryl borates is also reflected in the synthetic chemistry mentioned above. The lack of oxidative features between 0 and 0.6 V suggests that the dicationic species **6** is potentially air-stable. To test this possibility, a $CDCl_3$ solution of **6** was exposed to air for 12 hours and then analyzed by NMR

spectroscopy. Comparison of the ^{1}H and ^{31}P NMR spectra before and after this exposure indicate nearly no decomposition with the exception of a very small amount of oxidized phosphine (<2%, **Figure C.23** and **Figure C**.24). While crude, this initial test indicates that materials composed of typically air-sensitive TTFtt synthons may be made air-stable by tuning the charge state of the TTF core.

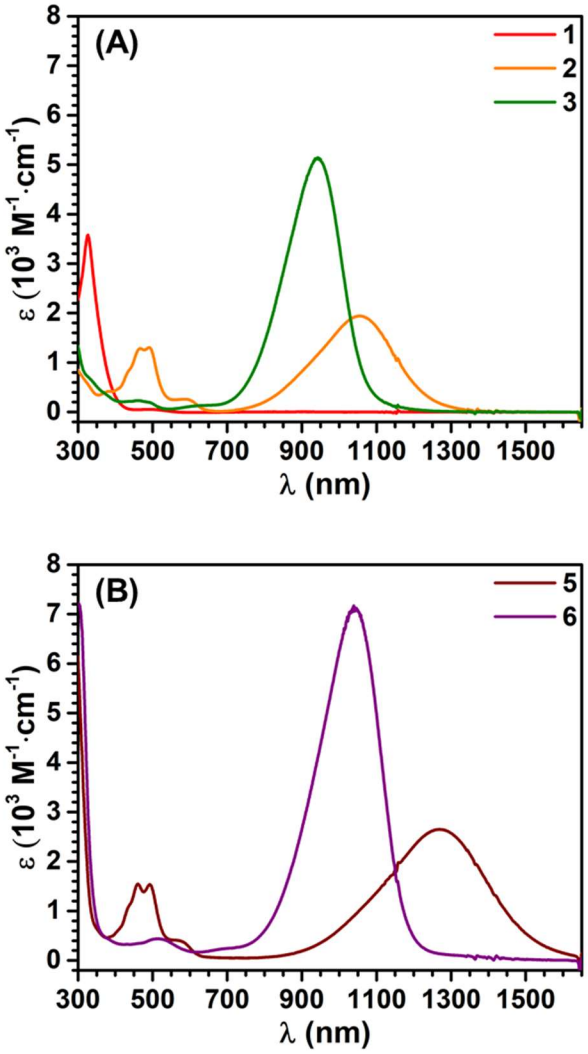

Figure 4.3. UV-vis-NIR absorption spectra of 1-3 (A), 5 and 6 (B) in DCM. Concentration: **1**, 92 μM; **2**, **3**, **5** and **6**, 50 μM.

In order to more firmly assign the redox features observed by CV, UV-vis-NIR investigations were carried out on the Sn compounds **1-3** and on the soluble Ni complexes **5** and **6** (**Figure 4.3**).

Compound **1** has an intense feature at 328 nm, assigned as arising mainly from π-π* transitions.[6] Upon oxidation to **2** a broad feature emerges at 1053 nm. Appearance of this new low-energy absorption band has been previously interpreted as arising from the formation of π-dimers.[7] This absorption band blue-shifts to 941 nm upon further oxidation. Similar spectral features are observed in the Ni complexes **5** and **6** (**Figure 4.3**B). Compared to **2** and **3**, the NIR absorption features of **5** and **6** both show a distinct red-shift (**Figure C.42** and **Figure C**.43).

In addition to UV-vis-NIR spectra, the signals of the TTF radicals were investigated by EPR spectroscopy. The EPR spectrum of **2** in THF (**Figure C.25**) shows an isotropic feature at g = 2.008, consistent with an organic radical. Conversely, anisotropic signals at g = 2.013, 2.007, and 2.003, were observed in the EPR spectrum of **5** (**Figure C.26**). Similarly, anisotropic signals have been observed in other TTF radical systems.[8] The spectroscopic and structural data for these compounds is very similar to that observed for other TTF systems again suggesting that the redox events of TTFtt are largely localized on the TTF core.

4.2.4 Transmetalation to Pd

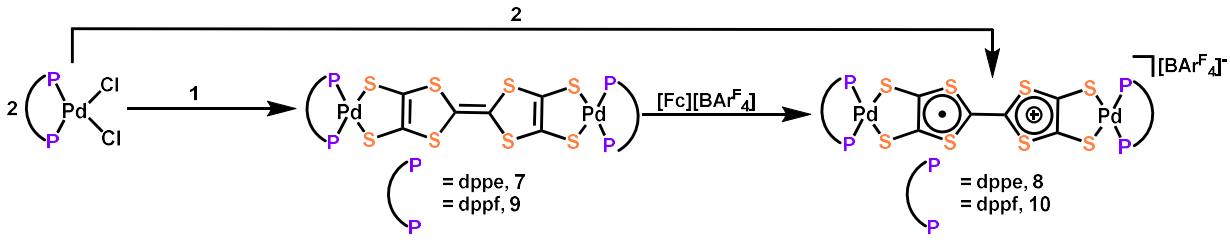

Scheme 4.2. The synthesis of Pd complexes with TTFtt as a bridging ligand.

To further demonstrate the versatility and generality of transmetalation with these tin precursors to other transition metals, we prepared the Pd complexes, $(dppePd)_2$TTFtt,

[(dppePd)$_2$TTFtt][BAr$^F{}_4$], (dppfPd)$_2$TTFtt and [(dppfPd)$_2$TTFtt][BAr$^F{}_4$] (**7**-**10**; dppf = 1,1'-bis(diphenylphosphino)ferrocene) (**Scheme 4.2**). Analogously to the Ni examples above, mixing dppePdCl$_2$ or dppfPdCl$_2$ with complexes **1** and **2** results in the new bridged Pd congeners. Complexes **7** and **9** which contain neutral TTF cores were isolated as insoluble pink/orange powders, while complexes **8** and **10** were crystalized as dark brown needles and were characterized by SXRD analysis (**Figure C.54** and **Figure C**.55). The radical species **8** and **10** possess similar geometric parameters, UV-vis-NIR features (**Figure C.44**), and EPR signals (**Figure C.27** and **Figure C**.28) to compound **5**.

Both sets of Pd complexes are also redox-active. As the CV of **10** shows (**Figure C.41**), two quasi-reversible peaks assigned to oxidation of the TTF core are observed below 0 V (-0.53 and -0.08 V vs. Fc^+/Fc). Three additional quasi-reversible features are also observed at 0.72, 0.94 and 1.26 V and are attributed to a two-electron oxidation of both ferrocene units from dppf and two separate one-electron [Pd-dithiolene]$^{0/1+}$ processes by comparison to the CV spectrum of (dppfPd)dmit (dmit = 1,3-dithiole-2-thione-4,5-dithiolate).[9] Complex **8** shows similar but more negative redox features without the additional ferrocene oxidations (**Figure C.40**).

The synthesis of (dppfPd)$_2$TTFtt has previously been reported by using *in-situ* formed TTFtt anions.[10] The material from this previous report did not show any redox peaks in its CV with a glassy-carbon electrode. When using a Pt-button working electrode, only three features were found at −0.05, 0.42 and 0.90 V vs. Ag/Ag^+ assigned as the oxidations of the ferrocene units (−0.05) and TTF core (0.42 and 0.90). Our CV experiment was performed on crystalline **10**, whose composition and structure are firmly confirmed by a variety of techniques including SXRD. Furthermore, the redox behaviour of **10** is consistent with the redox behaviour of complexes **5** and

8. We also note that the color and solubility of $(dppfPd)_2TTFtt$ from the previous literature report is quite different than what we have observed for this complex.

These results raise questions about the previous report of the preparation of $(dppfPd)_2TTFtt$ with *in-situ* formed $TTFtt^{4-}$. To address these inconsistencies, we repeated the synthesis of $(dppfPd)_2TTFtt$ following the previously reported procedure three times and consistently obtained low yields of 10% or less (versus 66% reported). The small amount of collected product prevented us from detailed characterization of this material. Taken all together, the direct comparison with previous preparations of $(dppfPd)_2TTFtt$ prepared through the conventional method highlights the versality and efficiency of the TTFtt-tin precursors we report here. This new synthetic protocol enables isolation of new pure complexes and may challenge previous preparations and assignments of these species that suffer from the *in-situ* generation of $TTFtt^{4-}$.

4.2.5 Packing and Dimerization of TTFtt Units

Although the NIR absorptions for radical cations and dications may indicate the presence of π-dimer formation in solution, this interpretation has been questioned.[11] To probe the possibility of dimerization in solution, room temperature Evans method experiments on $CDCl_3$ solutions of **5** were performed. The experimentally measured magnetic moment μ_{eff} =1.19 B.M. is smaller than the predicted spin-only value of 1.73 B.M. suggesting that some degree of oligomerization is occurring. Additionally, spin quantitation of the EPR spectrum of **5** at 15 K indicates < 10 % of the expected signal based on the concentration of **5**, also supporting some degree of dimerization. Variable-temperature UV-vis-NIR spectroscopic experiments (**Figure C.45**) indicate an increase of the absorption peak in the NIR region with cooling, suggesting that the equilibrium shifts to oligomerization as the temperature decreases.[11]

In addition to these solution studies, we were also interested in examining the effect of the solid-state packing of these molecules. As mentioned, solid-state packing of TTF cores is well-known, and much of the bulk transport properties of TTF based systems arises from their π-π and sulfur-sulfur interactions in the solid state, particularly in single component conductors.[12] The packing of these compounds has been discussed above and is largely similar to previously reported systems. Solid state magnetic measurements were performed on **5** and indicate a diamagnetic compound, which is also similar to previously reported radical cations of TTF.[13]

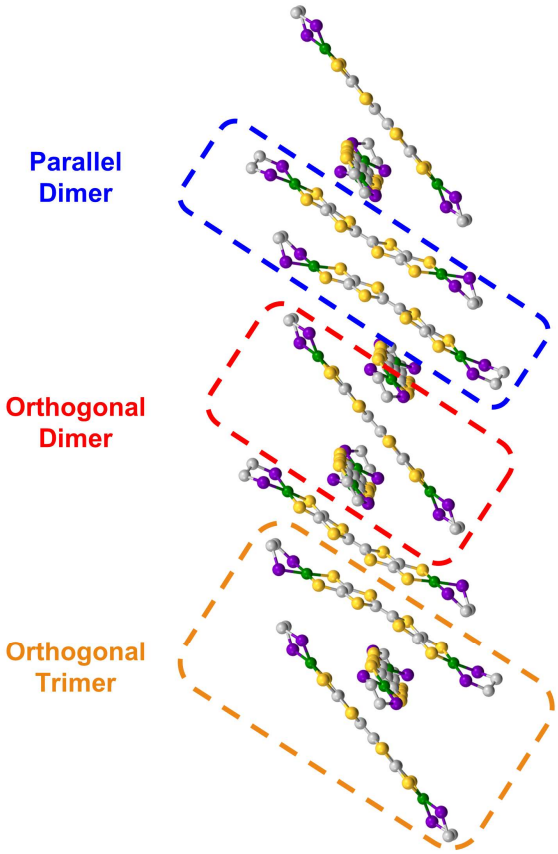

Figure 4.4. Stacking diagram for twisted polymorph of 5 with phenyl groups, hydrogen atoms, and anions removed for clarity. Ni is shown in green, S in yellow, P in purple, and C in grey. The computationally examined parallel dimer, orthogonal dimer, and orthogonal trimer are indicated.

During the course of these studies, however, we isolated a poorly diffracting alternative polymorph of **5**. While the poor quality of this crystal prevented a full structural solution, we have

been able to obtain sufficient resolution to observe a stacking interaction which has a twist of the TTF cores by a nearly orthogonal ~90° (**Figure 4.4**). TTF stacking most commonly has a parallel arrangement, although there are examples of similar twisted interactions, particularly when supported by auxiliary polymeric superstructures.[14] This structure of **5** is somewhat unusual in that the rotated 1D column of **5** is composed of two elements: trimers with asymmetric orthogonally crossed interactions and dimers with more typical parallel interactions (**Figure 4.4**,**Figure C.**56, **Figure C**.57 and **Figure C**.58). Higher-quality crystals of complex **8** were obtained and the structure of this species displays very similar chains (**Figure C.54**), verifying this unusual structural motif. The strength of TTF-TTF interactions and overlap is dependent on S-S interactions between TTF cores. In these unusual stacks however, the orthogonal and parallel interactions may lead to different overlaps which prompted us to investigate what additional effect the twisting of the TTF-TTF cores has on their interaction.

4.2.6 Computational Analysis of TTFtt-TTFtt Interactions

We then undertook calculations on **5** as a model for the effect of the twisted TTF-TTF interactions. Understanding the interactions in the dimer and trimer units in detail and how the twisting of the TTF-TTF interaction affects electronic structure requires large scale CASSCF calculations with extensive active spaces, leading to prohibitively high computational costs with conventional methods. Instead, we employed variational 2-electron reduced density matrix (V2RDM) techniques,[15] which have previously been demonstrated to successfully describe the electronic structure of a variety of strongly correlated large molecules.[16] V2RDM calculations were carried out as implemented in the Maple Quantum Chemistry Package.[17] The phenyl ligands were replaced with methyl groups and [18,20] active space V2RDM calculations with the 3-21G

basis set were performed for both geometries providing the data shown in **Table C.7**.[18] The electronic structures of both arrangements show significant degrees of correlation as demonstrated by partial occupancies in their frontier natural orbitals (NOs). The orthogonal arrangement shows more radical character, with frontier orbital natural occupation numbers (NON) of 1.224860 and 0.771141 suggesting significant bi-radical character, compared to 1.49923 and 0.51331 in the parallel arrangement. Mulliken charges show an effective charge of +1/2 for the Ni centers in both geometries, with a slightly higher cumulative charge of 1.94745 in the parallel arrangement compared to 1.70585 in the orthogonal system.

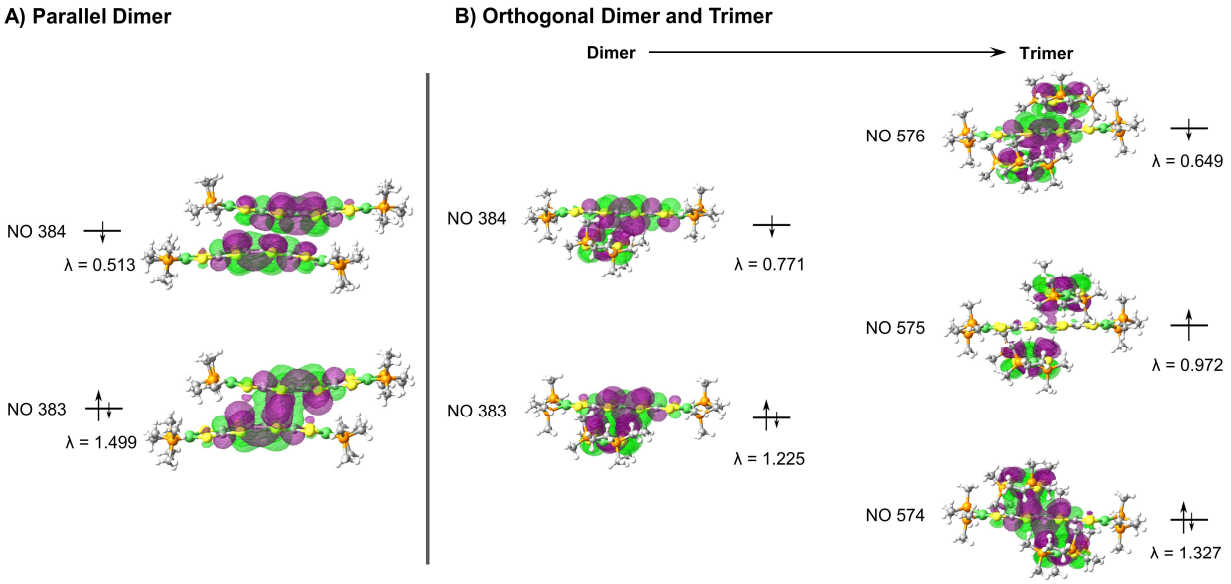

Figure 4.5. Frontier NO occupations and densities for A) the parallel dimer, showing the splitting into bonding and antibonding orbitals. Data and densities obtained via [18,20] V2RDM calculations with a 3-21G basis set. B) for the orthogonal dimer and trimer. Good overlap and correspondingly small splitting in the orthogonal dimer give way to a clear splitting into bonding, non-bonding and antibonding frontier NOs upon transitioning to the orthogonal trimer. Data and densities obtained via V2RDM calculations with a 3-21G basis set and [18,20] and [17,20] active spaces for the dimer and trimer respectively.

Frontier orbital densities, occupations and splittings for the parallel dimer and orthogonal dimer and trimer are shown diagrammatically in **Figure 4.5**A and B, respectively. All frontier NOs are localized on the bridging ligand with no involvement of the Ni centers, consistent with

experimental results. There are significant differences in the orbital configurations elucidating the variation in frontier NON across the two arrangements. The larger splitting of the NO occupancy in the parallel arrangement clearly arises from better orbital overlap between the two monomers, allowing for greater energetic orbital splitting into NO 384 with significant antibonding character, showing no overlap between the two monomers, and NON 383 with significant bonding character and orbital overlap. In contrast, the orthogonal dimer shows two frontier NOs with very similar densities, both showing significant bonding character and overlap between the two monomers, yielding a smaller splitting and correspondingly greater bi-radical character.

As the orthogonal dimeric arrangement is actually part of a larger asymmetrically stacked unit, a trimeric unit was run separately in V2RDM using a [17,20] active space and the 3-21G basis set, giving a SCF calculation with 1308 orbitals. Data are shown in **Table C.8**. Similar to the dimeric case, the trimer unit exhibits clear radical character and three partially occupied NOs with NON of 1.32748, 0.97218 and 0.64935. Mulliken charges in this arrangement are particularly symmetric with each nickel showing a charge of 0.43 to 0.45 with very little variation between the individual centers. Transitioning from a dimeric to a trimeric unit gives rise to splittings and symmetries in line with a classic Hückel picture with the orbitals splitting into bonding, non-bonding and antibonding. The bonding and antibonding orbitals NO 574 and 576 both show roughly equal distribution of the electron density across all three units within the trimer. NO 574 has good matching of the phases between the orbitals localized on each of the units in the trimer leading to overlap between the orbitals on all units and giving rise to significant bonding character and a NO occupancy of 1.32748. Constituent orbitals of NO 576 in contrast constitute a worse matching of the phases, reducing overlap between the individual units and leading to an overall antibonding interaction and a NO occupancy of 0.64935. Singly occupied non-bonding NO 575 is localized on

the top and bottom molecules with a nodal plane and negligible density on the central unit, leading to an electron entangled across the two isolated top and bottom units within the trimer.

The results from V2RDM CASSCF calculations help rationalize the appearance and stability of the different morphologies in the TTFtt stacks. Packing geometries in both the parallel and orthogonal arrangement allow for good orbital overlap between the individual units. Both morphologies show the frontier natural orbitals form via π-π stacking utilizing orbitals localized on the TTF linkers. The resulting NOs differ slightly between the different morphologies with overlap in the parallel geometry allowing for better splitting into clear bonding and antibonding frontier orbital pairs, reducing radical character. The splitting is less pronounced in the orthogonal dimer; however, as the chain size increases clear splitting into bonding, non-bonding and antibonding frontier orbital pairs is recovered in the trimer. In all cases partial occupations in the frontier NOs is retained, allowing for radical chain development and electron entanglement across multiple units.

In 1985, Hoffman and coworkers predicted possible stacking structures of metal bisdithiolenes based on qualitative molecular orbital and band structure calculations.[19] Soon afterwards, in 1988, a LAXS (Large Angle X-ray Scattering) and EXAFS (Extended X-ray Absorption Fine Structure) investigation was performed on amorphous nickel tetrathiolate polymers, proposing two types of polymers with hexagonal (honeycomb) and tetragonal packings for small and large cations, respectively.[20] However, the stackings of the TTFtt radicals in **5** and **8** highlight the key role of strong intermolecular interactions between radicals in the control of morphology. In sum, the stabilization and synthetic access provided by the Sn capped compounds reported here enables the observation of a variety of solid-state interactions of the TTF core. We anticipate that the redox

flexibility of these synthons will enable the observation of novel interactions and electronic structures in TTFtt based coordination polymers.

4.3 Conclusion

TTFtt is an attractive building block for redox-switchable and highly conjugated metal-organic materials. The work presented here demonstrates that capping TTFtt with dialkyl Sn groups stabilizes this ligand and facilitates the use of redox-active TTFtt moieties. Furthermore, the redox flexibility of these synthons helps to precisely control doping, charge, and crystallinity via homogeneous molecular reactions. The synthesis and characterization of the corresponding dinickel and dipalladium complexes validates the ease of transmetalation as a synthetic strategy. We have also observed an unusual "twisted" geometry in the solid state which impacts the electronic structure of the TTF-TTF interaction, effectively demonstrating the utility of these new synthons. Overall, this work demonstrates the usefulness of molecular TTFtt compounds and offers exciting promise for the design and synthesis of multi-functional TTFtt-based coordination polymers.

4.4 Experimental Section

General Methods

All manipulations were performed under an inert atmosphere of dry N_2 using a Schlenk line or MBraun UNIlab glovebox unless otherwise noted. Elemental analyses (C, H, N) were performed by Midwest Microlabs. Acetone was sparged with N_2 and stored in the glovebox over 4 Å

molecular sieves. MeOH was dried with NaOH overnight, distilled, transferred into the glovebox and stored over 4 Å molecular sieves. All other solvents used in molecular synthesis were initially dried and purged with N_2 on a solvent purification system from Pure Process Technology. THF was further stirred with liquid NaK alloy and then filtered through activated alumina and stored over 4 Å molecular sieves. Other solvents were passed through activated alumina and stored over 4 Å molecular sieves. Unless noted, all other chemicals were purchased from commercial sources and used as received. TTFttPG (PG=-C_2H_4CN),[21] dppeNiCl_2[22] and [Fc][BAr^F_4][23] were prepared as previously described. [Fc^{AcO}][BAr^F_4] and [Fc^{BzO}][BAr^F_4] were prepared using the same synthetic method as [Fc][BAr^F_4] but stirred at room temperature instead of boiling DCM during [BAr^F_4]$^-$ anion exchange to avoid decomposition of Fc^{AcO} or Fc^{BzO} cations. Nuclear Magnetic Resonance (NMR) spectra for ^{1}H, ^{13}C, ^{31}P, ^{119}Sn were recorded on either Bruker DRX-400 or AVANCE-500 spectrometers. Tetramethyltin in CD_2Cl_2 and 85% phosphoric acid were used as reference for ^{119}Sn and ^{31}P NMR spectra, respectively. Note that ^{119}Sn NMR shifts can be affected by concentration, so caution must be used in interpreting any reported shifts.[24] All experiments were performed at room temperature. Residual solvent peaks were referenced and labelled as the deuterated solvents. Electron paramagnetic resonance (EPR) spectra were recorded on a Bruker Elexsys E500 spectrometer with an Oxford ESR 900 X-band cryostat and a Bruker Cold-Edge Stinger. Spin quantitation was performed by double integration of derivative spectra and compared to a standard Cu^{II} solution. Electrochemical experiments were performed using cyclic voltammetry (CV) on a BASi Epsilon potentiostat/galvanostat. A glassy carbon working electrode, platinum wire counter electrode, and silver wire pseudo-reference electrode were used for all measurements. $FeCp_2^+$/$FeCp_2$ was used as an internal reference. Infrared spectra were recorded on a Bruker Tensor II FTIR spectrometer with MCT detector operated at 77 K. Data were processed and background

corrected with OPUS software (version 7.5). An additional manual correction for scattering was also applied. Samples were prepared under N_2 by grinding solid **1-10** with Nujol, placed between two KBr crystal plates, and measured in air under ambient conditions. UV-visible-NIR absorption spectra were recorded on a Shimadzu UV-3600 Plus spectrophotometer. All solutions were prepared in an N_2-filled glovebox and transferred into a 1×1 cm quartz cuvette for room-temperature measurements in sequence. The spectrum of pure DCM in the same cuvette was used for background calibration. A Hellma Analytics Excalibur Immersion Probe with a 10 mm path length (article no. 661-202-10-S-46) was used for variable-temperature UV-vis-NIR spectroscopic measurements and the solution of **5** in DCM was transferred to a custom-made, airtight apparatus equipped with 14/20 ground glass joint, #2 size ground glass plug and #25 size threaded Teflon plug for the immersion probe to go through which was sealed with a Teflon coated O-ring. The entire apparatus was sealed inside the glovebox before connecting to the spectrophotometer. The temperature was adjusted by adding dry ice into an isopropanol bath and each temperature point was the average of reads before and after a spectroscopic scan. Solid-state magnetic measurements were carried out with a MPMS-XL Quantum Design SQUID operating at temperatures between 1.8 and 300 K and dc magnetic fields ranging from -2 to 2 T. Measurements were performed on powder samples of **5** in sealed plastic heat-shrink tubing, whose diamagnetic contribution was corrected after experiment. All measured samples were diamagnetic in the solid state. Evans method on a $CDCl_3$ solution of **5** at room temperature was used for solution phase magnetic measurements. The diffraction data were measured at 100 K on a Bruker D8 VENTURE with PHOTON 100 CMOS detector system equipped with a Mo-target micro-focus X-ray tube (λ = 0.71073 Å). Data reduction and integration were performed with the Bruker APEX3 software package (Bruker AXS, version 2015.5-2, 2015). Alternatively, data were also collected at the

Advanced Photon Source of Argonne National Laboratory (beamline 15-ID-B,C,D) using X-ray radiation with a wavelength of λ=0.41328 Å at 110 K. Data were scaled and corrected for absorption effects using the multi-scan procedure as implemented in SADABS (Bruker AXS, version 2014/5, 2015, part of Bruker APEX3 software package). The structure was solved by the dual method implemented in SHELXT[25] and refined by a full-matrix least-squares procedure using OLEX23[26] software package (XL refinement program version 2014/7[27]). Suitable crystals were mounted on a cryo-loop and transferred into the cold nitrogen stream of the Bruker D8 VENTURE diffractometer. Most of the hydrogen atoms were generated by geometrical considerations and constrained to idealized geometries and allowed to ride on their carrier atoms with an isotropic displacement parameter related to the equivalent displacement parameter of their carrier atoms. Disorder was modeled with common constraints or restraints.

Since compounds, **3**, **5**, **6**, **8**, and **10** can be prepared via multiple approaches, the primary bulk procedure is described in detail below while other alternative ways are reported with product formation verified by NMR spectroscopic monitoring of the reactions.

TTFtt(SnBu$_2$)$_2$ (1)

TTFtt(C_2H_4CN)$_4$ (11 mmol, 5.9 g) and NaOMe (86.4 mmol, 4.75 g) were added into a 500 mL Schlenk flask with dry MeOH (27 mL) in a N_2-filled glovebox. The resulting suspension was stirred at room temperature overnight until all solids disappeared and a homogeneous dark red solution was observed. This solution was transferred into a sealed Schlenk flask and brought outside the glovebox. Volatiles were then removed under vacuum. Note that the higher vacuum from a Schlenk line is required to remove the volatile byproducts of the deprotection. When the solution was dried, the Schlenk flask was sealed and transferred back into the glovebox. The

remaining solid was re-dissolved in MeOH (144 mL) and treated with Bu_2SnCl_2 (43.2 mmol, 13.1 g) in MeOH (36 mL). After the mixture was stirred over an additional night at room temperature, MeOH was removed again under Schlenk line vacuum. The remaining solid was extracted with DCM and filtered sequentially through Celite and silica. After flash silica chromatography with DCM or THF, all of the filtrate was collected and dried under vacuum to provide red solid. The crude solid was washed with 10 mL of cold acetone and dried under vacuum to yield **1** as a pink powder (3.5 g, yield: 41 %). Crystals were prepared by either recrystallization from boiling MeCN followed by cooling to −35 ºC or DCM/Et_2O vapor diffusion overnight at −35 ºC. Crystals suitable for single crystal XRD were selected from the MeCN recrystallization. ^{1}H NMR (400 MHz, $CDCl_3$, 298 K): δ 0.94 (3H, t, *J* = 0.94 Hz), 1.38 (2H, q, *J* = 1.38 Hz), 1.76 (4H, m, *J* = 1.75 Hz) ppm. ^{119}Sn{^{1}H} NMR (149 MHz, $CDCl_3$, 298 K): δ 220.89 ppm. ^{13}C{^{1}H} NMR (126 MHz, CD_2Cl_2, 298 K) δ 13.61, 24.89, 26.77, 28.14, 111.59, 117.89 ppm. UV-vis-NIR (DCM, nm): 328.5, 515.6. IR (Nujol, KBr plates, cm^{-1}): 2724(m), 2668(m), 1304(m), 1288(m), 1242(w), 1173(m), 1146(m), 1075(m), 1016(w), 979(m), 966(w), 936(w), 885(s), 866(m), 846(w), 773(s), 722(s), 666(m). Anal. calc. for **1**, $C_{22}H_{36}S_8Sn_2$: C 33.26%, H 4.57%, N 0%; found: purification via DCM/Et_2O vapor diffusion: C 33.24%, H 4.52%, N none; purification via MeCN recrystallization: C 32.89%, H 4.66%, N none.

[TTFtt(SnBu$_2$)$_2$][BAr$^F{}_4$] (2)

1 (0.03 mmol, 24 mg) was treated with [Fc][BAr$^F{}_4$] (0.027 mmol, 28 mg) in Et_2O (1 mL). After stirring for 10 mins, the solution was filtered through Celite and concentrated to about 0.5 mL volume. Petroleum-ether (4 mL) was added dropwise leading to the formation of a brown precipitate. The yellow petroleum-ether supernatant was decanted gently. The solid was washed with fresh petroleum-ether and dried under vacuum to provide **2** as a brown solid (35 mg, 78 %).

Suitable crystals for single crystal XRD were obtained by Et_2O/petroleum-ether layered diffusion at −35 ºC for 3 days. UV-vis-NIR (DCM, nm): 384.1, 428.6, 465.4, 490.8, 591.0, 1053.7. IR (Nujol, KBr plates, cm^{-1}): 3174(m), 2728(m), 1650(m), 1608(w), 1309(s), 1276(s), 1110(bs), 1003(w), 966(w), 887(m), 848(m), 838(m), 818(w), 769(w), 741(m), 720(s), 680(m), 668(m). EPR (THF, 15K, 9.63 GHz, 6 μW): g_{eff} = 2.008. Anal. calc. for **2**, $C_{54}H_{48}BF_{24}S_8Sn_2$: C 39.13%, H 2.92%, N 0%; found: C 38.85%, H 3.03%, N 0%.

[TTFtt(SnBu$_2$)$_2$][BAr$^F{}_4$]$_2$ (3)

Compound **1** (0.03 mmol, 24 mg) was treated with $[Fc^{BzO}][BAr^F{}_4]$ (0.066 mmol, 76 mg) in THF (1 mL). After stirring for 5 mins, the dark green solution was filtered through Celite and concentrated to about 0.5 mL volume. Petroleum-ether (4 mL) was added dropwise leading to the formation of a dark green oil-like precipitate and the orange supernatant was decanted gently. The precipitate was washed with fresh petroleum-ether (2 mL) for 3 times, redissolved in THF (1 mL), and reprecipitated by adding petroleum-ether (4 mL). The petroleum-ether supernatant was removed and the solid was washed with fresh petroleum-ether 3 times and dried under vacuum. The green solid was then collected and recrystallized from THF/petroleum-ether layered diffusion at −35 ºC for 2 days to obtain **3** as dark green-brown crystals (56 mg, 74%). The resulting crystals are suitable for single crystal XRD. ^{1}H NMR (400 MHz, $CDCl_3$, 298 K): δ 0.94 (3H, bt), 1.42 (2H, bs), 1.77 (4H, bs), 1.98 (s, THF adduct), 3.87 (s, THF adduct), 7.52 (s, $[BAr^F{}_4]^-$), 7.72 (s, $[BAr^F{}_4]^-$) ppm. ^{119}Sn{^{1}H} NMR (149 MHz, $CDCl_3$, 298 K): δ −192.70 ppm. ^{13}C{^{1}H} NMR (126 MHz, CD_2Cl_2, 298 K) δ 13.52, 26.83, 28.07, 117.95 (m, $[BAr^F{}_4]^-$), 125.04 (q, $[BAr^F{}_4]^-$), 129.36 (q, $[BAr^F{}_4]^-$), 162.21 (q, $[BAr^F{}_4]^-$) ppm. UV-vis-NIR (DCM, nm): 469.5, 940.5. IR (Nujol, KBr plates, cm^{-1}): 2723(w), 2666(w), 1651(s), 1608(m), 1352(s), 1278(s), 1237(w), 1119(bs), 886(m), 839(m), 742(m), 721(m), 682(m), 670(m). Anal. calc. for **3•2THF**, $C_{94}H_{76}B_2F_{48}O_2S_8Sn_2$: C

42.36%, H 2.87%, N 0%; found: C 41.91%, H 3.05%, N none. Note that the ^{1}H NMR spectrum of crystalline **3** in $CDCl_3$ shows broad peaks and uneven splitting patterns which suggests a small amount of radical **3** may be present (**Figure C.2**). Similarly, the TTF peaks in the ^{13}C NMR are not visible, again likely due to exchange with some small amount of a radical species.

If the same reaction is finished in Et_2O instead of THF, then the product is dark purple throughout the workup and **3**•2Fc^{BzO} is obtained as dark purple crystals from a Et_2O/petroleum ether layered diffusion at −35 ºC for 3 days (**Figure C.53**). Transmetalation of **3**•2Fc^{BzO} is also facile as judged by ^{1}H NMR.

Alternative method: Compound **3** can also be generated by oxidation of **2** with 1.1 equivalents of [Fc^{BzO}][BAr^{F}_4] in THF and purified as described above.

(dppeNi)$_2$TTFtt (4)

dppe$NiCl_2$ (0.2 mmol, 105 mg) was suspended in DCM (3 mL) and mixed with **1** (0.1 mmol, 80 mg) in DCM (3 mL) and then stirred for 15 mins. The yellow-orange precipitate was separated by centrifugation (additional THF can help the separation). The solid was washed with THF (3 mL) 3 times and dried under vacuum. **4** was obtained as an orange powder (115 mg, 93 %). IR (Nujol, KBr plates, cm^{-1}): 2724(w), 2671(w), 1305(m), 1185(w), 1159(w), 1101(m), 1073(w), 1025 (w), 996(w), 971(w), 907(m), 873(w), 820(w), 764(w), 744(m), 690(s), 649(m). Anal. calc. for **4**, $C_{58}H_{48}Ni_2P_4S_8$: C 56.05%, H 3.89%, N 0%; found: C 55.79%, H 4.11%, N none.

[(dppeNi)$_2$TTFtt][BAr^{F}_4] (5)

Compound **4** (0.03 mmol, 37.2 mg) was treated with [Fc][BAr^{F}_4] (0.027 mmol, 29 mg) in DCM (3 mL) and stirred for 10 mins. After filtration through Celite, the filtrate was concentrated to about 0.5 mL and slow addition of petroleum-ether (4 mL) caused a brown precipitate to form. The

petroleum-ether supernatant was removed and the precipitate was washed with fresh petroleum-ether 3 times and dried under vacuum to provide **5** as a brown solid (50 mg, 88 %). Brown crystals were obtained via PhCl/petroleum-ether vapor diffusion at room temperature for one day (32 mg, 57%). ^{1}H NMR (400 MHz, $CDCl_3$, 298 K): δ 2.44 (bs, dppe), 7.51 (s, $[BAr^F{}_4]^-$), 7.61 (bs, dppe), 7.63 (bs, dppe), 7.71 (s, $[BAr^F{}_4]^-$), 8.00 (bs, dppe) ppm. UV-vis-NIR (DCM, nm): 429.9, 457.4, 491.1, 570.3, 1268.4. IR (Nujol, KBr plates, cm^{-1}): 2721(w), 2664(w), 1274(s), 1118(bs), 1098(m), 1028(w), 998(w), 968(w), 932(w), 878(m), 838(m), 817(w), 772(w), 743(m), 680(m). Evans method ($CDCl_3$, room temperature): μ_{eff} = 1.19 B.M. EPR (THF, 15K, 9.63 GHz, 0.2 μW): g_{eff} = 2.013, 2.007, 2.003. Anal. calc. for **5**, $C_{90}H_{60}BF_{24}Ni_2P_4S_8$: C 51.33%, H 2.87%, N 0%; found: C 51.64%, H 2.98%, N none.

Alternative method: Complex **5** was also prepared through the metalation of **2** with 2 equivalents of dppe$NiCl_2$ in DCM as indicated by ^{1}H NMR spectra (**Figure C.13** and **Figure C**.14).

[(dppeNi)$_2$TTFtt][BAr$^F{}_4$]$_2$ (6)

*To simplify the synthesis, **3** was generated in situ and used directly for the preparation of **6**.*

Compound **1** (0.01 mmol, 8 mg) was treated with $[Fc^{BzO}][BAr^F{}_4]$ (0.022 mmol, 25 mg) in Et_2O (0.5 mL). The resulting dark purple solution was added to dppe$NiCl_2$ (0.02 mmol, 11 mg) which over 3 mins resulted in the dissolution of the yellow dppe$NiCl_2$. The solution was then filtered through Celite and concentrated to about 0.5 mL volume. Petroleum-ether (4 mL) was added to the resulting dark purple solution to precipitate the product. After gently removing the orange supernatant and washing with fresh petroleum-ether several times, the purple-red powder was dried under vacuum. Compound **6** can then be obtained as purple-red crystals by PhCl/petroleum-ether vapor diffusion at room temperature for 2 days (24 mg, 81 %). ^{1}H NMR (400 MHz, $CDCl_3$, 298 K): δ 2.47 (d, dppe), 7.48 (s, $[BAr^F{}_4]^-$), 7.50-7.60(m, dppe), 7.61-7.70 (m, dppe), 7.70 (s,

$[BAr^{F}_4]^-$) ppm. $^{31}P\{^1H\}$ NMR (162 MHz, $CDCl_3$, 298 K): δ 62.95 ppm. $^{13}C\{^1H\}$ NMR (126 MHz, CD_2Cl_2, 298 K) δ 27.00 (t, dppe), 117.95 (m, $[BAr^{F}_4]^-$), 125.04 (q, $[BAr^{F}_4]^-$), 126.79 (t, dppe), 129.36 (q, $[BAr^{F}_4]^-$), 130.10(t, dppe), 133.53 (s, dppe), 133.71 (t, dppe) 156.09 (s, TTFtt), 162.21 (q, $[BAr^{F}_4]^-$), 173.46 (s,TTFtt) ppm. UV-vis-NIR (DCM, nm):515.6, 1039.5. IR (Nujol, KBr plates, cm^{-1}): 2723(w), 2670(w), 2585(w), 1354 (s), 1277(s), 1119(bs), 999(w), 958(m), 878(m), 839(m), 816(w), 745(m), 682(m). Anal. calc. for **6**, $C_{122}H_{72}B_2F_{48}Ni_2P_4S_8$: C 49.35%, H 2.44%, N 0%; found: C 49.02%, H 2.69%, N none.

Alternative method 1: Complex **6** can be obtained by direct metalation of isolated **3** or **3**•$2Fc^{BzO}$ with 2 equivalents of $dppeNiCl_2$. The products were verified by ^1H NMR spectra (**Figure C.15Figure C**.19).

Alternative method 2: **6** was also prepared by oxidation of **4** with 2 equivalents $[Fc^{AcO}][BAr^{F}_4]$ or **5** with 1 equivalent $[Fc^{AcO}][BAr^{F}_4]$ in Et_2O and the purification is the same as above (**Figure C.20**).

(dppePd)$_2$TTFtt (7)

$dppePdCl_2$ (0.06 mmol, 35 mg) was partially dissolved in DCM (2 mL) and mixed with **1** (0.029 mmol, 23 mg) in DCM (2 mL) and then stirred for 15 mins. The shiny pink precipitate was separated by centrifugation. The solid was washed with DCM (3 mL) 3 times and dried under vacuum. **7** was obtained as a pink powder (38 mg, 99 %). IR (Nujol, KBr plates, cm^{-1}): 2724(w), 2671(w), 1305(m), 1185(w), 1159(w), 1101(m), 1073(w), 1025 (w), 996(w), 971(w), 894(m), 876(m), 843(w), 822(w), 766(w), 747(m), 690(s), 649(m). Anal. calc. for **7•0.5DCM**, $C_{58.5}H_{49}ClPd_2P_4S_8$: C 50.89%, H 3.58%, N 0 %; found: C 50.70%, H 3.68%, N none. Note that the combustion analysis was calculated for a half of DCM solvate since the collected product was precipitate directly from DCM and washed with DCM.

[(dppePd)$_2$TTFtt][BAr$^F{}_4$] (8)

Compound **1** (0.025 mmol, 20 mg) was treated with [Fc][BAr$^F{}_4$] (0.025 mmol, 27 mg) in Et_2O (5 mL). The resulting dark brown solution was added to dppePdCl_2 (0.05 mmol, 29 mg) which over 5 mins resulted in the dissolution of the pale yellow dppePdCl_2. After filtration through Celite, the filtrate was concentrated to about 0.5 mL and slow addition of petroleum-ether (4 mL) caused a brown precipitate to form. The petroleum-ether supernatant was removed. After being washed with fresh petroleum-ether 3 times and dried under vacuum, brown crystals were obtained via PhCl/petroleum-ether vapor diffusion at room temperature for one day (28 mg, 51 %). ^{1}H NMR (400 MHz, $CDCl_3$, 298 K): δ 2.72 (bs, dppe), 7.50 (s, [BAr$^F{}_4$]$^-$), 7.58 (bs, dppe), 7.66 (bs, dppe), 7.71 (s, [BAr$^F{}_4$]$^-$), 8.00 (bs, dppe) ppm. UV-vis-NIR (DCM, nm): 429.9, 457.4, 491.1, 570.3, 1078.1, 1271.4. IR (Nujol, KBr plates, cm^{-1}): 2721(w), 2664(w), 1274(s), 1165(w), 1118(bs), 1098(m), 1028(w), 998(w), 968(w), 932(w), 887.4(w), 878(w), 838(m), 772(w), 743(m), 684(m). EPR (THF, 10K, 9.63 GHz, 1 μW): g_{eff} = 2.013, 2.008, 2.002. Anal. calc. for **8**, $C_{90}H_{60}BF_{24}Pd_2P_4S_8$: C 49.10%, H 2.75%, N 0%; found: C 48.88%, H 2.77%, N none.

Alternative method: Compound **7** (0.006 mmol, 10 mg) was treated with [Fc][BAr$^F{}_4$] (0.057 mmol, 6 mg) in Et_2O (2 mL) and stirred for 10 mins. Complex **8** was then purified with the same procedure as outlined above. (**Figure C.21**).

(dppfPd)$_2$TTFtt (9)

dppfPdCl_2 (0.06 mmol, 44 mg) was dissolved in DCM (3 mL) and mixed with **1** (0.03 mmol, 24 mg) in DCM (2 mL) and then stirred for 15 mins. The orange precipitate was separated by centrifugation. The solid was washed with DCM (3 mL) 3 times and dried under vacuum. **9** was obtained as an orange powder (46 mg, 94 %). IR (Nujol, KBr plates, cm^{-1}): 2724(w), 2671(w), 1667(m), 1301(m), 1185(w), 1165(m), 1101(m), 1087(s), 1028 (m), 996(w), 971(w), 901(m),

873(w), 820(w), 746(m), 690(s), 632(m). Anal. calc. for **9•DCM**, $C_{75}H_{58}Cl_2Pd_2P_4S_8$: C 51.92%, H 3.37%, N 0 %; found: C 51.32%, H 3.37%, N non. Note that the combustion analysis was calculated for a DCM solvate since the collected product was precipitate directly from DCM and washed with DCM.

[(dppfPd)$_2$TTFtt][BAr$^F{}_4$] (10)

Compound **1** (0.009 mmol, 7.2 mg) was treated with [Fc][BAr$^F{}_4$] (0.009 mmol, 9.5 mg) in Et_2O (2 mL). The resulting dark brown solution was added to dppfPdCl_2 (0.02 mmol, 15 mg) which over 5 mins resulted in the dissolution of the red dppfPdCl_2. After filtration through Celite, the filtrate was concentrated to about 0.5 mL and slow addition of petroleum-ether (4 mL) caused a brown precipitate to form. The petroleum-ether supernatant was removed. After being washed with fresh petroleum-ether 3 times and dried under vacuum, brown crystals were obtained via PhCl/petroleum-ether vapor diffusion at room temperature for one day (18 mg, 80 %). ^{1}H NMR (400 MHz, $CDCl_3$, 298 K): δ 4.25 (bs, dppf), 4.55 (bs, dppf), 7.28-7.35 (m, dppf), 7.52 (s, [BAr$^F{}_4$]$^-$), 7.71 (s, [BAr$^F{}_4$]$^-$) ppm. UV-vis-NIR (DCM, nm): 429.9, 457.4, 491.1, 570.3, 1342.3. IR (Nujol, KBr plates, cm^{-1}): 2721(w), 2664(w), 1667(m), 1353(s), 1274(s), 1157(m), 1118(bs), 1089(m), 1035(w), 1028(w), 998(w), 968(w), 924(w), 885(m), 838(m), 821(m), 743(m), 711(m), 692(m), 680(m), 668(m), 628(m). EPR (THF, 10K, 9.63 GHz, 0.4 μW): g_{eff} = 2.014, 2.008, 2.001. Anal. calc. for **10**, $C_{106}H_{68}BF_{24}Fe_2Pd_2P_4S_8$: C 50.66%, H 2.73%, N 0%; found: C 50.78%, H 2.86%, N none.

Alternative method: Compound **9** (0.005 mmol, 8 mg) was treated with [Fc][BAr$^F{}_4$] (0.045 mmol, 4.5 mg) in Et_2O (2 mL) and stirred for 10 mins. Complex **10** was then purified with the same procedure as outlined above. However, the product collected via the direct oxidation is typically associated with an impurity, likely **9**, although pure crystals can be grown (**Figure C.22**).

4.5 References

[1] (a)McCullough, R. D.; Belot, J. A. Toward New Magnetic, Electronic, and Optical Materials: Synthesis and Characterization of New Bimetallic Tetrathiafulvalene Tetrathiolate Building Blocks. *Chem. Mater.* **1994**, *6* (8), 1396–1403. (b) McCullough, R. D.; Belot, J. A.; Rheingold, A. L.; Yap, G. P. A. Toward New Electronic, Magnetic, and Optical Materials: Structure and Properties of the First Homobimetallic Tetrathiafulvalene Tetrathiolate Building Block. *J. Am. Chem. Soc.* **1995**, *117* (39), 9913–9914. (c) McCullough, R. D.; Belot, J. A.; Seth, J.; Rheingold, A. L.; Yap, G. P. A.; Cowan, D. O. Building Block Ligands for New Molecular Conductors: Homobimetallic Tetrathiafulvalene Tetrathiolates and Metal Diselenolenes and Ditellurolenes. *J. Mater. Chem.* **1995**, *5* (10), 1581. (d) McCullough, R. D.; Seth, J.; Belot, J. A.; Majetich, S. A.; Carter, A. C. Novel Coordination Complexes of Tetrathiafulvalene Derivatives. *Synth. Met.* **1993**, *56* (1), 1989–1994.

[2] (a)Ashton, P. R.; Balzani, V.; Becher, J.; Credi, A.; Fyfe, M. C. T.; Mattersteig, G.; Menzer, S.; Nielsen, M. B.; Raymo, F. M.; Stoddart, J. F.; et al. A Three-Pole Supramolecular Switch. *J. Am. Chem. Soc.* **1999**, *121* (16), 3951–3957. (b)Wang, L.; Zhang, J.-P.; Zhang, B. Bis[Tetrakis(Methylsulfanyl)Tetrathiafulvalenium] Oxalate Dichloride. *Acta Crystallogr. Sect. E Struct. Reports Online* **2005**, *61* (6), o1674–o1676. (c)Beck, J.; Bof de Oliveira, A. On the Oxidation of Octamethylenetetrathiafulvalene by CuBr 2 - Synthesis, Crystal Structure and Magnetic Properties of $(OMTTF)_2[Cu_4Br_{10}]$. *Zeitschrift für Anorg. und Allg. Chemie* **2009**, *635* (3), 445–449. (d)Wang, Y.; Cui, S.; Li, B.; Zhang, J.; Zhang, Y. Synthesis and Characterization of Monosubstituted TTF and Its Solvent Dependent Mono- and Dication Charge-Transfer Salts. *Cryst. Growth Des.* **2009**, *9* (9), 3855–3858. (e)Barin, G.; Frasconi, M.; Dyar, S. M.; Iehl, J.; Buyukcakir, O.; Sarjeant, A. A.; Carmieli, R.; Coskun, A.; Wasielewski, M. R.; Stoddart, J. F. Redox-Controlled Selective Docking in a [2]Catenane Host. *J. Am. Chem. Soc.* **2013**, *135* (7), 2466–2469. (f)Gao, F.; Zhu, F.; Wang, X.-Y.; Xu, Y.; Wang, X.; Zuo, J. Stabilizing Radical Cation and Dication of a Tetrathiafulvalene Derivative by a Weakly Coordinating Anion. *Inorg. Chem.* **2014**, *53* (10), 5321–5327.

[3] (a)Mori, T.; Inokuchi, H. Crystal and Electronic Structures of (BEDT-TTF)$AuCl_2AuCl_4$. *Chem. Lett.* **1986**, *15* (12), 2069–2072. (b)Shibaeva, R. P.; Lobkovskaya, R. M.; Korotkov, V. E.; Kusch, N. D.; Yagubskii, É. B.; Makova, M. K. ET Cation-Radical Salts with Metal Complex Anions. *Synth. Met.* **1988**, *27* (1–2), A457–A463. (c)Abboud, K. A.; Clevenger, M. B.; De Oliveira, G. F.; Talham, D. R. Dication Salt of Bis(Ethylenedithio)Tetrathiafulvalene: Preparation and Crystal Structure of BEDT-TTF(ClO4)2. *J. Chem. Soc. Chem. Commun.* **1993**, No. 20, 1560–1562. (d)Mori, T.; Inokuchi, H. A BEDT-TTF Complex Including a Magnetic Anion, $(BEDT-TTF)_3(MnCl_4)_2$. *Bull. Chem. Soc. Jpn.* **1988**, *61* (2), 591–593. (e)Clemente-León, M. Hybrid Molecular Materials Based upon Organic π-Electron Donors and Inorganic Metal Complexes. Conducting Salts of Bis(Ethylenediseleno)Tetrathiafulvalene (BEST) with the Octahedral Anions Hexacyanoferrate(III) and Nitroprusside. *J. Solid State Chem.* **2002**, *168* (2), 616–625. (f)Xiao, X.; Xu, H.; Xu, W.; Zhang, D.; Zhu, D. Two Dication Salts of ET: Preparation and Crystal Structures of $ET[Fe^{II}(CN)_4(CO)_2]$. *Synth. Met.* **2004**, *144* (1), 51–53. (g)Belo, D.; Rodrigues, C.; Santos, I. C.; Silva, S.; Eusébio, T.; Lopes, E. B.; Rodrigues, J. V.; Matos, M. J.; Almeida, M.; Duarte, M. T.; et al. Synthesis, Crystal Structure and Magnetic Properties of Bis(3,4;3′,4′-Ethylenedithio)2,2′,5,5′-Tetrathiafulvalene-Bis(Cyanoimidodithiocarbonate)Aurate(III), (BEDT-

TTF)[Au(CDC)$_2$]. *Polyhedron* **2006**, *25* (5), 1209–1214. (h)Minemawari, H.; Naito, T.; Inabe, T. (ET)$_3$(Br$_3$)$_5$: A Metallic Conductor with an Unusually High Oxidation State of ET (ET = Bis(Ethylenedithio)Tetrathiafulvalene). *Chem. Lett.* **2007**, *36* (1), 74–75. (i)Minemawari, H.; Jose, J. F. F.; Takahashi, Y.; Naito, T.; Inabe, T. Structural Characteristics in a Stable Metallic ET Salt with Unusually High Oxidation State (ET: Bis(Ethylenedithio)Tetrathiafulvalene). *Bull. Chem. Soc. Jpn.* **2012**, *85* (3), 335–340. (o)Zecchini, M.; Lopez, J. R.; Allen, S. W.; Coles, S. J.; Wilson, C.; Akutsu, H.; Martin, L.; Wallis, J. D. Exo-Methylene-BEDT-TTF and Alkene-Functionalised BEDT-TTF Derivatives: Synthesis and Radical Cation Salts. *RSC Adv.* **2015**, *5* (39), 31104–31112.

[4] Bryce, M. R. Recent Progress on Conducting Organic Charge-Transfer Salts. *Chem. Soc. Rev.* **1991**, *20* (3), 355.

[5] Arumugam, K.; Shaw, M. C.; Chandrasekaran, P.; Villagrán, D.; Gray, T. G.; Mague, J. T.; Donahue, J. P. Synthesis, Structures, and Properties of 1,2,4,5-Benzenetetrathiolate Linked Group 10 Metal Complexes. *Inorg. Chem.* **2009**, *48* (22), 10591–10607.

[6] Wu, J.-C.; Liu, S.-X.; Keene, T. D.; Neels, A.; Mereacre, V.; Powell, A. K.; Decurtins, S. Coordination Chemistry of a π-Extended, Rigid and Redox-Active Tetrathiafulvalene-Fused Schiff-Base Ligand. *Inorg. Chem.* **2008**, *47* (8), 3452–3459.

[7] (a)Spanggaard, H.; Prehn, J.; Nielsen, M. B.; Levillain, E.; Allain, M.; Becher, J. Multiple-Bridged Bis-Tetrathiafulvalenes: New Synthetic Protocols and Spectroelectrochemical Investigations. *J. Am. Chem. Soc.* **2000**, *122* (39), 9486–9494. (b)Massue, J.; Bellec, N.; Chopin, S.; Levillain, E.; Roisnel, T.; Clérac, R.; Lorcy, D. Electroactive Ligands: The First Metal Complexes of Tetrathiafulvenyl−Acetylacetonate. *Inorg. Chem.* **2005**, *44* (24), 8740–8748. (c)Nielsen, M. B.; Lomholt, C.; Becher, J. Tetrathiafulvalenes as Building Blocks in Supramolecular Chemistry II. *Chem. Soc. Rev.* **2000**, *29* (3), 153–164.

[8] Di Valentin, M.; Bisol, A.; Agostini, G.; Liddell, P. A.; Kodis, G.; Moore, A. L.; Moore, T. A.; Gust, D.; Carbonera, D. Photoinduced Long-Lived Charge Separation in a Tetrathiafulvalene−Porphyrin−Fullerene Triad Detected by Time-Resolved Electron Paramagnetic Resonance. *J. Phys. Chem. B* **2005**, *109* (30), 14401–14409.

[9] Noh, D.-Y.; Seo, E.-M.; Lee, H.-J.; Jang, H.-Y.; Choi, M.-G.; Kim, Y. H.; Hong, J. Syntheses and Characterization of Heterobimetallic Complexes (dppf)Pt(dithiolate) (dppf: Bis(Diphenylphosphino)Ferrocene); X-Ray Crystal Structures of (dppf)PtL Where L=dmit, phdt and i-mnt. *Polyhedron* **2001**, *20* (15–16), 1939–1945.

[10] Shin, K.; Han, Y.; Noh, D. Synthesis and Redox Property of Heterometallic ((dppf)M($C_8H_4S_8$ and (dppf)M(C_6S_8 (M = Pd and Pt, dppf = 1,1'-Bis(Diphenylphosphino)Ferrocene). *Bull. Korean Chem. Soc.* **2003**, *24* (2), 235–238.

[11] Khodorkovsky, V.; Shapiro, L.; Krief, P.; Shames, A.; Mabon, G.; Gorgues, A.; Giffard, M. Do π-Dimers of Tetrathiafulvalene Cation Radicals Really Exist at Room Temperature? *Chem. Commun.* **2001**, *1* (24), 2736–2737.

[12] (a)Tanaka, H. A Three-Dimensional Synthetic Metallic Crystal Composed of Single-Component Molecules. *Science.* **2001**, *291* (5502), 285–287. (b)Matsubayashi, G.; Nakano, M.; Tamura, H. Structures and Properties of Assembled Oxidized Metal Complexes with C8H4S8 and Related Sulfur-Rich Dithiolate Ligands. *Coord. Chem. Rev.* **2002**, *226* (1–2), 143–151. (c)Kobayashi, A.; Fujiwara, E.; Kobayashi, H. Single-Component Molecular Metals with Extended-TTF Dithiolate Ligands. *Chem. Rev.* **2004**, *104* (11), 5243–5264. (d)Okano, Y.; Zhou, B.; Tanaka, H.; Adachi, T.

High-Pressure (up to 10 . 7 GPa) Crystal Structure of Single-Component Molecular Metal [Au(tmdt)$_2$]. **2009**, No. 6, 7169–7174. (e)Zhou, B.; Idobata, Y.; Kobayashi, A.; Cui, H.; Kato, R.; Takagi, R.; Miyagawa, K.; Kanoda, K.; Kobayashi, H. Single-Component Molecular Conductor [Cu(dmdt)$_2$] with Three-Dimensionally Arranged Magnetic Moments Exhibiting a Coupled Electric and Magnetic Transition. *J. Am. Chem. Soc.* **2012**, *134* (30), 12724–12731. (f)Cui, H.; Kobayashi, H.; Ishibashi, S.; Sasa, M.; Iwase, F.; Kato, R.; Kobayashi, A. A Single-Component Molecular Superconductor. *J. Am. Chem. Soc.* **2014**, *136* (21), 7619–7622. (g)Zhou, B.; Ogura, S.; Liu, Q. Z.; Kasai, H.; Nishibori, E.; Kobayashi, A. A Single-Component Molecular Conductor with Metal–Metal Bonding, [Pd(hfdt)$_2$] (hfdt: Bis(Trifluoromethyl)Tetrathiafulvalenedithiolate). *Chem. Lett.* **2016**, *45* (3), 303–305. (h)Valade, L.; de Caro, D.; Faulmann, C.; Jacob, K. TTF[Ni(dmit)$_2$]$_2$: From Single-Crystals to Thin Layers, Nanowires, and Nanoparticles. *Coord. Chem. Rev.* **2016**, *308*, 433–444. (i)Silva, R.; Vieira, B.; Andrade, M.; Santos, I.; Rabaça, S.; Lopes, E.; Coutinho, J.; Pereira, L.; Almeida, M.; Belo, D. Gold and Nickel Extended Thiophenic-TTF Bisdithiolene Complexes. *Molecules* **2018**, *23* (2), 424. (j)Zhou, B.; Ishibashi, S.; Ishii, T.; Sekine, T.; Takehara, R.; Miyagawa, K.; Kanoda, K.; Nishibori, E.; Kobayashi, A. Single-Component Molecular Conductor [Pt(dmdt)$_2$]—a Three-Dimensional Ambient-Pressure Molecular Dirac Electron System. *Chem. Commun.* **2019**, *55* (23), 3327–3330.

[13] Lu, W.; Zhang, Y.; Dai, J.; Zhu, Q.-Y.; Bian, G.-Q.; Zhang, D.-Q. A Radical-Radical and Metal–Metal Coupling Tetrathiafulvalene Derivative in Which Organic Radicals Directly Coordinate to CuII Ions. *Eur. J. Inorg. Chem.* **2006**, *2006* (8), 1629–1634.

[14] (a)Narayan, T. C.; Miyakai, T.; Seki, S.; Dincă, M. High Charge Mobility in a Tetrathiafulvalene-Based Microporous Metal–Organic Framework. *J. Am. Chem. Soc.* **2012**, *134* (31), 12932–12935. (b)Sun, L.; Park, S. S.; Sheberla, D.; Dincă, M. Measuring and Reporting Electrical Conductivity in Metal-Organic Frameworks: Cd$_2$(TTFTB) as a Case Study. *J. Am. Chem. Soc.* **2016**, *138* (44), 14772–14782. (c)Xie, L. S.; Dincă, M. Novel Topology in Semiconducting Tetrathiafulvalene Lanthanide Metal-Organic Frameworks. *Isr. J. Chem.* **2018**, *58* (9–10), 1119–1122. (d) Xie, L. S.; Alexandrov, E. V.; Skorupskii, G.; Proserpio, D. M.; Dincă, M. Diverseπ–π Stacking Motifs Modulate Electrical Conductivity in Tetrathiafulvalene-Based Metal–Organic Frameworks. *Chem. Sci.* **2019**, 10, 8558-8565.

[15] (a) Mazziotti, D. A. Two-Electron Reduced Density Matrix as the Basic Variable in Many-Electron Quantum Chemistry and Physics. *Chem. Rev.* **2012**, 112, 244−262. (b) Mazziotti, D. A., Ed. Variational Two-Electron Reduced-Density Matrix Theory. In Reduced-Density-Matrix Mechanics: With Application to Many-Electron Atoms and Molecules; John Wiley and Sons, Inc.: Hoboken, NJ, **2007**; pp 19−59. (c) Nakata, M.; Nakatsuji, H.; Ehara, M.; Fukuda, M.; Nakata, K.; Fujisawa, K. Variational Calculations of Fermion Second-Order Reduced Density Matrices by Semidefinite Programming Algorithm. *J. Chem. Phys.* **2001**, 114, 8282−8292. (d) Mazziotti, D. A. Realization of Quantum Chemistry without Wave Functions through First-Order Semidefinite Programming. Phys. Rev. Lett. 2004, 93, 213001. (e) Gidofalvi, G. and Mazziotti, D. A. Active-Space Two-Electron Reduced-Density-Matrix Method: Complete Active-Space Calculations without Diagonalization of the N-electron Hamiltonian. J. Chem. Phys. 2008, 129, 134108. (f) Shenvi, N.; Izmaylov, A. F. Active-Space N-Representability Constraints for Variational Two-Particle Reduced Density Matrix Calculations. *Phys. Rev. Lett.* **2010**, 105, 213003. (g) Mazziotti, D. A. Large-Scale Semidefinite Programming for Many-Electron Quantum Mechanics *Phys. Rev. Lett.* **2011**, 106, 083001. (h) Verstichel, B.; van Aggelen, H.; Poelmans, W.; Van Neck, D. Variational Two-Particle Density Matrix Calculation for the Hubbard Model Below Half Filling

Using Spin-Adapted Lifting Conditions. *Phys. Rev. Lett.* **2012**, 108, 213001. (i) Fosso-Tande, J.; Nguyen, T.-S.; Gidofalvi, G.; DePrince, A. E., III Large-Scale Variational Two-Electron Reduced-Density-Matrix Driven Complete Active Space Self-Consistent Field Methods. *J. Chem. Theory Comput.* **2016**, 12, 2260−2271. (j) Mazziotti, D. A. Enhanced Constraints for Accurate Lower Bounds on Many-Electron Quantum Energies from Variational Two Electron Reduced Density Matrix Theory. *Phys. Rev. Lett.* **2016**, 117, 153001.

[16] (a) Schlimgen, A. W.; Heaps, C. W.; Mazziotti, D. A. Entangled Electrons Foil Synthesis of Elusive Low-Valent Vanadium Oxo Complex. *J. Phys. Chem. Lett* **2016**, 7, 627–631. (b) Schlimgen, A. W.; Mazziotti, D. A. Static and Dynamic Electron Correlation in the Ligand Noninnocent Oxidation of Nickel Dithiolates. *J. Phys. Chem. A* **2017**, 121, 9377–9384. (c) Montgomery, J. M.; Mazziotti, D. A. Strong Electron Correlation in Nitrogenase Cofactor, FeMoco. *J. Phys. Chem. A* **2018**, 122, 4988–4996. (d) McIsaac, A. R.; Mazziotti, D. A. Ligand Non-innocence and Strong Correlation in Manganese Superoxide Dismutase Mimics. Phys. Chem. Chem. Phys. **2017**,19, 4656–4660.

[17] Maple Quantum Chemistry Toolbox (2019). Maplesoft, a division of Waterloo Maple Inc., Waterloo, Ontario.

[18] alence Basis Sets for First-row Elements. *J. Am. Chem. Soc.* **1980**, 102, 939−947. (b) Gordon, M.; Binkley, J.; Pople, J.; Pietro, W.; Hehre, W. Self-consistent Molecular Orbital Methods. 22. Small Split-valence Basis Sets for Second-row Elements. *J. Am. Chem. Soc.* **1982**, 104, 2797−2803. (c) Dobbs, K.; Hehre, W. Molecular Orbital Theory of the Properties of Inorganic and Organometallic Compounds. 5. Extended Basis Sets for First-row Transition Metals. *J. Comput. Chem.* **1987**, 8, 861−879. (d) Dobbs, K.; Hehre, W. Molecular Orbital Theory of the Properties of Inorganic and Organometallic Compounds. 6. Extended Basis Sets for Second-row Transition Metals. *J. Comput. Chem.* **1987**, 8, 880−893.

[19] Alvarez, S.; Vicente, R.; Hoffmann, R. Dimerization and Stacking in Transition-Metal Bisdithiolenes and Tetrathiolates. *J. Am. Chem. Soc.* **1985**, *107* (22), 6253–6277.

[20] Vogt, T.; Faulmann, C.; Soules, R.; Lecante, P.; Mosset, A.; Castan, P.; Cassoux, P.; Galy, J. A LAXS (Large Angle X-Ray Scattering) and EXAFS (Extended X-Ray Absorption Fine Structure) Investigation of Conductive Amorphous Nickel Tetrathiolato Polymers. *J. Am. Chem. Soc.* **1988**, *110* (6), 1833–1840.

[21] Svenstrup, N.; Rasmussen, K. M.; Hansen, T. K.; Becher, J. The Chemistry of TTFTT; 1: New Efficient Synthesis and Reactions of Tetrathiafulvalene-2,3,6,7-Tetrathiolate (TTFTT): An Important Building Block in TTF-Syntheses. *Synthesis.* **1994**, 809–812.

[22] (a)Van Hecke, G. R.; Horrocks, W. D. Ditertiary Phosphine Complexes of Nickel. SpeCtral, Magnetic, and Proton Resonance Studies. A Planar-Tetrahedral Equilibrium. *Inorg. Chem.* **1966**, *5* (11), 1968–1974. (b)Angulo, I. M.; Bouwman, E.; van Gorkum, R.; Lok, S. M.; Lutz, M.; Spek, A. L. New Nickel-Containing Homogeneous Hydrogenation Catalysts. *J. Mol. Catal. A Chem.* **2003**, *202* (1–2), 97–106.

[23] Chávez, I.; Alvarez-Carena, A.; Molins*, E.; Roig, A.; Maniukiewicz, W.; Arancibia, A.; Arancibia, V.; Brand, H.; Manuel Manríquez*, J. Selective Oxidants for Organometallic Compounds Containing a Stabilising Anion of Highly Reactive Cations: $(3,5(CF_3)_2C_6H_3)_4B^-)Cp_2Fe^+$ and $(3,5(CF_3)_2C_6H_3)_4B^-)Cp^*_2Fe^+$. *J. Organomet. Chem.* **2000**, *601* (1), 126–132.

[24] Hunter, B. K.; Reeves, L. W. Chemical Shifts for Compounds of the Group IV Elements Silicon and Tin *Can. J. Chem.* **1968**, *46*, 1399-1414.

[25] Sheldrick, G. M. SHELXT- Integrated space-group and crystal-structure determination. *Acta Cryst***. 2015**, *A71*, 3- 9

[26] Dolomanov, O.V.; Bourhis, L. J.; Gildea, R. J.; Howard, A. K.; and Puschmann, H., Olex2, a complete structure solution, refinement, and analysis program. *J. Appl. Cryst*. **2009**. *42*, 339

[27] (a) Sheldrick, G. M. A Short History of SHELX. *Acta Cryst*. **2008***, A64*, 112-122; (b) Sheldrick, G. M. Crystal structure refinement with SHELXL. *Acta Cryst*. **2015,** *C71*, 3-8.

Chapter 5: Organic Diradical Characters Induced by Iron Spin Crossover

5.1 Introduction

Organic diradicals feature two unpaired electrons which can populate either triplet or open-shell singlet ground states.[1] These unusual species have attracted attention both for their fundamental properties and for applications in organic semiconductors, non-linear optics, singlet fission, and spintronics.[2] Significant progress has been made in generating stable species and in understanding their ground states and electronic structures.[3] Tuning or switching diradical character with external stimuli, however, remains challenging.[4] This advance is crucial for responsive properties as would be required in spintronics or optical applications.

Spin-crossover is a well-known phenomenon in inorganic chemistry,[5] particularly in six-coordinate Fe(II) complexes.[6] The ability to switch between high- (S = 2) and low-spin (S = 0) states with light (i.e. the LIESST effect)[7] or heat makes spin-crossover complexes attractive targets for applications in memory, displays, sensors, and, most relevantly, switches.[8] Combining spin-crossover phenomena with appropriate organic ligands is therefore a compelling strategy for generating switchable diradicals. Merging radical containing ligands with transition metal centers has been an area of active study.[9] While several metal containing organic diradicals have been reported in recent years, these examples are largely limited to transient intermediates or pairs of monoradical ligands.[10] The viability of spin-crossover modulated diradical character remains untested.

In targeting radical ligands, the archetypal organic electronic material tetrathiafulvalene (TTF) and its derivatives are attractive targets due their redox-activity and electronic

properties. [11] Recently, we have synthesized multiple tetrathiafulvalene-2,3,6,7-tetrathiolate ($TTFtt^{n-}$; n = 4, 3, and 2) complexes.[12] While TTF-based diradicals have not been previously reported, we hypothesized that a compressed π manifold in oxidized $TTFtt^{2-}$ ligands combined with variable π interactions between low- and high-spin Fe centers might enable switchable diradical behavior.

Herein, we report the compounds $(FeTPA)_2TTFtt$ (**1**) (TPA = tris(2-pyridylmethyl)amine) and $[(FeTPA)_2TTFtt][BAr^F{}_4]_2$ (**2**) ($BAr^F{}_4$ = tetrakis[3,5- bis(trifluoromethyl)phenyl]borate) as well as their monomeric analogues Fe(TPA)(dmit) (**3**) and $[Fe(TPA)(dmit)][BAr^F{}_4]$ (**4**) (dmit = 1,3-dithiole-2-thione-4,5-dithiolate, **Scheme 5.1**A). Compound **2** represents the first thoroughly characterized example of $TTFtt^{n-}$ ligands coordinated to Fe ions. Compound **2** exhibits spin-crossover induced switching of $TTFtt^{2-}$-based diradical character and is thus an unusual example showing how inorganic spin transitions can be used to change organic diradical character.

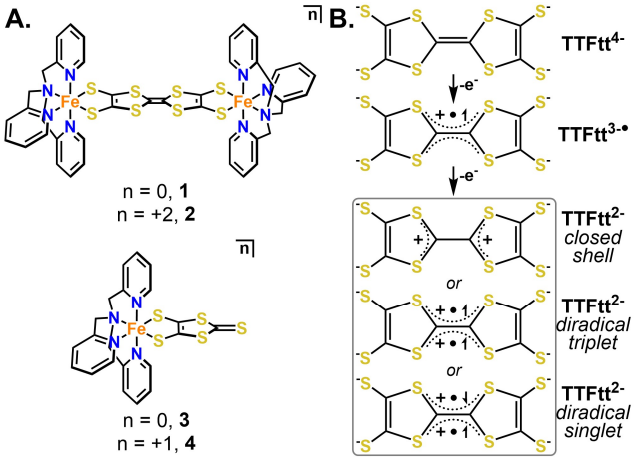

Scheme 5.1. A. Synthesized dinuclear compounds of $TTFtt^{n-}$ and mononuclear $dmit^{n-}$ analogues that serve as half-unit models. B. Possible redox and spin isomers of $TTFtt^{n-}$ ligands discussed in the text.

5.2 Results and Discussion

5.2.1 Synthesis and Structural Parameters

Complex **1** was synthesized via reaction with the deprotected proligand 2,3,6,7-tetrakis(2-cyanoethylthio)tetrathiafulvalene (TTFtt($C_2H_4CN)_4$) in good yield. Complex **1** was insoluble in all solvents we investigated which precluded detailed characterization but is pure as indicated by combustion analysis and behaves as a suitable synthon for subsequent chemistry. Complex **1** can be doubly oxidized with [Cp_2Fe][$BAr^F{}_4$] to form **2** which is more soluble, enabling common solution characterization including ^{1}H NMR and cyclic voltammetry measurements (**Figure D.1** and **Figure D**.2). Oxidation from **1** to **2** could be ligand-centered ($TTFtt^{4-}\rightarrow TTFtt^{2-}$), metal-centered (2 Fe(II)→2 Fe(III)), or some intermediate case, but the data acquired for **2** supports a $TTFtt^{2-}$ structure arising from ligand-centered oxidation (**Scheme 5.1B**, see below).

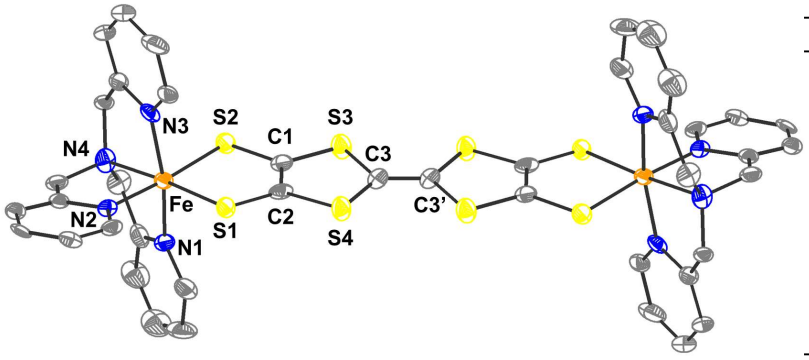

Å	2-HT	2-LT	Δ (from HT)
Fe–S1	2.368(3)	2.239(2)	−0.129(4)
Fe–S2	2.479(3)	2.289(2)	−0.190(4)
Fe–N1	2.138(8)	1.958(6)	−0.180(10)
Fe–N2	2.168(7)	1.979(6)	−0.189(9)
Fe–N3	2.160(9)	1.976(6)	−0.184(11)
Fe–N4	2.261(8)	2.017(6)	−0.244(11)
C3–C3'	1.408(18)	1.353(15)	−0.05(2)
C3–S3	1.701(11)	1.757(8)	+0.056(14)
C3–S4	1.690(10)	1.719(8)	+0.029(13)

Figure 5.1. Molecular structure for 2 collected at 100 K by SXRD (2-LT). H atoms, counterions, and solvent molecules are omitted for clarity and ellipsoids are shown at 50%. Selected bond length parameters for 2 at 293 K (2-HT) and 100 K (2-LT).

Compound **2** was structurally characterized via single-crystal X-ray diffraction (SXRD) at 293 K (**2-HT**; **Figure D.3**) and 100 K (**2-LT**; **Figure 5.1**). In both structures $TTFtt^{2-}$ is bridged between two TPA-capped Fe centers with two outer-sphere $BAr^F{}_4{}^-$ counter anions. The most striking difference between these temperatures is markedly longer Fe bond lengths in **2-HT**. The Fe–$N_{pyridine}$ and Fe–N_{amine} bond lengths in **2-LT** are 1.958(6)–1.979(6) and 2.017(6) Å (**Figure 5.1**), respectively. These values are consistent with Fe–N bonds in other low-spin complexes with a Fe-TPA moiety.[6a, e] In **2-HT**, these bonds are 0.18–0.19 and 0.244(11) Å longer than their counterparts

at 100 K, respectively, and are consistent with high-spin Fe-TPA complexes. The shorter Fe bonds at lower temperature indicate that **2** exhibits a temperature dependent spin-crossover as observed in related compounds.[6a, 7c]

In addition to the geometric changes at Fe, the central C3–C3′ bond and the central C–S bonds (C3–S3 and C3–S4) in the TTF core of **2** show temperature dependent differences of ~0.04 Å (**Figure 5.1**) suggesting some electronic structure change on this ligand as well. These bonds are markers for the oxidation state of $TTFtt^{n-}$, where similar increases in the C3–C3′ bond length and decreases in the C3-S3/4 bond lengths of ~0.02 Å are correlated to the change from $TTFtt^{3-\cdot}$ to $TTFtt^{2-}$, potentially suggesting that the geometric changes at Fe and the $TTFtt^{n-}$ ligand are due to a charge transfer induced spin transition (**Table D.1**).[12, 13] Theory and experiment, however, suggest that these changes instead arise from increased diradical character on $TTFtt^{2-}$ upon cooling from **2-HT** to **2-LT** leading to differential population of C–C and C–S π orbitals (see below). In sum, the structural data on **2** support an Fe centered spin transition with additional electronic structure changes of the $TTFtt^{2-}$ ligand.

The mononuclear compounds **3** and **4** were also synthesized as half-unit analogues to **1** and **2**, respectively, using the related $dmit^{2-}$ ligand in place of $TTFtt^{4-}$. The structure of **3** was determined by SXRD (**Figure D.4**), and the Fe–N bonds fall within in the range commonly observed for high-spin Fe(II). While the data quality for **4** was poor, connectivity could be determined by SXRD (**Figure D.5**) and confirms the assigned structure.

5.2.2 Mössbauer Spectroscopy

The neutral compound **1** exhibits two Fe signals over the temperature range from 250 K to 80 K (**Figure D.6-Figure D**.9). Both signals are characteristic of TPA ligated 6-coordinate HS Fe(II) with isomer shifts (δ) of 0.968(2) mm/s and 1.084(2) mm/s and quadrupole splitting (ΔE_Q) values

of 3.588(5) mm/s and 2.773(1) mm/s at 80 K. The percent composition of these two signals varies batch-to-batch, and therefore likely represents different packing morphologies of **1** leading to subtle differences at the Fe sites.

At 250 K, the ^{57}Fe Mössbauer spectrum of solid **2** shows a high-spin Fe(II) species comprising 46(5)% of the sample with an isomer shift (δ) of 0.880(9) mm/s and quadrupole splitting (ΔE_Q) of 3.22(2) mm/s (**Figure 5.2**A, green).[6e, 14] The remaining sample has a broad, poorly resolved signal (blue) potentially composed of multiple sites with an δ of 0.23(2) mm/s and ΔE_Q of 0.81(2) mm/s which we assign as low-spin Fe(II) sites. These parameters are outside of the typical ranges for both low-spin Fe(II) (δ: 0.36–0.52 mm/s; ΔE_Q: 0.23–0.52 mm/s) and low-spin Fe(III) (δ: 0.20-0.28 mm/s; ΔE_Q: 1.5–1.7 mm/s) reported for TPA ligated 6-coordinate complexes, but are similar to other low-spin Fe(II) species.[15]

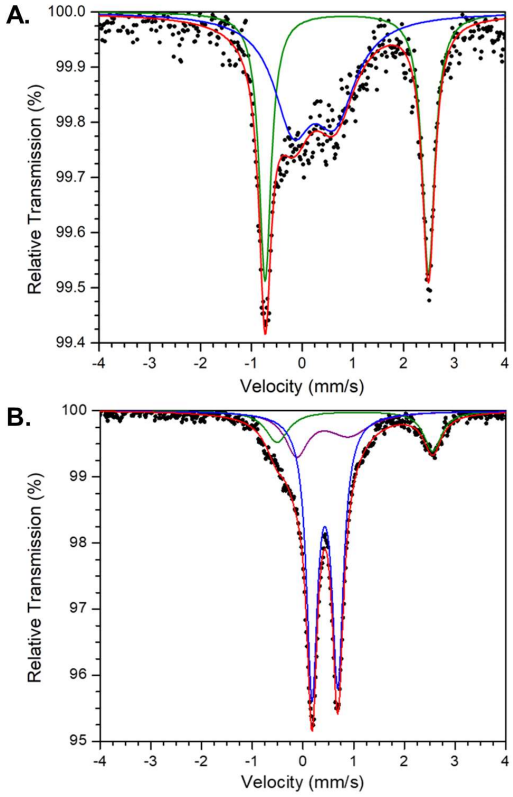

Figure 5.2. A. ^{57}Fe Mössbauer data for solid 2 collected at 250 K. B. ^{57}Fe Mössbauer data for 2 collected at 80 K. The data is in black, the red line is the overall fit and the blue, green, and purple lines show the fits to the three Fe sites, as outlined in the text.

Upon cooling, the proportion of low-spin Fe(II) in **2** increases while the signal for high-spin Fe(II) decreases as expected for spin-crossover. At 80 K (**Figure 5.2**B), the low-spin species (blue) has an δ of 0.314(1) mm/s and ΔE_Q of 0.490(3) mm/s, and constitutes 74(1)% of the sample, while the high-spin species (green; δ: 0.9(1), ΔE_Q: 2.87(2)) mm/s) comprises 19(1)%. A small amount (<10%) of an unidentified Fe species is present (purple; δ: 0.39(2) mm/s, ΔE_Q: 1.26(4) mm/s). This site may either correspond to some high-spin Fe(III) impurity or another low-spin Fe(II) species, potentially from different solid state packing of **2**. Similar convoluted features have been observed at low-temperature in other Fe-based spin-crossover compounds.[16] EPR features indicative of Fe(III) are absent in **2** (see below) suggesting that this small signal does arise from an Fe(II) site in another form of **2**. This is supported by the fact that spectra of frozen solutions of **2** in PEG-2000 are better fit to only two sites (**Figure D.10** and **Figure D**.11).

If the ligand bond changes between **2-HT** and **2-LT** represented reduction from $TTFtt^{2-}$ to radical $TTFtt^{3-\cdot}$ a concomitant, presumably Fe-based, oxidation must be occurring. In this case one would either expect: (i) two fully localized, unequal Fe centers (i.e. Fe(II) and Fe(III)) or (ii) two mixed-valent Fe(II/III) centers. The low-temperature Mössbauer data only shows a single major Fe feature eliminating possibility (i). The absence of an inter-valence charge transfer band in the low-temperature electronic spectra of **2** (see below) alternatively eliminates possibility (ii). This suggests that **2** is predominantly Fe(II) with a $TTFtt^{2-}$ ligand at all temperatures and any resonance structures invoking Fe(III) with a $TTFtt^{3-\cdot}$ ligand are minor contributors. Therefore, the changes in C–C and C–S bond lengths between **2-HT** and **2-LT** arise from a different type of change in the electronic structure of $TTFtt^{2-}$.

Complex **3** has a straightforward Mössbauer spectrum at both 250 K and 80 K, which features a single signal characteristic of a HS Fe(II) (**Figure D.12** and **Figure D**.13). The Mössbauer

spectrum of **4** has a signal with a δ of 0.282 to 0.338 mm/s and ΔE_Q of 1.32 to 1.40 mm/s between 250 K and 80 K, respectively (**Figure D.14** and **Figure D**.15). These data indicate that **4** is best thought of as a low-spin Fe(II) center bound to a $dmit^{\cdot -}$ radical, and corroborate similar low-spin Fe(II) features in **2**.

5.2.3 Magnetometry

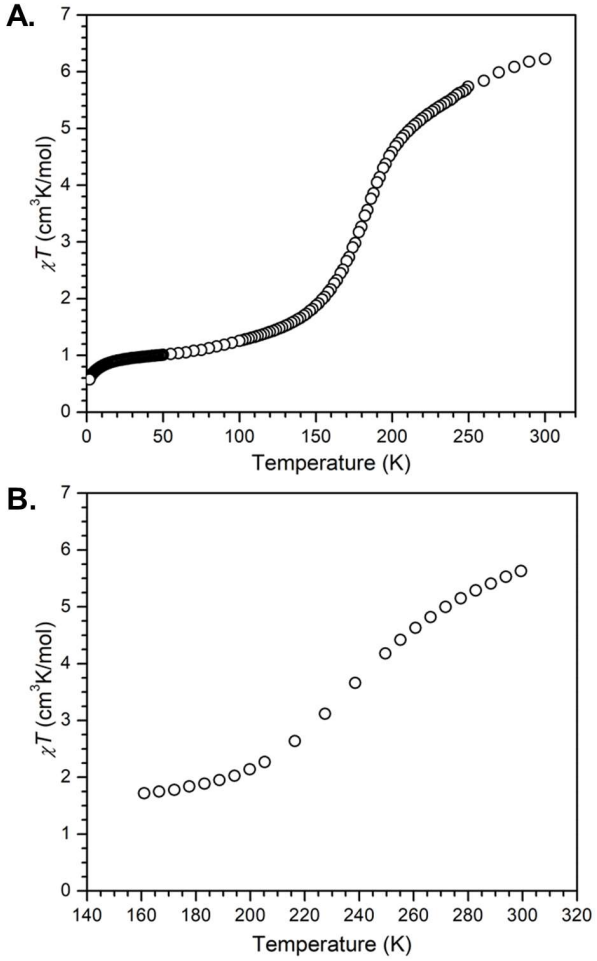

Figure 5.3. A. Temperature dependent magnetic susceptibility of 2 in the solid state, collected under an applied field of 0.1 T. B. Temperature dependent magnetic susceptibility of 2 in 95% 2-chlorobutane/5% C_6D_6 obtained via the Evans method.

The magnetic properties of **1** suggest two magnetically isolated high-spin Fe(II) ($S = 2$) centers (**Figure D.16**) and thus no coupling between the Fe centers were included in treating the magnetic data. However, the variable temperature χT differ drastically upon oxidation to **2** (**Figure 5.3**A).

The χT of **2** is near the spin-only value of 6 cm^3K/mol at 300 K, but decreases sharply between ~200–150 K. This behavior is completely reversible upon warming (**Figure D.17**). These data indicate two primary regions: high-temperature with high χT and low-temperature with low χT, separated by spin-crossover. From the molecular structures and Mössbauer data in the high- and low-temperature regions, the Fe centers show clear indications of undergoing spin-crossover from high- to low-spin, consistent with the observed decrease in χT. However, a low-temperature χT = 0 would be expected for low-spin Fe(II) (S = 0) centers without significant temperature independent paramagnetism, which is not observed.

One possible explanation is that **2** undergoes incomplete spin-crossover as has been previously observed in related systems.[7c, 17] Indeed, the magnetic behavior of **2** shows high sensitivity to batch effects, which is commonly observed in spin-crossover compounds.[18] However, no sample of **2** shows a χT approaching zero. Instead, χT is near the values expected for a diradical triplet (S = 1, χT ~ 1 cm^3K/mol) or a diradical system with weak coupling (2 S = ½, χT ~ 0.75 cm^3K/mol). Fitting the magnetic data to the Boltzmann equation gives a ΔH = 1030 cm^{-1} and $T_{1/2}$ = 185 K (**Figure D.18**).[19]

Solution phase variable temperature ^2H NMR Evans method measurements of **2** were performed to determine the χT of **2-LT** in the absence of possible incomplete spin-crossover due to packing effects in the solid state. These data (**Figure 5.3**B) show a significant drop upon cooling and a plateau at χT = 1.7(1) cm^3K/mol at 160 K. Importantly, the electronic spectrum of **2** under the same conditions (see below) shows that spin-crossover is complete by ~170 K. This indicates that the χT at 160 K arises from **2-LT**, which therefore cannot be diamagnetic. The above mentioned Mössbauer data rule out any major resonance contribution from Fe(III) with a $TTFtt^{3-\cdot}$ ligand which suggests that the nonzero χT across the low temperature region must arise from unpaired

spin density on $TTFtt^{2-}$. Fitting the solution phase magnetic data to the Boltzmann equation gives ΔH = 1400 cm^{-1} and $T_{1/2}$ = 260 K (**Figure D.19**).

The neutral compound **3** exhibits magnetic behavior as expected for a HS Fe(II) (S = 2) center (**Figure D.20**) and cooling to 1.8 K does not yield any notable features which would contradict a simple assignment of a HS Fe(II) and a diamagnetic $dmit^{2-}$ ligand. Monocationic **4** has a χT near the expected value for a S = ½ species (χT_{SO} = 0.375 cm^3K/mol; **Figure D.21**). The room temperature solution moment of **4** was also measured by Evans method as 2.1(1) μ_B (0.5 cm^3K/mol; **Figure D.22**) and supports the assignment of the species as S = ½ overall.

5.2.4 Variable Temperature UV-Vis-NIR Spectroscopy

The combined SXRD, Mössbauer, and magnetic measurements suggest that the Fe(II) centers in **2** undergo spin-crossover to a low-spin state upon cooling with an additional change on the $TTFtt^{2-}$ fragment that gives rise to unpaired electrons. The distinct electronic structure dependent changes in the absorption spectra of $TTFtt^{n-}$ ligands prompted us to collect variable temperature UV-Vis-Near-IR (UV-Vis-NIR) spectra of **2** (**Figure 5.4**).[12,15] As expected for a species with a diamagnetic $TTFtt^{2-}$ core, **2** shows an intense feature at 1074 nm in the NIR region. Upon cooling, the 1074 nm peak decreases in intensity while a broad feature at 1615 nm and sharper features at 325 and 396 nm increase. This spectroscopic behavior is fully reversible upon warming. Fitting the normalized intensity of the NIR feature at 1074 nm to the Boltzmann equation gives a ΔH = 1500 cm^{-1} and $T_{1/2}$ = 265 K, in good agreement with solution magnetic data (**Figure D.23**). Importantly, the spectra of **3**, **4** and $[(dppeNi)_2TTFtt][BAr^F{}_4]_2$, which is well described as a closed shell singlet, do not show similar changes with temperature, supporting fundamentally different properties in **2** at low temperature (**Figure D.24** and **Figure D**.26).

Radical $TTFtt^{3-\cdot}$ cores have a lower energy NIR feature than diamagnetic $TTFtt^{2-}$ cores.[12, 20] Additionally, the new high energy features (325 and 396 nm) of **2** at low temperature are similar to those reported for radical $TTFtt^{3-\cdot}$ complexes attributed to $\pi \rightarrow \pi^*$ transitions.[13b] However, these features in **2** at low temperature cannot be due to reduction of the $TTFtt^{2-}$ ligand to $TTFtt^{3-\cdot}$ as there is no significant oxidation of Fe upon cooling. We therefore used time-dependent density functional theory (TD-DFT) to better understand the observed features in the UV-Vis-NIR spectra.

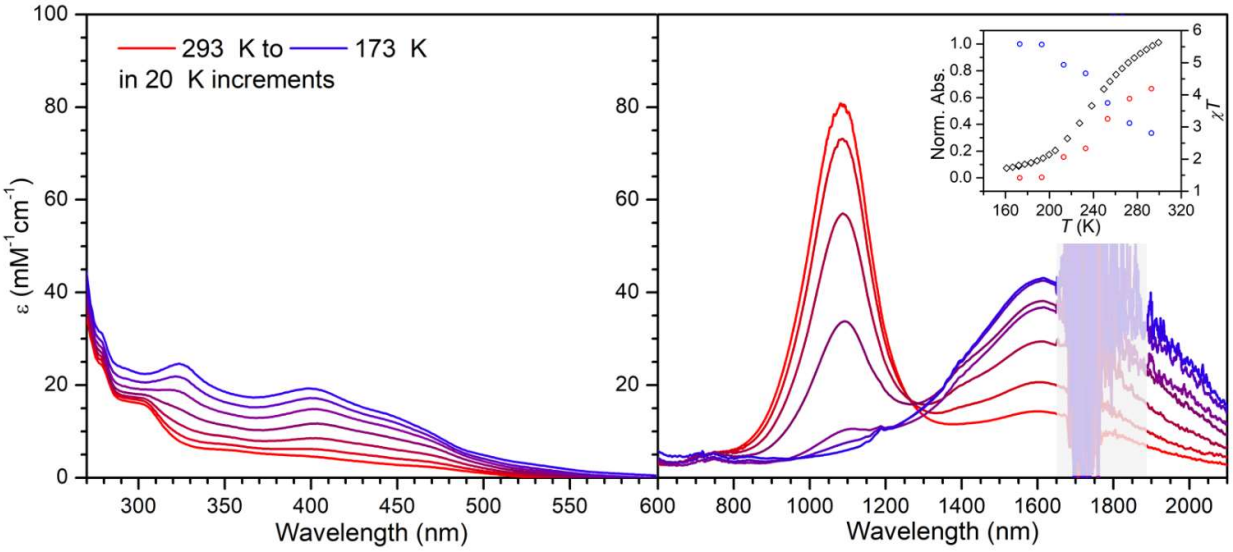

Figure 5.4. Variable temperature electronic spectra of 2 in the UV-visible (left) and visible-NIR (right) regions collected in 2-chlorobutane at 50 µM. The grey box (right) covers the strong NIR absorbances due to solvent. Inset at right shows the normalized maximum absorbance (left-axis) of the NIR features near 1100 nm (red) and 1600 nm (blue) versus temperature, along with the χT values (black, right-axis) of 2 obtained via Evans method in 95% 2-chlorobutane/5% C_6D_6.

Ground states for **2-HT** ($S = 4$) and for two potential forms of **2-LT** (diradical triplet, $S = 1$, with spin density localized on $TTFtt^{2-}$ and closed shell singlet, $S = 0$) were calculated using the corresponding SXRD structures. Similar calculations were carried out for $[(dppeNi)_2TTFtt][BAr^F{}_4]_2$ as a comparison and calibration standard (**Figure D.27**). The NIR transitions were well predicted from TD-DFT as $TTFtt^{2-}$ π-based transitions (**Figure D.28** and **Figure D**.30). Importantly, the calculated spectrum of the $S = 1$ diradical closely matches the low-

temperature NIR feature in **2-LT** (**Figure D.31**). The prominent NIR transition of **2** at 293 K also closely matches the calculated features of species with closed-shell forms of $TTFtt^{2-}$, specifically **2-HT** (S = 4, with ~90% of spin density localized on the FeTPA fragments), the calculated closed-shell $S = 0$ state of **2-LT**, and the known singlet $[(dppeNi)_2TTFtt][BAr^F{}_4]_2$.[12] This analysis explains the observed UV-vis-NIR features in **2** and suggests that the $TTFtt^{2-}$ ligand gains substantial diradical character upon Fe centered spin-crossover.

The electronic spectrum of **3** in DCM was collected at room temperature and features two absorbances at 310 and 498 nm (**Figure D.32**), assignable to dmit transitions.[21] In the visible region, **4** has a strong peak at 417 nm with a shoulder near 370 nm (**Figure D.32**). As this absorbance is between the typical range of a Fe(II)→TPA metal-to-ligand charge transfer and the previously reported π→π* transition of the $dmit^{2-}$ ligand, it is not straightforward to assign based on the room temperature spectrum alone.[22] A broad band centered near 1050 nm is present in **4**, and notably absent in **3**. A broad absorbance in this range has been observed to appear when oxidizing a $dmit^{2-}$ containing complex to the radical $dmit^{\cdot-}$ species.[23] Upon cooling to 193 K, the high energy visible features increase in intensity, although to a lesser degree than was observed in **2**.

5.2.5 EPR Spectroscopy

The above data on **2** suggests that Fe spin-crossover mediates increased diradical character on the $TTFtt^{2-}$ ligand so we employed EPR spectroscopy to directly probe this proposed diradical character. The EPR spectrum of **2** at 15 K in DCM displays an intense signal near $g = 2$, consistent with a $|\Delta m_s| = 1$ transition of an organic $S = ½$ or $S = 1$ species (**Figure 5.5**A). Importantly, a much lower intensity feature around $g = 4$ is observed, characteristic of the $|\Delta m_s| = 2$ feature of organic diradical species.[1, 3c, 4c] Using the relative intensity of the $|\Delta m_s| = 2$ and 1 signals, the distance

between the radicals can be estimated.[1] In **2** this value is around 3.3–4.6 Å which is similar to the centroid-to-centroid distance between the two 5-membered rings in TTF (~4.1 Å). The observed signals for **2** are distinct from possible impurities,[18a] are reproducible over several samples (**Figure D.33** and **Figure D**.34), and are reasonably well simulated as a diradical (**Figure 5.5**A, red line). The intensity (I) of the $|\Delta m_s| = 2$ signal of **2** between 26–15 K implies a singlet (i.e. antiferromagnetically coupled diradical) ground-state wherein a decrease in I*T* upon cooling is expected as the EPR active triplet state is depopulated in favor of the EPR silent singlet state (**Figure 5.5**B).[1] Overall, these data support that **2-LT** has significant diradical character. The EPR spectrum of **4** shows a nearly isotropic signal near $g = 2$, confirming the organic radical character of this species and supporting a low-spin assignment for the Fe center (**Figure D.35**).

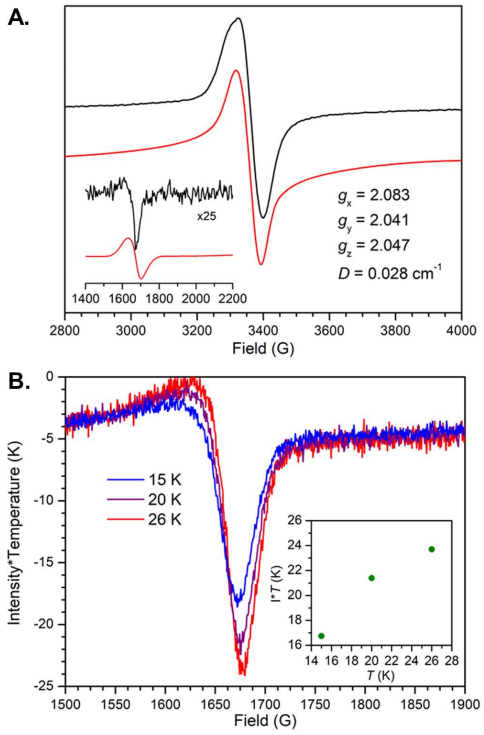

Figure 5.5. A. X-band EPR spectrum of 2 at 15 K in DCM at 5 mM with a power of 1.99 mW and frequency of 9.633 GHz. The inset shows the half-field signal centered around 1680 G increased in intensity by a factor of 25. Red lines indicate simulations with the parameters shown. Experimental data is shown in black. **B. Variable temperature change in intensity of the half-field signal of 2 by EPR.** Collected in DCM at 5 mM. Baselines have been normalized by shifting to overlap. Inset: Peak-to-peak intensity times temperature of the half-field signal versus temperature.

5.2.6 Computational Results

Advanced theoretical techniques were utilized to predict and understand the electronic character of the $TTFtt^{2-}$ ligand. Calculations were performed on **2-LT** using experimental geometries obtained via SXRD. DFT calculations with the B3LYP functional[24] and a 6-311G* basis set[25] as implemented in g16/a.01,[26] yielded a triplet ground state with a singlet-triplet gap of $\Delta E(S–T)$ = 409 cm^{-1}. The obtained spin density of the triplet state (**Figure 5.6**A and B) shows the vast majority of the unpaired electron density is localized on the linker with $\rho_{Fe} = 0.135$ on each FeTPA fragment, and $\rho_{TTFtt} = 1.730$.

Given the fact that DFT is not expected to accurately describe the complex electronic structure of open-shell singlet states we turned towards advanced theoretical techniques to validate the B3LYP results. Variational 2-electron reduced density matrix (V2RDM) calculations[27] were run in Maple 2019 Quantum Chemistry Package (QCP)[28] with a [18,20] active space and a 6-31G basis set, covering the entire spin manifold of singlet, triplet, quintet, septet, and nonet states. The results predict the ground state of **2-LT** to be a singlet ($\Delta E(S–T) = -373$ cm^{-1}) with strongly correlated, diradical character and frontier natural occupation numbers (NON) of $\lambda_{261} = 1.28$ and $\lambda_{262} = 0.72$ (**Figure 5.6**C, **Table D.3**). Based on the magnetic and spectroscopic data for **2**, the magnitude of the computed $\Delta E(S–T)$ is almost certainly overestimated. Inspection of the frontier NOs reveals the diradical to be localized almost exclusively on the $TTFtt^{2-}$ linker with negligible involvement of the Fe d-orbitals, in good agreement with the triplet result from DFT. Hartree Fock MO coefficients reveal similar distributions. Further calculations were performed to verify that these results were not an artifact of the choice of basis set or orbitals (**Table D.2**).

A.

B3LYP Triplet Spin Density

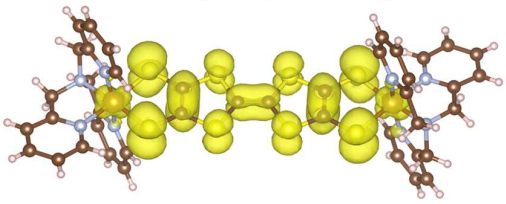

B.

DFT Spin Density

	ρFe_1	ρFe_2	$\rho TTFtt$
HT	3.69	3.87	0.25
LT	0.13	0.13	1.73

C. Singlet Triplet

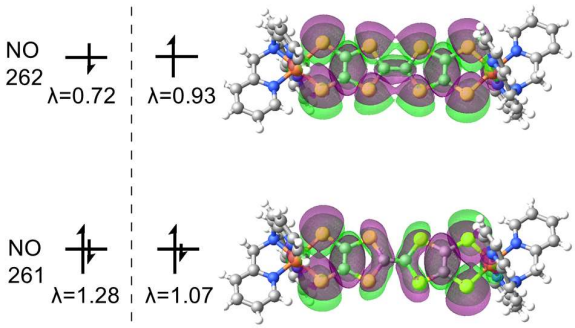

D.

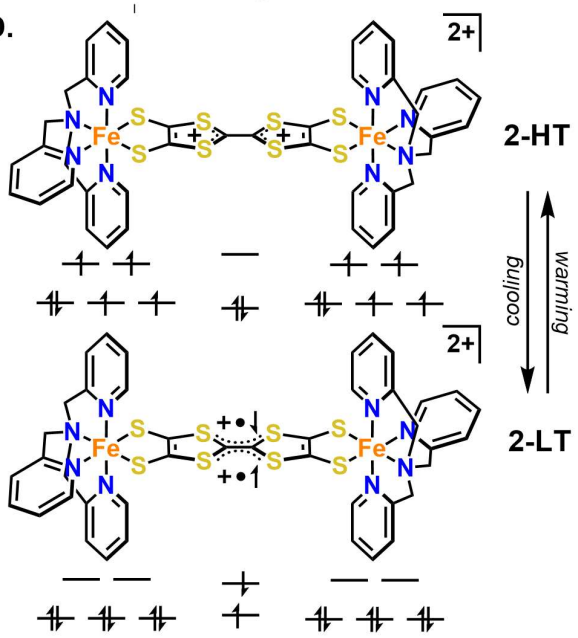

Figure 5.6. A. Spin density obtained for the triplet state of 2-LT in DFT with the B3LYP functional and a 6-311G* basis set as implemented in g16/a.01. B. Spin density obtained for the triplet state of 2-LT and 2-HT in DFT with the B3LYP functional and a 6-311G* basis set as implemented in g16/a.01. The values for "Fe" include all density on the FeTPA fragment. **C. Partially occupied frontier NOs and their corresponding NON of 2-LT from a diradical state [18,20] V2RDM calculation with a 6-31G basis set. D. Dominant resonance structures for 2-HT and 2-LT with qualitative frontier orbital diagrams.**

Additional calculations were performed on the $S = 4$ ground state of **2-HT** (**Figure D.36**). In **2-HT** weakening of the interaction between the Fe d-orbitals and the ligand orbitals raises the metal-based orbitals to yield eight singly occupied, Fe-based, frontier NOs. These results show a significant reduction in diradical character in the organic $TTFtt^{2-}$ linker in **2-HT**, as compared to **2-LT**. The unpaired electron density previously localized on the $TTFtt^{2-}$ π system in **2-LT** ($\rho_{TTFtt} = 1.730$) is instead in Fe-based NOs in **2-HT**, with $\rho_{TTFtt} = 0.25$.

The computational analysis clearly supports the assignment of a $TTFtt^{2-}$-based, strongly correlated diradical with open shell singlet and triplet states close in energy in **2-LT**. The temperature driven Fe-based spin transition gives rise to enhanced diradical character on the $TTFtt^{2-}$ core, that is an increase in the occupancy of the higher-lying NO262 at the expense of decreased occupancy in the lower-lying NO261. The DFT calculations suggest that this arises from the shrinking of the energy gap between the NO261 and NO262 in **2-LT** (19.59 kcal/mol), as compared to the analogous orbitals (NO254 and NO 268, respectively) in **2-HT** (26.01 kcal/mol).

The spin-crossover from **2-HT** to **2-LT** gives rise to enhanced diradical character on the $TTFtt^{2-}$ core. This spin transfer moves electron density from a C–C bonding and C–S antibonding orbital (NO 262 in **2-LT**, NO 268 in **2-HT**) to a C–C antibonding and C–S bonding orbital (NO 261 in **2-LT**, NO 254 in **2-HT**, **Figure 5.6**D). These changes in orbital populations correlate with the observed variations in bond lengths (**Figure 5.1**) and suggest that there should be bond length changes of similar trend, but of potentially larger magnitude when $TTFtt^{2-}$ undergoes a spin transition as compared to an electron transfer. This is indeed the case when comparing the larger bond length changes of **2** versus those between $[(dppeNi)_2TTFtt][BAr^F{}_4]_2$ and $[(dppeNi)_2TTFtt][BAr^F{}_4]$ (**Table D.1**).[12] Finally, as illustrated above with TD-DFT calculations, this orbital picture also supports the observed spectroscopic changes in **2**. Taken together, all the

computational analysis is consistent with the experimental data supporting that an Fe-based spin transition shrinks the gap between $TTFtt^{2-}$-based orbitals thereby increasing organic diradical character.

5.3 Conclusion

We have synthesized and characterized a family of novel Fe-thiolate compounds with intriguing electronic structures. Theory suggests that **2** shows temperature dependent Fe-based spin-crossover which decreases orbital energy separations on the $TTFtt^{2-}$ core generating significant diradical character. This is corroborated by SXRD data illustrating Fe-based spin-crossover alongside distinctive $TTFtt^{2-}$ bond changes. Mössbauer spectroscopy confirms a spin transition at Fe and the assigned Fe(II) oxidation state while variable temperature electronic spectra and magnetic susceptibility support the proposed change from a closed shell $TTFtt^{2-}$ to a diradical. Finally, the EPR data of **2** reveal signals diagnostic of organic diradicals.

Organic diradicals, as seen in **2** at low temperature, are relatively rare in general and are unknown in the well-studied TTF moiety. The reversible modulation of spin between this unusual organic diradical and the Fe centers in **2** represents a fundamentally new form of spin transition and opens the possibility to switch organic diradicals via stimulation of metal-based spin-crossover.

5.4 Experimental Section

General Methods

Syntheses and general handling were carried out in a nitrogen-filled MBraun glovebox unless otherwise noted. TTFtt-C_2H_4CN, [29] $Fe(TPA)(OTf)_2(MeCN)_2$, [30] dmit-(COPh) [31] and $[Fc][BAr^F{}_4]$ [32] were prepared according to literature procedures. Elemental analyses were performed by Midwest Microlabs. Electrochemical measurements were made on an Epsilon BAS potentiostat. THF and Et_2O were dried and degassed in a Pure Process Technologies solvent system, stirred over NaK amalgam for >24 hours, filtered through alumina, and stored over 4 Å molecular sieves. Methanol was dried with sodium hydroxide overnight, distilled, transferred into the glovebox and stored over 4 Å molecular sieves. 2-Chlorobutane was degassed by the freeze, pump, thaw method and stored over 4 Å molecular sieves. All other solvents were dried and degassed in a Pure Process Technologies solvent system, filtered through activated alumina, and stored over 4 Å molecular sieves. Solvents were tested for O_2 and H_2O with a standard solution of sodium benzophenone ketyl radical. All other reagents were used as purchased without further purification.

$(FeTPA)_2TTFtt$ (1)

$TTFtt(C_2H_4CN)_4$ (0.054 g, 0.099 mmol) was stirred with sodium tert-butoxide (0.076 g, 0.791 mmol) in THF (6 mL) overnight. The solid material was collected, washed with THF (4 mL x 3), and dried under vacuum to yield a pink powder. The pink solid was then stirred with $Fe(TPA)(OTf)_2(MeCN)_2$ (0.152 g, 0.209 mmol) in THF (6 mL) for 2 days. The resulting brick red solid was collected, washed with THF (4 mL x 3), and dried under vacuum (0.102 g, 100%). Elemental analysis: expected for $C_{42}H_{36}Fe_2N_8S_8$: % C, 49.41; H, 3.56; N, 10.98. Found: % C, 49.78; H, 3.77; N, 10.88.

[(FeTPA)$_2$TTFtt][BAr$^F{}_4$]$_2$ (2)

[Fc][BAr$^F{}_4$] (0.102 g, 0.097 mmol) was dissolved in DCM (12 mL) and added in 4 portions to (FeTPA)$_2$TTFtt (0.065 g, 0.064 mmol) and stirred for 5 minutes after each addition. The mixture was filtered through Celite and the filtrate was layered with petroleum ether. After cooling at −38 °C for several days, dark brown crystalline solid formed and was washed with petroleum ether and dried under vacuum (0.081 g, 60%). Crystals suitable for X-ray diffraction were similarly grown from DCM and petroleum ether. ^{1}H NMR (400 MHz, 25 °C, CD_2Cl_2) δ = 57.5, 56.1, 7.7, 7.5, −4.8. Elemental analysis: expected for $C_{106}H_{60}B_2F_{48}Fe_2N_8S_8$: % C, 46.34; H, 2.20; N, 4.08. Found: % C, 46.54; H, 2.26; N, 4.02. EPR (DCM): g_x = 2.083, g_y = 2.041, g_z = 2.047, D = 0.028 cm^{-1}. UV-vis-NIR at 20 °C, 2-chlorobutane (ϵ, M^{-1} cm^{-1}): 1025 nm (8 x10^4), 280 nm (3 x10^4), 300 nm (2 x10^4); (−100 °C, 2-chlorobutane): 1615 nm (4 x10^4), 325 nm (3 x10^4), 396 nm (2 x10^4).

Fe(TPA)(dmit)·0.5CH$_2$Cl$_2$ (3)

The deprotection and metalation procedure was adapted from similar procedures previously reported in the literature.[33] dmit-(COPh) (0.080 g, 0.196 mmol) was stirred with sodium methoxide (0.022 g, 0.407 mmol) in methanol (6 mL) for 1 hour, then Fe(TPA)(OTf)$_2$(MeCN)$_2$ (0.152 g, 0.209 mmol) was added and stirred overnight. Complex **3** was collected, washed with DCM (4 mL x 3), and dried under vacuum to yield a bright red solid (0.070 g, 61%). Crystals suitable for X-ray diffraction were grown from DCM and petroleum ether. ^{1}H NMR (400 MHz, 25 °C, $CDCl_3$) δ = 81.1, 59.9, 59.8, 35.7, −2.99. Elemental analysis: expected for $C_{21.5}H_{21}ClFeN_4S_5$: % C, 44.14; H, 3.27; N, 9.58. Found: % C, 44.65; H, 3.22; N, 9.01. UV-vis-NIR (20 °C, DCM): 310 nm, 498 nm.

[Fe(TPA)(dmit)][BAr$^F_4$] (4)

Fe(TPA)(dmit)·0.5CH_2Cl_2 (0.054 g, 0.092 mmol) was stirred with [Fc][BAr^F_4] (0.102 g, 0.097 mmol) in DCM (4 mL) for 10 minutes before filtering through Celite. The filtrate was layered with petroleum ether and cooled to −38 °C for several days which yielded green-brown crystals. The solids were washed with petroleum ether and dried under vacuum (0.112 g, 87%). Crystals which diffracted poorly were similarly grown from DCM and petroleum ether. ^{1}H NMR (400 MHz, 25 °C, CD_2Cl_2) δ = 16.9, 9.1, 7.7, 7.5. Elemental analysis: expected for $C_{47}H_{32}BF_6FeN_4S_5$: % C, 45.29; H, 2.15; N, 3.99. Found: % C, 45.33; H, 2.32; N, 3.81. EPR – g_x = 2.056, g_y = 2.071, g_z = 2.082, σ_{gx} = 0.034, σ_{gy} = 0.000, σ_{gz} = 0.105, σ_B = 25.994 G. UV-vis-NIR at 20 °C, DCM (ϵ, M^{-1} cm^{-1}): 417 nm (2 x10^3), 1050 nm (6 x10^3).

5.5 References

[1] Abe, M., Diradicals. *Chem. Rev.* **2013,** *113* (9), 7011-7088.

[2] (a)Kamada, K.; Ohta, K.; Shimizu, A.; Kubo, T.; Kishi, R.; Takahashi, H.; Botek, E.; Champagne, B.; Nakano, M., Singlet Diradical Character from Experiment. *J. Phys. Chem. Lett.* **2010,** *1* (6), 937-940. (b) Smith, M. B.; Michl, J., Singlet Fission. *Chem. Rev.* **2010,** *110* (11), 6891-6936. (c) Morita, Y.; Suzuki, S.; Sato, K.; Takui, T., Synthetic organic spin chemistry for structurally well-defined open-shell graphene fragments. *Nat. Chem.* **2011,** *3* (3), 197-204. (d) Schweicher, G.; Garbay, G.; Jouclas, R.; Vibert, F.; Devaux, F.; Geerts, Y. H., Molecular Semiconductors for Logic Operations: Dead-End or Bright Future? *Adv. Mater.* **2020,** *32* (10), 1905909.

[3] (a) Suzuki, S.; Furui, T.; Kuratsu, M.; Kozaki, M.; Shiomi, D.; Sato, K.; Takui, T.; Okada, K., Nitroxide-Substituted Nitronyl Nitroxide and Iminonitroxide. *J. Am. Chem. Soc.* **2010,** *132* (45), 15908-15910. (b) Fukuzumi, S.; Ohkubo, K.; Ishida, M.; Preihs, C.; Chen, B.; Borden, W. T.; Kim, D.; Sessler, J. L., Formation of Ground State Triplet Diradicals from Annulated Rosarin Derivatives by Triprotonation. *J. Am. Chem. Soc.* **2015,** *137* (31), 9780-9783. (c) Gallagher, N.; Zhang, H.; Junghoefer, T.; Giangrisostomi, E.; Ovsyannikov, R.; Pink, M.; Rajca, S.; Casu, M. B.; Rajca, A., Thermally and Magnetically Robust Triplet Ground State Diradical. *J. Am. Chem. Soc.* **2019,** *141* (11), 4764-4774. (d) Tang, S.; Zhang, L.; Ruan, H.; Zhao, Y.; Wang, X., A Magnetically Robust Triplet Ground State Sulfur-Hydrocarbon Diradical Dication. *J. Am. Chem. Soc.* **2020**.

[4] (a) Trabolsi, A.; Khashab, N.; Fahrenbach, A. C.; Friedman, D. C.; Colvin, M. T.; Cotí, K. K.; Benítez, D.; Tkatchouk, E.; Olsen, J.-C.; Belowich, M. E.; Carmielli, R.; Khatib, H. A.; Goddard, W. A.; Wasielewski, M. R.; Stoddart, J. F., Radically enhanced molecular recognition. *Nature Chem.* **2010,** *2* (1), 42-49. (b) Wang, J.; Hou, L.; Browne, W. R.; Feringa, B. L., Photoswitchable Intramolecular Through-Space Magnetic Interaction. *J. Am. Chem. Soc.* **2011,** *133* (21), 8162-8164. (c) Su, Y.; Wang, X.; Wang, L.; Zhang, Z.; Wang, X.; Song, Y.; Power, P. P., Thermally controlling the singlet–triplet energy gap of a diradical in the solid state. *Chem. Sci.* **2016,** *7* (10), 6514-6518. (d) Schuler, B.; Fatayer, S.; Mohn, F.; Moll, N.; Pavliček, N.; Meyer, G.; Peña, D.; Gross, L., Reversible Bergman cyclization by atomic manipulation. *Nature Chem.* **2016,** *8* (3), 220-224. (e) Zhang, R.; Peterson, J. P.; Fischer, L. J.; Ellern, A.; Winter, A. H., Effect of Structure on the Spin–Spin Interactions of Tethered Dicyanomethyl Diradicals. *J. Am. Chem. Soc.* **2018,** *140* (43), 14308-14313. (f) Yin, X.; Low, J. Z.; Fallon, K. J.; Paley, D. W.; Campos, L. M., The butterfly effect in bisfluorenylidene-based dihydroacenes: aggregation induced emission and spin switching. *Chemical Science* **2019,** *10* (46), 10733-10739.

[5] Halcrow, M. A. *Spin-Crossover Materials: Properties and Applications*, Wiley-Blackwell: Oxford, 2013.

[6] (a) Batten, S. R.; Bjernemose, J.; Jensen, P.; Leita, B. A.; Murray, K. S.; Moubaraki, B.; Smith, J. P.; Toftlund, H. "Designing Dinuclear Iron(II) Spin Crossover Complexes. Structure and Magnetism of Dinitrile-, Dicyanamido-, Tricyanomethanide-, Bipyrimidine- and Tetrazine-Bridged Compounds" *Dalton Trans.* **2004**, 3370-3375. (b) Murray, K. S. "Advances in Polynuclear Iron(II), Iron(III) and Cobalt(II) Spin-Crossover Compounds" *Eur. J. Inorg. Chem.* **2008**, *2008*, 3101-3121. (c) Tissot, A.; Shepherd, H. J.; Toupet, L.; Collet, E.; Sainton, J.; Molnár, G.; Guionneau, P.; Boillot, M.-L., Temperature- and Pressure-Induced Switching of the Molecular Spin State of an Orthorhombic Iron(III) Spin-Crossover Salt. *European Journal of Inorg. Chem.* **2013,** *2013* (5-6), 1001-1008. (d) Shatruk, M.; Phan, H.; Chrisostomo, B. A.; Suleimenova, A., Symmetry-breaking structural phase transitions in spin-crossover complexes. *Coord. Chem. Rev.* **2015,** *289-290*, 62-73. (e) García-López, V.; Waerenborgh, J. C.; Vieira, B. J. C.; Clemente-León, M.; Coronado, E., Iron(II) complexes of tris(2-pyridylmethyl)amine (TPMA) and neutral bidentate ligands showing thermal- and photo-induced spin-crossover. *Dalton Trans.* **2018,** *47* (27), 9156-9163.

[7] (a) Mathonière, C.; Lin, H.-J.; Siretanu, D.; Clérac, R.; Smith, J. M. "Photoinduced Single-Molecule Magnet Properties in a Four-Coordinate Iron(II) Spin Crossover Complex" *J. Am. Chem. Soc.* **2013**, *135*, 19083-19086. (b) Feng, X.; Mathonière, C.; Jeon, I.-R.; Rouzières, M.; Ozarowski, A.; Aubrey, M. L.; Gonzalez, M. I.; Clérac, R.; Long, J. R., Tristability in a Light-Actuated Single-Molecule Magnet. *J. Am. Chem. Soc.* **2013,** *135* (42), 15880-15884. (c) Arroyave, A.; Lennartson, A.; Dragulescu-Andrasi, A.; Pedersen, K. S.; Piligkos, S.; Stoian, S. A.; Greer, S. M.; Pak, C.; Hietsoi, O.; Phan, H.; Hill, S.; McKenzie, C. J.; Shatruk, M., Spin-crossover in Fe(II) Complexes with N_4S_2 Coordination. *Inorg. Chem.* **2016,** *55* (12), 5904-5913.

[8] Senthil Kumar, K.; Ruben, M., Emerging trends in spin-crossover (SCO) based functional materials and devices. *Coord. Chem. Rev.* **2017,** *346*, 176-205.

[9] (a) Sutter, J.-P.; Fettouhi, M.; Li, L.; Michaut, C.; Ouahab, L.; Kahn, O. "Synergy between Magnetic Interaction and Spin Crossover in an Iron(III) Complex with an Organic Radical as Ligand" *Angew. Chem. Int. Ed.* **1996**, *35*, 2113-2116. (b) Rose, B. D.; Sumner, N. J.; Filatov, A. S.; Peters, S. J.; Zakharov, L. N.; Petrukhina, M. A.; Haley, M. M., Experimental and

Computational Studies of the Neutral and Reduced States of Indeno[1,2-b]fluorene. *J. Am. Chem. Soc.* **2014,** *136* (25), 9181-9189. (c) Alexandropoulos, D. I.; Dolinar, B. S.; Vignesh, K. R.; Dunbar, K. R., Putting a New Spin on Supramolecular Metallacycles: Co_3 Triangle and Co_4 Square Bearing Tetrazine-Based Radicals as Bridges. *J. Am. Chem. Soc.* **2017,** *139* (32), 11040-11043. (d) Thorarinsdottir, A. E.; Harris, T. D., Metal–Organic Framework Magnets. *Chem. Rev.* **2020**.

[10] (a) Gardiner, M. G.; Hanson, G. R.; Henderson, M. J.; Lee, F. C.; Raston, C. L., Paramagnetic Bis(1,4-di-tert-butyl-1,4-diazabutadiene) Adducts of Lithium, Magnesium, and Zinc. *Inorg. Chem.* **1994,** *33* (11), 2456-2461. (b) Barclay, T. M.; Hicks, R. G.; Lemaire, M. T.; Thompson, L. K., Weak Magnetic Coupling of Coordinated Verdazyl Radicals through Diamagnetic Metal Ions. Synthesis, Structure, and Magnetism of a Homoleptic Copper(I) Complex. *Inorg. Chem.* **2001,** *40* (25), 6521-6524. (c) Petrenko, T.; Ray, K.; Wieghardt, K. E.; Neese, F., Vibrational Markers for the Open-Shell Character of Transition Metal Bis-dithiolenes: An Infrared, Resonance Raman, and Quantum Chemical Study. *J. Am. Chem. Soc.* **2006,** *128* (13), 4422-4436. (d) O'Connor, J. M.; Friese, S. J., Transition-Metal Hydrides as Hydrogen Atom Donors: Stronger Metal−Hydrogen Bonds Can Be Advantageous. *Organometallics* **2008,** *27* (17), 4280-4281. (e) Gass, I. A.; Gartshore, C. J.; Lupton, D. W.; Moubaraki, B.; Nafady, A.; Bond, A. M.; Boas, J. F.; Cashion, J. D.; Milsmann, C.; Wieghardt, K.; Murray, K. S. "Anion Dependent Redox Changes in Iron Bis-Terdentate Nitroxide {NNO} Chelates" *Inorg. Chem.* **2011**, *50*, 3052-3064. (f) Ylijoki, K. E. O.; Lavy, S.; Fretzen, A.; Kündig, E. P.; Berclaz, T.; Bernardinelli, G.; Besnard, C., A Synthetic and Mechanistic Investigation of the Chromium Tricarbonyl-Mediated Masamune–Bergman Cyclization. Direct Observation of a Ground-State Triplet p-Benzyne Biradical. *Organometallics* **2012,** *31* (15), 5396-5404. (g) Paul, N. D.; Rana, U.; Goswami, S.; Mondal, T. K.; Goswami, S., Azo Anion Radical Complex of Rhodium as a Molecular Memory Switching Device: Isolation, Characterization, and Evaluation of Current–Voltage Characteristics. *J. Am. Chem. Soc.* **2012,** *134* (15), 6520-6523.

[11] (a) Wang, H.-Y.; Cui, L.; Xie, J.-Z.; Leong, C. F.; D'Alessandro, D. M.; Zuo, J.-L., Functional coordination polymers based on redox-active tetrathiafulvalene and its derivatives. *Coord. Chem. Rev.* **2017,** *345*, 342-361. (b) Segura, J. L.; Martin, N., New concepts in tetrathiafulvalene chemistry. *Angew. Chem., Int. Ed.* **2001,** *40* (8), 1372-1409.

[12] Xie, J.; Boyn, J.-N.; Filatov, A. S.; McNeece, A. J.; Mazziotti, D. A.; Anderson, J. S., Redox, transmetalation, and stacking properties of tetrathiafulvalene-2,3,6,7-tetrathiolate bridged tin, nickel, and palladium compounds. *Chem. Sci.* **2020**.

[13] (a) Hilfiger, M. G.; Chen, M.; Brinzari, T. V.; Nocera, T. M.; Shatruk, M.; Petasis, D. T.; Musfeldt, J. L.; Achim, C.; Dunbar, K. R. An Unprecedented Charge Transfer Induced Spin Transition in an Fe–Os Cluster *Angew. Chem. Int. Ed.* **2010**, *49*, 1410-1413. (b) Gao, F.; Zhu, F.-F.; Wang, X.-Y.; Xu, Y.; Wang, X.-P.; Zuo, J.-L., Stabilizing Radical Cation and Dication of a Tetrathiafulvalene Derivative by a Weakly Coordinating Anion. *Inorg. Chem.* **2014,** *53* (10), 5321-5327.

[14] (a) Paulsen, H.; Grünsteudel, H.; Meyer-Klaucke, W.; Gerdan, M.; Grünsteudel, H. F.; Chumakov, A. I.; Rüffer, R.; Winkler, H.; Toftlund, H.; Trautwein, A. X. The spin-crossover complex [Fe(tpa)$(NCS)_2$]. *Eur. Phys. J. B*, **2001,** *23*, 463-472. (b) Min, K. S.; Swierczek, K.; DiPasquale, A. G.; Rheingold, A. L.; Reiff, W. M.; Arif, A. M.; Miller, J. S., A dinuclear iron(II) complex, [(TPyA)Fe^{II}($THBQ_{2-}$)Fe^{II}(TPyA)]$(BF_4)_2$ [TPyA = tris(2-pyridylmethyl)amine; $THBQ^{2-}$ = 2,3,5,6-tetrahydroxy-1,4-benzoquinonate] exhibiting both spin-crossover with hysteresis and

ferromagnetic exchange. *Chem. Commun.*, **2008,** (3), 317-319. (c) Zheng, C.; Xu, J.; Wang, F.; Tao, J.; Li, D., Spin-crossover and reversible single-crystal to single-crystal transformation behaviour in two cyanide-bridged mixed-valence $\{Fe^{III}_2Fe^{II}_2\}$ clusters. *Dalton Trans.* **2016,** *45* (43), 17254-17263.

[15] Polam, J. R.; Wright, J. L.; Christensen, K. A.; Walker, F. A.; Flint, H.; Winkler, H.; Grodzicki, M.; Trautwein, A. X., Valence Electron Cloud Asymmetry from Two Points of View: A Correlation between Mössbauer Quadrupole Splittings and ^{57}Fe NMR Chemical Shifts of Diamagnetic Iron(II) Porphyrinates. *J. Am. Chem. Soc.* **1996,** *118* (22), 5272-5276.

[16] Schneider, C. J.; Cashion, J. D.; Moubaraki, B.; Neville, S. M.; Batten, S. R.; Turner, D. R.; Murray, K. S. "The Magnetic and Structural Elucidation of 3,5-Bis(2-Pyridyl)-1,2,4-Triazolate-Bridged Dinuclear Iron(II) Spin Crossover Compounds" *Polyhedron* **2007**, *26*, 1764-1772.

[17] Min, K. S.; DiPasquale, A.; Rheingold, A. L.; Miller, J. S., Room-Temperature Spin-crossover Observed for $[(TPyA)Fe^{II}(DBQ^{2-})FeII(TPyA)]^{2+}$ [TPyA = Tris(2-pyridylmethyl)amine; DBQ^{2-} = 2,5-Di-tert-butyl-3,6-dihydroxy-1,4-benzoquinonate]. *Inorg. Chem.* **2007**, *46* (4), 1048-1050.

[18] (a) Nihei, M.; Shiga, T.; Maeda, Y.; Oshio, H., Spin-crossover iron(III) complexes. *Coord. Chem. Rev.* **2007,** *251* (21), 2606-2621. (b) Olguín, J.; Brooker, S., Spin-crossover active iron(II) complexes of selected pyrazole-pyridine/pyrazine ligands. *Coord. Chem. Rev.* **2011,** *255* (1), 203-240.

[19] Scepaniak, J. J.; Harris, T. D.; Vogel, C. S.; Sutter, J.; Meyer, K.; Smith, J. M., Spin-crossover in a Four-Coordinate Iron(II) Complex. *J. Am. Chem. Soc.* **2011,** *133* (11), 3824-3827.

[20] (a) Xu, C.-H.; Sun, W.; Zhang, C.; Zhou, C.; Fang, C.-J.; Yan, C.-H., Luminescence Switching of a Cyclometalated Iridium(III) Complex through a Redox-active Tetrathiafulvalene-based Ligand. *Chem. Eur. J.* **2009,** *15* (35), 8717-8721. (b) Bellec, N.; Vacher, A.; Barrière, F.; Xu, Z.; Roisnel, T.; Lorcy, D., Interplay between Organic–Organometallic Electrophores within Bis(cyclopentadienyl)Molybdenum Dithiolene Tetrathiafulvalene Complexes. *Inorg. Chem.* **2015,** *54* (10), 5013-5020.

[21] (a) Matsubayashi, G.-e.; Takahashi, K.; Tanaka, T., X-Ray crystal structure of bis(N-ethylpyridinum) bis[4,5-dimercapto-1,3-dithiole-2-thionato(2–)]cuprate(II) and electrical properties of its oxidized salts. *Dalton Trans.* **1988,** (4), 967-972. (b) Ferreira, G. B.; Hollauer, E.; Comerlato, N. M.; Wardell, J. L., An experimental and theoretical study of the electronic spectra of tetraethylammonium [bis(1,3-dithiole-2-thione-4,5-dithiolato)zincate(II)], $[NEt_4]_2[Zn(dmit)_2]$, and tetraethylammonium [bis(1,3-dithiole-2-one-4,5-dithiolato)zincate(II)], $[NEt_4]_2[Zn(dmio)_2]$. *Inorganica Chim. Acta **2006**, 359 (4), 1239-1247.*

[22] (a) Hitomi, Y.; Furukawa, S.; Higuchi, M.; Shishido, T.; Tanaka, T., Alkane hydroxylation catalyzed by a series of mononuclear nonheme iron complexes containing 4-nitropyridine ligands. *J. Mol. Catal. A: Chem.* **2008,** *288* (1), 83-86. (b) Diebold, A.; Hagen, K. S., Iron(II) Polyamine Chemistry: Variation of Spin State and Coordination Number in Solid State and Solution with Iron(II) Tris(2-pyridylmethyl)amine Complexes. *Inorg. Chem.* **1998,** *37* (2), 215-223.

[23] (a) Akasaka, T.; Nakano, M.; Tamura, H.; Matsubayashi, G.-E., Preparation and Properties of Tin(IV) Complexes with the Sulfur-Rich Dithiolate C_3S_5 and $C_8H_4S_8$ Ligands and Their Oxidation. *Bull. Chem. Soc. Jpn.* **2002**, *75* (12), 2621-2628. (b) Kawabata, K.; Nakano, M.; Tamura, H.; Matsubayashi, G.-E., Crystal structures of $[Rh(\eta^5\text{-}C_5H_5)(C_3S_5)]$ and $[Rh(\eta^5\text{-}$

$C_5Me_5)(C_3S_5)]_2$ and properties of their oxidized species. *J. Organomet. Chem.* **2004**, *689* (2), 405-410.

[24] Becke, A. D, Density-functional thermochemistry. III. the role of exact exchange. *J. Chem. Phys*., **1993,** *98* (7), 5648-5652.

[25] Krishnan, R.; Binkley, J. S.; Seeger, R.; Pople, J. A., Self-consistent molecular orbital methods. XX. A basis set for correlated wave functions. *J. Chem. Phys.* **1980,** *72* (1), 650-654.

[26] Frisch, M. J. *et al.,* Gaussian 16 Revision A.01, 2016. Gaussian Inc. Wallingford CT.

[27] (a) Mazziotti, D. A. Realization of quantum chemistry without wave functions through first-order semidefinite programming. *Phys. Rev. Lett.,* **2004**, *93* (21), 213001. (b) Mazziotti, D. A. Large-Scale Semidefinite Programming for Many-Electron Quantum Mechanics *Phys. Rev. Lett.* **2011**, *106* (8), 083001. (c) Schlimgen, A. W.; Heaps, C. W.; Mazziotti, D. A., Entangled Electrons Foil Synthesis of Elusive Low-Valent Vanadium Oxo Complex *J. Phys. Chem. Lett.* **2016**, *7* (4), 627-631.

[28] Maple Quantum Chemistry Package from RDMChem 2020. Maplesoft, a division of Waterloo Maple Inc., Waterloo, Ontario.

[29] Svenstrup, N.; Rasmussen, K. M.; Hansen, T. K. & Becher, J. The Chemistry of TTFTT; 1: New Efficient Synthesis and Reactions of Tetrathiafulvalene-2,3,6,7-Tetrathiolate (TTFTT): An Important Building Block in TTF-Syntheses. *Synthesis.* **1994,** *8*, 809–812.

[30] Diebold, A.; Hagen, K. S., Iron(II) Polyamine Chemistry: Variation of Spin State and Coordination Number in Solid State and Solution with Iron(II) Tris(2-pyridylmethyl)amine Complexes. *Inorg. Chem.* **1998,** *37* (2), 215-223.

[31] Hansen, T. K., et al., 4,5-DIBENZOYL-1,3-DITHIOLE-1-THIONE, *Org. Synth.* **1996**, 73, 270.

[32] Chávez, I.; Alvarez-Carena, A.; Molins*, E.; Roig, A.; Maniukiewicz, W.; Arancibia, A.; Arancibia, V.; Brand, H.; Manuel Manríquez*, J., Selective Oxidants for Organometallic Compounds Containing a Stabilising Anion of Highly Reactive Cations: $(3,5(CF_3)_2C_6H_3)_4B^-)Cp_2Fe^+$ and $(3,5(CF_3)_2C_6H_3)_4B^-)Cp^*2Fe^+$. *J. Organomet. Chem.* **2000**, *601* (1), 126–132.

[33] Zadrozny, J. M.; Greer, S. M.; Hill, S.; Freedman, D. E., A flexible iron(II) complex in which zero-field splitting is resistant to structural variation. *Chem. Sci.* **2016,** *7* (1), 416-423.

Chapter 6: NiTTFtt: A Disordered Intrinsic Organic Metal

6.1 Introduction

Using molecular design to engender high conductivity in undoped amorphous materials would enable tunable and robust conductivity in many applications, but there are no intrinsically conducting organic materials which maintain high conductivity when completely disordered. Inorganic glassy metals have been discovered but require careful fabrication.[1] Furthermore, the relationship between metallic behavior, which classically requires periodicity giving rise to a well-defined band structure, and geometric disorder in these materials is still unclear.[2] Electron-rich and redox-active tetrathiafulvalene (TTF) motifs feature prominently as molecular building blocks in conducting materials.[3] Appending thiolate groups to TTF to generate tetrathiafulvalene-tetrathiolate (TTFtt) enables the formation of extended coordination polymers that combine the properties of TTF with the rich electronic structures of transition metal dithiolenes.[4] While the promise of these materials has been recognized, their structure, purity, composition, and hence properties are not well-defined due to synthetic challenges.[5]

We recently discovered syntheses that enable the isolation of a series of redox congeners of capped TTFtt compounds and their facile transmetalation to group 10 metals.[6] Here we report that this synthetic strategy enables the isolation of the material NiTTFtt in high purity as an amorphous powder. Despite its disordered structure, NiTTFtt exhibits remarkably high conductivity of 1280 S/cm (room temperature, four-probe measurement) and intrinsically glassy metallic behavior. Advanced theoretical analysis shows that these properties are enabled by strong molecular overlap and correlation that are robust to structural perturbations. This unusual set of structural and electronic features results in remarkably stable conductivity which is maintained in air for weeks and at temperatures up to 140 °C. The unusual properties of NiTTFtt demonstrate that molecular

design can enable metallic conductivity even in completely disordered materials. This finding raises fundamental questions about charge transport mechanisms in disordered materials and suggests exciting new applications for intrinsically metallic organic materials.

6.2 Results and Discussion

6.2.1 Synthesis, Composition and Structure

NiTTFtt is synthesized by mixing $[TTFtt(SnBu_2)_2][BAr^F{}_4]_2$ ($BAr^F{}_4$ = tetrakis(3,5-bis(trifluoromethyl)phenyl)borate) with excess $[TEA]_2[NiCl_4]$ (**Figure 6.1**a, TEA = tetraethylammonium). The composition of NiTTFtt was verified by several techniques which all support a Ni:S ratio of 1:8 (**Table E.2**). Combustion analysis confirms the proposed formula of NiTTFtt with $[Bu_2Sn][BAr^F]$ chain terminations. The absence of any ammonium counterions implies that the TTF cores have formal 2+ charges which is also supported by the absence of Electron Paramagnetic Resonance signals (**Figure E.16**).[3] X-ray photoelectron spectroscopy (**Figure E.12** and **Figure E**.13) reveals peaks at 871 and 854 eV, which can be assigned as Ni $2p_{1/2}$ and $2p_{3/2}$ peaks respectively, and a satellite at 860 eV associated with a plasmon loss, all of which are consistent with low-spin ($S = 0$) square planar Ni(II) centers. The S 2p spectra appear as head and shoulder patterns spanning 161-166 eV suggesting the existence of multiple sulfur sites in NiTTFtt similar to spectra of $TTF[Nidmit_2]$ (dmit, 1,3-dithole-2-thione-4,5-dithiolate).[7] Ni K-edge X-ray absorption spectroscopy shows an intense rising edge at 8338.6 eV which also supports the assignment of square planar Ni(II) centers (**Figure 6.1**b).[8]

Powder X-ray diffraction (PXRD) data was also collected (**Figure 6.1**c). There are no apparent features in the PXRD pattern for NiTTFtt, suggesting that this material is completely amorphous with domain sizes < 1 nm.[9] Therefore, we have investigated the structure of NiTTFtt with pairwise

distribution function (PDF) analysis (**Figure 6.1**d). The peaks below 3 Å can be assigned to C–C, C–S, and Ni–S bonds and intraring distances. The peaks between 3-4.5 Å represent interchain distances and are consistent with typical intermolecular S–S distances in TTF systems. Notably, the peaks in this region are broader, suggesting that the interchain interactions in NiTTFtt are irregular, consistent with its amorphous structure.

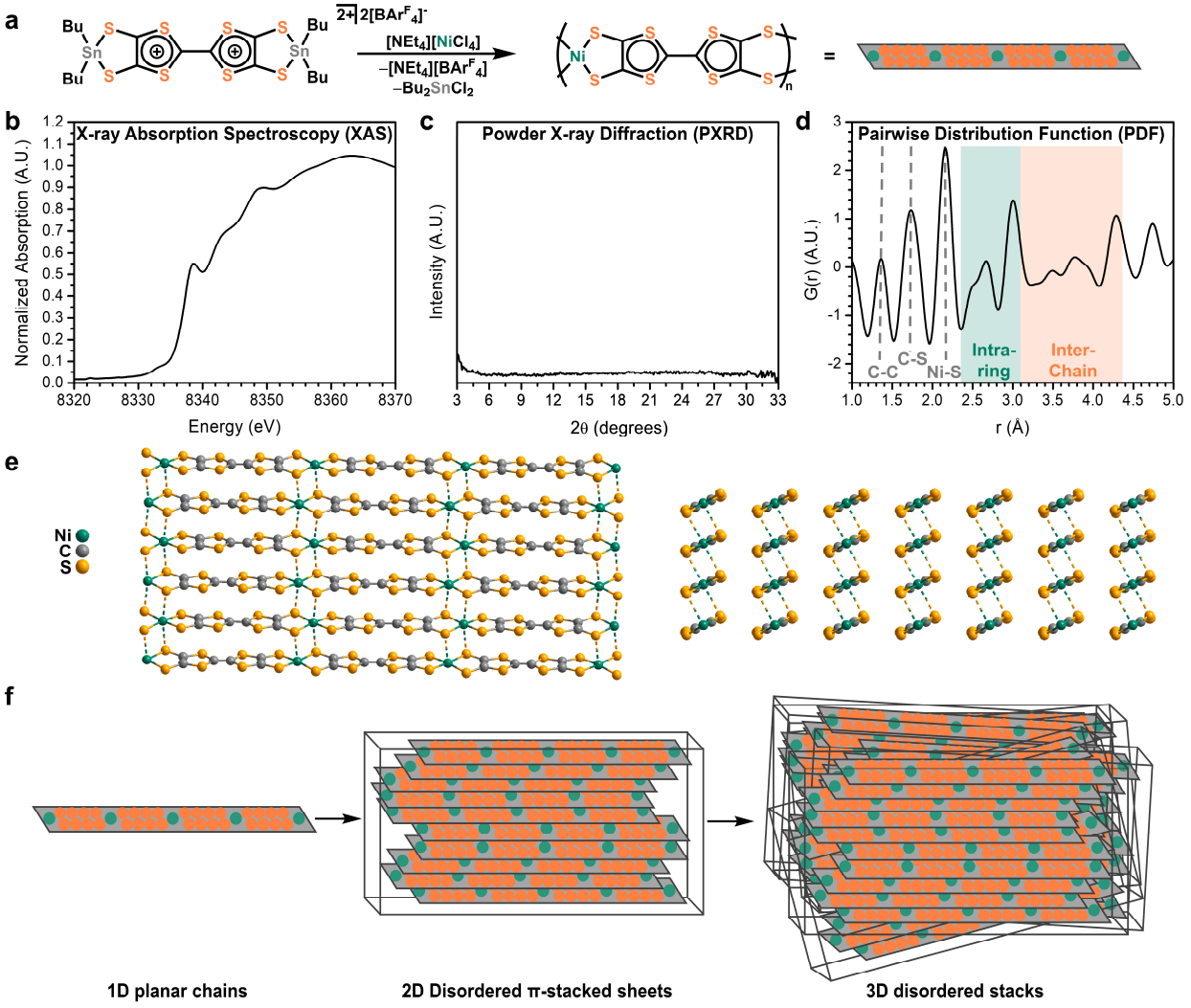

Figure 6.1. Synthesis and structure of NiTTFtt. a, Synthetic scheme. b, XAS spectrum. c, PXRD data. d, PDF data. e, Modeled structure. f, Hierarchical structure showing molecularly ordered chains but disordered packing in sheets and stacks.

Despite the amorphous nature of NiTTFtt, we have built a structural model based on experimental data (**Figure 6.1**e). This model is supported by attempts to grow more crystalline

NiTTFtt by slow diffusion which shows a PXRD pattern that can be indexed to a monoclinic unit cell (**Figure E.5**, **Figure E**.10 and **Figure E**.11). This unit cell constrains the model to staggered chain packing and the PDF data suggests S–S distances of ~3.4-3.7 Å along the π-stack and ~3 and 4 Å side-to-side between chains (**Figure 6.1**d and **Figure E**.8). These values are similar to those observed in the single-component molecular metal, [Ni(tmdt)$_2$] (tmdt, trimethylene-tetrathiafulvalene-dithiolate),[10] and also support tight packing as previously proposed.[11] Based on this model, the disordered structure of NiTTFtt arises from 1D chains that pack face-to-face to generate disordered 2D sheets which then pack side-to-side to generate a 3D structure (**Figure 6.1**f). Indeed, scanning electron microscopy (SEM) clearly reveals the presence of 2D flakes (**Figure E.9**).

6.2.2 Physical Properties

With this structural information on NiTTFtt we then turned to examine its electronic structure. Four-probe conductivity measurements on a hot pressed pellet of amorphous NiTTFtt reveal a remarkable room temperature conductivity of 1280 S/cm (**Figure 6.2**a). This value is similar to the most conductive coordination polymer (Cu$_3$BHT, 2500 S/cm, BHT = benzenehexathiolate)[12] even though Cu$_3$BHT is measured as a highly crystalline thin film while the pressed pellet of NiTTFtt has much higher contributions from grain boundaries. The thermal conductivity of NiTTFtt as measured by Raman thermometry (**Figure E.21**),[13] is 6.3 W/mK which is similar to inorganic glassy metals,[14] but much higher than what is typical for coordination polymers (< 0.4 W/mK).[15] The combination of high electrical and thermal conductivity suggests that electrons serve as carriers for both charge and thermal transport.

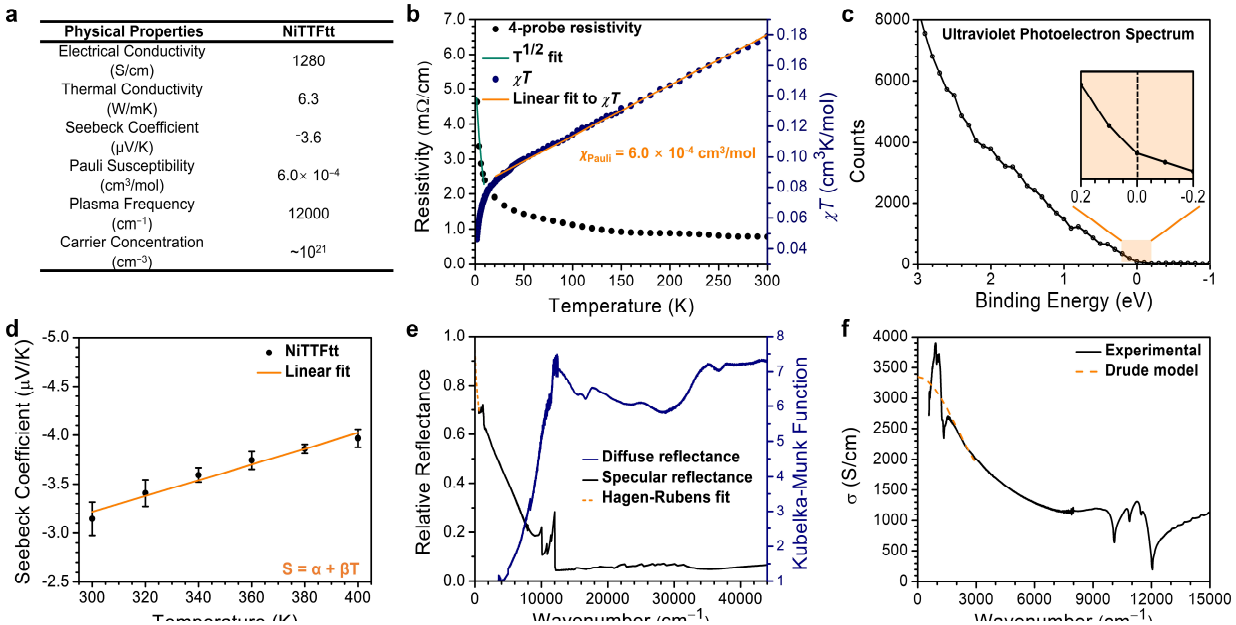

Figure 6.2. Physical properties of NiTTFtt. a, Summary of electronic, thermal, and magnetic properties. b, Variable temperature resistivity (black) and magnetic susceptibility (blue) data. The green line indicates a $T^{1/2}$ fit to the resistivity data at low temperature while the orange line indicates a linear fit to the magnetic susceptibility data with the shown Pauli paramagnetic contribution. c, Ultraviolet photoelectron spectrum showing a non-zero density of states at the Fermi level. d, Variable temperature Seebeck coefficient measurements showing a linear relationship (orange). e, Specular (black) and diffuse (blue) reflectance data. A Hagen-Rubens fit at low energy is shown as an orange dashed line. f, Optical conductivity at the low energy limit with a Drude model fit shown as an orange dashed line.

Variable temperature conductivity experiments on pressed pellets of amorphous NiTTFtt were then undertaken (**Figure 6.2**b). These measurements show an almost temperature-independent electrical resistivity with only a slight increase at low temperatures. Fitting this data with an Arrhenius plot indicates an activation energy of only 2.1 meV above 60 K and 0.08 meV below 20 K (**Figure E.24**).[12] These extremely small barriers may arise for two reasons. Firstly, macroscopic grain boundaries may provide a barrier to charge flow as is frequently observed in pressed pellets of conducting organic materials.[16, 17] Alternatively, a flat conductivity profile with temperature has been observed for glassy metals which have resistivities greater than 150 μΩ/cm.[18] The increase of resistivity as temperature decreases is proposed to arise from "weak localization"

with a characteristic $T^{1/2}$ upturn in resistivity due to electron-electron interactions. We observe this same $T^{1/2}$ dependence at low temperature, suggesting similar behavior in NiTTFtt. This observation, combined with the fact that extrapolation of the resistivity results in a finite zero-temperature limit, suggests that NiTTFtt is best thought of as having metallic character.[18]

Charge transport in disordered systems is typically analyzed with variable-range hopping models. Application of a 3D model to the resistivity data of NiTTFtt reveals a $T_0 < 100$ K which indicates a high density of states at the Fermi level (**Figure E.25**). Ultraviolet photoelectron spectroscopy (UPS) conducted on a pellet of NiTTFtt also supports a non-zero density of states at the Fermi level (**Figure 6.2**c). Values of T_0 between 1-10^4 K are commonly observed in granular metals and cermets where the model assumes hopping between metallic islands.[19] The observed $T^{1/2}$ upturn in resistivity led us to apply the Efros-Shklovskii model to the low temperature region. The observed linear relationship indicates the presence of a Coulomb gap which further suggests electron-electron interactions as discussed above. Interestingly, the T_{ES} value obtained from this fit is < 3 K, which is extremely small. Such a small value may suggest large delocalization lengths.[20] All these data support that NiTTFtt is best described as a glassy metal.

We then pursued additional orthogonal measurements to verify metallic character in NiTTFtt. The Seebeck coefficient (S) of NiTTFtt is −3.6 μV/K and the magnitude of this value increases in a linear fashion with temperature (**Figure 6.2**d). The negative Seebeck coefficient suggests that electrons are the charge carriers in NiTTFtt and the observed small magnitude and linear scaling with temperature are commonly observed in metallic inorganic conductors.[21] The magnetic susceptibility, χT, of NiTTFtt also has a weak temperature-dependence which may be attributed to a paramagnetic contribution from charge carriers, namely Pauli paramagnetism (**Figure 6.2**b). There is also a deviation from linearity in χT at low temperatures which we note coincides with

the above discussed increase in resistivity and putative localization. Regardless, the value of χ_{Pauli}, 6×10^{-4} cm^3/mol, is consistent with reported values in organic metals. [3, 16]

The combined data on NiTTFtt supports its assignment as a glassy metal, but we wanted to obtain more detailed quantification of its metallic nature and so we used both diffuse and specular reflectance spectroscopies (**Figure 6.2**e).[22, 23] NiTTFtt has a broad absorption over the UV-vis-NIR region up to ~12000 cm^{-1}. At the low frequency limit, the Hagen-Rubens relation can be used to extrapolate the specular reflectance to zero frequency and thereby estimate the optical dc conductivity as ~4200 S/cm, a value which is consistent with four-probe conductivity of pressed pellets (1280 S/cm). The observed plasma frequency of ~12,000 cm^{-1} suggests a carrier density of 10^{21} cm^{-3} which is similar to values in crystalline metallic polymers. [18, 24] Crude Hall effect measurements support this value (5×10^{21} cm^{-3}, **Figure E.28**).

We have further analyzed the reflectivity data by applying the Kramers-Kronig (KK) transformation (**Figure 6.2**f). Surprisingly, the optical conductivity from this analysis continuously increases as the frequency goes to zero. This behavior, particularly in the far-IR region below 3000 cm^{-1}, is suggestive of Drude behavior for a classic metal.[25] While the data range and quality limit fitting reliability, we have nonetheless analyzed this data with a Drude model, $\sigma_D(\omega) = (\omega_P^2\tau/4\pi)(1+\omega^2\tau^2)^{-1}$ **(Equation 6.1),** which gives a plasma frequency of about 12,100 cm^{-1}, a relaxation time of 9.0×10^{-15} s, a dc conductivity of ~3300 S/cm, and a carrier density of 3×10^{21} cm^{-3} (assuming $m^*=2m_e$). All fitted and measured values for NiTTFtt across different techniques are consistent with each other and again support metallic behavior. The Drude-like behavior and small T_{ES} values furthermore raise the possibility of band-like ballistic charge transport limited by hopping across macroscopic grain boundaries.

Amorphous organic conducting polymers also exhibit high conductivity, but the mechanism of charge transport in these materials is typically not metallic or intrinsic and relies upon doped charge carriers.[26] In intrinsic organic conductors, metallic character is always accompanied by crystalline order. The properties of NiTTFtt, which exhibits intrinsic metallic charge transport with a fundamentally disordered structure, are thus highly unusual. We have therefore undertaken detailed theoretical analyses of NiTTFtt to better understand this apparent dichotomy.

6.2.3 Theoretical Analysis

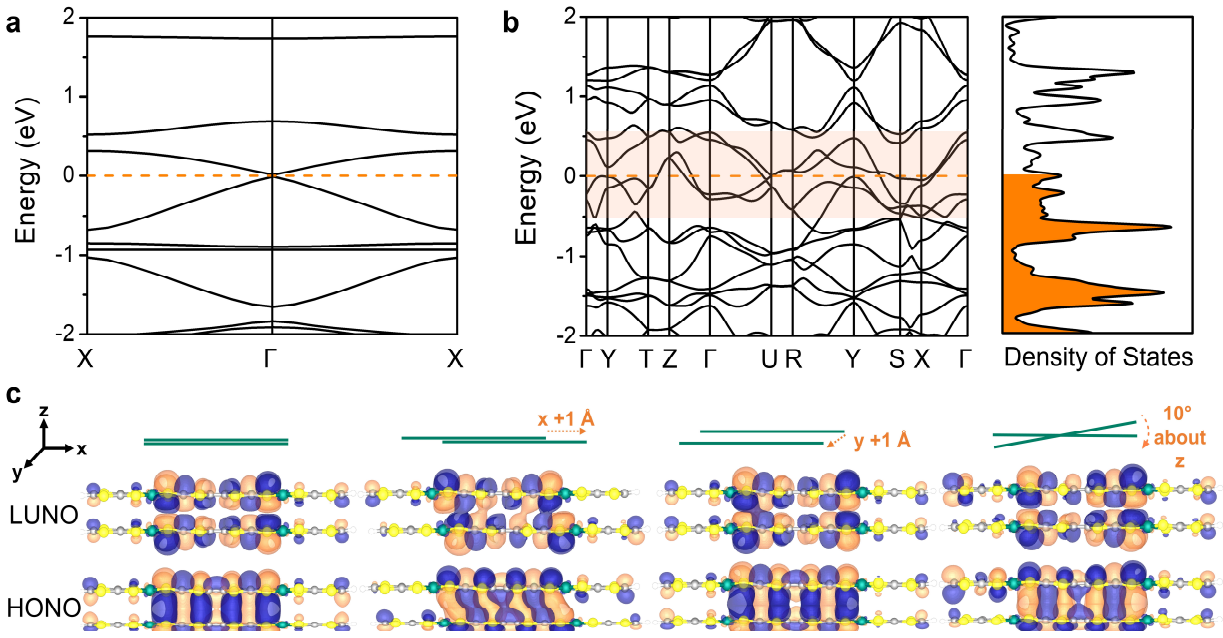

Figure 6.3. Theoretical analysis of NiTTFtt. a, Computed band structure of an isolated chain. b, Computed band structure of the idealized 3D structure determined from experimental data. c, Orbital diagrams of a molecular dimer of NiTTFtt building blocks showing that significant overlap is maintained regardless of structural distortions.

Density functional theory calculations were undertaken on 1D chains and 3D stacks of NiTTFtt based on our structural model. Interestingly, isolated 1D chains of NiTTFtt show semi-metallic behavior but exhibit a metallic band structure upon 3D assembly (**Figure 6.3**a and b respectively). Analysis of the band structure shows that metallic character arises from both π-stacking

interactions within the 2D sheets (Γ to Z), as well as side-to-side S–S interactions between sheets which broaden the bands near the Fermi level (Γ to X). Similar interactions have been invoked in single-component molecular conductors.[16] In addition to these periodic calculations, we have also analyzed why the metallic character of NiTTFtt is maintained with disorder by examining molecular models which can be systematically distorted (**Figure 6.2**c). Two molecular fragments of NiTTFtt were fixed at positions which vary the slip, π-stacking, and side-to-side distances as well as the interchain twist angle. The electronic structures of these models were analyzed by variational 2-electron reduced density matrix (V2RDM) complete active space self-consistent field (CASSCF) calculations.[27] This analysis demonstrates that the molecular fragments of NiTTFtt have significant overlap and correlation that is remarkably robust to disorder. This is perhaps best illustrated by the fact that the HONO-LUNO gaps have little to no change with structural distortions (**Table E.4**). These computations explain how metallic character is preserved in amorphous NiTTFtt: periodicity is disrupted by small scale structural disorder, but these defects are not significant enough to disrupt overlap, correlation, and delocalization.

6.2.4 Thermal and Aerobic Stability

The combination of structural disorder and intrinsic metallic character in NiTTFtt suggests some advantageous properties. Organic conductors, including n-type conducting polymers,[28] metallic coordination polymers like Cu_3BHT, and molecular conductors, typically suffer from fast degradation when exposed to air and heat.[18] Metallic character in these systems arises from their crystalline structure which can be disrupted with sufficient thermal energy (i.e. melting or decomposition), and exposure to air and heat leads to chemical reactions that remove charge carriers and reduce conductivity.[29] While these are significant issues in applications of conducting

organic materials, the disordered structure and intrinsic electronic properties of NiTTFtt suggest that this material should be significantly more robust.

Thermogravimetric analysis shows that NiTTFtt exhibits good stability both under N_2 gas (up to 270 °C) but also, remarkably, in air (up to 235 °C, **Figure 6.4**a). Inspired by the stability of NiTTFtt, we monitored sheet resistance (R_{sheet}) in air while heating and cooling between 20 and 140 °C (**Figure 6.4**b). The data clearly show that the high electrical conductivity of NiTTFtt is preserved even under these comparatively harsh conditions. The same sample was left in air over a month with no conductivity loss (**Figure 6.4**c). These data demonstrate that the unusual combination of intrinsic metallic character with an amorphous structure in NiTTFtt imparts substantial stability for conductivity with heat and air.

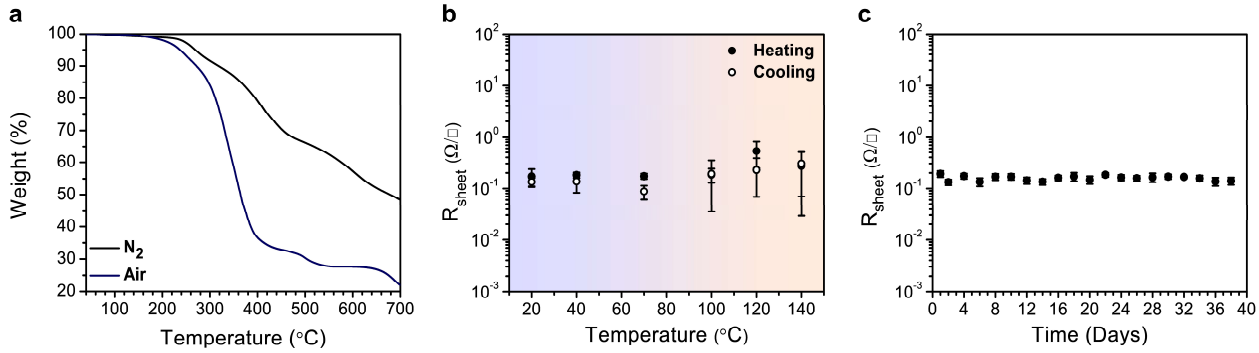

Figure 6.4. Thermal and aerobic stability of NiTTFtt. a, Thermogravimetric analysis under N_2 and air. b, Sheet resistance in air upon heating and cooling. c, Long-term stability of the resistance in air.

6.3 Conclusion

Organic conductors are an enormously important class of materials. To realize conductivity in normally insulating organic materials it is typically necessary to optimize their electronic structure through doping and their geometric structure through crystallinity. However, the requirement for

doping and crystallinity imposes restrictions on composition and stability. Here we report an unusual new material, NiTTFtt, that is structurally amorphous, precluding a classical band structure. Nevertheless, detailed characterization of NiTTFtt reveals high conductivity and metallic character. Theory shows that the presence of this metallic behavior is enabled by significant overlap between the molecular units of NiTTFtt that is insensitive to structural distortions. The exact mechanism of charge transport at the limit of no structural ordering is still unclear, with data raising the possibility of both hopping and band-like transport. Similar questions have been discussed in all-inorganic glassy metals, and NiTTFtt shows that the same interesting phenomena are present in organic materials composed of significantly more complex and tunable molecular building blocks. Regardless, the juxtaposition of metallic character and disorder in NiTTFtt provides remarkable thermally and aerobically stable conductivity. These results demonstrate that the use of molecular units that have strong overlap, and subsequently strong electronic delocalization, can lead to metallic character even in completely amorphous materials.

6.4 Experimental Section

General Methods

Unless otherwise noted, all synthetic manipulations were performed under an inert atmosphere of dry N_2 using a Schlenk line or a N_2-filled MBraun UNILab glovebox. Dichloromethane (DCM) was initially dried and sparged with Ar on a solvent purification system from Pure Process Technologies and stored over 4 Å molecular sieves. Methanol (MeOH) was dried with NaOH and distilled before being transferred into the glovebox. The dried MeOH was then passed through activated alumina and stored over 4 Å molecular sieves in the glovebox. $TTFtt(SnBu_2)_2$ (TTFtt =

tetrathiafulvalene-2,3,6,7-tetrathiolate; Bu=n-butyl), $Fc^{BzO}BAr^{F}_4$ (Fc^{BzO} = benzoyl ferrocenium; ([BAr^{F}_4] = tetrakis(3,5-bis(trifluoromethyl)phenyl)borate), and $[TEA]_2[NiCl_4]$ (TEA = tetraethylammonium) were synthesized following previously reported procedures.[6, 30]

NiTTFtt

$TTFtt(SnBu_2)_2$ (0.667 mmol, 266 mg) in 5 mL DCM was mixed with $Fc^{BzO}BAr^{F}_4$ (1.33 mmol, 1.54 g) in 5 mL DCM resulting in a homogenous dark purple solution. The resulting solution was added into a 10 mL MeOH solution of $[TEA]_2[NiCl_4]$ (2.00 mmol, 920 mg) with vigorous stirring. The mixture was kept stirring at 40 °C overnight. The solid product was isolated via centrifugation and washing with DCM (3×12 mL), MeOH (1×12 mL) and DCM (1×12 mL) sequentially. After being dried under vacuum at 100 °C overnight, 235 mg of NiTTFtt was isolated as a black powder (91%).

Semicrystalline NiTTFtt

$TTFtt(SnBu_2)_2$ (0.040 mmol, 43 mg) in 0.4 mL DCM was mixed with $Fc^{BzO}BAr^{F}_4$ (0.080 mmol, 93 mg) in 0.4 mL DCM to form a homogenous dark purple solution. After mixing, 0.8 mL of this dark purple solution was added into a clean 5 mL shell vial and 2.4 mL of a 1:1 DCM:MeOH solution (by volume) and then 0.8 mL of pure MeOH were slowly layered on the DCM layer sequentially, forming three distinct layers. Finally, a 0.8 mL MeOH solution of $[TEA]_2[NiCl_4]$ (0.12 mmol, 55 mg) was layered on top. The shell vial was carefully capped and placed in a secondary 24 mL vial which was allowed to sit and diffuse for 5 days. The resulting black powders were collected and washed identically to the procedure for amorphous NiTTFtt described above yielding 13 mg (85%).

6.5 References

[1] Plummer, J. Is metallic glass poised to come of age? *Nat. Mater.* **14**, 553–555 (2015).

[2] Hirata, A. *et al.* Geometric frustration of icosahedron in metallic glasses. *Science.* **341**, 376–379 (2013).

[3] Kobayashi, Y., Terauchi, T., Sumi, S. & Matsushita, Y. Carrier generation and electronic properties of a single-component pure organic metal. *Nat. Mater.* **16**, 109–114 (2017).

[4] Eisenberg, R. & Gray, H. B. Noninnocence in metal complexes: A dithiolene dawn. *Inorg. Chem.* **50**, 9741–9751 (2011).

[5] McCullough, R. D. *et al.* Building block ligands for new molecular conductors: homobimetallic tetrathiafulvalene tetrathiolates and metal diselenolenes and ditellurolenes. *J. Mater. Chem.* **5**, 1581 (1995).

[6] Xie, J. *et al.* Redox, transmetalation, and stacking properties of tetrathiafulvalene-2,3,6,7-tetrathiolate bridged tin, nickel, and palladium compounds. *Chem. Sci.* **11**, 1066–1078 (2020).

[7] de Caro, D. *et al.* Metallic Thin films of TTF[Ni(dmit)$_2$]$_2$ by electrodeposition on (001)-oriented silicon substrates. *Adv. Mater.* **16**, 835–838 (2004).

[8] Scott, R. A. Comparative X-ray absorption spectroscopic structural characterization of nickel metalloenzyme active sites. *Phys. B Condens. Matter* **158**, 84–86 (1989).

[9] Holder, C. F. & Schaak, R. E. Tutorial on powder X-ray diffraction for characterizing nanoscale materials. *ACS Nano* **13**, 7359–7365 (2019).

[10] Tanaka, H., Okano, Y., Kobayashi, H., Suzuki, W. & Kobayashi, A. A three-dimensional synthetic metallic crystal composed of single-component molecules. *Science.* **291**, 285–287 (2001).

[11] Vogt, T. *et al.* A LAXS (large sngle X-ray dcattering) and EXAFS (extended X-ray absorption fine structure) investigation of conductive amorphous Nickel tetrathiolato polymers. *J. Am. Chem. Soc.* **110**, 1833–1840 (1988).

[12] Huang, X. *et al.* Superconductivity in a Copper(II)-based coordination polymer with perfect Kagome dtructure. *Angew. Chemie Int. Ed.* **57**, 146–150 (2018).

[13] Liu, Z. *et al.* Controlling the Thermoelectric properties of organometallic coordination polymers via ligand fesign. *Adv. Funct. Mater.* **30**, 2003106 (2020).

[14] Xiang, L., Ji-hua, G. & Jun-hao, C. Thermal conductivity of metallic wires. *Chinese Phys.* **10**, 223–228 (2001).

[15] Sun, L. *et al.* A microporous and naturally nanostructured thermoelectric metal-organic gramework with ultralow thermal vonductivity. *Joule* **1**, 168–177 (2017).

[16] Kobayashi, A., Fujiwara, E. & Kobayashi, H. Single-Component Molecular Metals with Extended-TTF Dithiolate Ligands. *Chem. Rev.* **104**, 5243–5264, (2004).

[17] Dou, J. H. *et al.* Signature of metallic behavior in the metal-organic frameworks M$_3$(hexaiminobenzene)$_2$ (M = Ni, Cu). *J. Am. Chem. Soc.* **139**, 13608–13611 (2017).

[18] Kaiser, A. B. Electronic transport properties of conducting polymers and carbon nanotubes. *Reports Prog. Phys.* **64**, 1–49 (2001).

[19] Halim, J. *et al.* Variable range hopping and thermally activated transport in molybdenum-based MXenes. *Phys. Rev. B* **98**, 104202 (2018).

[20] Lan, X. *et al.* Quantum dot solids showing state-resolved band-like transport. *Nat. Mater.* **19**, 323–329 (2020).

[21] Kang, S. D.; Dylla, M.; Snyder, G. J. Thermopower-conductivity relation for distinguishing transport mechanisms: polaron hopping in CeO_2 and band conduction in $SrTiO_3$. *Phys. Rev. B* **97**, 235201 (2018).

[22]Heeger, A. J. Disorder-induced metal-insulator transition in conducting polymers. *J. Supercond.* **14**, 261–268 (2001).

[23] Jiang, Y. *et al.* Synthesis of a Copper 1,3,5-triamino-2,4,6-benzenetriol metal–organic gramework. *J. Am. Chem. Soc.* **142**, 18346–18354 (2020).

[24] Heeger, A. J. Nobel Lecture: Semiconducting and metallic polymers: The fourth generation of polymeric materials. *Rev. Mod. Phys.* **73**, 681–700 (2001).

[25] Lee, K. *et al.* Metallic transport in polyaniline. *Nature* **441**, 65–68 (2006).

[26] Bubnova, O. *et al.* Semi-metallic polymers. *Nat. Mater.* **13**, 190–194 (2014).

[27] Mazziotti, D. A. Large-dcale demidefinite programming for many-rlectron quantum mechanics. *Phys. Rev. Lett.* **106**, 083001 (2011).

[28] He, T., Stolte, M. & Würthner, F. Air-stable n-channel organic single crystal field-effect transistors based on microribbons of core-chlorinated naphthalene diimide. *Adv. Mater.* **25**, 6951–6955 (2013).

[29] Venkateshvaran, D. *et al.* Approaching disorder-free transport in high-mobility conjugated polymers. *Nature* **515**, 384–388 (2014).

[30] Gill, N. S. & Nyholm, R. S. 802. Complex halides of the transition metals. Part I. Tetrahedral nickel complexes. *J. Chem. Soc.* 3997 (1959).

Chapter 7: Redox-Active NiTTFtt Chains

7.1 Introduction

Photoelectric energy conversion, where light is converted into electricity, underpins solar energy capture and generation.[1] The most general route is the direct capture of photons and conversion into an electrical potential through photovoltaic (PV) materials. Although the efficiency of PVs has dramatically increased to more than 25% from 3.8% in the last two decades,[2] there are still fundamental challenges to the efficiency ceilings of this technology. For instance, it is reported that up to 40 % of the thermodynamic loss in PVs occurs due to carrier thermal relaxation.[3] Furthermore, the spectral windows of many PVs have a maximum onset of photogeneration around 800 nm, which means that nearly the entire near-IR spectrum is reflected or lost as waste heat.[4]

In addition to direct PV capture of photons, an alternative route is photothermal (PT) conversion of light into heat which can then generate a thermoelectric (TE) response through a net photothermoelectric (PTE) conversion. The development of PTE devices or solar thermoelectric generators (STEGs) could feasibly increase the utilization of solar energy by both allowing the harvesting of waste heat as well as increasing the solar absorption window.[5] However, the efficiency of STEGs is still limited by PT efficiency and performance.[5a] This motivates the development of new PTE materials.

Beyond energy capture, NIR-sensitive PTE materials also have utility in applications such as photodetectors[6] and night cameras.[7] A recent review has summarized the progress of photodetectors based on the PTE effect,[8] suggesting that PTE devices can realize ultra-broadband photodetection without cooling units and external bias. Such characters are highly desirable in the

military and civilian fields. For instance, the Mars Reconnaissance Orbiter launched by NASA in 2005 contained an uncooled PTE detector to monitor the climate of Mars.

Although PTE effects have now been observed in a wide variety of materials, including 2D materials such as graphene [9] and MoS_2, [10] organic PTE materials are comparatively rare, particularly for NIR applications. Conducting organic polymers are an important branch of TE materials as they are light, flexible, and exhibit intrinsically low thermal conductivity. The discovery of TE organic materials with prominent PT effects would be promising candidates for wearable PTE devices, as reported for NIR-sensitive poly(3,4-ethylenedioxyselenophene) derivatives (PEDOS).[11] Under 808 nm laser irradiation (2.33 W/cm), the output voltage of these materials was up to 900 μV in 3s. This work demonstrates the potential of organic materials in PTE applications, but this field is still under-explored. Indeed, aside from a single report of Cu-ethylenetetrathiolate (ett) polymers from 2015,[12] there are no other examples of organic PTE materials.

Tetrathiafulvalene (TTF)-based charge transfer salts and MOFs have recently been reported to exhibit excellent NIR PT conversions.[13] One example is even able to heat up to 250 °C in 25 s under 0.4 Wcm^{-2} irradiation at 808 nm. This rapid and efficient performance suggests that TTF-based materials exhibit exceptional PT properties, but the conductivity required for PTE applications is still an inherent limitation in this area.

Despite this issue, there have been enormous strides in realizing conductive coordination polymers over the past decade. Conducting coordination polymers or metal-organic-frameworks (MOFs) [14] have shown promising applications in superconductors, [15] energy storage, [16] thermoelectrics,[17] and other applications.[18] Among many conductive motifs, dithiolene-based frameworks in particular exhibit significant delocalization and high conductivity due to better

energy match between sulfur atoms and metal centers.[19] The poor thermal conduction of organic components also makes dithiolene-based coordination polymers potential candidates for thermal electronics. For example, in 2016, a ZT value 0.30(3) was reported for Ni-ett chains.[17c] In addition to the thermal and electrical conductivity, square-planar bis(dithiolene) complexes are also commonly characterized with strong NIR absorptions as well as PTE conversion properties. Some examples have been developed for photothermal therapy and photo-controlled drug delivery.[20]

Our laboratory has been interested in TTF-based materials, particularly those composed of tetrathiafulvalene-tetrathiolate units (TTFtt). We recently reported that these materials have extremely high conductivity and glassy metallic character while being thermally and aerobically robust.[21] Given the exemplary PT properties of TTF units and metal-dithiolenes in other reports, we hypothesized that these materials could be good candidates for PTE applications. Furthermore, we rationalized that modulating the redox-state of these materials via pre-synthetic doping might enable tuning of their PT or TE properties, and hence would reveal a new strategy for designing PTE properties in new materials. Here we demonstrate that this strategy of pre-synthetic doping,[22] using either neutral $TTFtt(SnBu_2)_2$ or dicationic $[TTFtt(SnBu_2)_2][BAr^F{}_4]$ ($BAr^F{}_4$ = tetrakis(3,5-bis(trifluoromethyl)phenyl)borate, Bu = n-Butyl) as transmetalating precursors, enables control over the redox state of Ni coordination polymers. In addition to the previously reported neutral NiTTFtt material, using $TTFtt(SnBu_2)_2$ leads to reduced $NiTTFtt^{2-}$ chains, with Li^+ and $Li(THF)_x^+$ as counter ions, in the materials $Li_{1.2}Ni_{0.4}$[NiTTFtt] and $[Li(THF)_{1.5}]_{1.2}Ni_{0.4}$[NiTTFtt], respectively. Interestingly, unlike n-type metallic NiTTFtt, physical characterization suggests these reduced polymers are typical p-type semiconductors. The broad spectral absorption and electrically conducting nature of these TTFtt-based materials enables highly efficient NIR-thermal conversion and good PTE performance. Furthermore, tuning of the PTE performance can be

achieved by changing the redox-state of these materials. Unlike conventional STEG materials made of several different materials combined in a composite, the materials presented here are single-component PTE candidates. Such single-component materials are desirable for ease of device fabrication and durability of performance. The NiTTFtt materials reported here represent the best single-component organic PTE materials for both p-type and n-type applications, and the tunable PT, TE, conductivity, and carrier properties demonstrate that using synthetic strategies to rationally change the redox-states of coordination polymer materials is a powerful strategy for generating new PTE candidates.

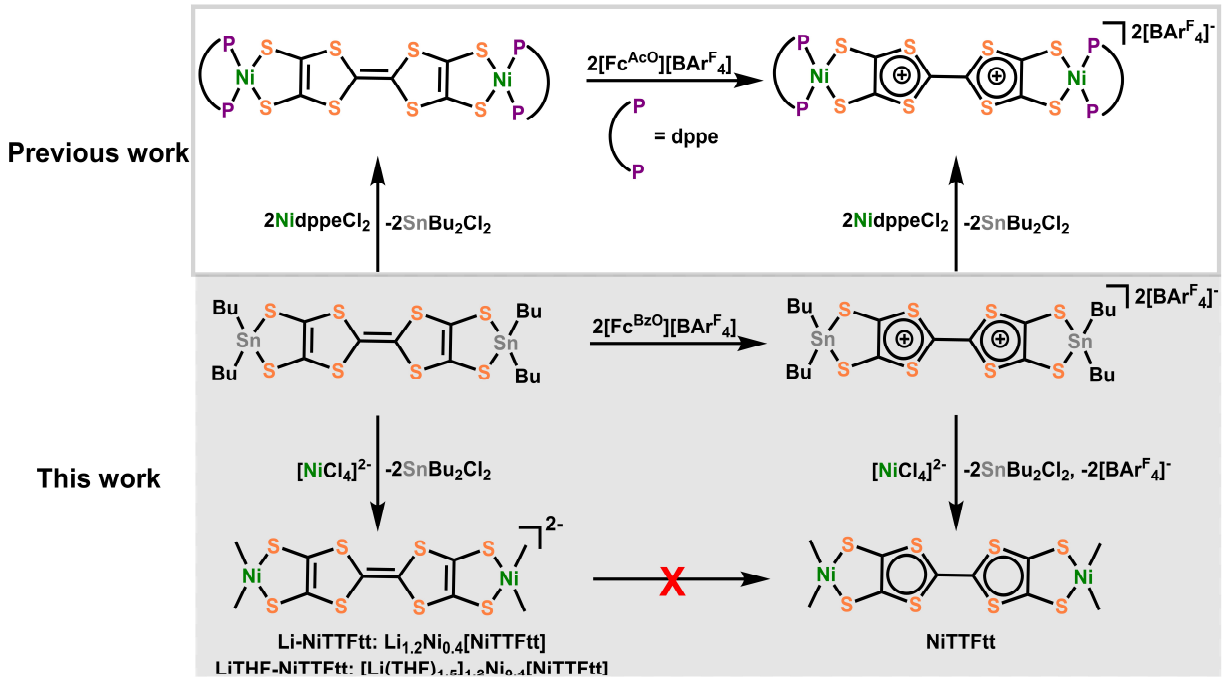

Scheme 7.1. Synthesis of Li-NiTTFtt, LiTHF-NiTTFtt, and NiTTFtt via a pre-synthetic redox control. The synthetic strategy is developed in a previous molecular study (top).

7.2 Results and Discussion

7.2.1 Synthesis and Redox Control

NiTTFtt is synthesized by mixing $[TTFtt(SnBu_2)_2][BAr^F{}_4]_2$ with excess $[TEA]_2[NiCl_4]$ (TEA = tetraethylammonium). To investigate the formation of alternative redox isomers of this material, the neutral linker precursor $TTFtt(SnBu_2)_2$ was mixed with *in situ* formed $Li_2[NiCl_4]$ in tetrahydrofuran (THF) resulting in new materials with anionic $NiTTFtt^{2-}$ chains (**Scheme 7.1**). The counterions for these chains depend on the workup of the material and are either $Li(THF)_x^+$ in the as-synthesized material **LiTHF-NiTTFtt** or Li^+ in the more-thoroughly dried material **Li-NiTTFtt**. The different redox-states of the TTF linkers in these materials from neutral **NiTTFtt** is immediately apparent in their air- stability. Unlike **NiTTFtt**, **Li-NiTTFtt** and **LiTHF- NiTTFtt** are extremely sensitive to air or chemical oxidants. As such, the characterization of these materials was carried out under anaerobic conditions.

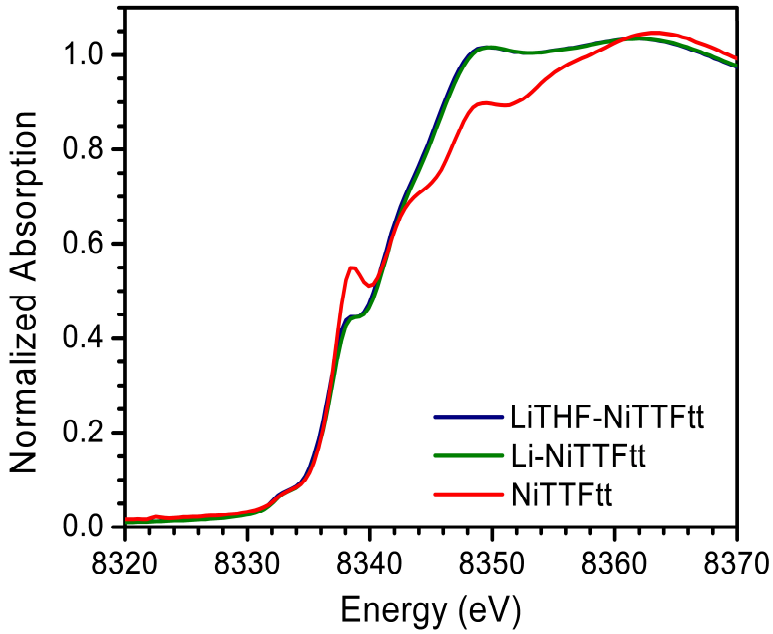

Figure 7.1. Ni K-edge XANES spectra of LiTHF-NiTTFtt (blue), Li-NiTTFtt (green) and NiTTFtt (red).

We initially turned to characterizing the composition and formulae of these materials by a suite of techniques including X-ray Fluorescence (XRF), Inductively Coupled Plasma-Optical Emission

Spectroscopy /Mass Spectrometry (ICP-OES/MS), and X-ray Photoelectron Spectroscopy (XPS) (see Appendix F). All analyses suggest a Ni:S ratio of 1:5.7 (1.4:8) and a Li:Ni ratio of 0.9:1 (1.2:1.4), which gives a formula of $Li_{1.2}Ni_{1.4}C_6S_8$ with only trace Sn (0.03:1 Sn:Ni) which we assign to chain ends (**Table F.1**). This empirical formula suggests Ni ions are not only incorporated into the backbone of the material but are also serving as counter cations, as has been observed in other Ni-dithiolene polymers.[17a] Multiple chemical environments for Ni are also supported by the fact that Ni-K edge X-ray Absorption Near Edge Structure (XANES) spectra of **Li-NiTTFtt** and **LiTHF-NiTTFtt** (**Figure 7.1**) are distinct from that of **NiTTFtt**, albeit with identical K-edge positions. Fits of the extended X-ray absorption fine structure (EXAFS) of **Li-NiTTFtt** reveal a Ni–S bond length of 2.161(6) Å, which is very similar to the Ni–S bond in **NiTTFtt** of 2.177(9) Å (**Table F.3**). The similarity of these distances supports similar structures and Ni oxidation states in the two materials and further suggests TTF-based redox differences. Accounting for Ni counter-cations verifies the presence of reduced chains with an overall 2− charge, indicating that a formally neutral TTF core is maintained in the final products. Combustion analysis (**Table F.2**) further confirms formula assignments of $[Li_{1.2}Ni_{0.4}]$NiTTFtt for **Li-NiTTFtt** and $[(LiTHF_{1.5})_{1.2}Ni_{0.4}]$NiTTFtt for **LiTHF-NiTTFtt**.

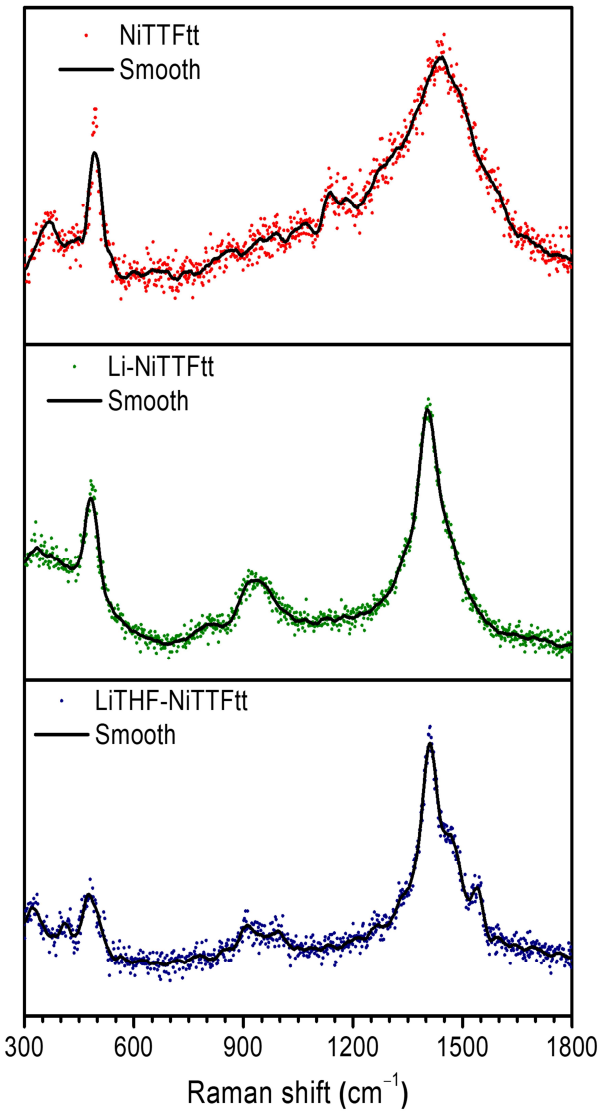

Figure 7.2. Raman spectra of LiTHF-NiTTFtt (blue), Li-NiTTFtt (green) and NiTTFtt (red).

In addition to the composition analysis, we also attempted to assign the redox differences spectroscopically. While XPS characterization of the S 2p peaks to assign redox states is ambiguous due to multiple sulfur chemical sites, we did observe a Raman peak for **NiTTFtt** at around 1170 cm^{-1}, corresponding to C=S modes (**Figure 7.2**, red). This feature shifts to 950 cm^{-1} in the case of the reduced congener **Li-NiTTFtt** (**Figure 7.2**, green). Similar shifts to lower energy have been observed in $[Ni(dmit)_2$ (dmit = 1,3-dithiole-2-thione-4,5-dithiolate) systems with the general interpretation that higher frequencies indicate more positive charge character on the metal-

dithiolene skeleton.[23] This supports the conclusion from XAS of ligand based redox-changes. Unfortunately, the Raman spectrum of **LiTHF-NiTTFtt** is convoluted by overlapping THF vibrational modes.

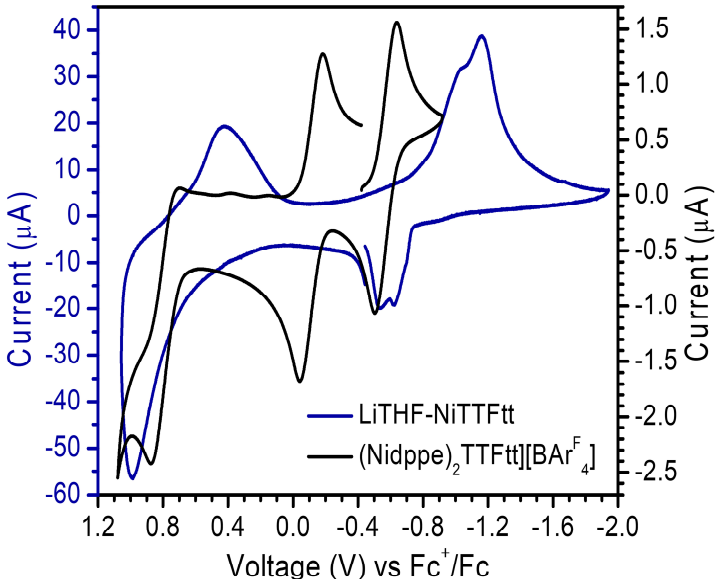

Figure 7.3. Solid-state cyclic voltammograms of LiTHF-NiTTFtt. Conditions: 0.1 M $LiPF_6$/MeCN at 10 mV/s scan rate. The CV plot of molecular $[(Nidppe)_2TTFtt][BAr^F{}_4]$ is reproduced from Ref. 22 .

We then performed solid-state cyclic voltammetry (CV) measurements on **LiTHF-NiTTFtt** to explore the redox-properties of this system (

Figure 7.3, blue). Similar to the CV plot of $[(Nidppe)_2TTFtt][BAr^F]$ (

Figure 7.3, black),[22] two quasi-reversible oxidation processes for **LiTHF-NiTTFtt** at –0.89 V and –0.78 V vs. Fc^+/Fc are assigned as TTF-based redox events. The irreversible peak at 0.70 V vs Fc^+/Fc is tentatively attributed to a Ni^{II}/Ni^{III} oxidation although we cannot exclude the possibility that these features arise from the dithiolene moieties. Regardless, all observed redox potentials are shifted more negative compared to the molecular analogue ($TTF/TTF^{\bullet+}/TTF^{2+}$, –0.58 and –0.11 V; Ni^{II}/Ni^{III}, 0.79 V). The exact reason for this negative shift is not immediately

apparent but may be due to differences in packing between the two materials, and subsequent differences in delocalization of negative charges. Regardless, these negative potentials explain why early reports of NiTTFtt materials synthesized without inert gas protection were all partially oxidized. Indeed, we noticed that in our hands the use of typically redox-neutral solvents such as methanol (as widely used in the literature) in **Li-NiTTFtt** syntheses resulted in oxidized materials. This observation underscores the importance of using rigorously anaerobic and anhydrous conditions to reliably access different redox congeners of dithiolene based materials in a reliable manner.

7.2.2 Band Engineering: Redox Induced Crossing of the Metal-to-Semiconductor Transition

Once we had established the overall composition of these materials, we then turned to examine their electrical properties. Compared to **NiTTFtt**, which is highly conductive (1280 S/cm), the room temperature conductivities of **Li-NiTTFtt** and **LiTHF-NiTTFtt** (via a two-probe measurement on pressed pellets) are much lower at 9.2 S/cm and 4.9×10^{-6} S/cm, respectively. The Seebeck coefficients of **Li-NiTTFtt** and **LiTHF-NiTTFtt** are also positive at +8.3 and +34.2 uV/K, respectively, which is notably different than the value of −3.6 uV/K found in **NiTTFtt** (**Figure 7.4**A). The sign of the Seebeck coefficients suggests that the reduced Li_xNiTTFtt materials are p-type semiconductors with bandgaps of 0.5 eV based on Ultraviolet Photoelectron Spectroscopy (UPS) analysis (**Figure 7.4**C).

(A)

	LiTHF-NiTTFtt	Li-NiTTFtt	NiTTFtt
Seebeck coefficient (uV/K)	+34.2	+8.3	-3.6
Electrical conductivity (S/cm)	4.9×10^{-6}	9.2	1280 (hot press)
Bandgap, UPS (eV)		0.5	0.5
E_a, Arrhenius fit (eV)	2.1×10^{-3}	0.18	0.23
T_0, VRH model (K)	13	5.1×10^{6}	1.1×10^{9}
π-π* bandgap, IR spectra (cm^{-1})		3200	3200

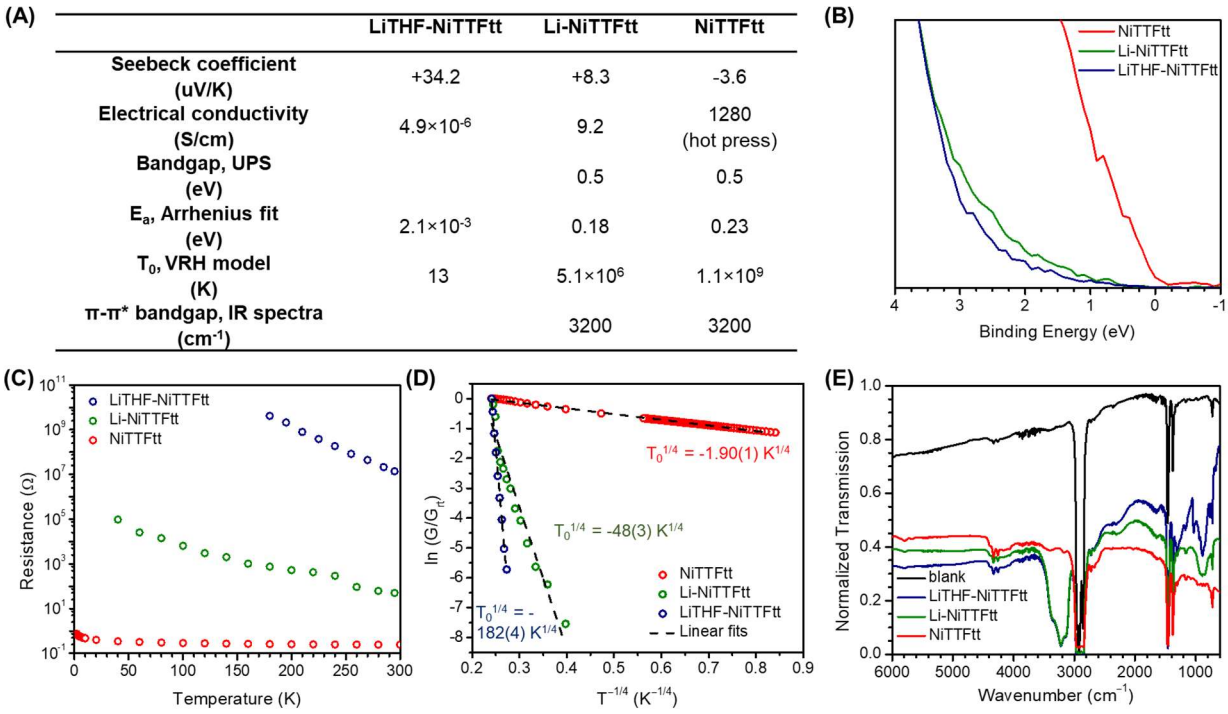

Figure 7.4. Physical characterization supporting a metal-to-semiconductor transition via redox control. (A) A summary of each species' physical properties. (B) Ultraviolet photoelectron spectra. (C) Plots of variable-temperature resistance. (D) 3D Variable-Range Hopping Models and linear fits. (E) IR transmittance spectra (baselined) as Nujol mulls. Blue: LiTHF-NiTTFtt; Green: Li-NiTTFtt; Red: NiTTFtt.

To further study the charge transport mechanism, we carried out variable-temperature (VT) resistance measurements on **Li-NiTTFtt** and **LiTHF-NiTTFtt**. As shown in **Figure 7.4**D, the resistance of both **Li-NiTTFtt** and **LiTHF-NiTTFtt** materials increase exponentially as the temperature decreases, in contrast to the resistance curve of NiTTFtt which is almost flat. Arrhenius fits (above 200 K) provide activation energies of **Li-NiTTFtt** and **LiTHF-NiTTFtt** of ~0.17 eV and ~0.23 eV, respectively. Due to their amorphous nature, the temperature-dependent conductivity behaviors deviate from the Arrhenius law at low temperature, especially for **Li-NiTTFtt** (**Figure F.11**). Therefore, three-dimension Variable-Range Hopping (3D VRH) models were applied as shown in **Figure 7.4**E. We recently reported a T_0 value extracted from a 3D VRH analysis on a **NiTTFtt** pellet which is extremely small, below 100 K. Such a value is consistent

with a metallic glass but not with a semiconductor. In contrast, the obtained T_0 values for **Li-NiTTFtt** and **LiTHF-NiTTFtt** are 5.1×10^6 K and 1.1×10^9 K, respectively, which are typical for amorphous semiconductors. The larger T_0 value of **LiTHF-NiTTFtt** implies a lower density of states at the Fermi level as compared to **Li-NiTTFtt**. Taken together with the larger Seebeck coefficient of **LiTHF-NiTTFtt**, it indicates that larger counter ions between chains increase the hopping barriers and lower the carrier concentrations in the materials with anionic chains.

Semiconducting molecular materials commonly exhibit long-wavelength absorptions in their IR spectra due to the small HOMO-LUMO gaps of delocalized π-systems.[24] In the case of $NiTTFtt^{2-}$ chains, we also found a strong and broad absorption around 3200 cm^{-1} in the IR spectra of both **Li-NiTTFtt** and **LiTHF-NiTTFtt** (**Figure 7.4**B). The energy of this feature indicates a π-π* bandgap about 0.4 eV. Notably, this absorption band is absent in **NiTTFtt** which also supports a metallic transition upon oxidation. Similar trends have been observed in TTF-based organic metals.[24, 25] In addition to the bandgap, we also noted some weak persistent photo-currents in both **Li-NiTTFtt** and **LiTHF-NiTTFtt** under 850 nm LED irradiation but not **NiTTFtt**. Persistent photo-currents are commonly observed in amorphous semiconductors such as amorphous silicon.[26] Hence, this phenomenon is further support of a metal-to-semiconductor transition upon reduction.

In summary, all physical characterization supports that these reduced polymers are p-type semiconductors with bandgaps of ~0.2-0.5 eV, in contrast to the oxidized material **NiTTFtt** which is metallic. Furthermore, we observe that the large counter ion seemingly plays an important role in hopping transport between neighboring chains, as **LiTHF-NiTTFtt** exhibits significantly lower conductivity.

7.2.3 NIR Photo-Thermal Conversion

Despite different charge transport mechanisms, diffuse reflectance spectra demonstrate that all three materials have broad absorptions over the visible and NIR regions (**Figure 7.5**). These broad absorptions suggest that these materials may effectively capture light, and particularly low-energy light, to convert it into thermal energy.

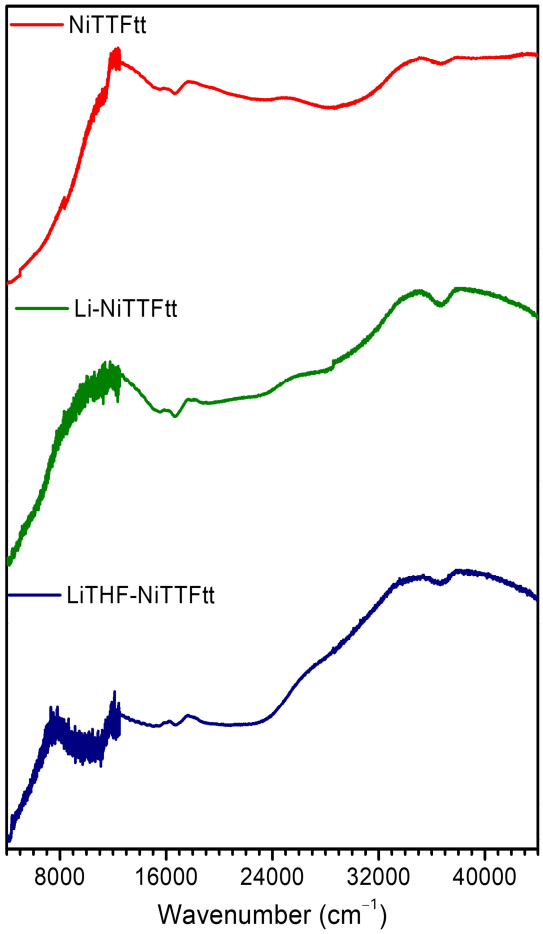

Figure 7.5. UV-vis-NIR diffuse reflectance spectra of LiTHF-NiTTFtt (blue), Li-NiTTFtt (green) and NiTTFtt (red) in KCl as a non-absorbing matrix.

Since **LiTHF-NiTTFtt** becomes desolvated with sufficient heating, only **Li-NiTTFtt** and **NiTTFtt** were tested for NIR photothermal behavior. Before testing PT conversion, the thermal stabilities of **Li-NiTTFtt** and **NiTTFtt** were examined by thermogravimetric analysis (TGA, **Figure F.12**) and differential scanning calorimetry (DSC, **Figure F.13**). Both materials are stable

up to at least 150 °C under appropriate testing conditions (**Li-NiTTFtt** under N_2 gas and **NiTTFtt** in air). Encouraged by this stability, we recorded the temperature of pressed pellets under 808 nm laser irradiation with an IR thermal camera. As shown in **Figure 7.6**A, **NiTTFtt** samples shows a linear temperature increase to values as high as 120 °C in 20 s when scanning the light power density from 0.50 to 2.0 W/cm^2. Similar behavior is observed with **Li-NiTTFtt** pellets with a maximum of 118 °C in 30 s at a much lower power density of 0.40 W/cm^2 (**Figure 7.6**D). Linear fits to these data reveal a temperature rise per 0.1 W/cm^2 radiation of 4.4 K and 23 K for **NiTTFtt** and **Li-NiTTFtt** respectively (**Figure 7.6**C). The performance of these materials, particularly with regard to the magnitude and speed of their PT response, are excellent. In fact, the performance of Li-NiTTFtt is among the very best reported for TTF-based MOFs. These remarkable properties are also quite durable; samples maintained their performance even after exposure to repeated laser on/off cycles (1.5 Wcm^{-2} for **NiTTFtt** and 0.3 Wcm^{-2} for **Li-NiTTFtt**, **Figure 7.6**B and E).

To assess the efficiency of the light-to-heat conversion, the PT efficiency, η_{PT}, was determined with a modified Roper's model (via a cooling process),[27] from the following equation:

$$\eta_{PT} = \frac{hS\Delta T_{max}}{I(1-10^{-A_{808}})} = \frac{\sum_i m_i C_{p_i} \Delta T_{max}}{\tau I(1-10^{-A_{808}})} \geq \frac{mC_p \Delta T_{max}}{\tau I(1-10^{-A_{808}})}$$

Equation 7.1

Where I is the laser power; A_{808} is the absorbance of the materials at the wavelength of 808 nm; h is the heat transfer coefficient; S is the surface area of the system; m_i and $C_{p,i}$ are the mass and heat capacity of system components; τ is the cooling time coefficient; ΔT_{max} is the temperature difference between the max and the ambient temperature.

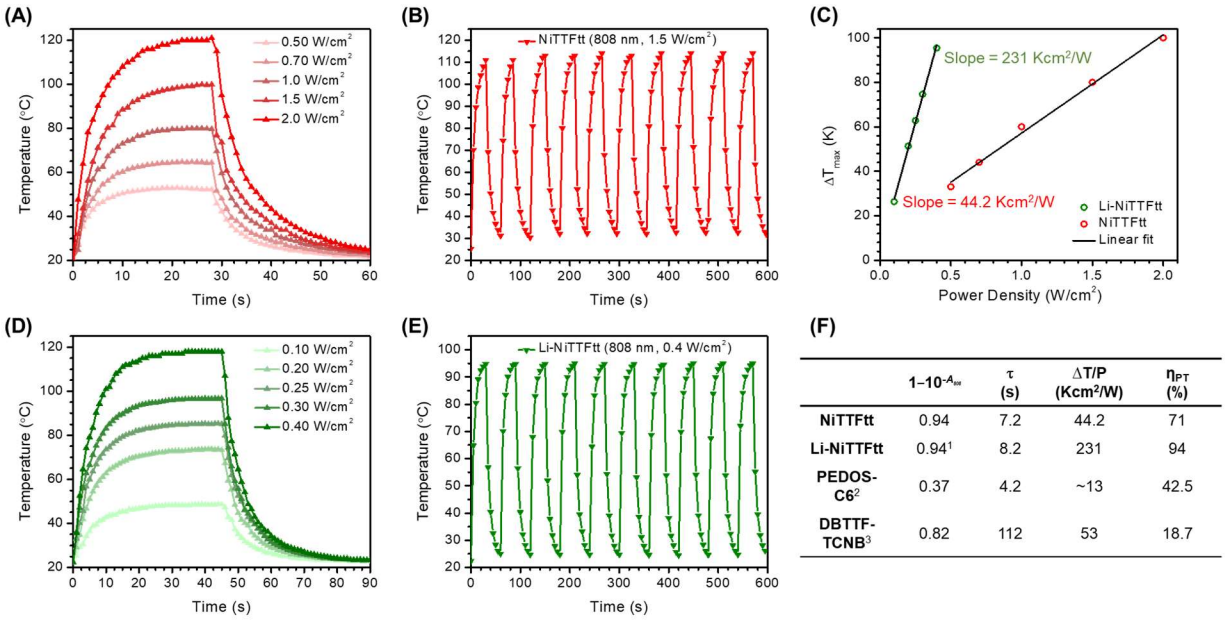

	$1-10^{-A_{808}}$	τ (s)	ΔT/P (Kcm²/W)	η_{PT} (%)
NiTTFtt	0.94	7.2	44.2	71
Li-NiTTFtt	0.94[1]	8.2	231	94
PEDOS-C6[2]	0.37	4.2	~13	42.5
DBTTF-TCNB[3]	0.82	112	53	18.7

Figure 7.6. Photo-thermal conversion of NiTTFtt (red) and Li-NiTTFtt (green). (A) Temperature rises with different NIR laser (808 nm) intensities from NiTTFtt pellet. (B) Reproducibility tests on NiTTFtt under 1.5 Wcm^{-2} (ten heating-cooling cycles). (C) Linear relationships between temperature increasements and irradiation power densities. (D) Temperature rises with different NIR laser (808 nm) intensities from Li-NiTTFtt pellet. (E) Reproducibility tests on Li-NiTTFtt under 0.3 Wcm^{-2} (ten heating-cooling cycles). (F) Comparison of PT parameters between NiTTFtt materials and reported PT organic materials. Note: experiments on Li-NiTTFtt were performed in the N_2-filled glovebox with the same setup as that of NiTTFtt. [1]The absorptance of Li-NiTTFtt is assumed to be identical to NiTTFtt for efficiency estimation due to similar NIR absorption;[2] Ref. 11; [3] Ref.13a.

Since the samples were laid on a white thermally-insulated foam, which displayed no detectable temperature change during the experiments, we assume the heat was only maintained in the pellet at thermal equilibrium. We determined the materials' specific heats by DSC (Figure F.15 and Figure F.16), revealing values of 0.87(1) Jg^{-1}K^{-1} for **NiTTFtt** and 0.86(4) Jg^{-1}K^{-1} for **Li-NiTTFtt**. The value of τ was determined by fitting the decay behavior of the temperature after the laser was turned off (**Figure F.18**) which provided values of 7.2(1) s and 8.2(2) s for **NiTTFtt** and **Li-NiTTFtt**, respectively. The absorbance of **NiTTFtt** at 808 nm was determined from its specular reflectance spectrum (6 % reflectance vs Al). Due to air-sensitivity, we were unable to collect the

specular reflectance spectrum of Li-NiTTFtt; however, as both **NiTTFtt** and **Li-NiTTFtt** have strong absorptions in NIR region, the A_{808} of **Li-NiTTFtt** here was assumed to be the same as that of **NiTTFtt**. With all these parameters, the PT efficiencies of **NiTTFtt** and **Li-NiTTFtt** are estimated as 71 % and 94 %, which are higher than the best reported PT materials (71 %) and even higher than many inorganic NPs including Au and quantum dots.[28]

These results demonstrate that both **NiTTFtt** and **Li-NiTTFtt** possess 1) broad absorption spectra stretching into the NIR; 2) a high temperature rise per unit power; 3) excellent stability and reproducibility; 4) remarkable PT conversion efficiency. These features are promising for PTE conversion, and thus we then investigated these materials in that context.

7.2.4 NIR-Seebeck Voltage

We also used pressed pellets to analyze PTE efficiency. The Seebeck voltage was measured with a homemade setup (**Figure F.19** and **Figure F**.20). Two diametrical ends of a circular pellet were contacted with gold or silver paste while one (hot) end was irradiated with a laser (**Figure 7.7**A). The temperatures of the cold and hot ends were monitored with an IR thermal camera. As shown in the **Figure 7.7**D, the temperature rise and generated voltage were linearly dependent on the NIR laser power for both **Li-NiTTFtt** and **NiTTFtt** while the sign of the voltage was reversed as expected due to the different charge carriers present in the two materials. It is noteworthy that the PTE responses for both materials, which are about 12s for **Li-NiTTFtt** and 1.5 s for **NiTTFtt**, reach equilibrium much faster than their PT effects. The substrate represents a significant cooling pathway which plays an important role in the PTE responsivity and response time. The response time can be dramatically improved with a moderate sacrifice in responsivity by replacing the substrate with other materials with low thermal conductivity, a strategy which has been widely

adopted in thin film-based PTE detectors.[8, 29] Therefore, the response time of both Li-NiTTFtt and NiTTFtt can be further improved as needed via simple modifications of the sample holder. Finally, we note that the calculated values of the Seebeck coefficients from PTE experiments (**Figure F.21**), −2.9 μVK^{-1} for **NiTTFtt** and 9.1 μVK^{-1} for **Li-NiTTFtt**, are consistent with the values measured within the Peltier setup at room temperature (−3.6 μVK^{-1} and 8.2 μVK^{-1}, respectively).

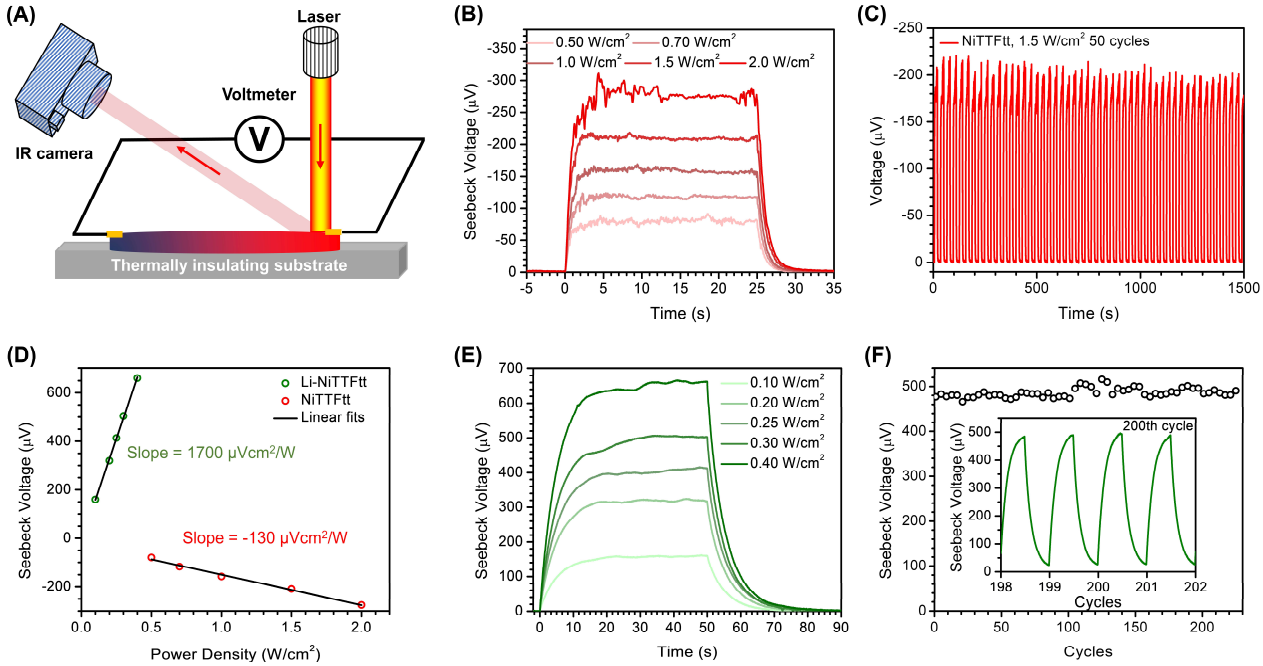

Figure 7.7. NIR-Seebeck voltage production from NiTTFtt (red) and Li-NiTTFtt (green). (A) Diagram of the photo-thermal voltage measurements. (B) Seebeck voltage generated from NiTTFtt pellets with various NIR laser intensities. (C) The cyclability test on NiTTFtt with a NIR laser intensity of 1.5 Wcm-2 at a switching time of 15 s. (D) Linear relationships between Seebeck voltages and irradiation power densities. (E) Seebeck voltage generated from Li-NiTTFtt pellets with various NIR laser intensities. (F) The cyclability test on Li-NiTTFtt with a NIR laser intensity of 0.3 Wcm^{-2} at a switching time of 20 s. Note: experiments on Li-NiTTFtt were performed under the same conditions as its PT experiments.

Optimized polyselenophene films exhibited a temperature rise of ~15 Kcm^2/W under 808 nm laser irradiation with η_{PT} = 42.5 %. Correspondingly, the previously reported Seebeck voltage is about 420 $\mu Vcm^2/W$. Under the same conditions, the produced voltage of **Li-NiTTFtt** is 1700

μVcm^2/W. Previously reported Cu-ett materials have PTE voltages that are also significantly smaller at ~360 μVcm^2/W. While this work was the first example of single-component organic PTE materials with a record PT efficiency for NIR lights, the PT and PTE performances of p-type **Li-NiTTFtt** materials significantly exceed these pioneering organic materials. In contrast, **NiTTFtt** is the first n-type organic PTE material yet reported.

More remarkably, both **NiTTFtt** and **Li-NiTTFtt** pellets show reproducible PTE effects; the light driven voltage was stable over multiple cycles of NIR switching (**Figure 7.7**C and F). Considering the temperature shift in the present case is over 60 °C, in contrast to a much smaller 9 °C difference in the PEDOS films, such stability is notable, particularly for **NiTTFtt** which exhibited this stability in air.

We note that the source of the PTE efficiency in these NiTTFtt materials is different from the conventional PTE materials that possess high Seebeck coefficients. In contrast, the TE properties of both NiTTFtt and Li-NiTTFtt are comparatively poor, and the PTE properties primarily arise from excellent PT properties. Such effective PT conversion leads to a significant temperature difference which is needed to optimize TE efficiency in STEG. As such, preserving this excellent PT conversion while improving the Seebeck coefficients of these materials is a promising strategy for improved PTE conversion. Indeed, we note that the NiTTFtt system itself provides the opportunity to chemically tune PTE properties. We have thus far explored the behaviors of **NiTTFtt** and **Li-NTTFtt** polymers, which are the two extreme oxidation states of NiTTFtt chains. However, pre-synthetic redox control of the TTFtt-tin transmetalation precursors also allows for programming intermediate oxidation states. This strategy should enable tuning of the Seebeck coefficient and ZT figures similarly to how these parameters can be optimized via doping of conducting polymers. Secondly, the counter ion size and identity is another dimension for chemical

modulation. Larger counterions may significantly reduce the carrier concentrations, which in turn would magnify the Seebeck voltage. We hypothesize that the TE performances of the materials can be enhanced by selecting counter ions with suitable sizes, such as tetramethylammonium, tetraethylammonium and tetrabutylammonium. Finally, installation of different transition metals in the chain skeleton is another approach to tune properties. The electron density on the metal will affect the chain's band-filling, the identity of the charge carriers, and their concentration. Thus, the modular properties of this metal-organic material offer a great deal of promise for tunable properties in PT, TE, and PTE applications.

7.3 Conclusion

In this work, we demonstrate that pre-synthetic redox control enables us to isolate both reduced and oxidized NiTTFtt chains. Reduction of the TTFtt linkers results in the metallic n-type NiTTFtt polymers becoming p-type semiconductors. Comprehensive physical characterization of optical, thermal and electrical properties demonstrates that these conducting NiTTFtt polymers exhibit efficient and high-performance PT conversion for NIR light. Furthermore, the heat generated from this conversion also enables promising PTE applications, particularly for single-component organic materials. Considering the UV to NIR optical absorption and fast and intense response, these materials show a great potential as a broadband PTE optical detector.

7.4 Experimental Section

General Methods

Unless otherwise noted, all synthetic manipulations were performed in N_2-filled MBraun UNILab glovebox. Dichloromethane (DCM) was initially dried and sparged with Ar on a solvent purification system from Pure Process Technologies and stored over 4 Å molecular sieves. Methanol (MeOH) was dried with NaOH and distilled before being transferred into the glovebox. The dried MeOH was then passed through activated alumina and stored over 4 Å molecular sieves in the glovebox. Tetrahydrofuran (THF) was stirred with liquid NaK alloy and then filtered through activated alumina and stored over 4 Å molecular sieves. $TTFtt(SnBu_2)_2$ (TTFtt = tetrathiafulvalene-2,3,6,7-tetrathiolate; Bu = n-butyl), $Fc^{BzO}BAr^F{}_4$ (Fc^{BzO} = benzoyl ferrocenium; ([$BAr^F{}_4$] = tetrakis(3,5-bis(trifluoromethyl)phenyl)borate), $Ni(DME)Cl_2$ (DME = 1,2-dimethyloxyethane) and NiTTFtt were synthesized following previously reported procedures. [21, 22, 30] Combustion elemental analyses (C, H, N) were performed by Midwest Microlabs.

Li(THF)/Li-NiTTFtt

$TTFtt(SnBu_2)_2$ (0.500 mmol, 400 mg) in 6 mL THF was added into a 12 mL THF solution of $Ni(DME)Cl_2$ (0.500 mmol, 110 mg) and LiCl (2.50 mmol, 105 mg) with vigorous stirring for 40 mins. The immediate precipitate was isolated via centrifugation and washed with THF (5 × 12 mL). After being dried under vacuum for 30 mins, the material was visibly dry and the dark purple powders were collected as LiTHF-NiTTFtt. To keep batch-to-batch consistency, the evacuation time was strictly kept at 30 mins and the product LiTHF-NiTTFtt was stored in a -35 °C freezer to avoid solvent loss over time. 131 mg Li-NiTTFtt was isolated as a black powder (85%) through further evacuation of LiTHF-NiTTFtt under 100 °C. Detailed characterization and composition data are provided in the main text as well as Appendix F.

Pressed pellets

Pressed pellets were prepared at 800 MPa in the glovebox by use of a hydraulic pellet press (TMAX-15T) and dies with different sizes (7 mm and 8 mm round dies and 6 mm square dies). Prior to pressing, powders were ground to particle sizes below 20 μm. During pressing the pressure was maintained for 20 mins after stabilizing at 800 MPa. The thickness of the pressed pellets is around 100-300 μm.

7.5 References

[1] (a) Mills, D. Advances in Solar Thermal Electricity Technology. *Sol. Energy* **2004**, *76* (1–3), 19–31. (b)Roeb, M.; Müller-Steinhagen, H. Concentrating on Solar Electricity and Fuels. *Science* **2010**, *329* (5993), 773–774.

[2] Kim, J. Y.; Lee, J.-W.; Jung, H. S.; Shin, H.; Park, N.-G. High-Efficiency Perovskite Solar Cells. *Chem. Rev.* **2020**, *120* (15), 7867–7918.

[3] Polman, A.; Atwater, H. A. Photonic Design Principles for Ultrahigh-Efficiency Photovoltaics. *Nat. Mater.* **2012**, *11* (3), 174–177.

[4] (a) Zhao, X.; Yao, C.; Liu, T.; Hamill, J. C.; Ngongang Ndjawa, G. O.; Cheng, G.; Yao, N.; Meng, H.; Loo, Y. Extending the Photovoltaic Response of Perovskite Solar Cells into the Near-Infrared with a Narrow-Bandgap Organic Semiconductor. *Adv. Mater.* **2019**, *31* (49), 1904494. (b) Bai, Y.; Lang, K.; Zhao, C.; Guo, Q.; Zeng, R.; Wang, J.; Hayat, T.; Alsaedi, A.; Tan, Z. Strategies Toward Extending the Near-Infrared Photovoltaic Response of Perovskite Solar Cells. *Sol. RRL* **2020**, *4* (2), 1900280.

[5] (a) Kraemer, D.; Poudel, B.; Feng, H.-P.; Caylor, J. C.; Yu, B.; Yan, X.; Ma, Y.; Wang, X.; Wang, D.; Muto, A.; McEnaney, K.; Chiesa, M.; Ren, Z.; Chen, G. High-Performance Flat-Panel Solar Thermoelectric Generators with High Thermal Concentration. *Nat. Mater.* **2011**, *10* (7), 532–538. (b) Park, T.; Na, J.; Kim, B.; Kim, Y.; Shin, H.; Kim, E. Photothermally Activated Pyroelectric Polymer Films for Harvesting of Solar Heat with a Hybrid Energy Cell Structure. *ACS Nano* **2015**, *9* (12), 11830–11839. (c) Limpert, S.; Burke, A.; Chen, I.-J.; Anttu, N.; Lehmann, S.; Fahlvik, S.; Bremner, S.; Conibeer, G.; Thelander, C.; Pistol, M.-E.; Linke, H. Bipolar Photothermoelectric Effect Across Energy Filters in Single Nanowires. *Nano Lett.* **2017**, *17* (7), 4055–4060.

[6] (a) Liu, H.; Liu, Y.; Dong, S.; Xu, H.; Wu, Y.; Hao, L.; Cao, B.; Li, M.; Wang, Z.; Han, Z.; Yan, K. Photothermoelectric SnTe Photodetector with Broad Spectral Response and High On/Off Ratio. *ACS Appl. Mater. Interfaces* **2020**, *12* (44), 49830–49839. (b) Wang, F.; Lv, Y.; Xu, Y.; Cao, L.; Chen, L.; Zhang, C.; Yao, S.; Xu, J.; Zhou, J.; Chen, Y. Enhanced Photothermoelectric Detection in Co:BiCuSeO Crystals with Tunable Seebeck Effect. *Opt. Express* **2022**, *30* (5), 8356.

[7] Koyama, S.; Inaba, Y.; Kasano, M.; Murata, T. A Day and Night Vision MOS Imager With Robust Photonic-Crystal-Based RGB-and-IR. *IEEE Trans. Electron Devices* **2008**, *55* (3), 754–759.

[8] Lu, X.; Sun, L.; Jiang, P.; Bao, X. Progress of Photodetectors Based on the Photothermoelectric Effect. *Adv. Mater.* **2019**, *31* (50), 1902044.

[9] (a) Antidormi, A.; Cummings, A. W. Optimizing the Photothermoelectric Effect in Graphene. *Phys. Rev. Appl.* **2021**, *15* (5), 054049. (b) Yamashita, H.; Tsunoda, K.; Nishino, H.; Sato, S. Signal-to-Noise Characteristics of Graphene Photodetectors Based on Photothermoelectric Effect. *J. Appl. Phys.* **2021**, *129* (17), 173101. (c) Viti, L.; Cadore, A. R.; Yang, X.; Vorobiev, A.; Muench, J. E.; Watanabe, K.; Taniguchi, T.; Stake, J.; Ferrari, A. C.; Vitiello, M. S. Thermoelectric Graphene Photodetectors with Sub-Nanosecond Response Times at Terahertz Frequencies. In *Frontiers in Optics and Photonics*; De Gruyter, **2021**; Vol. 10, pp 89–98.

[10] Buscema, M.; Barkelid, M.; Zwiller, V.; van der Zant, H. S. J.; Steele, G. A.; Castellanos-Gomez, A. Large and Tunable Photothermoelectric Effect in Single-Layer MoS_2. *Nano Lett.* **2013**, *13* (2), 358–363.

[11] Kim, B.; Shin, H.; Park, T.; Lim, H.; Kim, E. NIR-Sensitive Poly(3,4-Ethylenedioxyselenophene) Derivatives for Transparent Photo-Thermo-Electric Converters. *Adv. Mater.* **2013**, *25* (38), 5483–5489.

[12] Huang, D.; Zou, Y.; Jiao, F.; Zhang, F.; Zang, Y.; Di, C.; Xu, W.; Zhu, D. Interface-Located Photothermoelectric Effect of Organic Thermoelectric Materials in Enabling NIR Detection. *ACS Appl. Mater. Interfaces* **2015**, *7* (17), 8968–8973.

[13] (a) Wang, Y.; Zhu, W.; Du, W.; Liu, X.; Zhang, X.; Dong, H.; Hu, W. Cocrystals Strategy towards Materials for Near-Infrared Photothermal Conversion and Imaging. *Angew. Chemie Int. Ed.* **2018**, *57* (15), 3963–3967. (b) Su, J.; Xu, N.; Murase, R.; Yang, Z.; D'Alessandro, D. M.; Zuo, J.; Zhu, J. Persistent Radical Tetrathiafulvalene-Based 2D Metal-Organic Frameworks and Their Application in Efficient Photothermal Conversion. *Angew. Chemie Int. Ed.* **2021**, *60* (9), 4789–4795. (c) Yan, T.; Li, Y.; Su, J.; Wang, H.; Zuo, J. Charge Transfer Metal-Organic Framework Containing Redox-Active TTF/NDI Units for Highly Efficient Near-Infrared Photothermal Conversion. *Chem. – A Eur. J.* **2021**, *27* (43), 11050–11055. (d) Yan, T.; Li, Y.-Y.; Gu, Q.-Y.; Li, J.; Su, J.; Wang, H.-Y.; Zuo, J.-L. A Tetrathiafulvalene/Naphthalene Diimide-Containing Metal–Organic Framework with fsc Topology for Highly Efficient Near-Infrared Photothermal Conversion. *Inorg. Chem.* **2022**, *61* (7), 3078–3085.

[14] (a) Sun, L.; Campbell, M. G.; Dincă, M. Electrically Conductive Porous Metal-Organic Frameworks. *Angew. Chemie Int. Ed.* **2016**, *55* (11), 3566–3579. (b) Xie, L. S.; Skorupskii, G.; Dincă, M. Electrically Conductive Metal–Organic Frameworks. *Chem. Rev.* **2020**, *120* (16), 8536–8580.

[15] Huang, X.; Zhang, S.; Liu, L.; Yu, L.; Chen, G.; Xu, W.; Zhu, D. Superconductivity in a Copper(II)-Based Coordination Polymer with Perfect Kagome Structure. *Angew. Chemie Int. Ed.* **2018**, *57* (1), 146–150.

[16] Liu, J.; Song, X.; Zhang, T.; Liu, S.; Wen, H.; Chen, L. 2D Conductive Metal–Organic Frameworks: An Emerging Platform for Electrochemical Energy Storage. *Angew. Chemie Int. Ed.* **2021**, *60* (11), 5612–5624.

[17] (a) Sun, Y.; Sheng, P.; Di, C.; Jiao, F.; Xu, W.; Qiu, D.; Zhu, D. Organic Thermoelectric Materials and Devices Based on p- and n-Type Poly(Metal-1,1,2,2-Ethenetetrathiolate)s. *Adv. Mater.* **2012**, *24* (7), 932–937. (b) Jiao, F.; Di, C.; Sun, Y.; Sheng, P.; Xu, W.; Zhu, D. Inkjet-Printed Flexible Organic Thin-Film Thermoelectric Devices Based on p- and n-Type Poly(Metal-1,1,2,2-Ethenetetrathiolate)$_s$ Polymer Composites through Ball-Milling. *Philos. Trans. R. Soc. A Math. Phys. Eng. Sci.* **2014**, *372* (2013), 20130008. (c) Sun, Y.; Qiu, L.; Tang, L.; Geng, H.; Wang, H.; Zhang, F.; Huang, D.; Xu, W.; Yue, P.; Guan, Y.; Jiao, F.; Sun, Y.; Tang, D.; Di, C.; Yi, Y.; Zhu, D. Flexible N-Type High-Performance Thermoelectric Thin Films of Poly(Nickel-Ethylenetetrathiolate) Prepared by an Electrochemical Method. *Adv. Mater.* **2016**, *28* (17), 3351–3358.(d) Sun, L.; Liao, B.; Sheberla, D.; Kraemer, D.; Zhou, J.; Stach, E. A.; Zakharov, D.; Stavila, V.; Talin, A. A.; Ge, Y.; Allendorf, M. D.; Chen, G.; Léonard, F.; Dincă, M. A Microporous and Naturally Nanostructured Thermoelectric Metal-Organic Framework with Ultralow Thermal Conductivity. *Joule* **2017**, *1* (1), 168–177.

[18] (a) Noro, S.; Chang, H.-C.; Takenobu, T.; Murayama, Y.; Kanbara, T.; Aoyama, T.; Sassa, T.; Wada, T.; Tanaka, D.; Kitagawa, S.; Iwasa, Y.; Akutagawa, T.; Nakamura, T. Metal−Organic Thin-Film Transistor (MOTFT) Based on a Bis(o -Diiminobenzosemiquinonate) Nickel(II) Complex. *J. Am. Chem. Soc.* **2005**, *127* (28), 10012–10013. (b) Miner, E. M.; Fukushima, T.; Sheberla, D.; Sun, L.; Surendranath, Y.; Dincă, M. Electrochemical Oxygen Reduction Catalysed by Ni_3(Hexaiminotriphenylene)$_2$. *Nat. Commun.* **2016**, *7* (1), 10942. (c) Huang, X.; Yao, H.; Cui, Y.; Hao, W.; Zhu, J.; Xu, W.; Zhu, D. Conductive Copper Benzenehexathiol Coordination Polymer as a Hydrogen Evolution Catalyst. *ACS Appl. Mater. Interfaces* **2017**, *9* (46), 40752–40759. (d) DeGayner, J. A.; Jeon, I.-R.; Sun, L.; Dincă, M.; Harris, T. D. 2D Conductive Iron-Quinoid Magnets Ordering up to T_c = 105 K via Heterogenous Redox Chemistry. *J. Am. Chem. Soc.* **2017**, *139* (11), 4175–4184. (e) Hoppe, B.; Hindricks, K. D. J.; Warwas, D. P.; Schulze, H. A.; Mohmeyer, A.; Pinkvos, T. J.; Zailskas, S.; Krey, M. R.; Belke, C.; König, S.; Fröba, M.; Haug, R. J.; Behrens, P. Graphene-like Metal–Organic Frameworks: Morphology Control, Optimization of Thin Film Electrical Conductivity and Fast Sensing Applications. *CrystEngComm* **2018**, *20* (41), 6458–6471.

[19] Kusamoto, T.; Nishihara, H. Zero-, One- and Two-Dimensional Bis(Dithiolato)Metal Complexes with Unique Physical and Chemical Properties. *Coord. Chem. Rev.* **2019**, *380*, 419–439.

[20] Camerel, F.; Fourmigué, M. (Photo)Thermal Stimulation of Functional Dithiolene Complexes in Soft Matter. *Eur. J. Inorg. Chem.* **2020**, *2020* (6), 508–522.

[21] DOI: https://doi.org/10.21203/rs.3.rs-1281292/v1.

[22] Xie, J.; Boyn, J. N.; Filatov, A. S.; McNeece, A. J.; Mazziotti, D. A.; Anderson, J. S. Redox, Transmetalation, and Stacking Properties of Tetrathiafulvalene-2,3,6,7-Tetrathiolate Bridged Tin, Nickel, and Palladium Compounds. *Chem. Sci.* **2020**, *11* (4), 1066–1078.

[23] de Caro, D.; Fraxedas, J.; Faulmann, C.; Malfant, I.; Milon, J.; Lamère, J.-F.; Collière, V.; Valade, L. Metallic Thin Films of TTF[Ni(dmit)$_2$]$_2$ by Electrodeposition on (001)-Oriented Silicon Substrates. *Adv. Mater.* **2004**, *16* (910), 835–838.

[24] Kobayashi, A.; Fujiwara, E.; Kobayashi, H. Single-Component Molecular Metals with Extended-TTF Dithiolate Ligands. *Chem. Rev.* **2004**, *104* (11), 5243–5264.

[25] Kobayashi, Y.; Terauchi, T.; Sumi, S.; Matsushita, Y. Carrier Generation and Electronic Properties of a Single-Component Pure Organic Metal. *Nat. Mater.* **2017**, *16* (1), 109–114.

[26] (a) Kakalios, J.; Fritzsche, H. Persistent Photoconductivity in Doping-Modulated Amorphous Semiconductors. *Phys. Rev. Lett.* **1984**, *53* (16), 1602–1605. (b) Shimakawa, K. Persistent Photocurrent in Amorphous Chalcogenides. *Phys. Rev. B* **1986**, *34* (12), 8703–8708. (c) Hyun, K.-S.; Jang, J.; Lee, C. Persistent Photoconductivity Decay Mechanism in Compensated Amorphous Silicon. *J. Non. Cryst. Solids* **1991**, *137–138* (PART 1), 283–286.

[27] Paściak, A.; Pilch-Wróbel, A.; Marciniak, Ł.; Schuck, P. J.; Bednarkiewicz, A. Standardization of Methodology of Light-to-Heat Conversion Efficiency Determination for Colloidal Nanoheaters. *ACS Appl. Mater. Interfaces* **2021**, *13* (37), 44556–44567.

[28] Zhao, Y.; He, Z.; Zhang, Q.; Wang, J.; Jia, W.; Jin, L.; Zhao, L.; Lu, Y. 880 nm NIR-Triggered Organic Small Molecular-Based Nanoparticles for Photothermal Therapy of Tumor. *Nanomaterials* **2021**, *11* (3), 773.

[29] Yang, H.; Fu, B.; Li, D.; Tian, Y.; Chen, Y.; Mattila, M.; Yong, Z.; Li, R.; Hassanien, A.; Yang, C.; Tittonen, I.; Ren, Z.; Bai, J.; Li, Q.; Kauppinen, E. I.; Lipsanen, H.; Sun, Z. Broadband Laser Polarization Control with Aligned Carbon Nanotubes. *Nanoscale* 2015, *7* (25), 11199–11205.

[30] Boudier, A.; Breuil, P.-A. R.; Magna, L.; Olivier-Bourbigou, H.; Braunstein, P. Nickel(II) Complexes with Imino-Imidazole Chelating Ligands Bearing Pendant Donor Groups (SR, OR, NR_2, PR_2) as Precatalysts in Ethylene Oligomerization. *J. Organomet. Chem.* **2012**, *718*, 31–37.

Chapter 8: MoS_2-Like 2D Coordination Frameworks

8.1 Introduction

The beginning of the 21st century has seen a surge of interest in two-dimensional materials with layered structures, typified by graphene[1] and transition-metal dichalcogenides.[2] Inspired by these in-plane conjugated 2D inorganic materials, a new family of graphene-like 2D metal-organic frameworks has been reported exhibiting high electrical conductivity and porosity.[3] 2D π-d conjugated CPs based on metal-bis-dithiolene nodes display record conductivity and even superconductivity.[4] Transition metal chalcogenide clusters as nodes are less developed despite the fact that the combination of the delocalized electronic structure of clusters with highly conjugated linkers could produce a number of new conducting CP families. In addition to conductivity, nanoscale transition metal dichalcogenides frequently display semiconducting characteristics. As such, these mineral-like CPs are potentially attractive for applications in electronics and photonics.[5] Moreover, the distinct structures and unique chemical properties of both clusters and organic linkers endow these materials with advantages in some applications such as electrochemical energy storage and coupling of conductivity and magnetism.

In the literature, molecular clusters such as $Mo_3S_7^{4+}$ have been targeted as models of MoS_2 as these species demonstrate an ideal topology to mimic active sites in mechanistic studies.[6] Recently, Ji et al. have demonstrated that Mo_3S_7 clusters can be connected by 1,4-benzenedithiolate to generate highly crystalline 1D chains, which exhibited similar but enhanced HER activity compared to MoS_2 nanomaterials.[7] This work represents the first attempt of using Mo_3S_7 clusters as an SBU to build multifunctional CPs. Instead of BDT, the combination of Mo_3S_7 clusters with TTFtt linkers could potentially lead to extended 2D frameworks. Indeed, molecular Mo_3S_7-tris-

dithiolene complexes have been used to prepare single-component molecular conductors with intriguing spin frustration and low-bandgap semiconducting characteristics.[15b,8] A number of subsequent theoretical investigations attempted to model these spin interactions.[9] All of these studies shed light on the potential of MoS_2-like coordination frameworks for electrical and spintronic applications. In addition, according to the previous research, we propose that organic analogues of 2D sheets of MoS_2 should be porous and their electronic properties should be tunable by redox events at either nodes or linkers. Herein, we report the initial synthesis and characterization of the MoS_2-like coordination frameworks based on TTFtt linkers (**Scheme 8.1**).

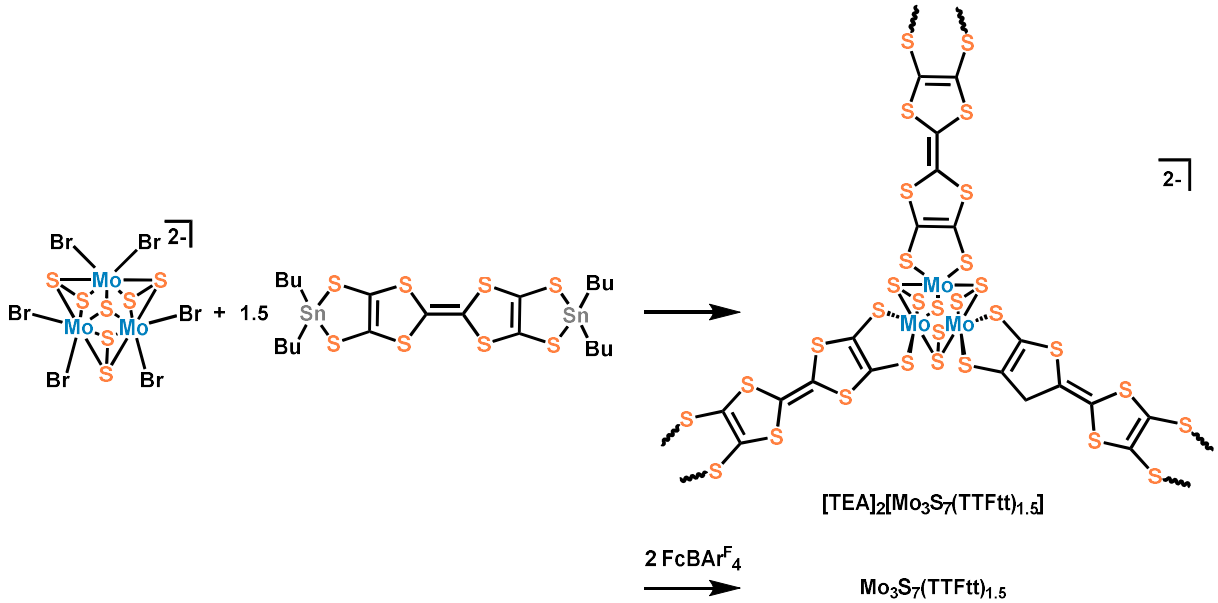

Scheme 8.1. Synthesis of MoS_2-like coordination frameworks based on TTFtt linkers and its in situ redox reaction.

8.2 Results and Discussion

8.2.1 Bulk Material Synthesis and Initial characterizations

To synthesize these proposed materials, the previously reported $[TEA]_2[Mo_3S_7Br_6]$ cluster was treated with 1.5 equivalents of the $TTFtt(SnBu)_2$ precursor in a mixture of MeCN and DCM

generating black amorphous materials termed as $[TEA]_2[(Mo_3S_7)(TTFtt)_{1.5}]$. Adding 2 equivalents of $FcBAr^F{}_4$ with the $TTFtt(SnBu_2)_2$ precursors before metalation resulted instead in tan powders. We propose that in situ oxidation leads to a neutral framework, the product of which is labelled as $(Mo_3S_7)(TTFtt)_{1.5}$.

XPS confirms the ratios of Mo and S as about 1:6.2, which is consistent with the prediction of Mo:S ratio, 3:19 (1:6.3). Furthermore, XAS studies (**Figure 8.1**, **Table 8.1**) of both the dianionic and neutral materials indicate that the oxidation state of Mo does not change upon oxidation and that the Mo-S and Mo-Mo distances are close to nano-MoS_2 in both cases.[10] It confirms that the redox event is based on TTF cores, potentially avoiding significant structural changes associated with metal centers.

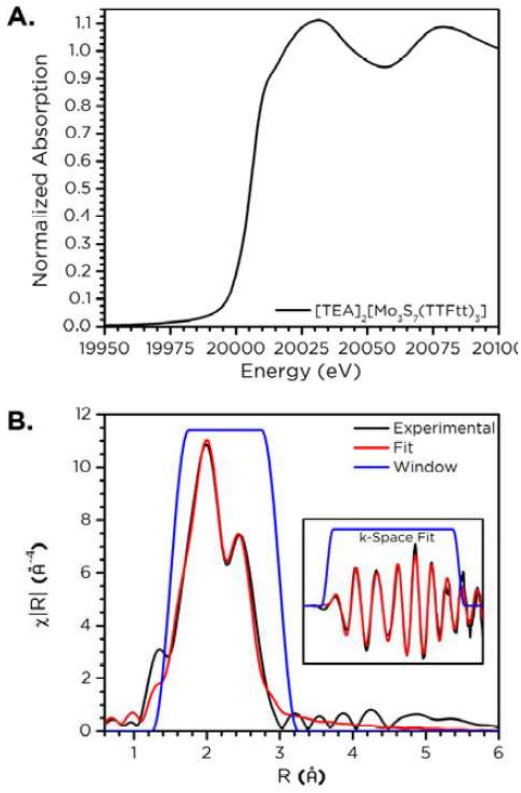

Figure 8.1. Mo K-edge XAS data for $[TEA]_2[Mo_3S_7(TTFtt)_3]$. A. XANES region showing an overall oxidation state similar to monolayer MoS_2. B. EXAFS region with fits and k-space fit inset. The bond lengths discussed in the text are from this fit.

Table 8.1. XAS data and bond length's comparison.

	$[TEA]_2[(Mo_3S_7)(TTFtt)_{1.5}]$	$(Mo_3S_7)(TTFtt)_{1.5}$	Nano MoS_2[a]	Bulk MoS_2[b]
Mo K-edge (eV)	20007(1)	20008(1)	20007(1)	20007
Mo-S (Å)	2.429(8)	2.435(5)	2.410(7)	2.40(2)
Mo-Mo (Å)	2.772(5)	2.761(3)	2.76(1)	~3.17

a, b: Ref 10 a and b.

Besides an obvious color difference, initial two-probe conductivity measurements on pressed pellets of these two materials suggest a significant difference in conductivity from ~ 10^{-3} S/cm to 0.3 S/cm, upon in situ oxidation from the dianionic to the neutral framework. This result supports our proposal of tuning the framework's electronic structure via the redox events on organic comparts.

8.2.2 Attempt of thin film synthesis

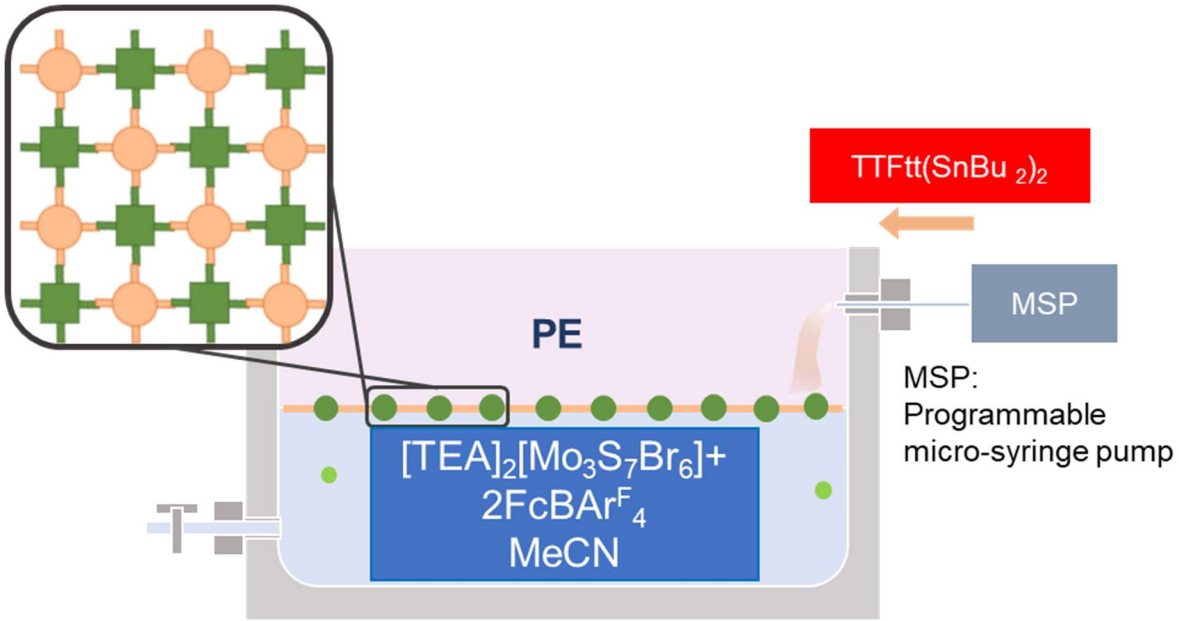

Figure 8.2. Demonstration of the film fabrication via the liquid-liquid interface method.

In addition to bulk materials, we also attempted to grow a thin film of these 2D frameworks. Recently, Zhong et al. has reported the wafer-scale synthesis of monolayer 2D porphyrin polymers by using a liquid-liquid interface growth method.[11] In collaboration with this team, a similar device and setup was used to grow the MoS_2-like coordination framework in a N_2-filled glovebox **(Figure 8.2)**. Due to water-sensitivity of tin precursors, we replaced the original water layer with MeCN generating a petroleum ether (PE)-MeCN interface. While the metal salts and oxidizing agents were pre-injected into the bottom MeCN layer, the DCM solution of $TTFttSn(Bu)_2$ was slowly added into the top layer by using the microsyringe pump. As $TTFttSn(Bu)_2$ is not soluble in either pentane or MeCN at room temperature, the tin precursors were expected to expand in the interface and react with the metal salts leading to thin film products. Atomic force microscopy (AFM) suggests that a crude thin film with thickness below 10 nm was obtained, but many cracks are evident (**Figure 8.3**). As the fact that all cracks have the same orientation, it may indicate that cracks are generated after the film formation due to external forces such as vibrations. To improve the film quality, we are scanning other synthetic conditions and methods.

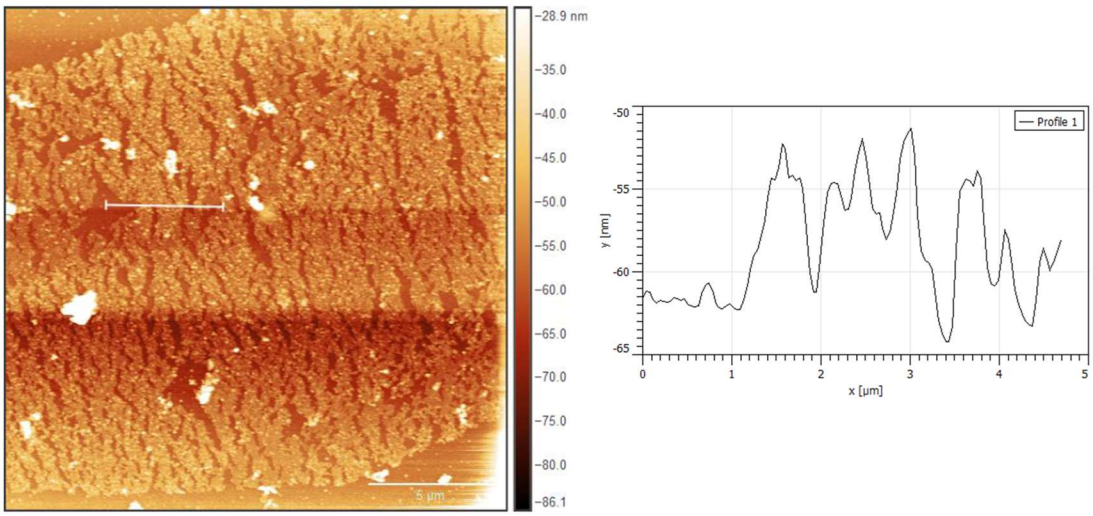

Figure 8.3. AFM spectrum of the as-synthesized thin film and its corresponding height image.

8.3 Conclusion

Based on previous studies of coordination frameworks constructed based on metal-sulfide clusters and TTFtt linkers, we proposed a 2D coordination framework mimicking MoS_2. Incorporating MoS-based clusters as nodes with conjugated, redox-active linkers will allow for the synthesis of porous structures with tunable electronic properties with potential applications in energy or ion storage. In addition, the magnetism and conduction shown in reported single-component complexes and TTFtt-based materials discussed in previous sections all indicate the promising applications in spintronics and advance electronics.

8.4 Experimental Section

General Methods

Unless otherwise noted, all synthetic manipulations were performed under an inert atmosphere of dry N_2 using a Schlenk line or a N_2-filled MBraun UNILab glovebox. DCM, MeCN and PE was initially dried and sparged with Ar on a solvent purification system from Pure Process Technologies, filtered with dry Al_2O_3 and stored over 4 Å molecular sieves. $TTFtt(SnBu_2)_2$, $FcBAr^F{}_4$, and $[TEA]_2[Mo_3S_7Br_6]$ were synthesized following previously reported procedures.[6]

$[TEA]_2[(Mo_3S_7)(TTFtt)_{1.5}]$

$[TEA]_2[Mo_3S_7Br_6]$ (0.010 mmol, 13 mg) in 2 mL MeCN was mixed with $TTFtt(SnBu)_2$ (0.015 mmol, 12 mg) in 2mL DCM yielding an immediate precipitate. The solid product was isolated via centrifugation and washing with DCM (3×3 mL), MeCN (1×3 mL) and DCM (1×3 mL)

sequentially. After being dried under vacuum, 12 mg of $[TEA]_2[(Mo_3S_7)(TTFtt)_{1.5}]$ was isolated as a black powder (80 %).

$(Mo_3S_7)(TTFtt)_{1.5}$

$TTFtt(SnBu_2)_2$ (0.015 mmol, 12 mg) in 1 mL DCM was mixed with $FcBAr^F{}_4$ (0.020 mmol, 21 mg) in 5 mL DCM resulting in a homogenous yellow solution. The resulting solution was added into a 2 mL MeCN solution of $[TEA]_2[Mo_3S_7Br_6]$ (0.010 mmol, 13 mg) with vigorous stirring. The solid product was isolated via centrifugation and washing with DCM (3×3 mL), MeOH (1×3 mL) and DCM (1×3 mL) sequentially. After being dried under vacuum, 7.5 mg of $(Mo_3S_7)(TTFtt)_{1.5}$ was isolated as a tan powder (74 %).

Film fabrication

Films were synthesized in both 1-inch by 5-inch and 2-inch by 5-inch reactors. For lateral structures with same width of each component, a multi-channel syringe pump (New Era Pump System Inc., NE-1800) was used to inject different precursors at the same rate and volume. 3 injection nozzles were employed to introduce $TTFtt(SnBu_2)_2$ and metal solutions with $FcBAr^F{}_4$ respectively in a 1-inch by 5-inch reactor with individual rate of 5 μL/min.

X-ray Photoelectron Spectroscopy (XPS)

XPS spectra were collected with the AXIS Nova spectrometer (Kratos Analytical) equipped with a monochromatic Al K_α X-ray source. The Al anode was powered at 10 mA and 15 kV. The instrument work function was calibrated to give a Au $4f_{7/2}$ metallic gold binding energy of 83.95 eV. The instrument base pressure was ca. 1×10^{-10} Torr. The analysis area size was 0.3×0.7 mm^2. For calibration purposes, the binding energies were referenced to the C 1s peak at 284.8 eV. Survey

spectra were collected with a step size of 1 and 160 eV pass energy. Samples were affixed to conductive carbon tape under N_2 before loading into the spectrometer.

X-ray Absorption Spectroscopy (XAS)

Powder samples of amorphous $[TEA]_2[(Mo_3S_7)(TTFtt)_{1.5}]$ and $(Mo_3S_7)(TTFtt)_{1.5}$ were prepared by grinding finely with polypropylene as a binder. A Teflon washer (5.3 mm internal diameter) was sealed on one side with Kapton tape and the ground powder was then transferred to the inside of this ring before compacting with a Teflon rod and sealing the remaining face with Kapton tape. X-ray absorption near-edge spectra (XANES) of Mo K-edge (20000 eV) data were acquired at the MRCAT 10-BM beam line in transmission at the Advanced Photon Source at Argonne National Laboratory with a bending magnet source with ring energy at 7.00 GeV. Data collected was processed using the Demeter software suite[12] by extracting the EXAFS oscillations $\chi(k)$ as a function of photoelectron wavenumber k. The theoretical paths were generated using FEFF6[13] and the models were done in the conventional way using the fitting program Artemis.

Electrical conductivity measurements

Electrical conductivity measurements were performed in a two-contact geometry at room temperature under N_2. Samples were prepared as pressed pellets clamped between two brass electrodes (4.8 mm diam.) in a plastic sleeve, allowing measurement of the sample thickness with calipers. Linear sweep voltammetry was conducted using a BASi Epsilon potentiostat/galvanostat, with the reference and counter electrode terminals connected to one electrode and the working

electrode terminal to the other. The resulting data were fit to a straight line to obtain the sample resistance.

Atomic Force Microscopy (AFM)

AFM measurements of 2DP films were conducted on either a Bruker Dimension Icon AFM with ScanAsyst® or a Cypher ES AFM. All measurements were done at room temperature under ambient air conditions.

8.4 References

[1] (a) M. J. Allen, V. C. Tung and R. B. Kaner, Honeycomb Carbon: A Review of Graphene, *Chem. Rev.*, 2010, **110**, 132–145. (b) K. S. Novoselov, V. I. Fal′ko, L. Colombo, P. R. Gellert, M. G. Schwab and K. Kim, A Roadmap for Graphene, *Nature*, 2012, **490**, 192–200.

[2] S. Manzeli, D. Ovchinnikov, D. Pasquier, O. V. Yazyev and A. Kis, 2D Transition Metal Dichalcogenides, *Nat. Rev. Mater.*, 2017, **2**, 17033.

[3] (a) D. Sheberla, L. Sun, M. a Blood-forsythe, S. Er, C. R. Wade, C. K. Brozek, A. Aspuru-guzik, M. Dincă, R. Casey, C. K. Brozek, A. Aspuru-guzik, M. Dinc and S. Experimental, A Semiconducting Metal-Organic Graphene Analogue Supporting Information, *J. Am. Chem. Soc.*, 2014, **3**, 1–13. (b) B. Hoppe, K. D. J. Hindricks, D. P. Warwas, H. A. Schulze, A. Mohmeyer, T. J. Pinkvos, S. Zailskas, M. R. Krey, C. Belke, S. König, M. Fröba, R. J. Haug and P. Behrens, Graphene-like Metal–Organic Frameworks: Morphology Control, Optimization of Thin Film Electrical Conductivity and Fast Sensing Applications, *CrystEngComm*, 2018, **20**, 6458–6471.

[4] (a) X. Huang, P. Sheng, Z. Tu, F. Zhang, J. Wang, H. Geng, Y. Zou, C.-a. Di, Y. Yi, Y. Sun, W. Xu and D. Zhu, Two-Dimensional *π–d* Conjugated Coordination Polymer with Extremely High Electrical Conductivity and Ambipolar Transport Behavior, *Nat Commun*, 2015, **6**, 7408–7416; (b) X. Huang, S. Zhang, L. Liu, L. Yu, G. Chen, W. Xu and D. Zhu, Superconductivity in a Copper(II)-Based Coordination Polymer with Perfect Kagomè Structure, *Angew. Chem. Int. Ed.*, 2018, **57**, 146–150; (c) Y. Cui, J. Yan, Z. Chen, J. Zhang, Y. Zou, Y. Sun, W. Xu and D. Zhu, $[Cu_3(C_6Se_6)]_n$: The First Highly Conductive 2D *π –d* Conjugated Coordination Polymer Based on Benzenehexaselenolate, *Adv. Sci.*, 2019, **6**, 1802235–1802240.

[5] K. F. Mak and J. Shan, Photonics and Optoelectronics of 2D Semiconductor Transition Metal Dichalcogenides, *Nat. Photonics*, 2016, **10**, 216–226.

[6] (a) D. Recatalá, R. Llusar, A. L. Gushchin, E. A. Kozlova, Y. A. Laricheva, P. A. Abramov, M. N. Sokolov, R. Gómez and T. Lana-Villarreal, Photogeneration of Hydrogen from Water by

Hybrid Molybdenum Sulfide Clusters Immobilized on Titania, *ChemSusChem*, 2015, **8**, 148–157. (b) P. D. Tran, T. V. Tran, M. Orio, S. Torelli, Q. D. Truong, K. Nayuki, Y. Sasaki, S. Y. Chiam, R. Yi, I. Honma, J. Barber and V. Artero, Coordination Polymer Structure and Revisited Hydrogen Evolution Catalytic Mechanism for Amorphous Molybdenum Sulfide, *Nat. Mater.*, 2016, **15**, 640–646.

[7] Z. Ji, C. Trickett, X. Pei and O. M. Yaghi, Linking Molybdenum–Sulfur Clusters for Electrocatalytic Hydrogen Evolution, *J. Am. Chem. Soc.*, 2018, **140**, 13618–13622.

[8] R. Llusar, S. Uriel, C. Vicent, J. M. Clemente-Juan, E. Coronado, C. J. Gómez-García, B. Braïda and E. Canadell, Single-Component Magnetic Conductors Based on Mo 3 S 7 Trinuclear Clusters with Outer Dithiolate Ligands, *J. Am. Chem. Soc.*, 2004, **126**, 12076–12083.

[9] (a) C. Janani, J. Merino, I. P. McCulloch and B. J. Powell, Low-Energy Effective Theories of the Two-Thirds Filled Hubbard Model on the Triangular Necklace Lattice, *Phys. Rev. B - Condens. Matter Mater. Phys.*, 2014, **90**, 1–10. (b) C. Janani, J. Merino, I. P. McCulloch and B. J. Powell, Haldane Phase in the Hubbard Model at 2/3-Filling for the Organic Molecular Compound $Mo_3S_7(dmit)_3$, *Phys. Rev. Lett.*, 2014, **113**, 267204. (c) A. C. Jacko, C. Janani, K. Koepernik and B. J. Powell, Emergence of Quasi-One-Dimensional Physics in a Nearly-Isotropic Three-Dimensional Molecular Crystal: Ab Initio Modeling of $Mo_3S_7(dmit)_3$, *Phys. Rev. B*, 2015, **91**, 125140. (d) B. J. Powell, J. Merino, A. L. Khosla and A. C. Jacko, Heisenberg and Dzyaloshinskii-Moriya Interactions Controlled by Molecular Packing in Trinuclear Organometallic Clusters, *Phys. Rev. B*, 2017, **95**, 094432. (e) A. C. Jacko, A. L. Khosla, J. Merino and B. J. Powell, Spin-Orbit Coupling in $Mo_3S_7(dmit)_3$, *Phys. Rev. B*, 2017, **95**, 155120.

[10] (a) Joensen, P.; Crozier, E. D.; Alberding, N.; Frindt, R. F. A Study of Single-Layer and Restacked MoS 2 by X-Ray Diffraction and X-Ray Absorption Spectroscopy. *J. Phys. C Solid State Phys.* **1987**, *20* (26), 4043–4053. (b) Quilty, C. D.; Housel, L. M.; Bock, D. C.; Dunkin, M. R.; Wang, L.; Lutz, D. M.; Abraham, A.; Bruck, A. M.; Takeuchi, E. S.; Takeuchi, K. J.; Marschilok, A. C. Ex Situ and Operando XRD and XAS Analysis of MoS 2 : A Lithiation Study of Bulk and Nanosheet Materials. *ACS Appl. Energy Mater.* **2019**, *2* (10), 7635–7646.

[11] Zhong, Y.; Cheng, B.; Park, C.; Ray, A.; Brown, S.; Mujid, F.; Lee, J.-U.; Zhou, H.; Suh, J.; Lee, K.-H.; Mannix, A. J.; Kang, K.; Sibener, S. J.; Muller, D. A.; Park, J. Wafer-Scale Synthesis of Monolayer Two-Dimensional Porphyrin Polymers for Hybrid Superlattices. *Science.* **2019**, *366* (6471), 1379–1384

[12] Ravel, B. & Newville, M. ATHENA , ARTEMIS , HEPHAESTUS : data analysis for X-ray absorption spectroscopy using IFEFFIT. *J. Synchrotron Radiat.* **12**, 537–541 (2005).

[13] Rehr, J. J. & Albers, R. C. Theoretical approaches to X-ray absorption fine structure. *Rev. Mod. Phys.* **72**, 621–654 (2000).

Appendix A:Supporting Data for Chapter 2

A.1 Methods and Procedures

Digestion Experiments

1 and **2** (~5 mg) were digested in 12 M hydrochloric acid (~1 mL) under air to check for BDT and PhSH content. The acid solution was extracted with C_6D_6 or CD_2Cl_2 (~0.5-1 mL; in the presence of TBA, Fe-containing digestion products were found to be soluble in CD_2Cl_2) and analyzed by ^{1}H NMR spectroscopy.

To test for the presence of quaternary ammonium ions, **1** and **2** (~5 mg) were digested in D_2SO_4 (~0.1-0.2 mL),[1] resulting in oxidation of BDT to an insoluble polymer. This suspension was diluted with $(CD_3)_2SO$ and analyzed by ^{1}H NMR spectroscopy. Addition of [TBA][PF_6] or [TMA][Cl] standards was used to confirm the identity of the species in solution.

Sample Preparation for ICP-MS

Solutions for ICP-MS were prepared by digesting 2 mg of material in 2 mL HNO_3 (trace metal grade) solution in a fume hood overnight at room temperature. Samples analyzed for Na content were digested in polypropylene to avoid contamination of Na from glass containers. The solution was diluted with ultra-filtered deionized water for ICP-MS analysis. Reported errors are the standard deviation of measurements on three batches of each material, except for the Co content before reduction (measured in duplicate).

X-ray Powder Diffraction

Reaction screening:

X-ray powder diffraction measurements for screening reaction conditions were performed on a SAXSLAB Ganesha equipped with a Xenocs GeniX3D Cu Kα source. Samples were loaded into

0.8-1.1 mm ID, 0.25 mm wall borosilicate capillaries and sealed with wax under N_2. Data reduction/integration was performed using Saxsgui software and a background correction for the capillary was applied.

11-BM APS synchrotron beamline (bending magnet source) / Argonne National Laboratory (Lemont, Il, USA):

The samples were loaded into 1.0 mm OD, 0.01 mm wall borosilicate capillaries in a N_2-filled glovebox (using an ionizer to reduce static and repeatedly dropping the capillary into a glass vial) and then capped with a septum with a small amount of vacuum grease. Capillaries were then evacuated via an inserted needle through a septum, and sealed using an electric arc lighter. The powders were rotated during the measurement at ~50 cycles per second. The powder patterns were measured at 295 K at beamline 11-BM of the Advanced Photon Source at Argonne National Laboratory using a wavelength of $\lambda = 0.41275$ Å, from 0.5 to 50° 2θ with a step size of 0.001° and a counting time of 0.1 sec/step.PROXIMA 2A / SOLEIL synchrotron beamline (Saint-Aubin, France).

To confirm the stability of **1** under the intense X-ray beam of the synchrotron (~1 hour under the beam at APS at ambient conditions), additional powder X-ray diffraction data for **1** were recorded at the PROXIMA 2A beamline (PX2A) of the SOLEIL synchrotron (E = 17 keV , $\lambda = 0.7293$ Å) using an EIGER X 9M 2D hybrid photon counting detector and measured at 295 K.[2] The optical layout included a cryogenically cooled channel-cut Si [111] monochromator, a convex horizontal prefocusing mirror and a pair of focusing bimorph mirrors in Kirpatrick-Baez configuration, resulting in a 100 μm wide X-ray beam at the sample position. The 2D detector was set at a distance of 300 mm from the sample. **1** was packed in a flame-sealed 1.0 mm diameter glass capillary, which was not only rotated during the measurement, but was also translated along its spinning

axis, resulting in a helical path of the beam along the exterior of the capillary, all to minimize sample damage from the intense X-ray beam. The capillary was translated along a 0.8 mm path (i.e. ca. 10 times the horizontal beamsize). The measurement time was 72 s, much smaller than for the 11-BM/APS related measurement, making radiation damage to the sample very unlikely. The 2D nature of the measurement, a 2D image displaying full Debye-Scherrer rings, provided a direct check for the maintenance of the crystallinity and homogeneity of the sample, as well as for the absence of significant preferred orientation in the latter (Figure A.8).

The free ALBULA / DECTRIS software was used to convert the PX2A synchrotron data from 2D I(x,y) binary frames (CBF & HDF5 formats) into conventional 1D ASCII I(2θ) XRPD histograms, with an average 2θ step size of 0.015°.[3] For both the 11-BM/APS and the PX2A/SOLEIL data, the two ubiquitous indexing programs DICVOL14[4] and N-TREOR14[5] were used, together with their respective graphical interfaces PreDICT[6] and EXPO2014,[7] yielding nearly identical unit cells for a given 1D histogram (**Table A.2** and **Table A**.3). For structure solution, the 11-BM data for **1** and **2** were used and simulated annealing applied as implemented in EXPO2014[7] and FOX,[8] yielding similar starting models albeit with different success rates. The Rietveld least-squares refinement of the structure solutions against the synchrotron data was carried out using the GSAS-I software,[9] based on starting models obtained with FOX. Restraints for bond distances and bond angles were introduced in the refinements based on published Fe_4S_4 cubane structures,[10] as well as from geometry information gathered from the CCDC/MOGUL module of the Cambridge Structural Database (CSD).[11] Besides appraisal of the usual figures of merit for powder structures, the crystallographic arrangements were also analyzed graphically using the CCDC Mercury software[12] to ensure that the obtained refined crystallographic structures were chemically plausible. It is worth noting that even the PX2A data allowed for a successful

structure solution, and not merely for successful indexing and Rietveld refinement. Eventually, the two GSAS-I Rietveld-refined structures for both **1** and **2** were obtained as CIF (Crystallographic Information; CCDC 1869639-1869640) files which were themselves validated by the standard IUCr / CheckCIF procedure.[13] Details of the structure solution and refinement are listed in Tables S2 and S3. Atomic coordinates are collected in Tables S4 and S5. Final Rietveld refinement fits are shown in Figures S9-S12.

Small Angle X-ray Scattering

Small angle X-ray scattering (SAXS) experiments were performed on a SAXSLAB Ganesha equipped with a Xenocs GeniX3D Cu Kα source. SAXS samples were loaded into 1.0 mm OD x 0.01 mm wall borosilicate glass tubes and sealed under N_2 with wax. A near-saturated solution of **2** in dry DMF (approx. 2 mg/mL) was prepared and passed through a 0.2 μm PET syringe filter prior to loading into the tube. A tube with neat DMF was used as the blank. SAXS data were collected in six 1-hour increments and compared to check for radiation damage, which was not found. All experiments were performed at ambient temperature. Data reduction/integration was performed using Saxsgui software, and background subtraction and fitting were performed in the Irena software suite.[14c] Linear fits were performed in OriginPro software. Data were also fit using the Unified Fit module in Irena, based on the work of Beaucage.[14]

Optical Spectroscopy

UV-visible absorption spectra were recorded on a Thermo Scientific Evolution 300 spectrometer with the VISIONpro software suite. All spectra were recorded at room temperature. Diffuse reflectance spectra were obtained with the use of a Harrick Praying Mantis accessory. Solid **1** or **2** was ground with [Mg][SO_4] in air to produce the diffuse reflectance sample and pure [Mg][SO_4]

was used as a white reference material. All spectra were normalized and had a background subtraction applied.

X-ray Photoelectron Spectroscopy

X-ray photoelectron spectra (XPS) were collected with the AXIS Nova spectrometer (Kratos Analytical) equipped with a monochromatic Al Kα X-ray source. The Al anode was powered at 10 mA and 15 kV. The instrument work function was calibrated to give an Au $4f_{7/2}$ metallic gold binding energy of 83.95 eV. Instrument base pressure was *ca*. 1×10^{-10} Torr. The analysis area size was 0.3 x 0.7 mm^2. For calibration purposes, the binding energies were referenced to C 1s peak at 284.8 eV. Survey spectra were collected with a step size of 1 eV and 160 eV pass energy. The high-resolution spectra were collected with a pass energy of 40 eV and 0.1 eV step size. Powder samples were affixed to conductive carbon tape in air before loading into the spectrometer.

For **1**, Fe, S, N, C, and O (likely from atmospheric adsorbates) are present. Quantification results provide the molar ratio of Fe:S:N = 1:1.96:0.52. For **2**, Fe, S, N, C, and O are again detected. Only Fe and S could be quantified, giving a molar ratio Fe:S = 1:1.95. For both **1** and **2**, XPS seems consistent with mixed valent Fe in the $Fe^{2+/3+}$ state; C 1s shows C-C/C-H and C-N bonds (indicated by broadening at about 286 eV); The S $2p_{3/2}$ shift of 161.5 eV corresponds to S^{2-} as in a sulfide ion or organic thiols – these species have close shifts and closely overlap. The N 1s spectrum appears as a sharp single peak located at 401.8 eV that fits well with reported binding energies of alkyl ammonium salts.[41] Li 1s overlaps with Fe 3p so it is difficult to assess Li content by XPS.

Mössbauer Spectroscopy

^{57}Fe Mössbauer spectra were measured at 80 K, 25 K, or 4.2 K with zero applied magnetic field, using a constant acceleration spectrometer with a ^{57}Co on Rh source. Samples were encased in Paratone-N oil and placed in a polyethylene sample cup inside a N_2-filled glovebox. Samples were

frozen in liquid N_2 immediately upon removal from the glovebox and kept cold while loading into the spectrometer. Spectra were analyzed using WMOSS software. The sample of reduced, air-exposed **2** was prepared by exposing the reduced **2** Mössbauer sample to dry air (passed over P_2O_5) for 15 minutes.

Infrared Spectroscopy

Infrared spectra were recorded on a Bruker Tensor II FTIR spectrometer with MCT detector operated at 77 K. Data were processed and background corrected with OPUS software (version 7.5). An additional manual correction for scattering was also applied. Samples were prepared under N_2 by grinding solid **1** or **2** with Nujol, placed between two KBr crystal plates, and measured in air under ambient conditions.

Electrochemical Measurements

Electrical conductivity measurements were performed in a two-contact geometry at room temperature under N_2. Samples were prepared as pressed pellets clamped between two brass electrodes (4.8 mm diam.) in a plastic sleeve, allowing measurement of the sample thickness with calipers. Linear sweep voltammetry was conducted using a BASi Epsilon potentiostat/galvanostat, with the reference and counter electrode terminals connected to one electrode and the working electrode terminal to the other. The resulting data were fit to a straight line to obtain the sample resistance. All values have been measured in triplicate on separate batches.

Electrochemical experiments were performed using cyclic voltammetry (CV) or differential pulse voltammetry (DPV) on a BASi Epsilon potentiostat/galvanostat. A glassy carbon working electrode, platinum wire counter electrode, and silver wire pseudoreference electrode were used for all measurements. Due to overlap of the irreversible $[Fe_4S_4]^{2+}$ oxidation with the $FeCp_2^+/FeCp_2$ couple, $CoCp_2$ was used as an internal standard, and the $CoCp_2^+/CoCp_2$ and $CoCp_2/CoCp_2^-$ couples

were referenced to $FeCp_2^+/FeCp_2$ in a separate electrolyte solution under the same conditions. Unless otherwise noted, all scans were performed with a reductive initial scan direction.

A.2 ICP-MS Analysis

Table A.1. Li^+ content (mol% related to TBA^+/TMA^+) in 1 and 2. Reported errors before treatment with $[R_4N][PF_6]$ are the standard deviation of measurements on three batches of each material. Measurements after treatment with $[R_4N][PF_6]$ or $[Li][CF_3SO_3]$ were performed on a single batch of each material.

Li^+ mol% to TBA^+/TMA^+	Compound **1**	Compound **2**
As-synthesized	1.4(7)%	7(3)%
After treatment with $[R_4N][PF_6]$	0.59%	2.84%
After treatment with $[Li][CF_3SO_3]$	2.0%	6.2%

A.3 NMR Spectra

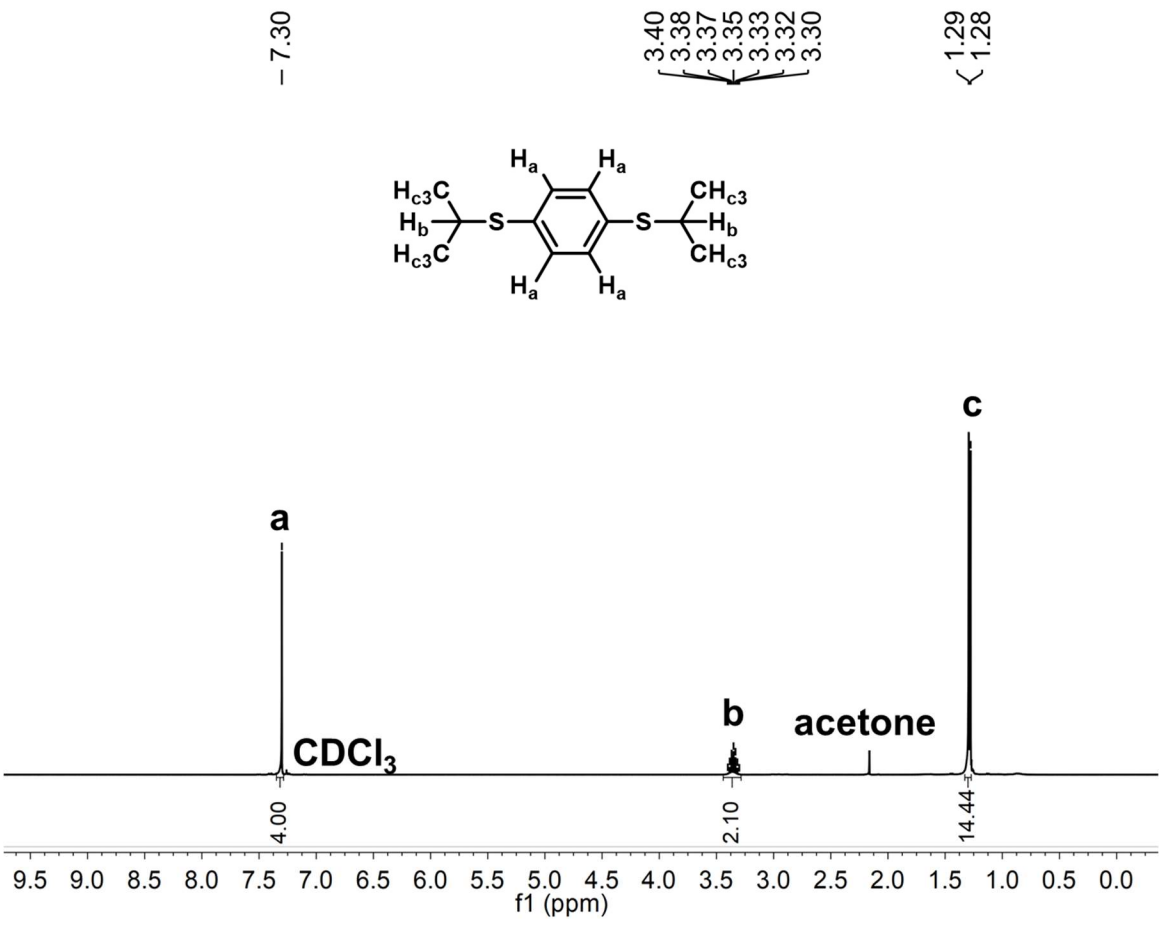

Figure A.1. ^1H NMR spectrum of 1,4-Bis(isopropylthio)benzene in $CDCl_3$.

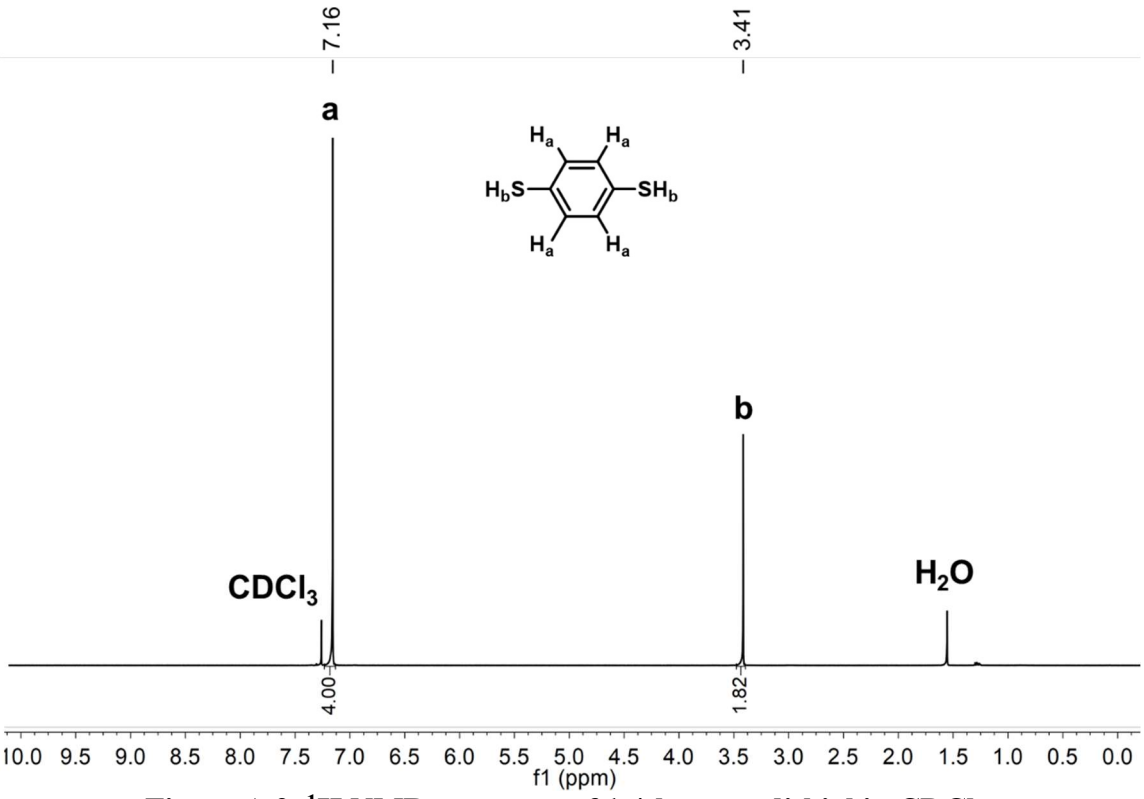

Figure A.2. ^{1}H NMR spectrum of 1,4-benzenedithiol in $CDCl_3$.

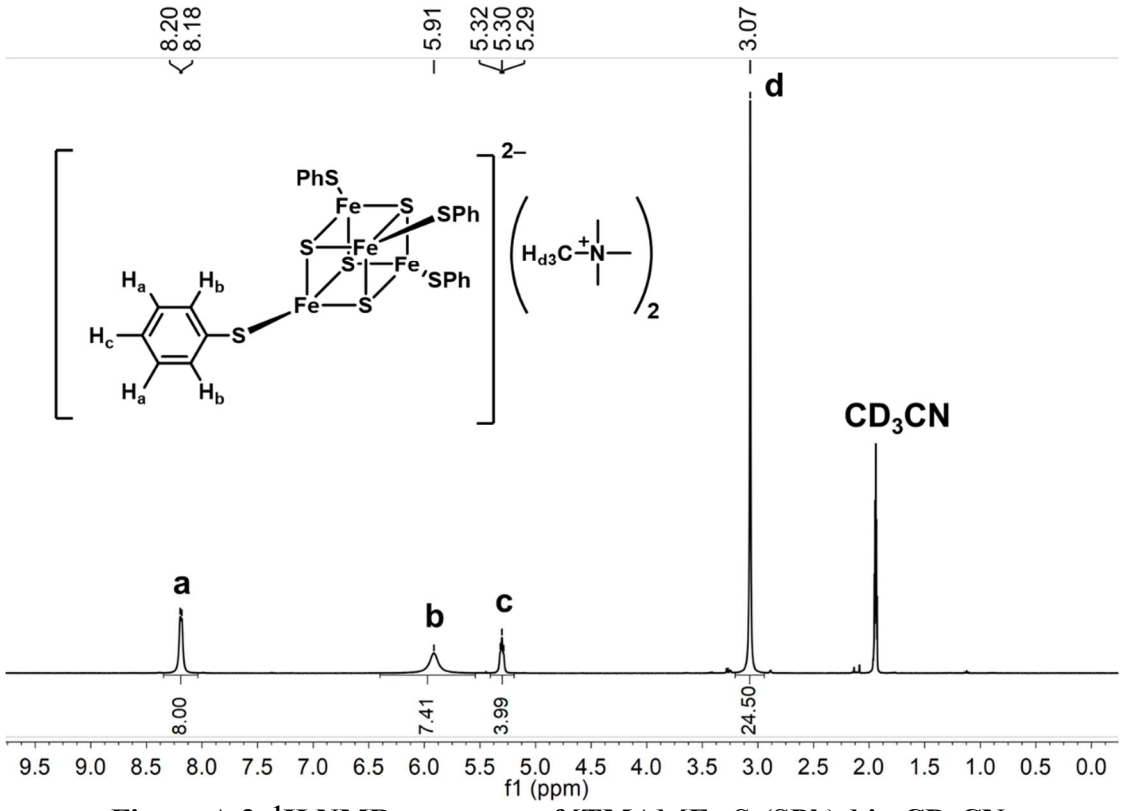

Figure A.3. ^{1}H NMR spectrum of $[TMA]_2[Fe_4S_4(SPh)_4]$ in CD_3CN.

A.4 Digestion Experiments

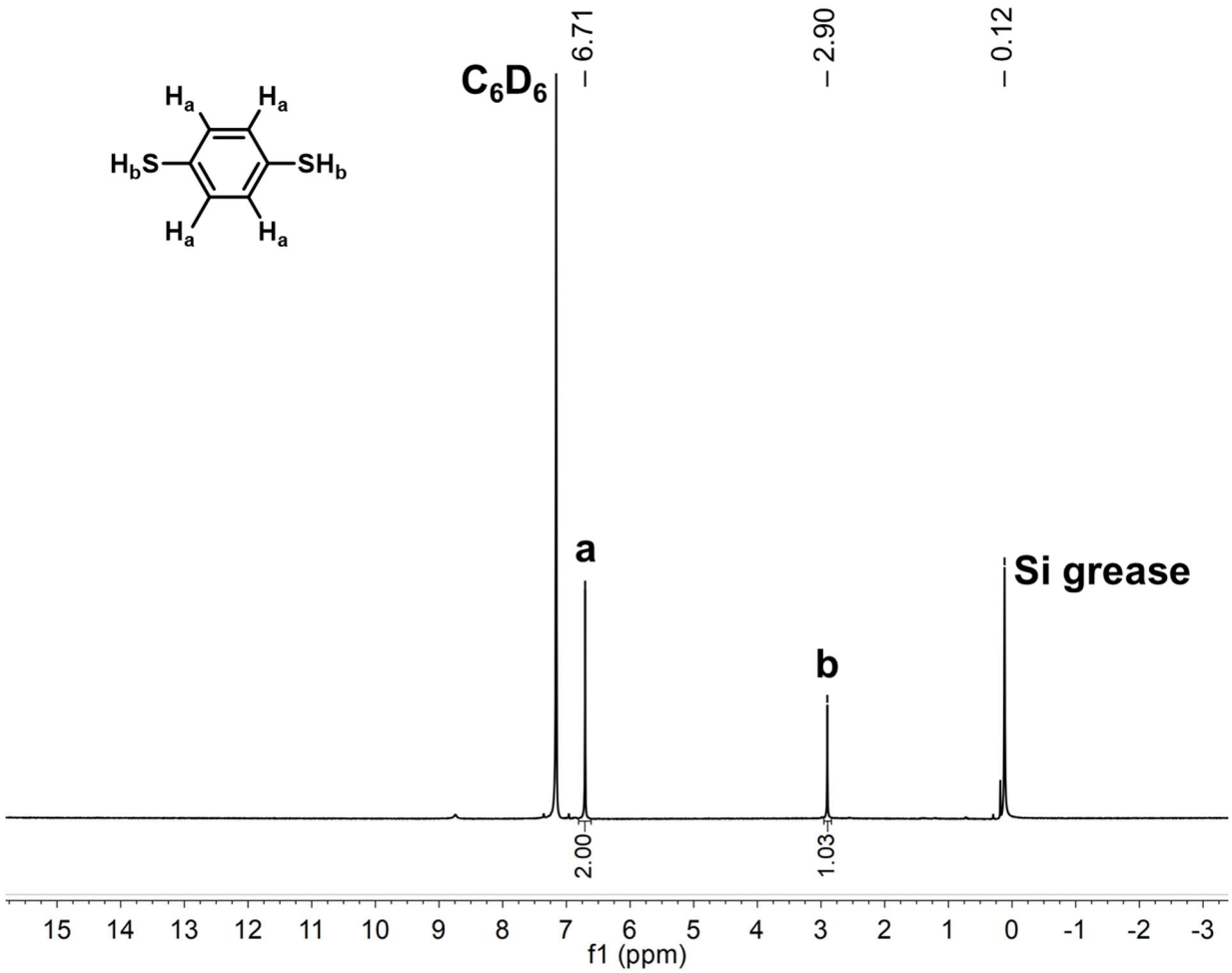

Figure A.4. ^{1}H NMR spectrum of C_6D_6 extract of 1 HCl digest.

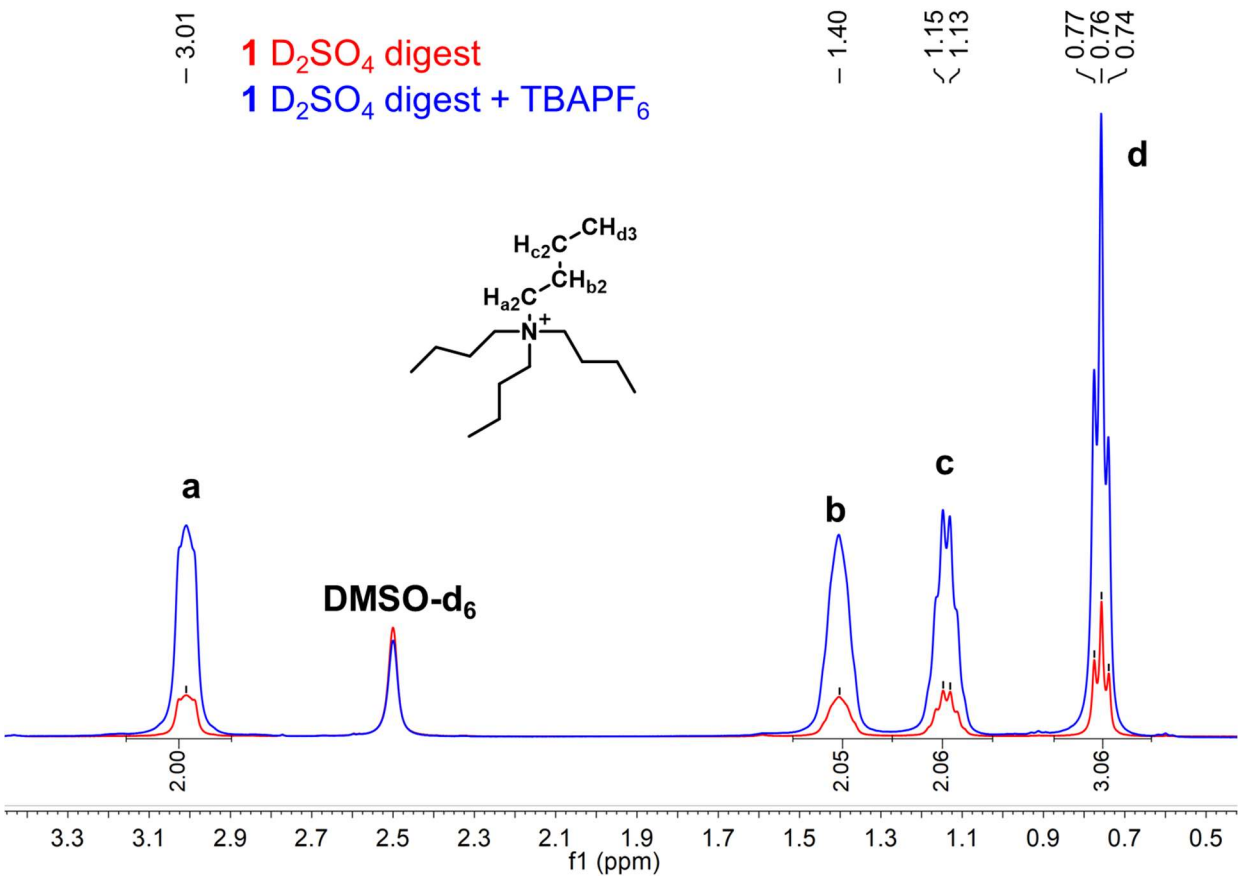

Figure A.5. ^{1}H NMR spectrum of 1 D_2SO_4 digest in $(CD_3)_2SO$. A singlet at 12.8 ppm (not shown) is attributed to H_2O+D_2SO_4.

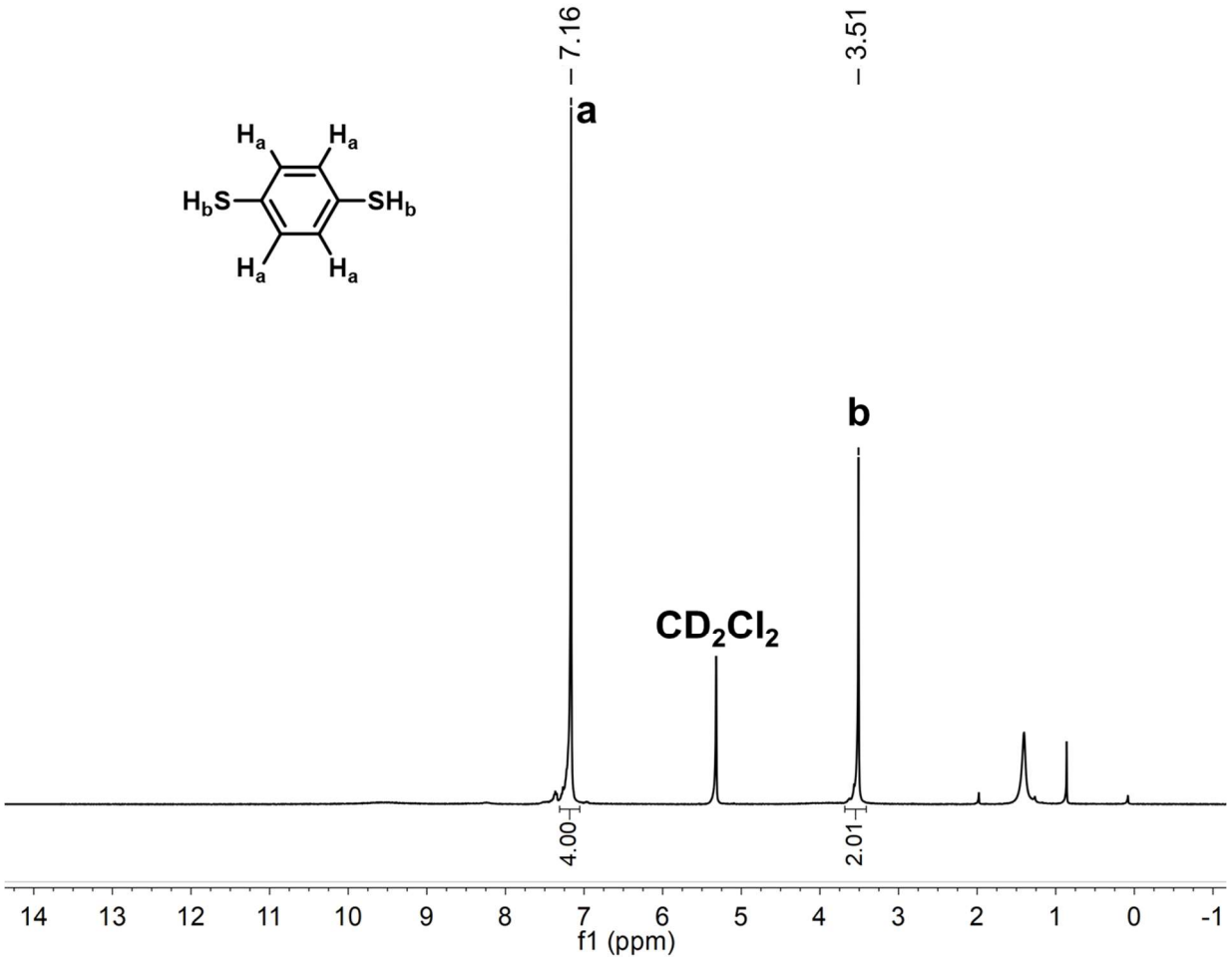

Figure A.6. ^{1}H NMR spectrum of CD_2Cl_2 extract of 2 HCl digest.

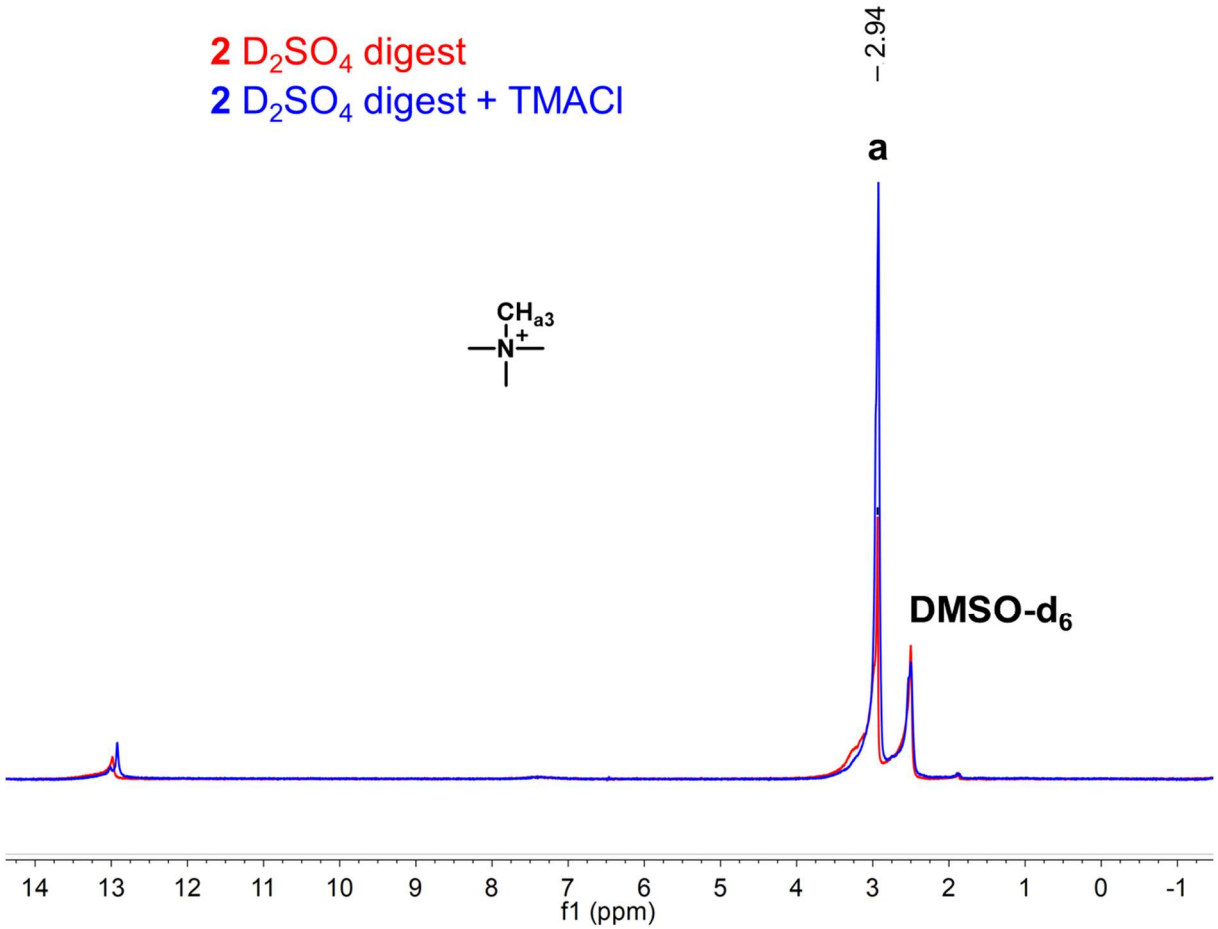

Figure A.7. ^{1}H NMR spectrum of 2 D_2SO_4 digest in $(CD_3)_2SO$.

A.5 X-ray Powder Diffraction

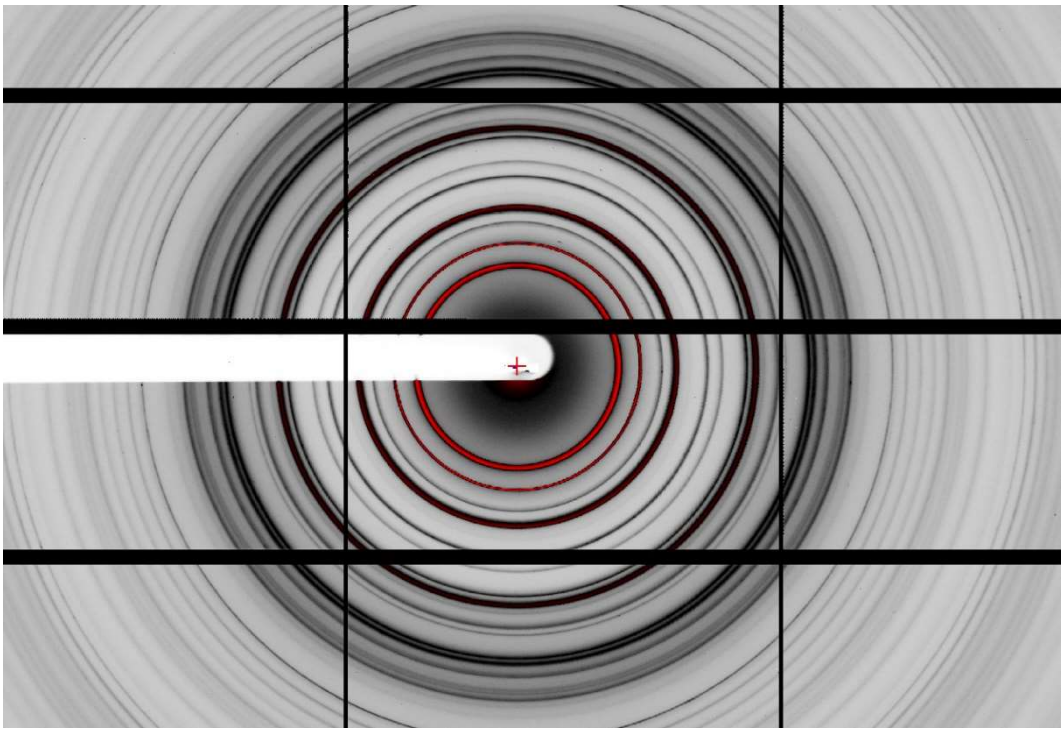

Figure A.8. X-ray powder diffraction data for 1 recorded at the PROXIMA 2A beamline.

Table A.2 Structural parameters and refinement results for 1 based on 1D (11-BM/APS) and 2D (PROXIMA 2A/SOLEIL) synchrotron X-ray powder diffraction data.

Compound # 1 : TBA	11-BM / APS	PROXIMA 2A / SOLEIL
Chemical formula	$C_{44}H_{80}Fe_4N_2S_8$ $Fe_4S_4(C_6H_4S_2)_2 \cdot 2N(C_4H_9)_4$	$C_{44}H_{80}Fe_4N_2S_8$ $Fe_4S_4(C_6H_4S_2)_2 \cdot 2N(C_4H_9)_4$
Crystal system	Tetragonal	Tetragonal
Space group (#)	P 4_2 c m (# 101)	P 4_2 c m (# 101)
Unit cell (Refinement)		
a (Å)	11.9266(3)	12.0246(31)
b (Å)	11.9266(3)	12.0246(31)
c (Å)	19.8484(5)	19.8533(36)
α (°)	90.0	90.0
β (°)	90.0	90.0
γ (°)	90.0	90.0
V (Å^3)	2823.32(12)	2870.6(12)
Z	2	2
Mol. wt. (g/mol)	1117.037	1117.037
ρ (g/cm^3)	1.314	1.292
Wavelength (Å)	0.4127	0.7293
2θ range (°)	1.600-24.600	2.400-19.925
Indexing (Figures of merit)		
N-TREOR / EXPO2014	M(15) = 32 F(15) = 220(0.0021,32)	M(20) = 12 F(20) = 45.0(0.0091,49)
DICVOL14 / PreDICT	M(17) = 39.6 F(17) = 282.5(0.0019,32)	M(18) = 21.7 F(18) = 75.9(0.0048,49)
(GSAS) Rietveld refinement		
Observed reflections	960	109
Variables	37	29
Restraints	95	0
Rp (%)	0.0943	0.0912
Rwp (%)	0.1341	0.1218
R (F^2)	0.2622	0.1539
Reduced χ^2	7.768	30.89
Refinable	0.1001	0.1616
Uoverall_isotropic		
Preferred Orientation		
Spherical harmonics order	10	10

Texture Index	1.102	1.108

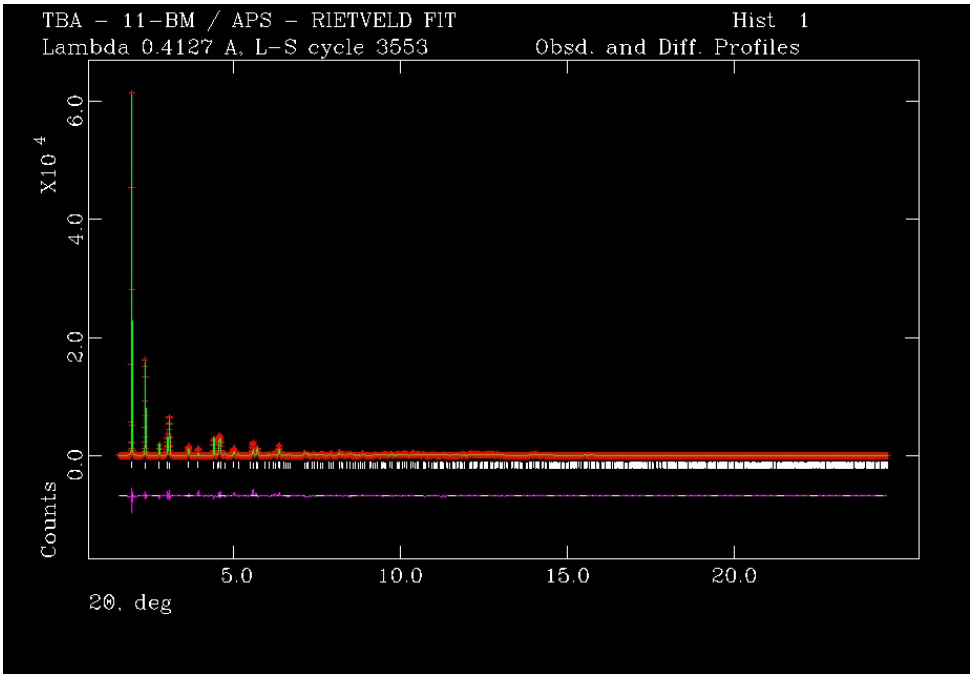

Figure A.9. The Rietveld plot for the refinement of the structure of 1. The red crosses represent the observed data points, and the green line is the calculated pattern. The magenta curve is the difference pattern, plotted at the same vertical scale as the other patterns. Full 2θ scale.

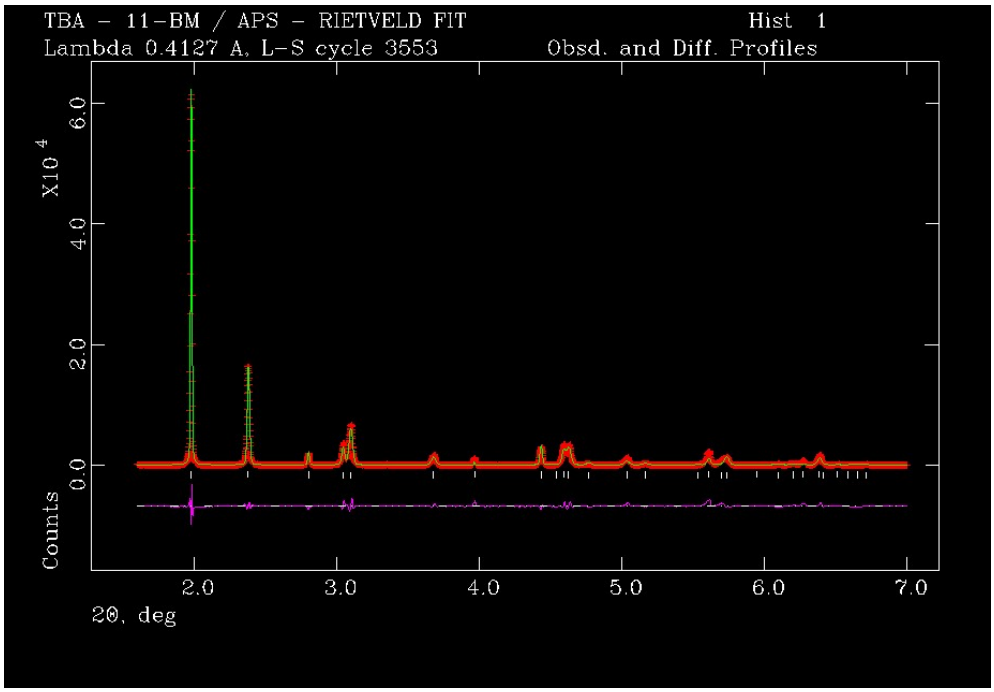

Figure A.10. The Rietveld plot for the refinement of the structure of 1. The red crosses represent the observed data points, and the green line is the calculated pattern. The magenta curve is the difference pattern, plotted at the same vertical scale as the other patterns. 2θ scale from 0.5 to 7°.

Table A.3 Structural parameters and refinement results for 2 based on 1D (11-BM/APS) synchrotron X-ray powder diffraction data

Compound # 2 : TMA	11-BM / APS
Chemical formula	$C_{20}H_{32}Fe_4N_2S_8$ $Fe_4S_4(C_6H_4S_2)_2,2N(CH_3)_4$
Crystal system	Tetragonal
Space group (#)	I 4_1/a (# 88 :2)
Unit cell (Refinement)	
a (Å)	17.1853(2)
b (Å)	17.1853(2)
c (Å)	20.4819(4)
α (°)	90.0
β (°)	90.0
γ (°)	90.0
V (Å^3)	6049.00(17)
Z	8
Mol. wt. (g/mol)	780.39
ρ (g/cm^3)	1.7136
Wavelength (Å)	0.4127
2θ range (°)	1.600-12.600
Indexing (Figures of merit)	
N-TREOR / EXPO2014	M(20) = 77 F(20) = 611(0.0010, 33)
DICVOL14 / PreDICT	M(20) = 109.2 F(20) = 959.3(0.0002,84)
(GSAS) Rietveld refinement	
Observed reflections	310
Variables	13
Restraints	55
Rp (%)	0.0587
Rwp (%)	0.0768
R (F^2)	0.0437
Reduced χ^2	4.055
Refinable Uoverall_isotropic	0.0636
Preferred Orientation	
Spherical harmonics order	10
Texture Index	1.028

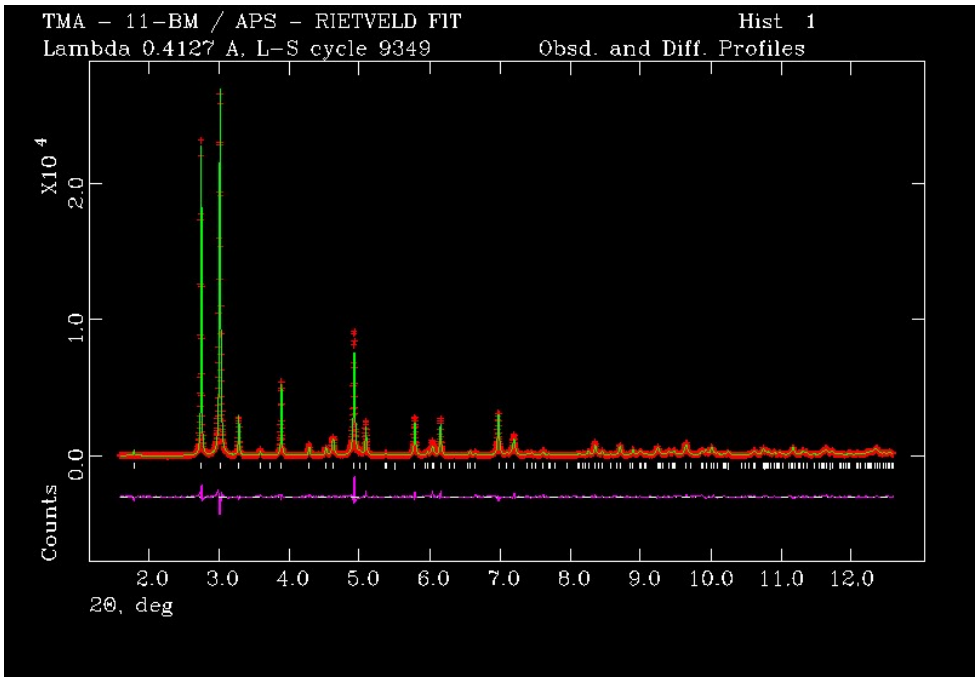

Figure A.11. The Rietveld plot for the refinement of the structure of 2. The red crosses represent the observed data points, and the green line is the calculated pattern. The magenta curve is the difference pattern, plotted at the same vertical scale as the other patterns. Full 2θ scale.

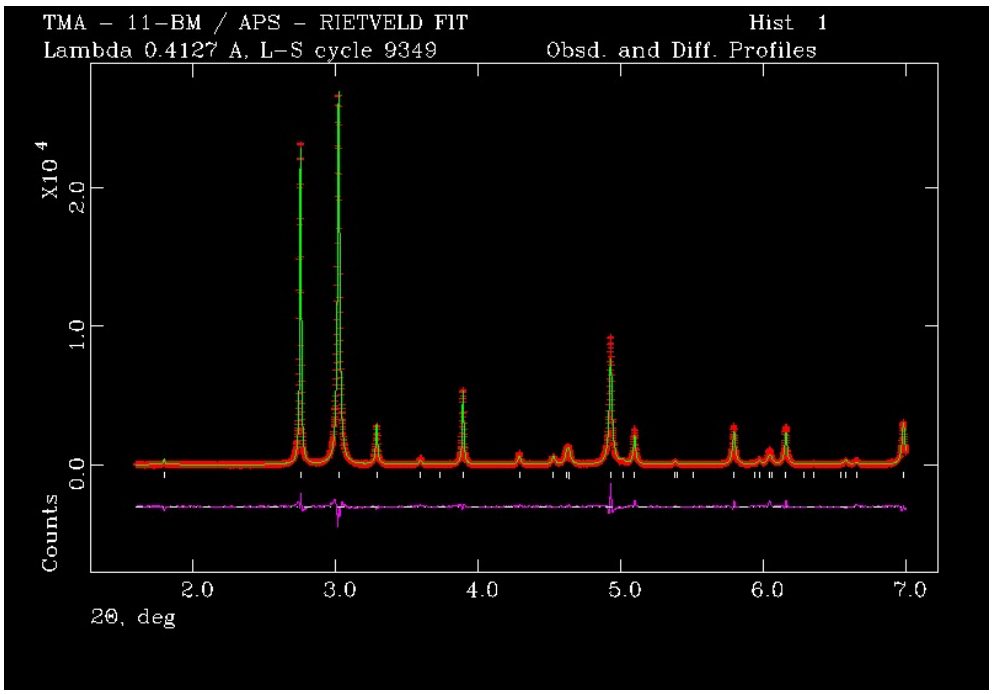

Figure A.12. The Rietveld plot for the refinement of the structure of 2. The red crosses represent the observed data points, and the green line is the calculated pattern. The magenta curve is the difference pattern, plotted at the same vertical scale as the other patterns. 2θ scale from 0.5 to 7°.

Table A.4 Atomic coordinates of 1.

Name	X	Y	Z
Fe1	0.582000	0.418000	0.472900
Fe2	0.582000	0.418000	0.071400
S1	0.606500	0.606500	0.457600
S2	0.607200	0.392790	0.586600
S3	0.707500	0.292500	0.431400
S4	0.707500	0.292500	0.112900
C1	0.707500	0.292500	0.341700
C2	0.636600	0.363400	0.306900
C3	0.636600	0.363400	0.237400
C4	0.707500	0.292500	0.202600
C5	0.778400	0.221600	0.237400
C6	0.778400	0.221600	0.306900
C7	0.053900	0.589820	0.577320
C8	-0.006700	0.641280	0.636180
C9	0.076800	0.645200	0.694080
C10	0.056300	0.742800	0.739710
C11	0.093890	0.458560	0.488700
C12	0.122420	0.338860	0.474050
C13	0.073490	0.301850	0.407440
C14	0.000140	0.200650	0.413680
N1	0.000000	0.500000	0.534840
Ha1	0.583600	0.416390	0.332890
Ha2	0.583600	0.416390	0.211400
Ha3	0.831390	0.168600	0.211400
Ha4	0.831390	0.168600	0.332890
Hb1	0.129200	0.552300	0.599000
Hb2	0.085100	0.654800	0.544930
Hb3	-0.075700	0.589800	0.650350
Hb4	-0.033100	0.724000	0.624200
Hb5	0.159000	0.652800	0.672400
Hb6	0.073000	0.568700	0.721800
Hb7	0.041100	0.816700	0.710500
Hb8	0.128100	0.756000	0.771100
Hb9	-0.015100	0.726400	0.770900
Hb10	0.078300	0.498000	0.440240
Hb11	0.170010	0.497800	0.507300
Hb12	0.096500	0.283500	0.513150
Hb13	0.212370	0.331900	0.469900
Hb14	0.141500	0.283800	0.373740
Hb15	0.026100	0.370300	0.386960
Hb16	0.014000	0.161000	0.461500
Hb17	0.020000	0.142000	0.375000

Hb18	-0.086100	0.223900	0.409000

Table A.5 Atomic coordinates of 2.

Name	X	Y	Z
Fe1	0.050231	0.188201	0.577047
Fe2	0.014770	0.171649	0.172788
S3	-0.081746	0.184388	0.562973
S4	0.121090	0.095576	0.524544
S5	0.031707	0.057885	0.226946
C6	0.096101	0.085952	0.440096
C7	0.107309	0.147543	0.397704
C8	0.087720	0.138894	0.332953
C9	0.057150	0.069189	0.311036
C10	0.045912	0.007759	0.353464
C11	0.065458	0.016348	0.418093
H12	0.130194	0.199231	0.414581
H13	0.095749	0.184202	0.300565
H14	0.023035	-0.043960	0.336487
H15	0.057465	-0.028985	0.450512
S16	0.020132	0.147691	0.062651
N1t	0.828842	0.963782	0.093534
C2t	0.853503	0.911453	0.149861
C3t	0.772498	1.025367	0.118499
C4t	0.900301	1.003370	0.064722
C5t	0.789071	0.915047	0.041160
H6t	0.801490	0.883602	0.170001
H7t	0.882025	0.947386	0.186937
H8t	0.893918	0.867616	0.131060
H9t	0.802202	1.060205	0.155658
H10t	0.721878	0.995946	0.139546
H11t	0.754849	1.061935	0.077320
H12t	0.928545	1.037362	0.103211
H13t	0.881413	1.041404	0.024887
H14t	0.939684	0.958375	0.046311
H15t	0.736049	0.889903	0.061944
H16t	0.829131	0.869002	0.025867
H17t	0.774864	0.952947	-0.000110

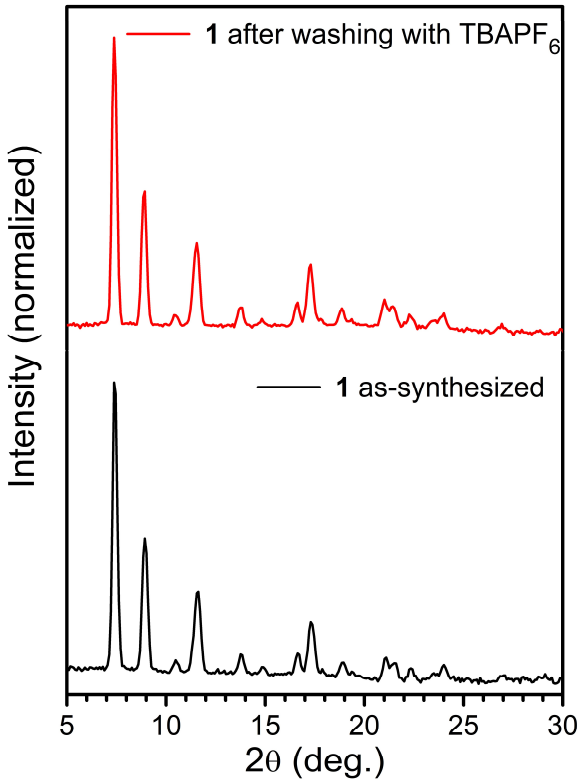

Figure A.13. XRPD patterns of 1 before and after treatment with [TBA][PF_6].

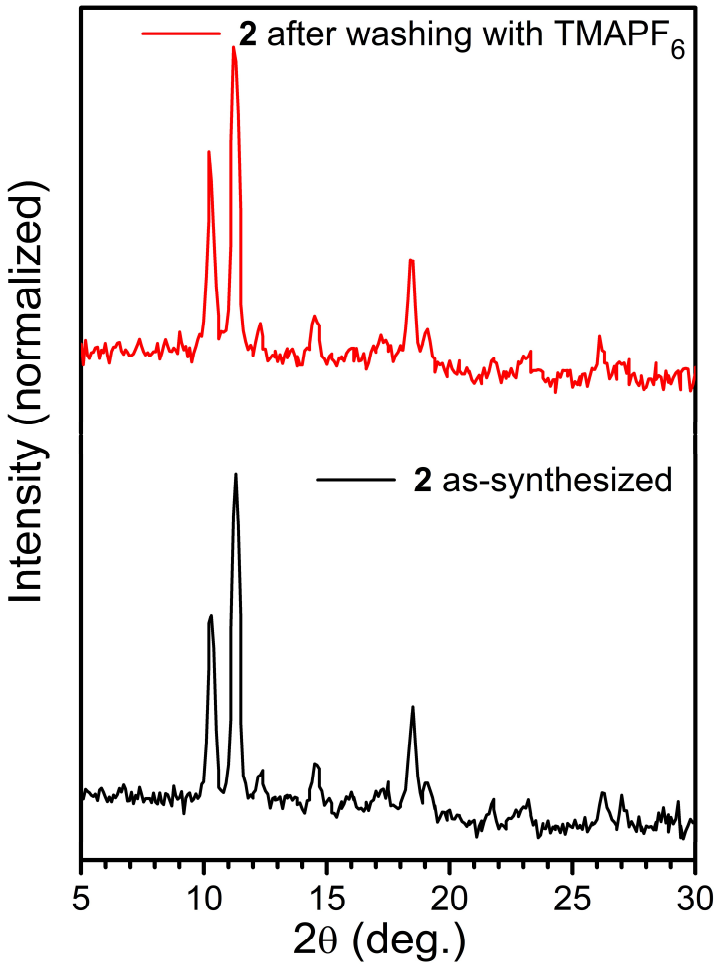

Figure A.14. XRPD patterns of 2 before and after treatment with [TMA][PF_6].

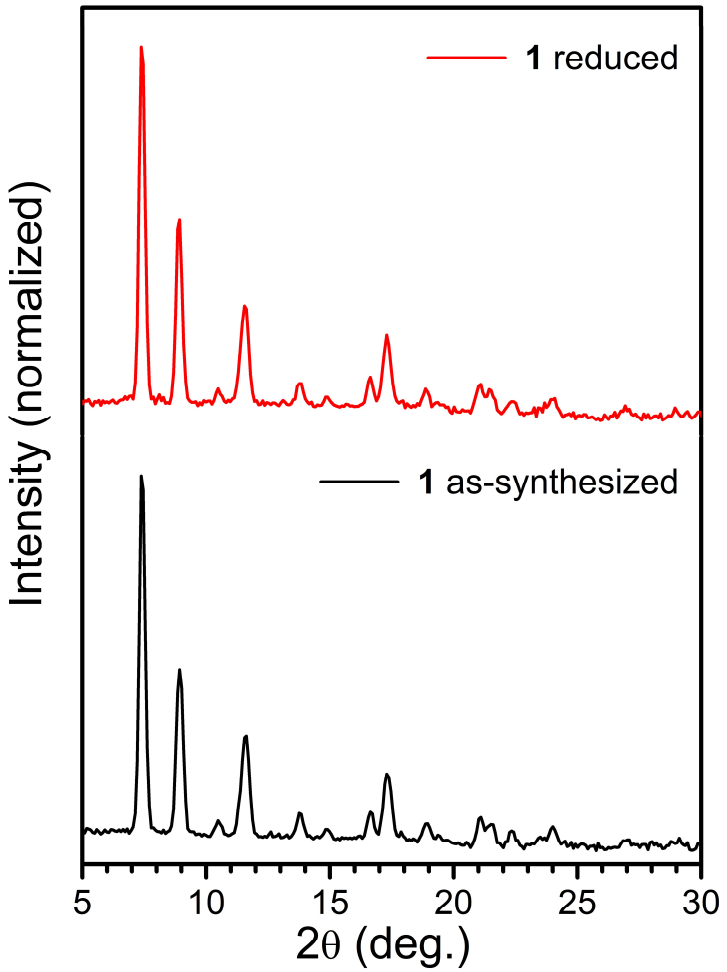

Figure A.15. XRPD patterns of 1 before and after chemical reduction.

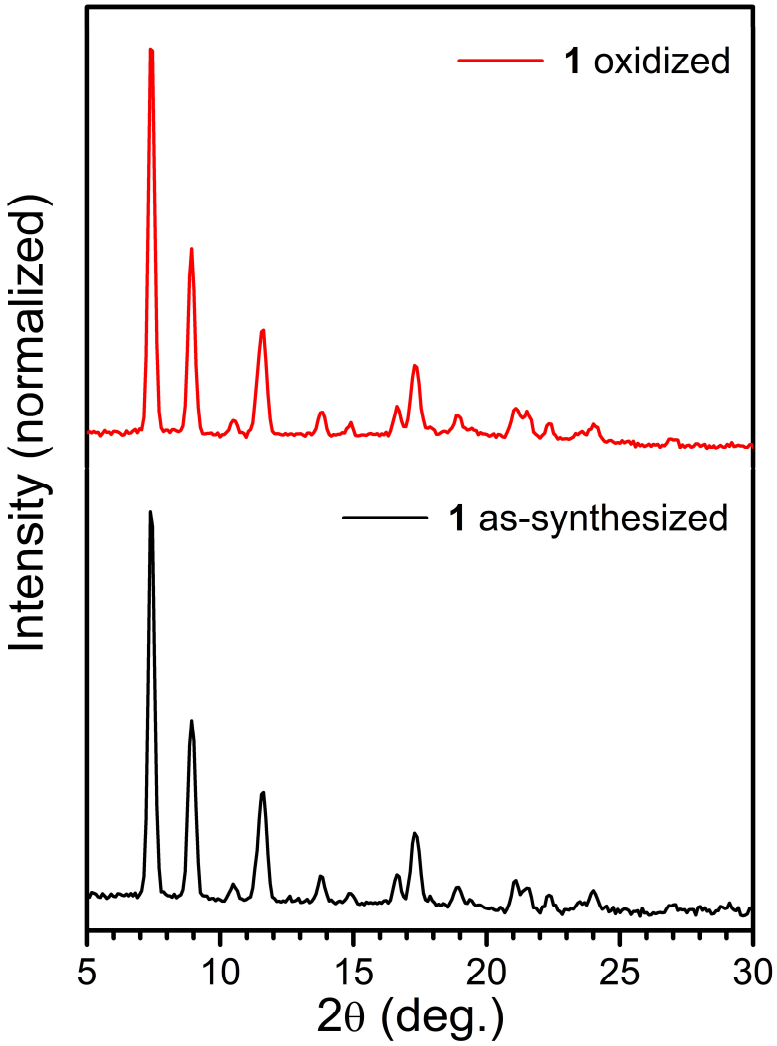

Figure A.16. XRPD patterns of 1 before and after chemical oxidation.

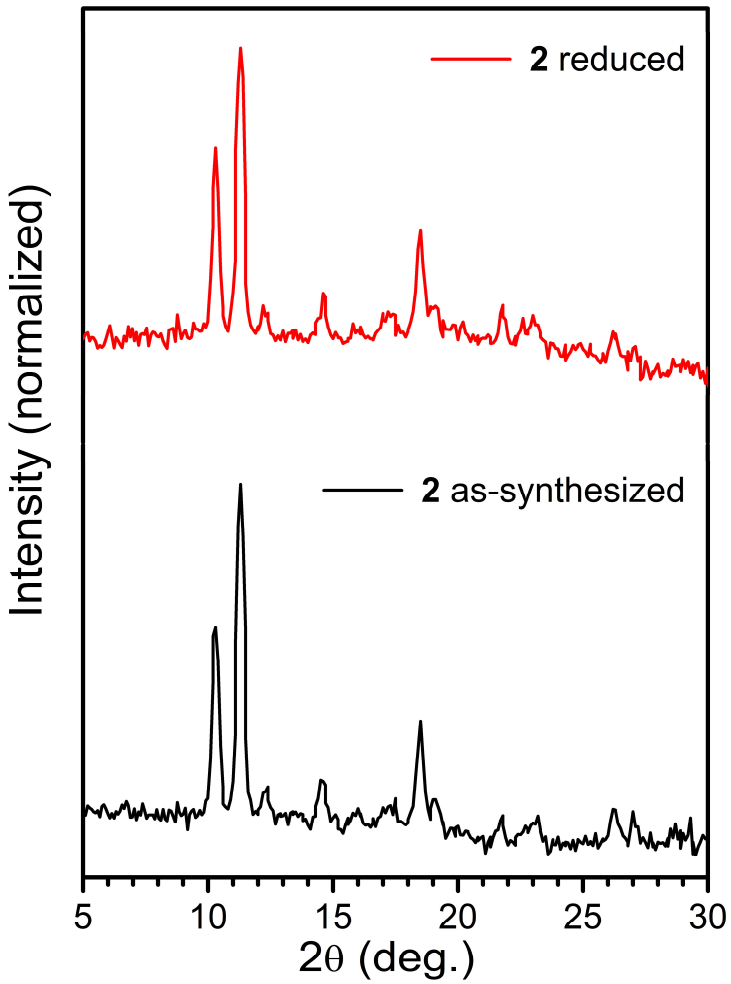

Figure A.17. XRPD patterns of 2 before and after chemical reduction.

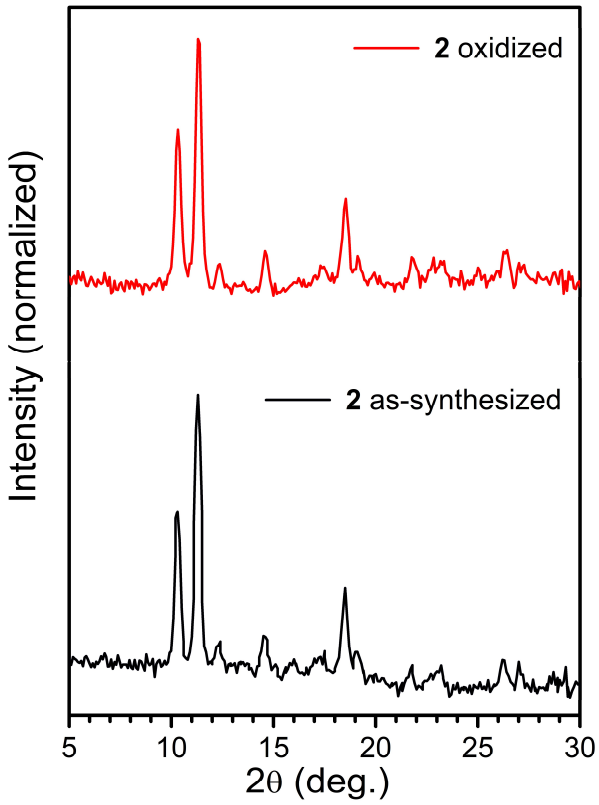

Figure A.18. XRPD patterns of 2 before and after chemical oxidation.

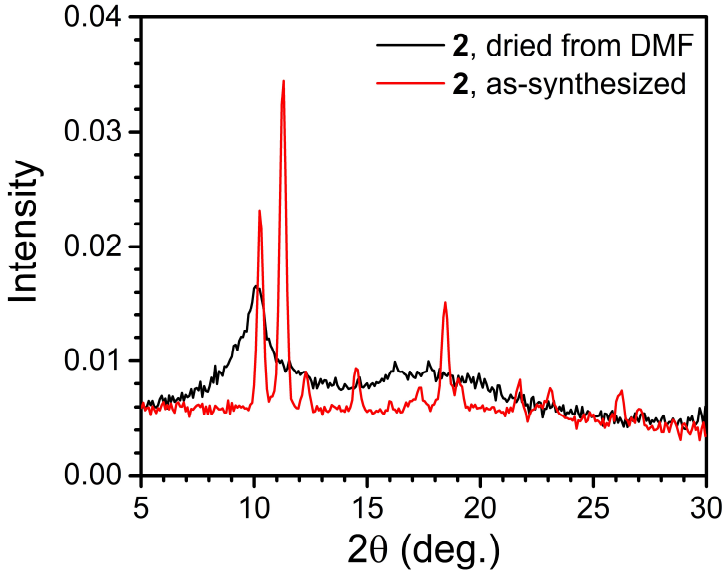

Figure A.19. XRPD pattern of solid material obtained by evaporation of a DMF solution of 2 under vacuum, compared to pattern of as-synthesized 2.

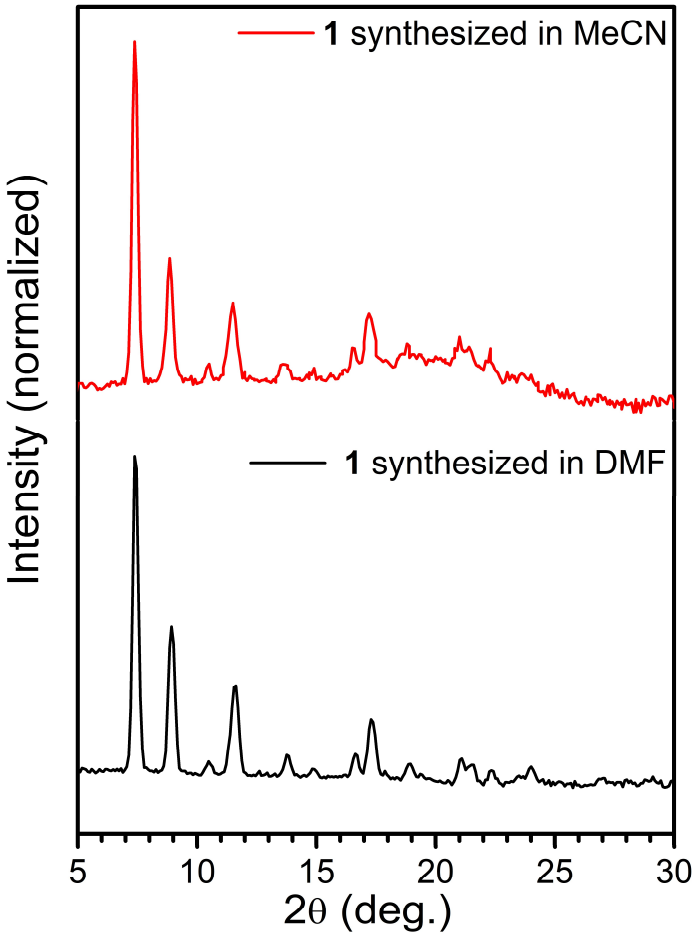

Figure A.20. XRPD patterns of 1 synthesized in MeCN with 40 equivalents [Li][CF_3SO_3] and in DMF with 5 equivalents [Li][CF_3SO_3].

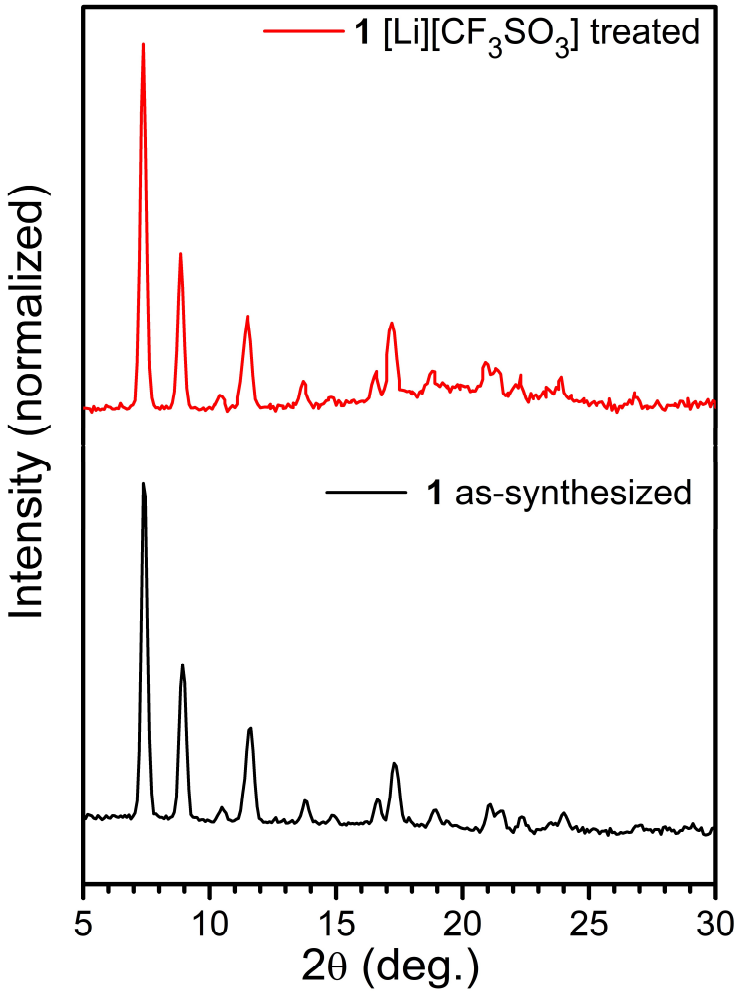

Figure A.21. XRPD patterns of 1 before and after soaking in [Li][CF_3SO_3] solution in THF.

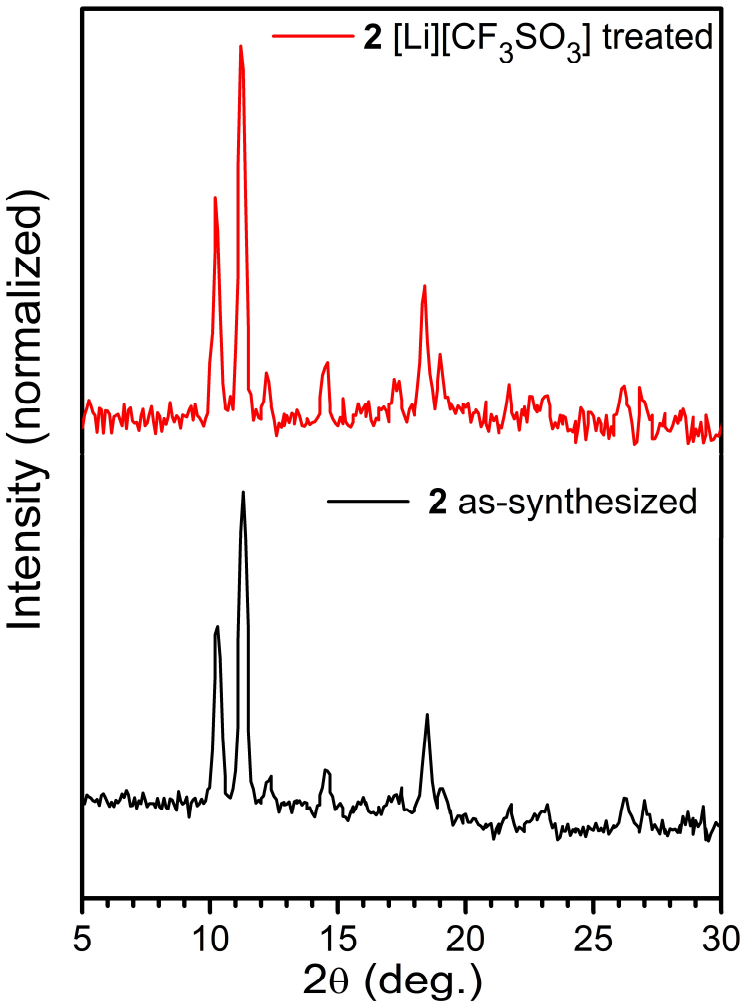

Figure A.22. XRPD patterns of 2 before and after soaking in [Li][CF_3SO_3] solution in THF.

A.6 Small Angle X-ray Scattering

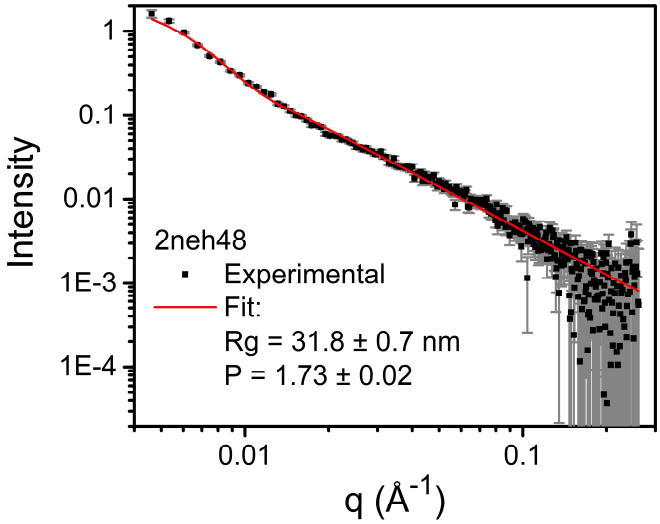

Figure A.23. SAXS data from a DMF solution of 2, fitted using Beaucage's unified exponential/power law model.

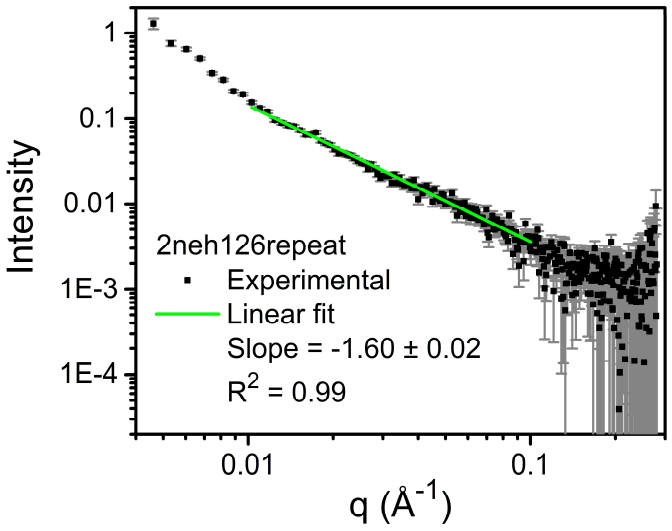

Figure A.24. SAXS data from a DMF solution of 2 after reduction with [Na][$C_{12}H_8$], with linear fit.

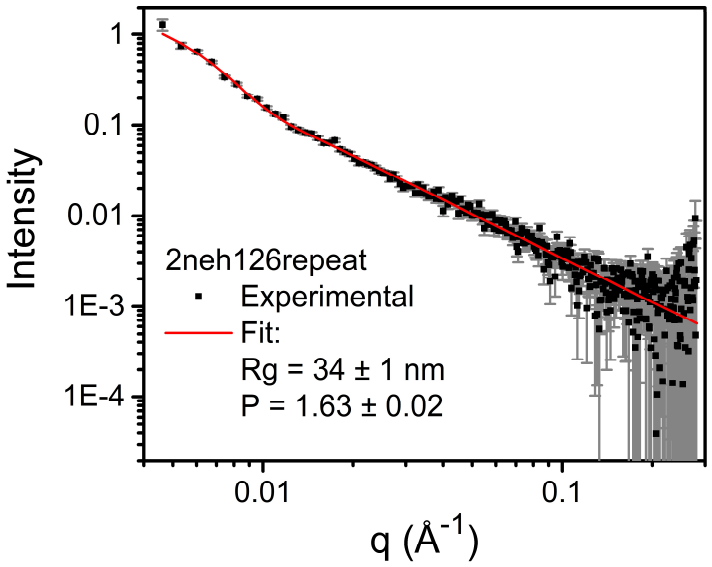

Figure A.25. SAXS data from a DMF solution of 2 after reduction with [Na][$C_{12}H_8$], fitted using Beaucage's unified exponential/power law model.

A.7 Optical Spectroscopy

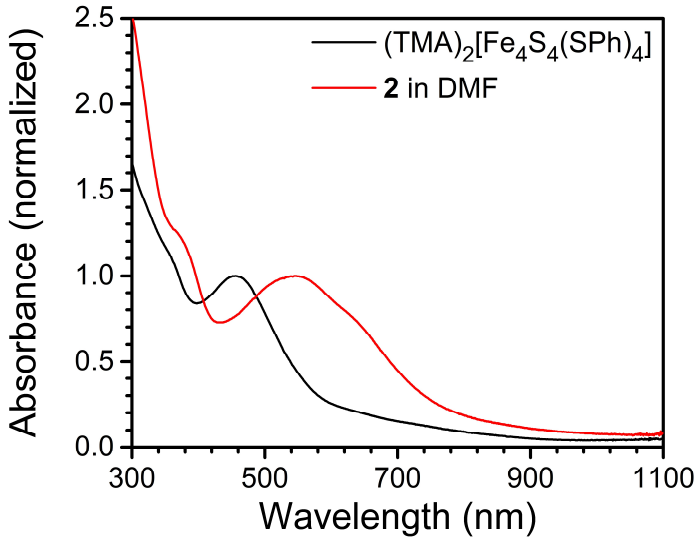

Figure A.26. UV-visible absorption spectra of DMF solutions of [TMA]$_2$[Fe_4S_4(SPh)$_4$] and 2.

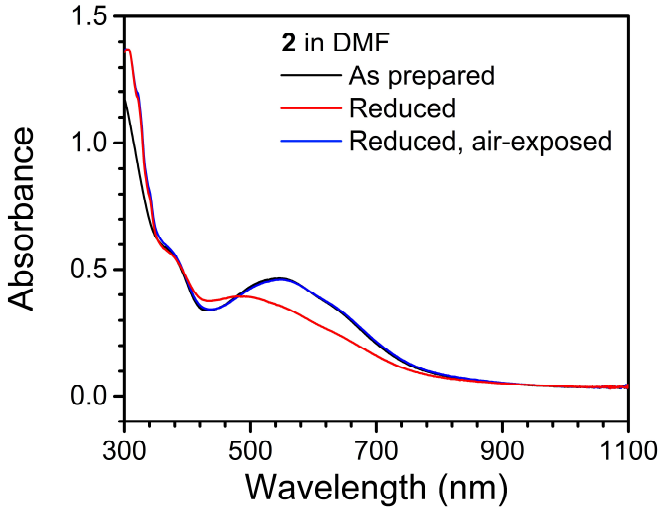

Figure A.27. UV-visible absorption spectra of DMF solutions of 2 following reduction by [Na][$C_{12}H_8$] and brief air exposure.

A.8 X-ray Photoelectron Spectroscopy

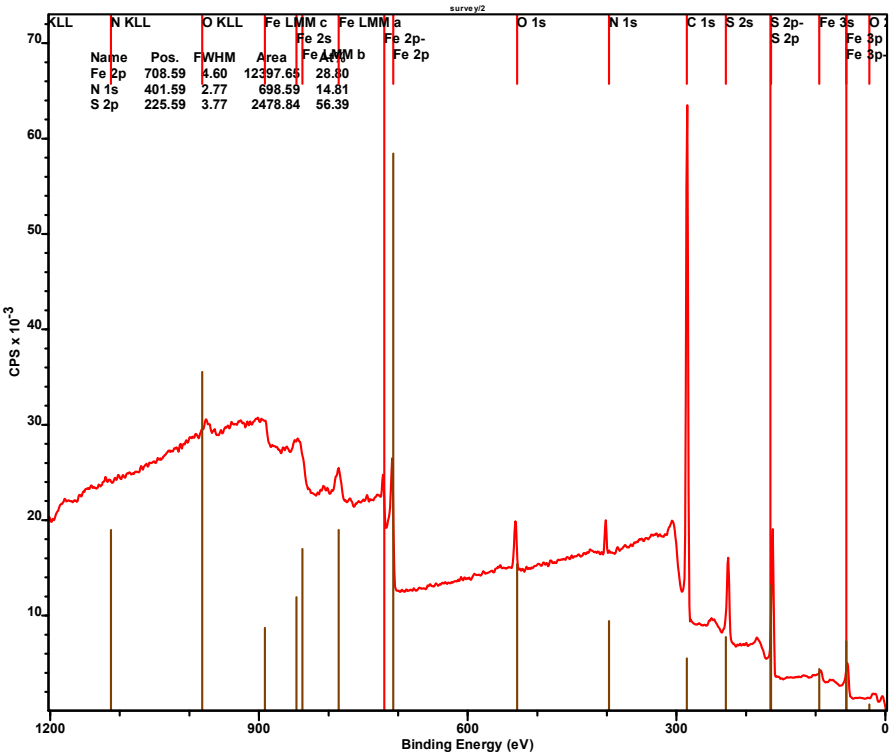

Figure A.28. XPS survey spectrum of 1.

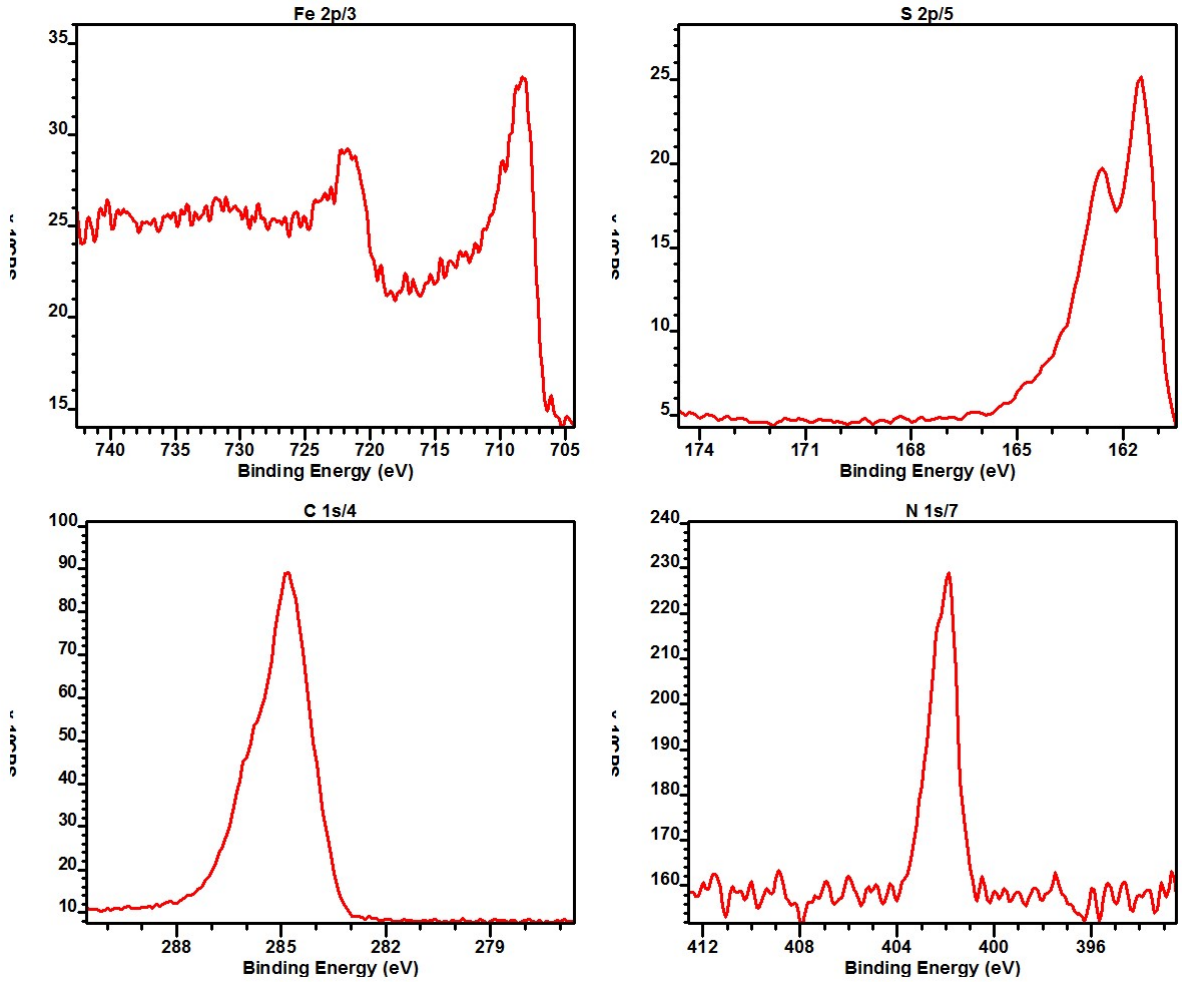

Figure A.29. High-resolution XPS data for 1.

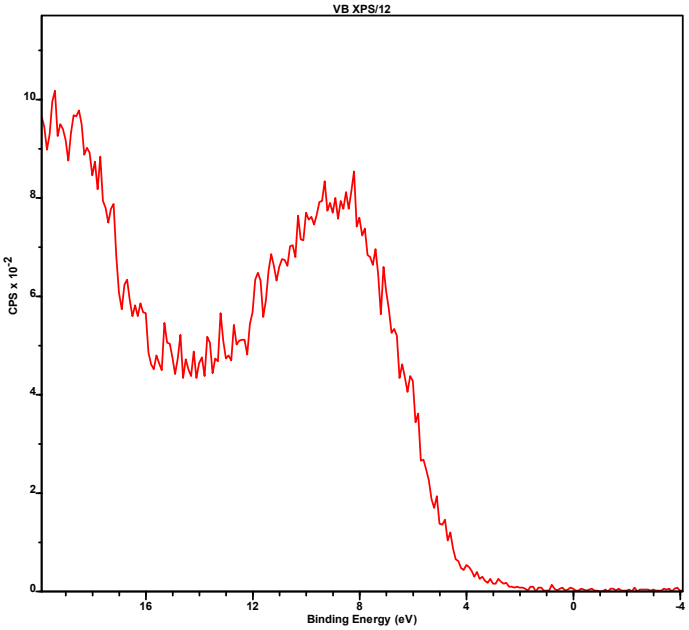

Figure A.30. XPS data from 1 in the valence band region.

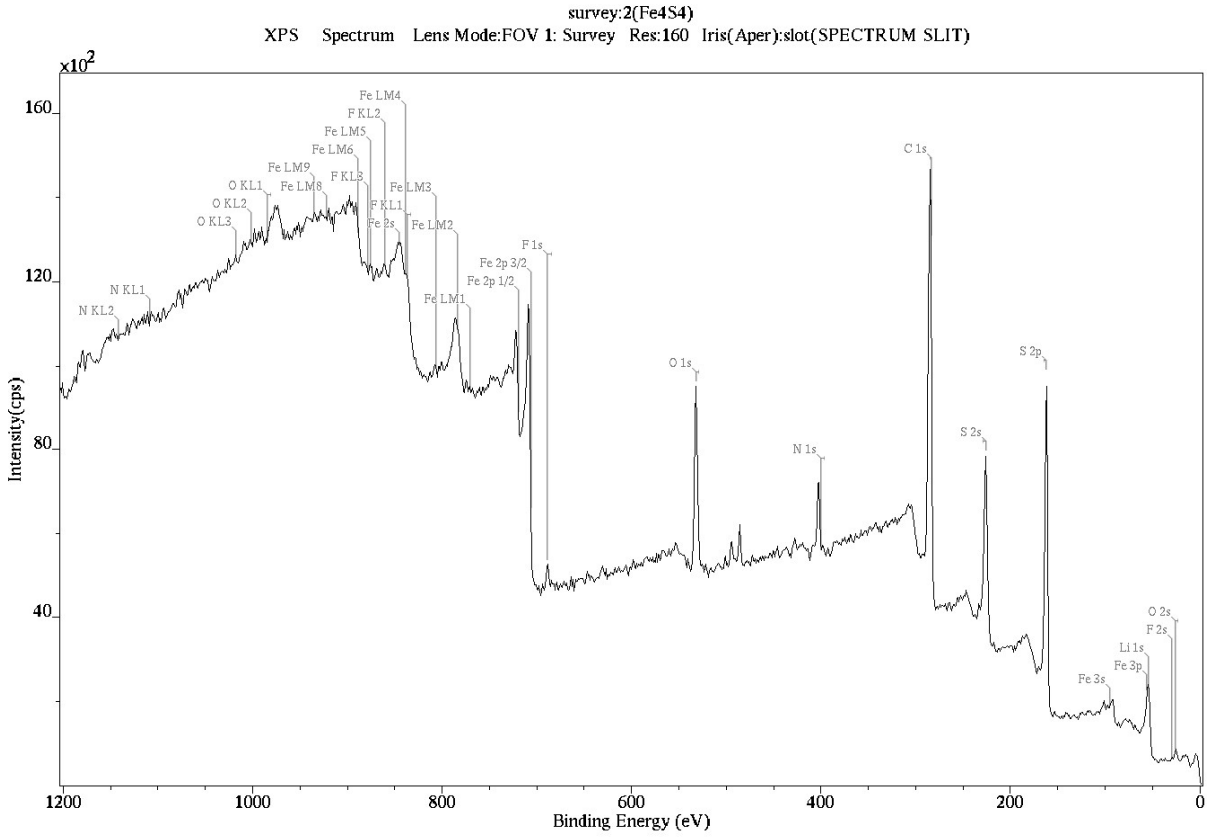

Figure A.31. XPS survey spectrum for 2.

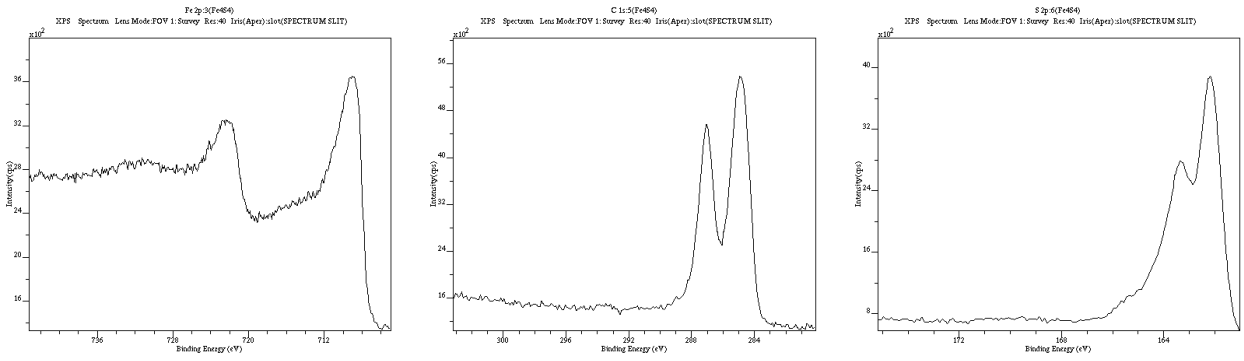

Figure A.32. High-resolution XPS data for 2 (L-R: Fe 2p, C 1s, S 2p).

A.9 Mössbauer Spectroscopy

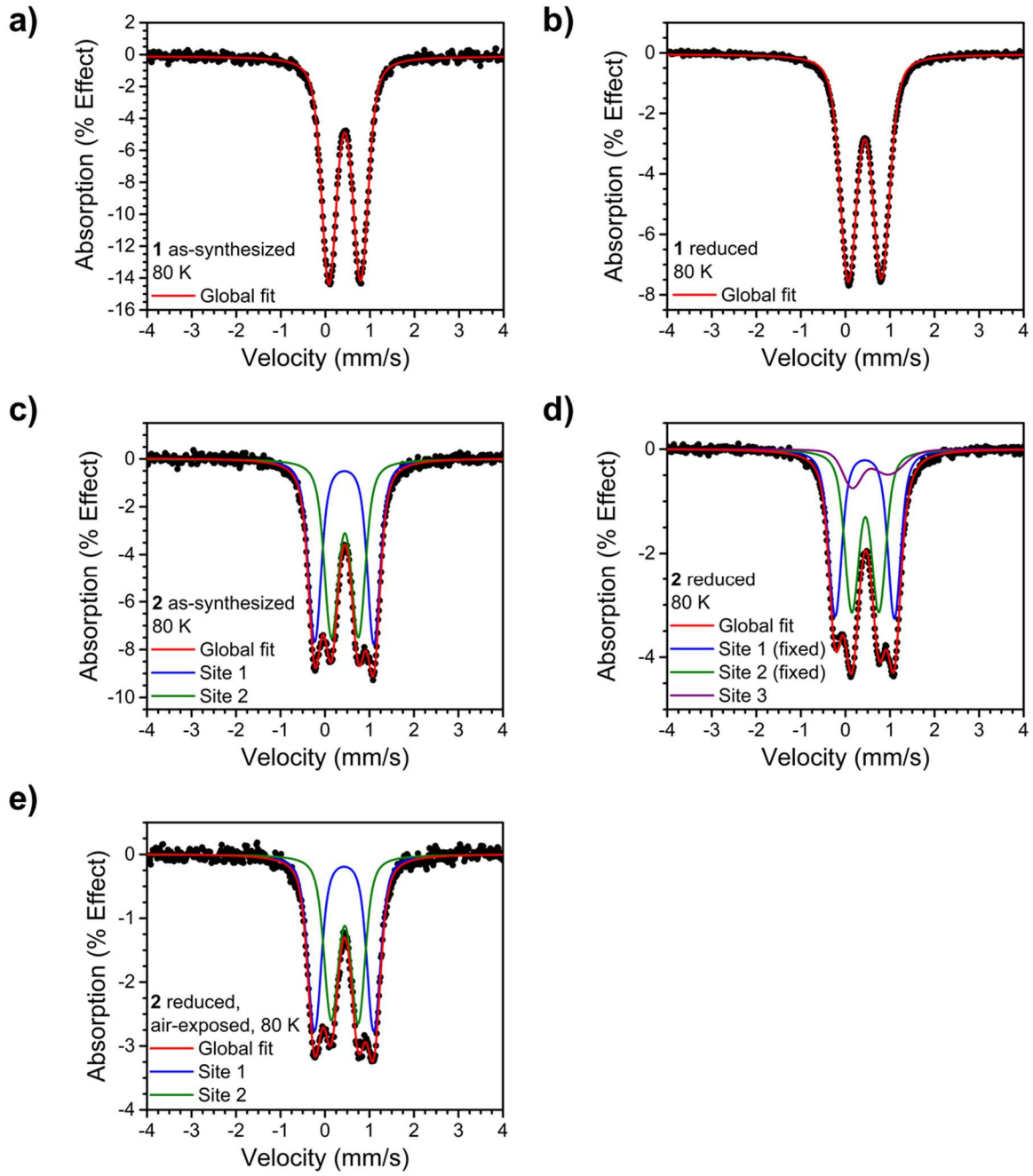

Figure A.33. 57Fe Mössbauer spectra at 80 K and fits: (a) 1 as-synthesized; (b) 1 following chemical reduction; (c) 2 as-synthesized; (d) 2 following chemical reduction; (e) 2 following chemical reduction and air exposure.

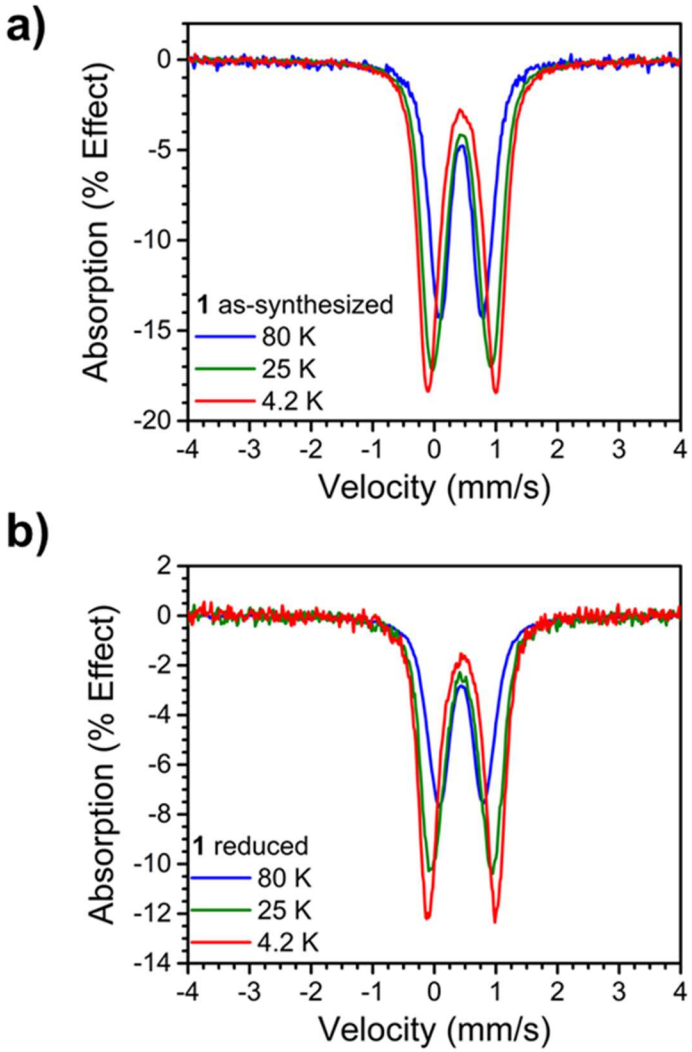

Figure A.34. ^{57}Fe Mössbauer spectra of 1 overlaid at 80 K, 25 K, and 4.2 K: (a) 1 as-synthesized; (b) 1 following chemical reduction.

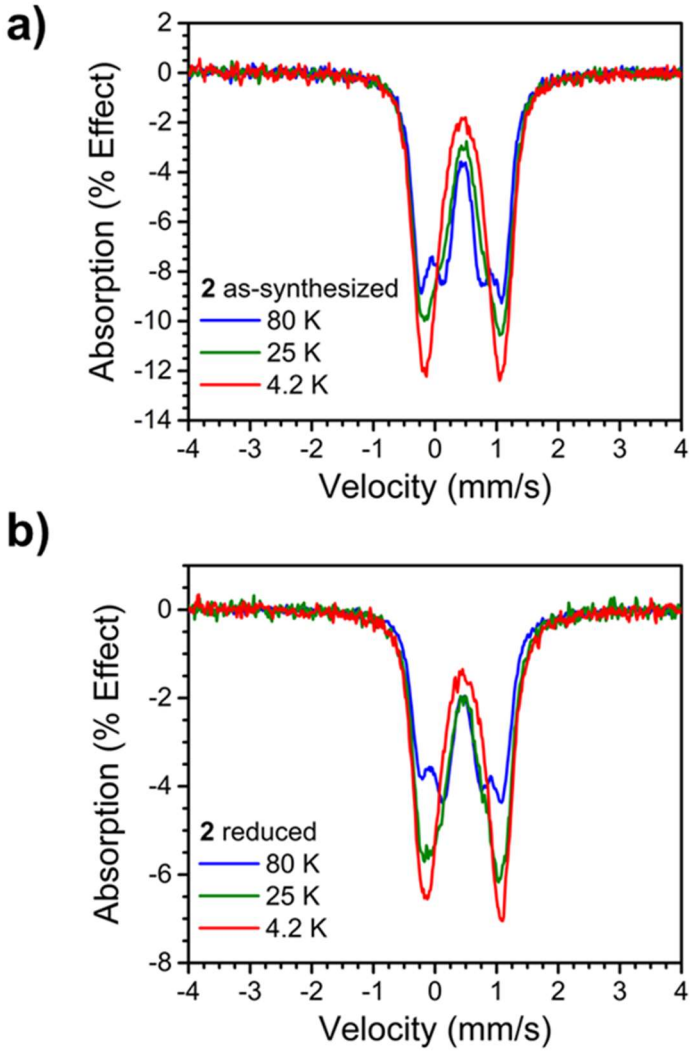

Figure A.35. 57Fe Mössbauer spectra of 2 overlaid at 80 K, 25 K, and 4.2 K: (a) 2 as-synthesized; (b) 2 following chemical reduction.

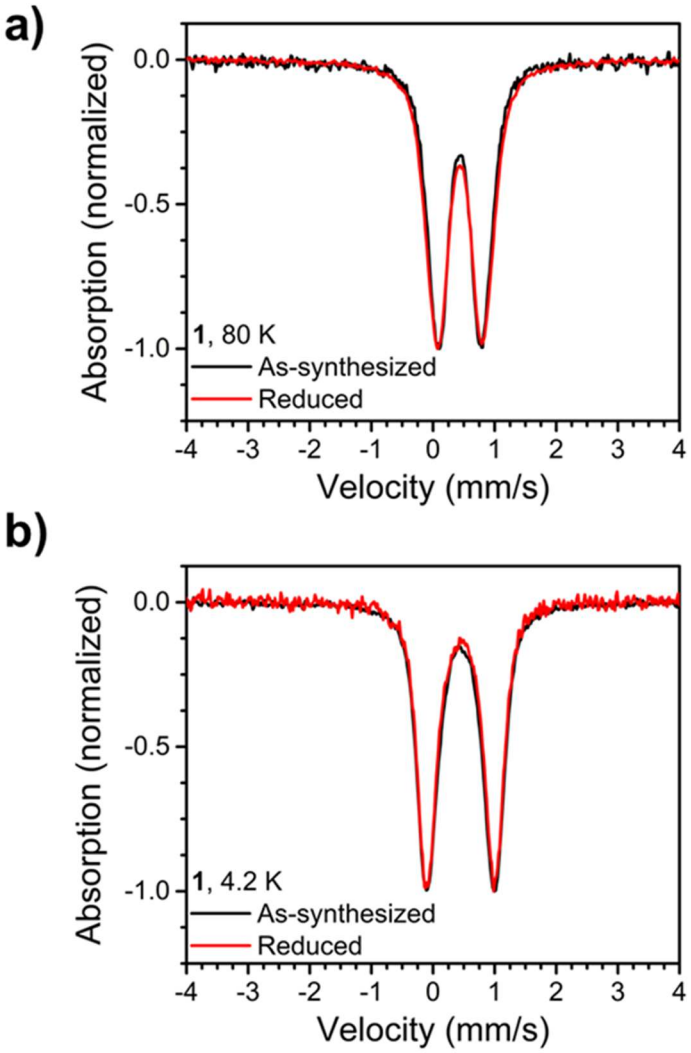

Figure A.36. Normalized ^{57}Fe Mössbauer spectra of 1 before and after chemical reduction: (a) 80 K; (b) 4.2 K.

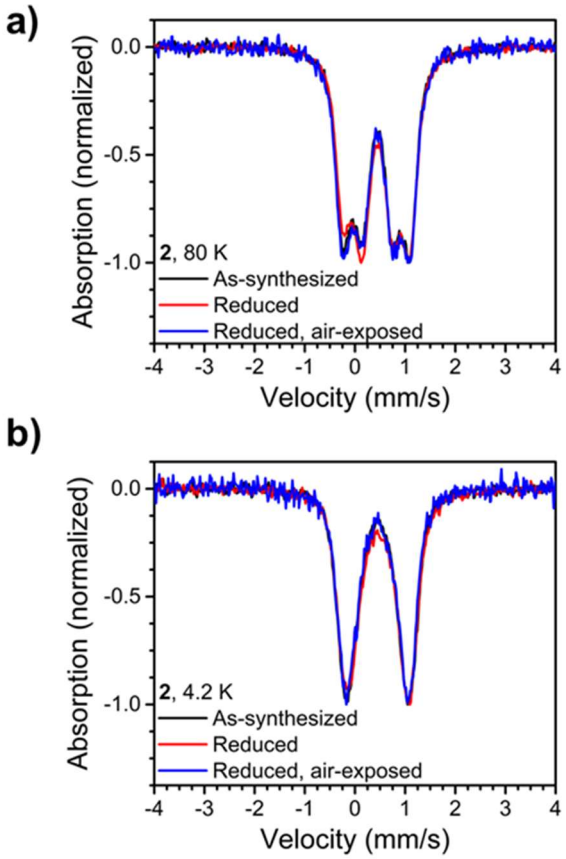

Figure A.37. Normalized ^{57}Fe Mössbauer spectra of 2 before and after chemical reduction: (a) 80 K; (b) 4.2 K.

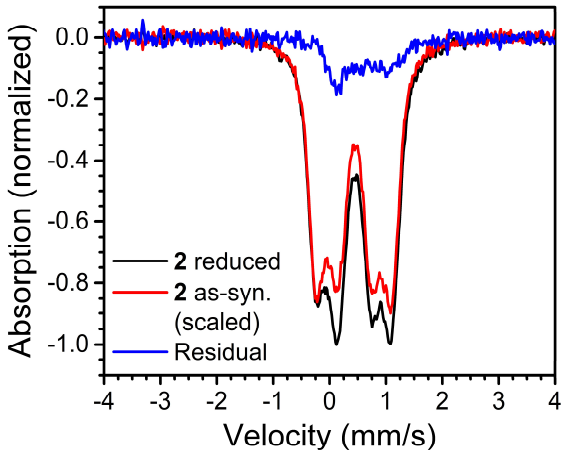

Figure A.38. Scaled ^{57}Fe Mössbauer spectra of 2 before and after chemical reduction, with subtraction showing additional signal due to reduction.

Table A.6 Fitting parameters for Mössbauer spectra. Spectra were fit using Voigt lineshapes with a fixed Lorentzian FWHM of 0.19 mm/s and a fitted Gaussian FWHM.

1 as-synthesized	Site 1
δ (mm/s)	0.4345(7)
ΔE_Q (mm/s)	0.714(1)
FWHM (left, mm/s)	0.346(3)
FWHM (right, mm/s)	0.355(3)
Relative area	*1*

1 reduced	Site 1
δ (mm/s)	0.4357(3)
ΔE_Q (mm/s)	0.7439(6)
FWHM (left, mm/s)	0.398(1)
FWHM (right, mm/s)	0.408(1)
Relative area	*1*

2 as-synthesized	Site 1	Site 2
δ (mm/s)	0.4339(9)	0.447(1)
ΔE_Q (mm/s)	1.330(4)	0.610(4)
FWHM (left, mm/s)	0.280(7)	0.313(7)
FWHM (right, mm/s)	0.272(7)	0.314(7)
Relative area	0.499(7)	0.501(7)

2 reduced	Site 1 (fixed)	Site 2 (fixed)	Site 3
δ (mm/s)	*0.4339(9)*	*0.447(1)*	0.561(8)
ΔE_Q (mm/s)	*1.330(4)*	*0.610(4)*	0.82(1)
FWHM (left, mm/s)	*0.280(7)*	*0.313(7)*	0.48(2)
FWHM (right, mm/s)	*0.272(7)*	*0.314(7)*	0.86(3)
Relative area	0.434(4)	0.434(4)	0.131(7)

2 reduced, air-exposed	Site 1	Site 2
δ (mm/s)	0.430(2)	0.443(2)
ΔE_Q (mm/s)	1.333(8)	0.607(9)
FWHM (left, mm/s)	0.30(1)	0.32(1)
FWHM (right, mm/s)	0.30(1)	0.31(1)
Relative area	0.52(1)	0.48(1)

A.10 Infrared Spectroscopy

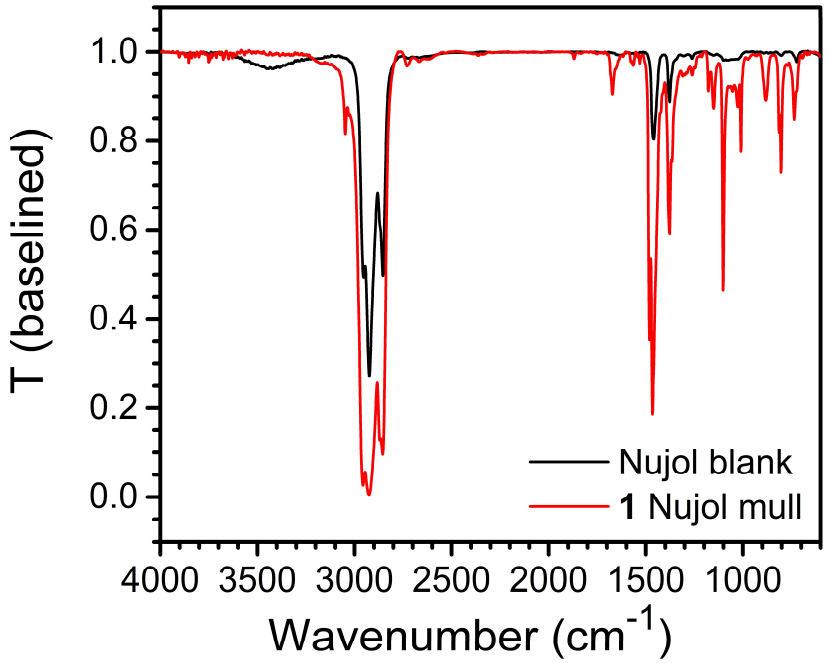

Figure A.39. Infrared transmittance spectrum of 1 as a Nujol mull.

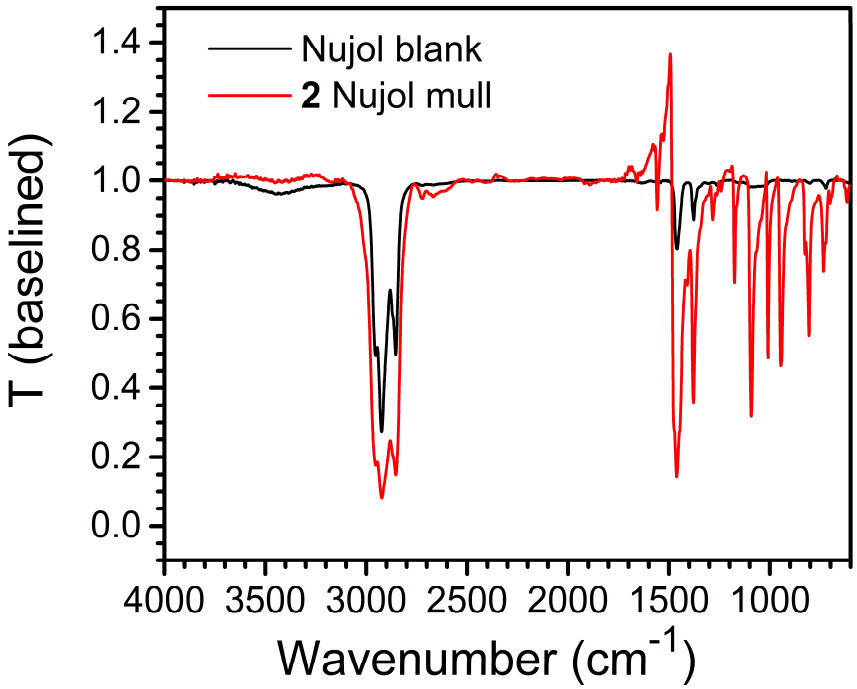

Figure A.40. Infrared transmittance spectrum of 2 as a Nujol mull.

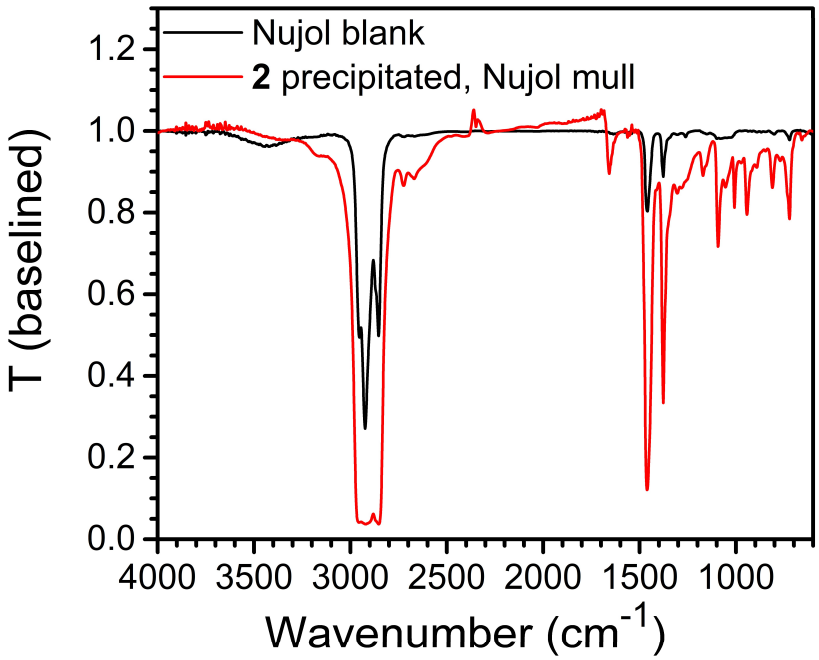

Figure A.41. Infrared transmittance spectrum of 2 reprecipitated from DMF solution by addition of Et_2O.

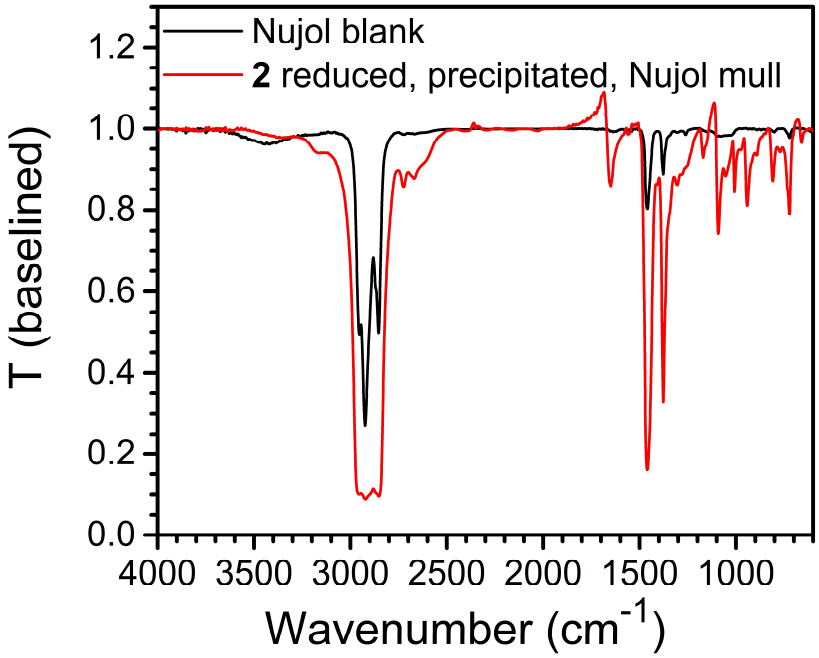

Figure A.42. Infrared transmittance spectrum of 2 reduced in DMF solution with $[Na][C_{12}H_8]$ and reprecipitated by addition of Et_2O.

A.11 Electrochemical Measurements

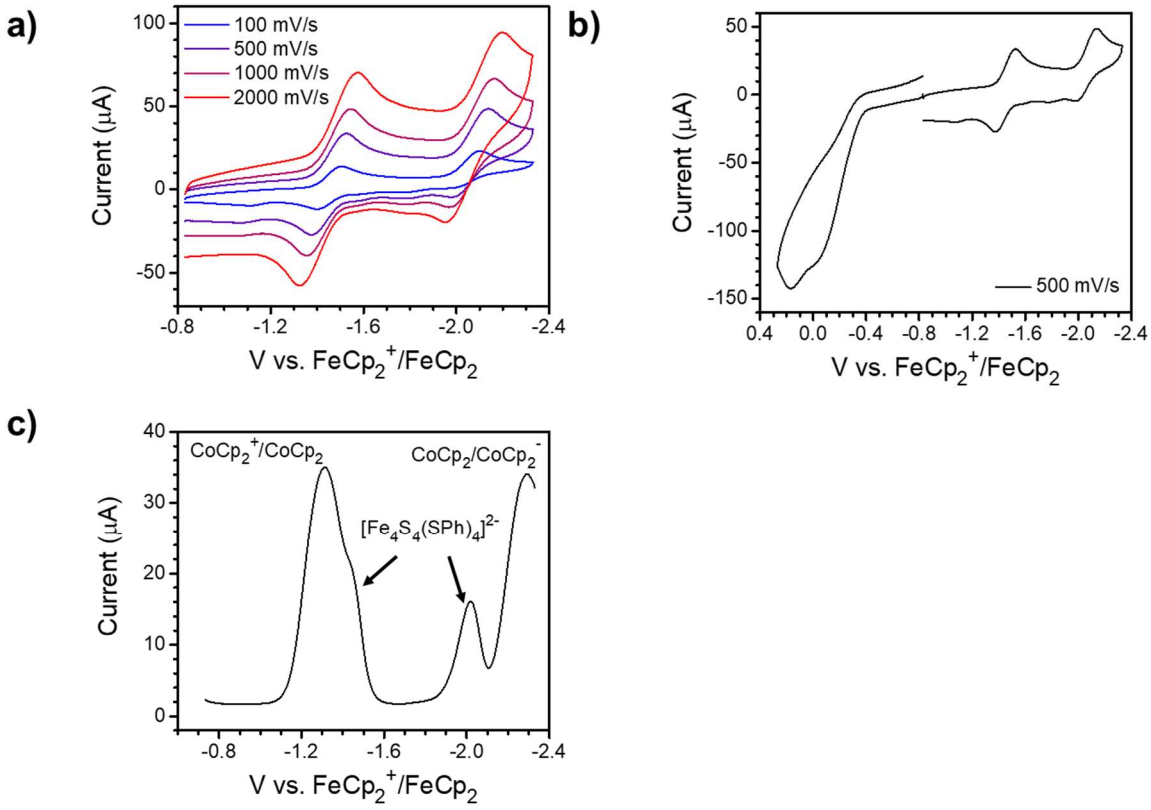

Figure A.43. Electrochemical data on $[TMA]_2[Fe_4S_4(SPh)_4]$ in 0.1 M [TMA][PF_6] in DMF. (a) Cyclic voltammograms showing reductive features collected at different scan rates; (b) cyclic voltammogram showing irreversible oxidation (note this is a composite of a reductive and an oxidative scan); (c) differential pulse voltammogram with added $CoCp_2$ internal reference.

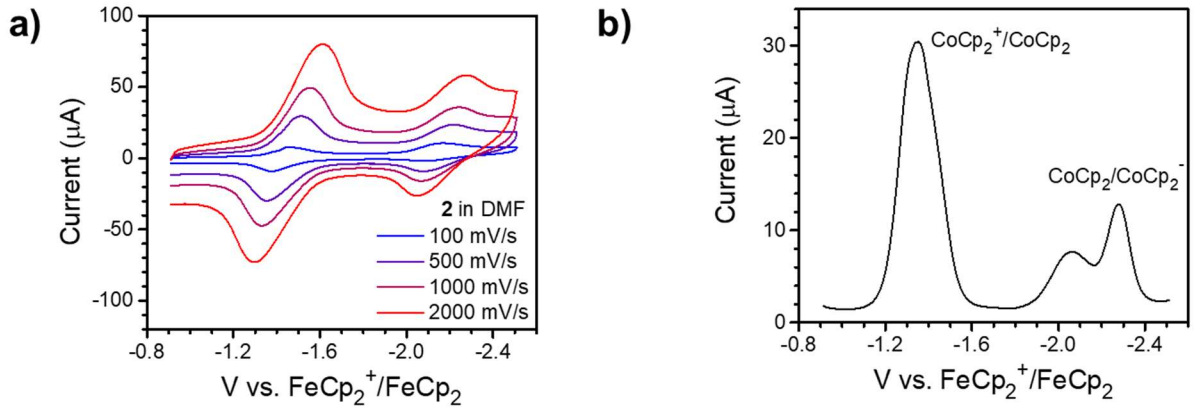

Figure A.44. Electrochemical data on 2 in 0.1 M [TMA][PF6] in DMF. (a) Cyclic voltammograms showing reductive features collected at different scan rates; (b) differential pulse voltammogram with added $CoCp_2$ internal reference.

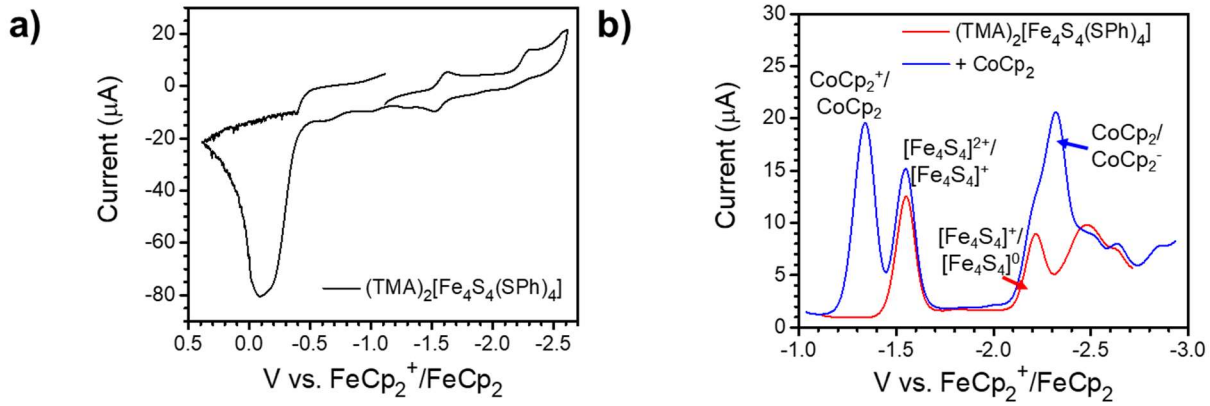

Figure A.45. Electrochemical data on $[TMA]_2[Fe_4S_4(SPh)_4]$ in 0.1 M $[Li][CF_3SO_3]$ in DMF. (a) Cyclic voltammogram at 100 mV/s showing reductive and oxidative features; (b) differential pulse voltammogram with added $CoCp_2$ internal reference.

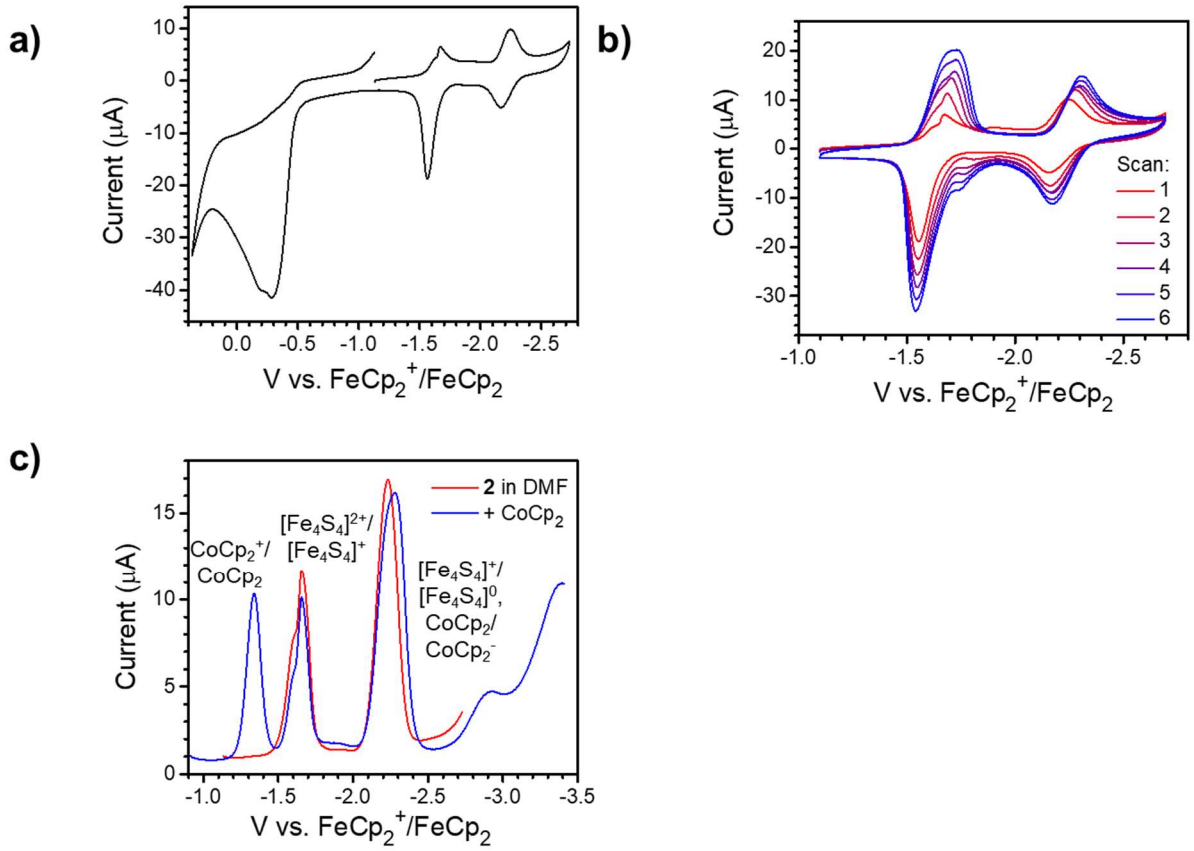

Figure A.46. Electrochemical data on 2 in 0.1 M $[Li][CF_3SO_3]$ in DMF. (a) Cyclic voltammogram at 100 mV/s showing reductive and oxidative features; (b) cyclic voltammograms at 100 mV/s showing changes in reductive features with repeated scans; (c) differential pulse voltammograms with and without $CoCp_2$ internal standard.

A.12 Precipitation Experiments

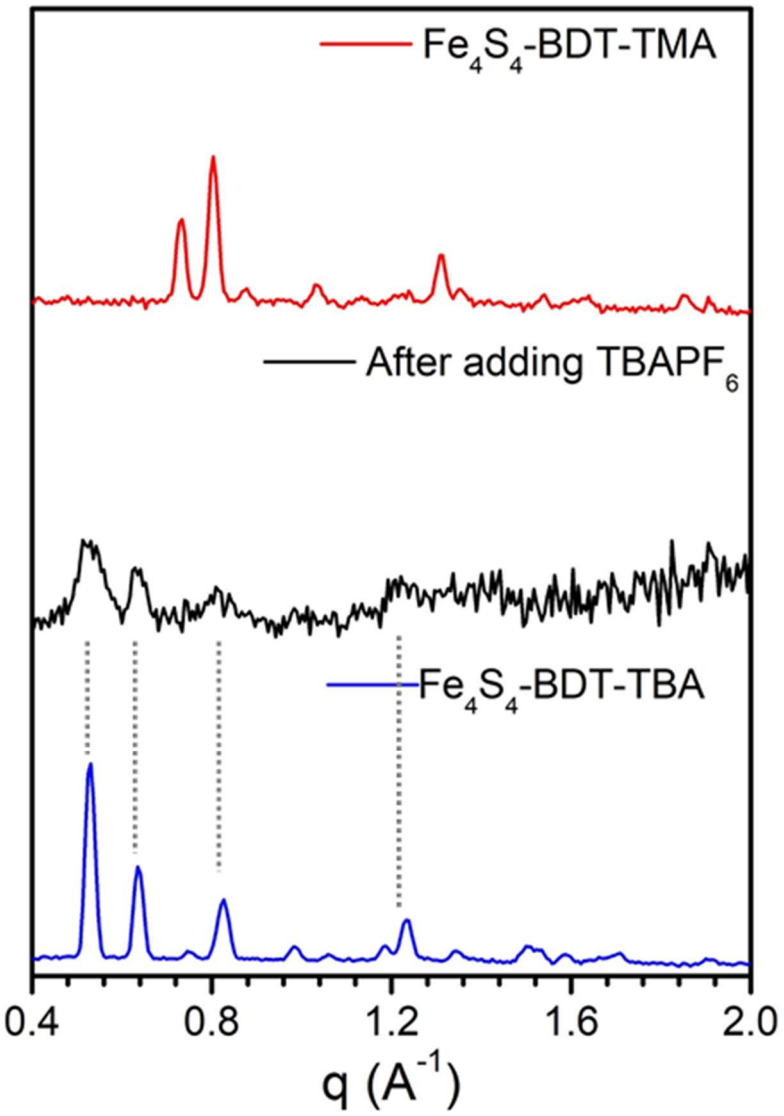

Figure A.47. XRPD patterns of (top to bottom) solid state 2, the precipitate formed from a DMF solution of 2 and **excess [Li][CF_3SO_3]** after adding [TBA][PF_6], and solid state of 1**.**

A.13 References

[1] Howarth, A. J.; Peters, A. W.; Vermeulen, N. A.; Wang, T. C.; Hupp, J. T.; Farha, O. K., Best Practices For The Synthesis, Activation, And Characterization Of Metal–Organic Frameworks. *Chem. Mater.* **2017,** *29* (1), 26-39.

[2] (a) https://www.synchrotron-soleil.fr/fr/lignes-de-lumiere/proxima-2a (b) Duran, D.; Le Couster, S.; Desjardins, K.; Delmotte, A.; Fox, G.; Meijers, R.; Moreno, T.; Savko, M.; Shepard, W., PROXIMA 2A – A New Fully Tunable Micro-focus Beamline for Macromolecular Crystallography. *J. Phys.: Conf. Ser.* **2013,** *425,* 012005.

[3] ALBULA (free) software (DECTRIS), https://www.dectris.com/products/albula-software.

[4] Louër, D. and Boultif, A., Some further considerations in powder diffraction pattern indexing with the dichotomy method. *Powder Diffr.* **2014,** *29* (Suppl. S2), S7-S12.

[5] Altomare, A.; Giacovazzo, C.; Guagliardi, A.; Moliterni, A.; Rizzi, R.; Werner, P.-E., New techniques for indexing: N-TREOR in EXPO. *J. Appl. Crystallogr.* **2000,** *33*, 1180-1186.

[6] PreDICT (free) software, International Centre for Diffraction Data, http://www.icdd.com.

[7] Altomare, A.; Cuocci, C.; Giacovazzo, C.; Moliterni, A.; Rizzi, R.; Corriero, N.; Falcicchio, A., EXPO2013: a kit of tools for phasing crystal structures from powder data. *J. Appl. Crystallogr.* **2013,** *46* (4), 1231-1235.

[8] Favre-Nicolin, V.; Cerny, R., FOX, `free objects for crystallography': a modular approach to ab initio structure determination from powder diffraction. *J. Appl. Crystallogr.* **2002,** *35* (6), 734-743.

[9] Larson A. C. and Von Dreele, R. B., General Structure Analysis System (GSAS), Los Alamos National Laboratory Report LAUR **1994,** 86-748.

[10] (a) Liu, Q.; Zhang, C.; Chen, C.; Zhu, H.; Deng, Y.; Cai, J., Syntheses and structural characterizations of Fe4S4 cubane-like cluster compounds containing cycloalkylthiolate ligands. *Sci. China Chem.* **1997**, *40* (6), 616-623. (b) Al-Rammahi, T. M. M.; Waddell, P. G.; Henderson, R. A. *CCDC 1472848: Experimental Crystal Structure Determination*, **2016,** DOI: 10.5517/ccdc.csd.cc1lfm7w. (c) Al-Rammahi, T. M. M.; Waddell, P. G.; Henderson, R. A., X-ray crystal structures of $[NHR_3]_2[Fe_4S_4X_4]$ (X = PhS, R = Et or nBu; X = Cl, R = nBu): implications for sites of protonation in Fe–S clusters. *Transition Metal Chemistry* **2016,** *41* (5), 555-561.

[11] https://www.ccdc.cam.ac.uk/solutions/csd-system/components/mogul.

[12] (a) Macrae, C. F.; Edgington, P. R.; McCabe, P.; Pidcock, E.; Shields, G. P.; Taylor, R.; Towler, M.; van de Streek, J., Mercury: visualization and analysis of crystal structures. *J. Appl. Crystallogr.* **2006,** *39* (3), 453-457. (b) Macrae, C. F.; Bruno, I. J.; Chisholm, J. A.; Edgington, P. R.; McCabe, P.; Pidcock, E.; Rodriguez-Monge, L.; Taylor, R.; van de Streek, J.; Wood, P. A., Mercury CSD 2.0 - new features for the visualization and investigation of crystal structures. *J. Appl. Crystallogr.* **2008,** *41* (2), 466-470.

[13] https://checkcif.iucr.org.

Appendix B:Supporting Data for Chapter 3

B.1 Chemical Composition

Chemical composition was examined by Inductively Coupled-Mass Spectrometry or Optical Emission Spectroscopy (ICP-MS/OES), X-ray Fluorescence Spectroscopy (XRF), and X-ray Photoelectron Spectrsocopy (XPS).

Solutions for ICP-MS were prepared by digesting 1 mg of material in a 0.5 mL HNO_3 (trace metal grade) solution in a fume hood overnight at room temperature. The solution was diluted with ultrafiltered deionized water for ICP-MS analysis. Data was obtained with an Agilent 7700x ICP-MS and analyzed using ICP-MS Mass Hunter version B01.03. The samples were diluted in 2% HNO_3 matrix and analyzed with a ^{159}Tb internal standard against a 12-point standard curve over the range from 0.1 ppb to 500 ppb.

ICP-OES data was obtained with an Agilent 700 Series instrument. The digestion method followed a procedure recently described in the literature.[1] Solutions for ICP-OES were prepared by adding 3 mg of material into a high-density polyethylene (HDPE) centrifuge tube. 1.5 mL of 30% aqueous hydrogen peroxide solution was then added using a micropipette and the tube was then quickly closed. After 20 minutes, this sample was digested with 1.5 mL HNO_3 (trace metal grade) solution in a fume hood overnight at room temperature. The solution was diluted with ultrafiltered deionized water for ICP-OES analysis.

XPS were collected with the AXIS Nova spectrometer (Kratos Analytical) equipped with a monochromatic Al Kα X-ray source. The Al anode was powered at 10 mA and 15 kV. The instrument work function was calibrated to give an Au $4f_{7/2}$ metallic gold binding energy of 83.95

eV. Instrument base pressure was ca. 1×10^{-10} Torr. The analysis area size was 0.3×0.7 mm^2. For calibration purposes, the binding energies were referenced to the C 1s peak at 284.8 eV. Survey spectra were collected with a step size of 1 and 160 eV pass energy. The high-resolution spectra were collected with a pass energy of 40 and 0.1 eV step size. Powder samples were affixed to conductive carbon tape under N_2 before loading into the spectrometer.

Samples (80 mg) for XRF analysis were ground in a mortar and pestle and passed sequentially through 60- and 120-mesh sieves. The sieved samples were placed in a polypropylene sample holder sealed with 4 mm polypropylene film under N_2. XRF measurements were performed on a Rigaku NEXDE VS spectrometer using N as a balancing element.

Table B.1. Li, S, and N ratios with respect to Fe in 1, 2, and 3.

Chemical Ratio	Compound **1**	Compound **2**	Compound **3**
Fe:Li (ICP-MS, ICP-OES)	Not Determined	3.4 (MS)	3.0 (OES)
Fe:S (XRF)	0.5	0.5	0.5
Fe:N (XPS)	1.6	3.7	5.4

B.2 NMR Spectra

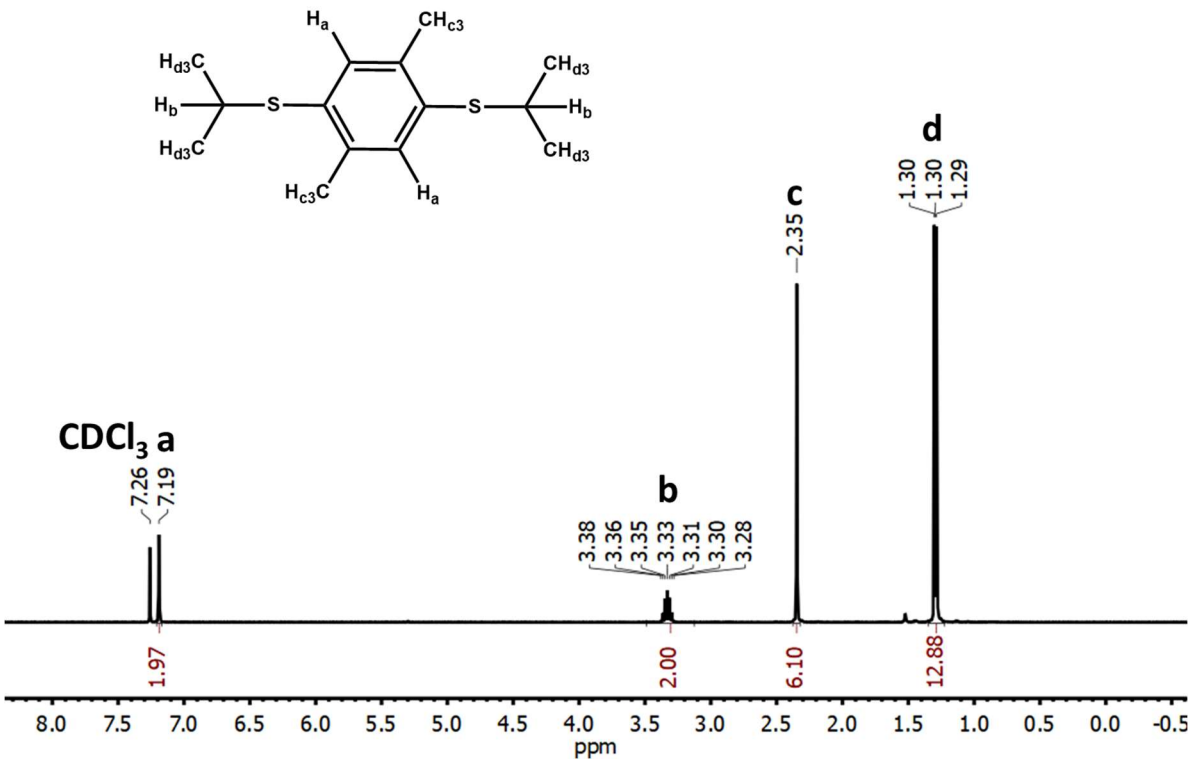

Figure B.1. ^{1}H NMR spectrum of 2,5-dimethyl-Bis(isopropylthio)benzene in $CDCl_3$.

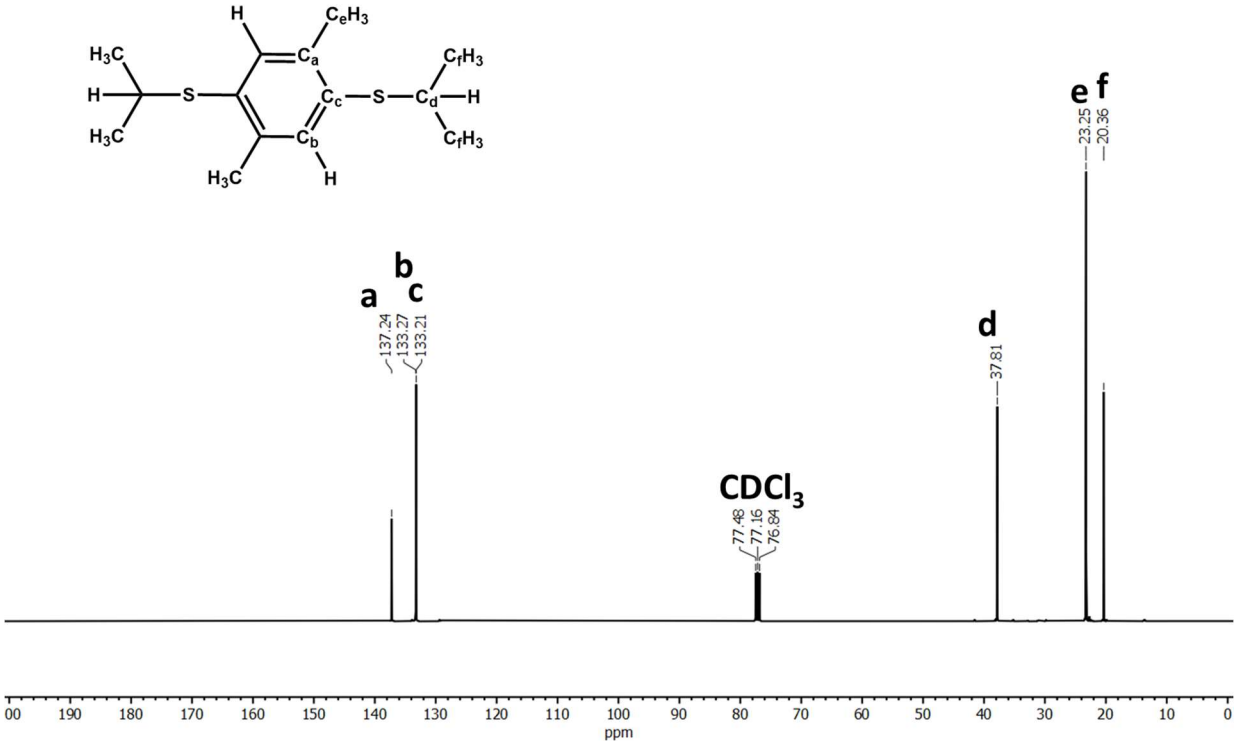

Figure B.2. ^{13}C NMR spectrum of 2,5-dimethyl-Bis(isopropylthio)benzene in $CDCl_3$.

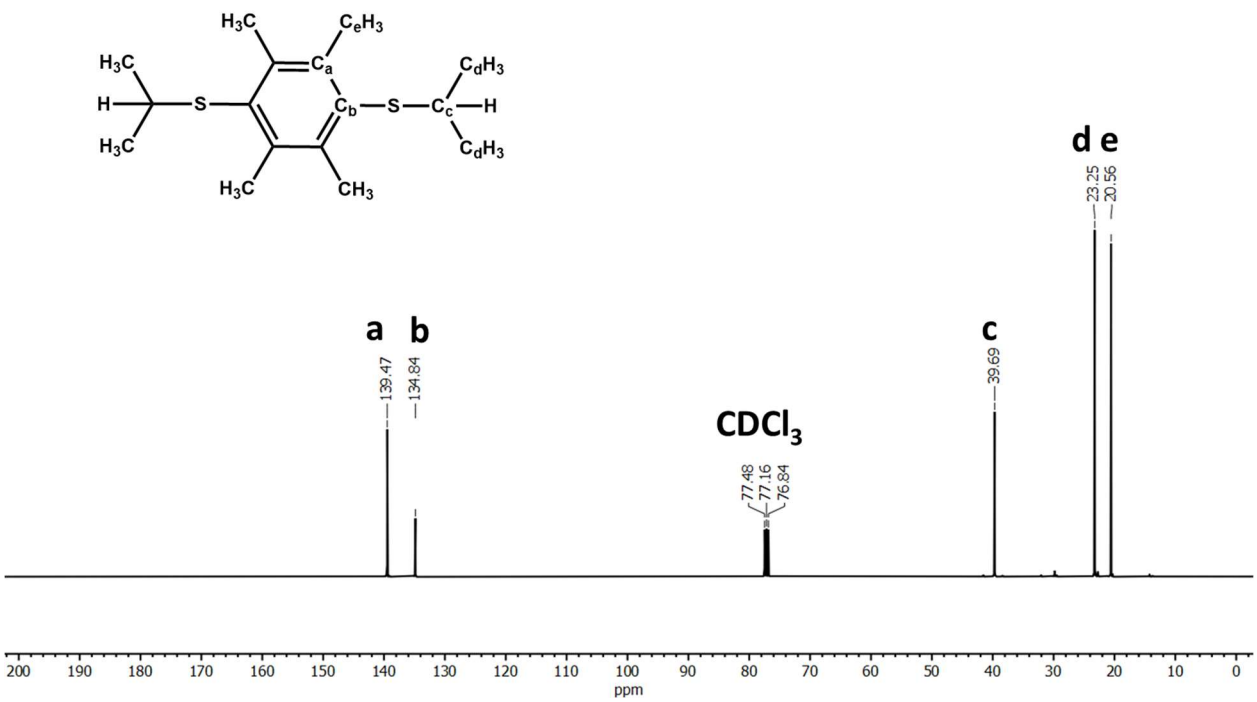

Figure B.3. ^{1}H NMR spectrum of 2,3,5,6-tetramethyl-Bis(isopropylthio)benzene in $CDCl_3$.

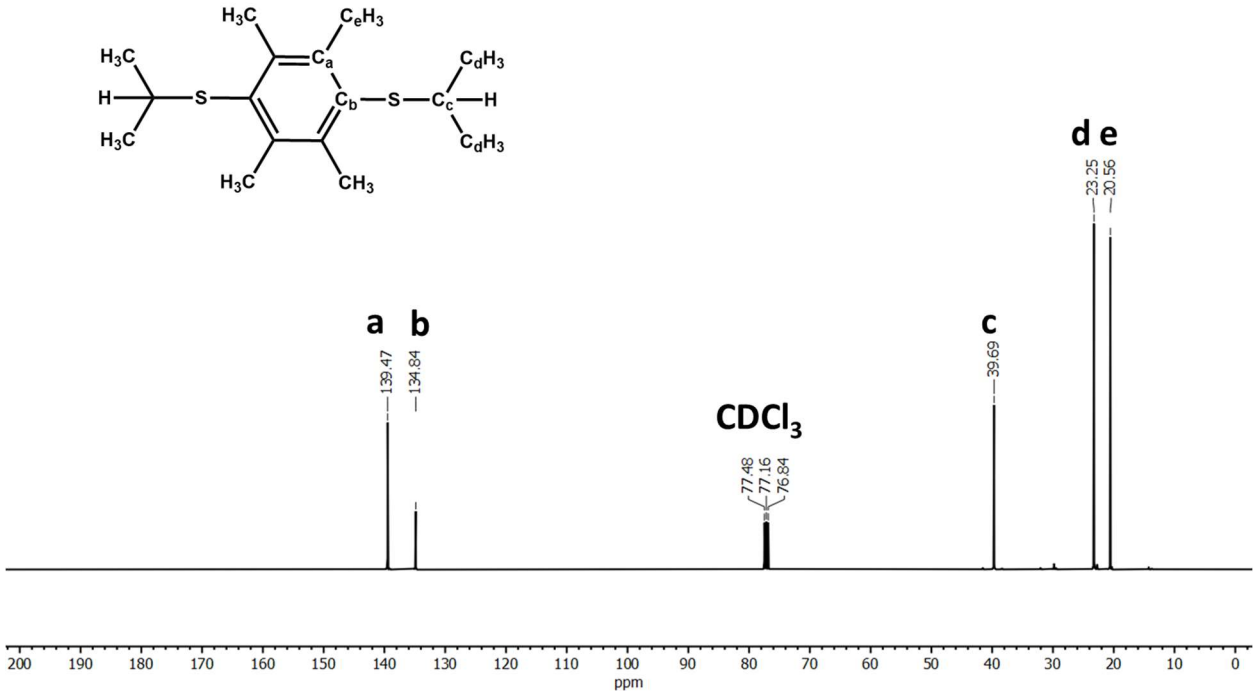

Figure B.4. ^{13}C NMR spectrum of 2,3,5,6-tetramethyl-Bis(isopropylthio)benzene in $CDCl_3$.

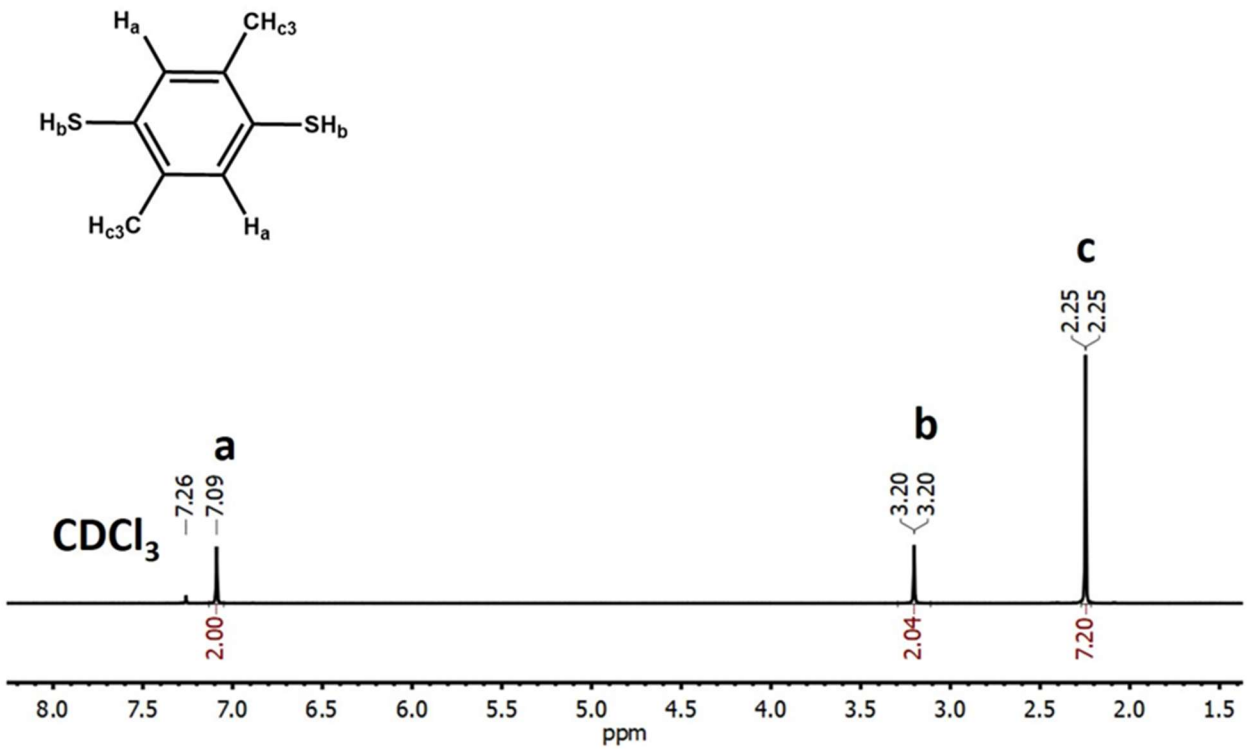

Figure B.5 ^{1}H NMR spectrum of 2,5-dimethyl-benzenethiol in $CDCl_3$.

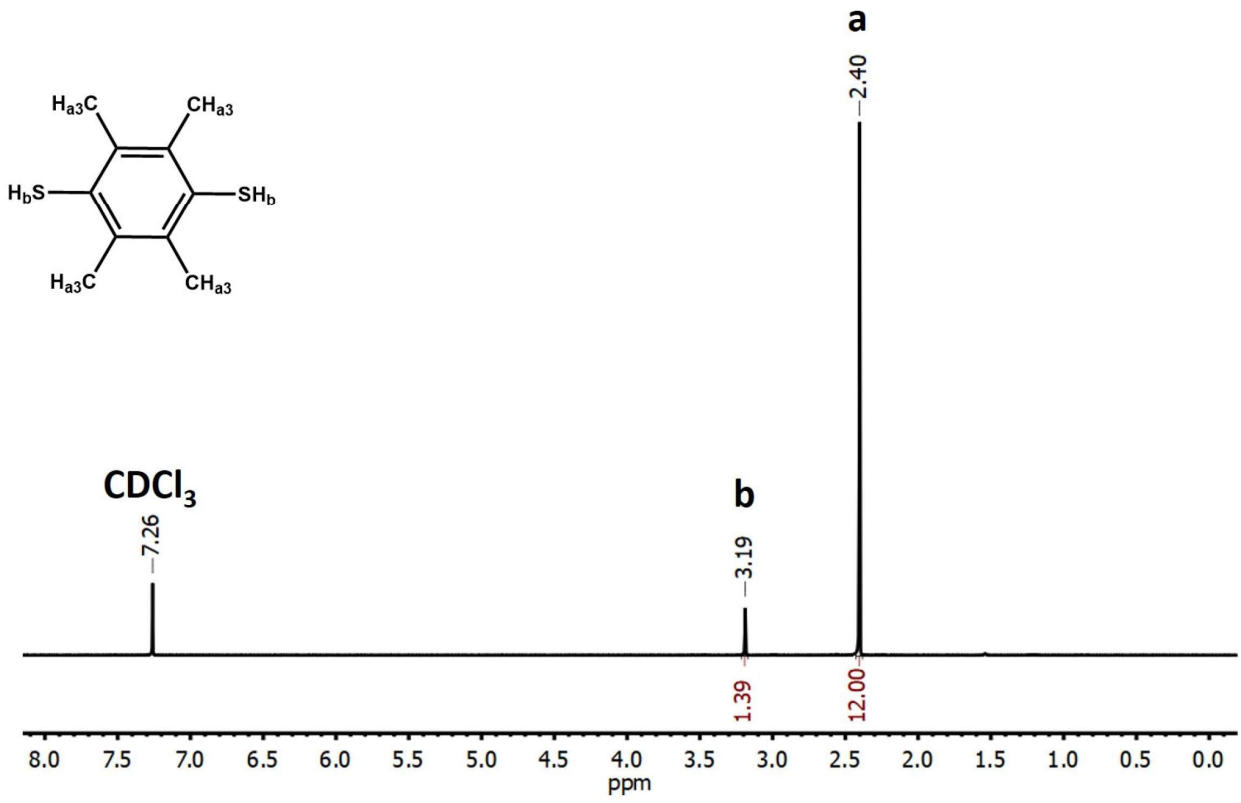

Figure B.6. ^{1}H NMR spectrum of 2,3,5,6-tetramethyl-1,4-benzenethiol in $CDCl_3$.

B.3 Digestion Experiments

1, 2, and 3 (~5 mg) were digested in 12 M hydrochloric acid (~1 mL) under air to check for ligand and PhSH content. The acid solution was extracted with C_6D_6 or $CDCl_3$ (~0.5−1 mL) and analyzed by ^{1}H NMR spectroscopy. To test for the presence of quaternary ammonium ions, 1 2, and 3 (~5 mg) were digested in D_2SO_4 (~0.1−0.2 mL), resulting in oxidation of the ligand to an insoluble polymer. This suspension was diluted with $(CD_3)_2SO$ and analyzed by ^{1}H NMR spectroscopy.

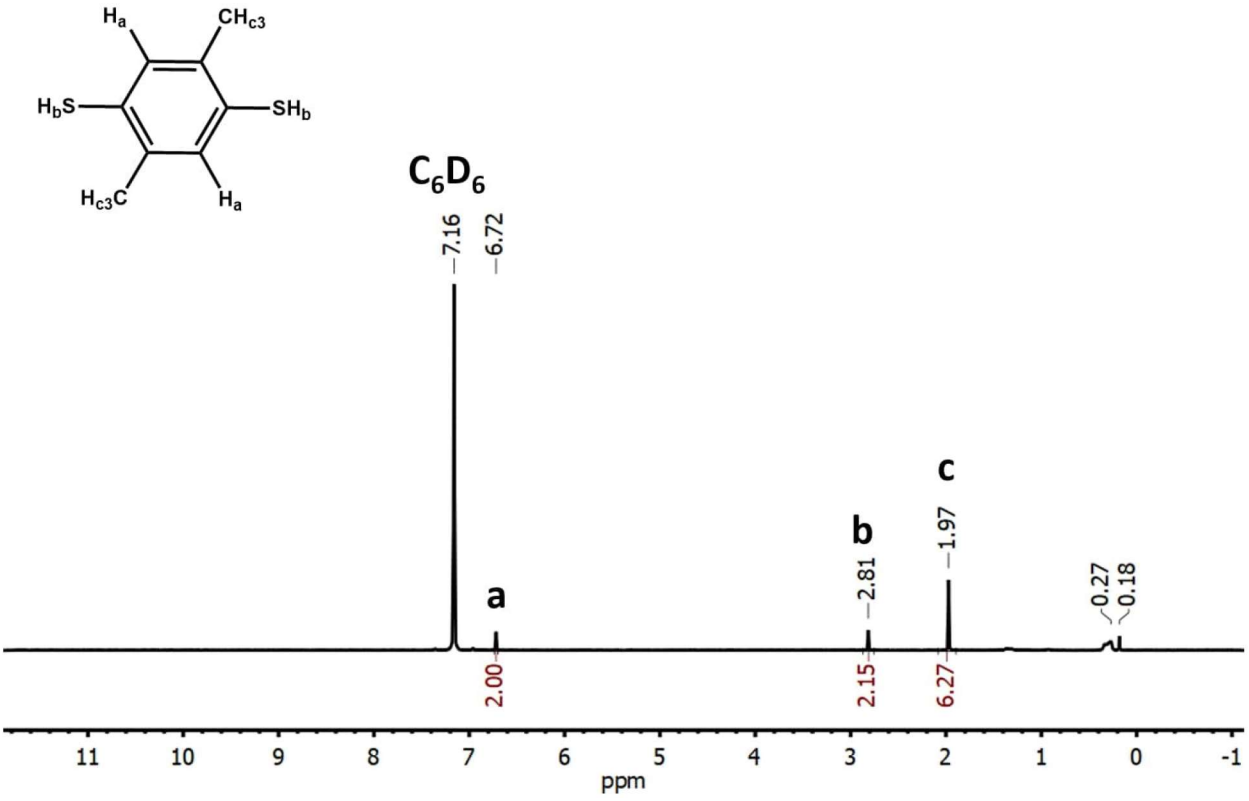

Figure B.7. ^{1}H NMR spectrum of C_6D_6 extract of 1 HCl digest.

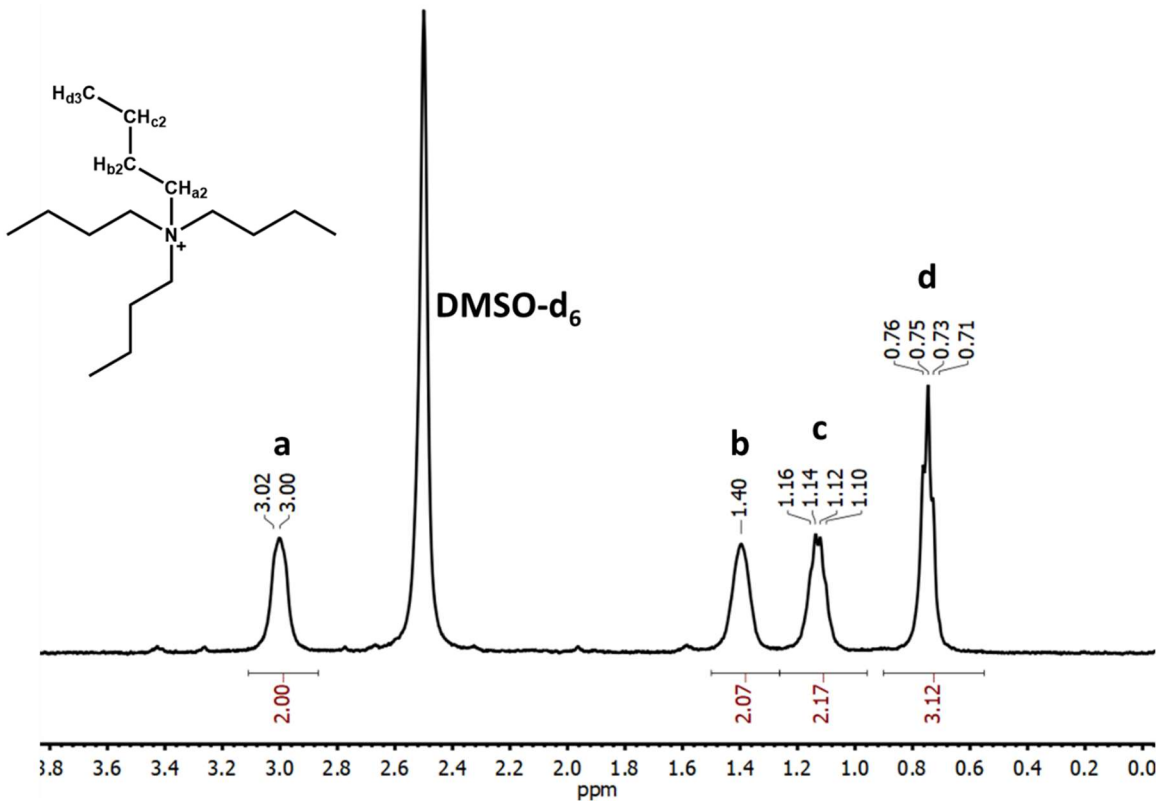

Figure B.8. ^{1}H NMR spectrum of 1 D_2SO_4 digest in $(CD_3)_2SO$.

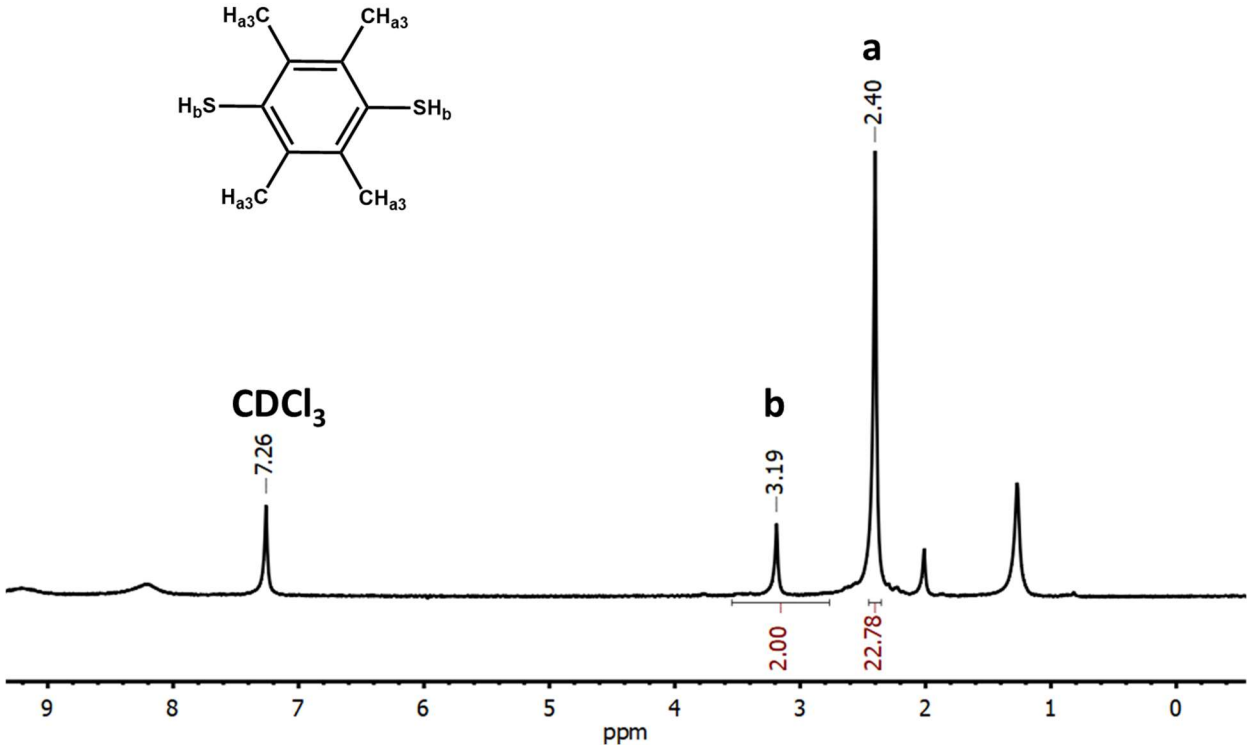

Figure B.9. ^{1}H NMR spectrum of 2 HCl digest in $CDCl_3$.

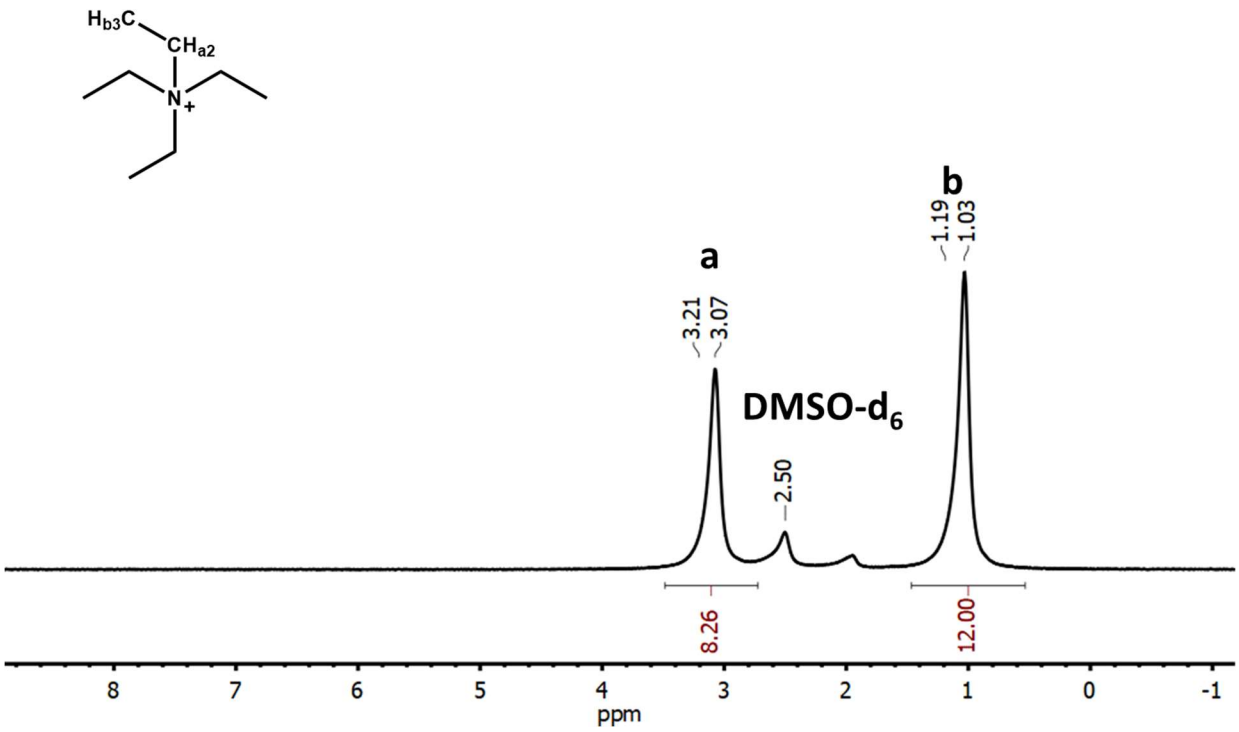

Figure B.10. ^{1}H NMR spectrum of 2 D_2SO_4 digest in $(CD_3)_2SO$.

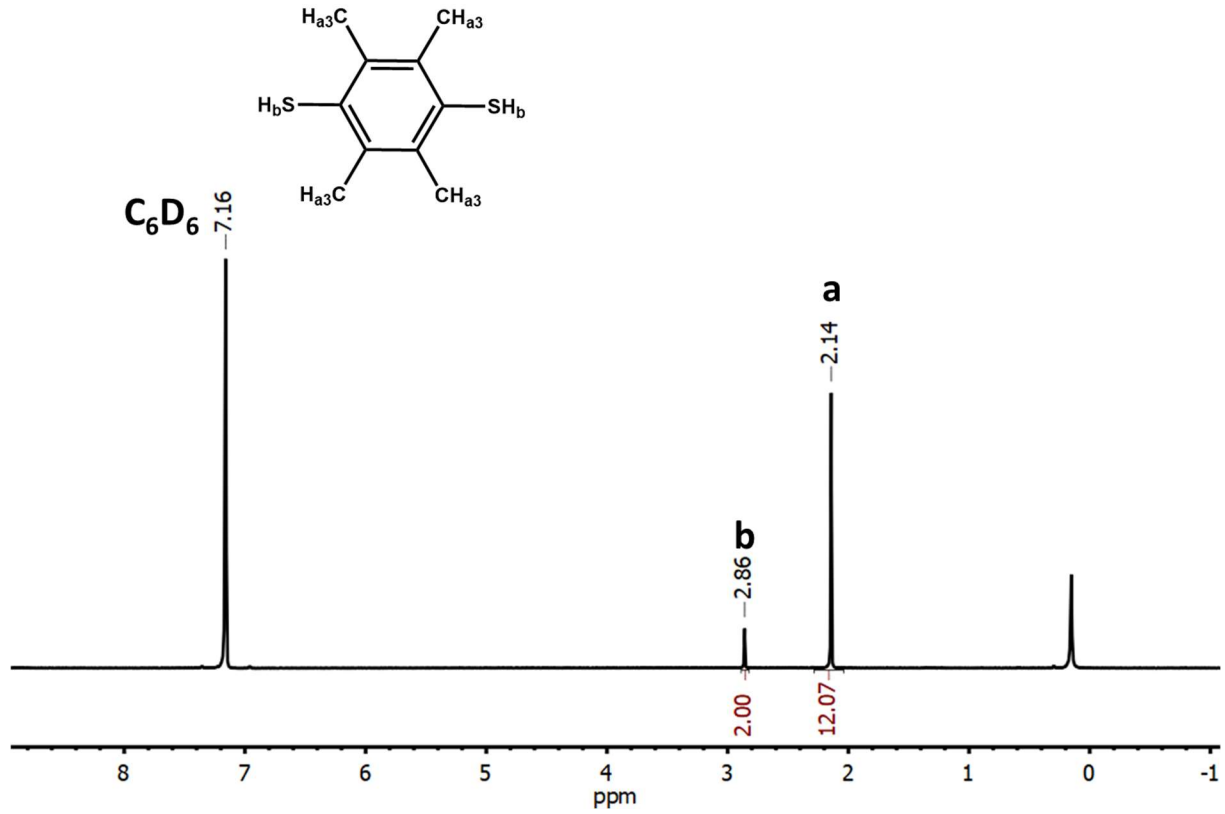

Figure B.11. ^{1}H NMR spectrum of C_6D_6 extract of 3 HCl digest.

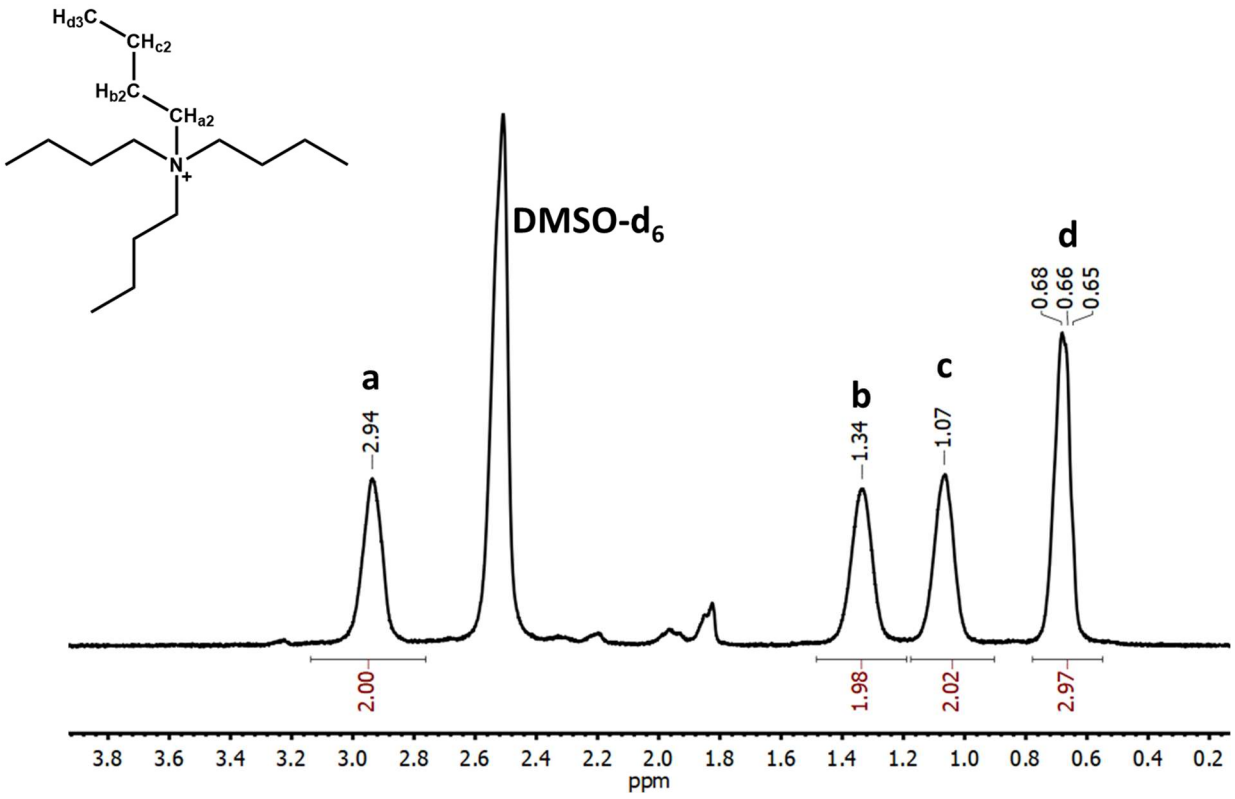

Figure B.12. ^{1}H NMR spectrum of 3 D_2SO_4 digest in $(CD_3)_2SO$.

B.4 Infrared Spectroscopy (IR)

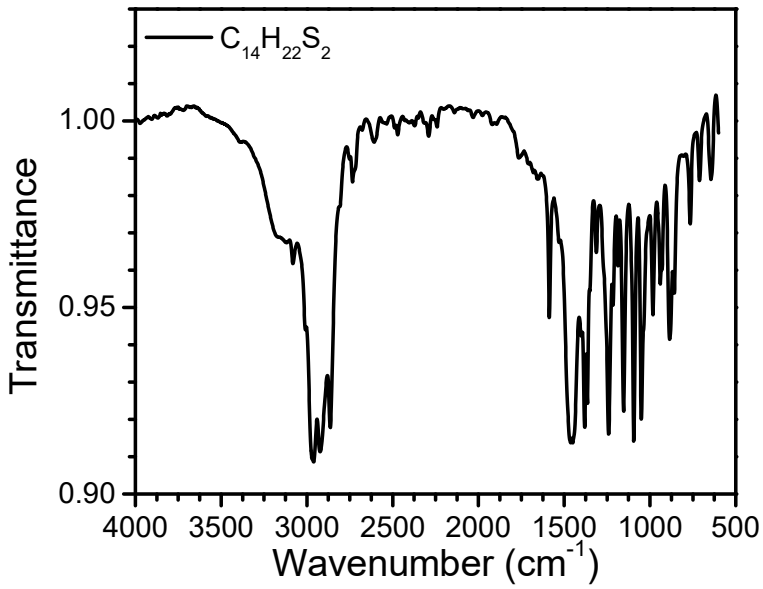

Figure B.13. Infrared transmittance spectrum of 2,5-dimethyl-Bis(isopropylthio)benzene.

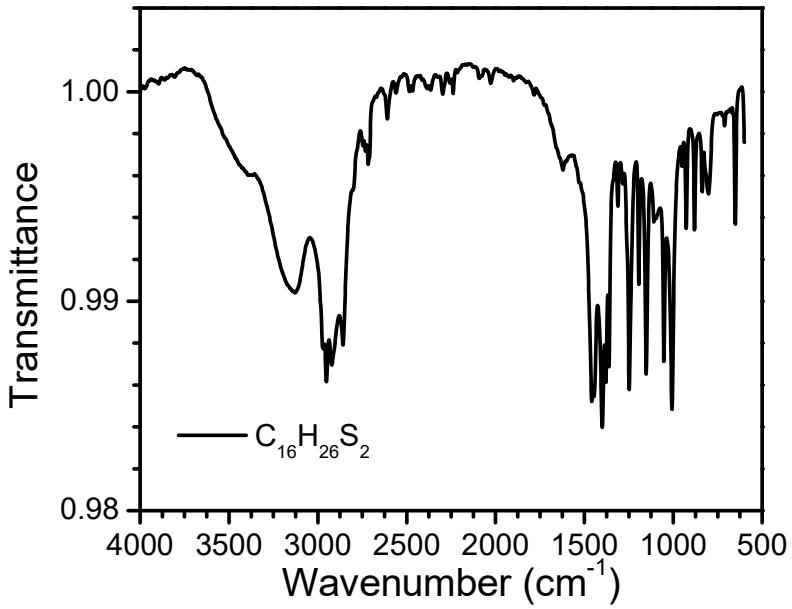

Figure B.14. Infrared transmittance spectrum of 2,3,5,6-tetramethyl-Bis(isopropylthio)benzene. Features around 3400 cm-1 correspond to water from the KBr pellet.

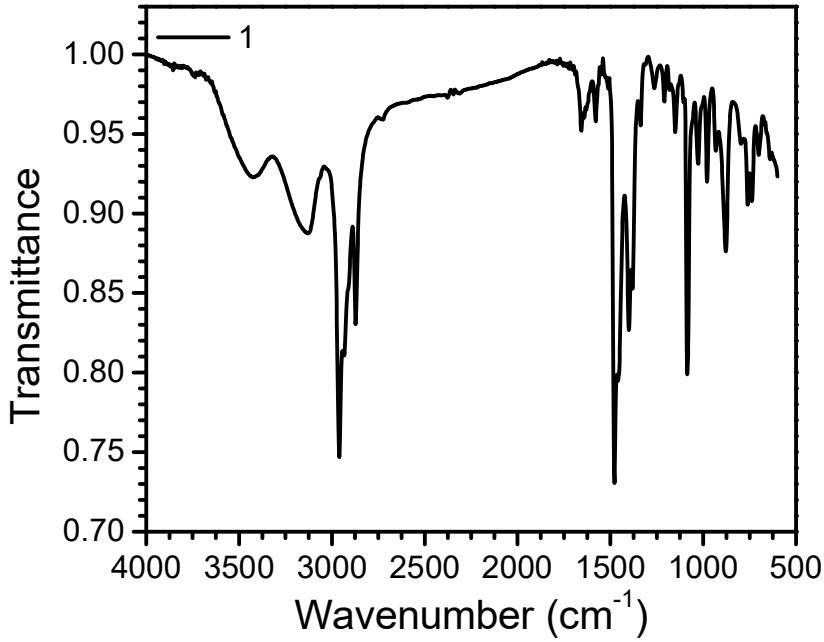

Figure B.15. Infrared transmittance spectrum of 1. Features around 3400 cm-1 correspond to water from the KBr pellet.

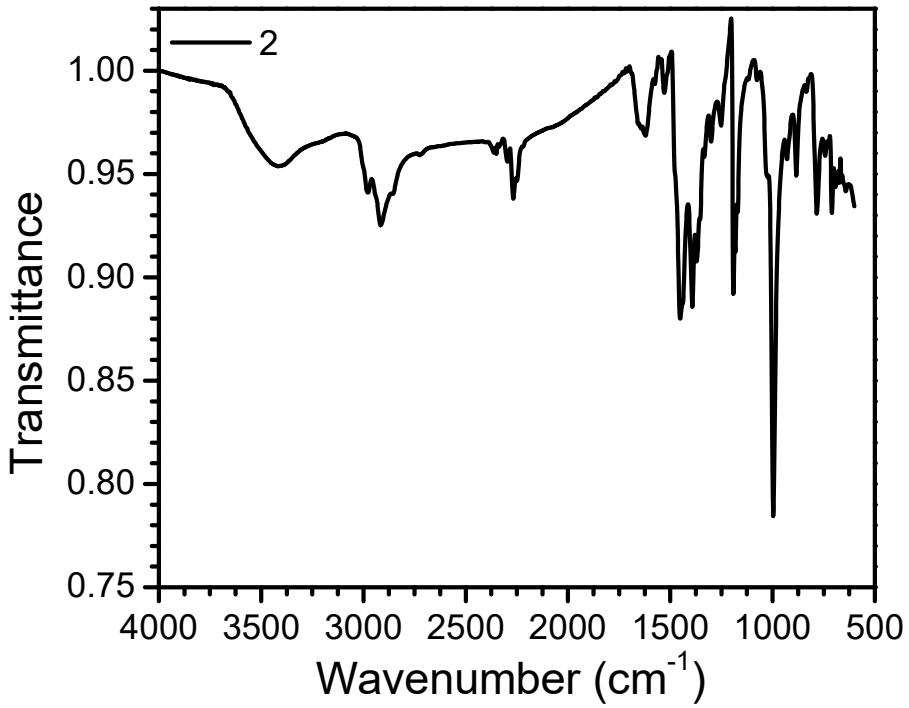

Figure B.16. Infrared transmittance spectrum of 2. Features around 3400 cm^{-1} correspond to water from KBr pellet.

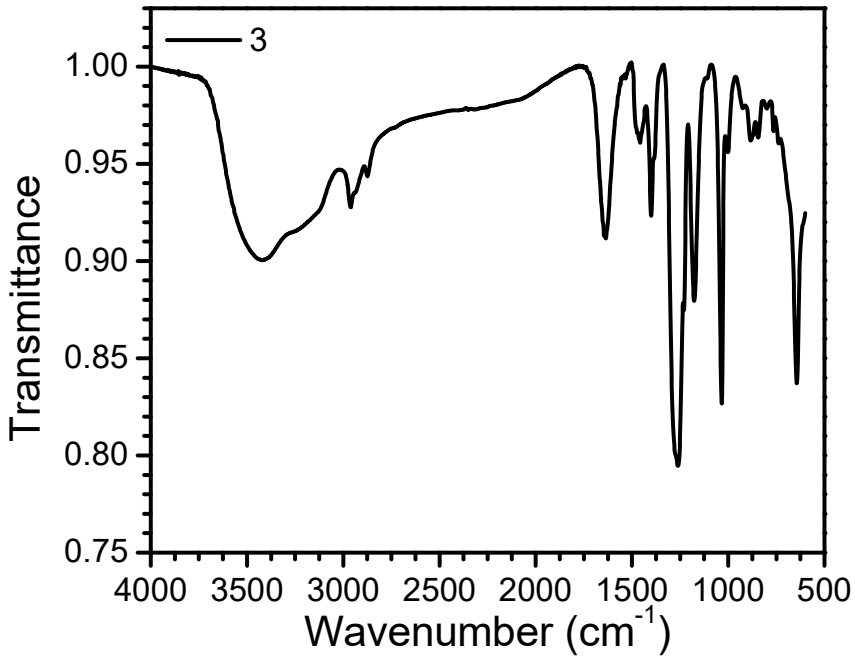

Figure B.17. Infrared transmittance spectrum of 3. Features around 3400 cm^{-1} correspond to water from the KBr pellet.

B.5 UV-Vis Spectroscopy

UV-visible absorption spectra were recorded on a Thermo Scientific Evolution 300 spectrometer with the VISIONpro software suite. Diffuse reflectance spectra were obtained with the use of a Harrick Praying Mantis accessory. Solid **1** was ground with [Mg][SO_4] in air to produce the diffuse reflectance sample. Solid **3** was finely ground under N_2 atmosphere and a thin layer was added to a [Mg]SO_4] sample. Pure [Mg][SO_4] was used as a white reference material and background subtraction was subsequently applied.

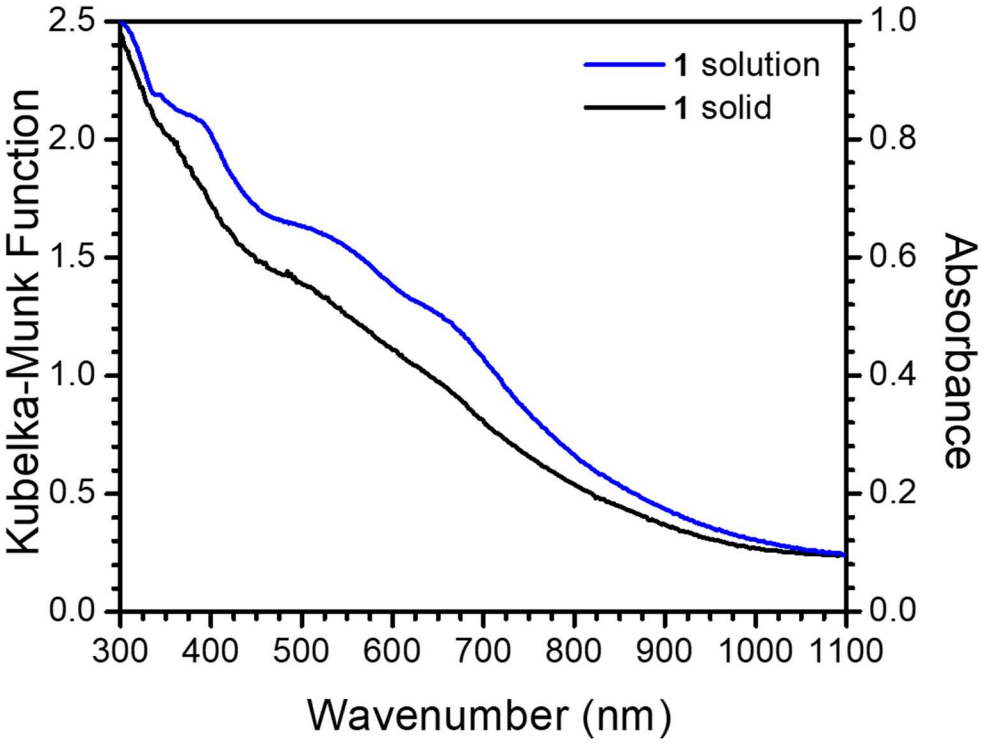

Figure B.18. UV-visible diffuse reflectance spectra of 1 in [Mg][SO_4] matrix plotted as Kubelka-Munk function and absorbance spectrum of 1 in DMF solution.

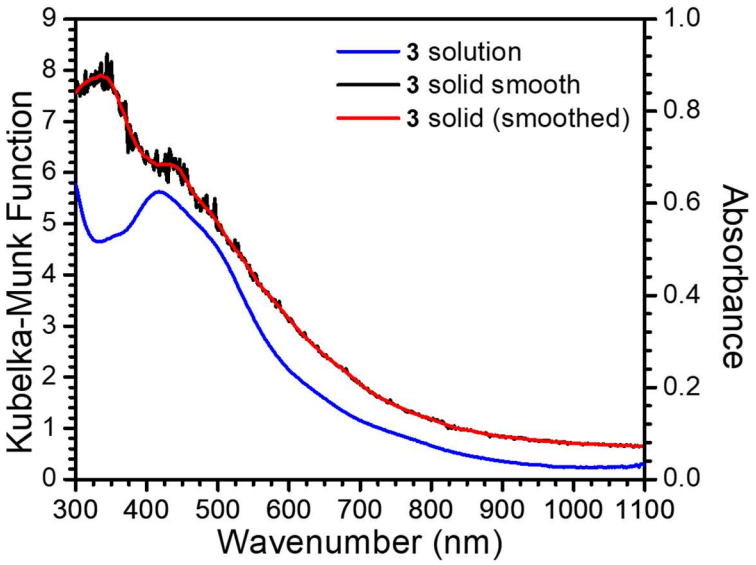

Figure B.19. UV-visible diffuse reflectance spectra of 3 in [Mg][SO_4] matrix plotted as Kubelka-Munk Function and absorbance spectrum of 3 in DMF solution. Note that due to high absorbance the solid spectra is somewhat noisy. While similar features corresponding to 3 in solution are clear, assignment of an additional feature near 300 nm is more tenuous.

B.6 Electrochemical Experiments

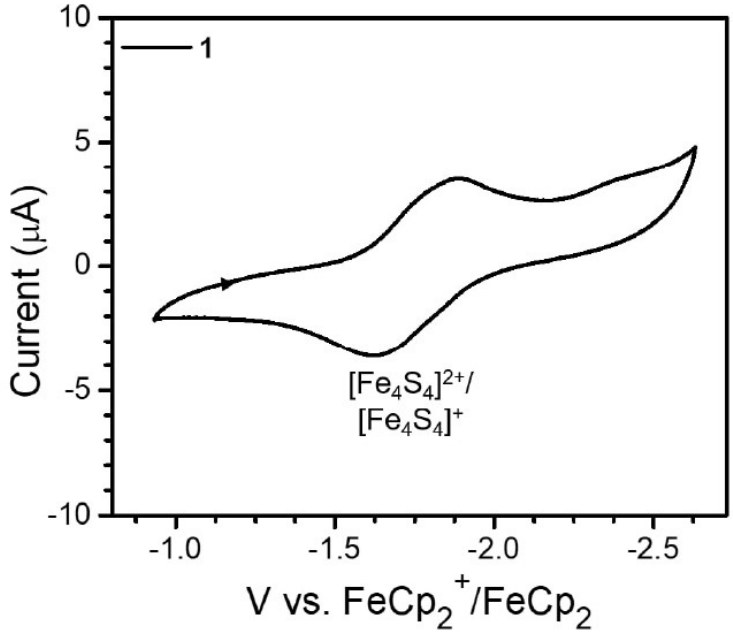

Figure B.20. Cyclic voltammogram of the reversible feature of 1. Conditions: DMF, 0.2 M [Li][CF_3SO_3], 0.1 V/s.

Electrical conductivity measurements were performed in a two-contact geometry at room temperature under N_2. Samples were prepared as pressed pellets clamped between two brass

electrodes (4.8 mm diam.) in a plastic sleeve, allowing measurement of the sample thickness with calipers. Linear sweep voltammetry was conducted using a BASi Epsilon potentiostat/galvanostat, with the reference and counter electrode terminals connected to one electrode and the working electrode terminal to the other. The resulting data were fit to a straight line to obtain the sample resistance.

Table B.2. Electrical conductivity of 1, 2, 3. Note that compounds 2 and 3 contain extra Li^+ cations.

Compound	Conductivity (S/cm)
1	1.8×10^{-11}
2	4.7×10^{-11}
3	4.3×10^{-10}

B.7 Structural Data

The X-ray data were first collected at the CRISTAL High Resolution (HR) beamline of the SOLEIL synchrotron [$l = 0.72800$ Å, calibrated with LaB_6 SRM (Standard Reference Material) on a first sample, which appeared to be laced with weak traces of impurities. To avoid any ambiguity, a second purer sample was subsequently synthesized and measured at the 11-BM beamline of the APS synchrotron [$l = 0.45793$ Å, calibrated with a Si-Al_2O_3 SRM]. The search for a suitable unit cell (using both PREDICT/DICVOL14 and EXPO/N-TREOR) was carried out independently on the powder diffraction data collected at both synchrotrons and revealed a tetragonal crystal structure with a very large volume of about 12000 Å. See Figure B.21 and **Table B.3** for the indexing results. The data sets collected at both synchrotrons point to nearly identical tetragonal primitive unit cells with very similar lattice parameters. These Indexing results were confirmed by excellent LeBail fits obtained from both diffractograms using the GSAS software.

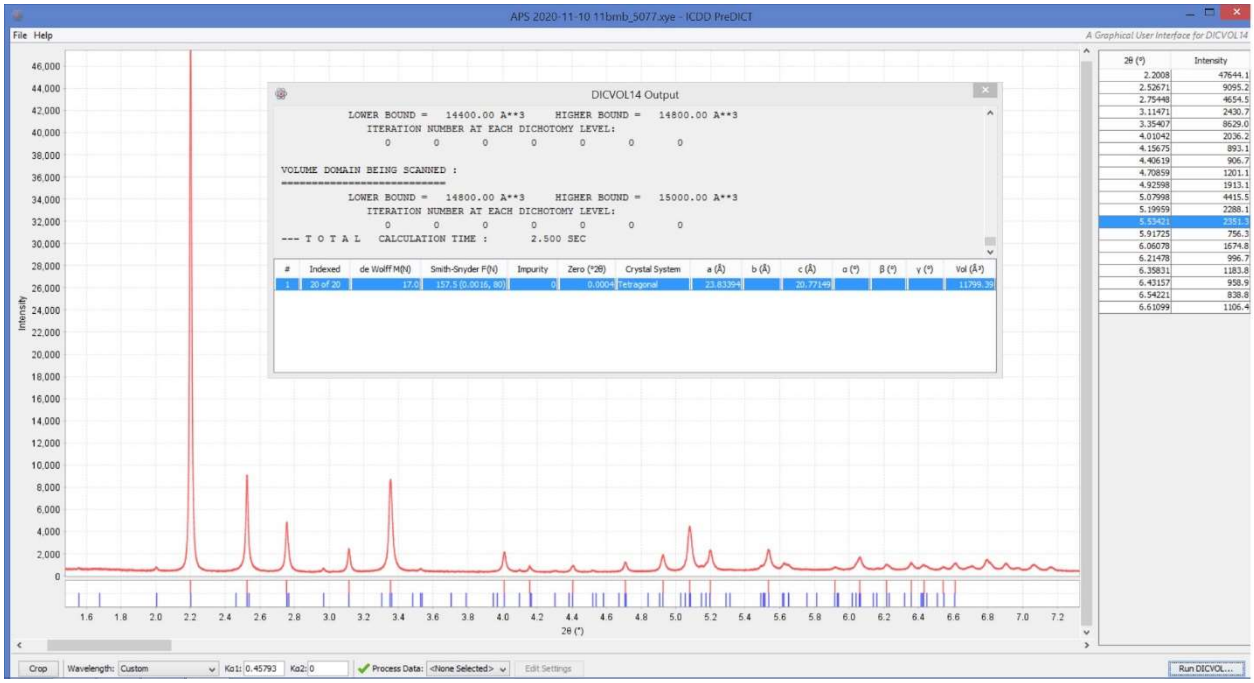
APS 2020-11-10 11bmb_5077.xye - ICDD PreDICT
File Help
A Graphical User Interface for DICVOL14
DICVOL14 Output
LOWER BOUND = 14400.00 A**3 HIGHER BOUND = 14800.00 A**3
ITERATION NUMBER AT EACH DICHOTOMY LEVEL:
0 0 0 0 0 0 0
VOLUME DOMAIN BEING SCANNED :
LOWER BOUND = 14800.00 A**3 HIGHER BOUND = 15000.00 A**3
ITERATION NUMBER AT EACH DICHOTOMY LEVEL:
0 0 0 0 0 0 0
--- T O T A L CALCULATION TIME : 2.500 SEC
Indexed de Wolff M(N) Smith-Snyder F(N) Impurity Zero (°2θ) Crystal System a (Å) b (Å) c (Å) α (°) β (°) γ (°) Vol (Å³)
1 20 of 20 17.0 157.5 (0.0016, 80) 0 0.0004 Tetragonal 23.83394 20.77149 11799.39
2θ (°) Intensity
Intensity
2θ (°)
Crop Wavelength: Custom Kα1: 0.45793 Kα2: 0 Process Data: <None Selected> Edit Settings Run DICVOL...

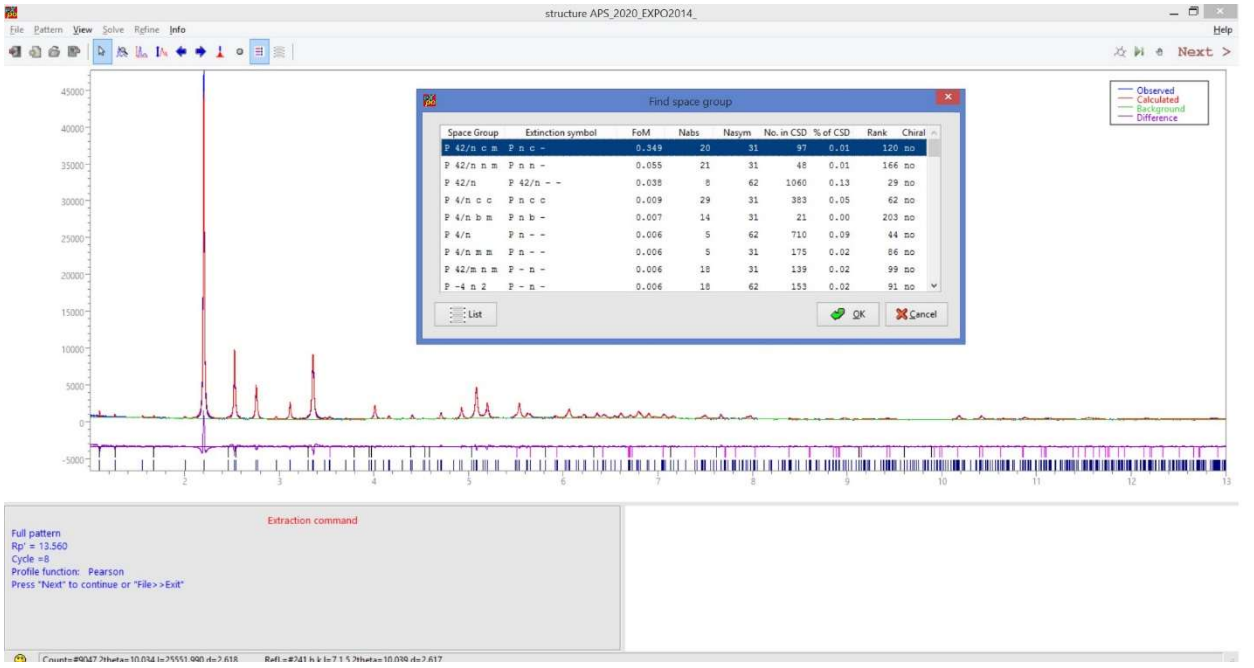
structure APS_2020_EXPO2014_
File Pattern View Solve Refine Info Help
Next >
Find space group
Space Group Extinction symbol FoM Nabs Nasym No. in CSD % of CSD Rank Chiral
P 42/n c m P n c - 0.349 20 31 97 0.01 120 no
P 42/n n m P n n - 0.055 21 31 48 0.01 166 no
P 42/n P 42/n - - 0.038 8 62 1060 0.13 29 no
P 4/n c c P n c c 0.009 29 31 383 0.05 62 no
P 4/n b m P n b - 0.007 14 31 21 0.00 203 no
P 4/n P n - - 0.006 5 62 710 0.09 44 no
P 4/n m m P n - - 0.006 5 31 175 0.02 86 no
P 42/m n m P - n - 0.006 18 31 139 0.02 99 no
P -4 n 2 P - n - 0.006 18 62 153 0.02 91 no
List OK Cancel
Observed
Calculated
Background
Difference
Extraction command
Full pattern
Rp' = 13.560
Cycle =8
Profile function: Pearson
Press "Next" to continue or "File>>Exit"

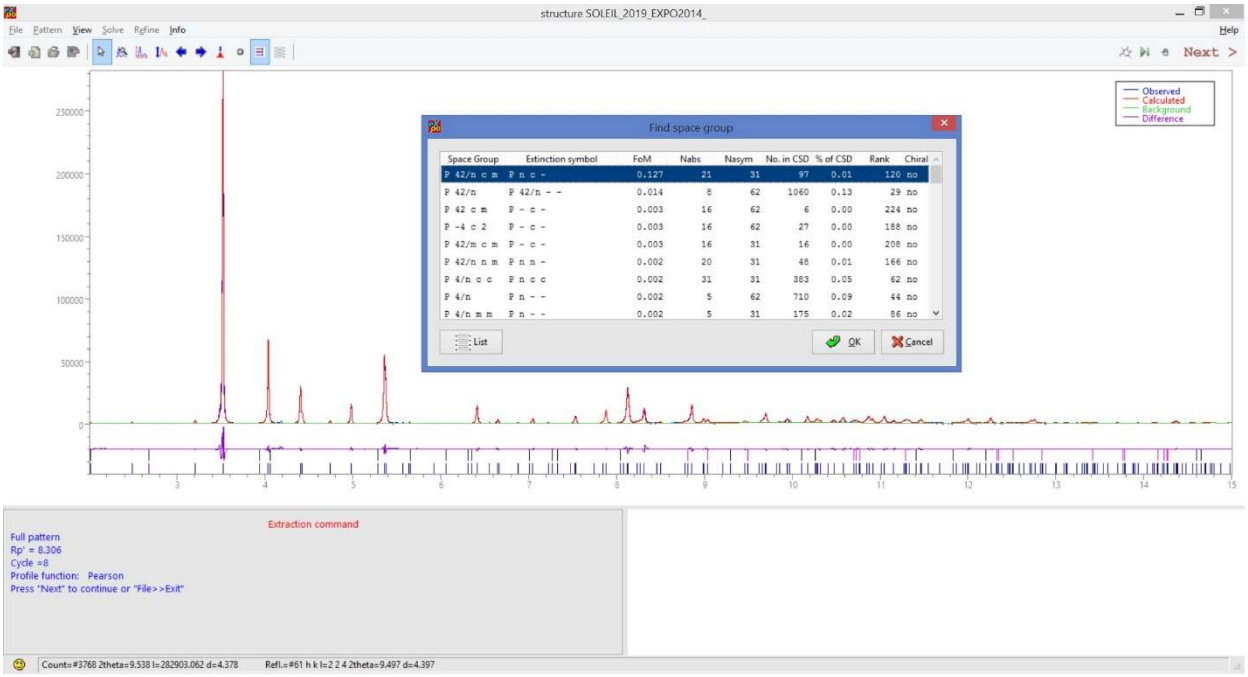

Figure B.21. Indexing of the 11-BM/APS XRPD data using the PREDICT/DICVOL[2] and EXPO/N-TREOR[3] indexing tools.

Table B.3. Unit cell determination and indexing results for both the SOELIL/CRISTAL and the APS/11-BM data using PREDICT/DICVOL.

	SOLEIL / CRISTAL	APS / 11-BM
Wavelength, Å	0.72800	0.45793
$2q_{max}$ [2 Å resolution], (°)	20.97	13.24
$2q_{max}$ [1 Å resolution], (°)	42.69	26.47
N [#peaks considered for indexing]:	17	20
M(N) [de Wolff FOM]	M(17) = 31	M(20) = 17
F(M) [Smith & Snyder FOM]	F(17) = 115(0.0013 , 117)	F(20) = 175.5(0;0016, 80)
Crystal system	tetragonal	tetragonal
a	23.69432	23.83394
c	20.66921	20.77149
Volume ($Å^3$)	11604	11799
Zero / 2q-offset (°)	-0.0027	0.0004

Whereas the indexing process evidenced six spurious weak lines in the SOLEIL data, none were found in the diffractogram collected at the APS. In the latter case, all relevant Bragg peaks down to the weakest peaks are accounted for by the suggested unit cell. The LeBail fitting of both the SOLEIL and the APS data showed that all observed Bragg peaks can be accounted for by the tetragonal unit cell and the high symmetry space group $P\ 4_2/n\ c\ m$ [#138]. As polymeric $Fe_4S_4(DMBDT)_2$ chains are incompatible with the diagonal mirror symmetry, the $P\ 4_2/n$ [#86] space group (a maximal subspace group of $P\ 4_2/n\ c\ m$) was chosen for a structure solution.

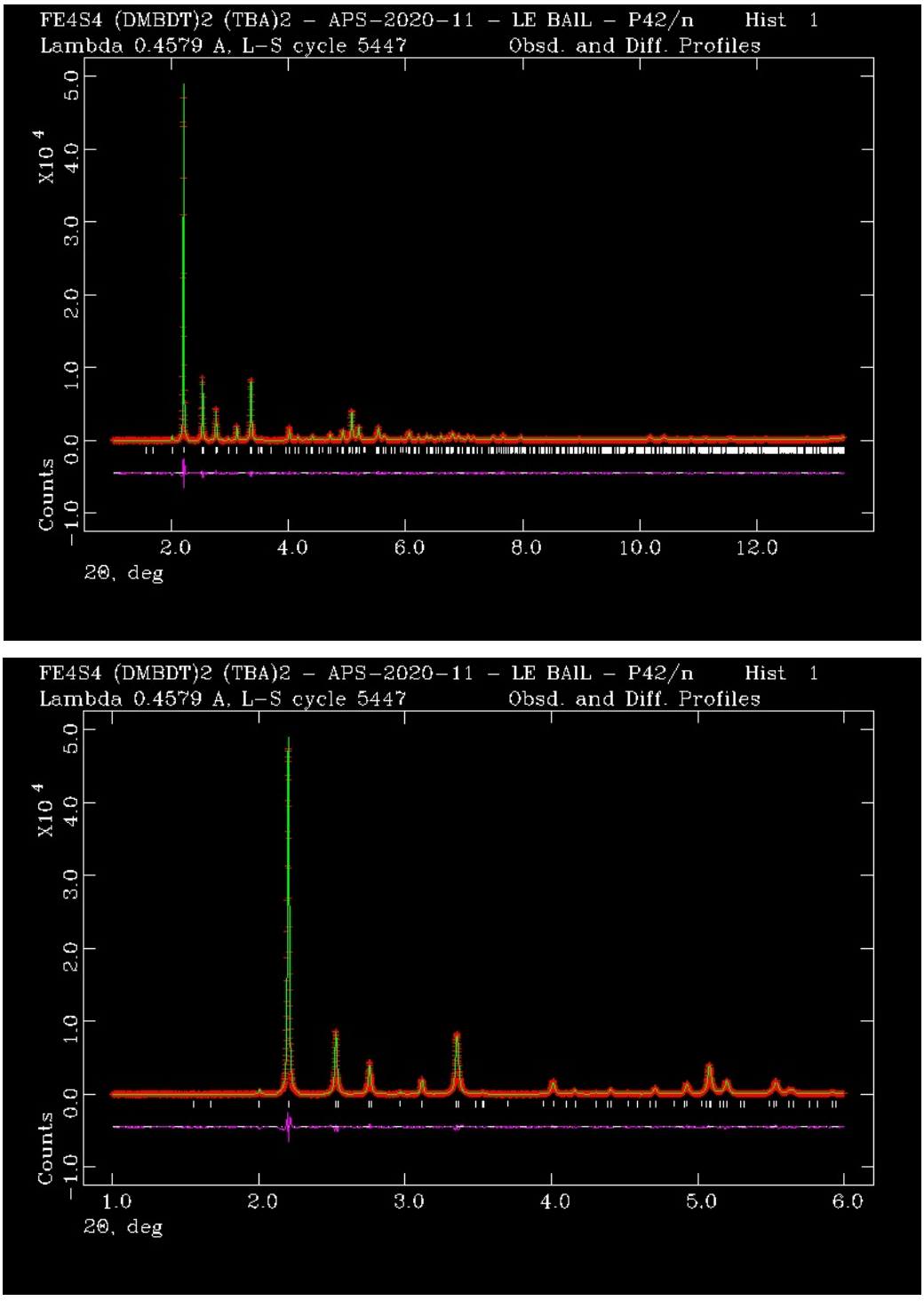

Figure B.22. LeBail refinement plots in P 42/n [#86] (2 Å resolution angular range, top and zoomed over a smaller range, bottom) for the refinement of the structure against the APS data. The red crosses represent the observed data points, and the green line is the calculated pattern. The magenta curve is the difference pattern, plotted at the same vertical scale as the other patterns. a = 23.8143(4); c = 20.7564(3).

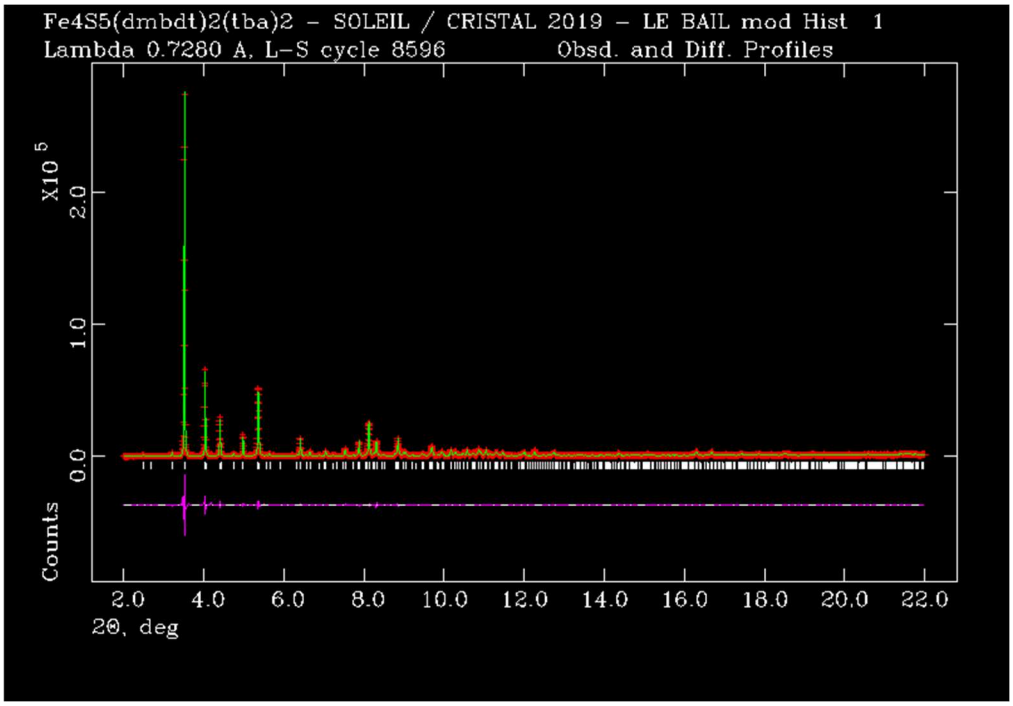

Figure B.23. LeBail refinement plots in $P\,4_2/n$ [#86] for the refinement of the structure against the SOLEIL/CRISTAL data (2 Å resolution angular range). The red crosses represent the observed data points, and the green line is the calculated pattern. The magenta curve is the difference pattern, plotted at the same vertical scale as the other patterns. a = 23.6904(2); c = 20.6668(2).

The initial Simulated Annealing runs using FOX[4] confirmed the plausibility that the structure may contain similar building blocks as observed in previously reported structures. The simulation was carried out assuming a less symmetric tetragonal $P4_2$ space group and $Fe_4S_4(DMBDT)_2$, and NC_8 rigid units, where the latter replaced the flexible TBA cations actually present in the crystal structure. In the obtained plausible solution, the positions of NC_8 units as replacements of TBA units are not correct but the 1D chains of $Fe_4S_4(DMBDT)_2$ are clearly recognizable.

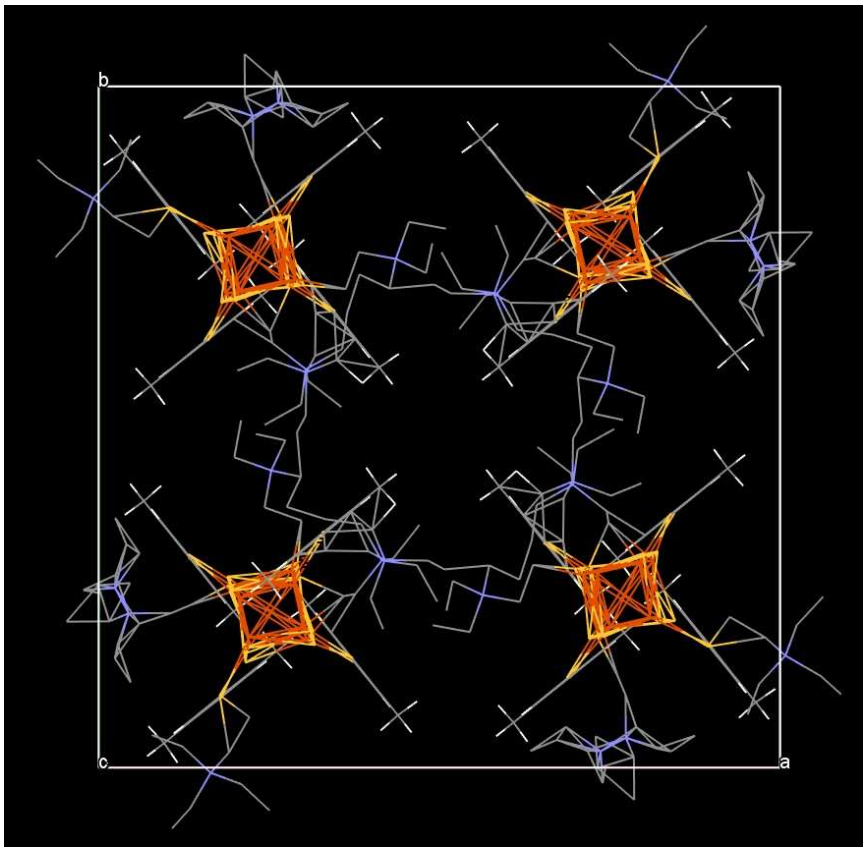

Figure B.24. Result of Simulated Annealing run using FOX and the APS data as visualized in the CCDC/Mercury software.[5]

The model of the polymeric $Fe_4S_4(DMBDT)_2$ chain was built using a previously reported chain containing a Fe_4S_4 cluster and a not-methylated dithiol ligand. To create the various parts of the crystal structure (positioned 1D chain and two independent TBA molecules sitting at two distinct Wyckoff positions), scripts written in PYTHON programming language were utilized (available as a part of a Supporting Information submission file). Each program generates (1) a LOG file for debugging, (2) a GSA file to enter the list of atoms into GSAS "in one click", and (3) a SHELX-format RES file for structure visualization. To further improve on the initial structure model and to avoid restrained Rietveld refinement that is prone for failure due to numerous required restraints, an additional Python script was written with the purpose of rotating fragments of the crystal structure around any axis (defined by any two atoms, real or fictious) and using any angular

stepping (we found 1° to be convenient) and any angular range (available as a part of a Supporting Information submission file).

The main purpose of this script is to rotate suitable local parts of the structure to remove too small short contacts and bring those close to their van der Waals values. The optimally rotated DMBDT molecules were determined in such a way as to adjust the H-H contacts to their van der Waals value of 2.4 Å. The above procedure resulted in two optimal configurations corresponding to the rotation of the two DMBDT sides by 19° (to adjust H-H contact) and to 65° (to further allow for the Fe-C van der Waals contacts [3.7 Å]) with respect to the main chain.

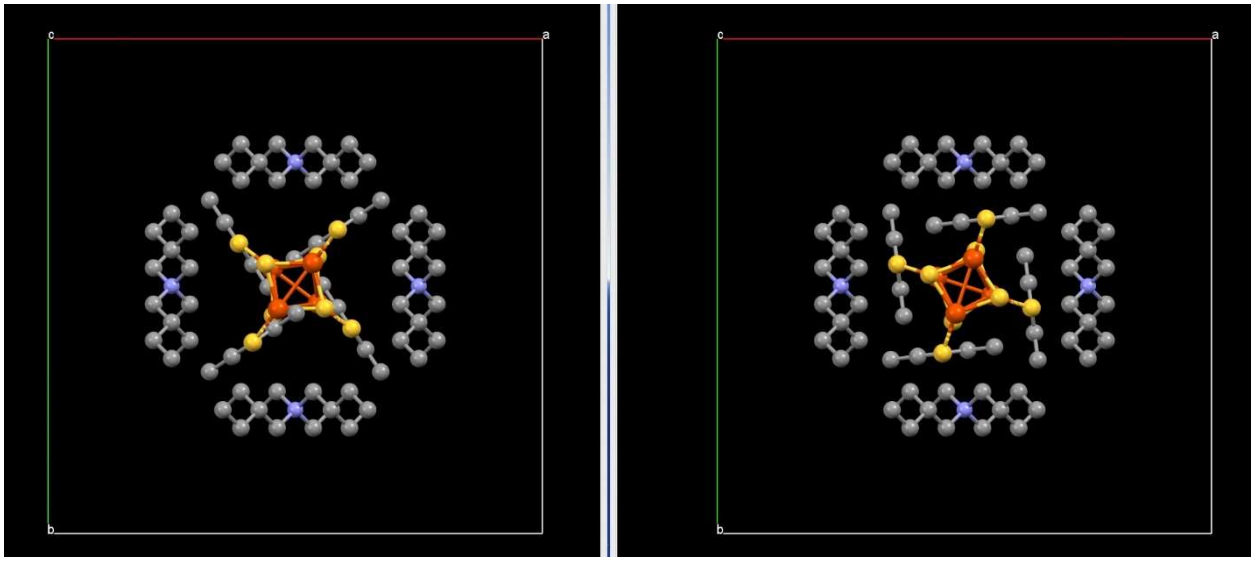

Figure B.25. Two optimal structures as results of rotations of the two DMBDT sides by 19° (left) or 65° (right) with respect to the main 1D chain.

Once the two independent DMBDT rings have been rotated by 19°, the whole 1D polymeric chain must itself be counter-rotated by -8° (ca. -0.42*19 °) to leave as much space as possible for the TBA cations. In the second case (65°), the counter-rotation angle is -27° (approx -0.42*65°). The model with 65° rotation was rejected based on the subsequent inferior Rietveld least-squares

results with a much higher R(F2) factor of merit and especially high refined Texture Index value (associated with a preferred orientation as modeled with spherical harmonics).

For symmetry reasons, the N atoms of TBA molecules were placed at midpoints between the centers of neighboring Fe_4S_4 clusters. This choice leads to the [0 1/4 1/4] and [0 3/4 1/4] independent positions in the unit cell. The positioning of the TBA moieties (in spite of an apparent but deceptive two-fold indetermination) was unequivocally chosen to produce the largest S-C interatomic contacts between the chains and the TBA molecules, in good agreement with the associated van der Waals distance [3.5 Å].

The 19° model was used for the final Rietveld refinement using the GSAS software package producing a final Rp value of 14.8%. A less than perfect fit is obtained due to the need to use more symmetric and rigid molecular subunits and a need to describe rather flexible crystal structure with an average highly symmetric structure. For example, missing intensity in the peak observed at about 2.7 degrees 2q can be pumped by moving Fe_4S_4 cluster slightly away from the perfect alignment along the *c* axis without changing the intramolecular geometry.

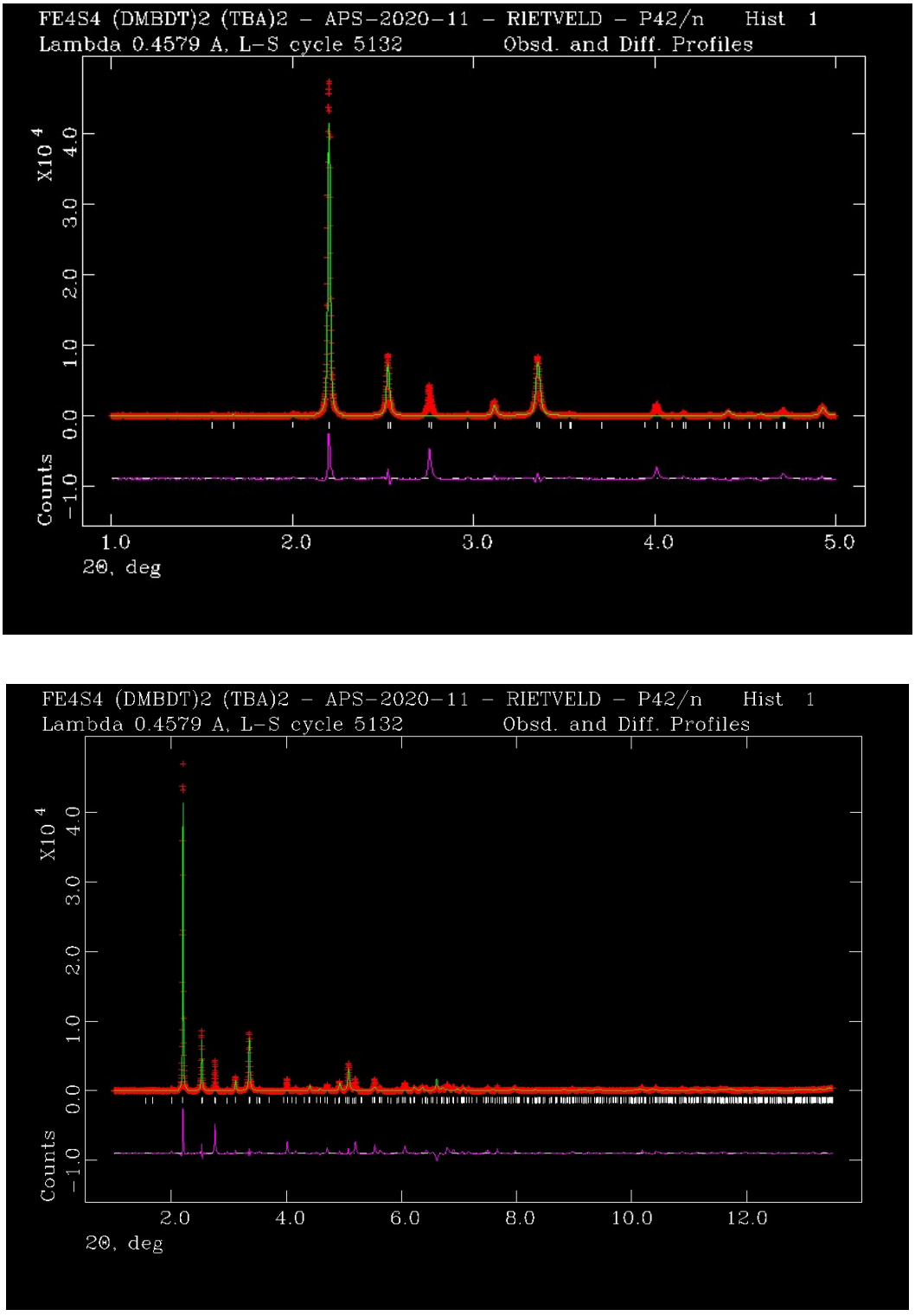

Figure B.26. Rietveld least-squares refinement plots (different scales above and below figures) of our proposed crystal structure solution. The red crosses represent the observed data points, and the green solid line is the calculated pattern. The magenta curve is the difference pattern plotted at the same vertical scale as that of the other two patterns.

Table B.4. Structural parameters and refinement results based on 1D [11-BM/APS] synchrotron powder X-ray diffraction data.

Chemical formula (unit cell)	**C 384 H 704 Fe 32 N 16 S 64**
Z	**8**
Crystal system	Tetragonal
Space group (#)	$P\,4_2/n$ (# 86)
X-ray data	
Wavelength (Å)	0.45793
2θ range (°) , 2θ step (°)	1.000 – 13.500 , 0.001
Unit cell (GSAS) LE BAIL REFINEMENT	
a (Å)	23.814318(366)
b (Å)	23.814318(366)
c (Å)	20.756374(311)
α (°)	90.0
β (°)	90.0
γ (°)	90.0
V ($Å^3$)	11771.4(5)
Molecular unit	**C 48 H 88 Fe 4 N 2 S 8**

Mol.wt. (g/mol)	1173.12
Calculated ρ (g/cm3)	1.323
(GSAS) RIETVELD REFINEMENT	
Observed reflections	854
Variables	49
Restraints	None (see text)
Rp (%)	0.1488
Rwp(%)	0.2181
$R(F^2)$	0.2607
Reduced χ^2	30.18
Refinable U overall_isotropic	0.000
Preferred Orientation Spherical harmonics order Texture Index	 10 1.778

The crystal structure of $Fe_4S_4(DMBDT)_2*(TBA)_2$ consists of chains of Fe_4S_4 clusters connected by pairs of DMBDT groups surrounded by TBA cations. Another way to look at the suggested crystal structure is in terms of TBA-built tubes or TBA-sheaths surrounding each of 1D $Fe_4S_4(DMBDT)_2$ polymeric chain.

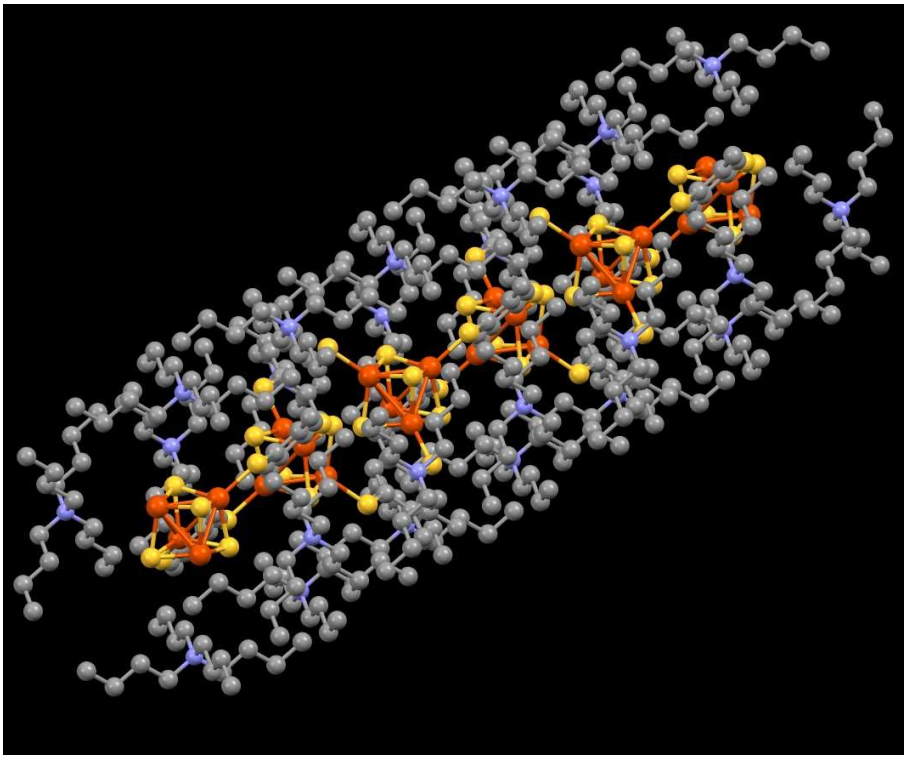

Figure B.27. TBA-built tubes surround each and every of 1D $Fe_4S_4(DMBDT)_2$ polymeric chain.

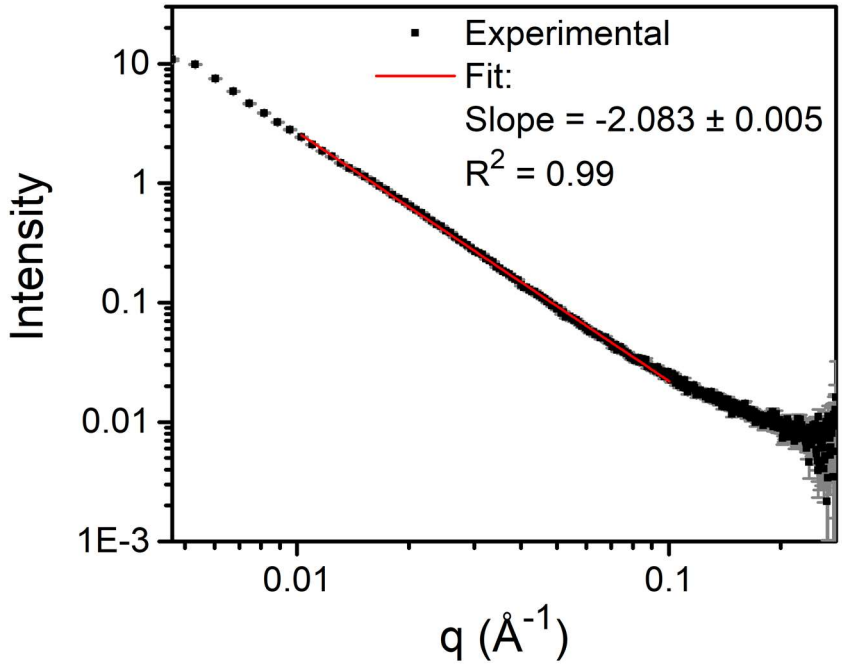

Figure B.28. Small-angle X-ray scattering (SAXS) of 3 and fit.

Small angle X-ray scattering (SAXS) experiments were performed on a SAXSLAB Ganesha equipped with a Xenocs GeniX3D Cu Kα source. SAXS samples were loaded into 1.0 mm OD × 0.01 mm wall borosilicate glass tubes and sealed under N_2 with wax. A near-saturated solution of **3** in dry DMF was prepared and passed through a 0.2 μm PET syringe filter prior to loading into the tube. A tube with neat DMF was used as the blank. SAXS data were collected in six one-hour increments and compared to check for radiation damage, which was not found. All experiments were performed at ambient temperature. Data reduction/integration was performed using Saxsgui software. Linear fits were performed in OriginPro software.

B.8 Referencess

[1] C. Morrison, H. Sun, Y. Yao, R. A. Loomis, and W. E. Buhro, *Chem. Mater.*, **2020**, 32, 1760-1768.

[2] J. Blanton, R. J. Papoular and D. Louër*, Powder Diffr.*, **2014**, 34, 233-241; b) D. Louër and A. Boultif, *Powder Diffr*., **2019**, 29, S7-S12.

[3] Altomare, C. Giacovazzo, A. Guagliardi, A. Moliterni, R. Rizzi and P.-E. Werner*, J. Appl. Crystallogr.*, **2000**, 33, 1180-1186.

[4] V. Favre-Nicolin and R. Cerny, *J. Appl. Crystallogr.*, **2002**, 35, 734-743.

[5] C.F. Macrae, I.J. Bruno, J.A. Chisholm, P.R. Edington, P. McCabe, E. Pidcock, L. Rodriguez-Monge, R. Taylor, J. van de Streek and P.A. Wood, *J. Appl. Crystallogr*., **2008**, 41, 466-470.

Appendix C:Supporting Data for Chapter 4

C.1 NMR Spectra

C.1.1 ^{1}H NMR Spectra

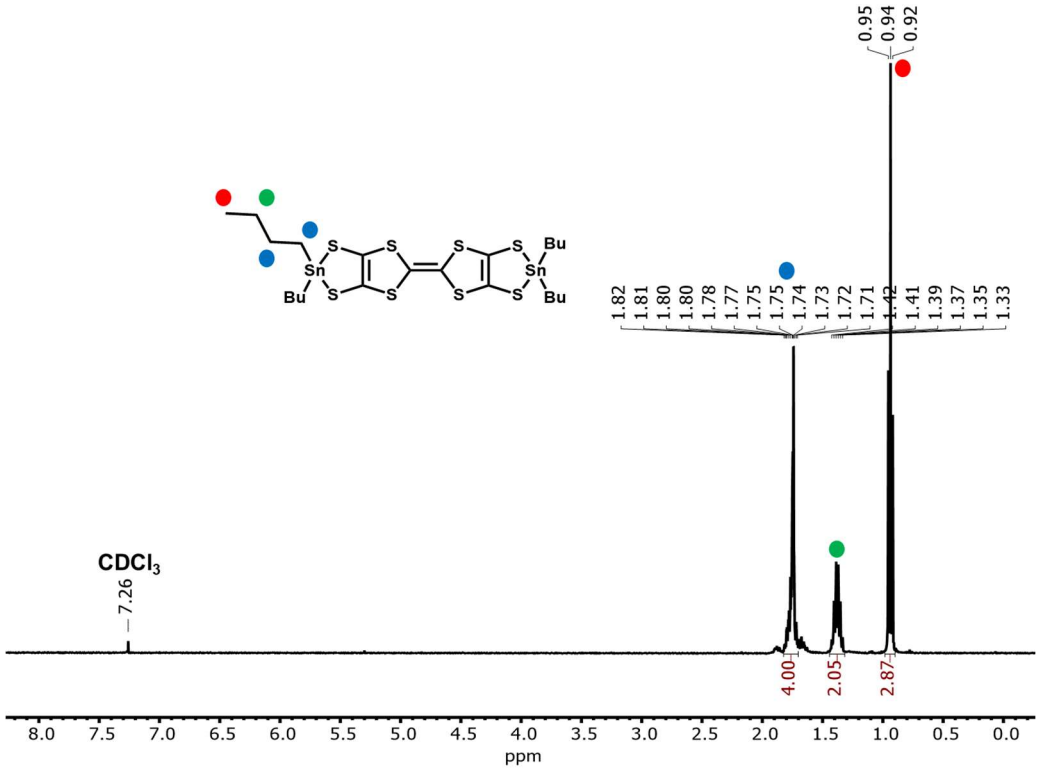

Figure C.1. ^{1}H NMR spectrum of 1 in $CDCl_3$.

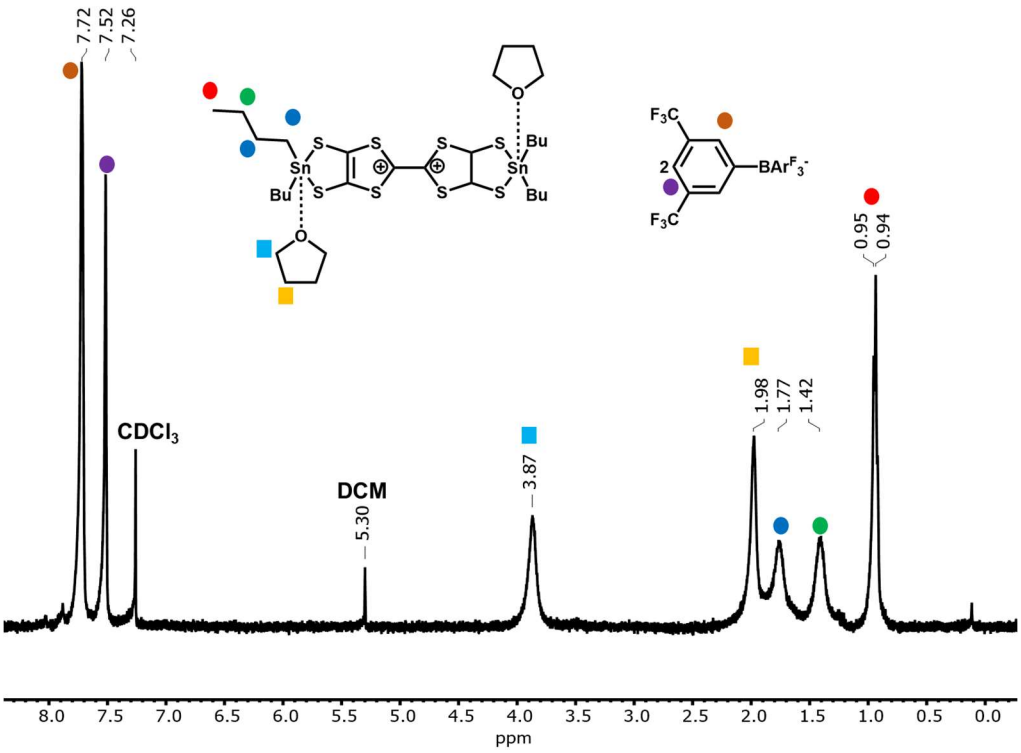

Figure C.2. ^{1}H NMR spectrum of 3•2THF in $CDCl_3$.

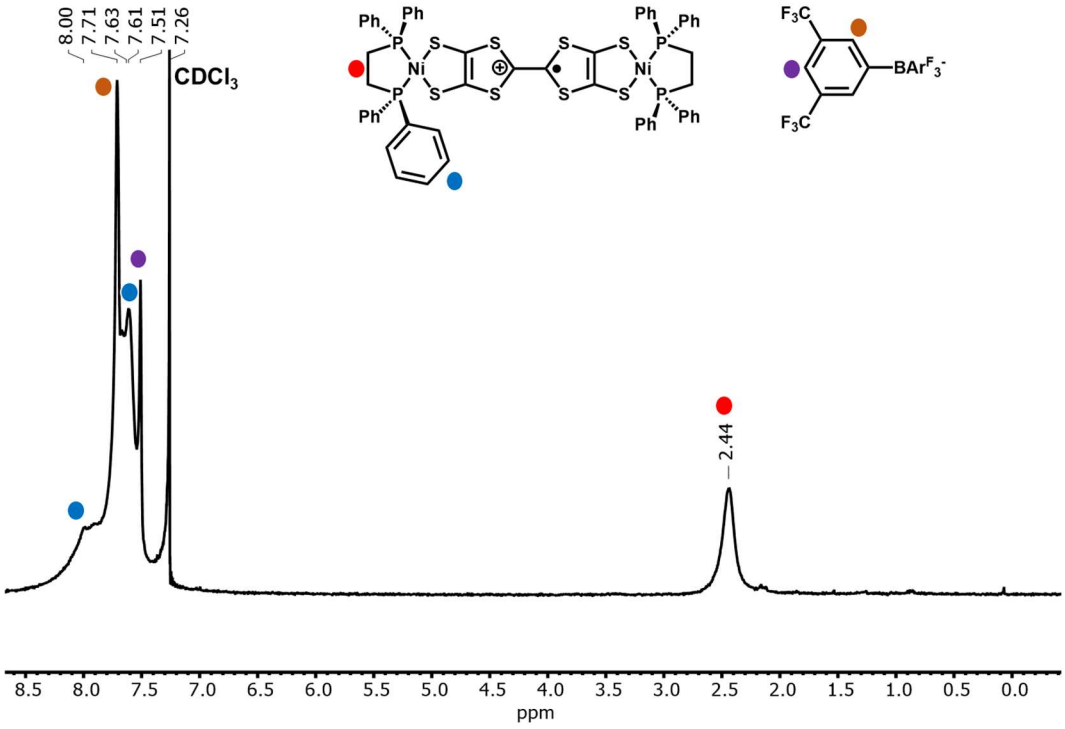

Figure C.3. ^{1}H NMR spectrum of 5 in $CDCl_3$

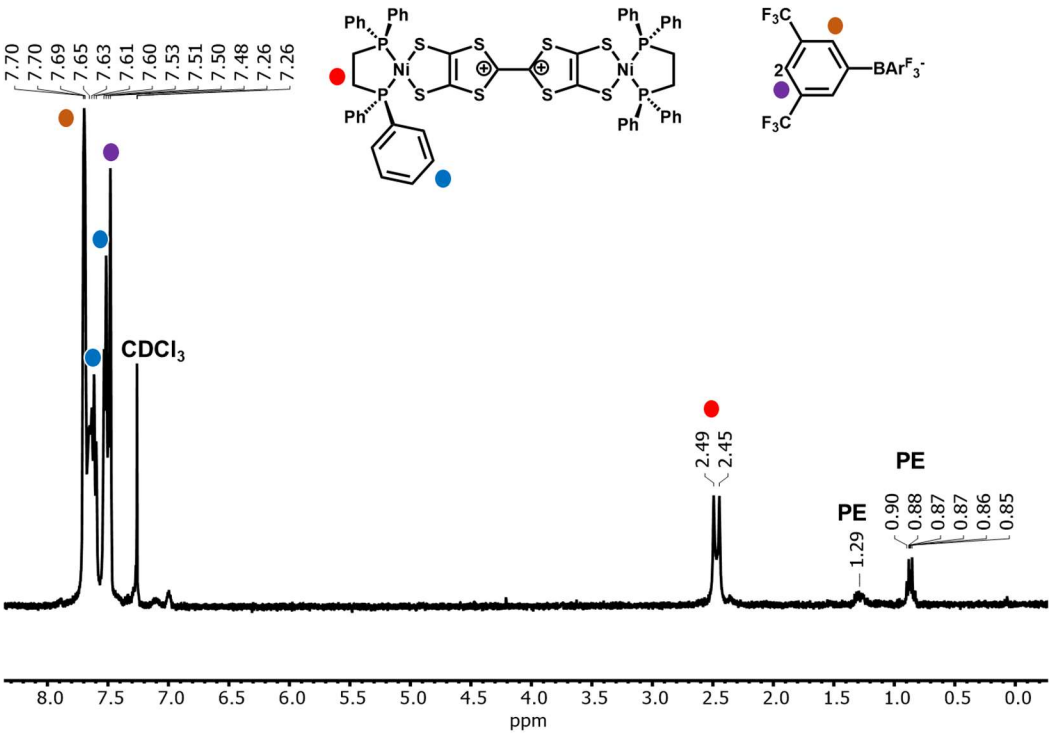

Figure C.4. ^{1}H NMR spectrum of 6 in $CDCl_3$.

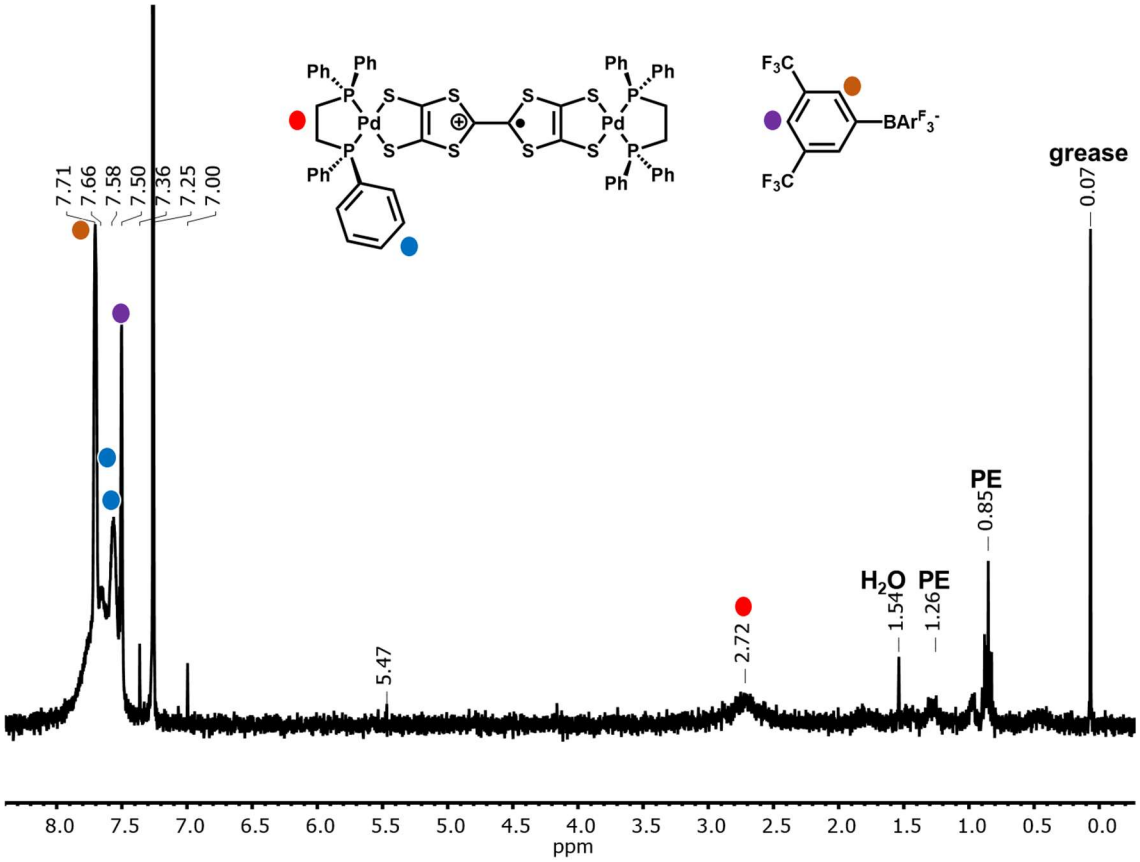

Figure C.5. ^{1}H NMR spectrum of 8 in $CDCl_3$.

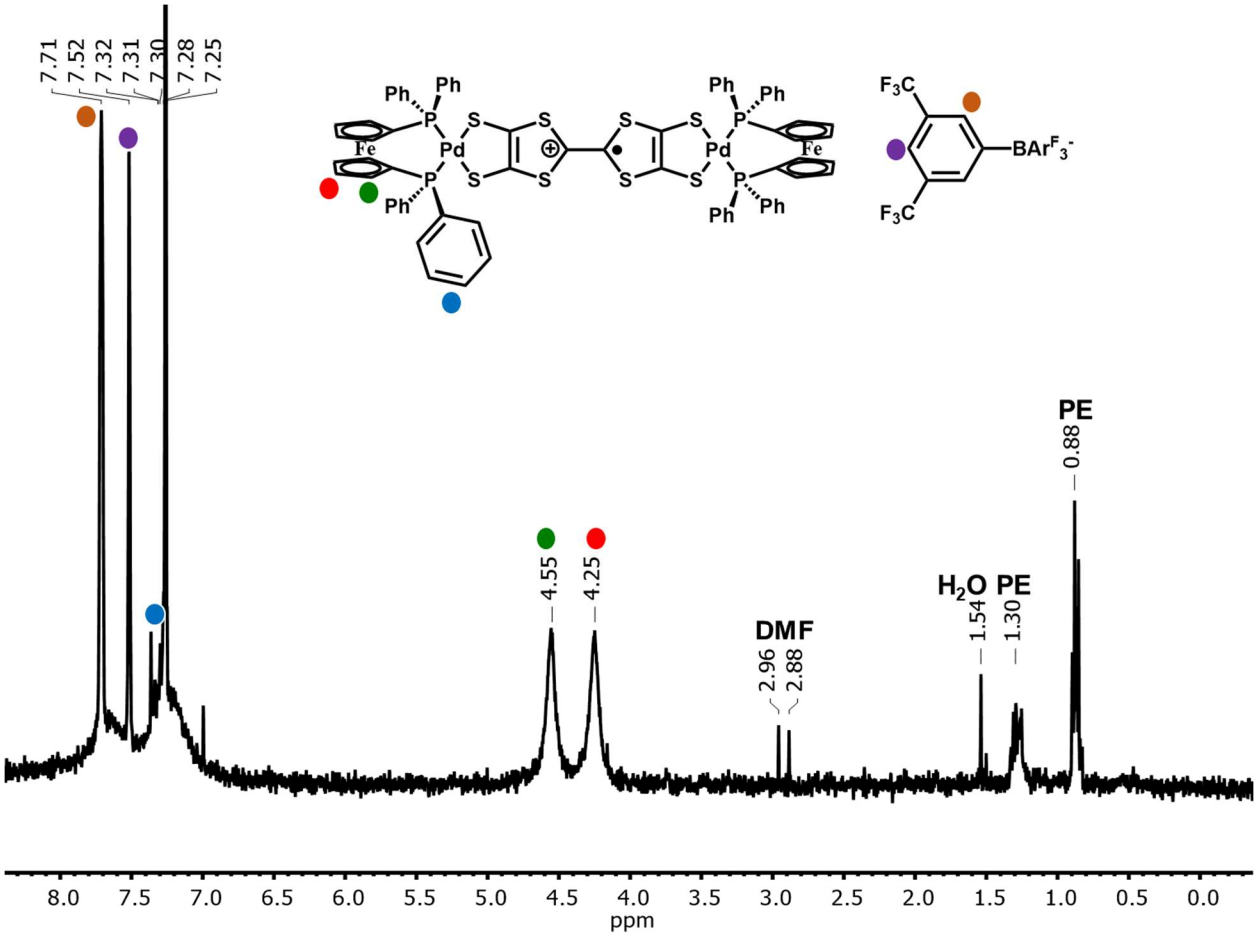

Figure C.6. ^{1}H NMR spectrum of 10 in $CDCl_3$.

C.1.2 ^{13}C NMR Spectra

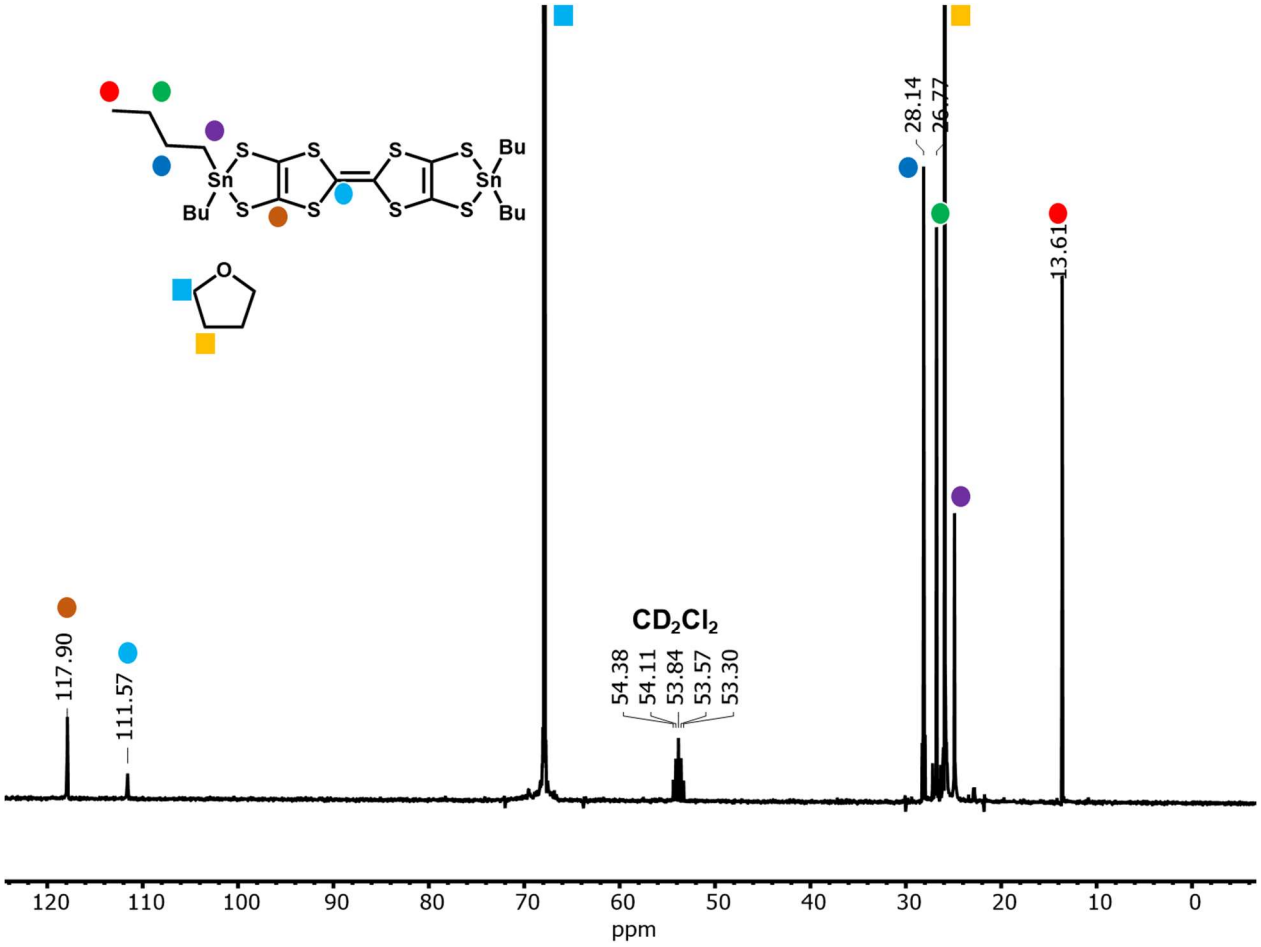

Figure C.7. ^{13}C{^{1}H} NMR spectrum of 1 in 0.5 mL THF + 0.1 mL CD_2Cl_2.

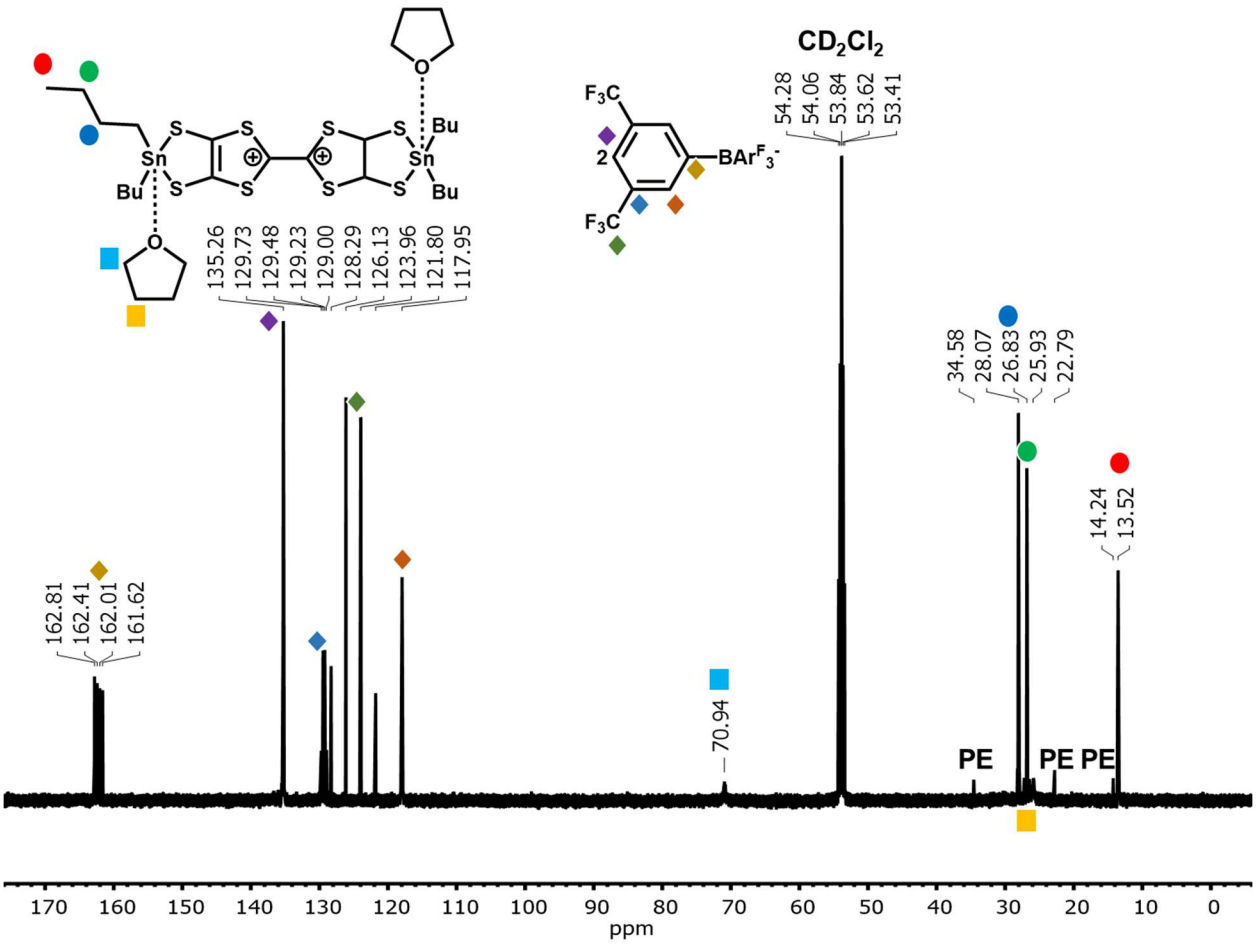

Figure C.8. $^{13}C\{^{1}H\}$ NMR spectrum of 3 in CD_2Cl_2. Due to a possible exchange with a small amount of radicals, the peaks of TTF and the first carbon of butyl groups connecting to the Sn atoms are not visible.

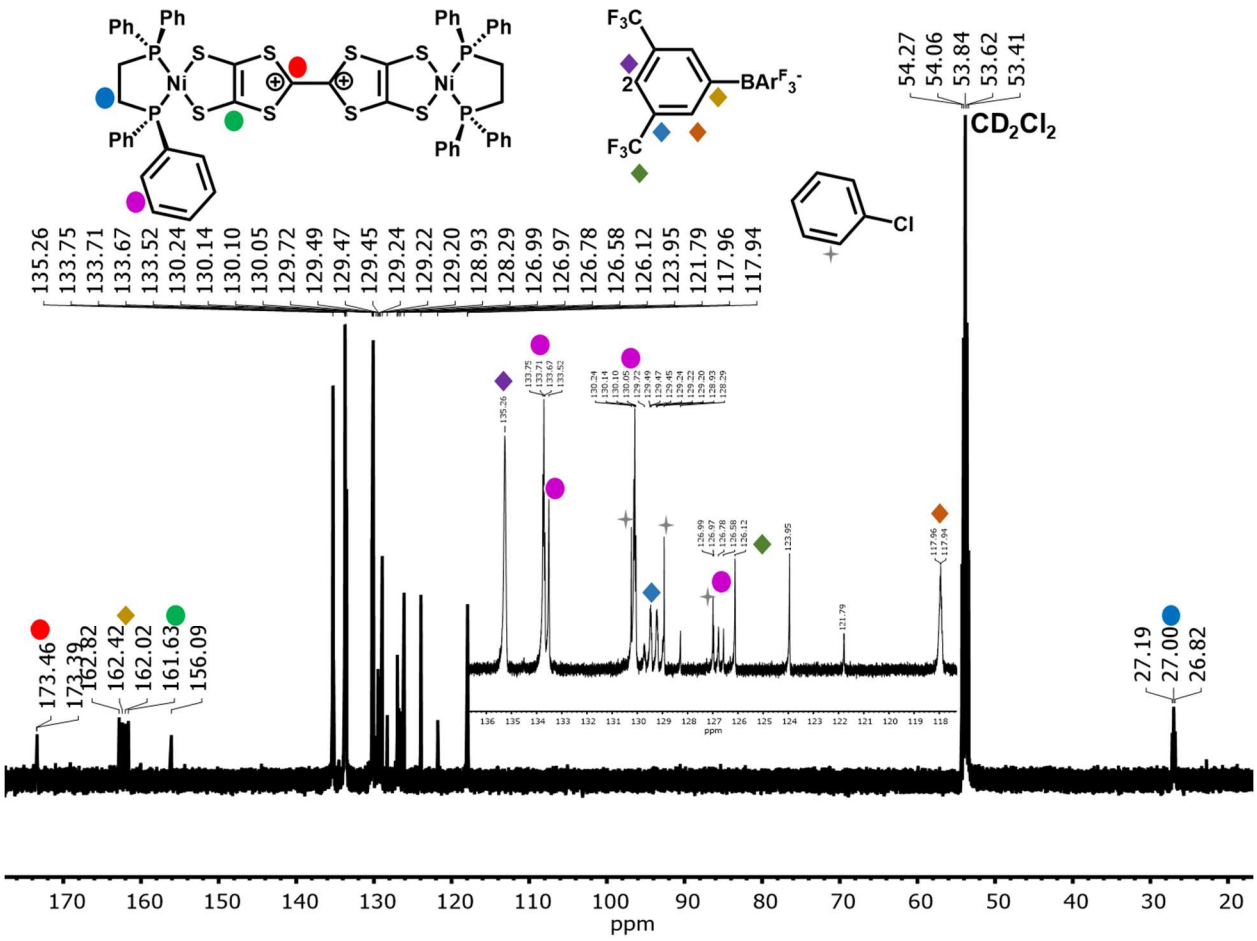

Figure C.9. $^{13}C\{^{1}H\}$ NMR spectrum of 6 in CD_2Cl_2. The spectrum from 118-136 ppm is expanded and shown in the inset graph.

C.1.3 ^{31}P NMR Spectra

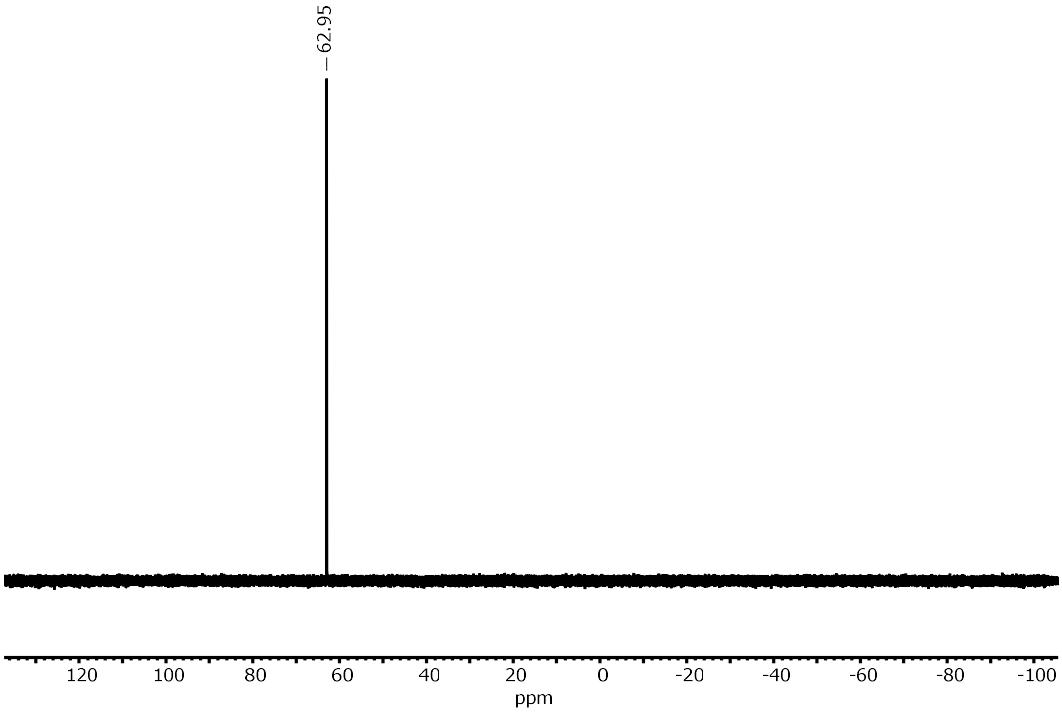

Figure C.10. $^{31}P\{^{1}H\}$ NMR spectrum of 6 in $CDCl_3$.

C.1.4 ^{119} Sn NMR Spectra

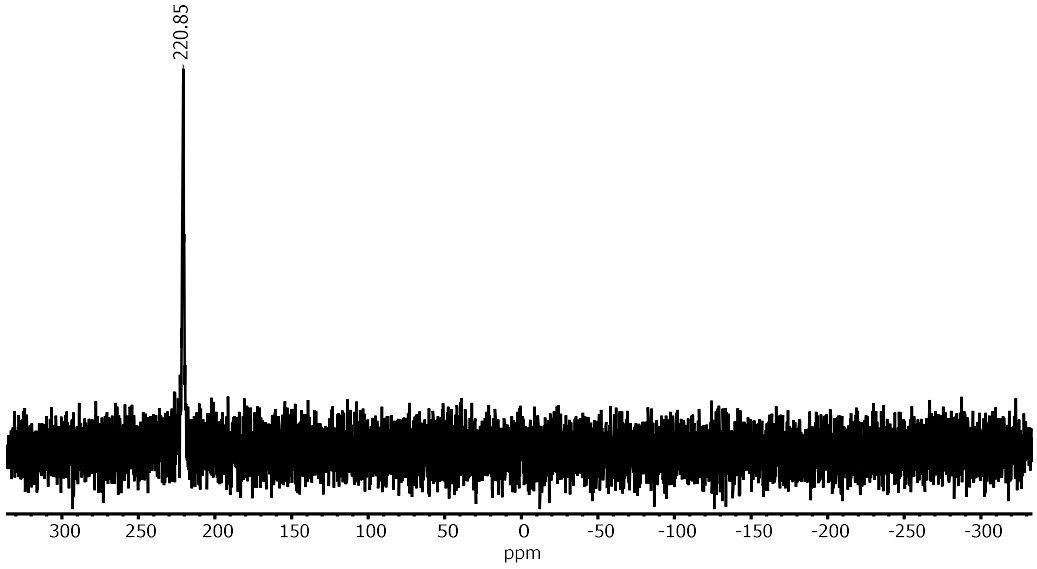

Figure C.11. $^{119}Sn\{^{1}H\}$ NMR spectrum of 1 in $CDCl_3$

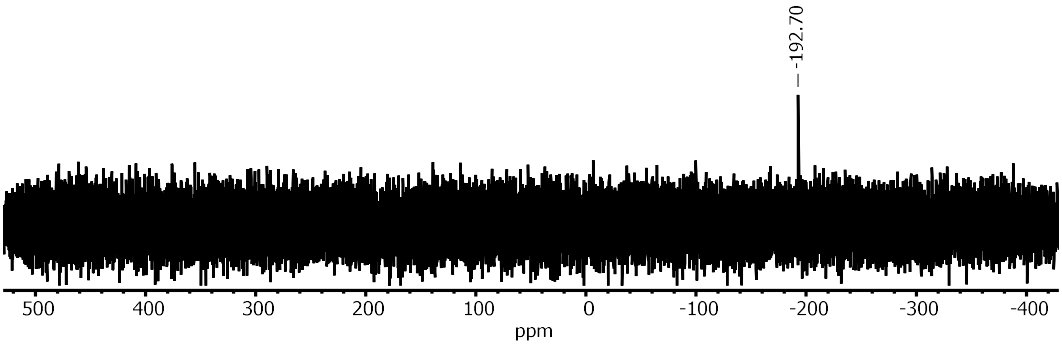

Figure C.12. $^{119}Sn\{^{1}H\}$ NMR spectrum of 3 in $CDCl_3$.

C.2 Alternative synthesis methods monitored by 1H NMR experiments

C.2.1 Synthesis of 5 by metalation of 2

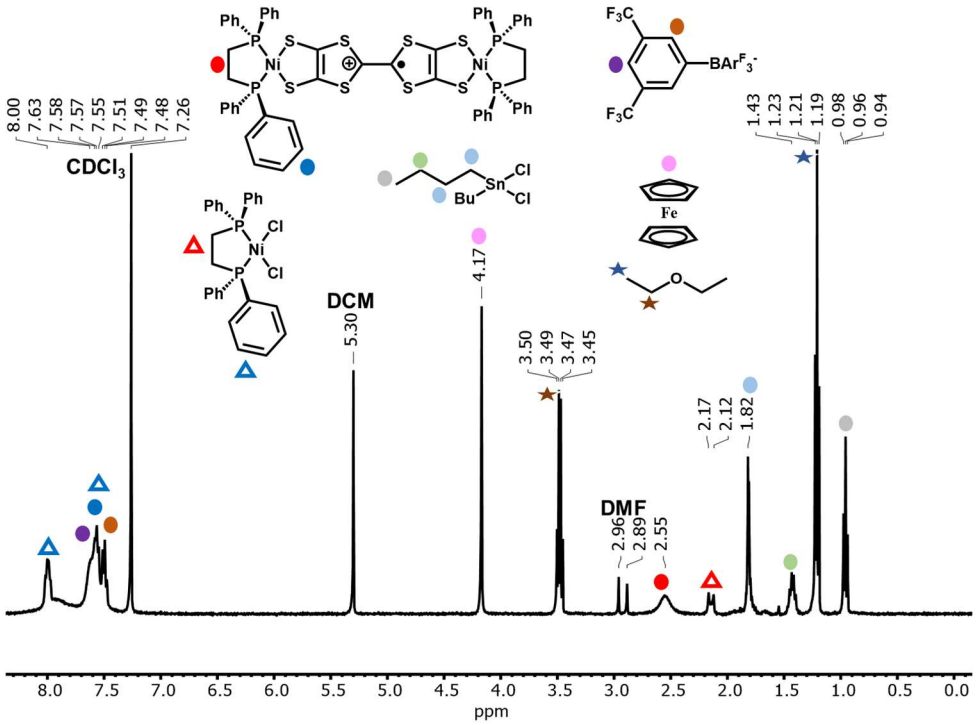

Figure C.13. ^{1}H NMR spectrum in $CDCl_3$ of metalation products of 2. Note the residual dppeNiCl_2 was due to an excess of this reagent added to the reaction.

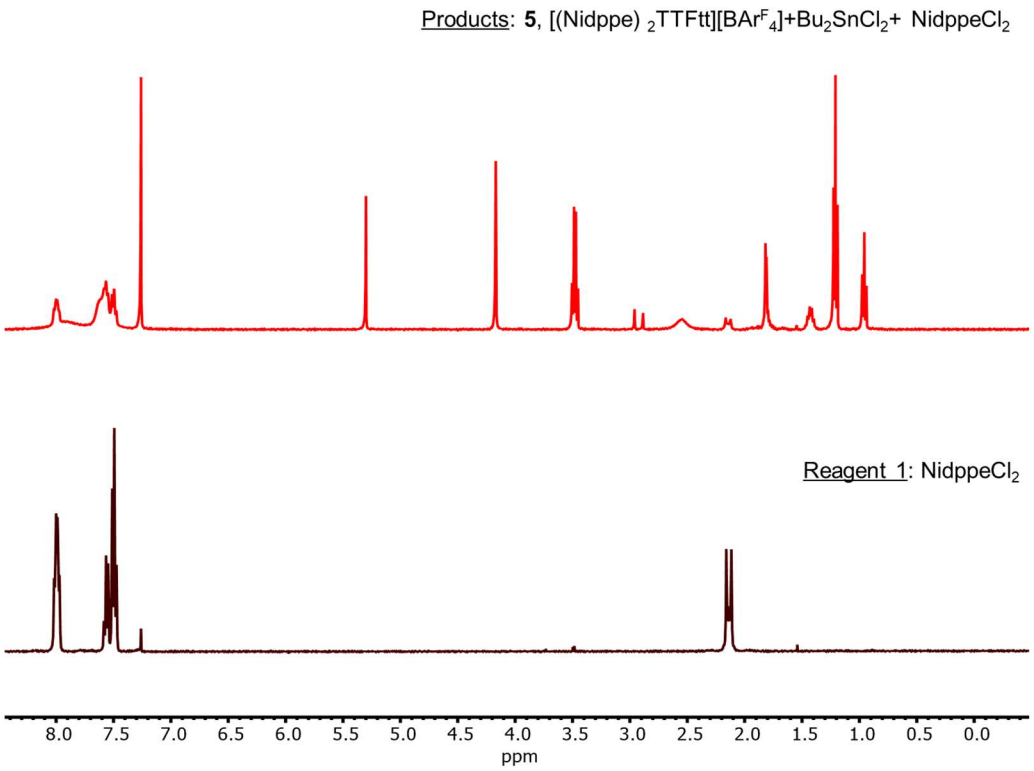

Figure C.14. ^{1}H NMR spectra in $CDCl_3$ monitoring the metalation process of 2.

C.2.2 Synthesis of 6 by metalation of 3•2THF

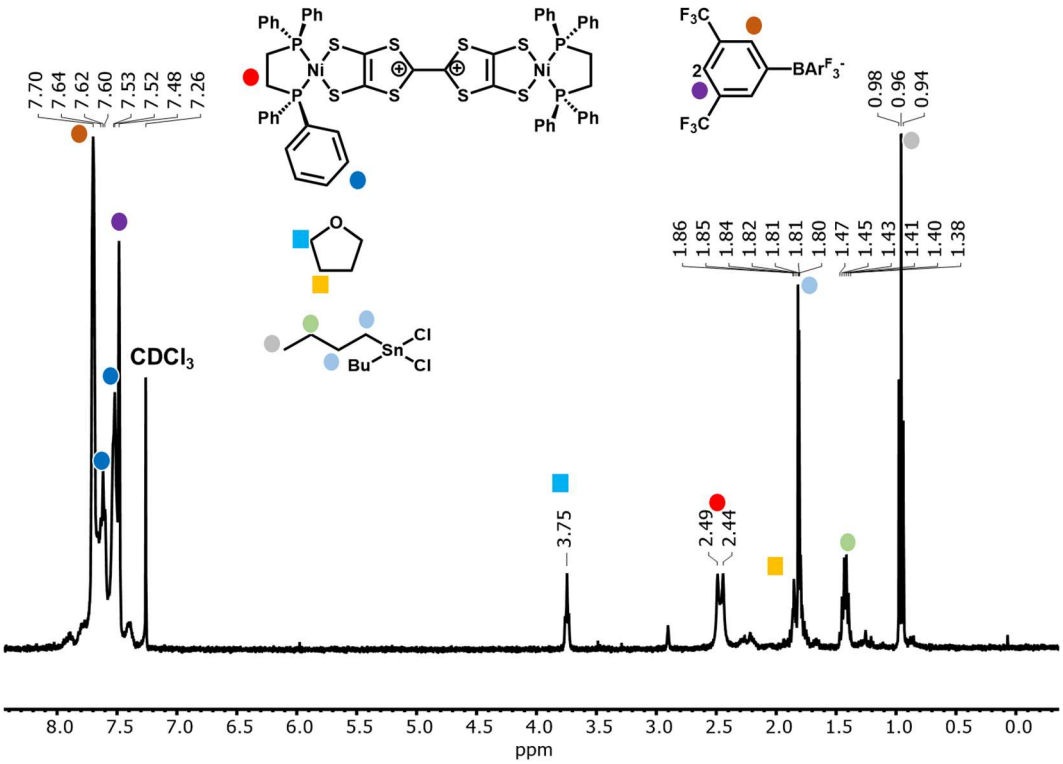

Figure C.15. ^{1}H NMR spectrum in $CDCl_3$ of metalation products of 3•2THF.

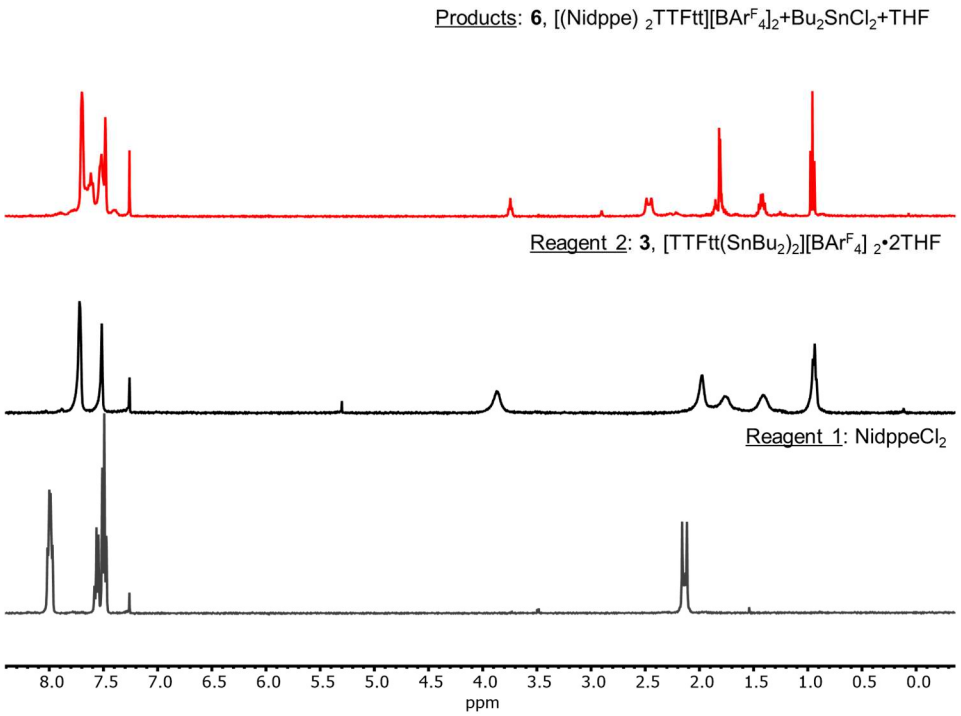

Figure C.16. ^{1}H NMR spectra in $CDCl_3$ monitoring the metalation process of 3•2THF.

C.2.3 Synthesis of 6 by metalation of 3•2Fc^{BzO}

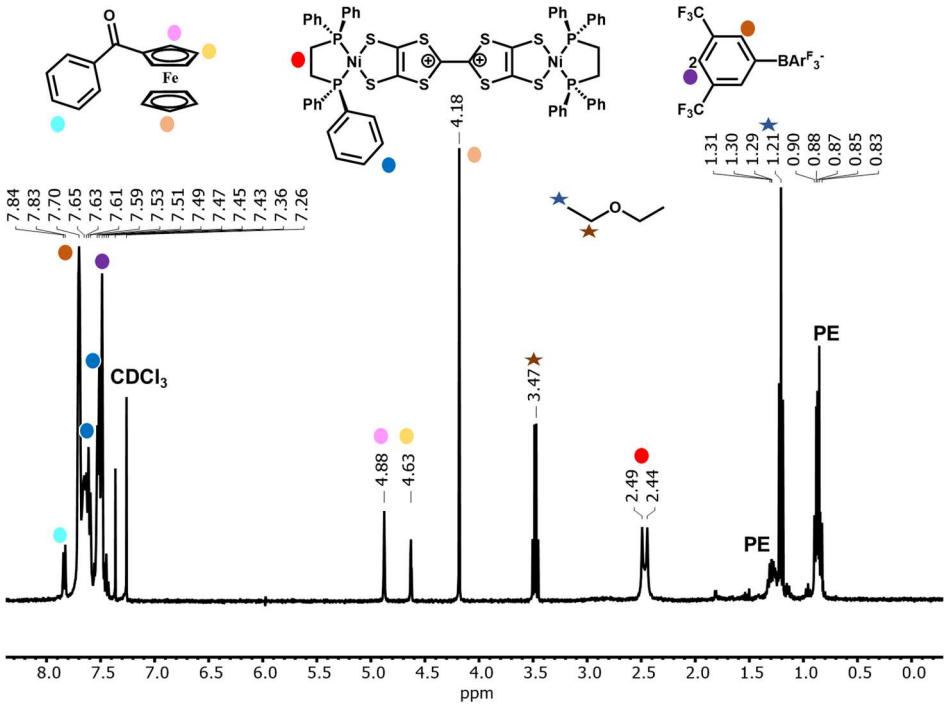

Figure C.17. ^{1}H NMR spectrum in $CDCl_3$ of metalation products of 3•2Fc^{BzO} after petroleum-ether extraction.

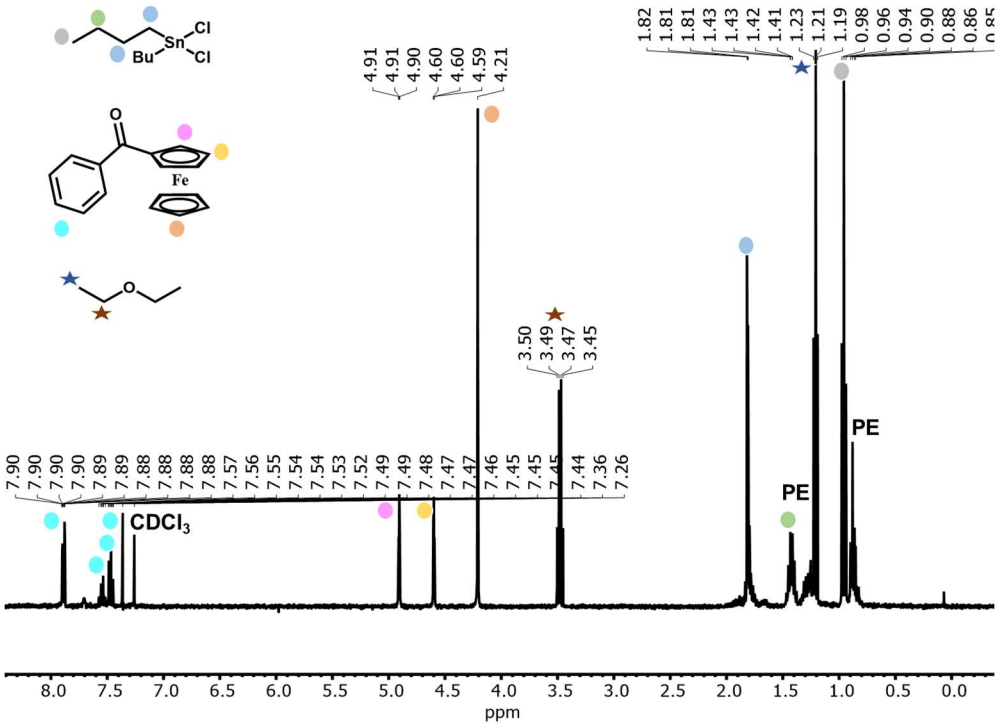

Figure C.18. ^{1}H NMR spectrum in $CDCl_3$ of metalation products of 3•2Fc^{BzO} in extracted petroleum-ether portion.

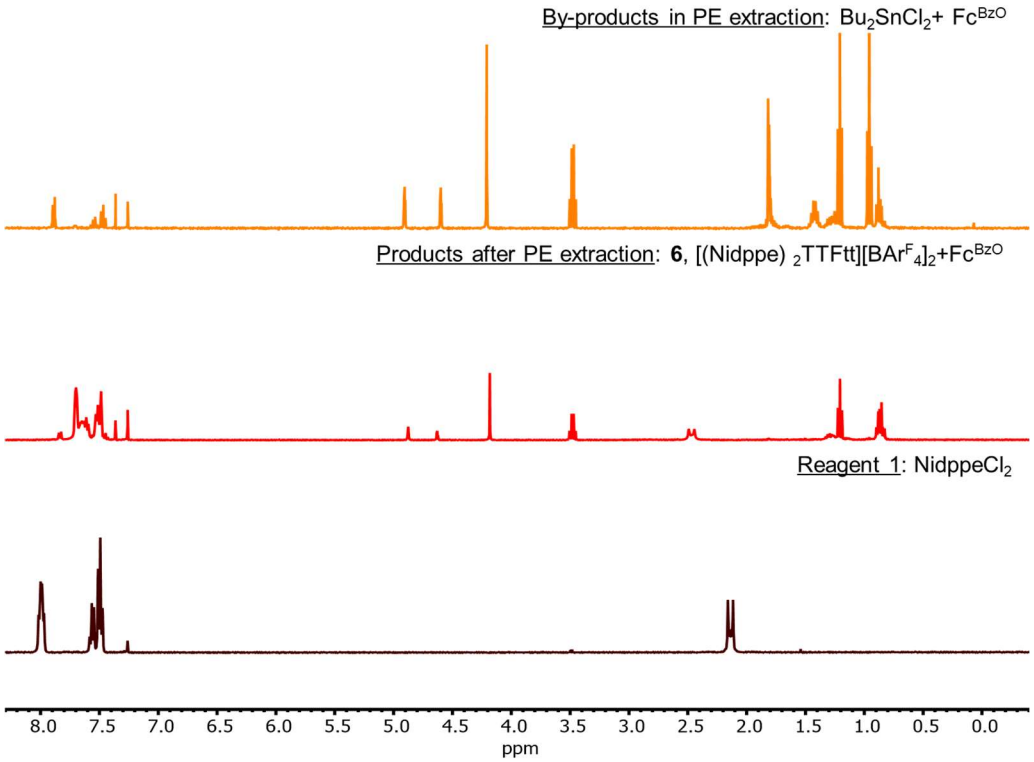

Figure C.19. ^{1}H NMR spectra in $CDCl_3$ monitoring the metalation process of 3•2Fc^{BzO}.

C.2.4 Synthesis of 6 by oxidation of 4.

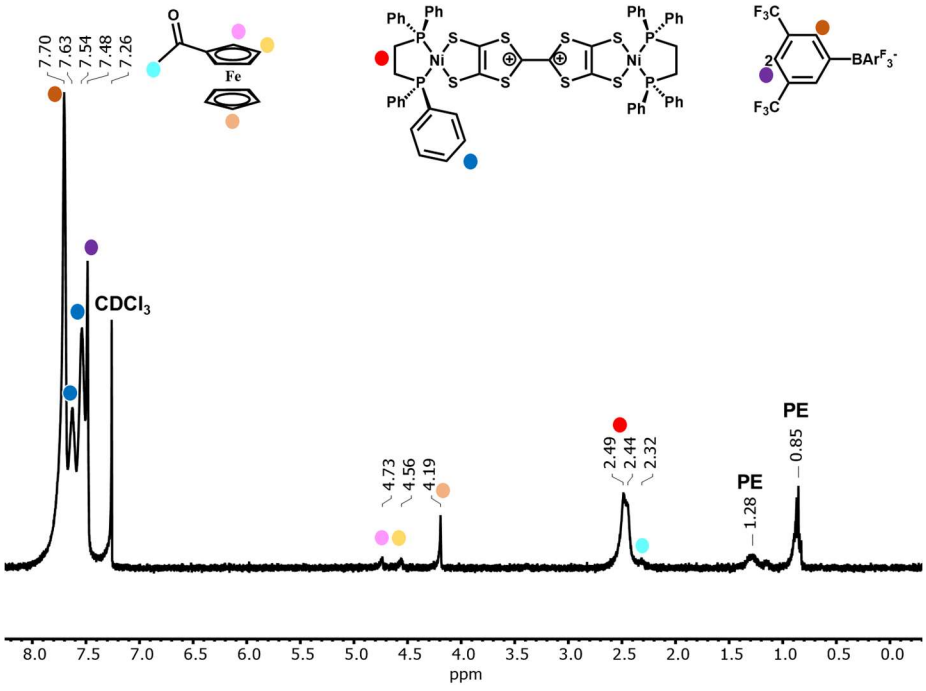

Figure C.20. ^{1}H NMR spectrum in $CDCl_3$ of oxidation products of 4.

C.2.5 Synthesis of 8 by oxidation of 7.

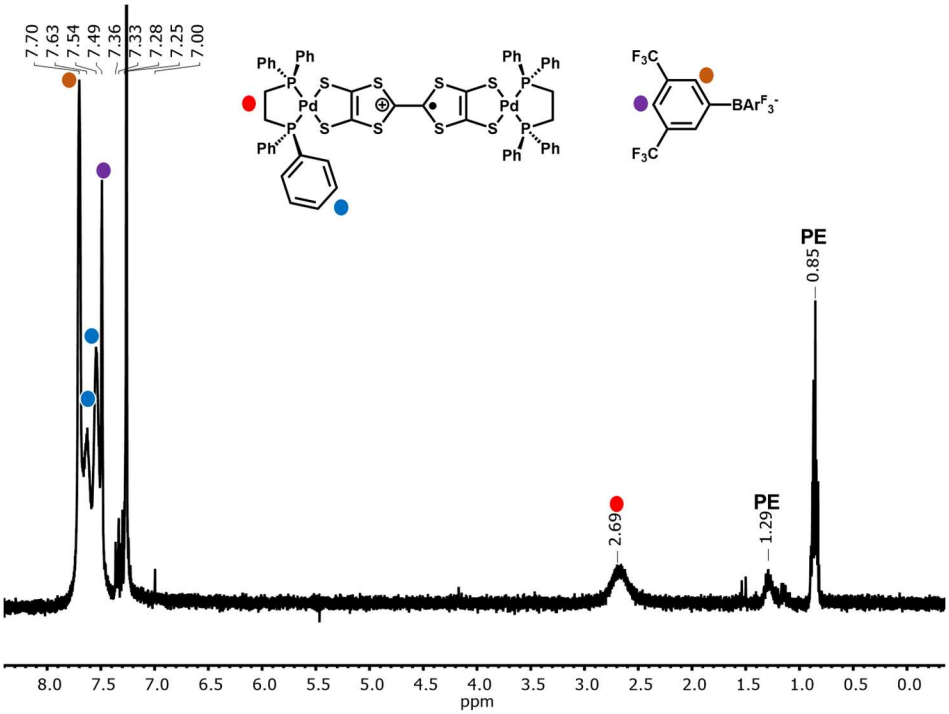

Figure C.21. ^{1}H NMR spectrum in $CDCl_3$ of 8 via oxidation of 7.

C.2.6 Synthesis of 10 by oxidation of 9.

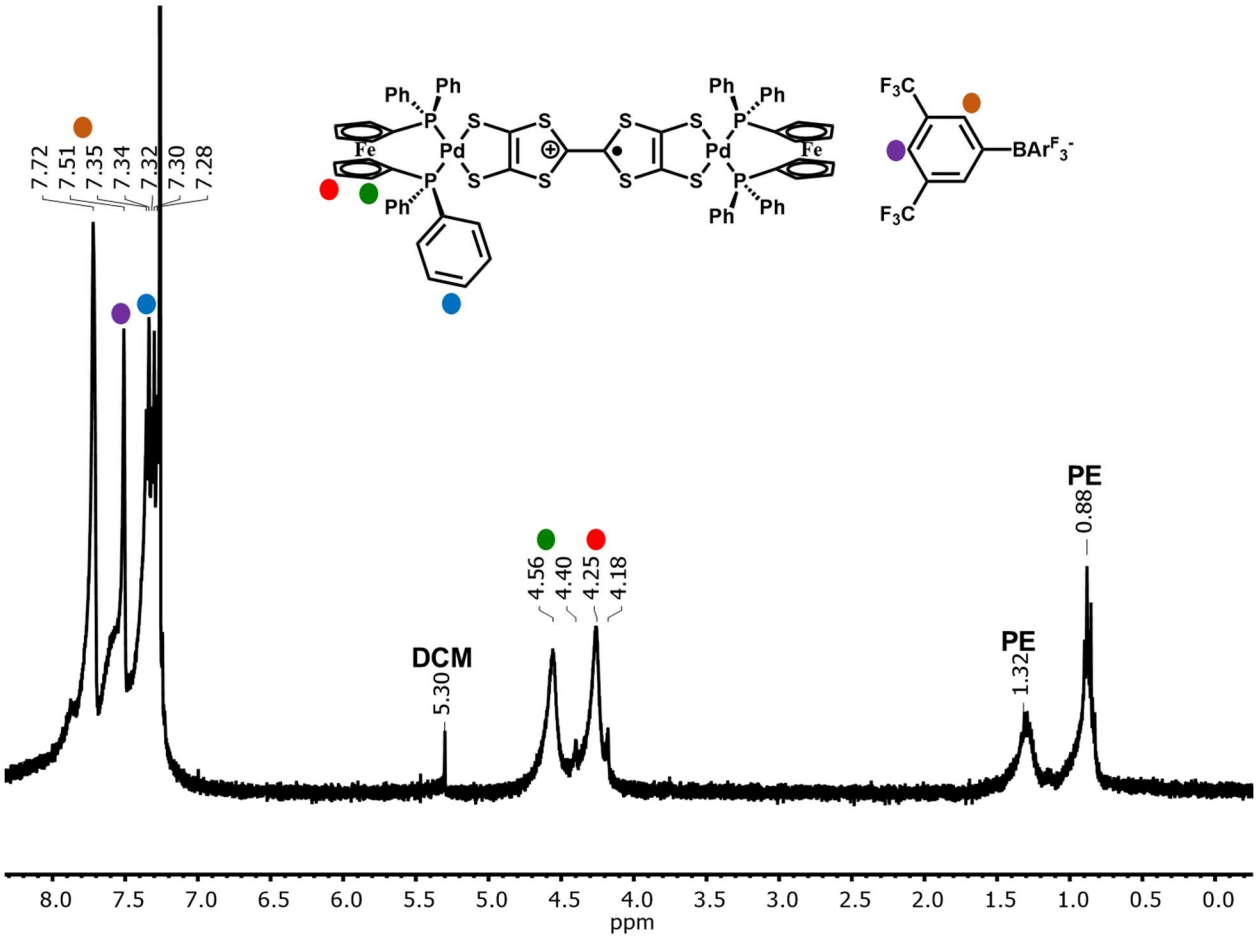

Figure C.22. ^{1}H NMR spectrum in $CDCl_3$ of 10 via oxidation of 9. Two additional peaks at 4.18 and 4.40 ppm are assigned as probably mixed 9.

C.3 Air stability test of 6 monitored by ^{1}H and ^{31}P NMR spectra

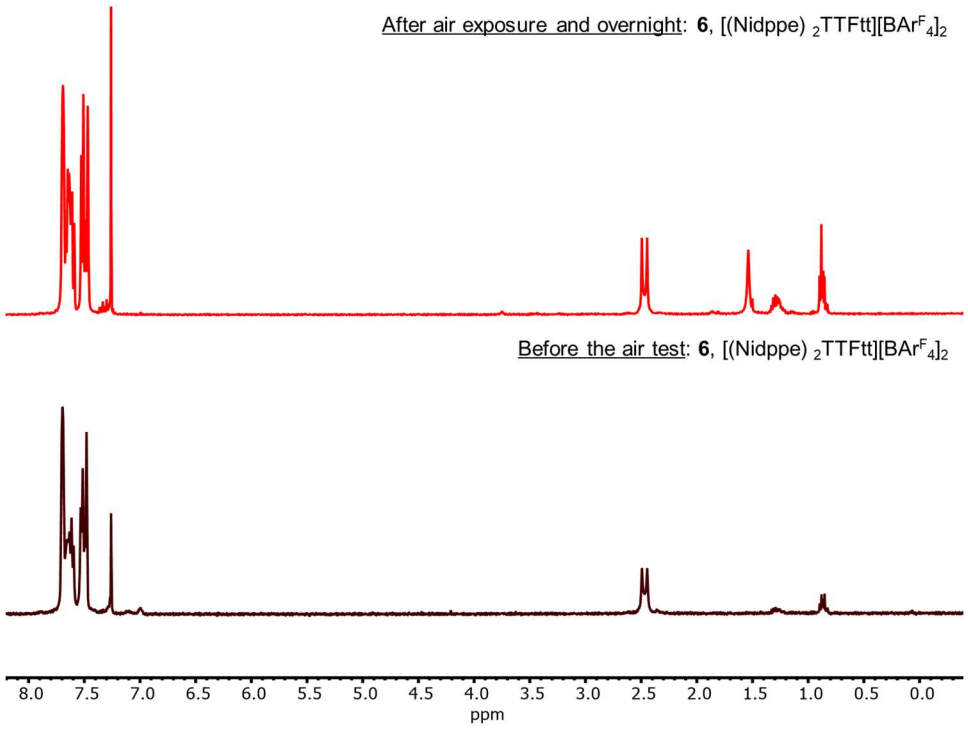

Figure C.23. ^{1}H NMR spectrum of 6 in $CDCl_3$ before and after air exposure for 35 mins and sealed placement overnight.

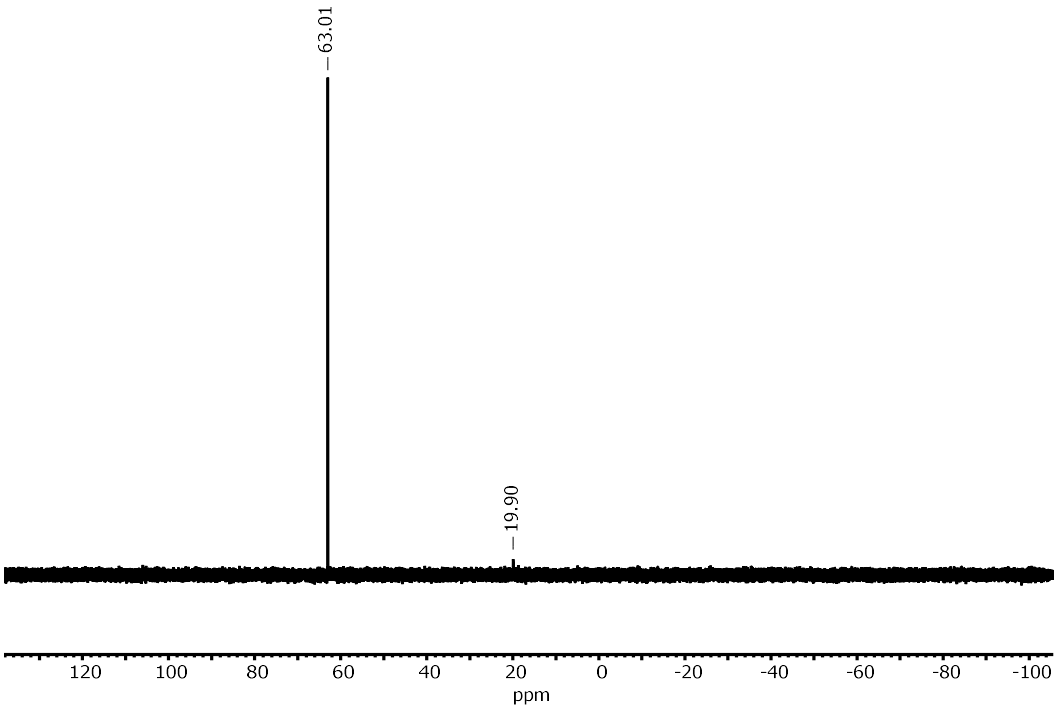

Figure C.24. ^{31}P{^{1}H} NMR spectrum of 6 in $CDCl_3$ after air exposure for 35 mins and sealed placement overnight.

C.4 EPR Spectra

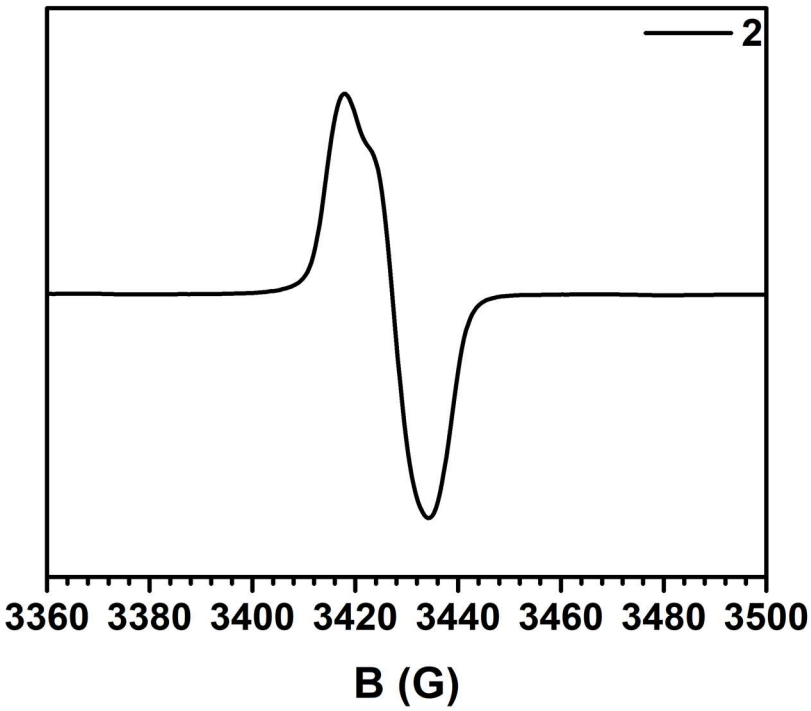

Figure C.25. X-band EPR spectrum of 2 collected on a 3 mM solution in THF at 15 K. Microwave frequency: 9.63 GHz, microwave power: 6 μW, and g_{eff} = 2.008.

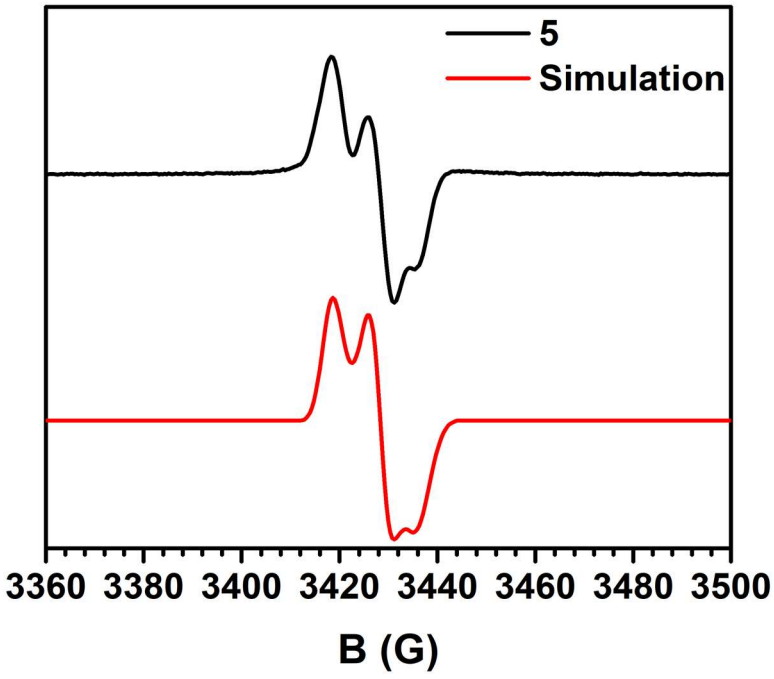

Figure C.26. X-band EPR spectrum of 5 collected on a 1 mM solution in THF at 15 K. Microwave frequency: 9.63 GHz, microwave power: 0.2 μW, and g_{eff} = 2.013, 2.007, 2.003.

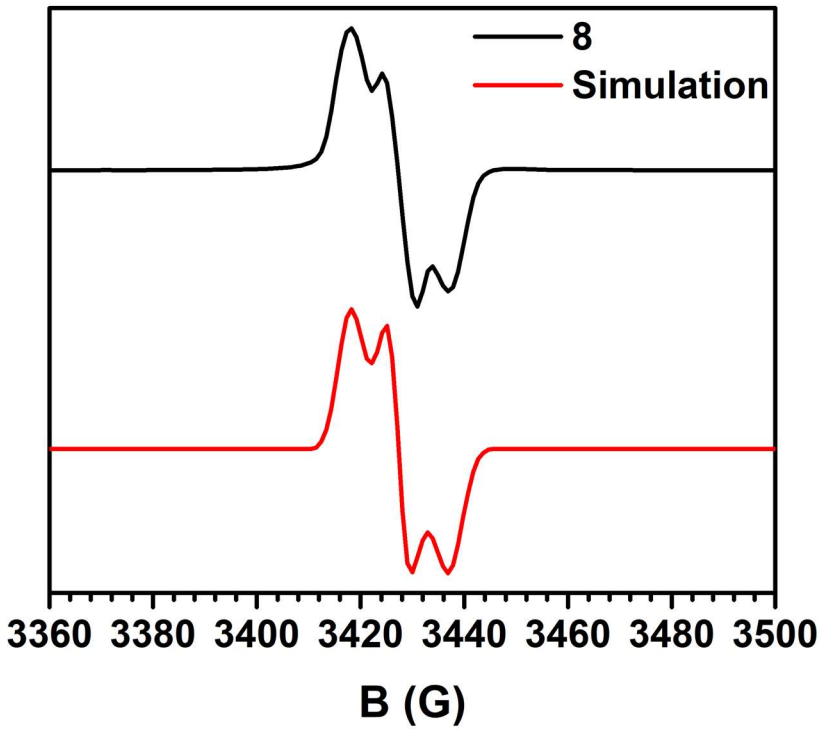

Figure C.27. X-band EPR spectrum of 8 collected on a 1 mM solution in THF at 10 K. Microwave frequency: 9.63 GHz, microwave power: 1 μW, and g_{eff} = 2.013, 2.008, 2.002.

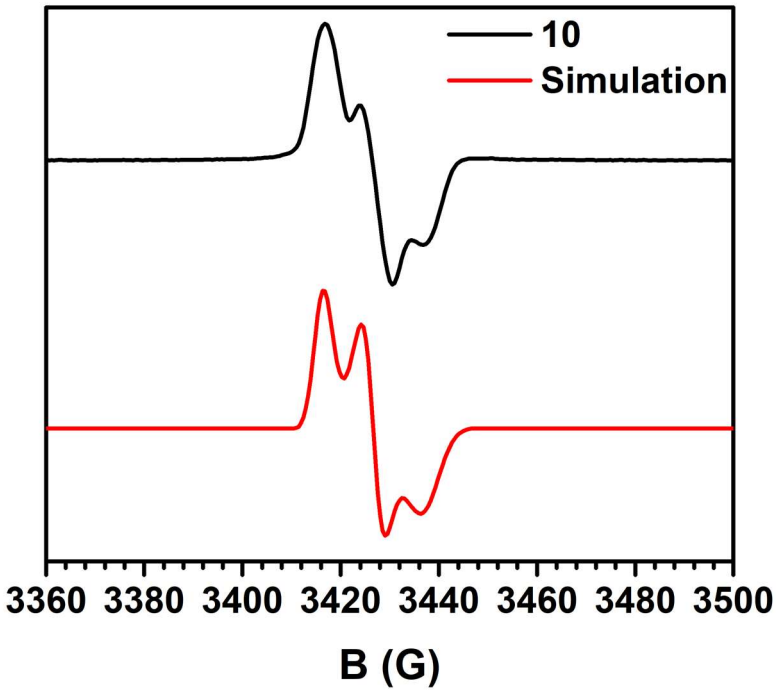

Figure C.28. X-band EPR spectrum of 10 collected on a 1 mM solution in THF at 10 K. Microwave frequency: 9.63 GHz, microwave power: 0.4 μW, and g_{eff} = 2.014, 2.008, 2.001.

C.5 Infrared Spectra

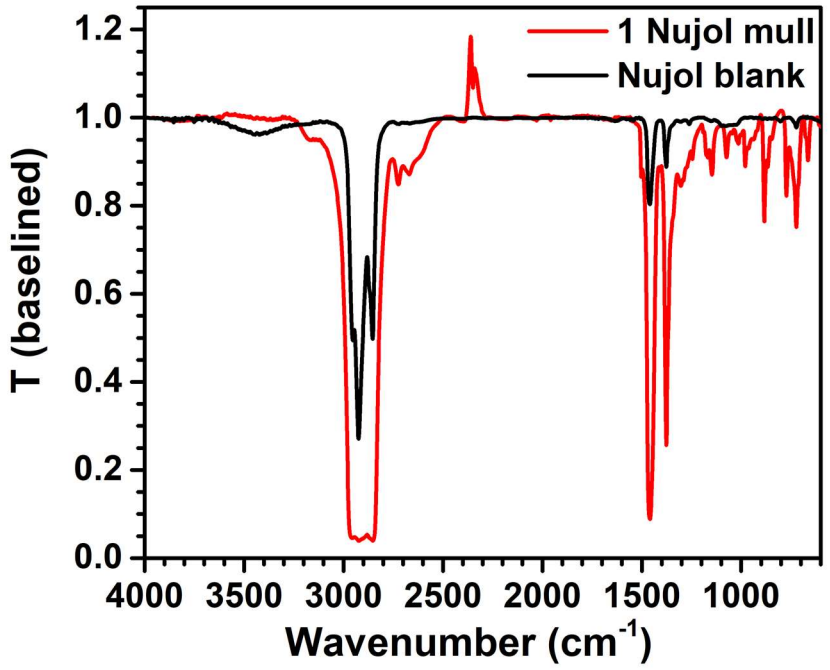

Figure C.29. Infrared transmittance spectrum of 1 as a Nujol mull. Note CO_2 signals at 2350 cm^{-1}.

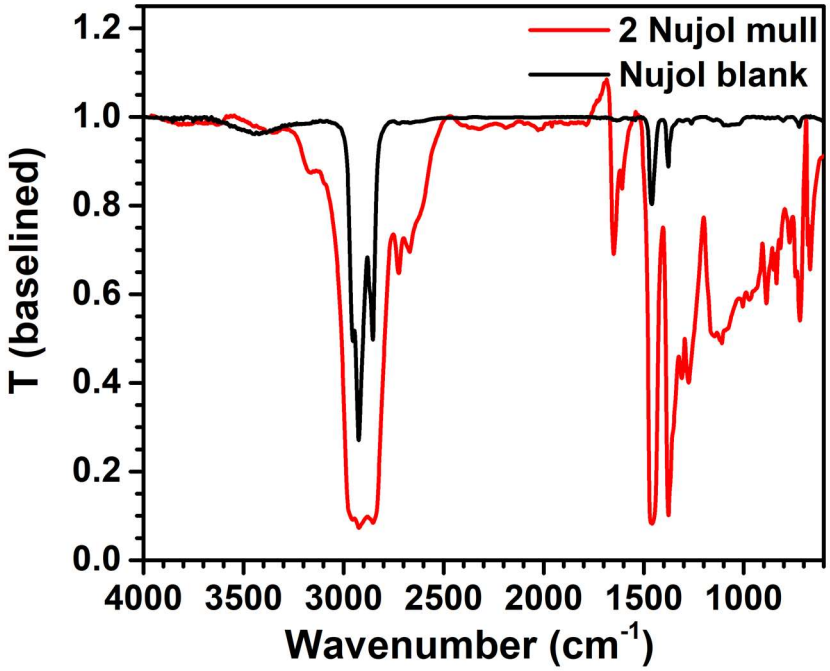

Figure C.30. Infrared transmittance spectrum of 2 as a Nujol mull.

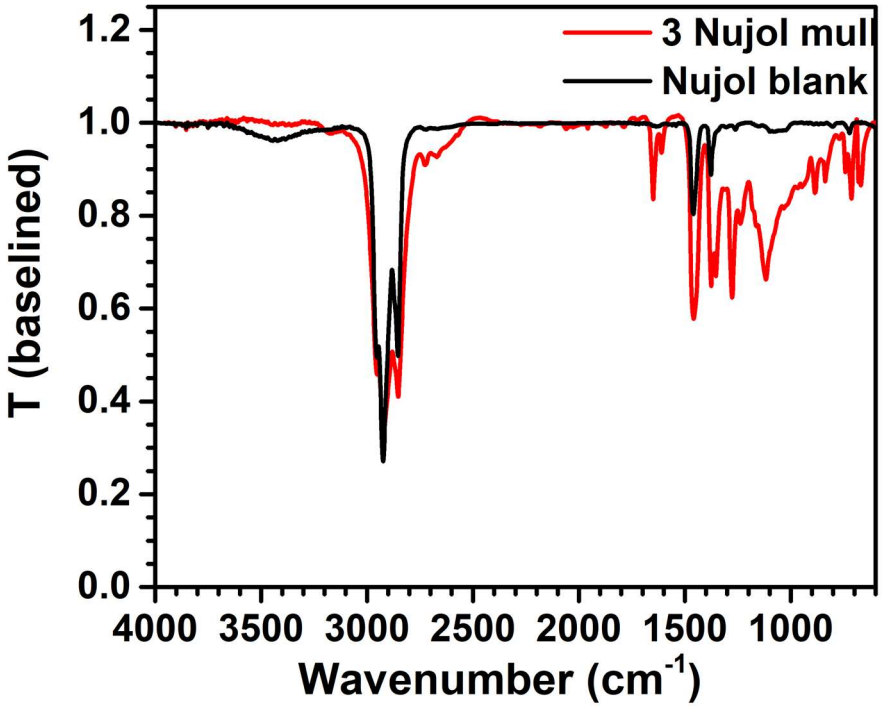

Figure C.31. Infrared transmittance spectrum of 3 as a Nujol mull.

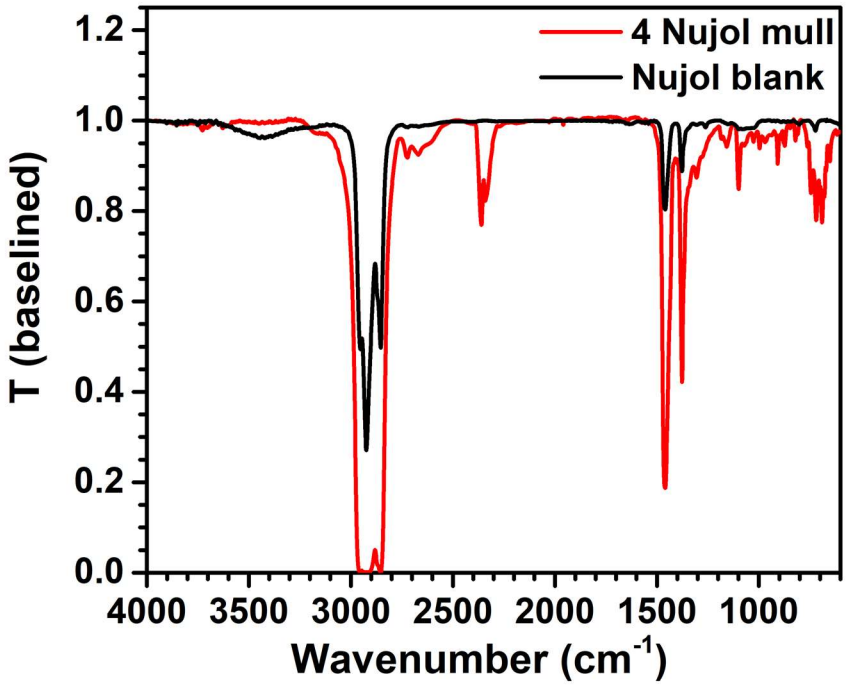

Figure C.32. Infrared transmittance spectrum of 4 as a Nujol mull. Note CO2 signals at 2350 cm^{-1}.

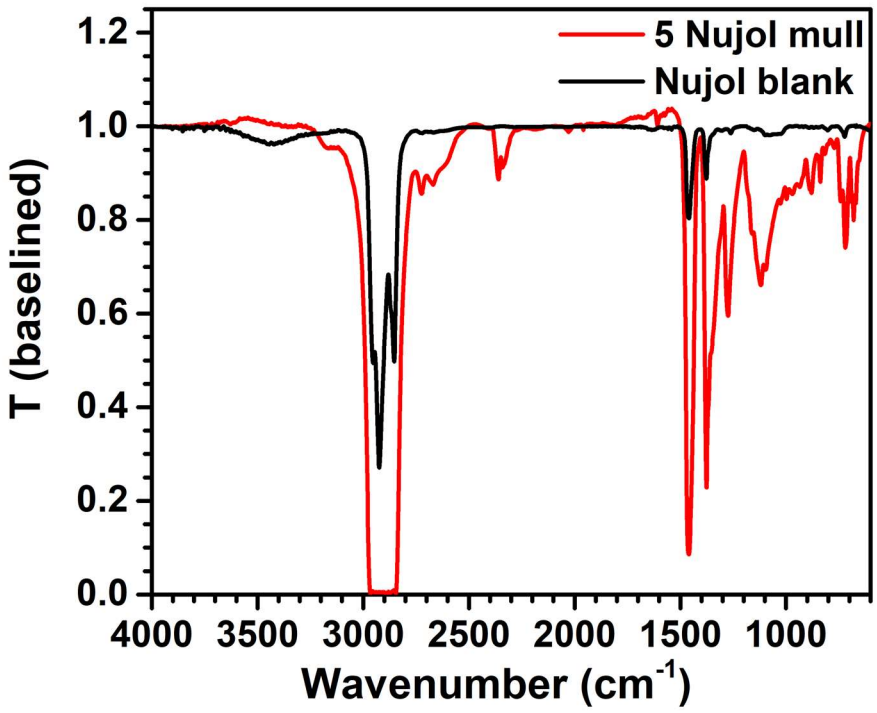

Figure C.33. Infrared transmittance spectrum of 5 as a Nujol mull. Note CO_2 signals at 2350 cm^{-1}.

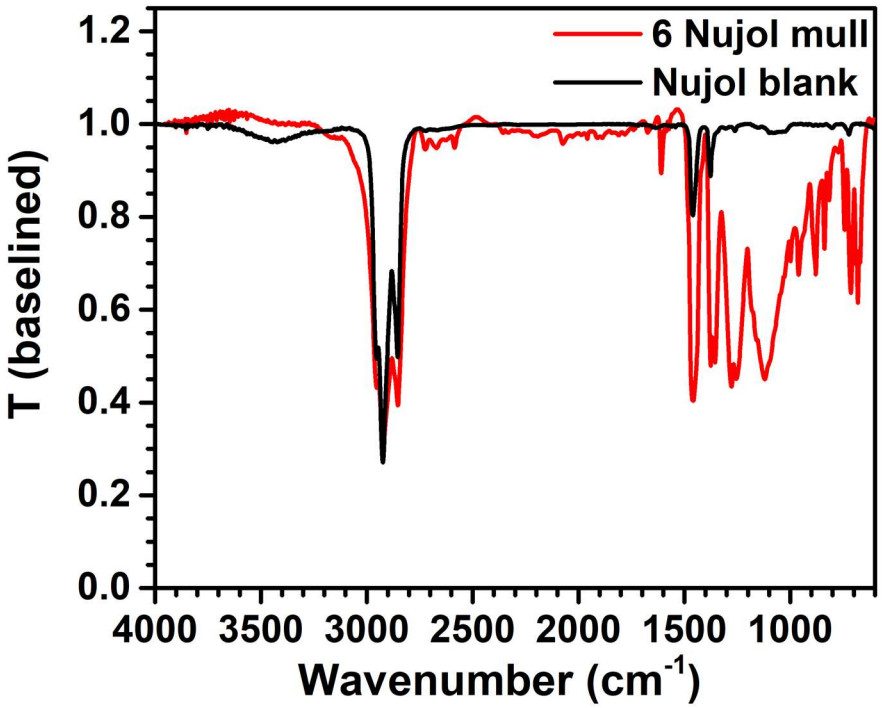

Figure C.34. Infrared transmittance spectrum of 6 as a Nujol mull.

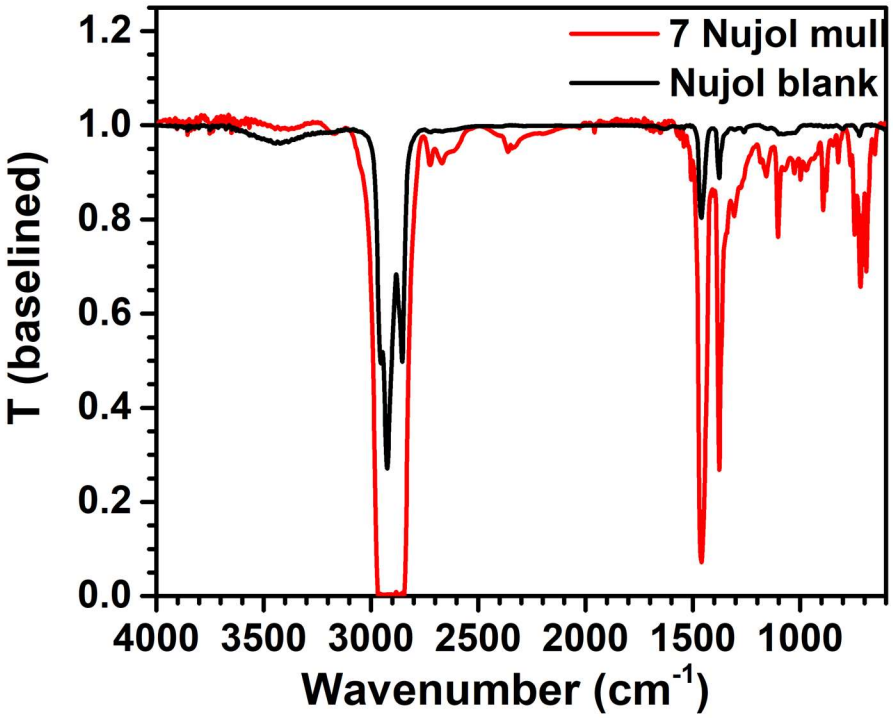

Figure C.35. Infrared transmittance spectrum of 7 as a Nujol mull.

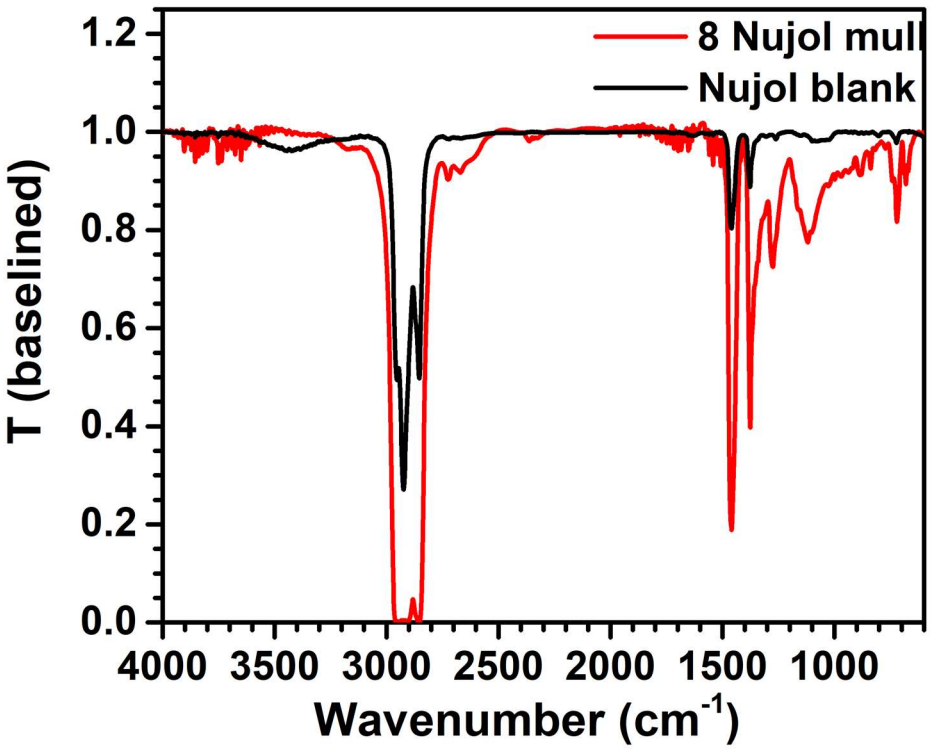

Figure C.36. Infrared transmittance spectrum of 8 as a Nujol mull.

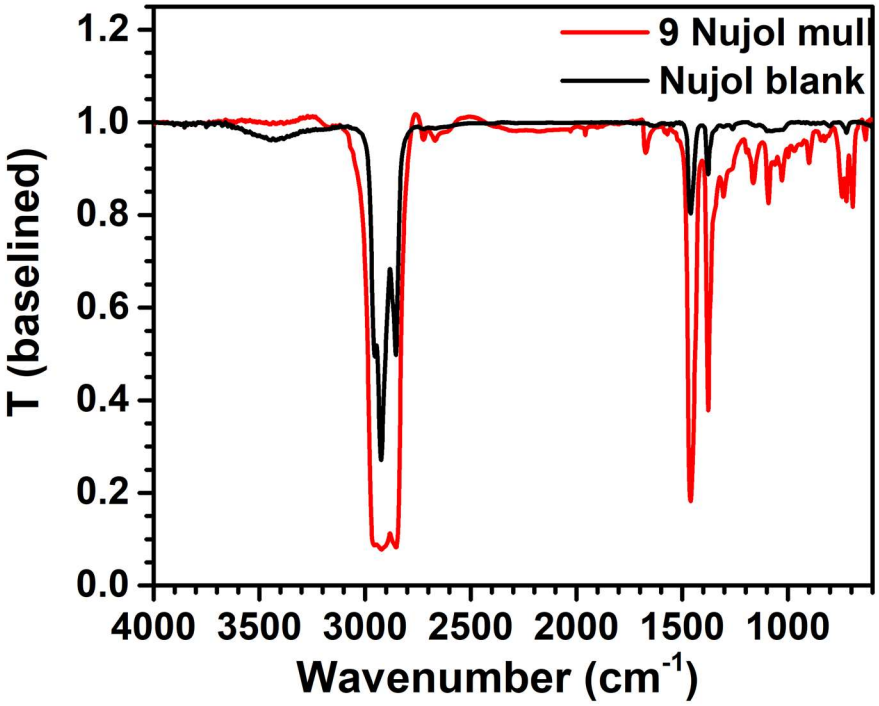

Figure C.37. Infrared transmittance spectrum of 9 as a Nujol mull.

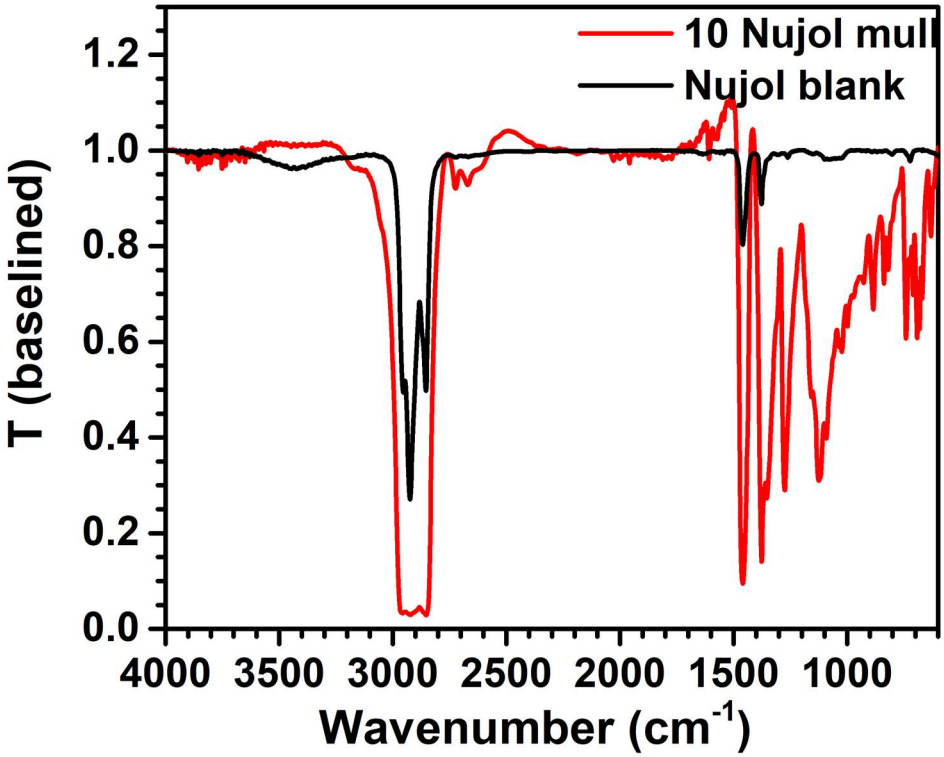

Figure C.38. Infrared transmittance spectrum of 10 as a Nujol mull.

C.6 Electrochemical Measurements

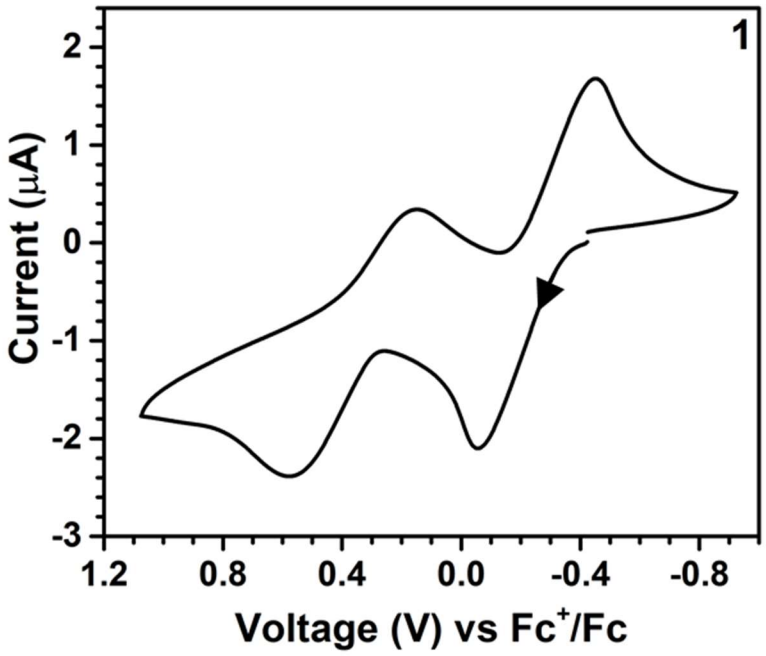

Figure C.39. Cyclic voltammogram of 1 in 0.01 M [Na][BAr$^{F}_{4}$] in DCM and Et$_2$O (10:1). Arrow denotes scan direction. Scan rate: 0.1V/s.

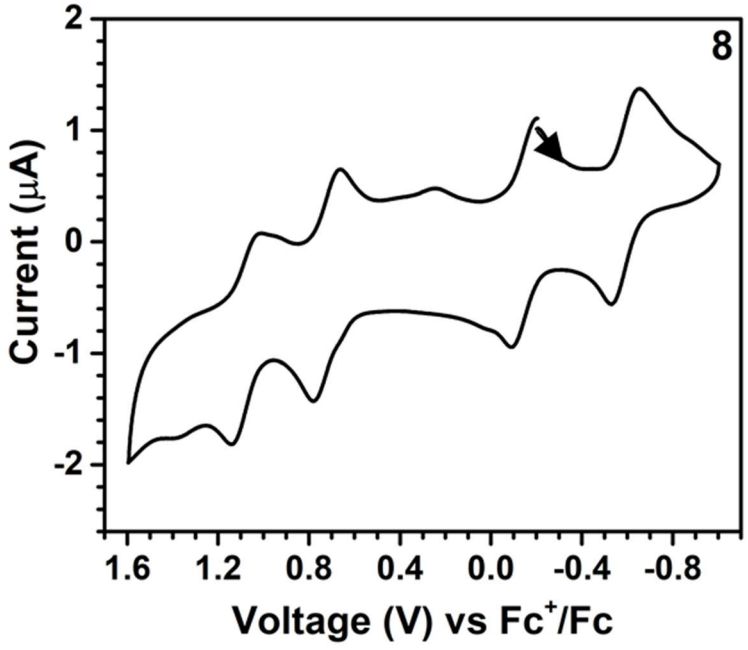

Figure C.40. Cyclic voltammogram of 8 in 0.1 M [TBA][PF$_6$] in DCM. Arrow denotes scan direction. Scan rate: 0.1V/s.

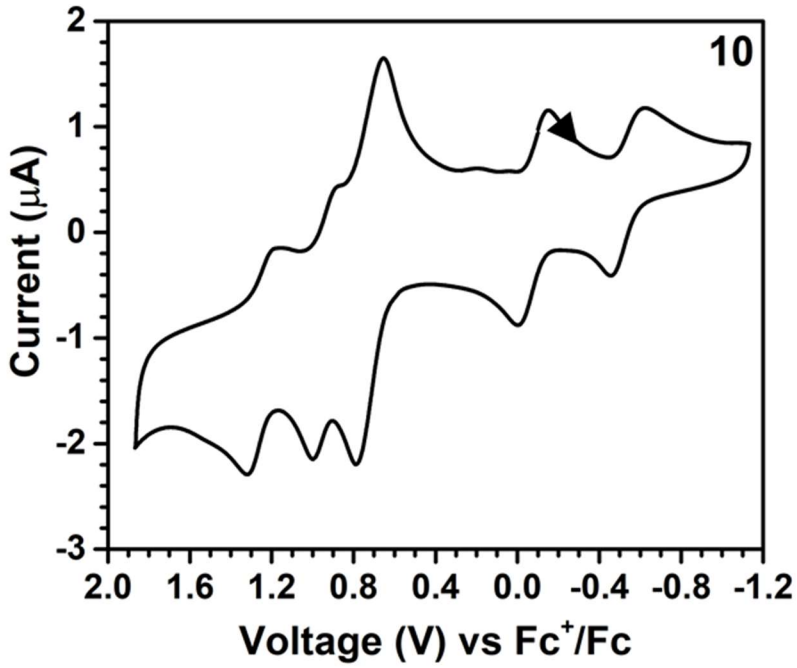

Figure C.41. Cyclic voltammogram of 10 in 0.1 M [TBA][PF_6] in DCM. Arrow denotes scan direction. Scan rate: 0.1V/s.

C.7 Optical Spectroscopy

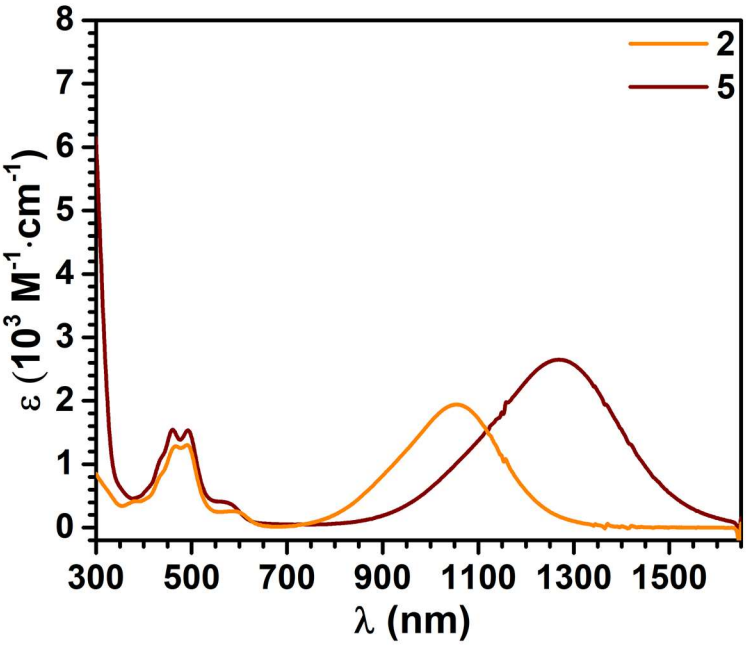

Figure C.42. UV-vis-NIR absorption spectra of 2 and 5 in DCM. Concentration: 50 μM.

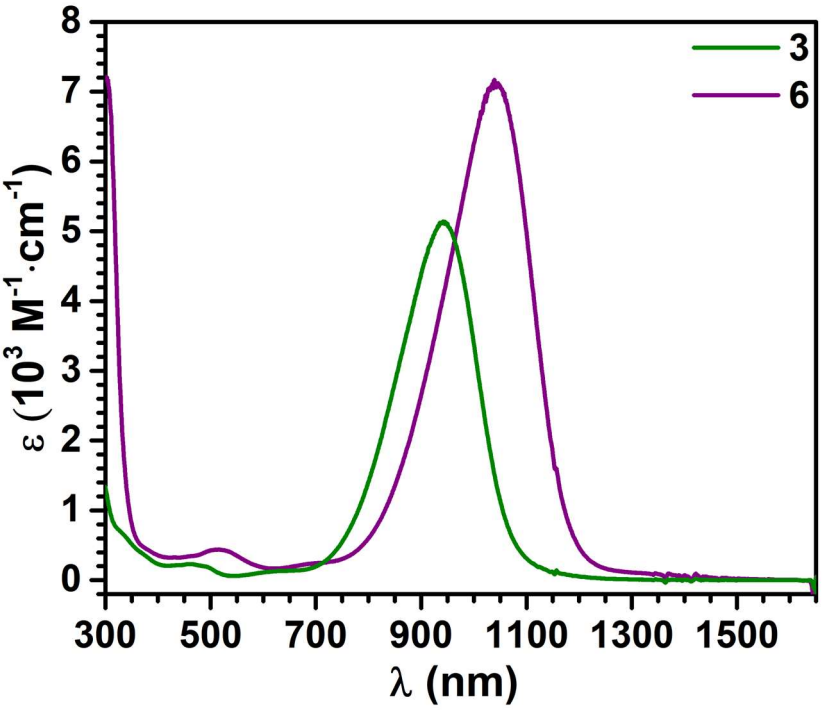

Figure C.43. UV-vis-NIR absorption spectra of 3 and 6 in DCM. Concentration: 50 μM.

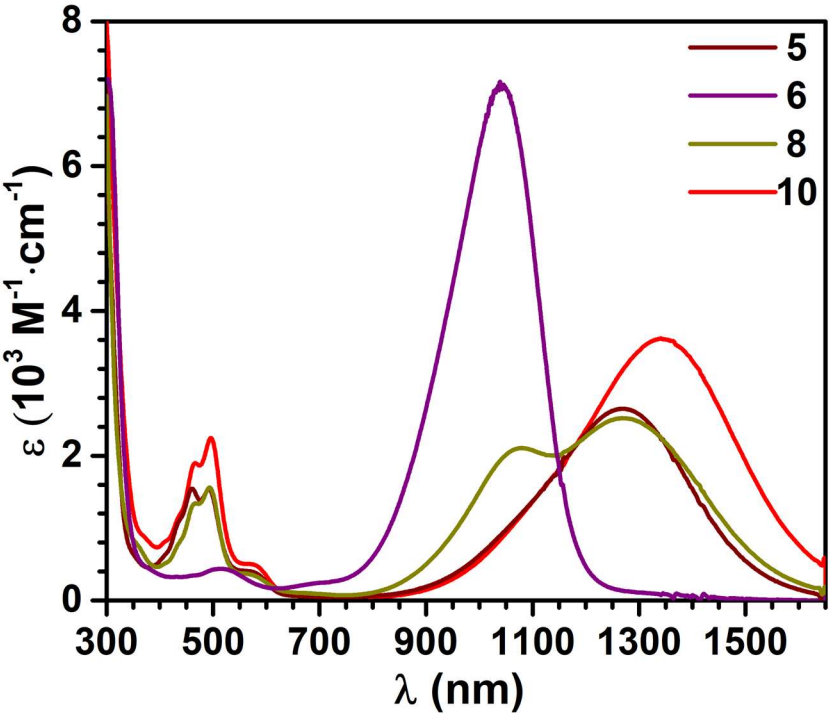

Figure C.44. UV-vis-NIR absorption spectra of 5, 6, 8 and 10 in DCM. Concentration: about 50 μM. Besides the same absorption at 1271.4 nm as 5, 8 has a shoulder absorption peak at 1078.1 nm. Since the energy of this band is obviously lower than the same feature in dicationic 6 (1039.5 nm) and no TTF-dication UV-vis peak is observed, this shoulder peak likely arises from some other speciation due to π-dimers or oligomers.

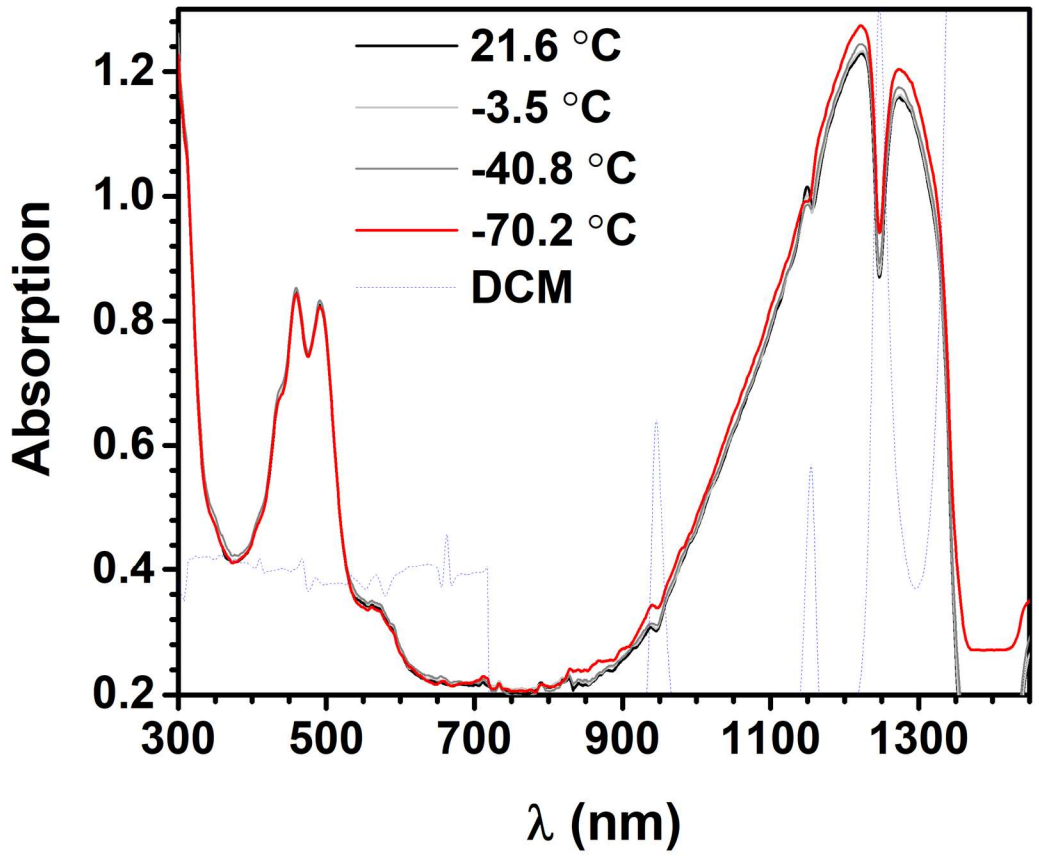

Figure C.45. Variable-temperature UV-vis-NIR absorption spectra of 5 in DCM. Concentration: about 30 μM. Due to the strong background absorptions of the instrument setup and DCM, the peaks in the NIR region are somewhat convoluted. However, a clear continuous increase of NIR feature with cooling suggests the equilibrium shifts to more π-dimers when the temperature decreases.

C.8 X-Ray Crystallography

C.8.1 Crystallogrphic Data

Table C.1. Crystallographic data for complexes 1, 2 and 3.

	1•2MeCN	**2•0.5THF•0.5MeCN**	**3•2THF**
Empirical formula	$C_{26}H_{42}N_2S_8Sn_2$	$C_{57}H_{53.5}BF_{24}N_{0.5}O_{0.5}S_8Sn_2$	$C_{102}H_{92}B_2F_{48}O_4S_8Sn_2$
Formula weight	876.47	1714.17	2809.23

Temperature/K	100(2)	100(2)	100(2)
Crystal system	triclinic	monoclinic	triclinic
Space group	P-1	$P2_1/c$	P-1
a/Å	7.7711(3)	9.5804(15)	12.9111(17)
b/Å	10.3961(4)	23.505(4)	15.863(2)
c/Å	12.6341(5)	30.294(5)	16.368(2)
α/°	113.062(2)	90	88.537(3)
β/°	96.284(2)	97.920(4)	88.979(3)
γ/°	98.114(2)	90	69.195(3)
Volume/$Å^3$	914.39(6)	6756.8(18)	3132.5(7)
Z	1	4	1
$\rho_{calc}g/cm^3$	1.592	1.685	1.489
μ/mm^{-1}	1.842	1.091	0.649
F(000)	440.0	3408.0	1406.0
Crystal size/mm^3	0.32 × 0.18 × 0.07	0.24 × 0.04 × 0.04	0.29 × 0.24 × 0.04
Radiation	MoKα (λ = 0.71073)	MoKα (λ = 0.71073)	MoKα (λ = 0.71073)

2Θ range for data collection/°	5.384 to 52.974	4.402 to 44.196	4.358 to 50.398
Index ranges	$-9 \leq h \leq 9$, $-12 \leq k \leq 13$, $-15 \leq l \leq 15$	$-9 \leq h \leq 10$, $-24 \leq k \leq 24$, $-31 \leq l \leq 31$	$-15 \leq h \leq 15$, $-18 \leq k \leq 18$, $-19 \leq l \leq 19$
Reflections collected	26492	103447	32479
Independent reflections	3767 [R_{int} = 0.0370, R_{sigma} = 0.0253]	8304 [R_{int} = 0.1444, R_{sigma} = 0.0648]	11153 [R_{int} = 0.1152, R_{sigma} = 0.1068]
Data/restraints/parameters	3767/0/175	8304/1098/850	11153/487/815
Goodness-of-fit on F^2	1.081	1.065	1.087
Final R indexes [I>=2σ (I)]	R_1 = 0.0271, wR_2 = 0.0569	R_1 = 0.0820, wR_2 = 0.1755	R_1 = 0.0977, wR_2 = 0.2003
Final R indexes [all data]	R_1 = 0.0343, wR_2 = 0.0590	R_1 = 0.1244, wR_2 = 0.1992	R_1 = 0.1437, wR_2 = 0.2241
Largest diff. peak/hole / e $Å^{-3}$	1.59/-0.33	0.96/-0.94	1.40/-0.98

Table C.2. Crystallographic data of complex 3•2Fc^{BzO}.

	3•2Fc^{BzO}

Empirical formula	$C_{120}H_{88}B_2F_{48}Fe_2O_2S_8Sn_2$
Formula weight	3101.08
Temperature/K	100(2)
Crystal system	monoclinic
Space group	$P2_1/c$
a/Å	12.734(2)
b/Å	31.568(5)
c/Å	18.543(3)
α/°	90
β/°	107.358(3)
γ/°	90
Volume/Å^3	7114(2)
Z	2
ρ_{calc}g/cm^3	1.448
μ/mm^{-1}	0.562
F(000)	3092.0
Crystal size/mm^3	0.001 × 0.001 × 0.001

Radiation	synchrotron (λ = 0.41328)
2Θ range for data collection/°	1.5 to 28.76
Index ranges	$-15 \leq h \leq 15$, $-37 \leq k \leq 37$, $-22 \leq l \leq 22$
Reflections collected	150144
Independent reflections	12839 [R_{int} = 0.1297, R_{sigma} = 0.0798]
Data/restraints/parameters	12839/728/991
Goodness-of-fit on F^2	1.028
Final R indexes [I>=2σ (I)]	R_1 = 0.0678, wR_2 = 0.1719
Final R indexes [all data]	R_1 = 0.1035, wR_2 = 0.1966
Largest diff. peak/hole / e Å^{-3}	1.07/-0.74

Table C.3. Crystallographic data of complexes 5 and 6.

	5	**6**
Empirical formula	$C_{122}H_{72}B_2F_{48}Ni_2P_4S_8$	$C_{90}H_{60}BF_{24}Ni_2P_4S_8$
Formula weight	2969.19	2105.97
Temperature/K	100(2)	100(2)
Crystal system	monoclinic	triclinic

Space group	C2/c	P-1
a/Å	40.752(3)	14.1624(15)
b/Å	18.9850(12)	18.3974(19)
c/Å	17.7197(11)	20.189(2)
α/°	90	94.073(2)
β/°	107.903(2)	103.397(2)
γ/°	90	106.515(2)
Volume/$Å^3$	13045.5(14)	4852.8(9)
Z	4	2
$\rho_{calc}g/cm^3$	1.512	1.441
μ/mm^{-1}	0.582	0.169
F(000)	5960.0	2130.0
Crystal size/mm^3	0.25 × 0.23 × 0.02	0.002 × 0.002 × 0.001
Radiation	MoKα (λ = 0.71073)	synchrotron (λ = 0.41328)
2Θ range for data collection/°	4.202 to 51.594	1.686 to 31.652

Index ranges	$-49 \leq h \leq 49$, $-23 \leq k \leq 23$, $-21 \leq l \leq 21$	$-18 \leq h \leq 18$, $-24 \leq k \leq 24$, $-26 \leq l \leq 26$
Reflections collected	166738	141909
Independent reflections	12520 [$R_{int} = 0.0661$, $R_{sigma} = 0.0320$]	22441 [$R_{int} = 0.0384$, $R_{sigma} = 0.0261$]
Data/restraints/parameters	12520/381/906	22441/174/1200
Goodness-of-fit on F^2	1.013	1.047
Final R indexes [$I>=2\sigma(I)$]	$R_1 = 0.0420$, $wR_2 = 0.0906$	$R_1 = 0.0352$, $wR_2 = 0.0910$
Final R indexes [all data]	$R_1 = 0.0617$, $wR_2 = 0.0987$	$R_1 = 0.0416$, $wR_2 = 0.0963$
Largest diff. peak/hole / e $Å^{-3}$	0.63/-0.54	0.96/-0.58

Table C.4. Crystallographic data of complexes 8 and 10.

	8	**10**
Empirical formula	$C_{540}H_{360}B_6F_{144}P_{24}Pd_{12}S_{48}$	$C_{106}H_{68}BF_{24}Fe_2P_4Pd_2S_8$
Formula weight	13208.08	2513.27
Temperature/K	100(2)	100(2)
Crystal system	triclinic	triclinic
Space group	P-1	P-1
a/Å	29.421(4)	13.503(3)
b/Å	31.324(5)	19.054(4)
c/Å	35.123(5)	28.239(6)
α/°	92.011(3)	105.082(5)
β/°	91.984(3)	91.975(4)
γ/°	99.304(3)	90.730(5)
Volume/Å^3	31896(8)	7009(3)
Z	2	2
ρ_{calc}g/cm^3	1.375	1.191
μ/mm^{-1}	0.637	0.688

F(000)	13212.0	2514.0
Crystal size/mm^3	0.22 × 0.01 × 0.01	0.28 × 0.24 × 0.02
Radiation	MoKα (λ = 0.71073)	MoKα (λ = 0.71073)
2Θ range for data collection/°	1.162 to 42.074	4.29 to 44.728
Index ranges	-29 ≤ h ≤ 29, -31 ≤ k ≤ 31, -35 ≤ l ≤ 35	-14 ≤ h ≤ 14, -20 ≤ k ≤ 20, -30 ≤ l ≤ 30
Reflections collected	362133	59637
Independent reflections	68469 [R_{int} = 0.1554, R_{sigma} = 0.1701]	17875 [R_{int} = 0.1086, R_{sigma} = 0.1360]
Data/restraints/parameters	68469/1269/2177	17875/754/1458
Goodness-of-fit on F^2	1.204	1.070
Final R indexes [I>=2σ (I)]	R_1 = 0.1770, wR_2 = 0.3523	R_1 = 0.0914, wR_2 = 0.1827
Final R indexes [all data]	R_1 = 0.2699, wR_2 = 0.3959	R_1 = 0.1467, wR_2 = 0.2038
Largest diff. peak/hole / e $Å^{-3}$	3.25/-3.71	1.25/-1.04

C.8.2 Molecular planarity diagram for complexes 1, 2, 3, 5 and 6.

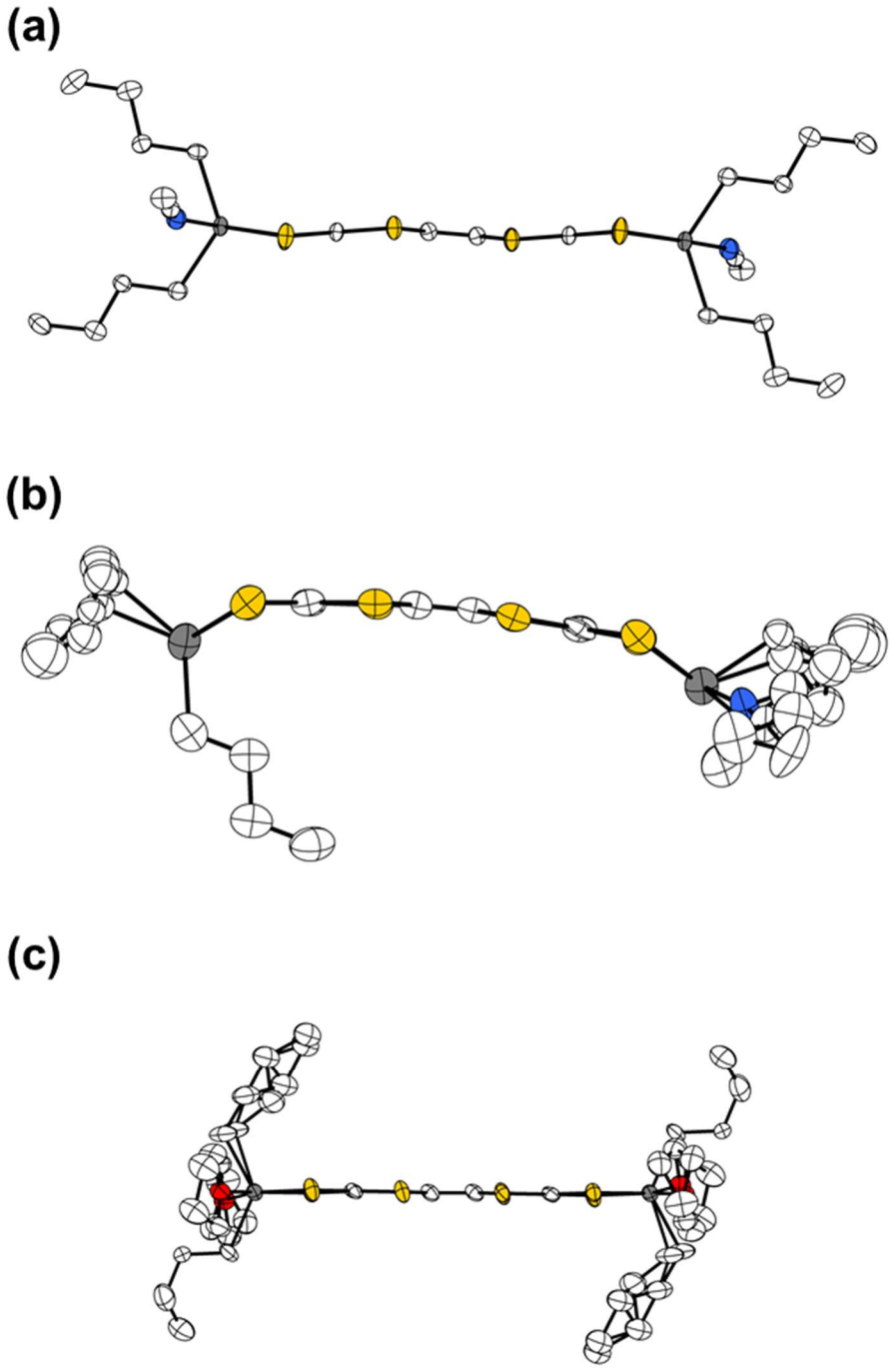

Figure C.46. Molecular planarity diagram for 1, 2 and 3. [BAr^{F}_{4}] anions and H atoms are omitted for clarity. Ellipsoids are shown at 50% probability. (Sn, grey; S, yellow; O, red; N, blue; C, white.). Disorder is shown.

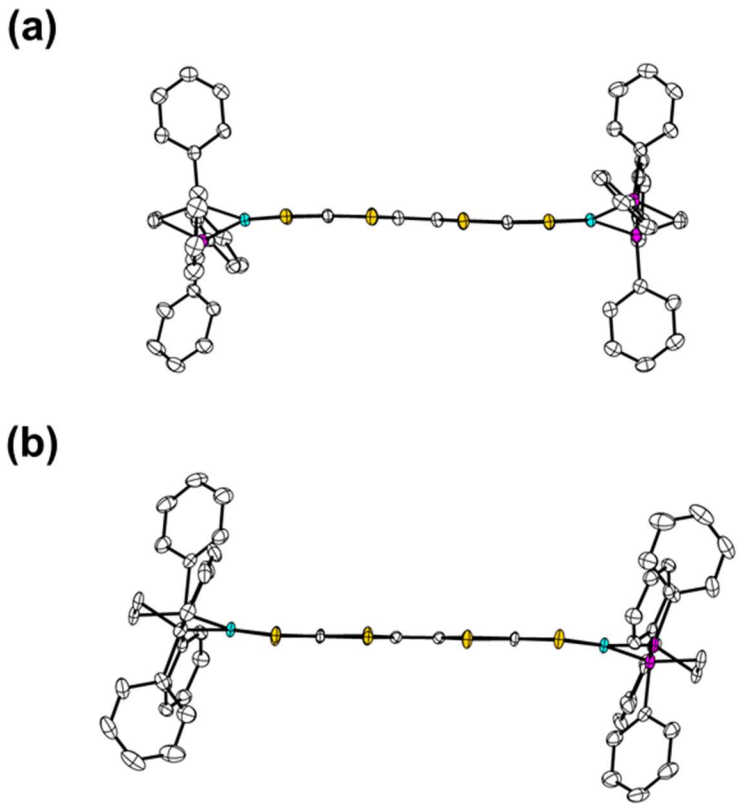

Figure C.47. Molecular planarity diagram for 5 and 6. [BAr^{F}_{4}] anions and H atoms are omitted for clarity. Ellipsoids are shown at 50% probability. (Ni, light blue; S, yellow; P, purple; C, white.)

C.8.3 The extended structures of 1, 2, 3, 5, and 6.

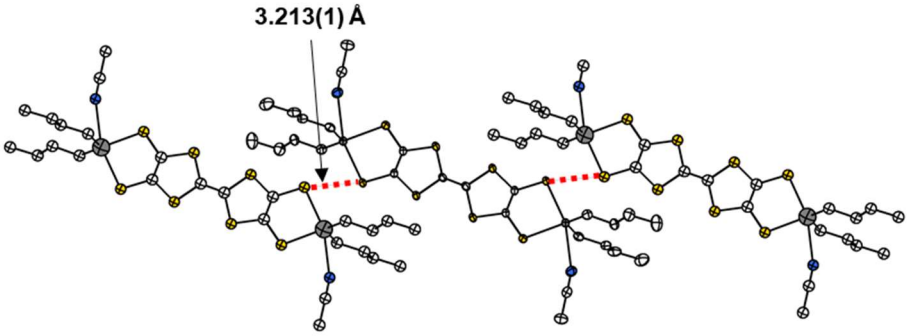

Figure C.48. Supermolecular structure of 1: 1D chain. The red dash lines represent the intermolecular S-S interactions. H atoms are omitted for clarity. Ellipsoids are shown at 50% probability. (Sn, grey; S, yellow; N, blue; C, white.)

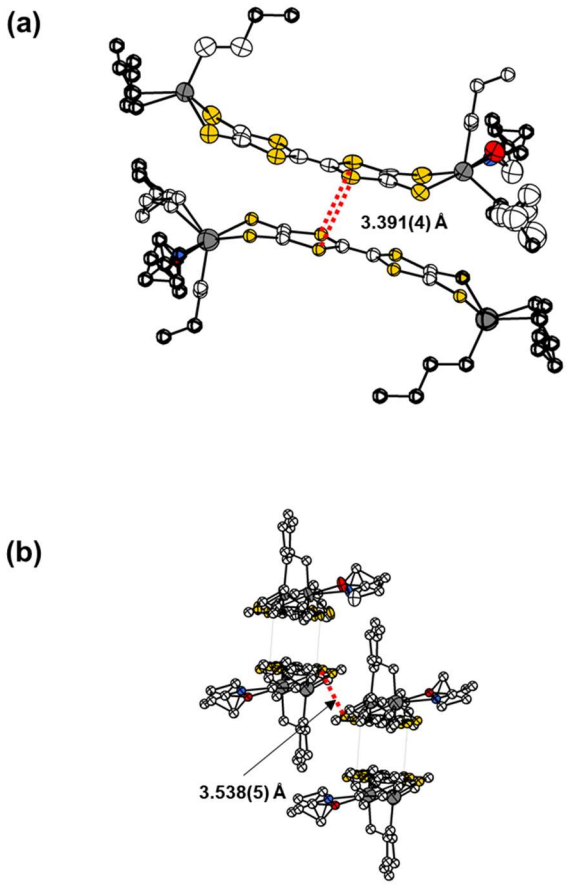

Figure C.49. The extended structure of 2: dimer unit (a) and 1D chain of dimers (b). The red dash lines represent the intermolecular S-S interactions. [$BAr^F{}_4$] anions and H atoms are omitted for clarity. Ellipsoids are shown at 50% probability. (Sn, grey; S, yellow; O, red; N, blue; C, white.). Disorder is shown**.**

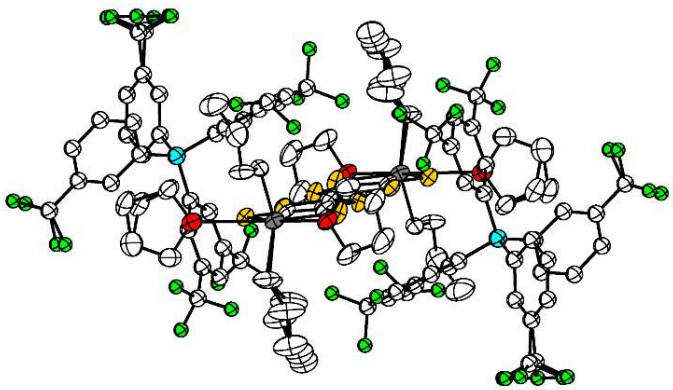

Figure C.50. The molecular structure of 3: the diactionic 3 encompassed by two bulk [$BAr^F{}_4$] anions. H atoms are omitted for clarity. Ellipsoids are shown at 50% probability. (Sn, grey; S, yellow; F, vivid green; B, light blue; O, red; C, white.). Disorder is shown.

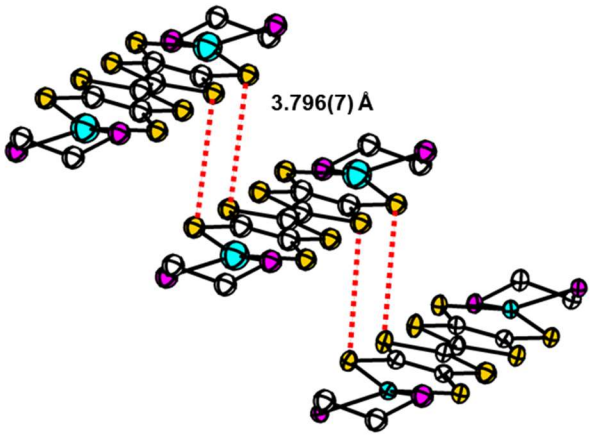

Figure C.51. The extended structure of 5: ladder-shaped 1D chain. The red dash lines represent the intermolecular S-S interactions. Phenyl groups of dppe, [BAr^F_4] anions and H atoms are omitted for clarity. Ellipsoids are shown at 50% probability. (Ni, light blue; S, yellow; P, purple; C, white.)

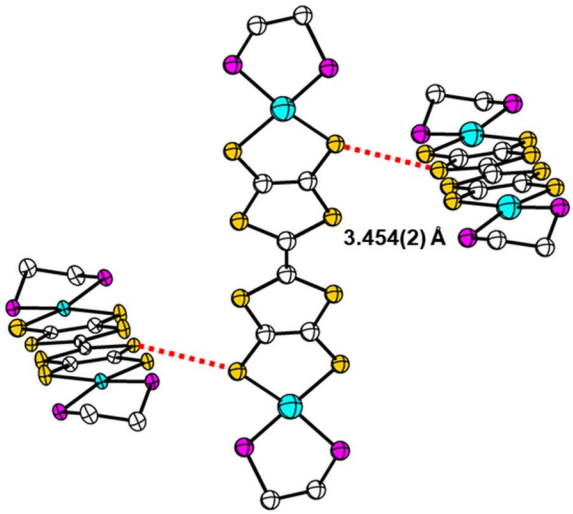

Figure C.52. The extended structure of 6: twisted 1D chain. The red dashed lines represent the intermolecular S-S interactions. Phenyl groups of dppe, [BAr^F_4] anions and H atoms are omitted for clarity. Ellipsoids are shown at 50% probability. (Ni, light blue; S, yellow; P, purple; C, white.)

C.8.4 Single-crystal X-ray Diffraction Structures of complex 3•2Fc^{BzO}, 8 and 10.

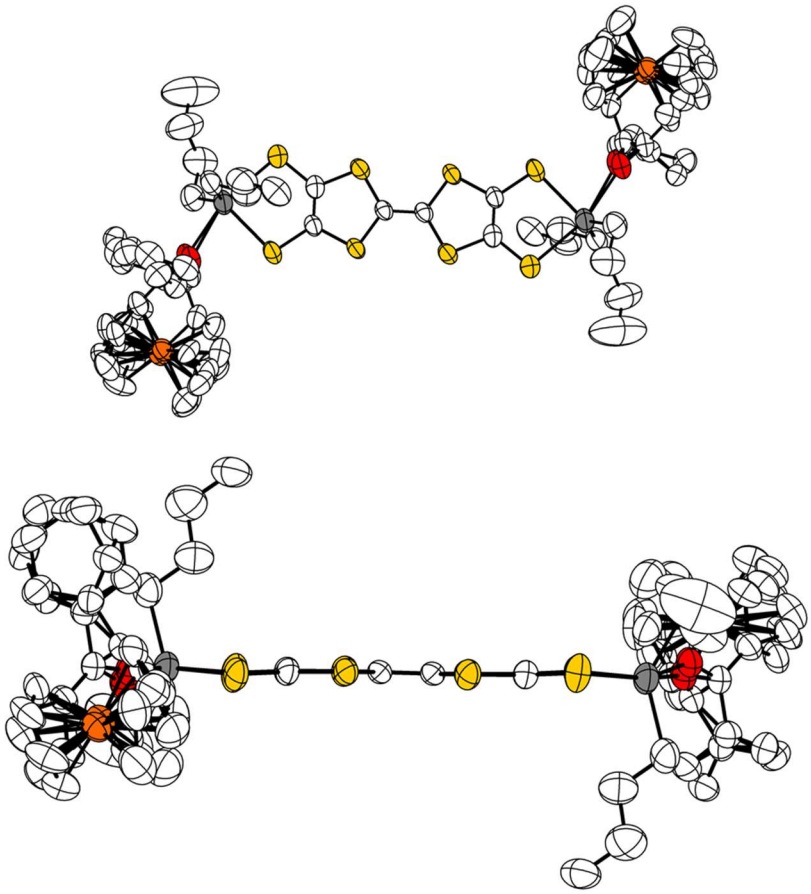

Figure C.53. Single-crystal X-ray diffraction structures of complex 3•2Fc^{BzO}. [BAr$^{F}_{4}$] anions and H atoms are omitted for clarity. Ellipsoids are shown at 50% probability. (Sn, grey; Fe, orange; S, yellow; O, red; C, white.). Disorder is shown.

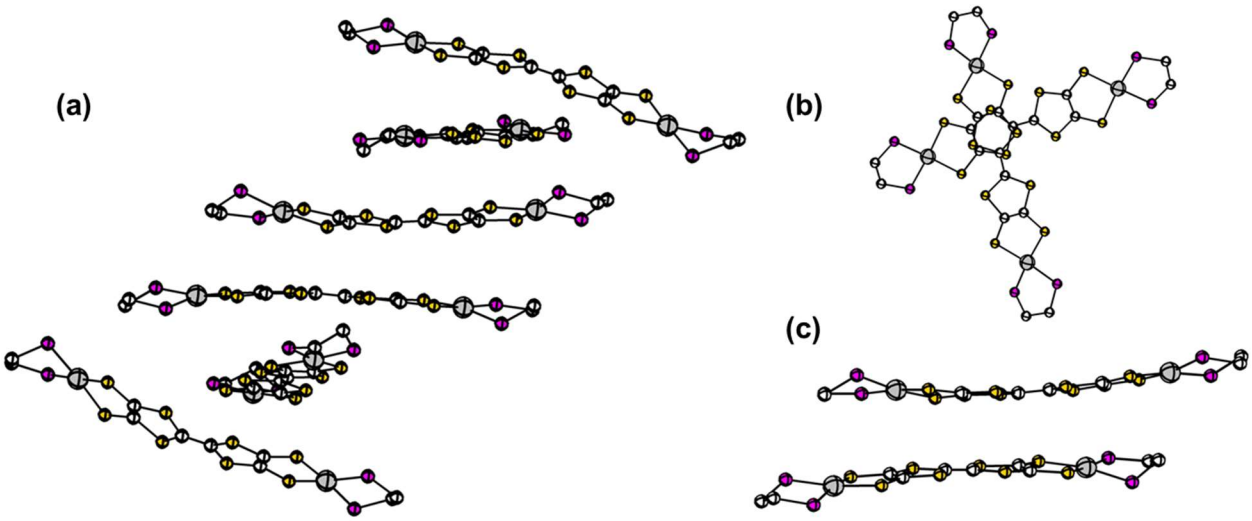

Figure C.54. Single-crystal X-ray diffraction structures of complex 8: a pentamer in 1D chain (a), a perpendicular dimer (b), and a parallel dimer (c). Phenyl groups of dppe, [BAr^F_4] anions and H atoms are omitted for clarity. Ellipsoids are shown at 50% probability. (Pd, light grey; S, yellow; P, purple; C, white.).

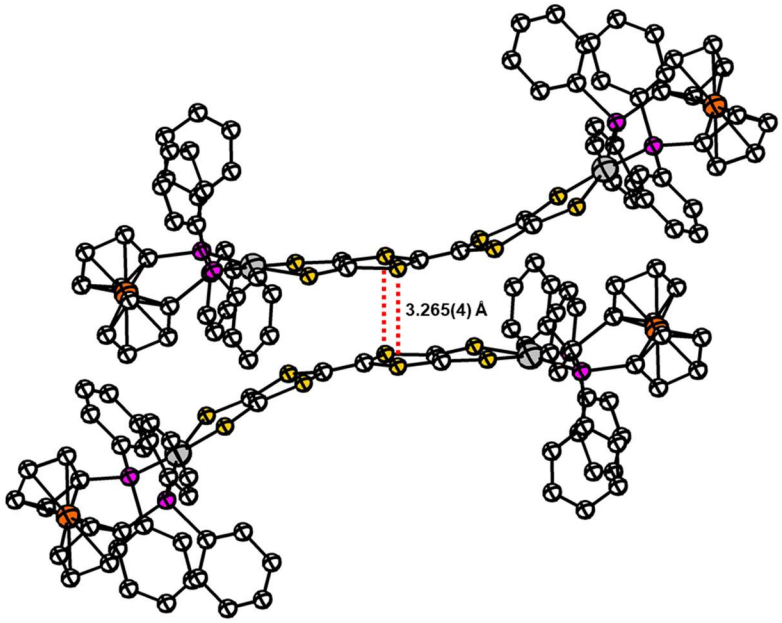

Figure C.55. Single-crystal X-ray diffraction structure of complex 10 in a dimer unit. The red dashed lines represent the intermolecular S-S interactions. [BAr^F_4] anions and H atoms are omitted for clarity. Ellipsoids are shown at 50% probability. (Pd, light grey; Fe, orange; S, yellow; P, purple; C, white.).

C.8.5 Crystallographic Characterization of a Polymorph of 5.

During attempts to obtain crystals of **5**, an alternative polymorph was found with an unusual packing interaction. The crystals of this polymorph are extremely unstable and quickly decompose and lose crystallinity. Many attempts failed to provide a better-quality data set. Attempts to collect data at a synchrotron only revealed a different polymorphic form. The polymorph crystallizes in a large unit cell of over 50000 $Å^3$ with many co-crystallized solvent molecules. Dichloromethane is the only solvent which provides this polymorph out of many variations that have been investigated. Both amorphous solvent regions and heavy disorder of several independent [BAr^F_4] anionic units led to diffraction only up to ~ 1.2 Å. Some atoms of the [BAr^F_4] anions could not be located in the difference Fourier map due to heavy disorder. These [BAr^F_4] anions were modeled by adding bis(trifluoromethyl)benzene moieties to boron in approximate tetrahedral geometry and utilizing the visible residual electron density of benzene rings for initial placement. After that, these moieties were allowed to freely move as a whole unit with a fixed internal geometry. All atoms of the cationic TTFtt portion were located in the difference Fourier map. This has allowed for accurate assignment of the charge, general 3D packing, and connectivity of the TTFtt units from this data. The coordinates of the TTFtt packing from this solution were then used for further calculations. In the figures below, Ni is blue, P is purple, S is yellow, F is green, B is pink, H is white, and C is grey.

Table C.5. Crystal data and structure refinement for the polymorph of 5.

Empirical formula	$C_{225}H_{150}B_{2.5}F_{60}Ni_5P_{10}S_{20}$
Formula weight	5264.92

Temperature/K	100(2)
Crystal system	monoclinic
Space group	C2/c
a/Å	53.053(5)
b/Å	21.9471(19)
c/Å	51.656(5)
α/°	90
β/°	118.338(2)
γ/°	90
Volume/Å^3	52938(8)
Z	8
ρ_{calc}g/cm^3	1.321
μ/mm^{-1}	0.656
F(000)	21300.0
Radiation	MoKα (λ = 0.71073)
2Θ range for data collection/°	4.238 to 35
Index ranges	-44 ≤ h ≤ 44, -18 ≤ k ≤ 18, -43 ≤ l ≤ 43

Reflections collected	187662
Independent reflections	16783 [R_{int} = 0.1277, R_{sigma} = 0.0503]
Data/restraints/parameters	16783/1154/761
Final R indexes [I>=2σ (I)]	R_1 = 0.2814, wR_2 = 0.6230
Final R indexes [all data]	R_1 = 0.3436, wR_2 = 0.6770

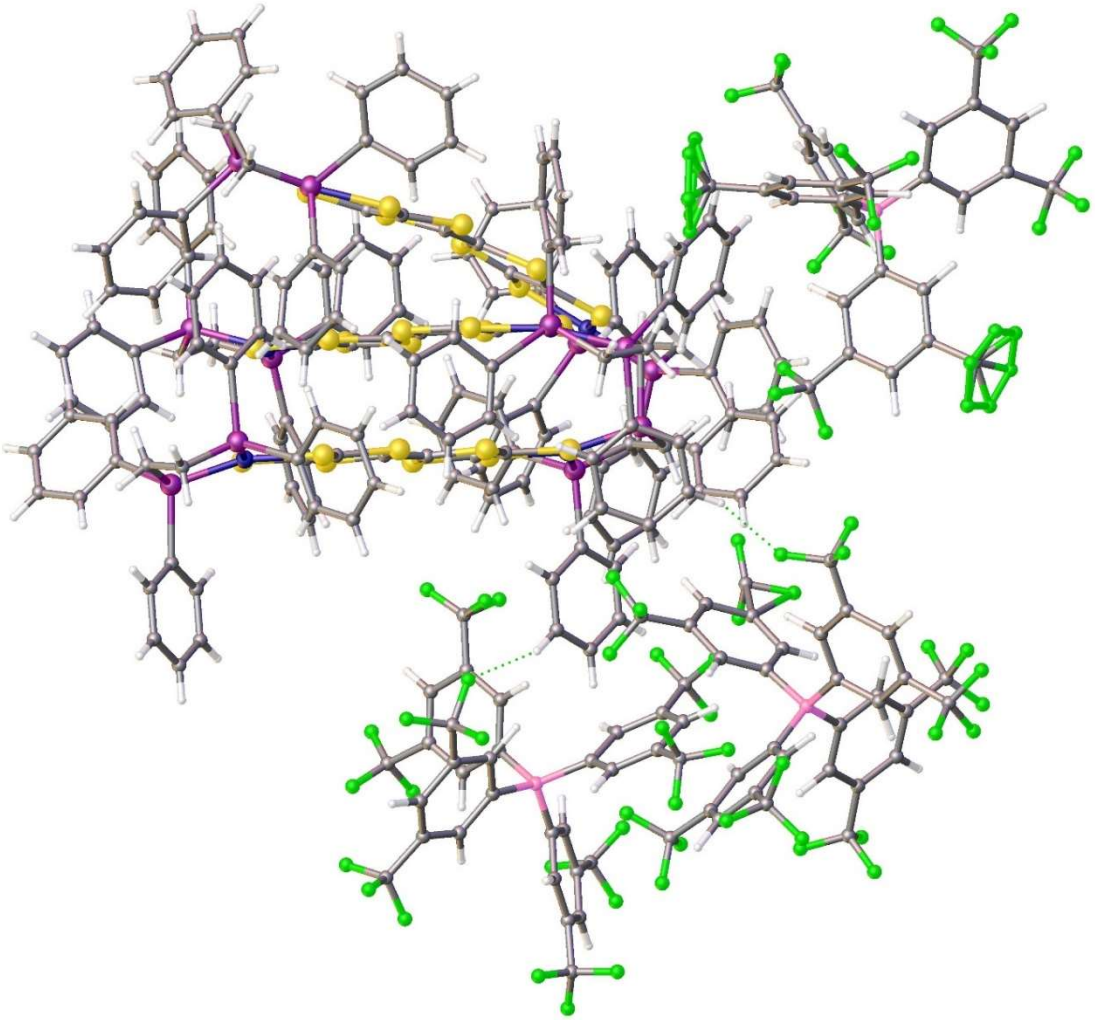

Figure C.56. Symmetry-grown unit showing 3 Ni complexes along with 3 $[BAr^F{}_4]^-$ counterions.

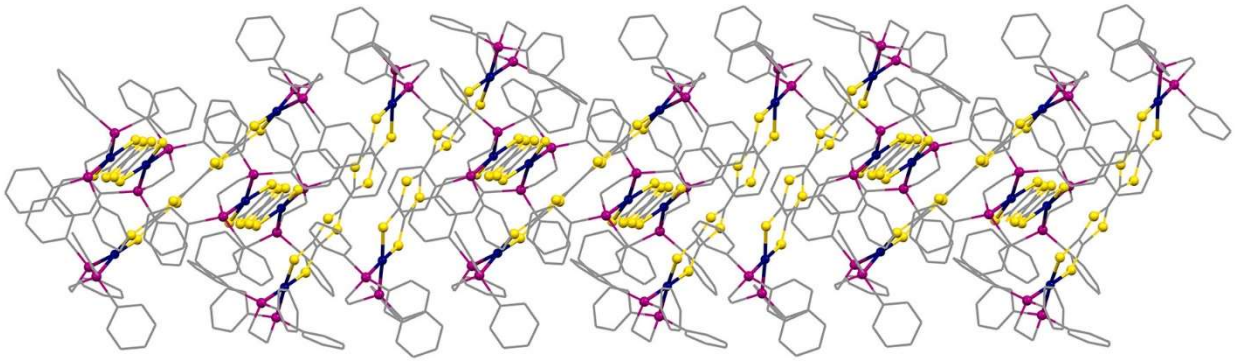

Figure C.57. Part of 3D packing showing the growth of a cationic chain.

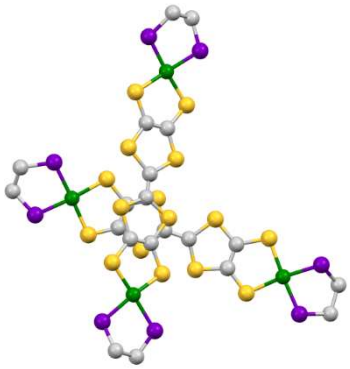

Figure C.58. Diagram showing the orthogonal dimeric stacking of two TTFtt units in the polymorphic version of 5. Note that Ni is green in this figure.

Table C.6 Fractional Atomic Coordinates for the polymorph of 5 (×10^4).

Atom	*x*	*y*	*z*
Ni1	5985.5(9)	-263(2)	5716.9(10)
Ni2	3770.8(9)	2607(2)	4764.1(10)
S1	5615(2)	-315(4)	5787(2)
S2	5765(2)	275(4)	5312(2)

S3	5180(2)	855(4)	5036(2)
S4	5049(2)	331(4)	5477(2)
S5	4496(2)	1143(4)	5266(2)
S6	4556(2)	1574(4)	4767(2)
S7	4063(2)	2458(4)	4589(2)
S8	3983(2)	1955(4)	5117(2)
P1	6226(2)	-801(5)	6106(2)
P2	6371(2)	-287(5)	5693(2)
P3	3554(2)	3302(4)	4437(2)
P4	3440(2)	2739(5)	4877(2)
C3	6469(11)	652(16)	6744(11)
C4	6735(10)	486(19)	6972(8)
C5	6848(8)	-90(20)	6972(8)
C6	6695(11)	-491(16)	6743(10)
C1	6430(11)	-320(20)	6515(7)
C2	6317(8)	250(20)	6515(8)
C7	5987(9)	-1440(20)	6211(12)

C8	5921(10)	-1347(16)	6438(10)
C9	5737(10)	-1740(20)	6476(9)
C10	5619(8)	-2240(20)	6287(12)
C11	5685(9)	-2332(17)	6060(10)
C12	5869(10)	-1940(20)	6022(9)
C13	6473(7)	-1283(17)	6056(5)
C14	6493(7)	-1099(18)	5787(5)
C15	6409(12)	-30(20)	5316(8)
C20	6601(9)	380(20)	5302(7)
C19	6581(10)	531(18)	5031(10)
C18	6369(11)	270(20)	4775(7)
C17	6177(9)	-140(20)	4789(8)
C16	6197(10)	-295(19)	5059(12)
C22	6611(7)	820(30)	6072(9)
C23	6809(11)	1210(16)	6282(11)
C24	7091(9)	1020(20)	6453(8)
C25	7175(7)	450(20)	6413(9)

C26	6977(11)	56(16)	6203(10)
C21	6695(9)	240(20)	6033(8)
C27	3741(9)	4174(12)	4452(12)
C32	3780(9)	4561(17)	4261(8)
C31	3945(10)	5084(15)	4368(11)
C30	4071(8)	5220(15)	4666(12)
C29	4032(10)	4830(20)	4858(8)
C28	3867(11)	4310(20)	4750(11)
C33	3422(12)	3010(20)	3996(5)
C38	3644(9)	3050(20)	3925(9)
C37	3596(10)	2890(20)	3645(11)
C36	3327(12)	2690(20)	3436(6)
C35	3106(9)	2650(20)	3506(7)
C34	3153(10)	2810(20)	3786(9)
C39	3228(4)	3579(13)	4461(6)
C40	3110(5)	3050(13)	4552(6)
C41	3530(12)	3362(18)	5228(8)

C46	3326(9)	3760(20)	5225(8)
C45	3398(10)	4171(18)	5455(11)
C44	3675(12)	4179(17)	5689(8)
C43	3880(8)	3780(20)	5692(8)
C42	3807(11)	3371(18)	5462(11)
C48	3219(10)	1490(20)	4812(9)
C47	3293(10)	1962(16)	5015(12)
C52	3275(9)	1880(16)	5272(10)
C51	3182(10)	1330(20)	5327(9)
C50	3108(10)	854(13)	5124(12)
C49	3126(10)	936(19)	4867(10)
C53	4265(7)	1722(16)	5054(8)
C54	4303(7)	1895(17)	4845(8)
C55	4702(7)	1111(16)	5100(8)
C56	4939(8)	784(16)	5184(8)
C57	5364(7)	169(16)	5509(8)
C58	5449(7)	396(16)	5322(8)

Ni3	4856.3(11)	2310(3)	6199.1(13)
Ni4	4651.3(14)	4069(3)	3877.1(16)
S9	5031(2)	1992(5)	5929(2)
S10	4623(3)	3042(7)	5917(3)
S11	4565(2)	3432(6)	5321(3)
S12	4982(2)	2522(5)	5368(2)
S13	4898(3)	2943(5)	4738(3)
S14	4876(3)	3309(6)	4162(3)
S15	4433(2)	4374(5)	4118(3)
S16	4489(2)	3884(5)	4693(2)
P5	4609(3)	2301(7)	6435(3)
P6	5125.6(12)	1629(3)	6556.3(10)
P7	4428.9(13)	4747(3)	3538.6(11)
P8	4930.4(14)	3962(3)	3695.1(12)
C63	4094(8)	3900(20)	6474(10)
C64	4154(9)	3301(16)	6434(9)
C59	4424(11)	3148(14)	6473(10)

C60	4634(8)	3590(30)	6552(10)
C61	4574(10)	4190(20)	6592(9)
C62	4304(12)	4345(12)	6553(10)
C65	4304(8)	1566(16)	6279(11)
C66	4171(11)	1610(18)	5975(12)
C67	3925(10)	1270(20)	5804(8)
C68	3812(7)	890(20)	5938(10)
C69	3945(9)	849(18)	6243(11)
C70	4191(9)	1185(19)	6414(8)
C71	4854(9)	2037(14)	6805(5)
C72	4992(5)	1442(15)	6813(5)
C78	5498(3)	510(6)	6516.2(14)
C73	5233(3)	765(5)	6444.6(15)
C74	4983(3)	441(6)	6273(2)
C75	4998(3)	-138(6)	6172(2)
C76	5263(3)	-393(6)	6244(2)
C77	5513(3)	-70(6)	6415.8(18)

C81	5946.4(13)	1875(4)	7213.4(13)
C80	5670.5(12)	1651(3)	7044.7(10)
C79	5487.9(12)	1924(3)	6777.6(10)
C84	5581.1(15)	2421(4)	6679.3(16)
C83	5856.9(17)	2646(4)	6848(2)
C82	6039.5(14)	2372(5)	7115.0(18)
C85	4715(10)	2940(20)	5637(10)
C86	4897(9)	2530(20)	5655(9)
C87	4735(9)	3150(20)	5165(10)
C88	4728(9)	3205(19)	4932(10)
C89	4575(9)	3830(20)	4417(9)
C90	4772(10)	3420(20)	4449(10)
C92	4086(4)	5696(5)	3650.0(14)
C91	4367(4)	5591(5)	3710.1(16)
C96	4579(4)	6017(6)	3869(2)
C95	4509(4)	6548(6)	3968(2)
C94	4228(4)	6653(6)	3908(2)

C93	4017(4)	6227(6)	3748.8(19)
C97	4053.2(14)	4235(5)	3257.0(18)
C98	3911(3)	3702(6)	3254(5)
C99	3657(3)	3547(10)	3005(6)
C100	3546(2)	3926(18)	2760(3)
C101	3689(2)	4459(18)	2764(3)
C102	3942(2)	4614(10)	3012(4)
C103	4659(5)	4978(15)	3384(5)
C104	4826(8)	4443(12)	3372(5)
C110	4727.3(16)	2732(6)	3342.9(15)
C105	4944.7(16)	3027(6)	3583.2(14)
C106	5192.7(17)	2713(7)	3770.2(18)
C107	5223(2)	2104(7)	3717(2)
C108	5006(2)	1809(6)	3477(2)
C109	4758(2)	2123(6)	3289.7(19)
C112	5552(4)	4288(4)	3921(2)
C111	5326(4)	4416(4)	3977(2)

C116	5365(4)	4813(6)	4202(3)
C115	5631(4)	5083(6)	4372(3)
C114	5857(4)	4955(6)	4316(3)
C113	5817(4)	4557(5)	4090(2)
F25	6429(7)	4884(13)	4959(6)
F26	6676(8)	4878(13)	5406(5)
F27	6364(5)	4229(15)	5180(7)
F28	6916(6)	2183(10)	5279(7)
F29	7293(6)	2663(17)	5575(5)
F30	7256(5)	2515(16)	5208(6)
C181	7470(2)	6535(4)	5226(2)
F37	7794(4)	5774(7)	5930.8(18)
F38	7379(4)	6204(7)	5784(3)
F39	7741(4)	6746(6)	5831(3)
F40	7568(4)	7079(5)	4702(3)
F41	7231(3)	7420(4)	4790(3)
F42	7131(4)	6756(5)	4440(3)

C178	7434.9(15)	5324(4)	5041.9(16)
C179	7370.1(19)	5797(4)	4839.5(18)
C180	7387(2)	6401(4)	4932(2)
C182	7535(2)	6057(5)	5427(2)
C183	7518(2)	5453(4)	5336.4(16)
C184	7328(3)	6913(4)	4717(3)
C185	7614(3)	6196(6)	5743(2)
C190	7114(4)	3289(6)	5204(4)
C191	7278(5)	3639(9)	5114(7)
C186	7214(7)	4252(10)	5048(8)
C187	6987(6)	4515(7)	5070(7)
C188	6824(4)	4165(10)	5160(6)
C189	6887(4)	3552(10)	5226(5)
C192	6586(3)	4503(10)	5176(4)
C193	7073(4)	2674(7)	5305(4)
C197	7003(2)	4786(5)	3961.4(18)
F43	7468(4)	5741(8)	3970(3)

F44	7745(3)	4947(9)	4139(3)
F45	7363(3)	4909(8)	3710(3)
F46	6406(2)	4763(8)	3656(2)
F47	6491(3)	3851(8)	3844(2)
F48	6375.8(16)	4576(9)	4056(3)
C194	7262.6(16)	4677(3)	4573.8(18)
C195	6971.1(16)	4554(4)	4404.1(19)
C196	6841.2(19)	4609(5)	4098.4(18)
C198	7294(2)	4908(5)	4133(2)
C199	7425.1(18)	4855(4)	4440(2)
C200	6529(2)	4453(7)	3914(2)
C201	7467(3)	5123(7)	3988(3)
C205	8214.0(19)	3514(5)	5350(2)
F31	7844(3)	2746(6)	4650(3)
F32	7902(3)	2258(4)	5041(4)
F33	8274(3)	2594(6)	5011(4)
F34	8611(2)	3806(8)	5927(2)

F35	8615.5(18)	4648(7)	5706(3)
F36	8361(3)	4589(8)	5934(2)
C202	7711.1(16)	4207(4)	5087.3(15)
C203	7731.4(19)	3670(4)	4954.3(18)
C204	7983(2)	3325(4)	5085(2)
C206	8191.0(18)	4051(5)	5482.6(19)
C207	7940.4(17)	4399(4)	5352.1(17)
C208	8001(3)	2734(5)	4947(3)
C209	8444(2)	4271(7)	5763(2)
B2	7415.0(17)	4612(4)	4933.8(18)
F7	8717(6)	5200(17)	7364(5)
F8	8873(5)	5234(17)	7833(5)
F9	8473(6)	5696(11)	7539(6)
F10	8870(4)	3064(17)	7888(6)
F11	8557(7)	2496(10)	7622(6)
F12	8579(6)	2932(17)	8028(5)
F13	7766(4)	3259(15)	8042(8)

F14	7430(6)	3952(10)	7973(7)
F15	7394(7)	2935(10)	7985(7)
F16	6706(5)	2352(15)	7033(6)
F17	6754(8)	2754(15)	6642(4)
F18	6971(7)	2047(10)	6889(7)
F19	7659(5)	1800(14)	6612(5)
F20	8077(4)	2035(17)	6657(6)
F21	7700(6)	2067(17)	6227(4)
F22	7396(3)	4408(13)	5876(6)
F23	7799(5)	4801(8)	6131(7)
F24	7757(4)	4011(12)	5885(4)
C149	7140(3)	5635(6)	6961(3)
F1	6665(4)	4751(9)	6326(4)
F2	6826(5)	5612(10)	6252(3)
F3	6583(3)	5596(10)	6495(4)
F4	7373(4)	6574(7)	7370(4)
F5	7391(4)	5833(11)	7658(3)

F6	7772(4)	6078(10)	7625(4)
C146	7496(5)	4642(9)	7024(5)
C147	7236(4)	4709(8)	6767(4)
C148	7058(3)	5204(6)	6737(3)
C150	7400(3)	5564(7)	7218(3)
C151	7579(4)	5070(9)	7250(4)
C152	7485(4)	6014(8)	7467(3)
C153	6783(4)	5290(8)	6454(3)
C157	7200(3)	3003(10)	7399(3)
C158	7433(4)	3354(11)	7587(3)
C159	7594(5)	3660(13)	7479(5)
C154	7520(6)	3614(16)	7183(5)
C155	7286(6)	3262(14)	6995(3)
C156	7126(4)	2956(10)	7103(3)
C160	6867(4)	2576(8)	6921(4)
C161	7491(4)	3412(9)	7900(3)
C166	8456(4)	4656(6)	7511(6)

C167	8166(4)	4619(10)	7312(6)
C162	8022(4)	4069(13)	7271(7)
C163	8168(6)	3557(9)	7429(7)
C164	8458(6)	3594(7)	7628(6)
C165	8602(3)	4144(10)	7669(5)
C168	8639(4)	5215(7)	7573(4)
C169	8588(4)	3002(7)	7776(4)
C172	7696(5)	3847(7)	6303(3)
C171	7687(7)	4077(7)	6548(5)
C170	7712(9)	3685(12)	6771(5)
C175	7746(8)	3063(11)	6747(5)
C174	7756(6)	2833(6)	6501(5)
C173	7731(6)	3225(8)	6279(4)
C176	7798(4)	2156(5)	6514(4)
C177	7666(3)	4266(6)	6060(3)
B1	7678(3)	4027(6)	7036(3)
Ni5	5834.4(12)	2938(2)	5154.7(14)

S17	5649(3)	3245(6)	5420(3)
S18	5623(3)	3623(6)	4810(3)
S19	5197(3)	4618(6)	4750(3)
S20	5250(3)	4325(6)	5323(3)
P9	6131.7(16)	2370(5)	5504.6(12)
P10	5947.0(14)	2373(5)	4891(2)
C120	5128(9)	1020(20)	4344(9)
C119	5406(11)	799(15)	4502(10)
C118	5634(7)	1200(30)	4639(9)
C117	5583(8)	1830(20)	4618(9)
C122	5305(11)	2047(15)	4460(10)
C121	5078(6)	1640(20)	4323(9)
C124	6007.0(15)	2365(7)	4365(4)
C125	6063.2(19)	2513(9)	4136(4)
C126	6177(3)	3080(11)	4130(4)
C127	6234(5)	3499(9)	4353(5)
C128	6178(5)	3351(8)	4582(5)

C123	6064(2)	2784(7)	4588(4)
C129	6264(9)	1870(20)	5143(9)
C130	6239(9)	1716(18)	5368(8)
C136	6779.9(19)	2602(8)	5862.6(12)
C135	7029(2)	2932(11)	6029.7(18)
C134	7012(4)	3540(10)	6095(3)
C133	6746(4)	3817(8)	5994(4)
C132	6497(3)	3486(6)	5827(3)
C131	6514(2)	2879(6)	5761.4(16)
C141	5681(7)	1519(17)	5934(7)
C140	5858(7)	1625(17)	6232(6)
C139	6111(7)	1953(16)	6323(4)
C138	6185(7)	2175(18)	6117(3)
C137	6007(6)	2069(16)	5819(4)
C142	5755(5)	1741(14)	5728(5)
C143	5447(7)	3952(15)	4988(8)
C144	5440(8)	3874(17)	5189(9)

C145	5110(6)	4746(12)	5017(3)
F49	4236(9)	634(18)	2555(8)
F50	4469(8)	-89(19)	2900(8)
F51	4359(8)	758(18)	2976(8)
F52	5486(7)	26(9)	3538(6)
F53	5573(7)	930(11)	3651(5)
F54	5723(4)	525(14)	3390(6)
F57A	5808(10)	2771(11)	2301(7)
F58A	6091(4)	3380(20)	2637(10)
F59A	5651(9)	3695(13)	2258(7)
C213	4952(4)	536(13)	3092(5)
C214	5219(3)	776(15)	3159(5)
C215	5241(5)	1240(15)	2988(7)
C210	4996(7)	1466(14)	2749(7)
C211	4729(5)	1226(16)	2682(6)
C212	4707(3)	762(15)	2853(6)
C216	5488(3)	563(9)	3420(4)

C217	4436(5)	480(20)	2820(11)
C221	5720(3)	3317(6)	2895(3)
F1G	5464(5)	3875(9)	3299(4)
F55	5613(5)	3005(10)	3522(4)
F56	5914(4)	3625(9)	3483(3)
F57	5645(5)	3217(12)	2164(3)
F58	6048(4)	2924(12)	2532(4)
F59	5896(5)	3852(10)	2518(4)
C218	5311(5)	2388(10)	2662(5)
C219	5376(4)	2644(9)	2934(4)
C220	5581(3)	3108(7)	3050(3)
C222	5652(3)	3059(8)	2622(3)
C223	5448(4)	2593(9)	2506(4)
C224	5644(4)	3401(8)	3338(3)
C225	5809(4)	3265(10)	2459(4)
B3	5000	2070(60)	2500

C.9 Computational Methodology

Variational two-electron reduced density matrix (V2RDM) calculations were performed using the Maple Quantum Chemistry Package (QCP).[1] Natural orbital density plots were obtained using the DensityPlot3D procedure in QCP. As with wave-function-based complete active-space self-consistent-field (CASSCF) techniques, active-space V2RDM variationally solves the Schrödinger equation for an active set of orbitals, known as an active space, followed by orbital rotations between the active and inactive orbitals to lower the energy until self-consistency is achieved.[2] V2RDM has been successfully used to account for most of the strong correlation in a variety of large transition-metal molecules.[3] The major advantage of V2RDM over traditional wave-function-based methods is its favorable polynomial scaling of $O(r^6)$, compared to the $O(r^N)$ exponential scaling of conventional wave-function-based methods (where r is the number of basis functions and N is the number of active electrons). This scaling is the result of the fact that in V2RDM calculations the 2-RDM is computed directly, avoiding the explicit calculation of the entire wave function.

As fermionic interactions are pairwise the energy of any system can be expressed as a linear functional of the 2-RDM: $E = Tr[{}^2K{}^2D]$, where ${}^2K$ is the 2-electron reduced Hamiltonian, and ${}^2D$ is the 2-RDM. The energy is variationally minimized using a semidefinite program,[4] which minimizes the energy as a functional of the 2-RDM subject to several N-representability constraints:[5]

$$ {}^2D \succeq 0 \tag{1} $$

$$ {}^2Q \succeq 0 \tag{2} $$

$$ {}^2G \succeq 0 \tag{3} $$

These conditions are termed the DQG conditions, where ${}^2D$ is the two-particle matrix, ${}^2Q$ is the two-hole matrix, ${}^2G$ the particle-hole matrix, and $M \succeq 0$ indicates that matrix M is positive semidefinite, meaning its eigenvalues are nonnegative. As the 2-RDM is calculated directly, without the wave function, the DQG conditions are necessary to ensure that the 2-RDM remains *N*-representable, meaning there must be a corresponding *N*-electron wave function. The minimized energy from a V2RDM calculation represents a lower bound to the true ground state energy. Calculations using [19,20] active spaces as carried out in this in study remain outside the scope of traditional wave-function-based CASSCF methods.

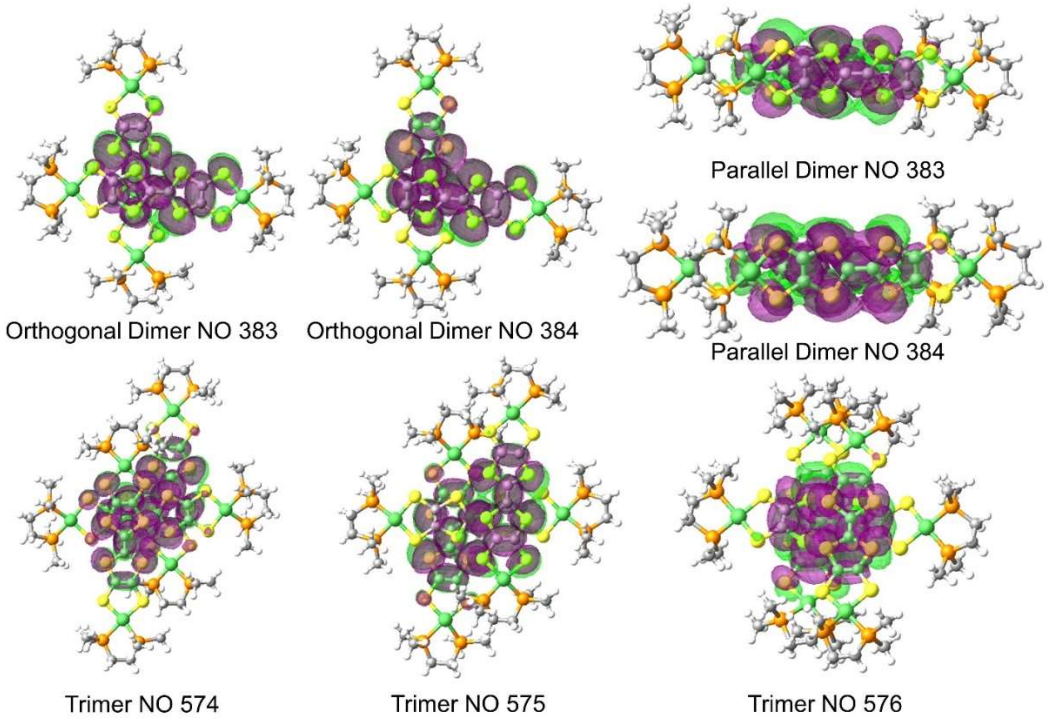

Figure C.59. Orbital density plots for the computationally treated dimers and trimers viewed along the stacking interaction.

Table C.7 Energies, NO occupations and Mulliken charges for the two different dimerization geometries. V2RDM calculations with a [19,20] active space and 3-21G basis set.

	Parallel	Orthogonal
E(a.u.)	-16430.761095	-16430.712292
λ382	1.88571	1.912486

$\lambda 383$	1.49923	1.224860
$\lambda 384$	0.51331	0.771141
$\lambda 385$	0.08481	0.073175
$q1$	0.40607	0.37830
$q2$	0.56836	0.43482
$q3$	0.57037	0.45403
$q4$	0.40265	0.43870

Table C.8. Energies, NO occupations and Ni atom Mulliken charges for the trimer unit. V2RDM calculations were performed with a [17,20] active space and 3-21G basis set.

	V2RDM
E(a.u.)	-24645.905214
$\lambda 573$	1.92977
$\lambda 574$	1.32748
$\lambda 575$	0.97218
$\lambda 576$	0.64935
$\lambda 577$	0.06524
$q1$	0.44168
$q2$	0.44892
$q3$	0.43547
$q4$	0.43356
$q5$	0.44406
$q6$	0.43699

C.10 References

[1] Maple Quantum Chemistry Toolbox (**2019**). Maplesoft, a division of Waterloo Maple Inc., Waterloo, Ontario.

[2] (a) Mazziotti, D. A. Two-Electron Reduced Density Matrix as the Basic Variable in Many-Electron Quantum Chemistry and Physics. *Chem. Rev.* **2012**, 112, 244−262. (b) Mazziotti, D. A., Ed. Variational Two-Electron Reduced-Density Matrix Theory. In Reduced-Density-Matrix Mechanics: With Application to Many-Electron Atoms and Molecules; John Wiley and Sons, Inc.: Hoboken, NJ, **2007**; pp 19−59. (c) Nakata, M.; Nakatsuji, H.; Ehara, M.; Fukuda, M.; Nakata, K.; Fujisawa, K. Variational Calculations of Fermion Second-Order Reduced Density Matrices by Semidefinite Programming Algorithm. *J. Chem. Phys.* **2001**, 114, 8282−8292. (d) Mazziotti, D. Realization of Quantum Chemistry without Wave Functions through First-Order Semidefinite Programming. *Phys. Rev. Lett.* **2004**, 93, 213001. (e) Gidofalvi, G. and Mazziotti, D. A. Active-Space Two-Electron Reduced-Density-Matrix Method: Complete Active-Space Calculations without Diagonalization of the N-electron Hamiltonian. *J. Chem. Phys.* **2008**, 129, 134108. (f) Shenvi, N.; Izmaylov, A. F. Active-Space N-Representability Constraints for Variational Two-Particle Reduced Density Matrix Calculations. *Phys. Rev. Lett.* **2010**, 105, 213003. (g) Verstichel, B.; van Aggelen, H.; Poelmans, W.; Van Neck, D. Variational Two-Particle Density Matrix Calculation for the Hubbard Model Below Half Filling Using Spin-Adapted Lifting Conditions. *Phys. Rev. Lett.* **2012**, 108, 213001. (h) Fosso-Tande, J.; Nguyen, T.-S.; Gidofalvi, G.; DePrince,

A. E., III Large-Scale Variational Two-Electron Reduced-Density-Matrix Driven Complete Active Space Self-Consistent Field Methods. *J. Chem. Theory Comput.* **2016**, 12, 2260−2271. (i) Mazziotti, D. A. Enhanced Constraints for Accurate Lower Bounds on Many-Electron Quantum Energies from Variational Two Electron Reduced Density Matrix Theory. *Phys. Rev. Lett.* **2016**, 117, 153001.

[3] (a) Schlimgen, A. W.; Heaps, C. W.; Mazziotti, D. A. Entangled Electrons Foil Synthesis of Elusive Low-Valent Vanadium Oxo Complex. *J. Phys. Chem. Lett* **2016**, 7, 627–631. (b) Schlimgen, A. W.; Mazziotti, D. A. Static and Dynamic Electron Correlation in the Ligand Noninnocent Oxidation of Nickel Dithiolates. *J. Phys. Chem. A* **2017**, 121, 9377–9384. (c) Montgomery, J. M.; Mazziotti, D. A. Strong Electron Correlation in Nitrogenase Cofactor, FeMoco. *J. Phys. Chem. A* **2018**, 122, 4988–4996. (d) McIsaac, A. R.; Mazziotti, D. A. Ligand Non-innocence and Strong Correlation in Manganese Superoxide Dismutase Mimics. Phys. Chem. Chem. Phys. **2017**,19, 4656–4660.

[4] (a) Mazziotti, D. A. First-order Semidefinite Programming for the Two-electron Treatment of Many-Electron Atoms and Molecules. *ESAIM: Math. Modell. Numer. Anal.* **2007**, 41, 249−259. (b) Mazziotti, D. A. Large-Scale Semidefinite Programming for Many-Electron Quantum Mechanics. *Phys. Rev. Lett.* **2011**, 106, 083001.

[5] (a) Mazziotti, D. A. Variational reduced-density-matrix method using three-particle *N*-representability conditions with application to many-electron molecules. *Phys. Rev. A: At., Mol., Opt. Phys.* **2006**, 74, 032501. (b) Garrod C. and Percus, J. Reduction of the *N*-Particle Variational Problem. J. Math. Phys. (N.Y.) **1964**, 5, 1756.

Appendix D:Supporting Data for Chapter 5

D.1 Characterization and Analysis Methods

Magnetometry. Magnetic measurements were carried out on a Quantum Design MPMS3 performed on bulk powder samples in polycarbonate capsules. The powder samples were suspended in an eicosane matrix to prevent movement and protect the sample from incidental air exposure. Frozen solution samples in PEG-2000 were prepared by dissolving **2** and PEG-2000 in DCM, then removing DCM under reduced pressure. Diamagnetic corrections for the capsule and eicosane were made by measuring temperature vs. moment in triplicate for each to determine a moment per gram correction. The diamagnetic correction for PEG-2000 was made by measuring sample versus moment to determine a moment per gram correction. Pascal's constants were used to correct for the diamagnetic contribution from the complexes.[1]

Single Crystal X-Ray Diffraction (SXRD). The diffraction data for **2-LT** and **2-HT** were measured at 100 K and 298 K, respectively, on a Bruker D8 VENTURE diffractometer equipped with a microfocus Mo-target X-ray tube (λ = 0.71073 Å) and PHOTON 100 CMOS detector. The diffraction data for **3** was measured at 100 K on a Bruker D8 fixed-chi with PILATUS1M (CdTe) pixel array detector (synchrotron radiation, λ = 0.41328 Å (30 KeV)) at the Chem-MatCARS 15-ID-B beam-line at the Advanced Photon Source (Argonne National Laboratory). Data reduction and integration were performed with the Bruker APEX3 software package (Bruker AXS, version 2015.5-2, 2015[2]). Data were scaled and corrected for absorption effects using the multi-scan procedure as implemented in SADABS (Bruker AXS, version 2014/54[3]). The structures were solved by SHELXT (Version 2014/55[4]) and refined by a full-matrix least-squares procedure using

OLEX26 (XL refinement program version 2018/17[5]). We have only been able to obtain a poor quality structure of **4** which verifies its connectivity.

X-Ray Powder Diffraction (XRPD) Diffraction patterns were collected on a SAXSLAB Ganesha diffractometer with a Cu K-α source (λ = 1.54 Å) in wide angle X-ray scattering (WAXS) transmission mode. The samples were contained in a ~1 mm diameter borosilicate capillary tube. A correction was made to subtract the broad peak from the capillary around 16–25° (2θ) from the baseline.

UV-vis-NIR. Variable temperature UV-vis-NIR measurements were performed on a Shimadzu UV-3600 Plus dual beam spectrophotometer with a Unisoku CoolSpeK 203-B cryostat. UV-vis region spectra were collected on Thermo Scientific Evolution 300 spectrometer with the VISIONpro software suite. Samples were stirred during cooling and during measurements colder than room temperature. Background spectra of the cuvette and solvent were collected at maximum and minimum temperatures within the range to account for temperature dependence of the background.

Cyclic Voltammetry. Electrochemical measurements were performed using a BAS Epsilon potentiostat and analyzed using BAS Epsilon software version 1.40.67NT. Cyclic voltammetry measurements were made using a glassy carbon working electrode, platinum wire counter electrode, and silver wire pseudo-reference electrode, and referenced to internal Fc/Fc^{+}.

EPR Spectroscopy. EPR spectra were recorded on a Bruker Elexsys E500 spectrometer equipped with an Oxford ESR 900 X-band cryostat and a Bruker Cold-Edge Stinger. Simulation of EPR spectra was performed using a least-squares fitting method with the SpinCount program.

Mössbauer Spectroscopy. Zero-field iron-57 Mössbauer spectra were with a constant acceleration spectrometer and a rhodium embedded cobalt-57 source. Prior to measurements, the

spectrometer was calibrated at 295 K with α-iron foil. Samples were prepared in a N_2-filled glovebox where powdered samples were placed in a polyethylene cup and frozen in liquid nitrogen prior to handling in air. All spectra were analyzed using the WMOSS Mössbauer Spectral Analysis Software.[6]

FT-IR Spectroscopy. Powder samples for FT-IR were formed into pellets in a potassium bromide matrix. Spectra were acquired in absorbance mode on a Bruker Tensor II with background subtractions used to account for air. A linear baseline correction was applied.

NMR Spectroscopy. ^{1}H and ^{2}H spectra were recorded on Bruker DRX 400 or 500 spectrometers. Chemical shifts of ^{1}H NMR are reported in ppm units referenced to residual solvent resonances. Variable temperature ^{2}H NMR spectra were collected in 95/5 w/w% of 2-chlorobutane/C_6D_6 with a capillary of 90/10 w/w% 2-chlorobutane/C_6D_6. The temperature dependent change in density of both 2-chlorobutane and C_6D_6 was accounted for at each temperature point, to yield an accurate solution concentration. Pascal's constants were used to correct for the diamagnetic contribution of the complex.

Fitting of Magnetic and NIR Data of 2 to a Boltzmann Distribution. The magnetic data and NIR spectroscopic data of **2** were fit to a Boltzmann distribution of the form:

$$\frac{p_{\mathrm{HT}}}{p_{\mathrm{LT}}} = e^{\Delta H / k_B (\frac{1}{T} - \frac{1}{T_{1/2}})}$$

Equation D.1

Where p_{HT} and p_{LT} are the fractions of HT and LT forms of **2**, respectively, ΔH is the enthalpy difference between **2-HT** and **2-LT**, k_{B} is the Boltzmann constant, T is the temperature of the measurement, and $T_{1/2}$ is the transition temperature.

For the spectroscopic data, the fraction of **2-HT** was estimated by assuming the fraction of **2-HT** at 173 K is zero, due to the lack of the characteristic NIR signal around 1100 nm. The fraction of **2-LT** at 173 K is correspondingly 100%, and a linear relationship between intensity and concentration of **2-LT** was assumed in order to calculate the fraction of each form at various temperatures.

TD-DFT Calculations. TD-DFT calculations were performed with ORCA[7,8,9,10] software suite using time-dependent density functional theory (TD-DFT). The PBE0 functional was used with a basis set of def2-TZVPP on Fe and def2-TZVP on all other atoms. Furthermore, an effective core potential of SDD was used on Fe. Starting coordinates for all calculations were from crystal structures determined by single crystal X-ray diffraction at 100 K or 293 K as indicated. Simulations of UV-vis spectra were generated using the orca_mapspc function with line broadening of 2000 cm^{-1}. Molecular orbitals were generated using the orca_plot function and visualized in Avogadro with an iso value of 0.3.

To calibrate the calculations, the electronic spectrum of the previously reported[12] reference complex $[(dppeNi)_2TTFtt][BAr^F{}_4]_2$ — which features a doubly oxidized TTF core, as in **2** — was calculated by the same methods using the reported crystal structure. Using the experimental spectral data, a weighted calibration was calculated using the shifts to the primary absorbances (i.e. at 1039 and 516 nm). This calibration was then applied to the calculated spectra of **2**. The predicted spectra of both $S = 0$ **2-LT** and $S = 4$ **2-HT** match well to the spectra of **2** at 20 °C. Conversely, the low temperature spectrum of **2** only matches well with the predicted spectrum of the $S = 1$ spin state of the **2-LT** structure. The are many predicted transitions for the $S = 4$ state of **2-HT** and their orbital composition is complicated and highly mixed. Nevertheless, the predicted spectrum matches experiment well, and TTFtt character is apparent in the NIR transitions. The

predicted transitions of the closed shell $S = 0$ state of **2-LT** are much simpler, match those in $[(dppeNi)_2TTFtt][BAr^F{}_4]_2$, and provide a clearer interpretation of the orbital composition. While we don't believe that the closed shell $S = 0$ state of **2-LT** is an accurate electronic structure description, it does serve as a simpler model to understand the orbital contributions of the NIR features of **2** at high temperature.

V2RDM and DFT Methods. Variational 2-electron reduced density matrix (V2RDM) and DFT calculations were carried out to elucidate the electronic structure of **2**. The V2RDM method allows large complete active space self-consistent field (CASSCF) to be carried out with polynomial $O(r^6)$ computational scaling, enabling calculations to be carried out that remain out of reach of traditional wave function based CASSCF methods which scale exponentially.[11] This is achieved by formulating the system energy as a linear functional of the 2RDM:

$$E = Tr[{}^2K\ {}^2D] \qquad (1)$$

where ${}^2K$ is the 2-electron reduced Hamiltonian, and ${}^2D$ is the 2-RDM. Minimization of the energy is subject to a set of constraints on the 2RDM that are termed N-representability constraints and ensure that variationally obtained 2RDM corresponds to a physically feasible system.[12,13]

$${}^2D \geq 0 \qquad (2)$$

$${}^2Q \geq 0 \qquad (3)$$

$${}^2G \geq 0 \qquad (4)$$

This procedure is carried out using a semi-definite program.[27,**Error! Bookmark not defined.**] The V2RDM method has been demonstrated to recover the vast majority of the correlation energy in strongly correlated systems and has recently been applied to a range of transition metal systems to successfully explain their electronic structure.[14,15,12] To ensure that the obtained NO and spin state splitting picture of the LT form of **2** is not an artifact of the choice of active space orbitals and size

or basis set further calculations on the singlet and triplet state were carried out using a [16,14] active apace and 6-31G basis sets and a [14,14] active space with a larger 6-31G* basis set, each time forcing iron 3d orbitals into the active space for the initial guess. The data are shown in **Table D.1**. While the [16,14] active space is not large enough to account for the full correlation energy yielding a significantly smaller singlet-triplet gap of $\Delta E(T–S) = 210$ cm^{-1}, the [14,14]/6-31G* calculation gives an almost identical gap to the larger [18,20] calculation with $\Delta E(T–S) = 379$ cm^{-1}. In both cases the CASSCF routine rotates the NOs with iron 3d contributions back into the core and virtual orbitals, obtaining identical Nos as those obtained in the [18,20] calculation.

D.2 Data and spectra

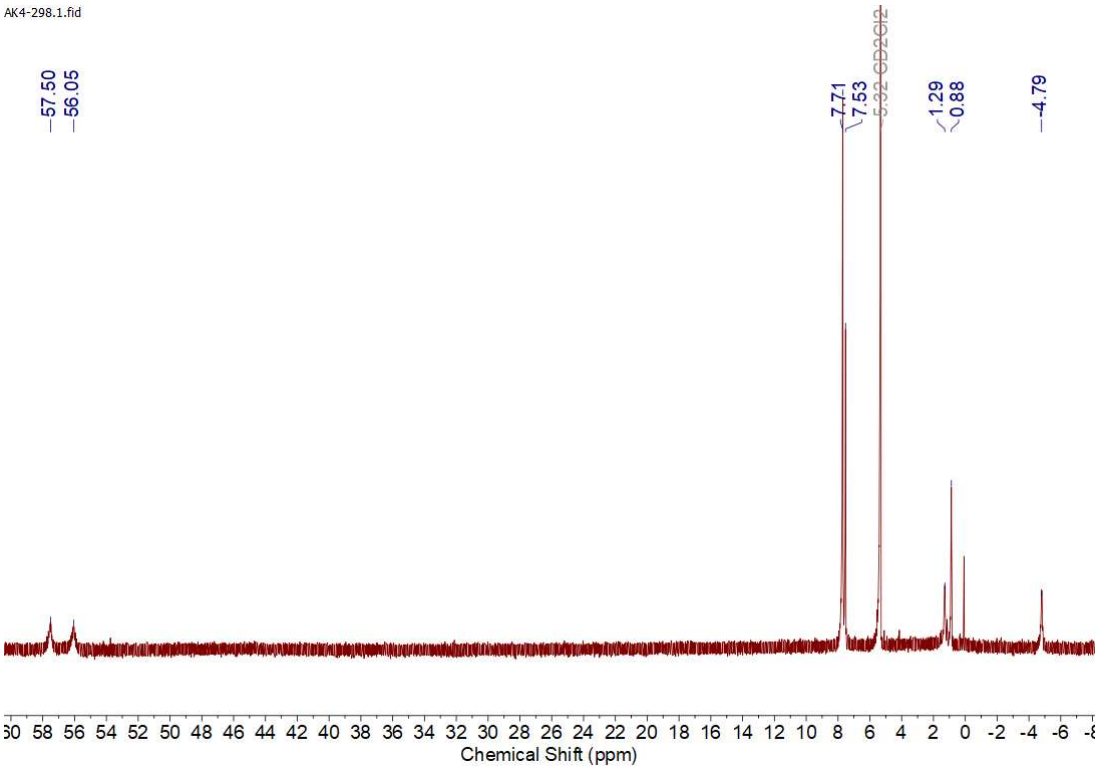

Figure D.1. ^{1}H NMR spectrum of 2 in CD_2Cl_2.

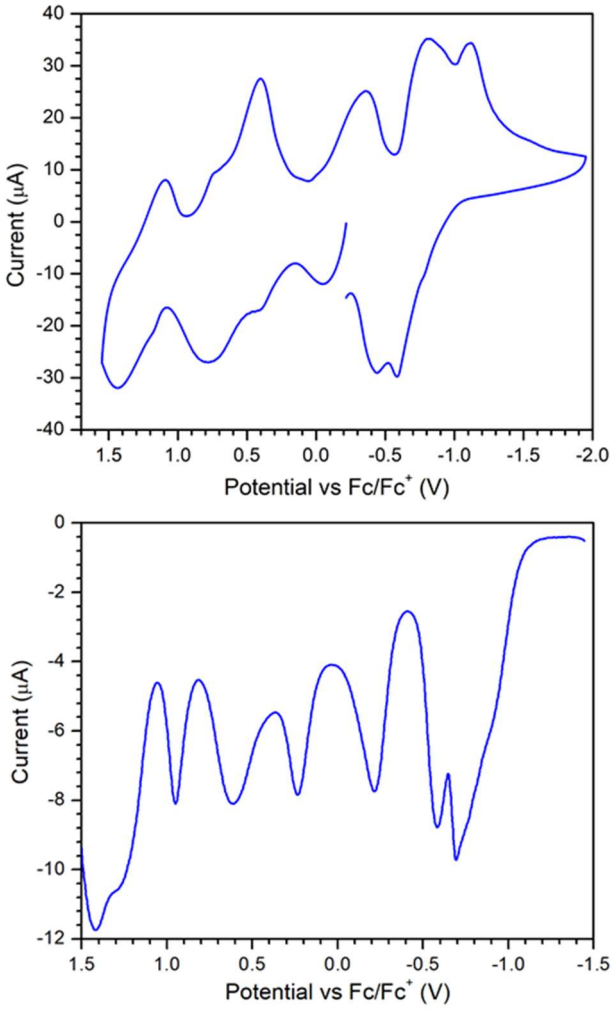

Figure D.2. Cyclic voltammogram (CV) and differential pulse voltammogram (DPV) of 2. It is collected in DCM with 0.1 M [TBA][PF_6]. The CV was collected at a scan rate of 250 mV/s. The DPV was collected with a 4 mV step, 50 mV pulse amplitude, 50 ms pulse width, and 200 ms pulse period.

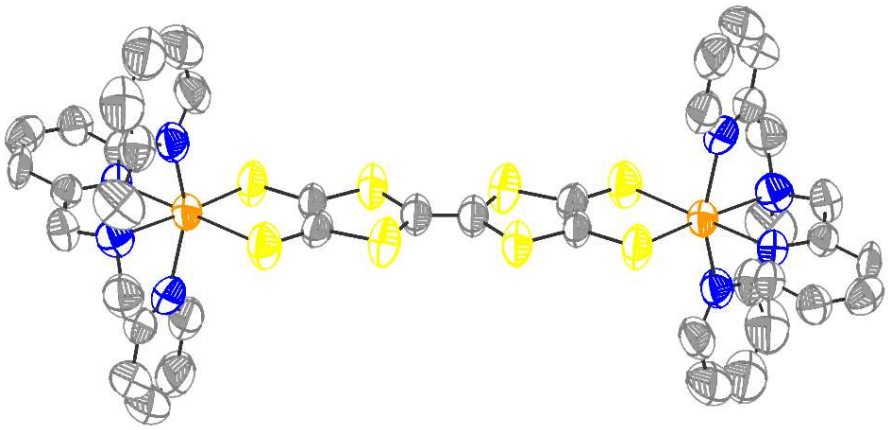

Figure D.3. Molecular structure of 2 at 293 K (2-HT). Atom colors: grey – carbon, yellow – sulfur, blue – nitrogen, orange – iron. H-atoms and BAr^F_4 counter anion omitted for clarity. Ellipsoids are shown at 50% probability.

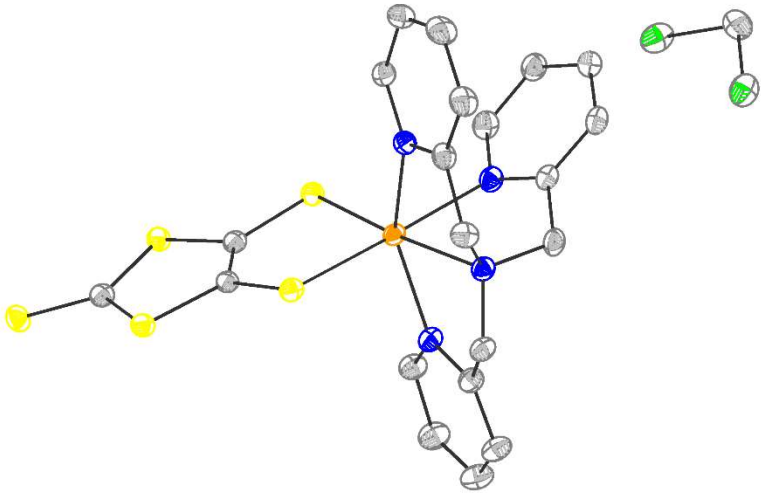

Figure D.4. Molecular structure of 3 at 100 K. Atom colors: grey – carbon, yellow – sulfur, blue – nitrogen, orange – iron, green – chlorine. H-atoms omitted for clarity. Ellipsoids are shown at 50% probability.

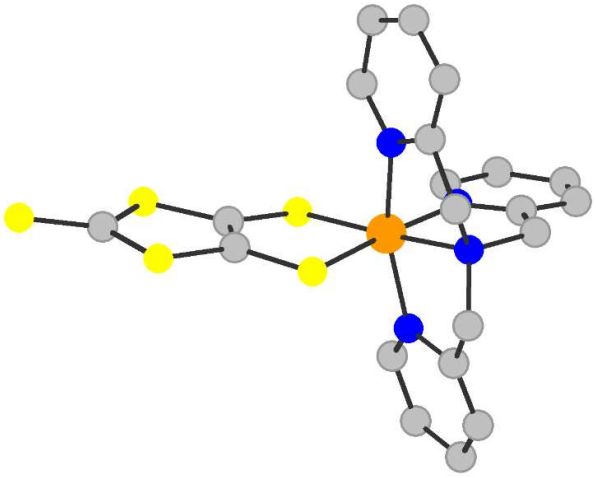

Figure D.5. Molecular structure of 4 at 100 K. Structure shown in ball-and-stick model for atom connectivity only, due to poor data quality. Atom colors: grey – carbon, yellow – sulfur, blue – nitrogen, orange – iron. H-atoms and BAr^{F}_{4} counter anion omitted for clarity.

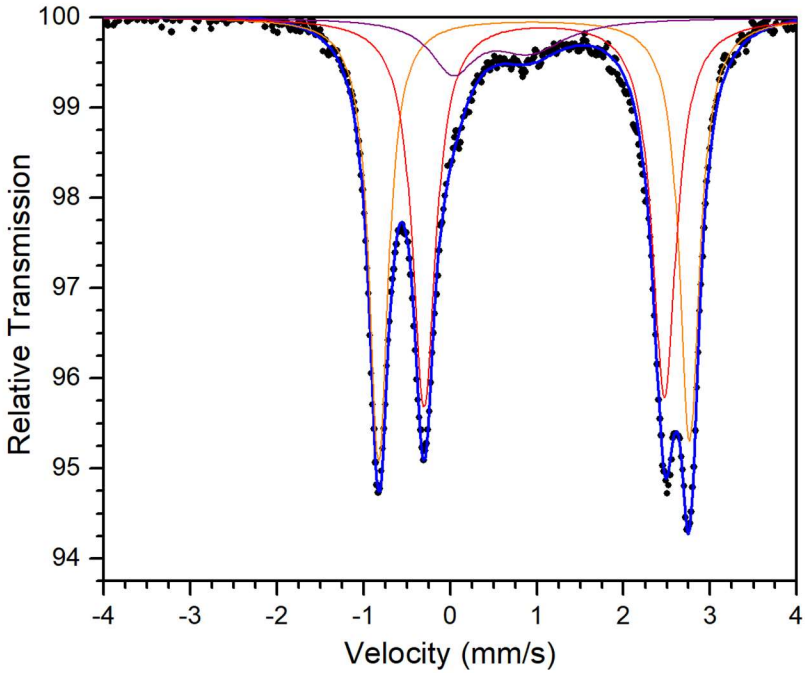

Figure D.6. Mössbauer spectrum of 1 at 80 K. Batch I. Site A (orange): δ = 0.968(2) mm/s; ΔE_Q = 3.588(5) mm/s; 48(2)%. Site B (red): δ =1.084(2) mm/s; ΔE_Q = 2.773(1) mm/s; 52(2)%. Overall Fit (blue): $R\chi^2$ = 0.839. Note: Overall fit includes minor Fe(III) impurity (purple): δ = 0.45 mm/s ; ΔE_Q = 0.90 mm/s.

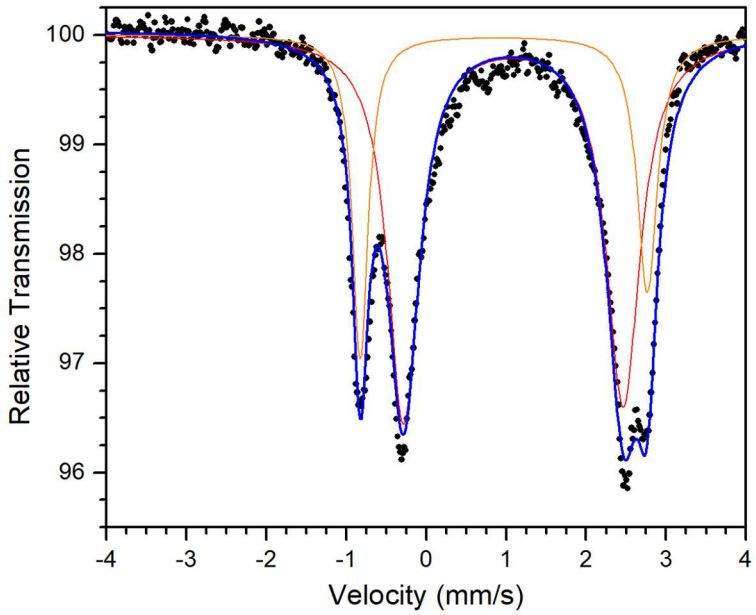

Figure D.7, Mössbauer spectrum of 1 at 80 K. Batch II. Site A (orange): δ = 0.969(4) mm/s; ΔE_Q = 3.589(9) mm/s; 30(2)%. Site B (red): δ = 1.089(3) mm/s; ΔE_Q = 2.748(8) mm/s; 70(1)%. Overall Fit (blue): $R\chi^2$ = 2.079.

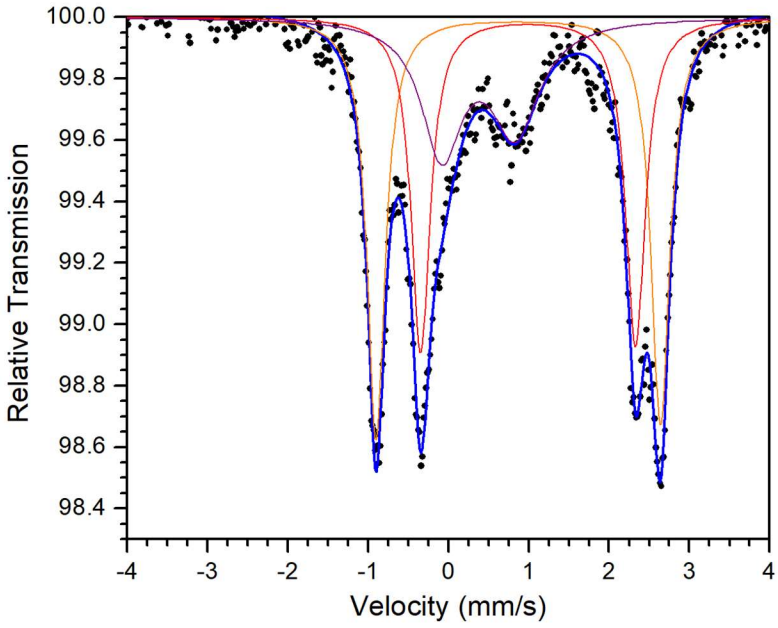

Figure D.8. Mössbauer spectrum of 1 at 250 K. Batch I. Site A (orange): δ = 0.8700(8) mm/s; ΔE_Q = 3.54(1) mm/s; 39(5)%. Site B (red): δ = 0.991(5) mm/s; ΔE_Q = 2.675(8) mm/s; 33(4)%. Overall Fit (blue): $R\chi^2$ = 0.558. Note: Overall fit includes minor Fe(III) impurity (purple): δ = 0.375 mm/s ; ΔE_Q = 0.915 mm/s.

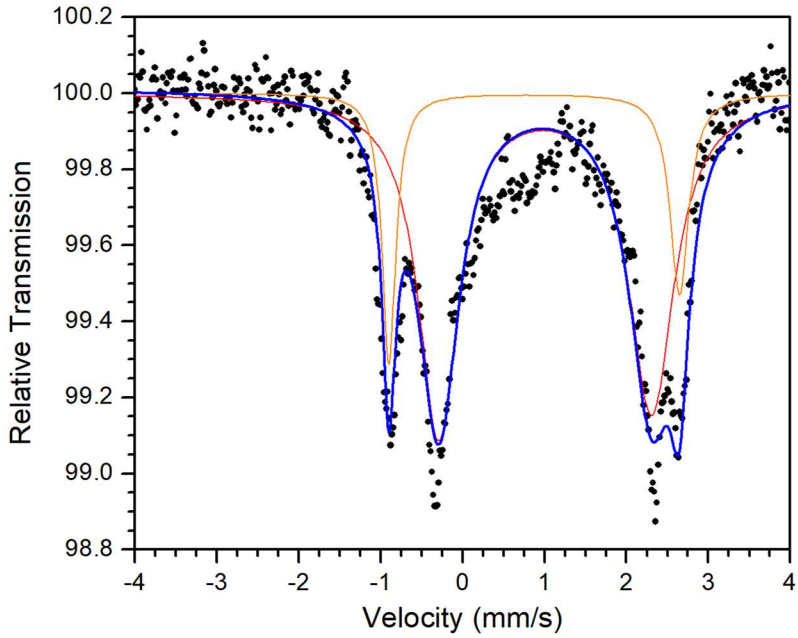

Figure D.9. Mössbauer spectrum of 1 at 250 K. Batch II. Site A (orange): δ = 0.87(1) mm/s; ΔE_Q = 3.55(2) mm/s; 21(2)%. Site B (red): δ = 1.01(2) mm/s ; ΔE_Q = 2.60(3) mm/s; 79(4)%. Overall Fit (blue): Rχ^2 = 1.476.

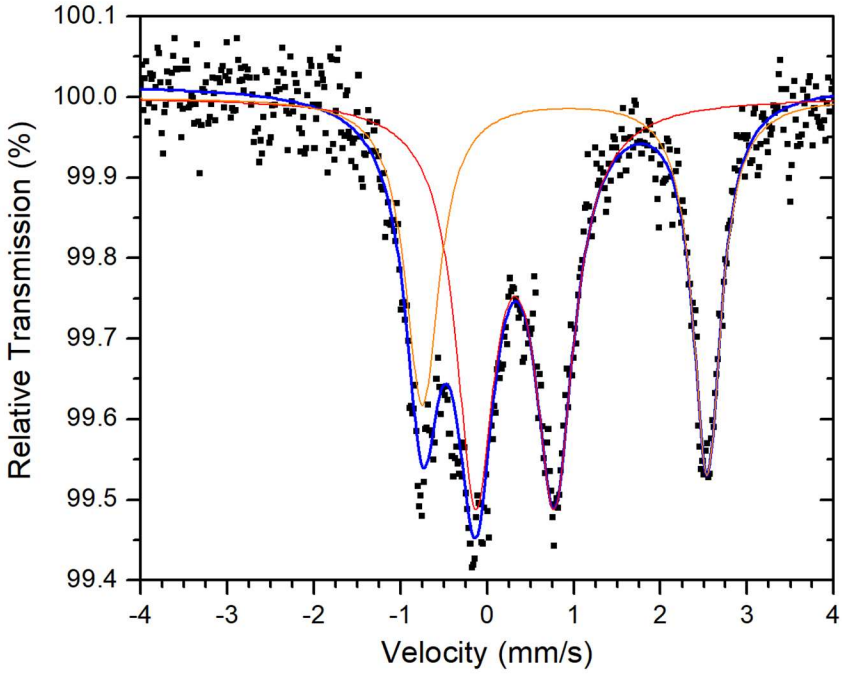

Figure D.10. Mössbauer spectrum of 2 in a frozen solution of PEG-2000 at 250 K. Site A (red): δ = 0.32(9) mm/s; ΔE_Q = 0.91(2) mm/s; 59(3)%. Site B (orange): δ = 0.89(5) mm/s; ΔE_Q = 3.29(3) mm/s; 41(5)%. Overall Fit (blue): Rχ^2 = 0.565.

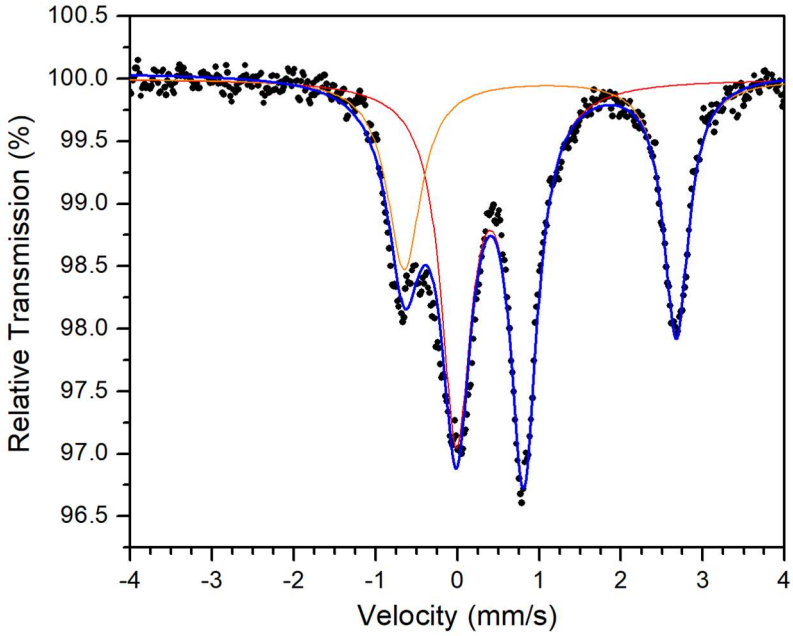

Figure D.11. Mössbauer spectrum of 2 in a frozen solution of PEG-2000 at 80 K. Site A (red): δ = 0.398(3) mm/s; ΔE_Q = 0.823(7) mm/s; 63(3)%. Site B (orange): δ = 1.01(1) mm/s; ΔE_Q = 3.32(1) mm/s; 37(3)%. Overall Fit (blue): Rχ^2 = 1.632.

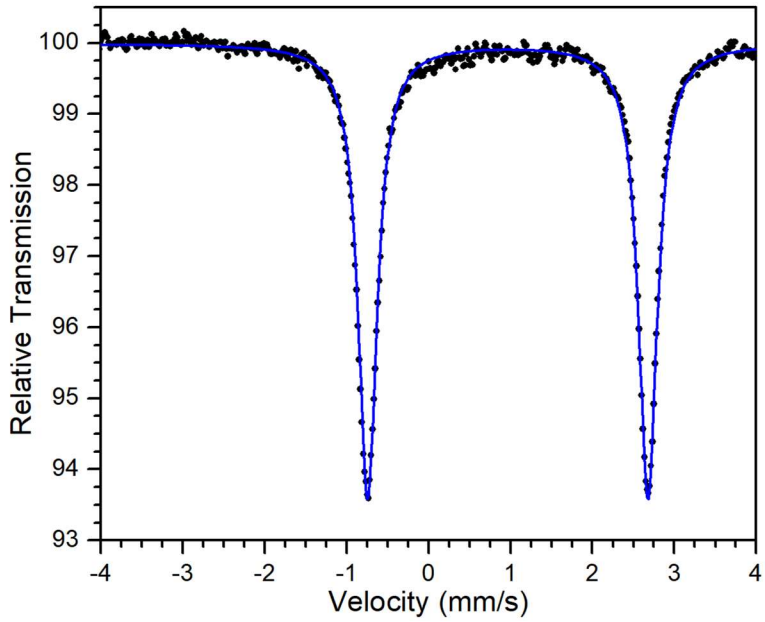

Figure D.12. Mössbauer spectrum of 3 at 80 K. δ = 0.966(1) mm/s; ΔE_Q = 3.422(3) mm/s. Fit (blue): Rχ^2 = 1.08.

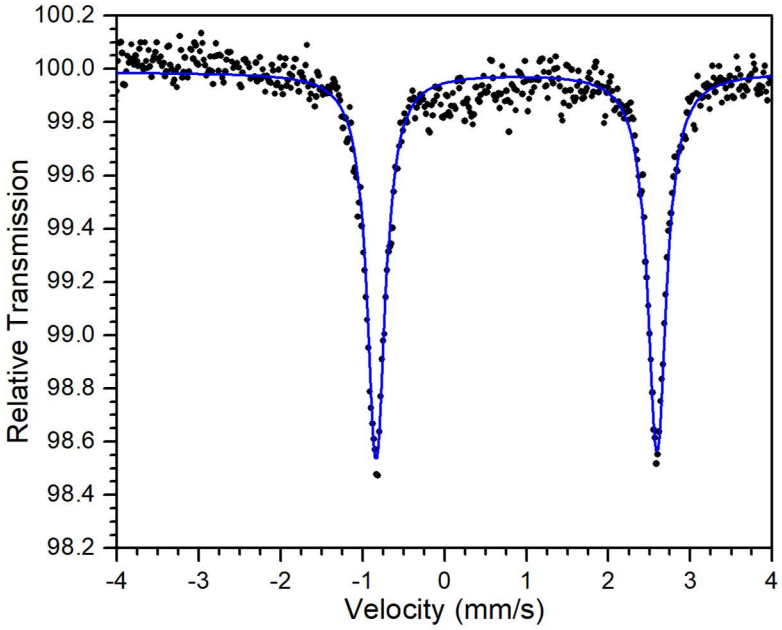

Figure D.13. Mössbauer spectrum of 3 at 250 K. Parameters: δ = 0.878(5) mm/s; ΔE_Q = 3.43(1) mm/s. Fit (blue): Rχ^2 = 0.766.

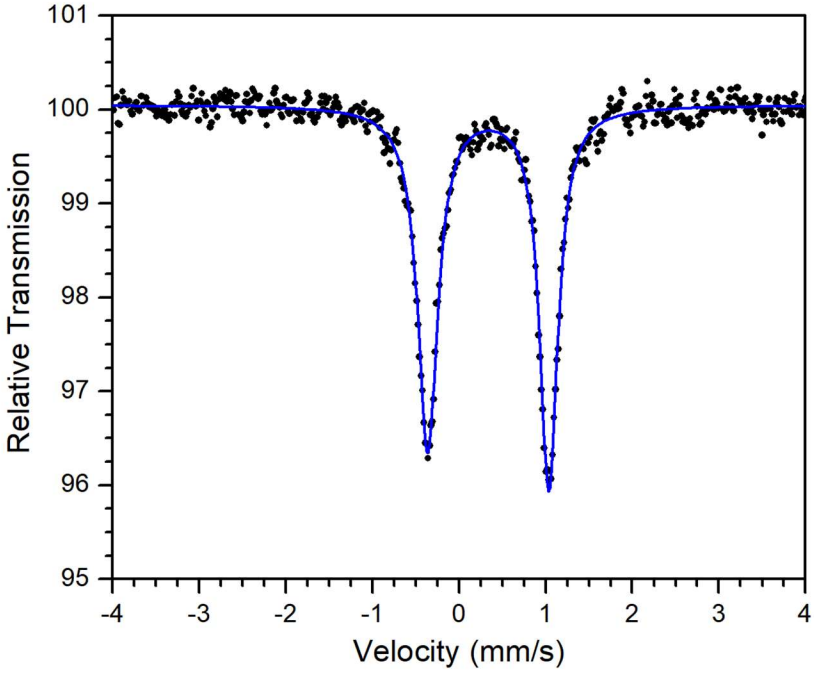

Figure D.14. Mössbauer spectrum of 4 at 80 K. Parameters: δ = 0.338(5) mm/s; ΔE_Q = 1.398(5) mm/s. Fit (blue): Rχ^2 = 0.508.

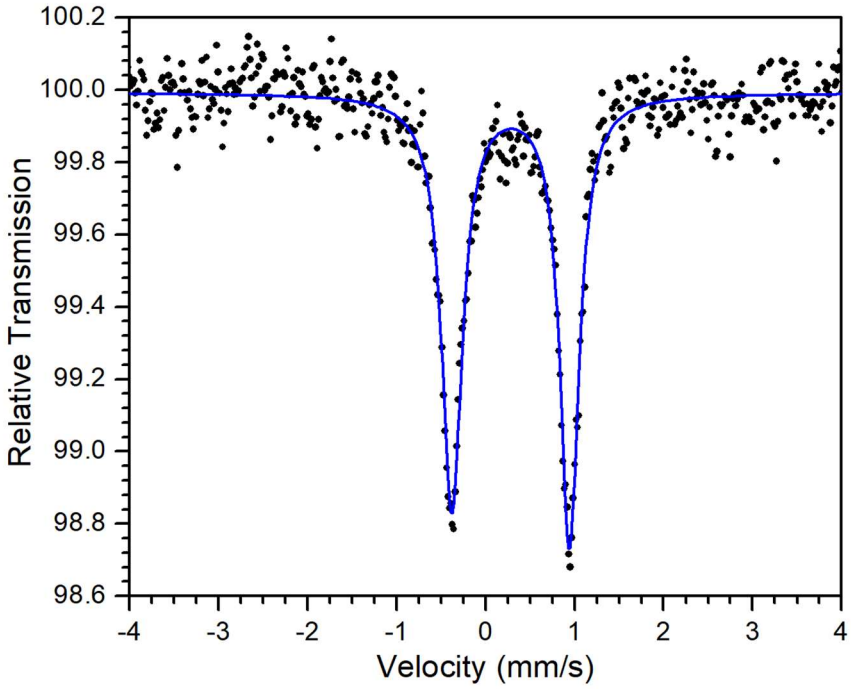

Figure D.15. Mössbauer spectrum of 4 at 250 K. Parameters: δ = 0.282(5) mm/s; ΔE_Q = 1.32(1) mm/s. Fit (blue): Rχ^2 = 0.619.

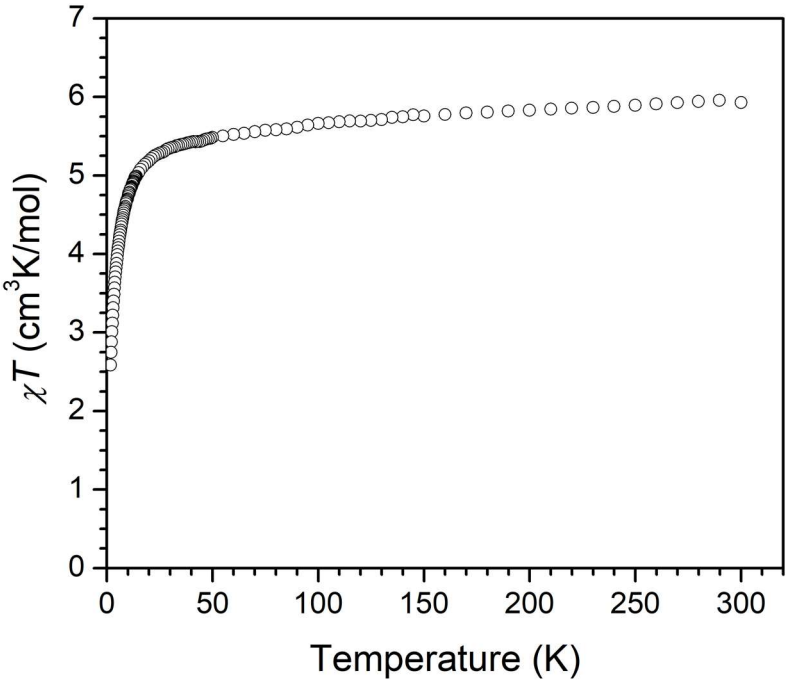

Figure D.16. Temperature dependent χT of 1. Collected under an applied field of 0.1 T.

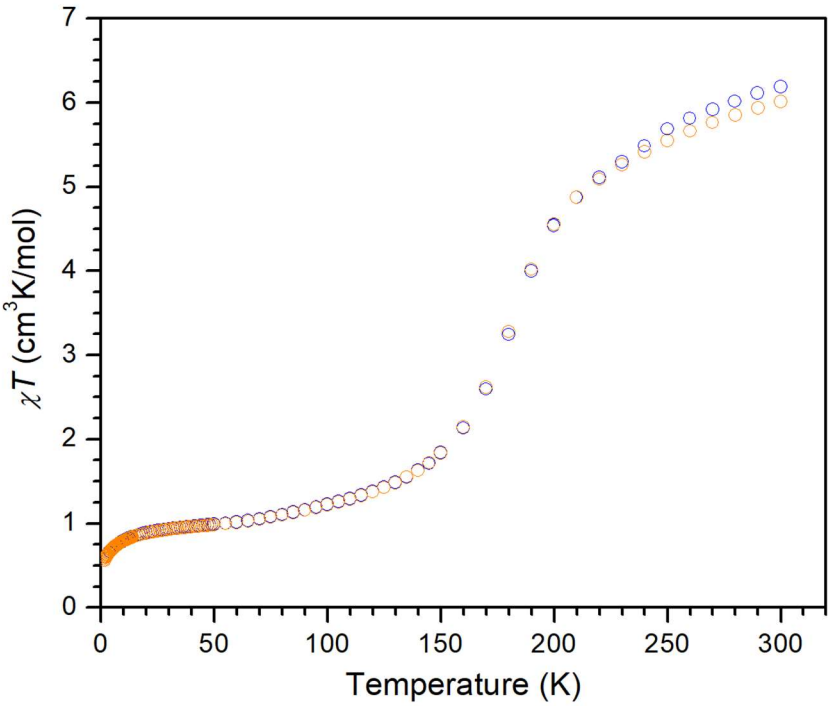

Figure D.17. Magnetic data for 2 upon cooling and warming. The sample was cooled (blue) then warmed (orange) under a static applied field of 0.1 T.

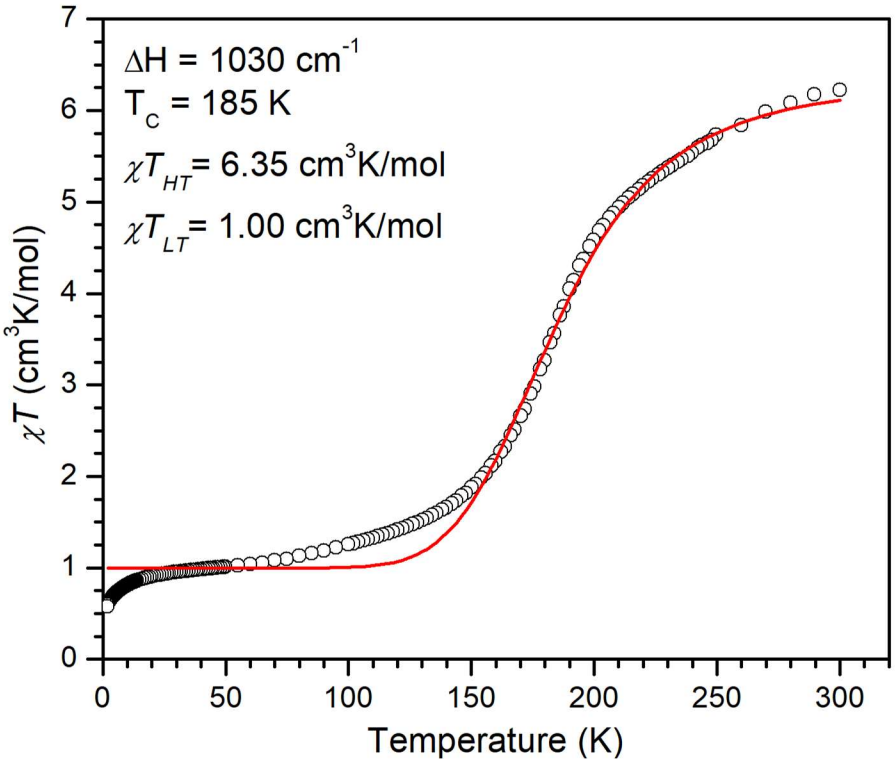

Figure D.18. Fit of the magnetic data of 2 to a Boltzmann distribution.

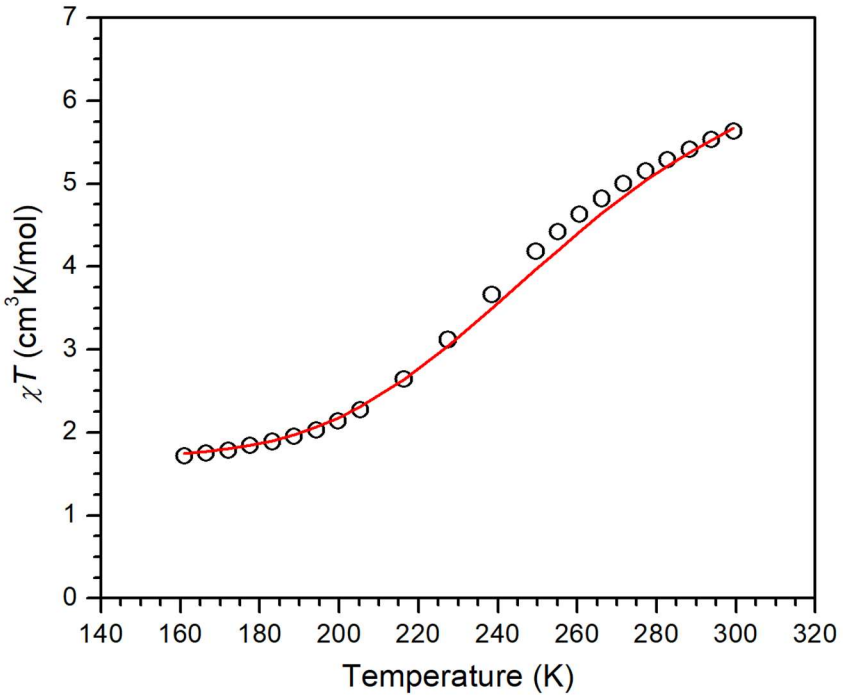

Figure D.19. Variable temperature Evans method of 2 in 2-chlorobutane.

A solution of **2** in 95/5 w/w% 2-chlorobutane and C_6D_6. The shift plotted is the difference in shift between the ^{2}H NMR signal of the C_6D_6 in solution and the C_6D_6 capillary. Red line is the Boltzmann fit to the data with χT_{HT} = 7.1 cm^{3}K/mol, χT_{LT} = 1.7 cm^{3}K/mol, ΔH = 1400 cm^{-1} and $T_{1/2}$ = 260 K

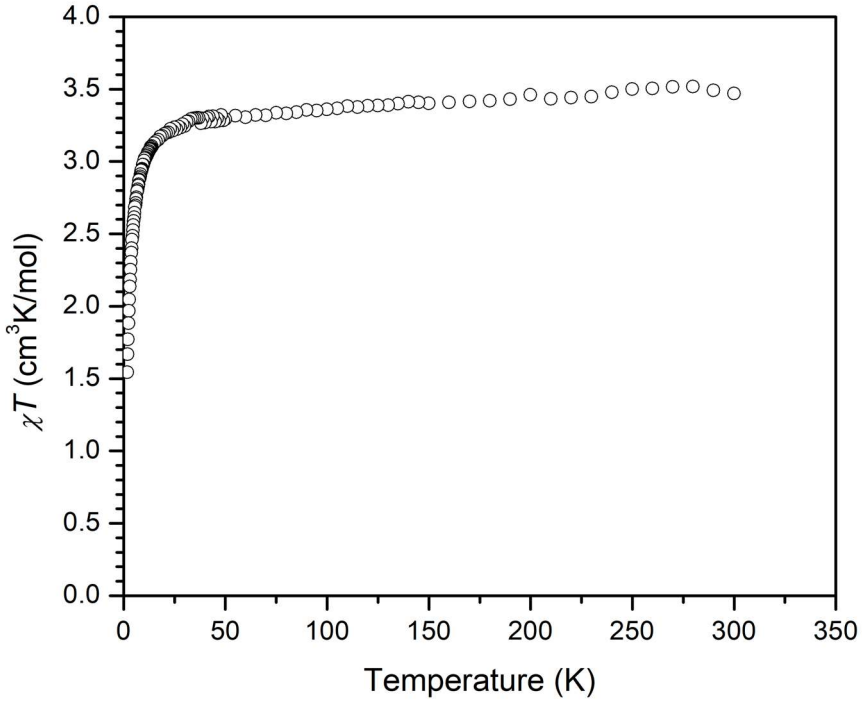

Figure D.20. Temperature dependent χT of 3. Collected under an applied field of 0.1 T.

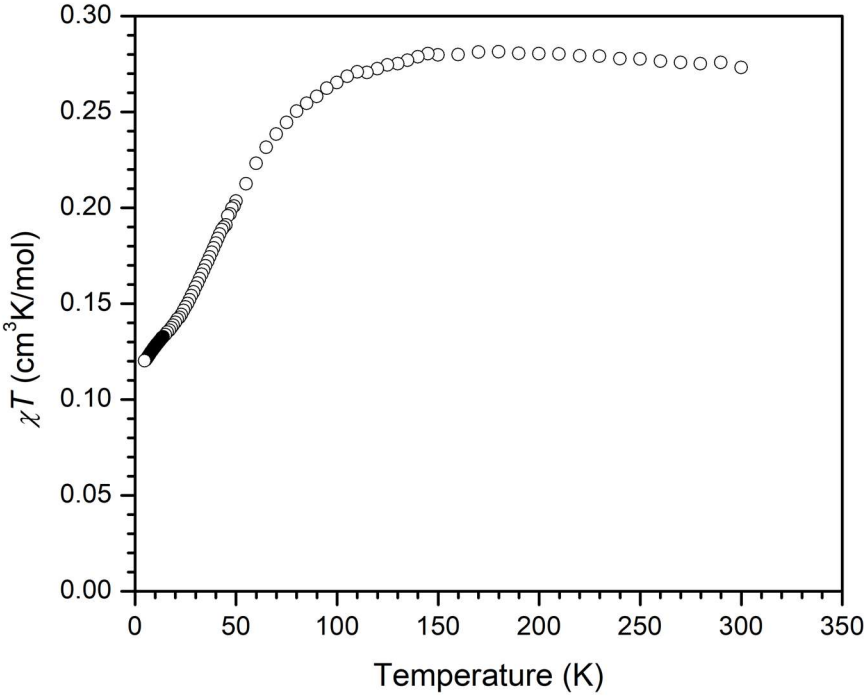

Figure D.21. Temperature dependent χT of 4. Collected under an applied field of 0.1 T.

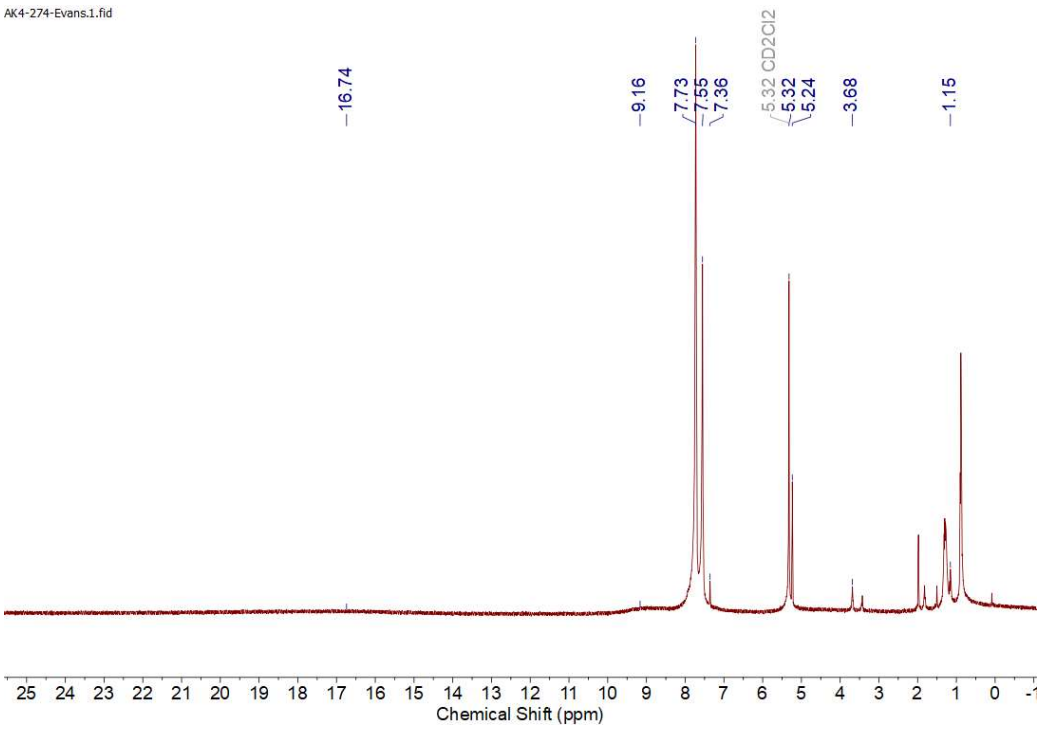

Figure D.22. Evans method ^{1}H NMR spectrum of 4 in CD_2Cl_2

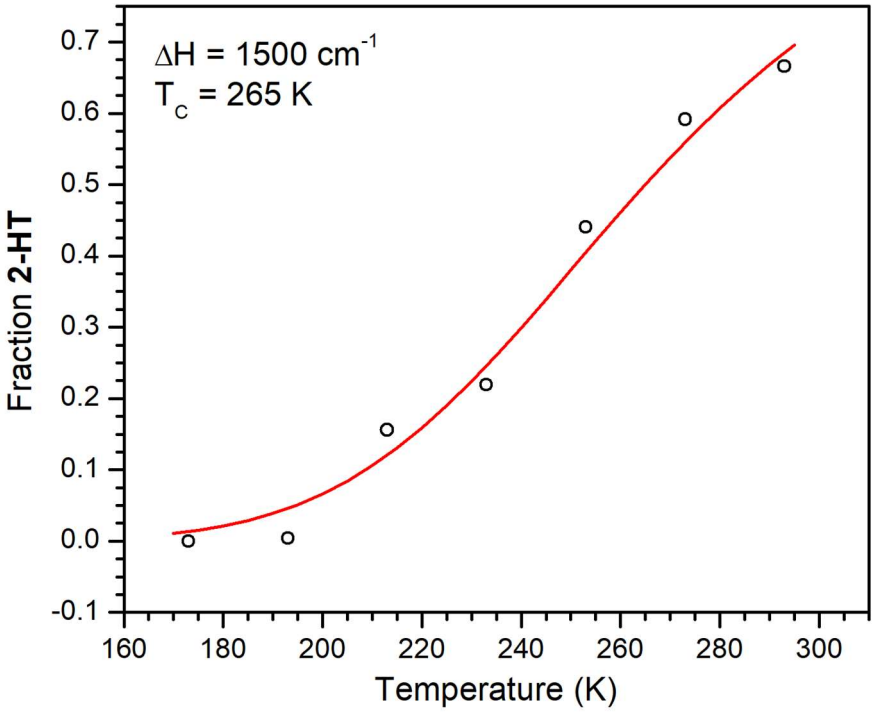

Figure D.23. Fit of the intensity of the NIR feature of 2-HT to a Boltzmann distribution. Collected in CD_2Cl_2.

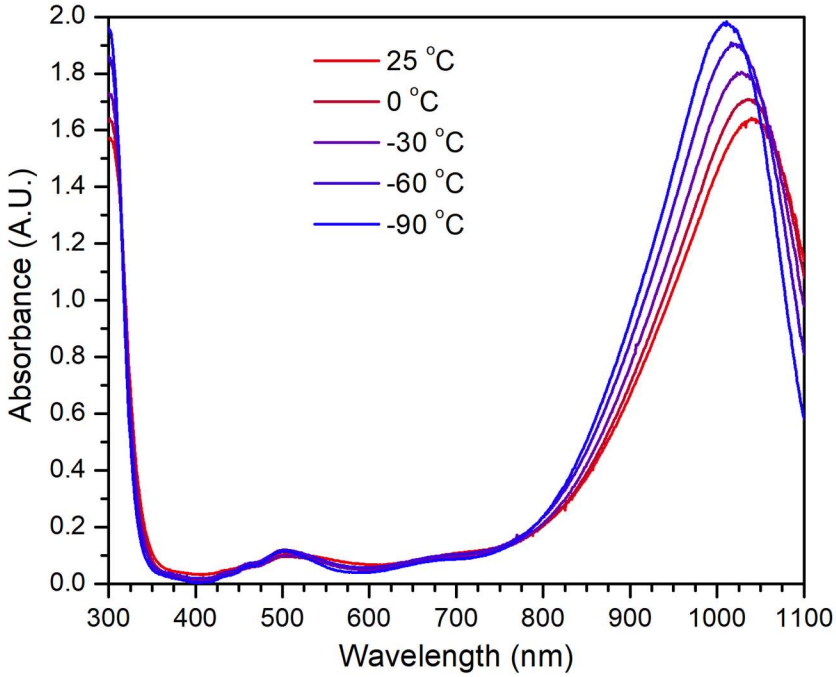

Figure D.24. Variable temperature UV-Vis spectra of [(dppeNi)$_2$TTFtt][BAr$^F{}_4$]$_2$. Collected in DCM at 25 μM

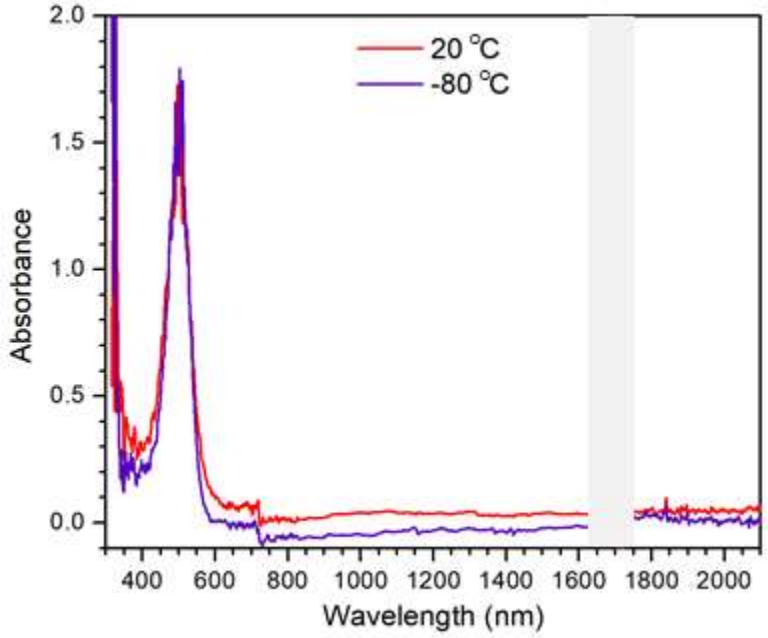

Figure D.25. Variable temperature electronic spectrum of 3 in DCM. The opaque box covers the strong NIR absorptions from the solvent.

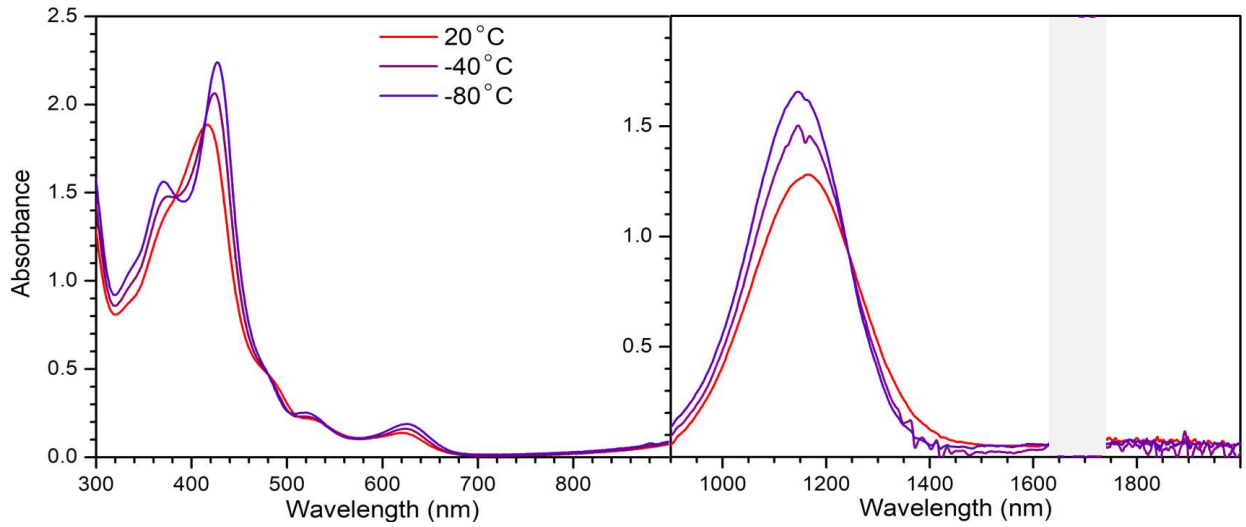

Figure D.26. Variable temperature electronic spectra of 4. Collected in DCM in the UV-Vis (left, 100 μM) and NIR (right, 200 μM). The opaque box (right) covers the strong NIR absorbances due to solvent.

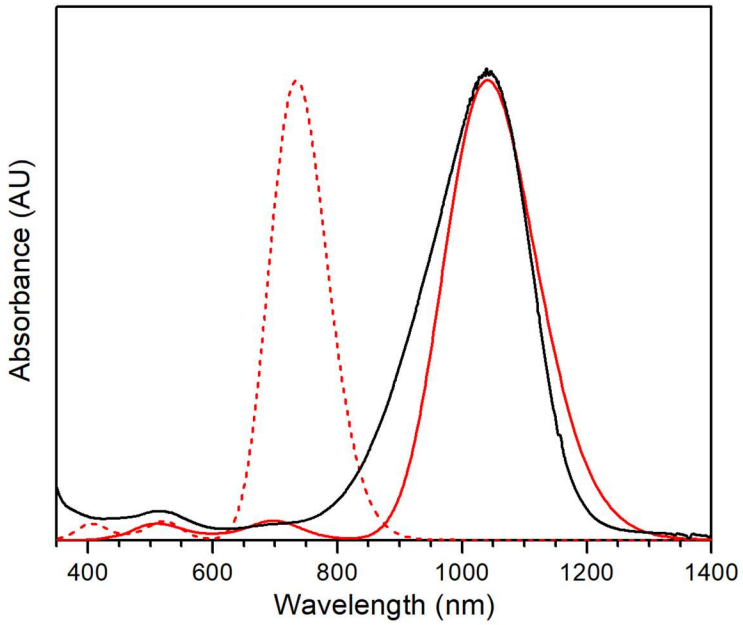

Figure D.27. Calibration from [(dppeNi)$_2$TTFtt][BAr$^F{}_4$]$_2$ reference complex. The black line shows the experimental data in 50 μM DCM at 20 °C, the dashed red line shows the unadjusted calculated spectrum from TD-DFT, and the solid red line is the calculated spectrum adjusted with the weighted calibration.

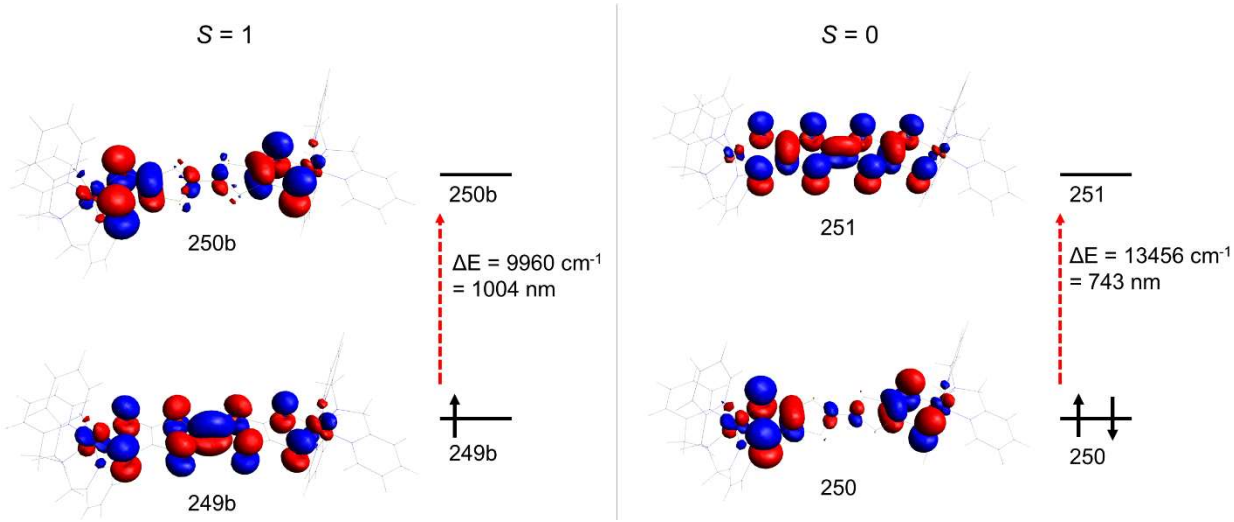

Figure D.28. Primary molecular orbitals associated with the NIR transition of 2-LT. Calculated by TD-DFT. The transitions shown account for >80% of the feature intensity at the associated energy. The listed energies of the transitions are shown without calibration. The calculations of the open shell (left) and closed shell (right) are shown.

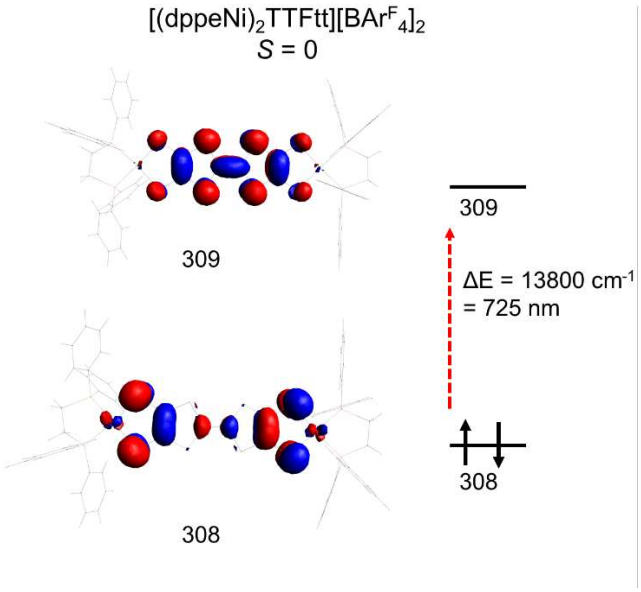

Figure D.29. Primary molecular orbitals associated with the NIR transitions of [(dppeNi)$_2$TTFtt][BAr$^F{}_4$]$_2$. Calculated by TD-DFT. The transitions shown account for >95% of the feature intensity at the associated energy. The listed energies of the transitions are shown without calibration.

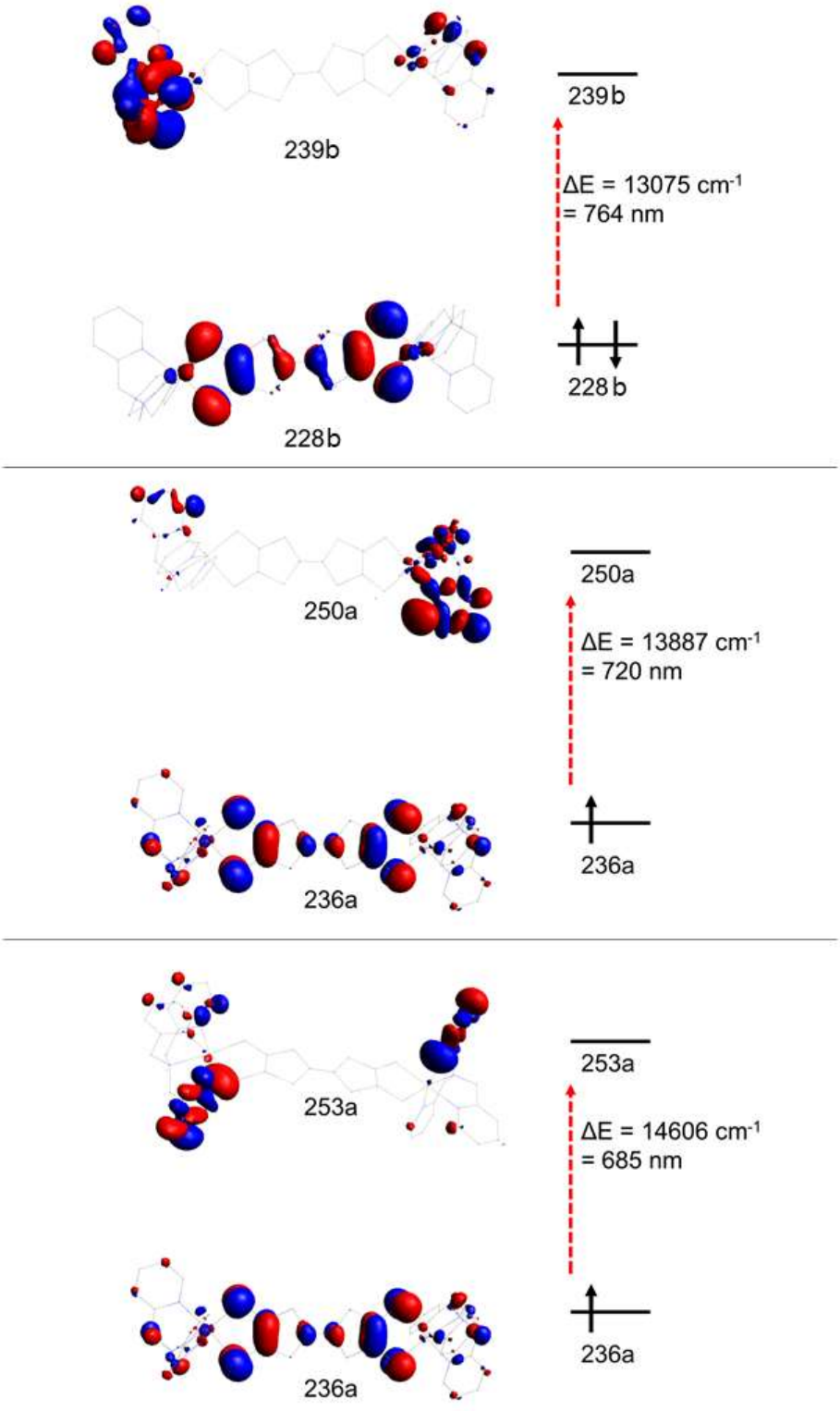

Figure D.30. Primary molecular orbitals associated with the NIR transitions of 2-HT. Calculated by TD-DFT. The transitions shown account for >60% of the feature intensity at the associated energies. The listed energies of the transitions are shown without calibration.

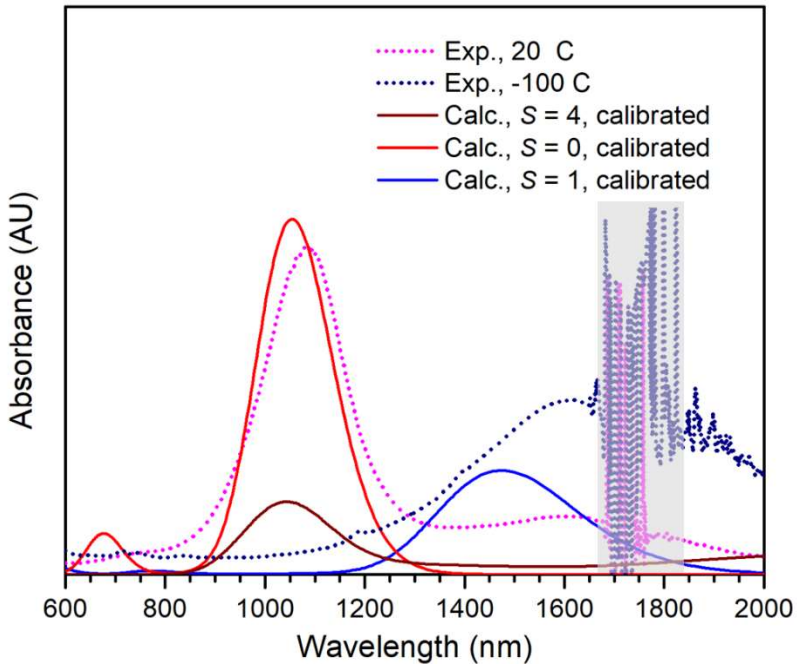

Figure D.31. Predicted spectra of 2 by TD-DFT versus experimental data. Experimental electronic spectra of 2 collected in 2-chlorobutane at 50 μM at indicated temperatures, grey box covers the strong NIR absorptions from solvent. Calculated spectra have been calibrated as noted in the methods section.

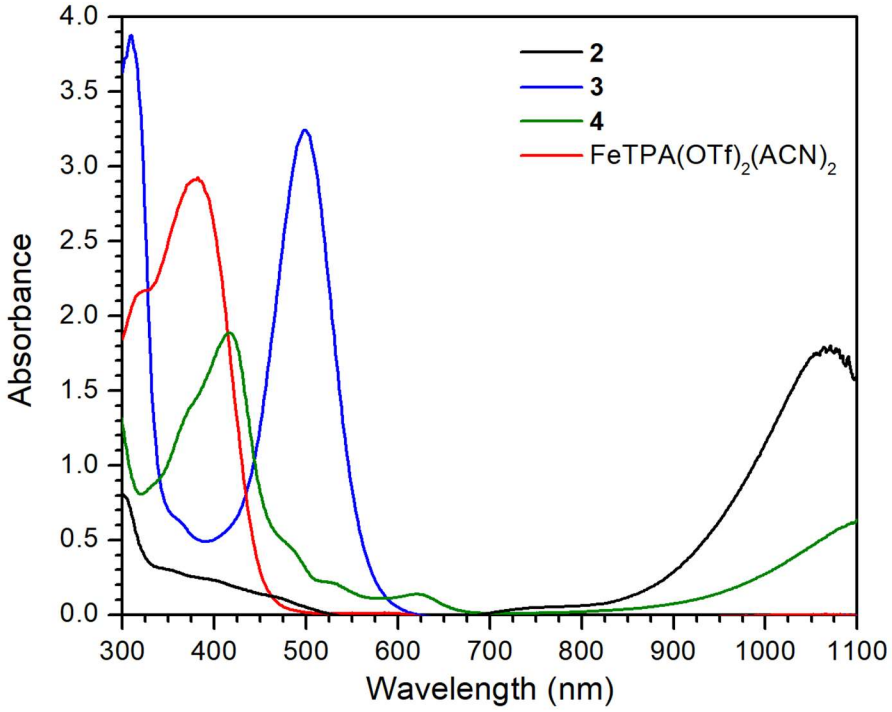

Figure D.32. Comparison of the UV-Vis spectra of 2, 3, 4, and the starting material.

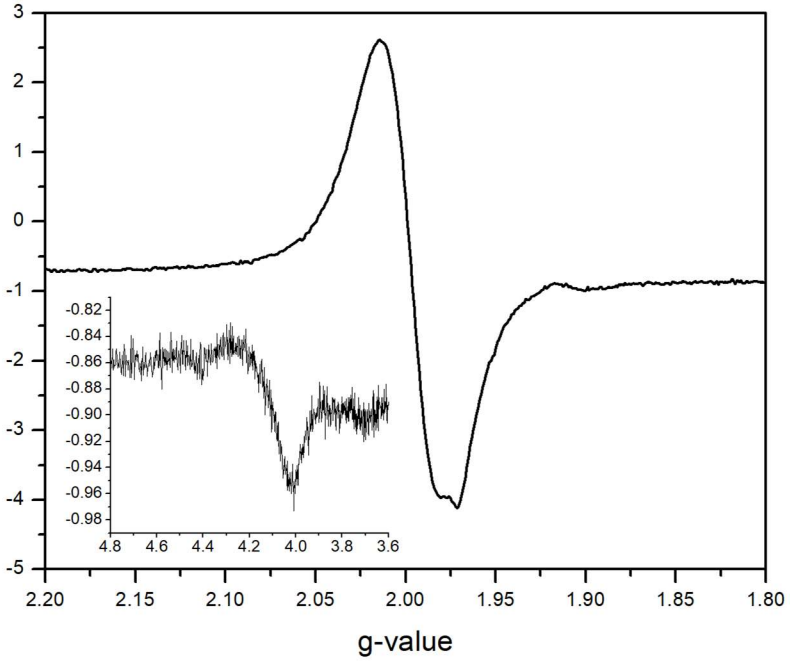

Figure D.33. Additional EPR spectrum of 2. Collected in DCM at 15 K with a power level of 1.998 mW and frequency of 9.632 GHz.

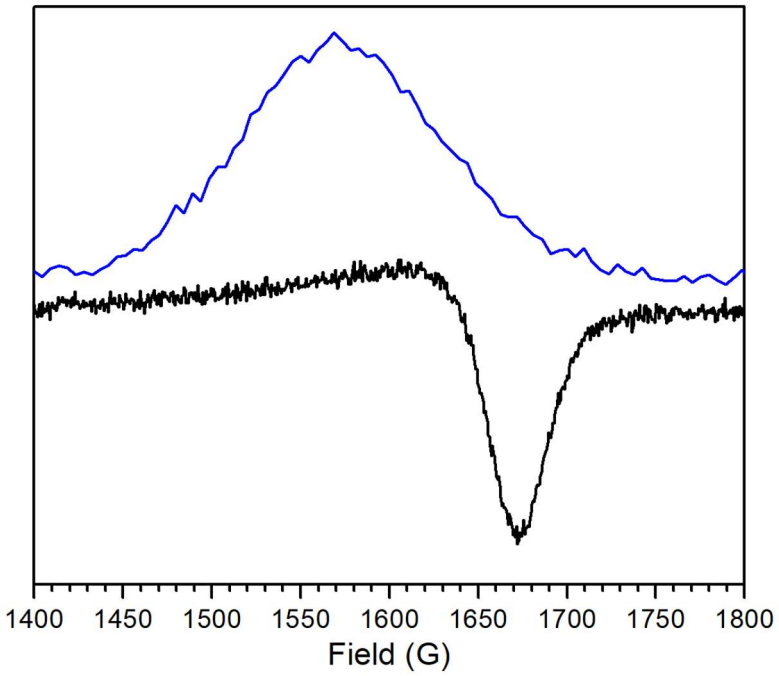

Figure D.34. EPR spectrum of [Fc][BAr^F] compared to 2. Both samples were collected in DCM. [Fc][BAr^F] is shown in blue and 2 is shown in black.

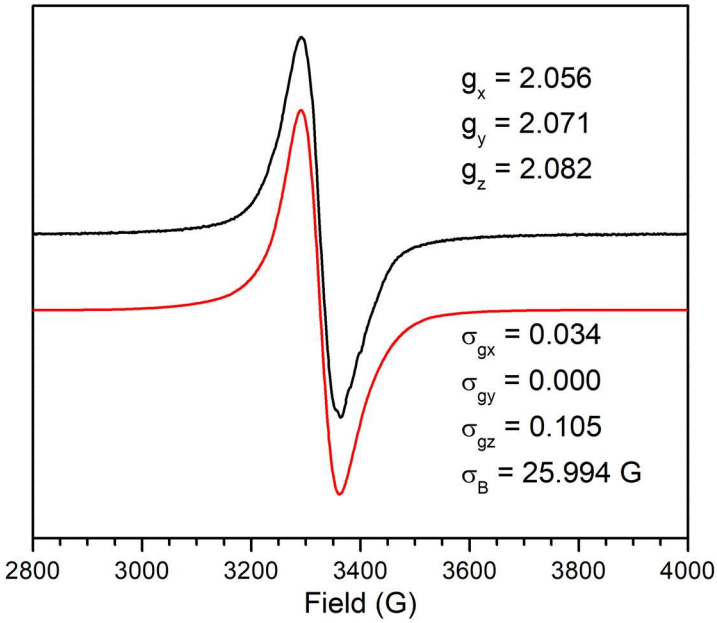

Figure D.35. EPR spectrum of 4. Collected at 15 K in DCM at 5 mM with a power of 1.998 mW and frequency of 9.387 GHz. Red lines indicate simulations with the parameters shown. Experimental data is shown in black.

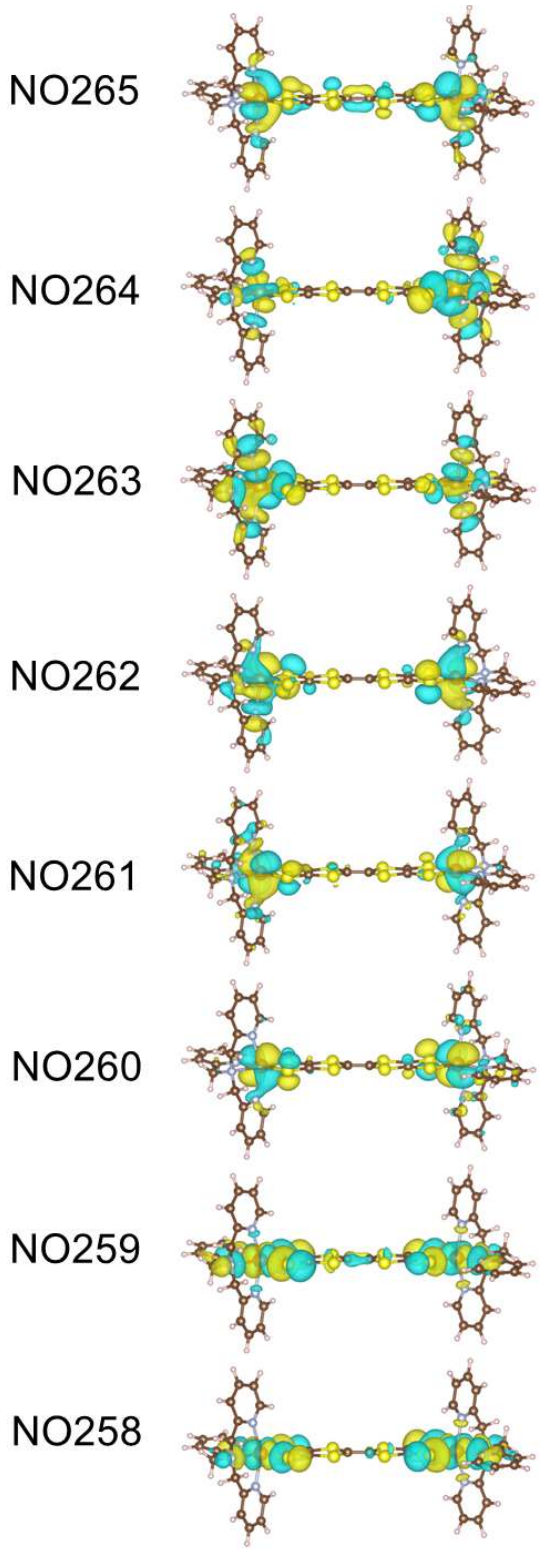

Figure D.36. Frontier NO's of 2-HT. Frontier NO's obtained for the triplet state of 2-HT by DFT with the B3LYP functional and a 6-311G* basis set as implemented in g16/a.01.

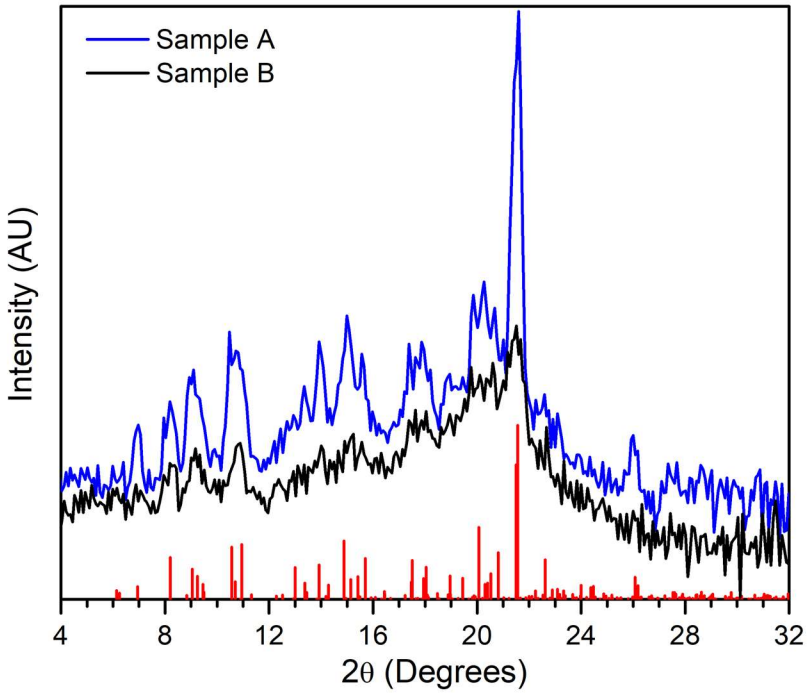

Figure D.37. XRPD patterns of two samples of 2. Calculated pattern of room temperature molecular structure from SXRD is shown in red. Both samples were pure and solvent-free by elemental analysis. Temperature dependent χT of samples A and B can be compared in Figure D.38.

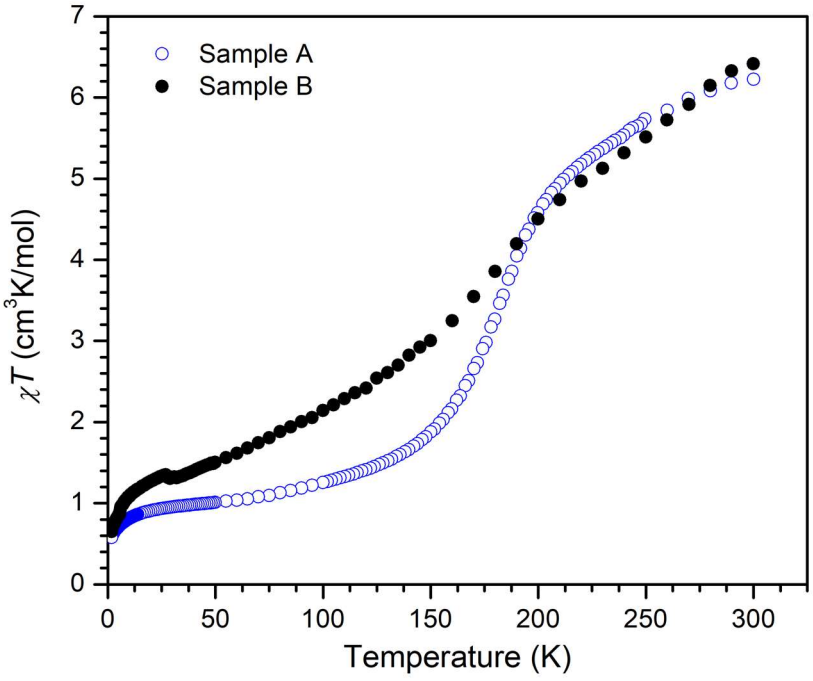

Figure D.38. Temperature dependent χT of two samples of 2. Both samples were pure and solvent-free by elemental analysis. XRPD of samples A and B can be compared in Figure D. 37.

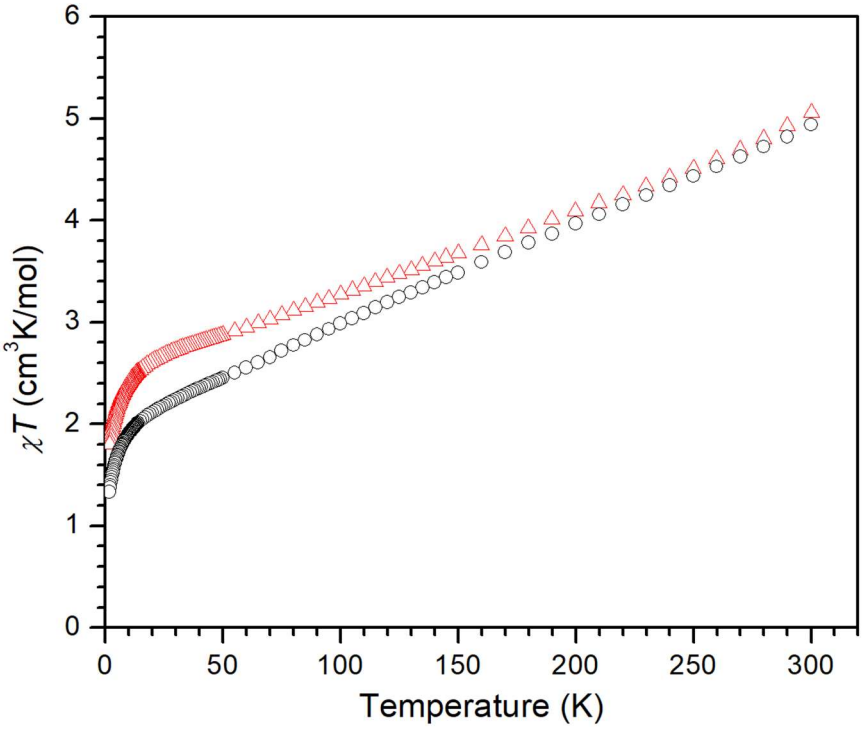

Figure D.39. Frozen solution magnetic behavior of different samples of 2 in PEG-2000.

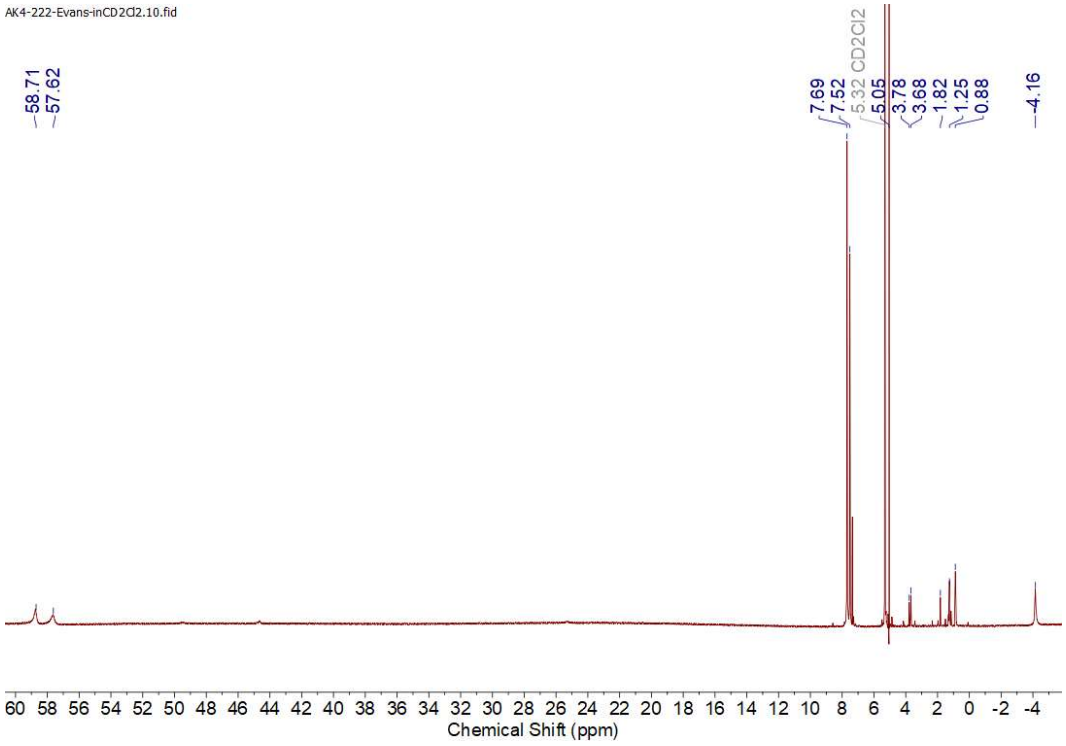

Figure D.40. Evans method ^{1}H NMR spectrum of 2 in CD_2Cl_2.

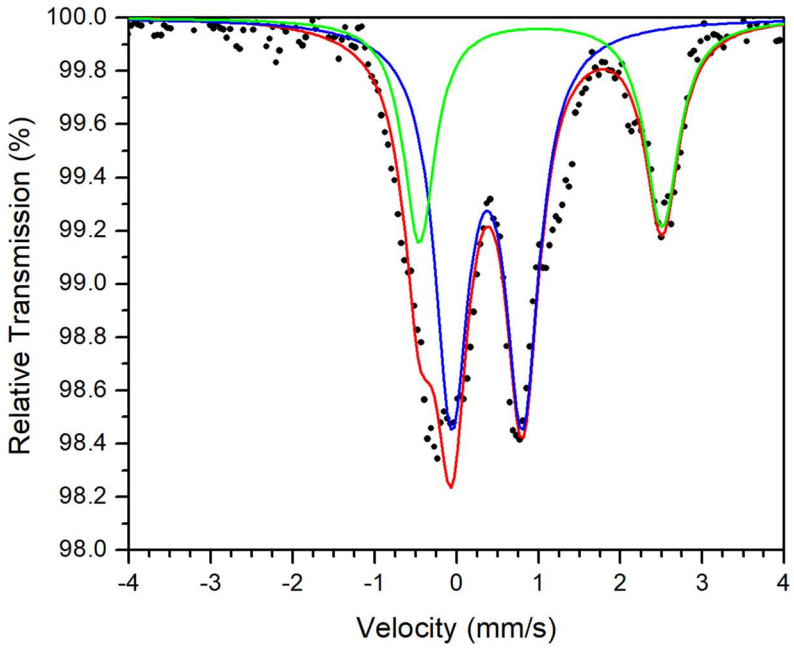

Figure D.41. Additional Mössbauer spectrum of 2 at 80 K. Site A (blue): δ = 0.37(1) mm/s; ΔE_Q = 0.86(2) mm/s; 65(2)%. Site B (green): δ = 1.02(2) mm/s; ΔE_Q = 2.964(8) mm/s; 33%. Overall Fit (red): Rχ^2 = 1.488

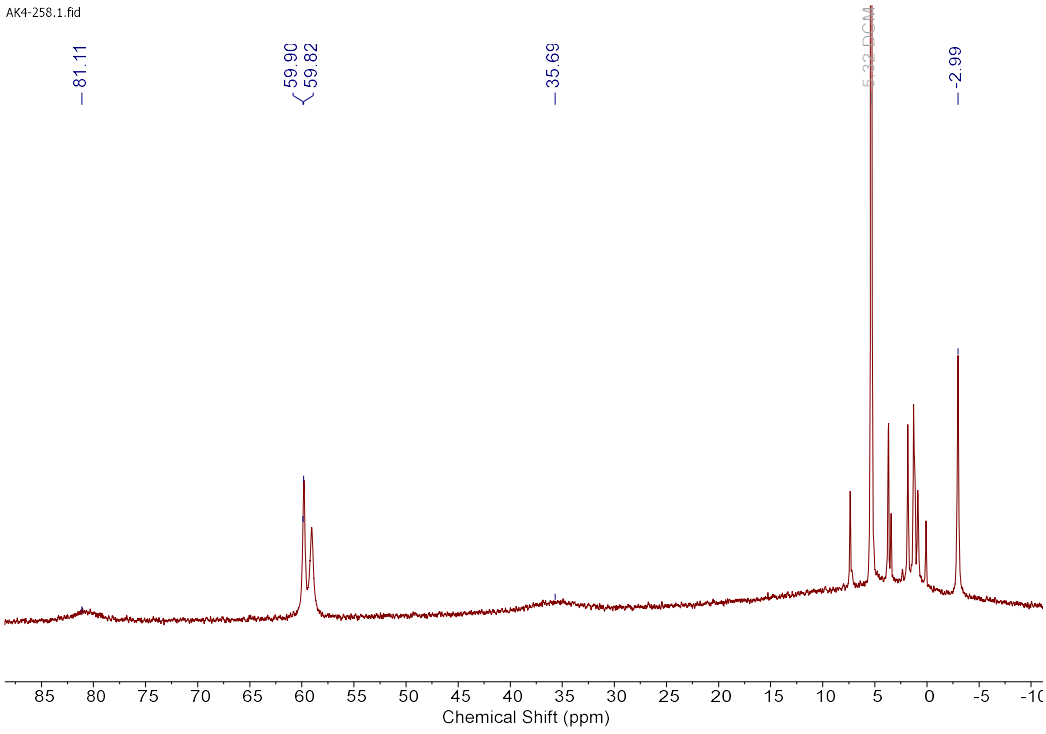

Figure D.42. ^{1}H NMR spectrum of 3 in CD_2Cl_2. Unlabelled peaks are residual solvent.

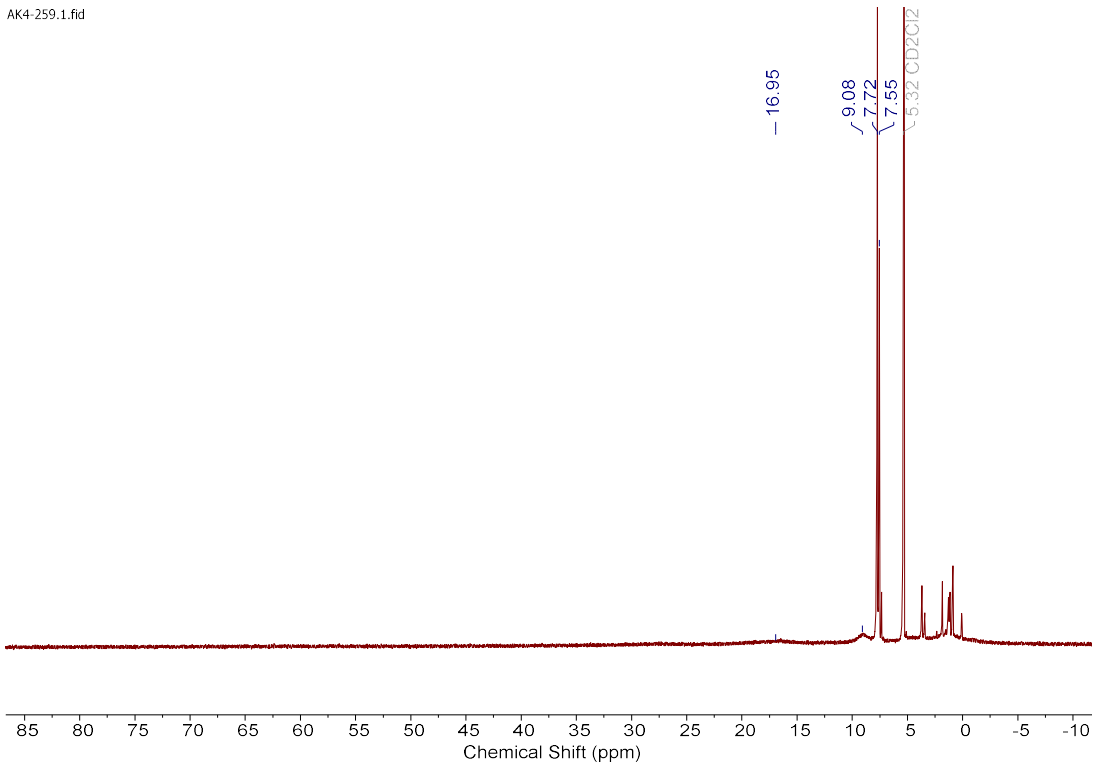

Figure D.43. ^{1}H NMR spectrum of 4 in CD_2Cl_2. Unlabelled peaks are residual solvent.

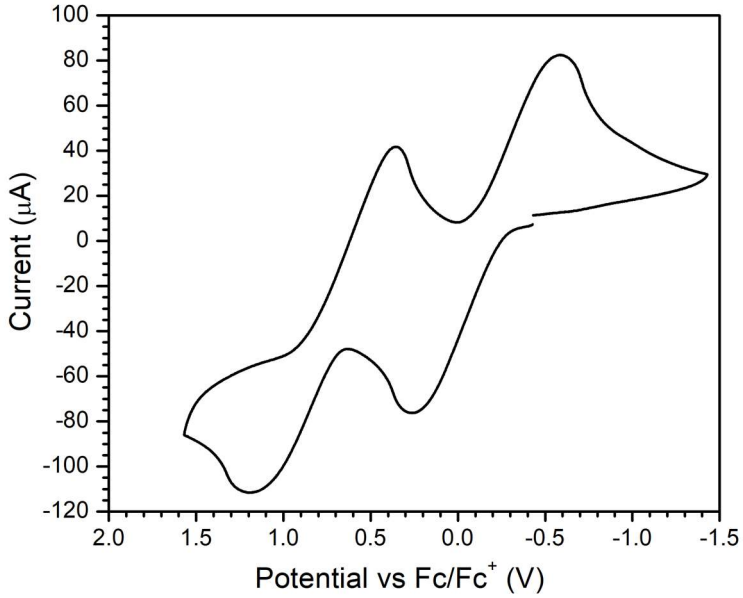

Figure D.44. CV of 3. Collected in DCM with 0.1 M of [TBA][PF_6] at a scan rate of 250 mV/s.

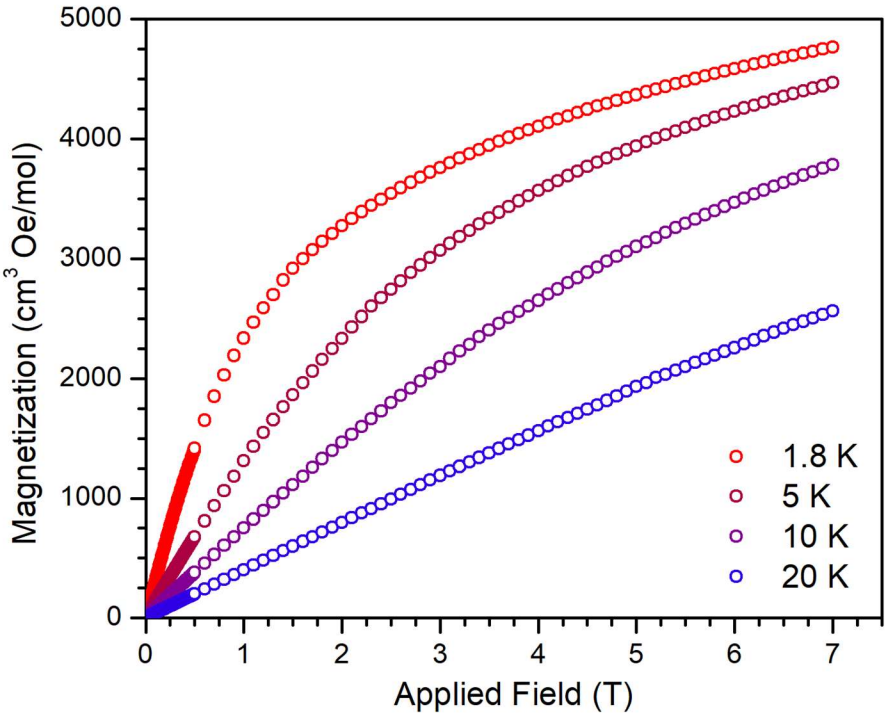

Figure D.45. Field-dependent magnetization of 2 at various temperatures.

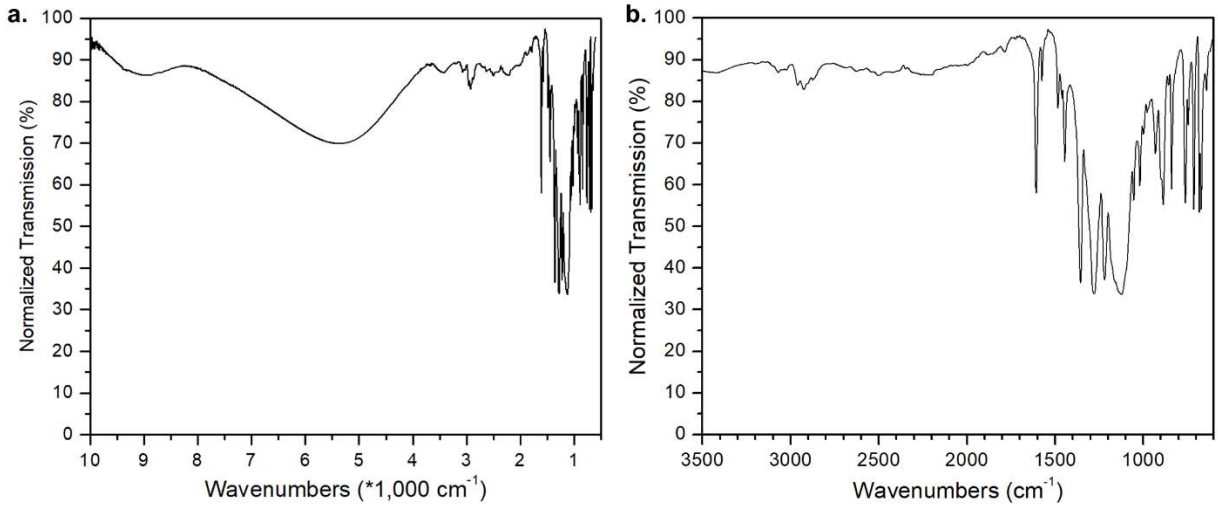

Figure D.46. Infrared spectrum of 2. a, extended window showing NIR features. b, region from 600 to 3500 cm^{-1}.

Table D.1. Comparison of TTFtt bond lengths in 2 and Ni reference compounds. C_{out} = C1,C1; C_{ctr} = C3; S_{thiol} =S1, S2; S_{ring} = S3, S4. Values are averages of the specified bonds. Ni complex data reproduced from ref. 20.

2-HT			2-LT			
Atom 1	**Atom 2**	**Distance (Å)**	**Atom 1**	**Atom 2**	**Distance (Å)**	**Δ (Å)**
C1	S1	1.701(10)	C1	S1	1.683(8)	-0.018(13)
C2	S2	1.675(11)	C2	S2	1.715(8)	+0.040(14)
C1	S4	1.708(10)	C1	S4	1.739(8)	+0.031(13)
C2	S3	1.724(9)	C2	S3	1.725(8)	0.001(12)
C3	S3	1.701(11)	C3	S3	1.757(8)	+0.056(14)
C3	S4	1.690(10)	C3	S4	1.719(8)	+0.029(13)
C1	C2	1.404(13)	C1	C2	1.375(10)	-0.029(16)
C_{out}	S_{thiol}	1.688(9)	C_{out}	S_{thiol}	1.699(6)	+0.011(11)
C_{out}	S_{ring}	1.716(7)	C_{out}	S_{ring}	1.732(6)	+0.016(9)
C_{ctr}	S_{ring}	1.695(7)	C_{ctr}	S_{ring}	1.738(6)	+0.043(9)
C_{out}	C_{out}	1.404(13)	C_{out}	C_{out}	1.375(10)	−0.029(16)
[(dppeNi)$_2$TTFtt][BAr$^F{}_4$]$_2$			**[(dppeNi)$_2$TTFtt][BAr$^F{}_4$]**			
Atom 1	**Atom 2**	**Distance (Å)**	**Atom 1**	**Atom 2**	**Distance (Å)**	**Δ (Å)**
C1	S1	1.713(2)	C1	S1	1.735(2)	
C2	S2	1.713(2)	C2	S2	1.727(2)	
C1	S4	1.723(2)	C1	S4	1.739(2)	
C2	S3	1.726(2)	C2	S3	1.740(2)	
C3	S3	1.704(2)	C3	S3	1.723(2)	
C3	S4	1.709(2)	C3	S4	1.727(2)	
C1	C2	1.379(3)	C1	C2	1.362(2)	
			C1'	S1'	1.732(2)	
			C2'	S2'	1.728(2)	
			C1'	S4'	1.740(2)	
			C2'	S3'	1.738(2)	
			C3'	S3'	1.726(2)	
			C3'	S4'	1.728(2)	
			C1'	C2'	1.361(2)	
C_{out}	S_{thiol}	1.713(1)	C_{out}	S_{thiol}	1.731(1)	+0.018(1)
C_{out}	S_{ring}	1.725(1)	C_{out}	S_{ring}	1.739(1)	+0.014(1)
C_{ctr}	S_{ring}	1.707(1)	C_{ctr}	S_{ring}	1.726(1)	+0.019(1)
C_{out}	C_{out}	1.379(2)	C_{out}	C_{out}	1.362(1)	−0.017(2)

Table D.2. Energies and NON of 2. [16,14] active space V2RDM calculations a 6-31G basis set and [14,14] and [16,22] active space calculations with a 6-31G* basis set.

	[16,14] 6-31G		[14,14] 6-31G*		[16,22] 6-31G*	
	Singlet	Triplet	Singlet	Triplet	Singlet	Triplet
E_{rel}/cm^{-1}	0	210	0	379	0	326

λ_{259}	1.95	1.95	1.92	1.92	1.92	1.92
λ_{260}	1.95	1.94	1.91	1.91	1.90	1.91
λ_{261}	1.25	1.04	1.30	1.06	1.33	1.13
λ_{262}	0.80	1.01	0.71	0.94	0.63	0.85
λ_{263}	0.06	0.06	0.09	0.09	0.09	0.09
λ_{264}	0.06	0.06	0.08	0.09	0.08	0.08

Table D.3. Energies and NON for 2-LT. Obtained with [18,20] active space calculations in V2RDM with a 6-31g basis set.

	Singlet	Triplet	Quintet	Septet	Nonet
E_{rel} (cm^{-1})	0	372	5990	28400	57100
λ_{259}	1.88	1.88	1.82	1.74	1.57
λ_{260}	1.88	1.87	1.81	1.73	1.57
λ_{261}	1.28	1.07	1.00	1.00	1.00
λ_{262}	0.72	0.93	1.00	1.00	1.00
λ_{263}	0.12	0.12	0.18	0.27	0.43
λ_{264}	0.12	0.12	0.17	0.27	0.43

Table D.4. Crystal data and structure refinement for 2-LT.

Identification code	**2-LT**
Empirical formula	$C_{54}H_{32}BCl_2F_{24}FeN_4S_4$
Formula weight	1458.63
Temperature/K	100(2)
Crystal system	monoclinic
Space group	$P2_1/c$
a/Å	12.6586(12)
b/Å	16.4126(15)
c/Å	32.380(3)
α/°	90
β/°	94.807(2)
γ/°	90
Volume/$Å^3$	6703.5(11)

Z	4
ρ_{calc}g/cm^3	1.445
μ/mm^{-1}	0.533
F(000)	2916.0
Radiation	MoKα (λ = 0.71073)
2Θ range for data collection/°	4.182 to 44.522
Index ranges	-13 ≤ h ≤ 13, -17 ≤ k ≤ 17, -33 ≤ l ≤ 34
Reflections collected	62339
Independent reflections	8454 [R_{int} = 0.1316, R_{sigma} = 0.0889]
Data/restraints/parameters	8454/168/811
Goodness-of-fit on F^2	1.017
Final R indexes [I>=2σ (I)]	R_1 = 0.0742, wR_2 = 0.1654
Final R indexes [all data]	R_1 = 0.1226, wR_2 = 0.1868
Largest diff. peak/hole / e Å^{-3}	0.69/-0.43

Table D.5. Fractional Atomic Coordinates (×10^4) and Equivalent Isotropic Displacement Parameters (Å^2×10^3) for 2-LT. U_{eq} is defined as 1/3 of of the trace of the orthogonalised UIJ. tensor.

Atom	*x*	*y*	*z*	U(eq)
Fe1	-753.1(8)	2279.9(6)	1274.0(3)	23.9(3)
S1	-958.6(15)	3634.8(11)	1249.8(6)	27.4(5)
S2	39.0(15)	2332.7(12)	664.6(6)	29.0(5)
S3	328.5(17)	3702.6(12)	75.1(7)	35.5(6)
S4	-657.0(17)	4883.2(12)	598.3(7)	34.0(5)
N1	652(4)	2242(4)	1576.9(18)	24.7(15)
N2	-1351(4)	2189(3)	1817.8(19)	23.5(15)
N3	-2120(5)	2016(4)	962.9(19)	28.5(16)
N4	-657(5)	1055(3)	1309.5(19)	29.6(16)
C1	-563(6)	3889(4)	784(2)	27.5(19)
C2	-108(6)	3340(5)	531(2)	29(2)
C3	-77(6)	4714(5)	145(3)	36(2)
C4	-2956(6)	2499(6)	875(2)	41(2)
C5	-3892(6)	2224(7)	665(3)	49(3)
C6	-3957(8)	1438(7)	534(3)	59(3)
C7	-3076(7)	932(6)	611(3)	49(3)
C8	-2190(6)	1232(5)	825(2)	34(2)
C9	-1198(6)	745(4)	920(2)	32(2)
C10	500(5)	853(4)	1351(3)	30(2)
C11	1108(6)	1491(4)	1594(2)	27.2(19)
C12	2092(6)	1354(5)	1799(3)	36(2)

C13	2673(6)	1995(6)	1992(3)	40(2)
C14	2215(6)	2748(6)	1971(3)	44(2)
C15	1209(6)	2864(5)	1769(2)	29(2)
C16	-1192(6)	783(5)	1673(2)	30(2)
C17	-1403(5)	1423(5)	1969(2)	24.5(19)
C18	-1656(6)	1260(5)	2364(3)	29(2)
C19	-1893(5)	1902(5)	2618(3)	28(2)
C20	-1870(5)	2691(5)	2464(2)	28.7(19)
C21	-1594(5)	2802(5)	2070(2)	26.5(19)
Cl1	7889(2)	2731.4(17)	4728.4(9)	76.2(9)
Cl2	7332(2)	1042.6(19)	4834.7(9)	82.1(9)
C54	7190(13)	1903(7)	4541(4)	127(6)
F1	8168(5)	4304(4)	3916.6(18)	80(2)
F2	7784(4)	4228(3)	3264.0(16)	56.5(15)
F3	8428(4)	3202(4)	3592(2)	74.5(18)
F4	4946(4)	4452(3)	4619.7(16)	59.5(15)
F5	4501(5)	3212(4)	4708.9(18)	74.3(18)
F6	3531(4)	3975(4)	4301.6(19)	88(2)
F7	8408(4)	589(4)	3753(2)	88(2)
F8	8039(4)	-637(4)	3892.0(19)	78.5(19)
F9	7893(4)	-219(3)	3271.8(19)	62.3(16)
F10	4108(4)	365(4)	4627.8(16)	66.3(16)
F11	4765(4)	-823(3)	4549.1(17)	69.2(17)
F12	3378(4)	-440(3)	4177.4(15)	51.5(14)
F13	1197(6)	3795(3)	3366.4(19)	88(2)
F14	1623(4)	4027(3)	2766.5(17)	58.3(15)
F15	191(4)	3437(3)	2851(3)	111(3)
F16	1710(4)	-209(3)	2858.9(18)	58.6(15)
F17	322(4)	360(3)	3049.3(16)	49.9(13)
F18	680(4)	453(3)	2423.4(15)	47.4(13)
F19	4609(5)	3899(3)	1915(2)	87(2)
F20	5515(9)	3403(4)	1485(2)	145(4)
F21	6201(5)	3900(4)	2017(3)	139(4)
F22	5926(5)	477(3)	1495.3(19)	84(2)
F23	6265(5)	-94(3)	2064.0(19)	85(2)
F24	4688(4)	-5(4)	1818(2)	90(2)
C22	5573(7)	407(5)	1861(3)	38(2)
C23	5455(5)	1193(5)	2078(2)	24.3(16)

C24	5249(5)	1182(4)	2488(2)	22.9(17)
C25	5094(5)	1901(4)	2718(2)	23.6(17)
C26	5172(5)	2623(5)	2495(2)	23.8(17)
C27	5379(5)	2644(5)	2086(2)	28.3(17)
C28	5531(5)	1920(5)	1871(2)	29.5(18)
C29	5429(7)	3453(5)	1872(3)	37(2)
C30	7726(7)	-37(5)	3659(3)	43(2)
C31	6591(6)	226(5)	3701(3)	29(2)
C32	6156(5)	809(4)	3439(2)	25.7(19)
C33	5121(5)	1106(4)	3452(2)	22.0(18)
C34	4565(6)	756(4)	3759(2)	26.3(19)
C35	4987(6)	161(5)	4027(2)	31(2)
C36	4319(7)	-169(6)	4344(3)	41(2)
C37	6014(6)	-115(5)	4003(3)	31(2)
C38	3407(5)	1912(4)	3106(2)	20.5(17)
C39	2808(6)	1212(4)	3015(2)	25.3(18)
C40	1723(6)	1222(5)	2916(2)	31.2(18)
C41	1120(6)	463(4)	2815(3)	29.2(17)
C42	1165(6)	1961(5)	2903(3)	33(2)
C43	1742(5)	2661(5)	2991(2)	29.0(18)
C44	1193(6)	3472(5)	2986(3)	42(2)
C45	2834(5)	2645(5)	3087(2)	27.2(18)
C46	5186(6)	2648(4)	3460(2)	22.8(18)
C47	6191(6)	2966(4)	3419(2)	25.2(19)
C48	6646(6)	3547(4)	3692(3)	31(2)
C49	7746(8)	3821(7)	3623(3)	53(3)
C50	6132(7)	3833(5)	4020(3)	36(2)
C51	5138(7)	3534(5)	4070(2)	33(2)
C52	4543(8)	3783(7)	4426(3)	53(3)
C53	4679(6)	2955(5)	3799(2)	30(2)
B1	4704(7)	1878(5)	3181(3)	25(2)

Table D.6. Anisotropic Displacement Parameters ($Å^2 \times 10^3$) for 2-LT. The Anisotropic displacement factor exponent takes the form: $-2\pi^2[h^2a^{*2}U_{11}+2hka^*b^*U_{12}+\ldots]$.

Atom	U_{11}	U_{22}	U_{33}	U_{23}	U_{13}	U_{12}
Fe1	18.7(6)	16.7(6)	36.8(7)	1.7(5)	4.5(5)	0.9(5)
S1	29.1(12)	16.4(11)	37.9(13)	2.2(10)	9.9(10)	2.5(9)

S2	29.1(12)	20.2(11)	39.0(13)	1.9(10)	10.6(10)	2.9(9)
S3	43.9(14)	24.8(12)	40.0(13)	3.1(10)	16.4(11)	3.5(10)
S4	42.0(13)	20.8(11)	40.9(13)	4.7(10)	13.5(11)	2.6(10)
N1	19(3)	19(4)	37(4)	-2(3)	10(3)	-6(3)
N2	19(3)	6(4)	45(4)	-1(3)	1(3)	0(3)
N3	19(4)	24(4)	43(4)	6(3)	1(3)	2(3)
N4	40(4)	16(3)	34(4)	-4(3)	7(3)	-1(3)
C1	19(4)	18(4)	45(5)	-7(4)	2(4)	8(4)
C2	19(4)	30(5)	38(5)	3(4)	0(4)	4(4)
C3	31(5)	30(5)	46(6)	12(4)	3(4)	6(4)
C4	28(5)	58(6)	37(5)	10(5)	10(4)	-1(5)
C5	17(5)	85(8)	45(6)	2(6)	-5(4)	1(5)
C6	42(7)	87(9)	46(7)	2(6)	-9(5)	-17(6)
C7	43(6)	58(7)	46(6)	-7(5)	-3(5)	-20(5)
C8	35(5)	37(6)	32(5)	7(4)	10(4)	-7(4)
C9	40(5)	15(4)	42(5)	-10(4)	-3(4)	-4(4)
C10	16(4)	19(4)	57(6)	10(4)	8(4)	5(4)
C11	22(5)	19(5)	41(5)	3(4)	8(4)	1(4)
C12	21(5)	38(5)	51(6)	14(5)	10(4)	14(4)
C13	19(5)	48(6)	52(6)	10(5)	2(4)	5(5)
C14	20(5)	68(7)	45(6)	0(5)	7(4)	-8(5)
C15	23(5)	29(5)	37(5)	3(4)	14(4)	6(4)
C16	18(4)	26(5)	46(5)	3(4)	2(4)	6(4)
C17	13(4)	23(5)	37(5)	2(4)	0(4)	-2(3)
C18	19(4)	17(5)	50(6)	3(4)	6(4)	1(4)
C19	11(4)	31(5)	45(5)	4(4)	13(4)	-2(4)
C20	17(4)	34(5)	36(5)	-4(4)	8(4)	0(4)
C21	19(4)	16(5)	45(6)	0(4)	1(4)	6(3)
Cl1	71.4(19)	64.3(18)	89(2)	11.2(16)	-16.3(16)	0.8(15)
Cl2	81(2)	88(2)	74(2)	17.0(17)	-9.2(16)	-36.3(17)
C54	194(16)	69(9)	101(11)	-19(8)	-89(11)	38(10)
F1	80(4)	92(5)	68(4)	-18(4)	11(3)	-66(4)
F2	63(4)	50(3)	59(4)	-2(3)	21(3)	-35(3)
F3	21(3)	71(4)	132(6)	10(4)	6(3)	-10(3)
F4	68(4)	51(3)	59(4)	-25(3)	1(3)	2(3)
F5	97(5)	78(4)	53(4)	-13(3)	34(3)	-22(4)
F6	45(4)	127(6)	92(5)	-65(4)	6(3)	23(4)
F7	22(3)	70(4)	168(7)	-8(4)	-7(3)	1(3)

F8	47(4)	85(5)	106(5)	38(4)	17(3)	48(3)
F9	41(3)	64(4)	84(5)	10(3)	19(3)	27(3)
F10	83(4)	74(4)	45(3)	-8(3)	24(3)	-20(3)
F11	59(4)	71(4)	78(4)	44(3)	9(3)	1(3)
F12	33(3)	64(4)	57(3)	10(3)	3(3)	-18(3)
F13	147(6)	39(3)	85(4)	4(3)	43(4)	45(4)
F14	64(4)	30(3)	85(4)	17(3)	30(3)	24(2)
F15	27(3)	33(3)	267(8)	-22(4)	-23(4)	15(2)
F16	31(3)	19(3)	122(5)	4(3)	-17(3)	2(2)
F17	37(3)	37(3)	77(4)	0(3)	16(3)	-13(2)
F18	56(3)	28(3)	55(3)	3(2)	-11(2)	-13(2)
F19	66(4)	60(4)	141(6)	57(4)	47(4)	32(3)
F20	327(13)	42(4)	80(5)	33(4)	99(7)	53(6)
F21	70(5)	91(5)	244(10)	111(6)	-61(6)	-45(4)
F22	135(6)	54(4)	72(4)	-19(3)	57(4)	-13(4)
F23	107(5)	48(4)	94(5)	-29(3)	-23(4)	40(4)
F24	49(4)	75(4)	151(6)	-66(4)	34(4)	-32(3)
C22	31(5)	38(5)	46(6)	-10(4)	14(5)	-1(5)
C23	7(4)	33(4)	32(4)	-3(3)	0(3)	2(3)
C24	16(4)	17(4)	35(4)	3(3)	2(3)	0(3)
C25	7(4)	23(4)	39(5)	2(3)	-6(3)	6(3)
C26	8(4)	21(4)	43(4)	-1(3)	5(3)	6(3)
C27	8(4)	36(4)	40(4)	7(3)	2(3)	3(3)
C28	12(4)	45(4)	33(4)	4(3)	3(3)	4(4)
C29	24(5)	39(5)	50(6)	15(4)	14(4)	4(5)
C30	30(6)	21(5)	77(8)	1(5)	-7(5)	9(4)
C31	18(5)	23(5)	45(6)	-3(4)	0(4)	-6(4)
C32	12(4)	23(4)	43(5)	0(4)	6(4)	0(4)
C33	17(4)	16(4)	35(5)	-1(4)	7(4)	0(3)
C34	20(4)	23(5)	35(5)	-5(4)	-2(4)	-1(4)
C35	35(5)	29(5)	28(5)	0(4)	-2(4)	-11(4)
C36	46(6)	48(6)	30(5)	-2(5)	4(5)	-14(5)
C37	26(5)	22(5)	43(5)	-2(4)	-7(4)	9(4)
C38	15(4)	16(3)	31(5)	1(3)	4(3)	1(3)
C39	20(3)	16(4)	42(5)	1(4)	8(3)	3(3)
C40	23(4)	27(4)	44(5)	3(4)	3(4)	-3(3)
C41	23(4)	18(4)	46(5)	7(4)	2(3)	4(3)
C42	14(4)	28(4)	57(6)	6(4)	5(4)	-1(3)

C43	12(3)	23(3)	54(5)	4(4)	8(4)	2(3)
C44	17(4)	31(4)	79(6)	1(4)	9(4)	-1(3)
C45	18(3)	22(4)	42(5)	-3(4)	6(3)	-4(3)
C46	20(4)	16(4)	33(5)	9(4)	2(4)	2(3)
C47	25(5)	20(4)	31(5)	0(4)	5(4)	2(4)
C48	26(5)	14(4)	51(6)	5(4)	-6(4)	-14(4)
C49	65(8)	57(7)	37(6)	-1(6)	0(5)	-32(6)
C50	50(6)	18(5)	40(6)	-5(4)	-4(5)	6(4)
C51	41(6)	25(5)	32(5)	4(4)	-9(4)	5(4)
C52	42(7)	72(8)	47(7)	-22(6)	6(5)	-4(6)
C53	19(4)	28(5)	41(5)	2(4)	-1(4)	6(4)
B1	20(5)	17(5)	39(6)	-1(4)	5(4)	6(4)

Table D.7. Bond Lengths for 2-LT.

Atom	Atom	Length/Å	Atom	Atom	Length/Å
Fe1	S1	2.239(2)	F11	C36	1.360(10)
Fe1	S2	2.289(2)	F12	C36	1.341(9)
Fe1	N1	1.958(6)	F13	C44	1.341(10)
Fe1	N2	1.979(6)	F14	C44	1.301(9)
Fe1	N3	1.976(6)	F15	C44	1.308(9)
Fe1	N4	2.017(6)	F16	C41	1.333(8)
S1	C1	1.683(8)	F17	C41	1.325(9)
S2	C2	1.715(8)	F18	C41	1.341(9)
S3	C2	1.725(8)	F19	C29	1.286(9)
S3	C3	1.757(8)	F20	C29	1.271(10)
S4	C1	1.739(8)	F21	C29	1.280(10)
S4	C3	1.719(8)	F22	C22	1.306(9)
N1	C11	1.361(9)	F23	C22	1.333(10)
N1	C15	1.361(9)	F24	C22	1.306(9)
N2	C17	1.353(9)	C22	C23	1.483(11)
N2	C21	1.346(9)	C23	C24	1.374(10)
N3	C4	1.334(10)	C23	C28	1.375(10)
N3	C8	1.362(10)	C24	C25	1.418(10)
N4	C9	1.475(9)	C25	C26	1.396(10)
N4	C10	1.496(9)	C25	B1	1.619(12)
N4	C16	1.476(9)	C26	C27	1.372(10)

C1	C2	1.375(10)	C27	C28	1.398(11)
C3	C3[1]	1.353(15)	C27	C29	1.503(11)
C4	C5	1.391(11)	C30	C31	1.518(11)
C5	C6	1.358(13)	C31	C32	1.363(10)
C6	C7	1.396(13)	C31	C37	1.385(11)
C7	C8	1.361(11)	C32	C33	1.401(10)
C8	C9	1.499(11)	C33	C34	1.390(10)
C10	C11	1.486(10)	C33	B1	1.605(11)
C11	C12	1.380(10)	C34	C35	1.384(10)
C12	C13	1.400(12)	C35	C36	1.486(11)
C13	C14	1.365(12)	C35	C37	1.385(11)
C14	C15	1.395(11)	C38	C39	1.395(10)
C16	C17	1.461(10)	C38	C45	1.404(10)
C17	C18	1.370(10)	C38	B1	1.640(11)
C18	C19	1.385(10)	C39	C40	1.384(10)
C19	C20	1.390(10)	C40	C41	1.483(11)
C20	C21	1.363(10)	C40	C42	1.403(10)
Cl1	C54	1.706(13)	C42	C43	1.379(10)
Cl2	C54	1.704(12)	C43	C44	1.501(11)
F1	C49	1.315(10)	C43	C45	1.391(10)
F2	C49	1.347(10)	C46	C47	1.392(10)
F3	C49	1.342(11)	C46	C53	1.411(10)
F4	C52	1.345(10)	C46	B1	1.642(11)
F5	C52	1.316(11)	C47	C48	1.391(10)
F6	C52	1.347(10)	C48	C49	1.498(12)
F7	C30	1.359(10)	C48	C50	1.373(11)
F8	C30	1.284(10)	C50	C51	1.373(11)
F9	C30	1.323(10)	C51	C52	1.486(12)
F10	C36	1.314(10)	C51	C53	1.386(11)

[1]-X,1-Y,-Z

Table D.8. Bond Angles for 2-LT.

Atom	Atom	Atom	Angle/°	Atom	Atom	Atom	Angle/°
S1	Fe1	S2	89.44(8)	C23	C28	C27	118.5(7)
N1	Fe1	S1	98.44(19)	F19	C29	C27	112.8(7)

N1	Fe1	S2	89.31(18)	F20	C29	F19	106.3(8)
N1	Fe1	N2	87.2(2)	F20	C29	F21	105.8(9)
N1	Fe1	N3	165.4(3)	F20	C29	C27	114.1(8)
N1	Fe1	N4	83.8(3)	F21	C29	F19	103.5(8)
N2	Fe1	S1	93.09(17)	F21	C29	C27	113.4(7)
N2	Fe1	S2	175.94(18)	F7	C30	C31	110.7(7)
N2	Fe1	N4	84.3(2)	F8	C30	F7	106.9(8)
N3	Fe1	S1	96.08(19)	F8	C30	F9	108.5(7)
N3	Fe1	S2	89.83(19)	F8	C30	C31	114.4(8)
N3	Fe1	N2	93.0(2)	F9	C30	F7	103.6(8)
N3	Fe1	N4	81.8(3)	F9	C30	C31	112.1(7)
N4	Fe1	S1	176.5(2)	C32	C31	C30	118.7(8)
N4	Fe1	S2	93.33(19)	C32	C31	C37	120.8(7)
C1	S1	Fe1	103.6(3)	C37	C31	C30	120.5(8)
C2	S2	Fe1	102.0(3)	C31	C32	C33	123.8(7)
C2	S3	C3	95.7(4)	C32	C33	B1	121.7(7)
C3	S4	C1	96.9(4)	C34	C33	C32	114.1(7)
C11	N1	Fe1	114.4(5)	C34	C33	B1	123.5(7)
C15	N1	Fe1	128.3(5)	C35	C34	C33	123.2(7)
C15	N1	C11	117.3(6)	C34	C35	C36	118.6(8)
C17	N2	Fe1	115.2(5)	C37	C35	C34	120.6(7)
C21	N2	Fe1	127.3(5)	C37	C35	C36	120.8(8)
C21	N2	C17	117.0(7)	F10	C36	F11	106.5(7)
C4	N3	Fe1	128.6(6)	F10	C36	F12	106.1(7)
C4	N3	C8	117.6(7)	F10	C36	C35	113.6(7)
C8	N3	Fe1	113.8(5)	F11	C36	C35	112.8(8)
C9	N4	Fe1	105.9(4)	F12	C36	F11	104.7(7)
C9	N4	C10	112.4(6)	F12	C36	C35	112.4(7)
C9	N4	C16	111.5(6)	C35	C37	C31	117.5(7)
C10	N4	Fe1	106.2(4)	C39	C38	C45	115.3(6)
C16	N4	Fe1	108.5(4)	C39	C38	B1	121.6(6)
C16	N4	C10	111.9(6)	C45	C38	B1	122.9(6)
S1	C1	S4	121.7(4)	C40	C39	C38	123.4(7)
C2	C1	S1	122.8(6)	C39	C40	C41	121.6(7)
C2	C1	S4	115.5(6)	C39	C40	C42	120.3(7)
S2	C2	S3	120.9(5)	C42	C40	C41	118.1(7)
C1	C2	S2	121.6(6)	F16	C41	F18	106.0(6)
C1	C2	S3	117.5(6)	F16	C41	C40	113.5(6)

S4	C3	S3	114.4(4)	F17	C41	F16	106.3(6)
C3[1]	C3	S3	120.5(9)	F17	C41	F18	105.3(6)
C3[1]	C3	S4	125.1(9)	F17	C41	C40	112.6(7)
N3	C4	C5	122.7(9)	F18	C41	C40	112.5(6)
C6	C5	C4	119.2(9)	C43	C42	C40	117.3(7)
C5	C6	C7	118.8(9)	C42	C43	C44	120.0(6)
C8	C7	C6	119.2(9)	C42	C43	C45	122.0(7)
N3	C8	C9	114.0(7)	C45	C43	C44	118.0(7)
C7	C8	N3	122.5(8)	F13	C44	C43	112.0(8)
C7	C8	C9	123.5(8)	F14	C44	F13	104.8(7)
N4	C9	C8	108.2(6)	F14	C44	F15	106.6(8)
C11	C10	N4	110.6(6)	F14	C44	C43	114.3(7)
N1	C11	C10	114.7(6)	F15	C44	F13	104.7(8)
N1	C11	C12	122.1(7)	F15	C44	C43	113.6(7)
C12	C11	C10	123.1(7)	C43	C45	C38	121.8(7)
C11	C12	C13	120.7(8)	C47	C46	C53	114.8(7)
C14	C13	C12	117.0(8)	C47	C46	B1	122.5(7)
C13	C14	C15	120.9(8)	C53	C46	B1	122.1(7)
N1	C15	C14	122.0(8)	C48	C47	C46	122.0(7)
C17	C16	N4	115.3(6)	C47	C48	C49	116.9(8)
N2	C17	C16	114.5(7)	C50	C48	C47	121.8(7)
N2	C17	C18	122.7(7)	C50	C48	C49	121.2(8)
C18	C17	C16	122.8(7)	F1	C49	F2	106.4(8)
C17	C18	C19	119.1(7)	F1	C49	F3	106.6(9)
C18	C19	C20	118.9(7)	F1	C49	C48	113.6(8)
C21	C20	C19	118.4(7)	F2	C49	C48	112.2(8)
N2	C21	C20	123.8(7)	F3	C49	F2	103.9(8)
Cl2	C54	Cl1	115.8(6)	F3	C49	C48	113.4(8)
F22	C22	F23	103.9(7)	C51	C50	C48	117.8(8)
F22	C22	C23	114.2(7)	C50	C51	C52	121.5(8)
F23	C22	C23	113.0(7)	C50	C51	C53	120.7(8)
F24	C22	F22	107.7(8)	C53	C51	C52	117.7(8)
F24	C22	F23	104.8(8)	F4	C52	F6	105.2(8)
F24	C22	C23	112.4(7)	F4	C52	C51	112.9(8)
C24	C23	C22	118.7(7)	F5	C52	F4	107.0(8)
C24	C23	C28	120.6(7)	F5	C52	F6	106.4(8)
C28	C23	C22	120.7(7)	F5	C52	C51	113.4(8)
C23	C24	C25	122.8(7)	F6	C52	C51	111.3(8)

C24	C25	B1	122.3(6)	C51	C53	C46	122.9(7)
C26	C25	C24	114.6(7)	C25	B1	C38	103.9(6)
C26	C25	B1	122.6(6)	C25	B1	C46	111.3(6)
C27	C26	C25	123.1(7)	C33	B1	C25	114.3(6)
C26	C27	C28	120.3(7)	C33	B1	C38	112.8(6)
C26	C27	C29	119.1(7)	C33	B1	C46	102.6(6)
C28	C27	C29	120.6(7)	C38	B1	C46	112.2(6)

[1]-X,1-Y,-Z

Table D.9. Crystal data and structure refinement for 2-HT.

Identification code	**2-HT**
Empirical formula	$C_{106}H_{60}B_2F_{48}Fe_2N_8S_8$
Formula weight	2747.42
Temperature/K	293(2)
Crystal system	monoclinic
Space group	$P2_1/c$
a/Å	12.7265(13)
b/Å	16.2243(16)
c/Å	28.827(3)
α/°	90
β/°	92.733(2)
γ/°	90
Volume/Å^3	5945.4(10)
Z	2
ρ_{calc}g/cm^3	1.535
μ/mm^{-1}	0.509
F(000)	2748.0
Radiation	MoKα (λ = 0.71073)
2Θ range for data collection/°	4.258 to 41.758
Index ranges	$-12 \leq h \leq 12$, $-16 \leq k \leq 16$, $-28 \leq l \leq 28$
Reflections collected	80374
Independent reflections	6267 [R_{int} = 0.1542, R_{sigma} = 0.0645]
Data/restraints/parameters	6267/1029/784
Goodness-of-fit on F^2	1.023
Final R indexes [I>=2σ (I)]	R_1 = 0.0804, wR_2 = 0.1941
Final R indexes [all data]	R_1 = 0.1501, wR_2 = 0.2351

Largest diff. peak/hole / e Å^{-3}	0.77/-0.43

Table D.10. Fractional Atomic Coordinates (×10^4) and Equivalent Isotropic Displacement Parameters (Å^2×10^3) for 2-HT. Ueq is defined as 1/3 of of the trace of the orthogonalised UIJ tensor.

Atom	*x*	*y*	*z*	U(eq)
Fe1	-570.9(11)	3378.5(8)	3931.0(5)	74.2(5)
S1	283(3)	2949.2(18)	4683.1(10)	103.7(10)
S2	-1062(3)	1983.9(17)	3813.3(9)	95.9(10)
S3	-661(2)	484.1(17)	4353.7(10)	95.4(10)
S4	428(3)	1282(2)	5109.5(11)	107.8(11)
N1	-1869(8)	3883(6)	4294(3)	93(3)
N2	-286(7)	4753(5)	3961(3)	83(2)
N3	-1277(6)	3800(5)	3274(3)	67(2)
N4	892(6)	3531(6)	3606(3)	84(2)
C1	-44(8)	380(6)	4883(4)	88(3)
C2	-528(7)	1527(6)	4300(4)	77(3)
C3	21(8)	1938(7)	4666(4)	82(3)
C4	-2749(10)	3487(8)	4360(4)	115(4)
C5	-3519(14)	3840(11)	4628(6)	174(7)
C6	-3321(17)	4593(13)	4828(7)	191(8)
C7	-2406(15)	4980(10)	4765(5)	158(6)
C8	-1695(12)	4636(8)	4490(4)	101(3)
C9	-675(12)	5016(8)	4398(4)	118(4)
C10	-888(8)	5158(6)	3576(4)	88(3)
C11	-1237(7)	4607(6)	3181(4)	69(3)
C12	-1551(8)	4912(7)	2746(4)	88(3)
C13	-1909(8)	4392(9)	2410(4)	91(3)
C14	-1949(7)	3579(8)	2500(4)	81(3)
C15	-1638(8)	3305(6)	2931(4)	75(3)
C16	864(10)	4862(8)	3941(5)	132(5)
C17	1333(9)	4267(8)	3628(4)	98(3)
C18	2253(10)	4451(10)	3402(6)	140(5)
C19	2663(13)	3833(12)	3139(6)	157(6)
C20	2229(11)	3089(10)	3113(6)	151(6)
C21	1338(9)	2970(8)	3350(4)	107(4)
F1	6850(8)	7804(6)	4918(3)	186(4)

F2	7257(6)	6853(5)	4503(3)	153(3)
F3	6074(6)	6652(6)	4949(3)	192(4)
F4	2708(9)	6517(9)	4108(4)	294(7)
F5	2592(8)	6885(8)	3458(4)	229(5)
F6	2223(8)	7623(10)	3940(7)	310(7)
F7	5313(7)	7013(5)	1917(4)	195(4)
F8	3864(9)	6987(6)	2044(5)	234(5)
F9	4265(13)	7456(5)	1461(4)	276(7)
F10	5079(8)	10871(7)	1699(5)	266(6)
F11	3788(10)	11053(5)	2017(3)	204(4)
F12	3710(9)	10429(5)	1433(3)	201(4)
F13	8256(5)	11275(3)	2720(2)	114(2)
F14	9123(6)	10519(4)	2275(2)	126(2)
F15	9774(5)	10840(4)	2930(3)	124(2)
F16	9329(12)	7403(9)	3529(6)	282(6)
F17	8740(9)	7065(6)	2955(6)	262(6)
F18	10036(8)	7682(6)	2964(6)	316(8)
F19	6846(9)	10511(9)	4855(4)	235(5)
F20	6656(12)	11600(8)	4640(3)	307(7)
F21	5726(7)	11099(8)	5080(3)	213(5)
F22	2379(7)	11446(9)	4109(4)	255(6)
F23	2076(7)	10263(9)	3975(6)	273(6)
F24	2305(6)	11010(6)	3464(3)	185(4)
C22	5324(7)	8346(5)	3627(3)	63(2)
C23	5963(7)	8057(5)	3994(3)	69(2)
C24	5665(9)	7471(6)	4296(3)	79(3)
C25	4682(9)	7144(6)	4257(4)	87(3)
C26	3991(9)	7411(7)	3901(4)	89(3)
C27	4333(7)	7995(6)	3597(3)	76(3)
C28	6405(12)	7194(9)	4678(5)	116(3)
C29	2964(14)	7074(13)	3864(7)	161(5)
C30	5092(6)	9082(5)	2784(3)	61(2)
C31	4962(7)	8322(6)	2552(3)	69(2)
C32	4616(7)	8275(6)	2098(4)	73(2)
C33	4383(7)	8981(6)	1850(3)	76(3)
C34	4500(7)	9740(6)	2063(3)	70(2)
C35	4845(7)	9773(6)	2520(3)	68(2)
C36	4310(12)	10484(8)	1802(5)	112(4)

C37	4529(13)	7479(8)	1872(5)	116(4)
C38	6912(7)	9145(5)	3211(3)	65(2)
C39	7537(7)	8443(6)	3213(3)	78(3)
C40	8572(8)	8457(7)	3089(4)	96(3)
C41	9007(8)	9173(6)	2942(4)	94(3)
C42	8411(7)	9870(6)	2911(3)	73(2)
C43	7387(7)	9869(6)	3053(3)	72(3)
C44	8858(10)	10628(7)	2714(5)	92(3)
C45	9202(14)	7714(10)	3126(9)	170(6)
C46	5255(7)	9893(5)	3611(3)	59(2)
C47	5874(7)	10218(5)	3979(3)	70(2)
C48	5470(9)	10739(6)	4305(4)	81(3)
C49	4421(9)	10947(6)	4274(4)	86(3)
C50	3792(8)	10643(6)	3911(4)	83(3)
C51	4206(7)	10132(6)	3594(3)	74(3)
C52	2707(12)	10888(12)	3877(6)	143(5)
C53	6089(13)	11033(10)	4691(6)	128(4)
B1	5645(8)	9120(6)	3301(4)	63(2)

Table D.11. Anisotropic Displacement Parameters ($Å^2 \times 10^3$) for 2-HT. The Anisotropic displacement factor exponent takes the form: $-2\pi^2[h^2a^{*2}U_{11}+2hka^*b^*U_{12}+\ldots]$.

Atom	U_{11}	U_{22}	U_{33}	U_{23}	U_{13}	U_{12}
Fe1	85.9(10)	67.1(9)	69.3(9)	12.3(7)	-1.8(7)	13.2(8)
S1	132(3)	87(2)	89(2)	14.2(17)	-27.9(18)	10.8(19)
S2	134(3)	72.1(17)	79.8(19)	22.5(15)	-16.6(17)	8.0(17)
S3	101(2)	78.6(19)	106(2)	37.5(17)	-5.7(18)	7.9(16)
S4	123(3)	100(2)	99(2)	39.3(19)	-20.3(19)	5.6(19)
N1	111(7)	102(7)	66(6)	20(5)	8(5)	17(6)
N2	93(7)	77(6)	79(6)	-12(5)	-11(6)	1(5)
N3	71(5)	59(5)	70(6)	10(5)	-1(4)	-1(4)
N4	76(6)	80(6)	96(6)	21(5)	3(5)	13(4)
C1	88(7)	79(7)	99(8)	33(6)	6(6)	11(6)
C2	72(7)	76(7)	85(7)	35(6)	12(6)	19(6)
C3	80(7)	93(8)	73(7)	29(6)	6(6)	16(6)
C4	121(9)	114(9)	114(10)	46(8)	30(8)	21(7)
C5	171(13)	166(13)	194(17)	93(12)	100(12)	57(11)

C6	202(16)	172(15)	209(18)	62(13)	121(15)	97(13)
C7	216(16)	128(11)	137(12)	22(9)	76(12)	73(10)
C8	139(10)	97(8)	68(8)	15(6)	14(7)	42(8)
C9	166(14)	96(9)	91(10)	-12(8)	-13(9)	18(9)
C10	100(8)	61(7)	103(9)	9(7)	-5(7)	4(6)
C11	68(7)	62(7)	78(8)	11(6)	12(6)	2(5)
C12	87(8)	81(8)	95(9)	55(8)	8(7)	16(6)
C13	85(8)	121(11)	65(8)	11(8)	-11(6)	2(8)
C14	77(7)	84(9)	82(9)	3(7)	-9(6)	2(6)
C15	85(7)	60(7)	81(8)	13(7)	4(6)	-3(6)
C16	114(11)	122(10)	157(12)	-36(8)	-24(8)	-16(8)
C17	85(8)	100(7)	107(9)	20(6)	-16(6)	-2(6)
C18	80(9)	143(12)	198(15)	48(10)	-1(8)	-7(8)
C19	105(11)	171(13)	199(16)	68(12)	32(10)	23(9)
C20	110(11)	152(11)	195(15)	33(12)	59(10)	46(9)
C21	89(8)	95(8)	139(11)	25(7)	17(7)	30(7)
F1	228(9)	183(8)	139(7)	-13(6)	-82(6)	46(6)
F2	134(6)	174(7)	152(6)	37(5)	7(5)	59(5)
F3	150(7)	253(10)	175(8)	139(7)	23(6)	27(6)
F4	218(10)	365(14)	290(12)	184(12)	-80(9)	-214(10)
F5	160(8)	327(13)	194(9)	30(8)	-49(7)	-143(8)
F6	92(7)	314(14)	530(20)	-84(13)	60(10)	-71(8)
F7	163(7)	118(6)	302(11)	-120(7)	-24(7)	33(5)
F8	239(9)	128(7)	343(12)	-119(8)	109(10)	-88(7)
F9	552(19)	115(7)	149(7)	-62(6)	-111(9)	46(9)
F10	148(7)	256(11)	392(15)	250(11)	9(8)	-31(7)
F11	317(12)	106(6)	188(8)	42(5)	11(8)	79(7)
F12	301(11)	133(6)	158(7)	55(5)	-96(7)	-2(7)
F13	115(5)	57(3)	174(6)	0(4)	34(4)	-5(3)
F14	164(6)	95(5)	124(5)	-11(4)	51(5)	-28(4)
F15	101(4)	102(5)	169(6)	-27(4)	24(4)	-37(4)
F16	308(15)	205(11)	331(14)	84(10)	7(10)	166(11)
F17	210(10)	92(6)	480(18)	-16(9)	-3(11)	70(6)
F18	172(8)	138(7)	660(20)	137(11)	217(11)	100(6)
F19	198(9)	320(12)	178(9)	-84(8)	-75(7)	47(9)
F20	458(16)	285(11)	164(8)	62(8)	-119(9)	-282(12)
F21	160(7)	356(14)	123(6)	-104(8)	-5(5)	-20(7)
F22	139(7)	364(13)	258(10)	-178(10)	-33(7)	141(8)

F23	79(6)	286(11)	459(18)	109(11)	61(9)	45(7)
F24	125(6)	240(10)	187(8)	-53(7)	-33(6)	87(6)
C22	63(5)	52(5)	74(5)	-5(4)	7(4)	-1(4)
C23	62(6)	60(6)	85(6)	1(4)	5(4)	-4(5)
C24	96(6)	65(6)	76(6)	2(4)	11(5)	7(5)
C25	108(7)	65(7)	91(7)	19(6)	23(5)	-9(6)
C26	89(6)	87(7)	91(7)	-1(5)	9(5)	-32(5)
C27	71(6)	77(6)	82(7)	2(5)	2(5)	-16(5)
C28	127(9)	116(9)	105(9)	25(6)	6(6)	31(7)
C29	112(9)	200(14)	171(11)	44(10)	-3(9)	-82(8)
C30	48(5)	57(5)	78(5)	0(4)	7(4)	2(4)
C31	62(6)	60(5)	87(6)	-2(5)	11(5)	0(5)
C32	72(6)	66(5)	83(6)	-10(4)	13(5)	3(5)
C33	74(6)	83(5)	74(6)	3(4)	16(5)	-6(5)
C34	60(6)	74(5)	76(5)	11(4)	5(5)	-1(5)
C35	68(6)	58(5)	77(5)	0(4)	3(5)	3(5)
C36	129(10)	94(7)	115(9)	51(7)	2(7)	-4(7)
C37	140(10)	88(7)	119(8)	-44(7)	4(8)	3(6)
C38	56(4)	59(5)	79(6)	-3(5)	-2(4)	3(4)
C39	68(5)	54(5)	112(7)	5(5)	25(6)	6(4)
C40	65(6)	73(5)	151(9)	18(6)	22(6)	18(5)
C41	59(6)	76(6)	149(10)	4(6)	25(6)	8(5)
C42	62(5)	56(5)	101(7)	-9(5)	10(5)	-2(4)
C43	64(5)	54(5)	98(7)	-9(5)	10(5)	6(4)
C44	101(7)	56(5)	122(7)	-16(6)	24(6)	-16(5)
C45	119(10)	88(8)	310(16)	59(10)	71(11)	48(7)
C46	62(5)	52(5)	66(5)	6(4)	16(4)	-5(4)
C47	70(6)	66(6)	73(6)	4(4)	4(4)	-3(5)
C48	90(6)	70(6)	83(6)	-8(5)	12(5)	-20(5)
C49	99(6)	77(7)	85(7)	-8(5)	30(5)	3(6)
C50	74(6)	84(7)	92(7)	-9(5)	20(5)	17(5)
C51	66(5)	77(6)	81(6)	-7(5)	10(5)	13(5)
C52	81(7)	202(13)	148(10)	-41(10)	20(7)	46(8)
C53	129(10)	130(10)	126(9)	-53(8)	1(7)	-47(7)
B1	55(5)	57(5)	77(6)	1(4)	9(5)	8(4)

Table D.12. Bond Lengths for 2-HT.

Atom	Atom	Length/Å	Atom	Atom	Length/Å
Fe1	S1	2.479(3)	F12	C36	1.282(14)
Fe1	S2	2.368(3)	F13	C44	1.301(12)
Fe1	N1	2.160(9)	F14	C44	1.336(12)
Fe1	N2	2.261(8)	F15	C44	1.340(12)
Fe1	N3	2.168(7)	F16	C45	1.27(2)
Fe1	N4	2.138(8)	F17	C45	1.29(2)
S1	C3	1.675(11)	F18	C45	1.180(16)
S2	C2	1.701(10)	F19	C53	1.351(17)
S3	C1	1.690(10)	F20	C53	1.183(14)
S3	C2	1.708(10)	F21	C53	1.237(15)
S4	C1	1.701(11)	F22	C52	1.211(16)
S4	C3	1.724(9)	F23	C52	1.331(19)
N1	C4	1.313(14)	F24	C52	1.290(17)
N1	C8	1.359(14)	C22	C23	1.386(11)
N2	C9	1.439(13)	C22	C27	1.383(11)
N2	C10	1.475(11)	C22	B1	1.630(13)
N2	C16	1.478(13)	C23	C24	1.354(12)
N3	C11	1.338(11)	C24	C25	1.359(13)
N3	C15	1.337(11)	C24	C28	1.485(16)
N4	C17	1.320(13)	C25	C26	1.388(13)
N4	C21	1.318(13)	C26	C27	1.376(13)
C1	$C1^{1}$	1.408(18)	C26	C29	1.416(17)
C2	C3	1.404(13)	C30	C31	1.408(11)
C4	C5	1.398(18)	C30	C35	1.383(11)
C5	C6	1.37(3)	C30	B1	1.620(13)
C6	C7	1.34(2)	C31	C32	1.364(12)
C7	C8	1.350(16)	C32	C33	1.373(12)
C8	C9	1.474(16)	C32	C37	1.449(15)
C10	C11	1.498(13)	C33	C34	1.381(12)
C11	C12	1.387(13)	C34	C35	1.370(12)
C12	C13	1.348(14)	C34	C36	1.437(15)
C13	C14	1.345(14)	C38	C39	1.390(11)
C14	C15	1.361(13)	C38	C43	1.407(11)
C16	C17	1.468(16)	C38	B1	1.645(13)
C17	C18	1.398(16)	C39	C40	1.382(12)

C18	C19	1.38(2)	C40	C41	1.363(13)
C19	C20	1.33(2)	C40	C45	1.449(17)
C20	C21	1.365(16)	C41	C42	1.362(12)
F1	C28	1.321(15)	C42	C43	1.384(11)
F2	C28	1.337(14)	C42	C44	1.480(13)
F3	C28	1.262(14)	C46	C47	1.395(11)
F4	C29	1.199(17)	C46	C51	1.389(11)
F5	C29	1.278(18)	C46	B1	1.631(13)
F6	C29	1.32(2)	C47	C48	1.381(12)
F7	C37	1.253(14)	C48	C49	1.376(13)
F8	C37	1.279(15)	C48	C53	1.416(16)
F9	C37	1.218(14)	C49	C50	1.377(13)
F10	C36	1.211(14)	C50	C51	1.359(12)
F11	C36	1.310(15)	C50	C52	1.436(16)

[1]-X,-Y,1-Z

Table D.13. Bond Angles for 2-HT.

Atom	Atom	Atom	Angle/°	Atom	Atom	Atom	Angle/°
S2	Fe1	S1	87.63(10)	F4	C29	F5	105.0(16)
N1	Fe1	S1	89.8(2)	F4	C29	F6	101.2(17)
N1	Fe1	S2	103.2(3)	F4	C29	C26	121.4(17)
N1	Fe1	N2	74.5(4)	F5	C29	F6	94.5(16)
N1	Fe1	N3	90.5(3)	F5	C29	C26	117.5(15)
N2	Fe1	S1	100.4(2)	F6	C29	C26	113.0(17)
N2	Fe1	S2	171.6(2)	C31	C30	B1	120.4(8)
N3	Fe1	S1	177.6(2)	C35	C30	C31	115.6(8)
N3	Fe1	S2	94.6(2)	C35	C30	B1	123.5(8)
N3	Fe1	N2	77.4(3)	C32	C31	C30	122.0(9)
N4	Fe1	S1	93.5(2)	C31	C32	C33	120.3(9)
N4	Fe1	S2	106.1(3)	C31	C32	C37	119.6(10)
N4	Fe1	N1	150.6(4)	C33	C32	C37	120.0(11)
N4	Fe1	N2	76.2(3)	C32	C33	C34	119.8(9)
N4	Fe1	N3	85.1(3)	C33	C34	C36	120.3(10)
C3	S1	Fe1	99.8(4)	C35	C34	C33	119.0(9)
C2	S2	Fe1	101.9(4)	C35	C34	C36	120.6(10)
C1	S3	C2	97.8(5)	C34	C35	C30	123.4(9)
C1	S4	C3	99.1(5)	F10	C36	F11	100.7(14)

C4	N1	Fe1	124.2(9)	F10	C36	F12	106.7(13)
C4	N1	C8	120.2(12)	F10	C36	C34	116.5(13)
C8	N1	Fe1	115.4(9)	F11	C36	C34	114.9(12)
C9	N2	Fe1	105.4(7)	F12	C36	F11	98.3(12)
C9	N2	C10	109.8(9)	F12	C36	C34	117.0(12)
C9	N2	C16	112.4(10)	F7	C37	F8	97.0(13)
C10	N2	Fe1	109.5(6)	F7	C37	C32	116.7(12)
C10	N2	C16	113.5(9)	F8	C37	C32	114.8(12)
C16	N2	Fe1	105.9(7)	F9	C37	F7	105.2(13)
C11	N3	Fe1	117.8(7)	F9	C37	F8	101.6(14)
C15	N3	Fe1	124.7(7)	F9	C37	C32	118.4(13)
C15	N3	C11	117.0(8)	C39	C38	C43	115.5(8)
C17	N4	Fe1	117.4(8)	C39	C38	B1	123.0(8)
C21	N4	Fe1	125.0(8)	C43	C38	B1	120.8(8)
C21	N4	C17	117.3(11)	C40	C39	C38	122.5(9)
S3	C1	S4	113.6(5)	C39	C40	C45	119.9(11)
$C1^1$	C1	S3	123.0(12)	C41	C40	C39	120.0(9)
$C1^1$	C1	S4	123.4(11)	C41	C40	C45	120.1(11)
S2	C2	S3	117.9(7)	C42	C41	C40	119.7(9)
C3	C2	S2	125.3(8)	C41	C42	C43	120.5(9)
C3	C2	S3	116.8(7)	C41	C42	C44	119.4(9)
S1	C3	S4	122.0(7)	C43	C42	C44	120.0(9)
C2	C3	S1	125.4(7)	C42	C43	C38	121.5(8)
C2	C3	S4	112.6(8)	F13	C44	F14	107.2(11)
N1	C4	C5	120.2(15)	F13	C44	F15	106.6(9)
C6	C5	C4	118.6(18)	F13	C44	C42	115.3(10)
C7	C6	C5	120.2(18)	F14	C44	F15	102.8(10)
C6	C7	C8	119.6(18)	F14	C44	C42	111.9(9)
N1	C8	C9	115.4(12)	F15	C44	C42	112.1(10)
C7	C8	N1	121.0(15)	F16	C45	F17	93.6(14)
C7	C8	C9	123.6(15)	F16	C45	C40	116.2(18)
N2	C9	C8	112.2(11)	F17	C45	C40	114.2(16)
N2	C10	C11	115.6(8)	F18	C45	F16	105.4(18)
N3	C11	C10	116.3(9)	F18	C45	F17	102.5(18)
N3	C11	C12	121.2(10)	F18	C45	C40	120.8(15)
C12	C11	C10	122.4(10)	C47	C46	B1	122.1(8)
C13	C12	C11	120.0(10)	C51	C46	C47	115.4(8)
C14	C13	C12	119.3(10)	C51	C46	B1	120.9(8)

C13	C14	C15	119.0(10)	C48	C47	C46	122.2(9)
N3	C15	C14	123.6(9)	C47	C48	C53	122.0(12)
C17	C16	N2	112.2(10)	C49	C48	C47	119.9(10)
N4	C17	C16	116.1(12)	C49	C48	C53	118.0(12)
N4	C17	C18	122.3(13)	C48	C49	C50	119.2(10)
C18	C17	C16	121.3(13)	C49	C50	C52	118.3(11)
C19	C18	C17	116.7(16)	C51	C50	C49	120.0(10)
C20	C19	C18	121.8(17)	C51	C50	C52	121.7(12)
C19	C20	C21	117.0(16)	C50	C51	C46	123.4(10)
N4	C21	C20	125.0(13)	F22	C52	F23	103.1(15)
C23	C22	B1	123.1(8)	F22	C52	F24	105.2(15)
C27	C22	C23	114.0(8)	F22	C52	C50	121.6(15)
C27	C22	B1	122.3(8)	F23	C52	C50	111.2(15)
C24	C23	C22	123.8(9)	F24	C52	F23	95.5(15)
C23	C24	C25	120.4(10)	F24	C52	C50	116.3(13)
C23	C24	C28	120.1(11)	F19	C53	C48	115.1(13)
C25	C24	C28	119.4(11)	F20	C53	F19	95.8(15)
C24	C25	C26	119.1(10)	F20	C53	F21	107.6(14)
C25	C26	C29	119.1(12)	F20	C53	C48	118.9(15)
C27	C26	C25	118.5(10)	F21	C53	F19	91.6(14)
C27	C26	C29	122.4(12)	F21	C53	C48	121.6(14)
C26	C27	C22	124.1(10)	C22	B1	C38	112.6(7)
F1	C28	F2	100.0(13)	C22	B1	C46	100.7(7)
F1	C28	C24	113.8(11)	C30	B1	C22	113.0(7)
F2	C28	C24	110.0(11)	C30	B1	C38	104.0(7)
F3	C28	F1	110.1(13)	C30	B1	C46	113.8(7)
F3	C28	F2	104.3(11)	C46	B1	C38	113.2(7)
F3	C28	C24	116.9(13)				

[1]-X,-Y,1-Z

Table D.14. Crystal data and structure refinement for 3.

Identification code	**3**
Empirical formula	$C_{22}H_{20}Cl_2FeN_4S_5$
Formula weight	627.47
Temperature/K	60(2)
Crystal system	monoclinic
Space group	$P2_1/c$

a/Å	12.277(2)
b/Å	15.270(3)
c/Å	14.049(2)
α/°	90
β/°	95.225(3)
γ/°	90
Volume/Å^3	2622.8(7)
Z	4
ρ_{calc}g/cm^3	1.589
μ/mm^{-1}	0.266
F(000)	1280.0
Radiation	synchrotron (λ = 0.41328)
2Θ range for data collection/°	1.936 to 30.604
Index ranges	$-15 \leq h \leq 15$, $-19 \leq k \leq 19$, $-17 \leq l \leq 17$
Reflections collected	59090
Independent reflections	5561 [R_{int} = 0.0718, R_{sigma} = 0.0291]
Data/restraints/parameters	5561/0/307
Goodness-of-fit on F^2	1.060
Final R indexes [I>=2σ (I)]	R_1 = 0.0309, wR_2 = 0.0823
Final R indexes [all data]	R_1 = 0.0377, wR_2 = 0.0847
Largest diff. peak/hole / e Å^{-3}	0.46/-0.45

Table D.15. Fractional Atomic Coordinates (×104) and Equivalent Isotropic Displacement Parameters (Å^2×10^3) for 3. U_{eq} is defined as 1/3 of the trace of the orthogonalized UIJ tensor.

Atom	*x*	*y*	*z*	U(eq)
Fe1	2675.4(2)	6663.5(2)	3772.6(2)	16.32(9)
S1	3705.4(4)	5702.8(3)	2868.5(4)	18.04(12)
S2	1064.0(4)	6440.9(3)	2619.6(4)	18.12(12)
S3	704.8(4)	4980.6(3)	1184.9(4)	18.69(12)
S4	1329.4(4)	3483.5(4)	-34.4(4)	22.39(13)
S5	2935.4(4)	4424.5(3)	1337.0(4)	18.44(12)
N1	2033.0(15)	5797.1(12)	4815.3(13)	19.7(4)
N2	1885.1(14)	7566.1(11)	4776.5(13)	18.9(4)
N3	3011.0(15)	7983.8(11)	3250.5(13)	19.1(4)
N4	4093.5(15)	7030.4(12)	4806.3(13)	19.8(4)
C1	1644.3(17)	4256.8(13)	784.5(15)	19.0(4)
C2	2639.2(17)	5283.0(13)	2093.4(15)	17.6(4)
C3	1577.1(17)	5563.8(13)	2013.9(15)	16.9(4)

C4	2290.9(19)	4943.7(14)	4919.3(16)	23.0(5)
C5	1812(2)	4409.6(16)	5558.3(18)	27.8(5)
C6	1075(2)	4771.0(16)	6133.5(18)	29.3(5)
C7	822.5(18)	5646.9(16)	6045.0(17)	25.5(5)
C8	1299.5(17)	6144.7(14)	5363.0(16)	20.4(4)
C9	968.8(18)	7082.4(14)	5140.5(16)	21.0(4)
C10	1521.3(18)	8337.6(14)	4196.2(17)	22.0(4)
C11	2429.9(18)	8634.5(14)	3613.1(16)	20.8(4)
C12	2648(2)	9512.1(15)	3449.0(18)	26.5(5)
C13	3495(2)	9717.6(16)	2895.8(18)	29.8(5)
C14	4092.6(19)	9057.5(15)	2521.8(17)	26.4(5)
C15	3826.3(18)	8194.3(14)	2718.1(16)	21.3(4)
C16	2697.7(17)	7811.1(15)	5575.7(16)	21.8(4)
C17	3866.8(18)	7734.9(14)	5329.3(15)	19.8(4)
C18	4657.9(18)	8340.4(14)	5648.6(16)	22.0(4)
C19	5725.7(19)	8207.8(15)	5441.4(16)	24.5(5)
C20	5974.1(18)	7468.1(15)	4934.7(16)	24.4(5)
C21	5136.8(18)	6899.4(15)	4626.6(17)	23.3(5)
Cl1	6915.5(5)	7875.0(4)	7678.6(4)	30.39(14)
Cl2	8339.9(5)	6685.5(4)	6745.3(5)	31.62(14)
C22	8290(2)	7609.3(17)	7496(2)	33.3(6)

Table D.16. Anisotropic Displacement Parameters ($Å^2 \times 10^3$) for 3. The Anisotropic displacement factor exponent takes the form: $-2\pi^2[h^2a^{*2}U_{11}+2hka^*b^*U_{12}+\ldots]$.

Atom	U_{11}	U_{22}	U_{33}	U_{23}	U_{13}	U_{12}
Fe1	19.63(16)	13.77(15)	16.21(16)	-0.53(10)	5.19(11)	0.33(11)
S1	19.0(2)	16.5(2)	19.1(3)	-2.66(18)	4.10(19)	0.07(19)
S2	19.8(2)	15.4(2)	19.7(3)	-1.34(18)	4.87(19)	1.51(19)
S3	19.5(3)	15.7(2)	21.2(3)	-1.50(18)	3.76(19)	-0.38(19)
S4	22.7(3)	19.2(3)	25.3(3)	-6.4(2)	2.7(2)	-1.1(2)
S5	19.7(3)	15.2(2)	20.8(3)	-3.13(19)	3.80(19)	0.34(19)
N1	22.1(9)	19.1(9)	18.3(9)	0.4(7)	4.6(7)	1.5(7)
N2	19.9(9)	18.6(9)	18.6(9)	-1.1(7)	3.7(7)	1.0(7)
N3	22.3(9)	16.5(8)	18.8(9)	-2.1(7)	3.3(7)	-2.5(7)
N4	22.0(9)	18.9(9)	18.9(10)	-1.8(7)	3.7(7)	1.7(7)
C1	22.5(10)	14.6(9)	20.3(11)	0.5(8)	4.4(8)	-0.3(8)

C2	22.1(10)	13.2(9)	18.1(11)	0.0(7)	5.1(8)	-0.7(8)
C3	22.1(10)	11.6(9)	17.3(10)	0.6(7)	3.8(8)	-2.0(7)
C4	25.7(11)	19.2(10)	24.7(12)	3.0(8)	5.0(9)	1.7(8)
C5	32.3(12)	21.8(11)	30.0(13)	6.9(9)	6.1(10)	2.4(9)
C6	29.5(12)	29.5(12)	29.9(13)	8.8(10)	8.0(10)	-1.1(10)
C7	22.0(11)	31.3(12)	24.4(12)	3.8(9)	8.7(9)	2.9(9)
C8	19.4(10)	21.8(11)	20.5(11)	-0.3(8)	4.1(8)	2.3(8)
C9	21.8(11)	21.8(11)	20.2(11)	0.2(8)	6.6(8)	1.7(8)
C10	22.6(11)	15.1(10)	28.6(12)	-0.4(8)	4.9(9)	2.7(8)
C11	24.6(11)	17.0(10)	20.5(11)	-0.8(8)	-0.3(8)	0.8(8)
C12	32.5(12)	16.5(10)	30.2(13)	-0.9(9)	1.5(10)	1.0(9)
C13	36.8(13)	18.8(11)	33.1(14)	5.0(9)	-0.1(10)	-5.2(10)
C14	29.3(12)	25.1(12)	25.0(12)	2.5(9)	3.0(9)	-8.8(9)
C15	25.3(11)	19.8(10)	19.1(11)	-1.7(8)	3.8(8)	-3.1(8)
C16	23.4(11)	24.6(11)	17.9(11)	-6.0(8)	3.6(8)	1.9(9)
C17	22.7(10)	21.8(10)	15.3(11)	-0.6(8)	3.4(8)	0.9(8)
C18	27.3(11)	22.6(11)	16.3(11)	-2.7(8)	2.8(8)	2.1(9)
C19	26.1(11)	27.5(12)	20.0(12)	-1.9(9)	2.5(9)	-4.5(9)
C20	22.3(11)	29.8(12)	21.5(12)	-2.5(9)	3.3(8)	1.8(9)
C21	22.5(11)	23.1(11)	24.7(12)	-3.5(9)	4.2(9)	5.3(9)
Cl1	37.5(3)	25.2(3)	28.9(3)	-1.4(2)	5.6(2)	6.5(2)
Cl2	37.7(3)	24.2(3)	34.8(3)	1.5(2)	13.3(3)	4.8(2)
C22	35.1(13)	29.8(13)	35.2(15)	-6.0(10)	4.6(10)	-6.9(10)

Table D.17. Bond Lengths for 3.

Atom	Atom	Length/Å	Atom	Atom	Length/Å
Fe1	S1	2.3783(6)	N4	C17	1.346(3)
Fe1	S2	2.4637(7)	N4	C21	1.343(3)
Fe1	N1	2.1745(18)	C2	C3	1.368(3)
Fe1	N2	2.2538(18)	C4	C5	1.383(3)
Fe1	N3	2.1971(18)	C5	C6	1.382(3)
Fe1	N4	2.2347(19)	C6	C7	1.376(3)
S1	C2	1.747(2)	C7	C8	1.393(3)
S2	C3	1.736(2)	C8	C9	1.513(3)
S3	C1	1.728(2)	C10	C11	1.512(3)
S3	C3	1.752(2)	C11	C12	1.390(3)

S4	C1	1.669(2)	C12	C13	1.390(4)
S5	C1	1.719(2)	C13	C14	1.378(4)
S5	C2	1.746(2)	C14	C15	1.392(3)
N1	C4	1.346(3)	C16	C17	1.511(3)
N1	C8	1.346(3)	C17	C18	1.386(3)
N2	C9	1.476(3)	C18	C19	1.383(3)
N2	C10	1.478(3)	C19	C20	1.384(3)
N2	C16	1.481(3)	C20	C21	1.385(3)
N3	C11	1.350(3)	Cl1	C22	1.777(3)
N3	C15	1.342(3)	Cl2	C22	1.765(3)

Table D.18. Bond Angles for 3.

Atom	Atom	Atom	Angle/°	Atom	Atom	Atom	Angle/°
S1	Fe1	S2	89.89(2)	S4	C1	S3	123.86(13)
N1	Fe1	S1	103.16(5)	S4	C1	S5	124.24(13)
N1	Fe1	S2	92.30(5)	S5	C1	S3	111.90(12)
N1	Fe1	N2	75.36(7)	S5	C2	S1	117.97(12)
N1	Fe1	N3	150.89(7)	C3	C2	S1	126.21(16)
N1	Fe1	N4	91.36(7)	C3	C2	S5	115.82(16)
N2	Fe1	S1	172.53(5)	S2	C3	S3	119.41(12)
N2	Fe1	S2	97.47(5)	C2	C3	S2	126.01(17)
N3	Fe1	S1	105.23(5)	C2	C3	S3	114.55(16)
N3	Fe1	S2	94.06(5)	N1	C4	C5	122.1(2)
N3	Fe1	N2	75.65(7)	C6	C5	C4	118.9(2)
N3	Fe1	N4	80.10(7)	C7	C6	C5	119.3(2)
N4	Fe1	S1	94.65(5)	C6	C7	C8	119.2(2)
N4	Fe1	S2	173.38(5)	N1	C8	C7	121.5(2)
N4	Fe1	N2	78.13(7)	N1	C8	C9	115.85(18)
C2	S1	Fe1	98.89(7)	C7	C8	C9	122.46(19)
C3	S2	Fe1	97.08(7)	N2	C9	C8	110.27(17)
C1	S3	C3	98.96(10)	N2	C10	C11	109.68(17)
C1	S5	C2	98.74(10)	N3	C11	C10	115.15(18)
C4	N1	Fe1	124.47(15)	N3	C11	C12	122.1(2)
C8	N1	Fe1	116.61(14)	C12	C11	C10	122.8(2)
C8	N1	C4	118.88(19)	C13	C12	C11	118.4(2)
C9	N2	Fe1	107.22(12)	C14	C13	C12	120.0(2)

C9	N2	C10	112.85(17)	C13	C14	C15	118.3(2)
C9	N2	C16	110.24(17)	N3	C15	C14	122.5(2)
C10	N2	Fe1	105.54(13)	N2	C16	C17	113.28(17)
C10	N2	C16	111.45(17)	N4	C17	C16	115.76(19)
C16	N2	Fe1	109.29(12)	N4	C17	C18	122.4(2)
C11	N3	Fe1	115.33(14)	C18	C17	C16	121.79(19)
C15	N3	Fe1	125.30(15)	C19	C18	C17	118.9(2)
C15	N3	C11	118.73(19)	C18	C19	C20	119.0(2)
C17	N4	Fe1	111.56(14)	C19	C20	C21	118.7(2)
C21	N4	Fe1	122.72(15)	N4	C21	C20	122.8(2)
C21	N4	C17	118.03(19)	Cl2	C22	Cl1	110.72(14)

D.3 References

[1] Bain, G. A.; Berry, J. F., Diamagnetic Corrections and Pascal's Constants. *J. Chem. Ed.* **2008,** *85* (4), 532.

[2] Krause, L.; Herbst-Irmer, R.; Sheldrick, G. M.; Stalke, D. Comparison of Silver and Molybdenum Microfocus X-Ray Sources for Single-Crystal Structure Determination *J. Appl. Crystallogr.* **2015**, *48*, 3-10.

[3] Sheldrick, G.M. Shelxt - Integrated Space-Group and Crystal-Structure Determination *Acta Crystallogr., Sect. A: Found. Adv*. **2015**, *71*, 3–8

[4] Dolomanov, O. V.; Bourhis, L. J.; Gildea, R. J.; Howard, J. A. K.; Puschmann, H. "Olex2: A Complete Structure Solution, Refinement and Analysis Program" *J. Appl. Crystallogr.* **2009**, *42*, 339-341.

[5] Sheldrick, G.M. Crystal Structure Refinement with ShelXL *Crystal Acta Crystallogr., Sect. C: Struct. Chem.* **2015**, *71*, 3–8.

[6] Prisecaru, I. "WMOSS4 Mössbauer Spectral Analysis Software, www.wmoss.org, 2009-2016"

[7] Neese, F. "The Orca Program System" Wiley Interdisciplinary Reviews: Computational Molecular Science, 2, 73-78, doi: 10.1002/wcms.81 (2012)

[8] H - Kr: A. Schaefer, H. Horn and R. Ahlrichs, Fully optimized contracted Gaussian basis sets for atoms Li to Kr *J. Chem. Phys.* 1992, *97*, 2571.

[9] Rb - Xe: A. Schaefer, C. Huber and R. Ahlrichs, Fully optimized contracted Gaussian basis sets of triple zeta valence quality for atoms Li to Kr *J. Chem. Phys.* **1994**, *100*, 5829.

[10] F. Weigend, R. Ahlrichs, Balanced basis sets of split valence, triple zeta valence and quadruple zeta valence quality for H to Rn: Design and assessment of accuracy *Phys. Chem. Chem. Phys.* **2005**, *7*, 3297.

[11] Mazziotti, D. A. Two-Electron Reduced Density Matrix as the Basic Variable in Many-Electron Quantum Chemistry and Physics. *Chem. Rev.* **2012**, *112*, 244-262.

[12] Mazziotti, D. A. Variational minimization of atomic and molecular ground-state energies via the two-particle reduced density matrix. *Phys. Rev. A,* **2002**, *65*, 062511

[13] Mazziotti, D. A. Structure of fermionic density matrices: Complete n-representability conditions. *Phys. Rev. Lett.,* **2012**, *108*, 263002.

[14] McIsaac, A.R. & Mazziotti, D. A. Ligand non-innocence and strong correlation in manganese superoxide dismutase mimics. *Phys. Chem. Chem. Phys.,* **2017**, *19*, 4656-4660.

[15] Montgomery, J.M. & Mazziotti, D. A. Strong electron correlation in nitrogenase cofactor, FeMoco. *J. Phys. Chem. A,* **2018**, *122*(22), 4988-4996.

Appendix E:Supporting Data for Chapter 6

E.1 Pressed Pellets

Pressed pellets were prepared at 800 MPa in the glovebox by using a hydraulic pellet press (TMAX-15T) and dies with different sizes (7 mm, 8 mm, and 12 mm round dies and 6 mm square dies). Hot pressing was carried out with an additional heated die (13 mm Across International heated die with digital controller, the same press machine in the glovebox was used). Prior to pressing, powders were ground to particle sizes below 20 μm. For hot pressed samples, 240 mg of powder was ground with a ball mill (Spex SamplePrep 5100 Mixer miller, 440C steel balls) for 15 mins (in air) and loaded into 13 mm round dies that were preheated to 200 °C (under N_2). During pressing the pressure was maintained for 20 mins after stabilizing at 800 MPa. The thickness of the pressed pellets is around 100-300 μm. The hot pressed pellet was only used for electrical conductivity measurements and most physical characterization was collected on normal pressed pellets (prepared at room temperature, "cold press"). The uniformity of the pressed pellets was examined under a reflected light microscope and the amorphousness of the powders was confirmed by PXRD measurements (see below).

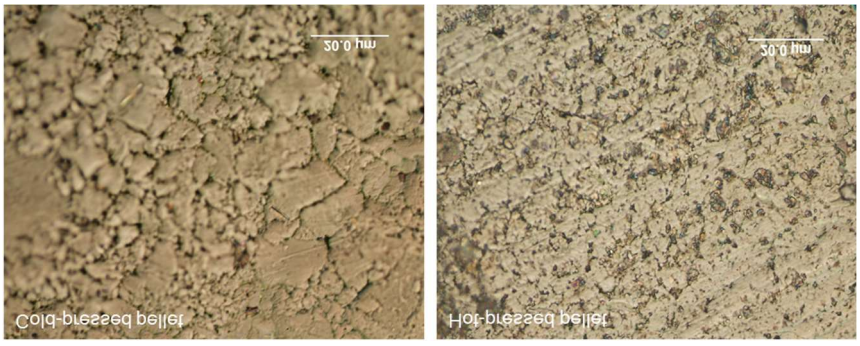

Figure E.1. The surface of cold (left) and hot (right) pressed pellets. Compared to the left figure, the right figure shows generally larger grains which suggests fewer grain boundaries. Fewer grain boundaries should improve the bulk pellet's electrical conductivity. The conductivity of the hot pressed is 1280 S/cm compared to that of the cold pressed pellet, 475 S/cm. Nevertheless, many pits remain after hot-pressing, resulting in limited improvements. The pellet's conductivity should therefore, still be below the intrinsic value for the material.

E.2 Structural Characterizations

E.2.1 X-ray Powder Diffraction on Commercial Diffractometers

X-ray Powder Diffraction (PXRD) for screening reaction conditions were performed on a SAXSLAB Ganesha equipped with a Xenocs GeniX3D Cu Kα source. Samples were loaded into 0.8−1.1 mm ID, 0.25 mm wall borosilicate capillaries and sealed with wax under N_2. Data reduction/integration was performed using the Saxsgui software and a background correction for the capillary was applied.

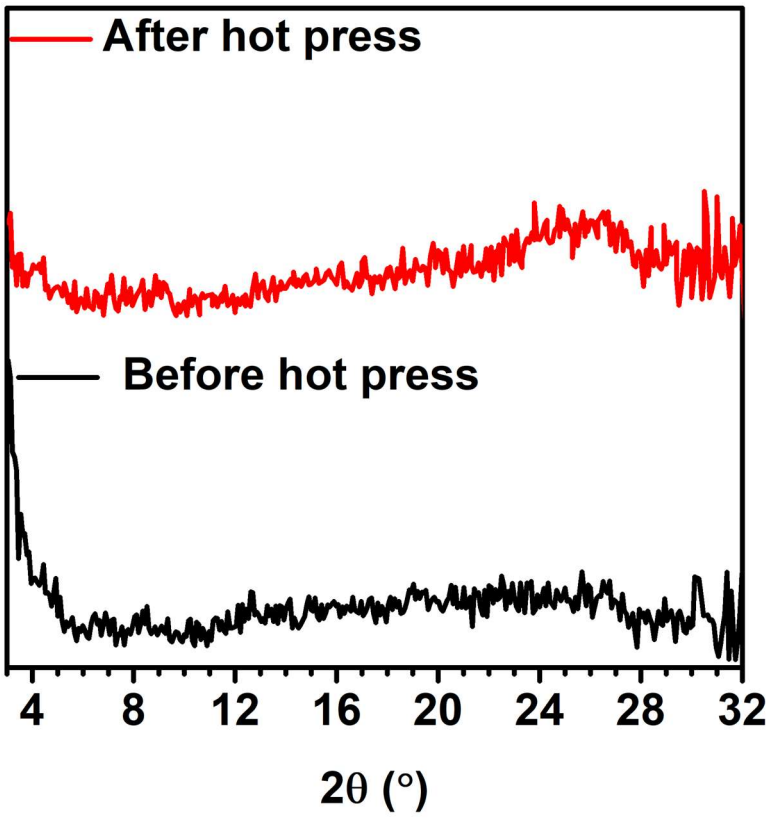

Figure E.2. PXRD spectra of NiTTFtt before and after hot press.

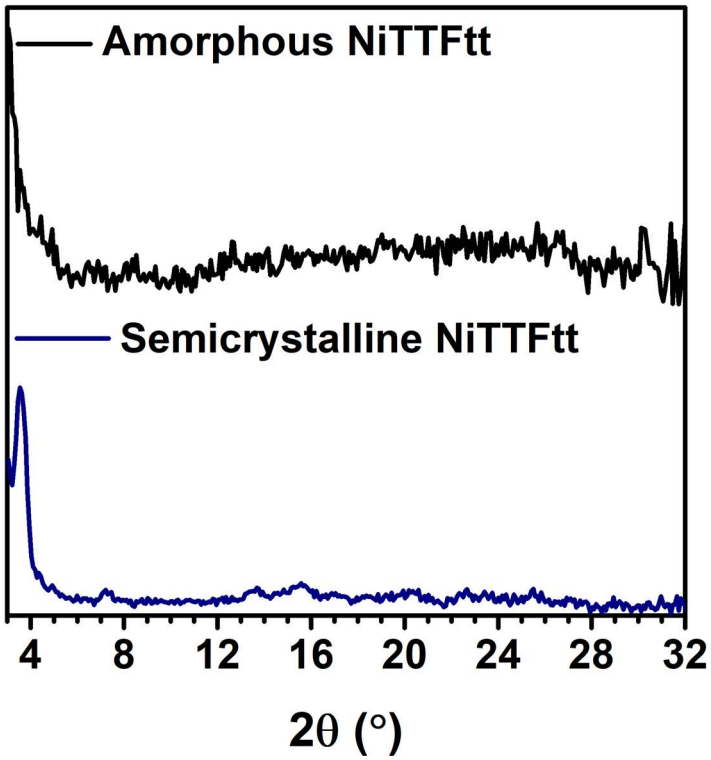

Figure E.3. PXRD spectra of both amorphous (top) and semicrystalline (bottom) NiTTFtt.

Domain Size Estimation

Scherrer fits were used on first two relatively sharp peaks to estimate the crystalline domain sizes.[1] According to the Scherrer equation,

$$D = \frac{\kappa\lambda}{\beta cos\theta}$$

Equation E.1

(D, crystalline domain size; θ, diffraction angle; β, the width of the peak at half of its height; κ, the Scherrer constant, typically considered to be 0.9), and Gaussian simulations shown in Figure E.4, the crystalline domain size is estimated as 2.5 (second peak) - 2.8 (first peak) nm. Since NiTTFtt is not a well-defined nanomaterial, namely that the assumption of a spherical shape in this analysis may be incorrect, the crystalline domain size is likely an upper limit or an overestimation.

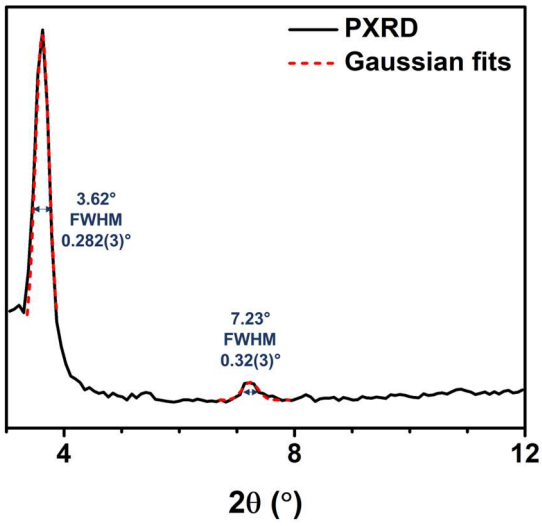

Figure E.4. PXRD spectrum of NiTTFtt and Gaussian fits of the first two peaks. The peak's full width at half-maximum was estimated.

Additionally, both amorphous and semicrystalline NiTTFtt samples were analyzed with a long-collection (24h) absorption measurement on a Rigaku SmartLab X-ray diffractometer equipped with a HyPix3000 detector. Both samples of amorphous and semicrystalline NiTTFtt were loaded into 1.0 mm OD, 0.01 mm wall borosilicate capillaries as fine powders in a N_2-filled glovebox and then sealed with wax. All measurements were carried out with a Cu Ka radiation (1.54186 Å) in a transmission mode. Scans were measured using a parallel beam mode selected through the attached Cross Beam Optics. The tube was energized at 44 mA and 40 kV. The data collections were completed in SmartLab Studio II software package (version 4.4.241.0).

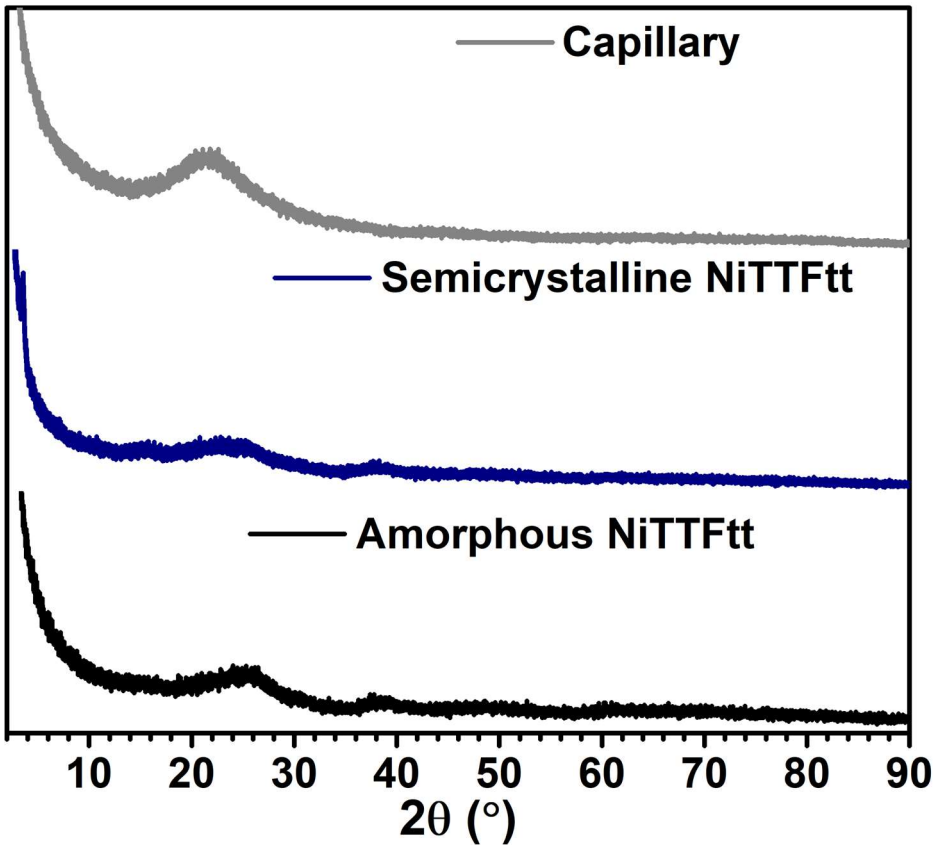

Figure E.5. In-house PXRD spectra of amorphous (bottom) and semicrystalline (middle) NiTTFtt and the capillary background (top).

E.2.2 Synchrotron X-ray Powder Diffraction

Synchrotron X-ray Powder Diffraction was collected at beamline 11-BM at the Advanced Photon Source at Argonne National Laboratory (Lemont, Il, USA). The sample of semicrystalline NiTTFtt was loaded into Cole-Parmer Polyimide tubing provided by the beamline and capped with clay. The powders were rotated during the measurement at ~50 Hz. The powder patterns were measured at 295 K using a wavelength of λ = 0.458126 Å, from 0.5 to 50° 2θ with a step size of 0.001° and a counting time of 0.1 s/step.

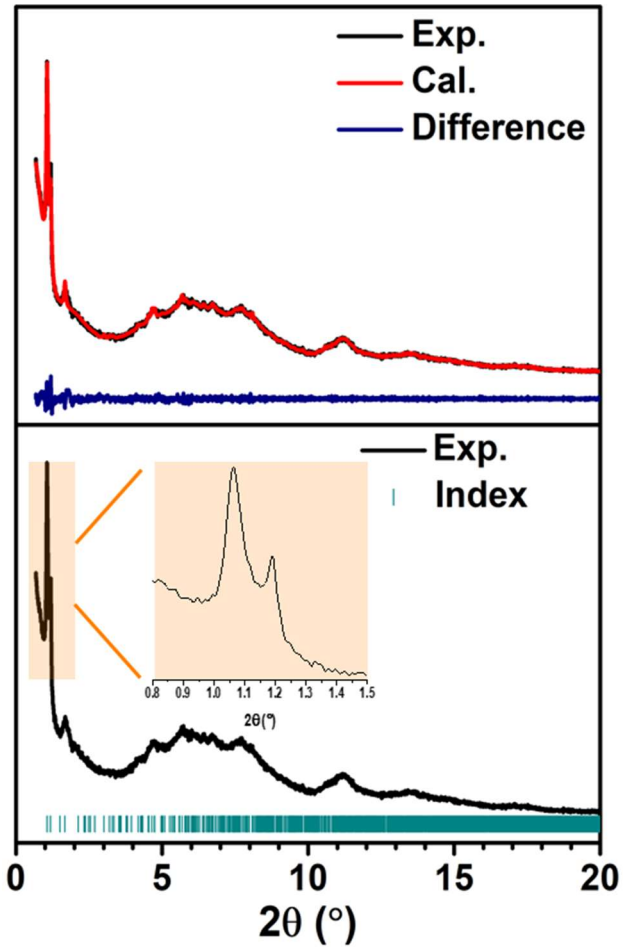

Figure E.6. Diffraction pattern with Le Bail fit (R_{wp}=2.13% and R_p = 1.60%) and residual (top) and indexing (bottom) of the synchrotron PXRD spectrum of semicrystalline NiTTFtt.

E.2.3 X-ray Absorption Spectroscopy

Powder samples of amorphous NiTTFtt were prepared by grinding finely with polypropylene as a binder. A Teflon washer (5.3 mm internal diameter) was sealed on one side with Kapton tape and the ground powder was then transferred to the inside of this ring before compacting with a Teflon rod and sealing the remaining face with Kapton tape. X-ray absorption near-edge spectra (XANES) were employed to probe the local environment around Ni. Data were acquired at the Advanced Photon Source at Argonne National Laboratory with a bending magnet source with ring energy at 7.00 GeV. Ni K-edge (8333 eV) data were acquired at the MRCAT 10-BM beam line in

transmission. The incident, transmitted, and reference X-ray intensities were monitored using gas ionization chambers. A metallic nickel foil standard was used as a reference for energy calibration and was measured simultaneously with experimental samples. X-ray absorption spectra were collected at room temperature.

Data collected was processed using the Demeter software suite[2] by extracting the EXAFS oscillations χ(k) as a function of photoelectron wavenumber k. The theoretical paths were generated using FEFF6[3] and the models were done in the conventional way using the fitting program Artemis.

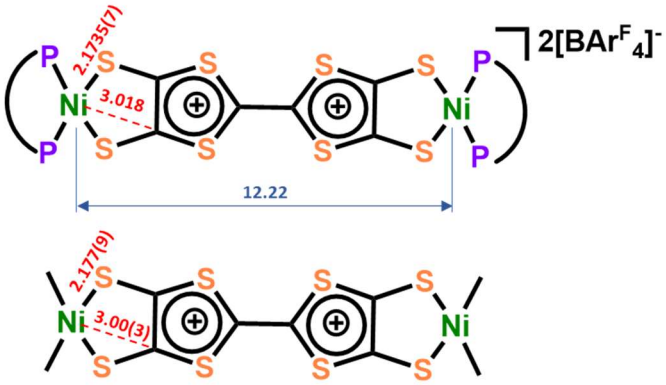

Figure E.7. Comparisons of bond lengths between [Ni(dppe)$_2$TTFtt][BArF$_4$]$_2$ crystal structure and the EXAFS fits of NiTTFtt. (dppe = 1,2-bis(diphenylphosphino)ethane)

Table E.1. EXAFS fit parameters for NiTTFtt.

NiTTFtt	N	R (Å)	σ^2 (Å^2)	R-factor	Reduced chi-square
Ni-S	4	2.177(9)	0.004(1)	0.022	319
Ni-C	4	3.00(3)	0.003(3)		

ΔE_0 = 5(2) eV; S_0^2 = 0.9; Independent Points: 11; Fitting Range: k: 2.0-12.5 Å^{-1}; R: 1.3-3 Å

N, Coordination numbers; R, interatomic distances; σ^2, Debye-Waller factors (the mean-square deviations in interatomic distance). The values in parentheses are the estimated standard deviations; ΔE_0, change in the photoelectron energy; S_0^2, amplitude reduction factor.

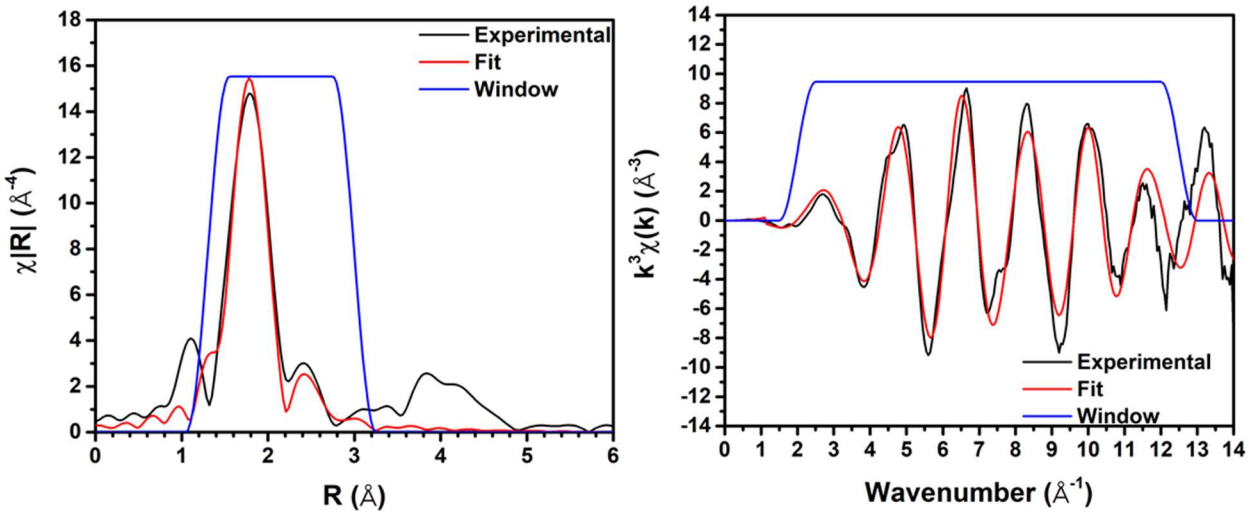

Figure E.8. EXAFS spectra in R-space(left) and k-space (right) of Ni K-edge absorption of amorphous NiTTFtt. The experimental data (black), simulated fit (red), and window (blue) are shown.

E.2.4 X-ray Total Scattering and Pair Distribution Function Analysis

Samples of semicrystalline and amorphous NiTTFtt were loaded into Cole-Parmer Polyimide tubing provided by the beamline and capped with clay. The pair distribution function (PDF), G(*r*), gives the probability of finding a pair of atoms separated by a distance *r*. High-energy X-ray total scattering experiments were performed at 11-ID-B at the Advanced Photon Source, with an X-ray wavelength of 0.2115 Å. The raw 2D data were azimuthally integrated and reduced to 1D intensity *versus* 2θ in GSAS-II[4] using CeO_2 powder for the calibration to determine sample to detector distance. PDFgetX2 program[5] was used to correct and normalize the diffraction data and then Fourier transform the reduced structure factor to obtain the PDF, G(*r*), according to:

$$G(r) = \frac{2}{\pi}\int_{q_{max}}^{q_{min}} dqq(S(q) - 1)\sin(qr)$$

Equation E.2

where q is the magnitude of the scattering momentum transfer and S(q) is the properly corrected and normalized powder diffraction intensity measured from q_{min} and q_{max}.

The length of structural coherence, namely the particle sizes, could be estimated by PDF real space.[6] The smaller the particles, the shorter the real space distance at which the respective atomic PDF decays to zero. For amorphous and semicrystalline NiTTFtt, the decay difference is not obvious; but the semicrystalline one does have more peaks overall. This may suggest that both are amorphous but the semicrystalline one has some small degree of ordering with a crystalline domain size of about 2 nm where G(r) decays to zero.

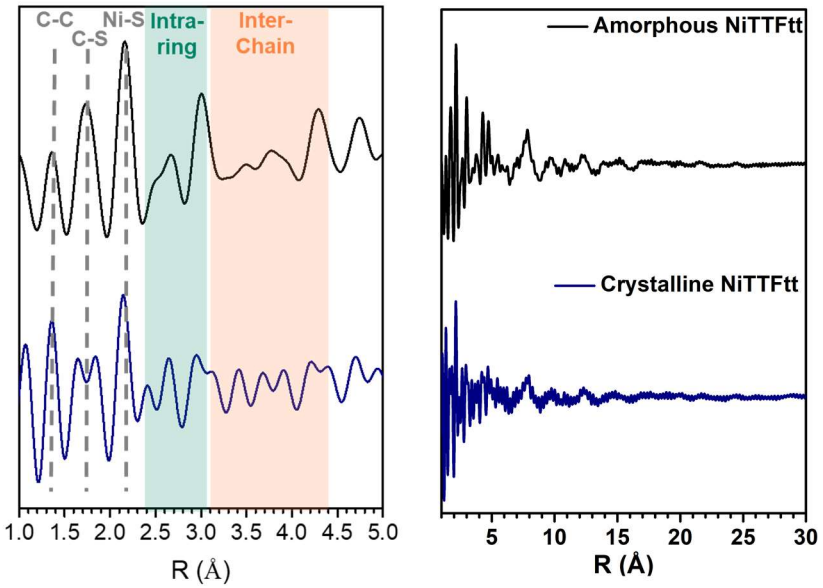

Figure E.9. PDF spectra of semicrystalline (bottom) and amorphous (top) NiTTFtt. The left and right figures present the spectra in the range of 1-5 and 1-30 Å, respectively. The y axis is G(r).

E.2.5 Scanning Electron Microscope

Scanning electron microscope (SEM) images were taken on a Carl Zeiss Merlin using the In-Lens detector in the Materials Research Science and Engineering Center (MRSEC) at the University of Chicago. The accelerating voltage is 5.00 kV.

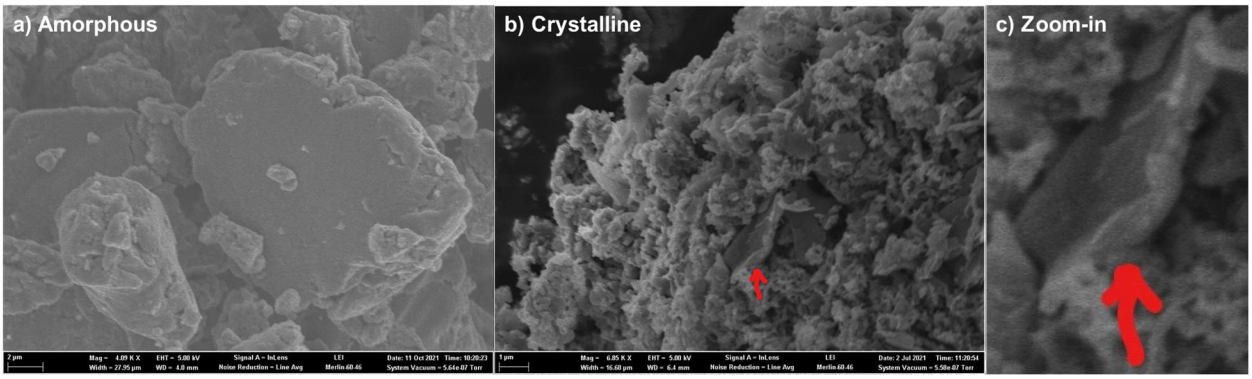

Figure E.10. SEM images of amorphous (a) and semicrystalline (b) NiTTFtt. A 2D-sheet structure of semicrystalline NiTTFtt was shown in a zoom-in figure(c) of b.

E.3 Structural Model

Due to the poor crystallinity of semicrystalline NiTTFtt, we are unable to solve the structure directly based on PXRD data. However, the various X-ray technologies used above and the predominant single-chain structure that should arise allow us to build a reasonable structural model. Herein, we demonstrate the detailed model-building procedure which was constructed in Materials Studio software.[7] In general, it is divided into two primary portions: 1) unit cell determination; 2) the packing of NiTTFtt chains in the unit cell.

1) Unit Cell determination

As shown in **Figure E.6**, the synchrotron PXRD spectrum, which has the first peak splitting, provides a more accurate but less symmetric unit cell, compared to the PXRD spectrum collected on commercial diffractometers (**Figure E.3**). However, both unit cells are generally similar and

have dimensions that are consistent with 2D sheets built from face-to-face NiTTFtt stacks. In the monoclinic unit cell based off of the synchrotron PXRD data, the 2D sheet is made of 8 NiTTFtt monomers stacked (see **Figure E.11**), which is similar to a twisted and rotated π-stacked column (5-6 MTTFtt per unit) found in crystal structures of $[(Ni/Pddppe)_2TTFtt][BAr^F{}_4]$ molecules.[1] Due to the twist of this stack, and the poor crystallinity of these materials, it is hard if not impossible to discriminate between all possible orientations of 8 chains. Therefore, we instead have used the more symmetric unit cell based on the commercial PXRD spectrum to build a structural model. In an orthorhombic unit cell, the 2D π-stacked sheet contains 3 chains indicating a simple AB pattern. In addition, the cell dimension, 24.7 Å in both unit cells, matches well with the length of 2 Ni-TTFtt-Ni monomers (12.4 Å). To further simplify the model, this dimension is reduced by half, namely the length of a Ni-TTFtt-Ni monomer. A likely reason why the unit cell has a two-monomer length is due to some more complicated twisting of the chains. In short, based on the PXRD spectra, a highly-symmetric smallest unit cell that contains two Ni-TTFtt-Ni monomers was selected as a model and a starting point for further calculations.

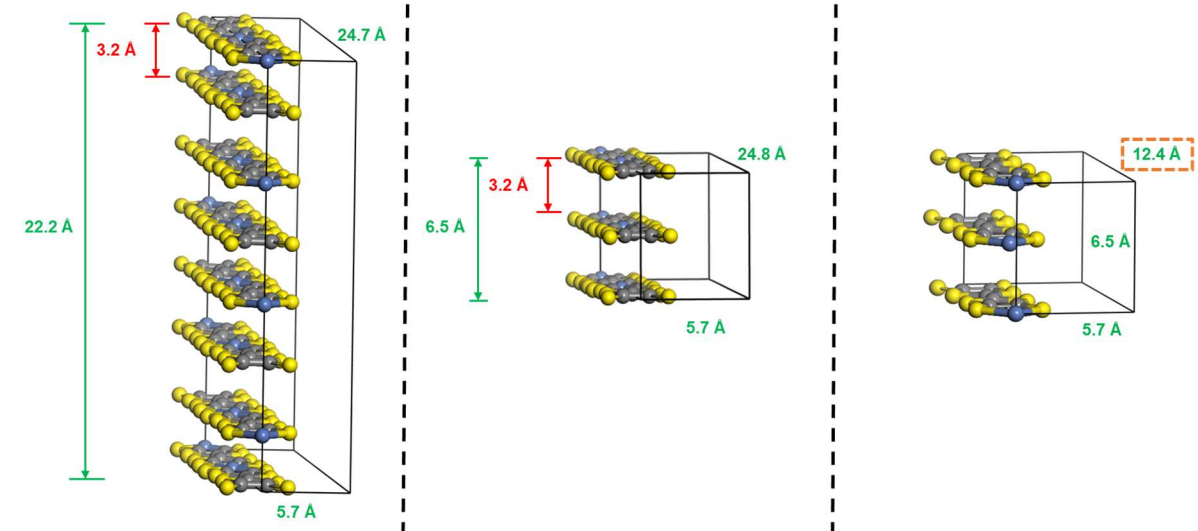

Figure E.11. Unit cells determined based on index of synchrotron PXRD and commercial PXRD and simplified model.

2) Packing of NiTTFtt chains in the unit cell

Although the unit cell dimensions constrain the contents of the unit cell, the orientation and relative positions of the two chains are not dictated. In this section, the modeling of specific atomic positions is described.

First, we simply input two identical chains with an AA stacking pattern into the unit cell. The general S–S distances in the face-to-face π-stacks are the same as the parallel chain's distance, 3.2 Å. Based on all reported S–S distances in TTF-stacks, distances of 3.3-3.8 Å[8, 9, 10] are expected while 3.2 Å is too short. Also, a distance of 3.2 Å should result in an intense feature in the PDF data, which is not observed. Lastly, if AA stacks are preferred, the unit cell should be smaller. These combined observations suggest that the neighboring chains need to be shifted from each other, namely resulting in an AB packing. When the second neighboring chain is shifted along the b direction to the point where the Ni atoms lie below the dithiolene S atoms of the first chain, the S–S distances the π-stacks are generally 3.4 and 3.7 Å. Notably, these peaks are both observed in the PDF data. This shifted geometry also suggests weak axial S-coordination to the Ni centers with a distance of ~2.7 Å. This is still consistent with the D_{4h} symmetry implied from the rising edge of the XAS data.

While the S–S distances in the π-stacks that result from shifting are reasonable, the side-to-side chain distances must also be considered. The initial value from the model, 2.8 Å, is physically unreasonable. Distances as short as 2.7 Å have been observed, but only under elevated pressures of 10 GPa.[8] Therefore, to maintain the overall structure but increase the side-to-side S–S distances, the chains are rotated along chain axis (the b direction). Once the chains are rotated 30°, the S–S distances in side-to-side packings are primarily 3.1, 3.9 and 4.3 Å, all of which match well with

peaks in the PDF data. Indeed, this rotation results in more S–S interactions with side-to-side neighboring chains. The pattern of these interactions is identical to that observed in crystal structures of $Ni(tmdt)_2$ (tmdt = trimethylenetetrathiafulvalenedithiolate), the first single-component metal which is composed of [tmdt-Ni-tmdt] blocks.[11] After these rough operations, the geometry was optimized using Quantum Espresso.[12] Calculations were run using the pbsesol ultrasoft-psuedopotential, an s-point mesh of 6x3x5, a wavefunction cutoff of 560 eV, and an SCF convergence threshold of 2e-9 eV. This optimization results in only minor changes to the structure, supporting the feasibility of this model.

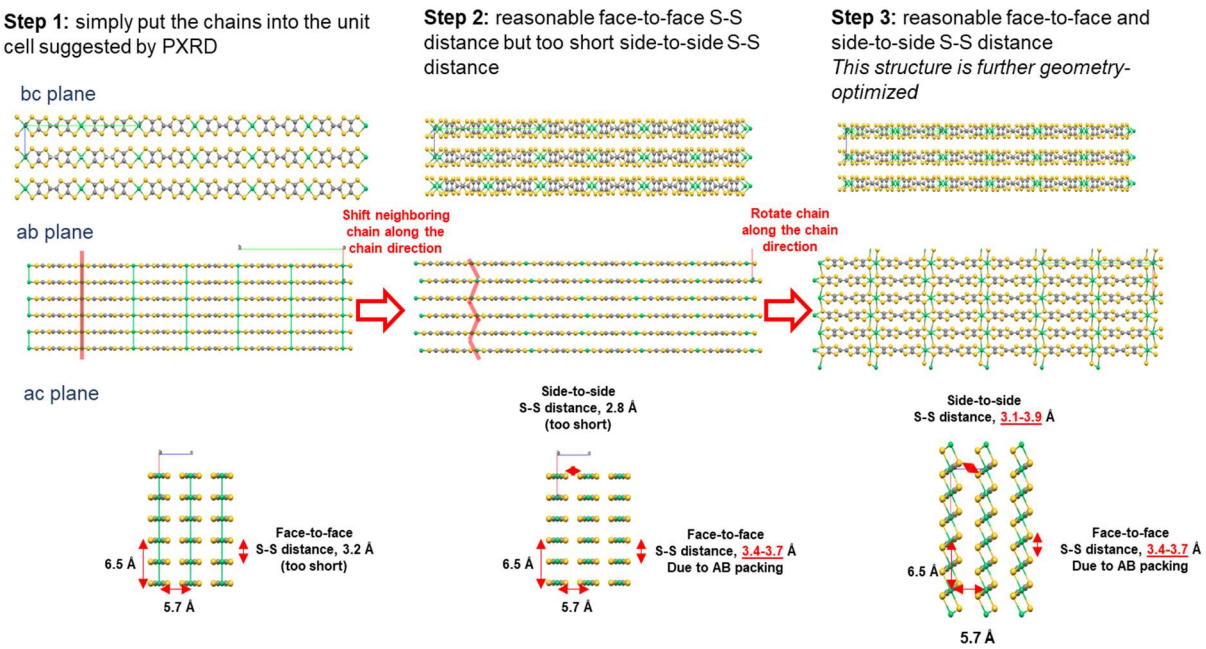

Figure E.12. Proposed NiTTFtt chains stackings which meets the S-S distances in general TTF stacks and PDF data.

In sum, the proposed structural model was built from both experimental data and literature precedent. The resulting structure is tightly-packed, which is consistent with previous literature hypotheses on this class of materials.[13] During the model building process, we have considered the effects of the twist, rotation, and shift of neighboring chains. In the actual materials, both semicrystalline and amorphous, the structure will be much more complicated. Therefore, in

theoretical calculations, the proposed structure is used for band structure calculations as a highest symmetric unit and then distortions in the positions of neighboring units are taken into account to see the effects on the orbital overlap and energy.

E.4 Composition and Vibrational Characterizations

E.4.1 X-Ray and Ultraviolet Photoelectron Spectroscopy

X-ray photoelectron spectra (XPS) were collected with the AXIS Nova spectrometer (Kratos Analytical) equipped with a monochromatic Al Kα X-ray source. The Al anode was powered at 10 mA and 15 kV. The instrument work function was calibrated to give a Au $4f_{7/2}$ metallic gold binding energy of 83.95 eV. The instrument base pressure was ca. 1×10^{-10} Torr. The analysis area size was 0.3×0.7 mm^2. For calibration purposes, the binding energies were referenced to the C 1s peak at 284.8 eV. Survey spectra were collected with a step size of 1 and 160 eV pass energy. Ultraviolet photoelectron spectra (UPS) were collected with the AXIS Nova spectrometer using UV-radiation source. The high-resolution spectra were collected with a pass energy of 40 and a 0.1 eV step size. 7 mm cold pressed pellets were affixed to conductive carbon tape under N_2 before loading into the spectrometer.

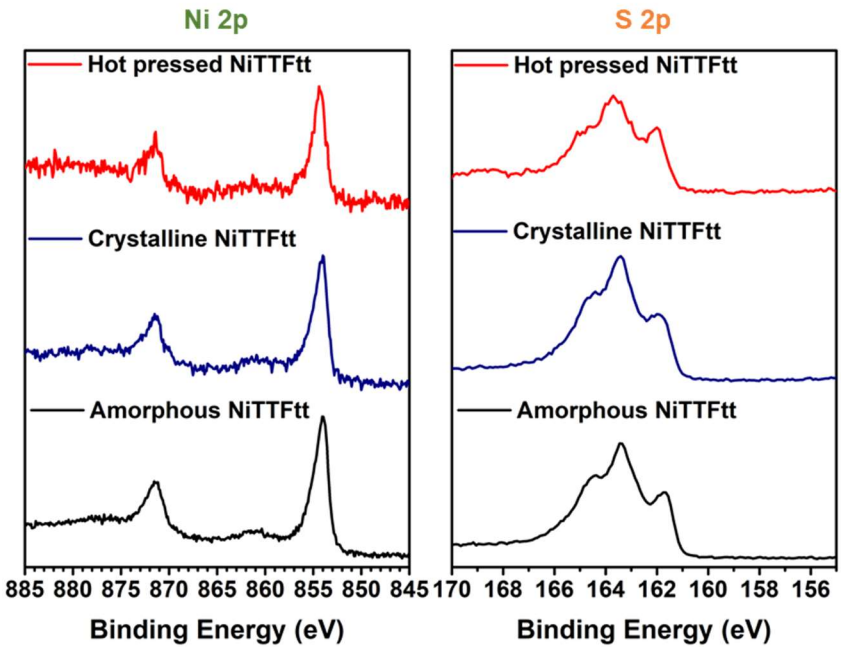

Figure E.13. High-resolution XPS spectra for amorphous (black), semicrystalline (blue), and hot-pressed (red) NiTTFtt.

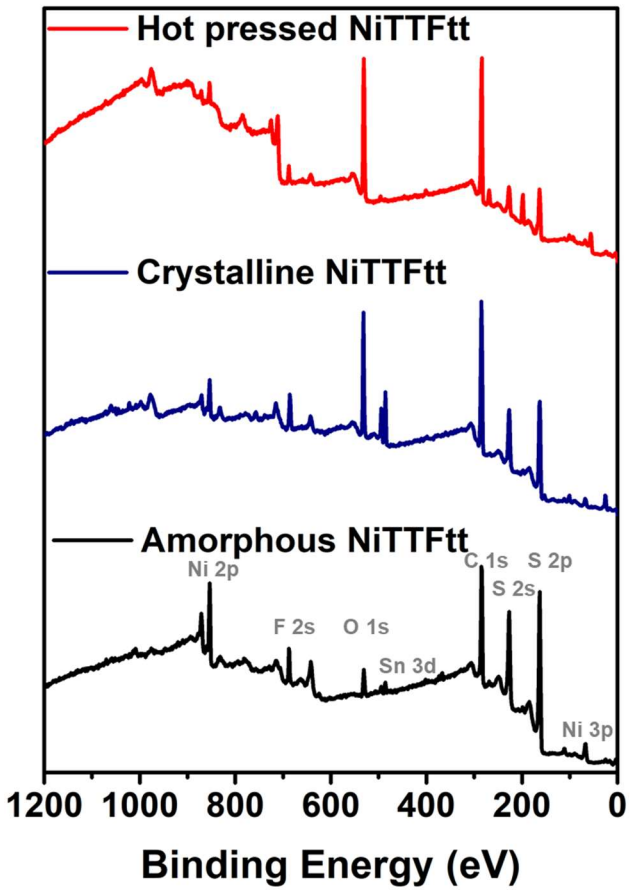

Figure E.14. XPS Survey spectra for amorphous (black), semicrystalline (blue), and hot-pressed (red) NiTTFtt.

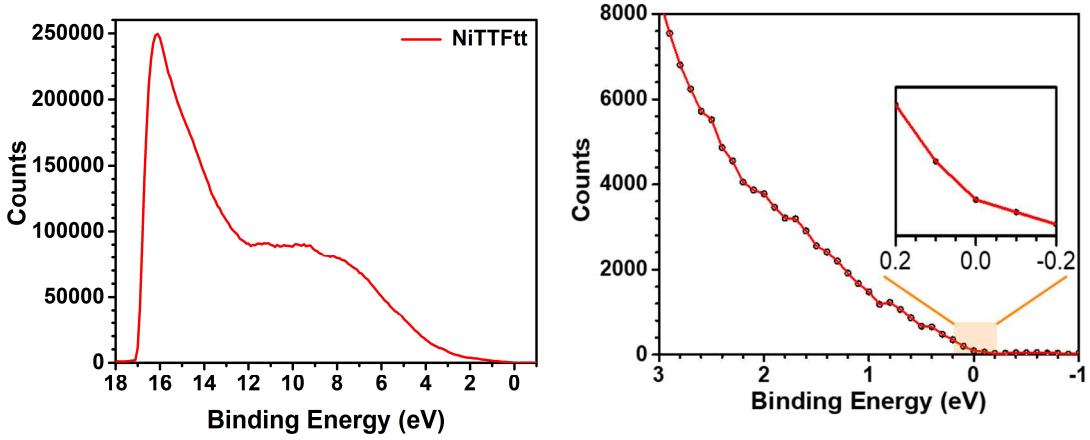

Figure E.15. UPS spectrum of amorphous NiTTFtt. The left and right figures present the spectra in the range of -1 - 18 and -1 - 3 eV, respectively.

E.4.2 Inductively Coupled Plasma- Mass Spectrometry/Optical Emission Spectrometry

Inductively coupled plasma mass spectrometry (ICP-MS) data was obtained with an Agilent 7700x ICP-MS and analyzed using ICP-MS Mass Hunter version B01.03. The samples were diluted in 2% HNO_3 matrix and analyzed with a ^{159}Tb internal standard against a 12-point standard curve over the range from 0.1 to 500 ppb. The correlation was >0.9997 for all analyses of interest. Data collection was performed in Spectrum Mode with five replicates per sample and 100 sweeps per replicate. Solutions for ICP-MS were prepared by digesting 2 mg of material in 1 mL HNO_3 (trace metal grade) solution in a fume hood overnight at room temperature. The solution was diluted with ultrafiltered deionized water for ICP-MS analysis.

An Agilent 700 series spectrometer was used for inductively coupled plasma optical emission spectroscopy (ICP-OES). The sample preparation was referred to the reported procedure[14] to improve the accuracy of Sulfur determination. Solutions for ICP-OES were prepared by digesting 2 mg of materials in 0.5 mL HNO_3 and 0.5 mL H_2O_2 (trace metal grade) solutions in tight-sealed

high-density polyethylene (HDPE) centrifuge tubes overnight and then diluted with ultrafiltered deionized water.

E.4.3 X-ray Fluorescence Measurements

X-ray fluorescence (XRF) measurements were performed on pressed pellets with a Rigaku NEX DE VS spectrometer under a He atmosphere.

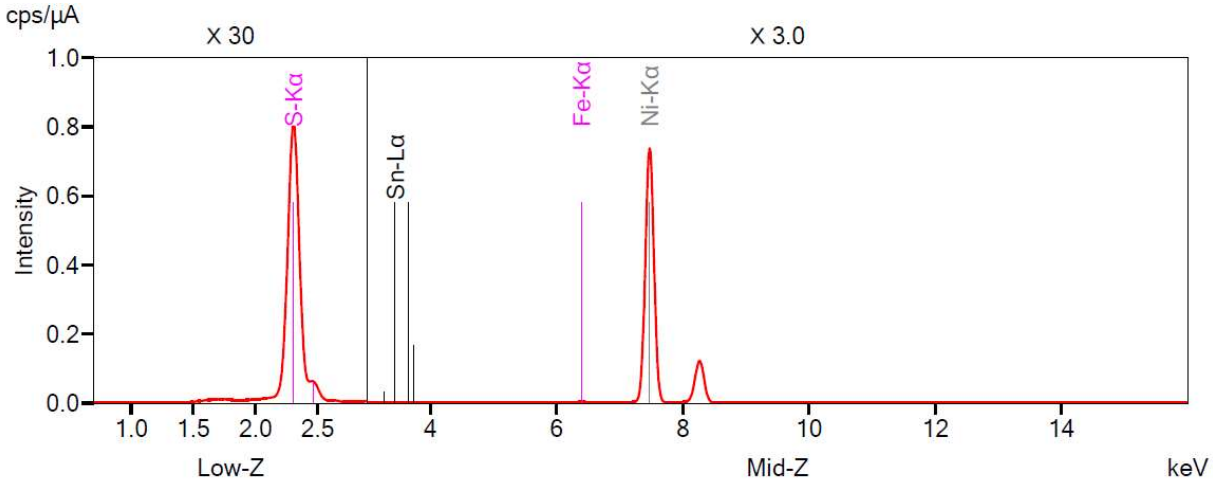

Figure E.16. A typical XRD spectrum of NiTTFtt.

Table E.2. Ni/S ratios summary based on various technologies

	Amorphous NiTTFtt	**Semicrystalline NiTTFtt**
Proposed formula	NiC_6S_8	NiC_6S_8
S/Ni (ICP-OES)	8.2	8.4
S/Ni (XPS)	7.7	7.9
S/Ni (XRF)	7.5	9.4
Sn/Ni (ICP-MS)	0.03	0.08

E.4.4 Elemental Analyses

Combustion elemental analyses (C, H, N) were performed by Midwest Microlabs.

Table E.3. Elemental analyses of different batches of NiTTFtt.

	C	H	N
Batch 1	22.05	0.98	0
Batch 2	21.94	1.20	0
Batch 3	22.30	1.31	0.02
Batch 4	22.20	0.22	0
Average	22.12	0.93	0
$Ni_{0.96}TTFtt(SnBu_2)_{0.04}[BAr^F]_{0.04}$	21.29	0.28	0
$C_{7.6}H_{1.2}B_{0.04}F_{0.96}Ni_{0.96}S_8Sn_{0.04}$			

E.4.5 Electron Paramagnetic Resonance

Electron paramagnetic resonance (EPR) spectra were recorded on a Bruker Elexsys E500 spectrometer with an Oxford ESR 900 X-band cryostat and a Bruker Cold-Edge Stinger. NiTTFtt was mixed and ground with dry KBr powder into a uniform mixture (concentration is ~0.5 mg/1g KBr). This "solid matrix" was loaded into the EPR tube to fill about 0.1 mL volume.

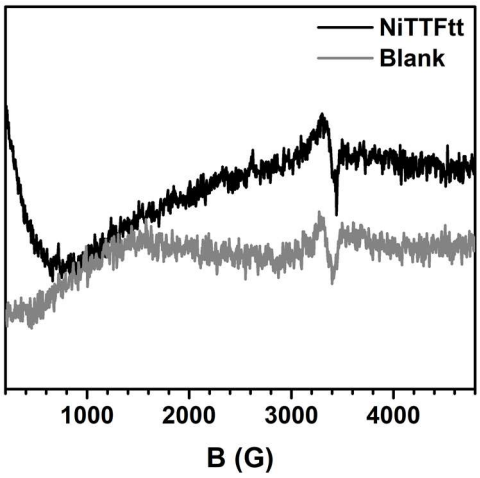

Figure E.17. EPR spectrum of NiTTFtt in KBr (black) and cavity blank (gray) at 10 K.
(MW Freq = 9.632GHz, MW power = 20dB)

E.4.6 Infrared Spectroscopy

Infrared spectra were recorded on a Bruker Tensor II FTIR spectrometer with MCT detector operated at 77 K. Data were processed and background corrected with OPUS software (version 7.5). An additional manual correction for scattering was also applied. Samples were prepared under N_2 by grinding solid sample with dry KBr powder, pressed as pellets, and measured in air under ambient conditions.

A NIR absorption was observed by IR spectroscopy, but the expected C–C and C–S vibrations around 1200-600 cm^{-1} are not obvious in the transmission IR spectra for both semicrystalline and amorphous samples. Such weak IR absorption have been previously noted in metallic conducting polymers[15] and this phenomenon implies a highly delocalized system and metallic character since infrared-active vibration (IRAV) modes are characteristic of more localized states and weaker IR features indicates greater delocalization.

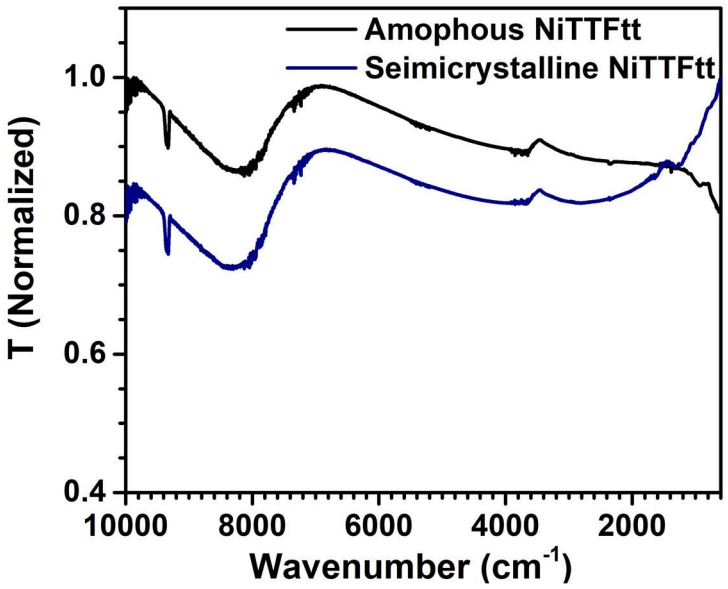

Figure E.18. Transmission IR spectrum of amorphous (black) and semicrystalline (blue) NiTTFtt KBr pellets.

E.4.7 Raman Spectroscopy

Raman spectra were obtained with a Horiba LabRamHR Evolution confocal microscope. A Si (111) wafer was used for calibration. The sample of a 7 mm round pressed pellet of NiTTFtt powder was excited using a 532 nm light source operating at 5 % of its power and using 100x long path objective and a 600 mm^{-1} grating. The expected C–C, C–S and Ni–S vibrations that were not shown in IR spectra are clearly observed in the Raman spectrum and they are consistent with previous literature examples.[16, 17]

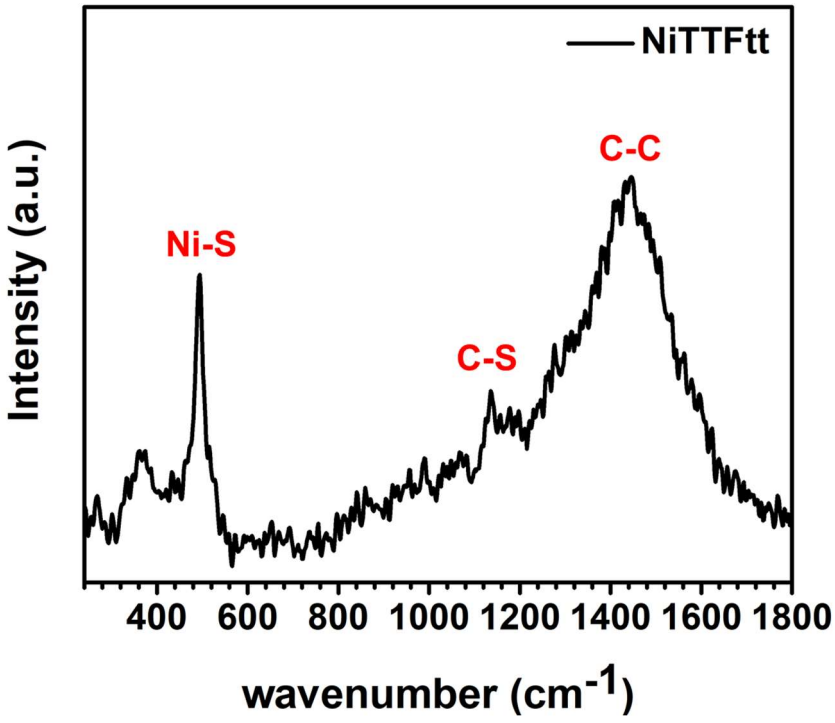

Figure E.19. Raman spectrum of NiTTFtt.

E.5 Physical Characterization

E.5.1 Room-Temperature Electrical Conductivity and Seebeck Measurements (in Ar-glovebox)

The measurements are based on a previously reported setup.[18] Gold electrical contacts (75 nm thick) for electronic conductivity (σ) and Seebeck coefficient (α) measurements were deposited

onto 8 mm pressed pellets via thermal evaporation through homemade shadow masks. The electric conductivity was measured in the in-plane direction by using a four-probe geometry with a 0.2 mm spacing between electrodes and electrodes length of 1 mm. The Seebeck coefficient was measured with two 1 mm^2 gold pads, which are each 3 mm apart. A detailed schematic is shown in a previous report.[18] Four probe conductivity measurements were performed using a custom-designed probe station in an argon-filled glovebox. Voltage and current measurements were performed using a Keithley 2400 source meter and a Keithley 6221 precision current source. A constant current was applied to the outer contacts, and the resultant steady state voltage response was recorded from the two inner contacts. The resistance (R, ohm) of the sample was extracted from the slope of the IV sweep by using Ohm's law (R = V/I). The conductivity σ was then calculated via the following equation:

$$\sigma = \frac{I}{V} \frac{\left(\frac{\sinh\left(\frac{t}{s}\right)}{\sinh\left(\frac{t}{2s}\right)}\right)}{\pi t}$$

Equation E.3

Where t is the thickness of the sample and s is the separation distance between neighboring probes.

This formula has been previously applied for a thick Si wafer, [19] which is similar to the round pressed pellet. The Seebeck coefficient measurements were performed on the same probe station. Two Peltier elements were placed 5 mm apart to provide the temperature difference ($\Delta T = T_H - T_C$). Two thermocouples were used to collect the hot and cold side temperatures, and two probes were used to measure the corresponding voltage value. A minimal amount of thermally conductive silicone paste was applied to the tips of the thermocouple to ensure good thermal contact between

the thermocouple and the gold pads. A delay of 200 s was used for voltage measurements to ensure that a steady-state temperature gradient and voltage were reached. The Seebeck coefficient was calculated from the slope of a linear fit for the ΔV vs ΔT plot. A representative plot can be found in Figure E.21. The measurements were taken within an approximate ΔT of ±3 K around 300 K so that the Seebeck coefficient did not change significantly over T ± ΔT. A series of measurements on Ni foil (0.03 mm, >99.9%) were performed at 25 °C to determine the systematic error. The measured Seebeck coefficient of Ni is −20.3 ± 1.3 μV/K, which matched well with reported values in the literature (−19 μV/K at 25 °C). [20, 21]

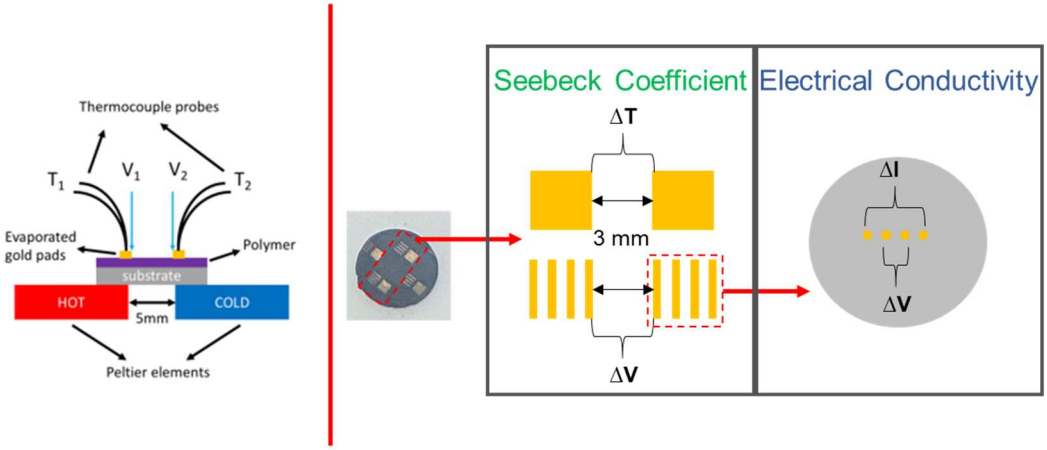

Figure E.20. The schematic for the homemade setup for Seebeck measurements (left) and a demonstration of the gold-deposited 8 mm pressed pellets for the measurements of Seebeck coefficient and electrical conductivity.

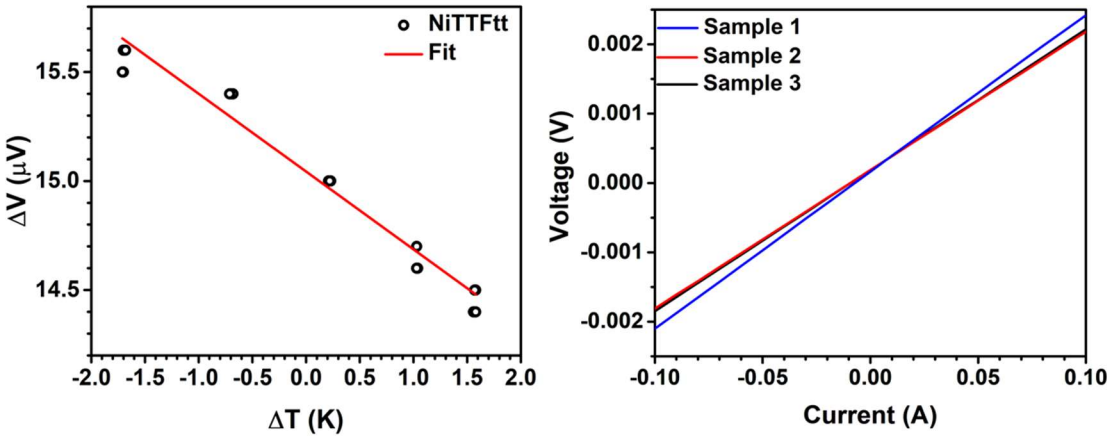

Figure E.21. ΔV-ΔT plot and fit for the Seebeck coefficient (left) and V-I curves of different pellets for electrical conductivity (right). The resistivity measurements (right) are performed on the cold pressed pellet and the average conductivity of cold pressed pellets is 475 S/cm.

E.5.2 Thermal Conductivity Measurement by Using Raman Thermometry

The thermal conductivities of the samples were determined through single-laser Raman thermometry using the same Confocal Raman Microscope discussed above based on a reported method.[17] In Raman thermometry, a focused laser beam is used as a heat source, while the temperature-dependent Raman spectra are used as a thermometer. In the first step, the shift in the spectral positions of the Raman peaks is recorded as a function of the absorbed laser power. In this work, the spectral positions of the Raman peaks around 495 cm^{-1} were measured as a function of the incident absorbed laser power (λ = 532 nm). The laser power was varied by using 0.1, 1, 2.5, and 5% of the max power of the 532 nm light source. The individual powers were examined with a Si power detector. The operational setup also includes a 100x long path objective and an 1800 mm^{-1} grating.

Typically, as the laser power increases, the Raman vibrations exhibit a red-shift which originates from the local temperature increase. In a second step, the shift in the spectral position of the Raman peaks is recorded as a function of temperature, which is controlled externally by a Linkam cryostat in air. This second step constitutes the calibration of our "thermometer" since it allows us to convert the shift in the spectral positions of the Raman peaks into a local temperature rise.

The temperature rise in the laser spot region for the case of a semi-infinite medium can be written as:

$$\Delta T = \frac{P_{abs}}{\pi R \kappa}$$

Equation E.4

where P_{abs} is the laser power absorbed by the sample, R is the Gaussian spot radius, and κ is the thermal conductivity of the specimen. R is calculated by using and the ToptiCalc™ program and based on the technical information of the laser source and the lens.

In short, the thermal conductivity is obtained measuring the temperature rise within the laser spot as a function of the laser power absorbed by the sample.

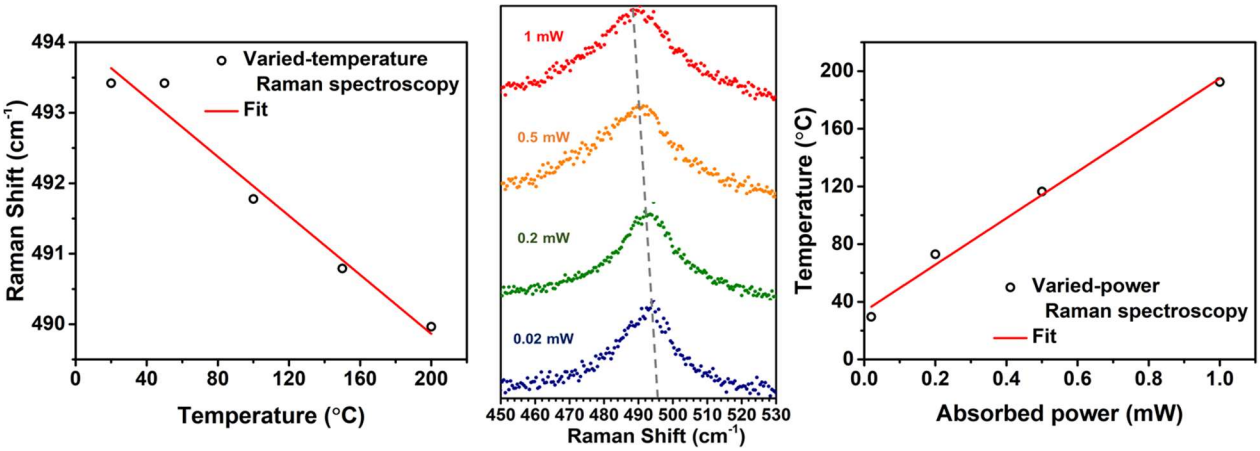

Figure E.22. The Raman shift-temperature plot and fit (left), Raman shift under varied laser power(middle), and the plot and fit of absorbed power and temperature (right).

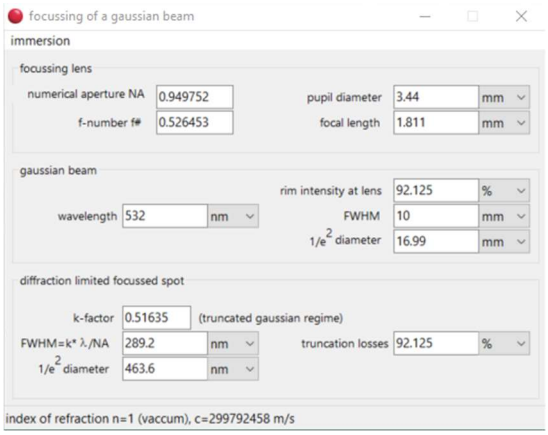

Figure E.23. The demonstration of the calculation of the Gaussian spot size in the ToptiCalc™ program. All technical information of lens and the laser source are included.

E.5.3 Variable-Temperature Electrical Resistance

A strip of double-sided polyimide tape was placed on a DC Resistivity/ETO Sample Puck (P102 from Quantum Design), which serves as an electrical insulator, and then pressed pellets with 75 nm thick deposited gold contacts were put on the top of the tape. Then 0.015 inch-OD indium wires were used to bond to the samples' gold nodes as shown in **Figure E.24**. The puck was then loaded into a physical property measurement system (PPMS, Quantum Design) under a He-filled inert atmosphere. The 4-point probe resistivity measurements on a 13 mm hot pressed pellet and 2-point probe resistivity measurements on 8 mm cold pressed pellets were carried out in an AC mode with a DC excitation of 1 mA. The temperature dependent resistivity/resistance measurements were performed from 300 K to 2 K. Since four-probe measurements were carried out on the hot pressed pellet, its conductivity at every temperature was calculated based on the previous formula.

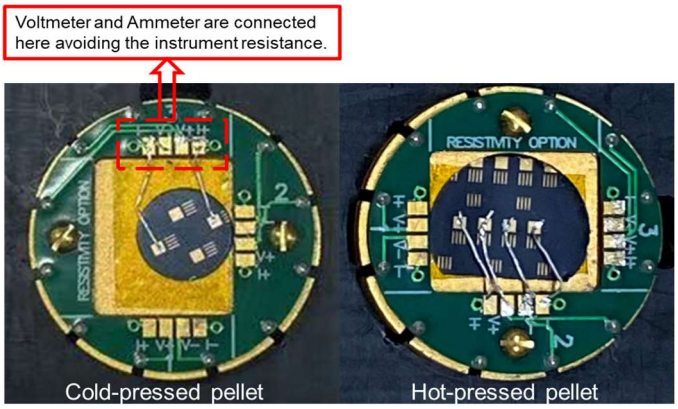

Figure E.24. demonstrations of the cold-pressed pellet (left) and the hot-pressed pellet (right) for PPMS.

For the variable-temperature (VT) conductance data, multiple models were applied. First, the activated energy (E_a) was estimated by Arrhenius plots, lnG-1/T. Unlike semiconductors, NiTTFtt has non-linear relationship overall the whole temperature zone and therefore, the max and min

values of E_a were calculated by fitting the high and low temperature regions. Even the max Ea, is only 2.1 meV, which is likely contributed by the grain boundaries.

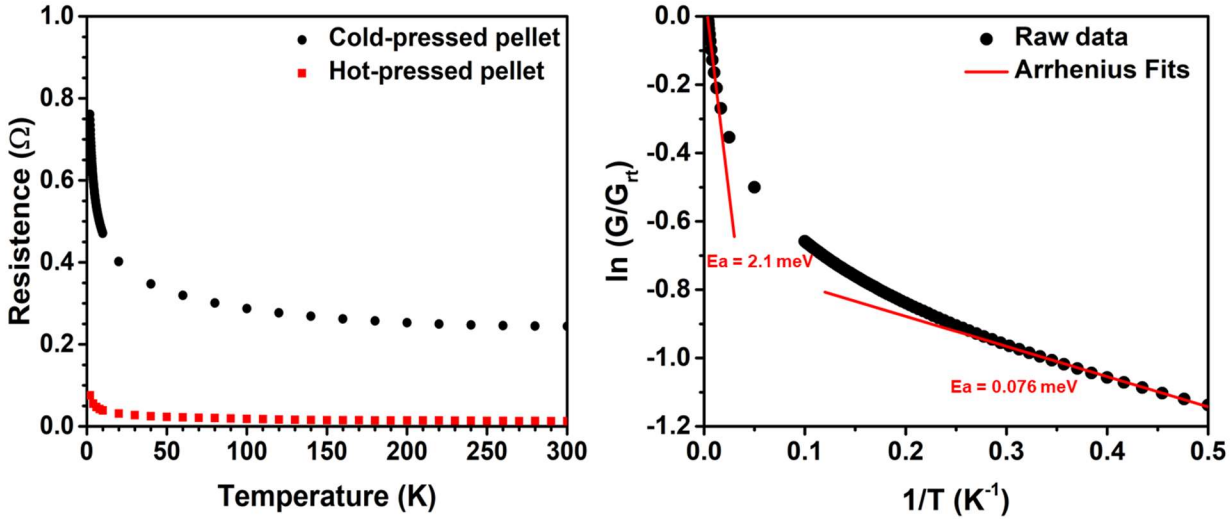

Figure E.25. Temperature-dependent resistance of both cold-pressed (black) and hot-pressed (red) pellets (left) and Arrhenius plot and fits of the cold-pressed pellet (right).

Since NiTTFtt is completely amorphous, to further explore the conduction mechanism, Variable-Range Hoping models were examined, the conductivity of which, σ_{VRH}, is described by

$$\sigma_{VRH} = \sigma_0 \, exp - (\frac{T_0}{T})^x$$

Equation E.5

where σ_0 is a conductivity prefactor and T_0 is a characteristic temperature with an exponent x. In our case, we applied the 3D hoping model (x=1/4) and the Efros-Shklovskii model (x=1/2, dimensionless but related to electron-electron interactions) to both the whole temperature range and specifically the low temperature region (below 15 K, both cold and hot pressed pellets).

Reasonable linear fits for $\ln(G/G_{rt})$-$T^{-1/4}$ provide T_0 = 13 and 92 K for cold and hot pressed pellets respectively. In Mott's model, T_0 is related to D(EF) by a relation of form

$$T_0 = \frac{a}{k_B D(E_F)\gamma^{-3}}$$

Equation E.6

where a is a constant; $1/\gamma$ is the decay length; $D(E_F)$ is the density of states(DOS) at Fermi level. T_0 below 10^4 K indicates a high DOS at the Fermi level and T_0's range from 1 to 10^4 K is usually found in granular metals and cermets rather than semiconductors.[22]

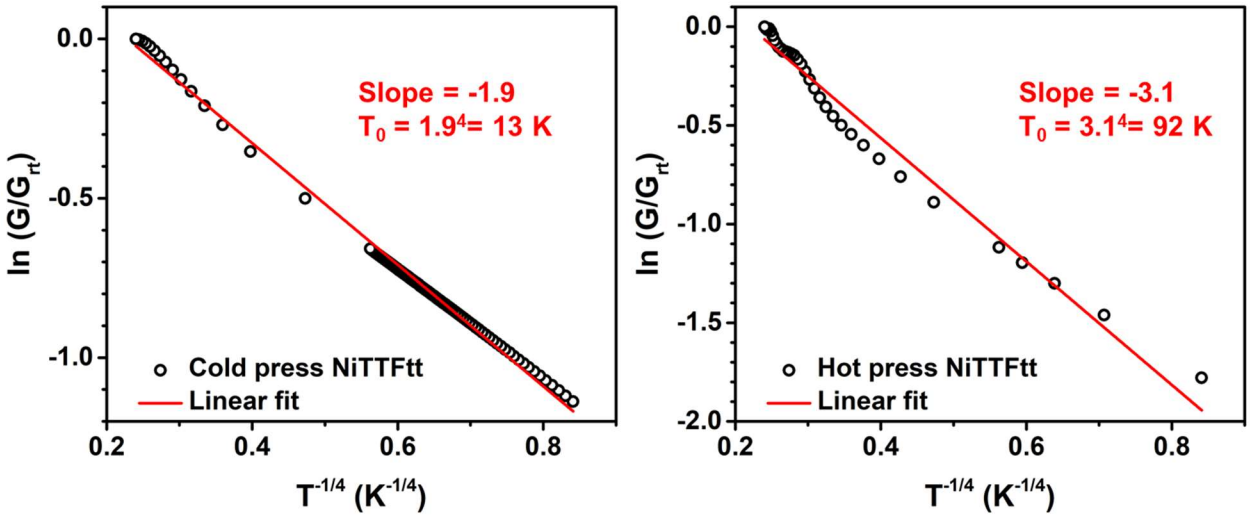

Figure E.26. 3D VRH application and fits on VT-conductance data of both cold (left) and hot (right) pressed pellets.

Furthermore, good linear fits for $\ln(G/G_{rt})$-$T^{-1/2}$ at low temperature suggests the system is a coulomb glass[23] and the electron-electron interactions dominate the transport at low temperature (the energy barrier is the coulomb gap), which is consistent with the $T^{-1/2}$ character observed.

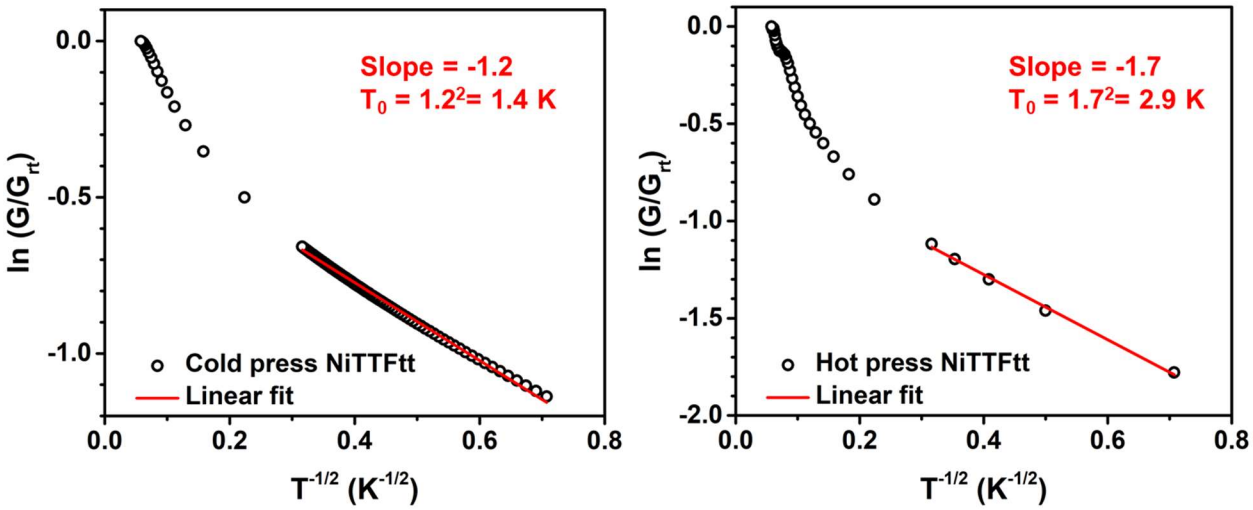

Figure E.27. Efros-Shklovskii model and fits on VT-conductance data of both cold (left) and hot (right) pressed pellets.

Overall, all analysis supports the conduction mechanism of NiTTFtt is more in an agreement with glassy metals rather than semiconductors. We note that the specific mechanism could be the electron cotunneling transport observed in gold nanocrystal arrays.[24]

E.5.4 Variable-Temperature Seebeck Coefficient Measurements

Variable-Temperature Seebeck Coefficients were measured with MMR Technologies Inc. K-20 Programmable Temperature Controller and P-100 Programmable Seebeck Controller. A 1 mm × 4 mm piece of a pressed pellet was gently put between electrodes of the sample chip (C3306 sample mounting stage). Ag epoxy (Epoxy Technology H20E) was used for the connection between the sample and the electrodes. The sample chip was heated in a muffle furnace at 175 °C for 0.5 h for a complete curing, before loading the chip into the sample device (MMR Technologies. Inc. Model 2900). The whole preparation was finished in air. Temperature-dependent Seebeck measurements were performed from 300 to 400 K and Seebeck measurements at each temperature repeated three times.

E.5.5 Magnetic Measurements

Solid-state magnetic measurements were performed on a Quantum Design MPMS3 SQUID magnetometer. The bulk powder of the sample (36.0 mg) was suspended in an eicosane matrix in a polycarbonate capsule to prevent movement and protect the sample from incidental air exposure. Diamagnetic corrections for the capsule and eicosane were made by measuring temperature vs moment in triplicate for each to determine a moment per gram correction. Diamagnetic corrections for the sample itself were applied using Pascal's constants of each atom based on the formula of NiC_6S_8.

E.5.6 Hall Effect Measurement

The setup for the Hall effect measurement mimicked the Hall device for aluminum foils reported for an education experiment.[25] A 6×6 mm squared pressed pellet (264 μm) and a double-sided polyimide tape was put on DC Resistivity/ETO Sample Puck (P102). By using fast-drying Ag paint (Ted Pella 16040-30) and In wires, the device was set up as shown in **Figure E.28**. The Hall effect experiments were carried out on a Quantum Design PPMS at room temperature (300 K). The max current, 5 mA was used during the test. While the magnetic field was scanned between 0-7 T, R_{xy} (V_{hall}/I) the Hall coefficient ($R_H=dR_{xy}/dH$) was calculated based on the linear fit. The charge density (n) is extracted using the following relation

$$n = \frac{1}{R_H de}$$

Equation E.7

(e, electron charge; d, the thickness of the pellet)

Although the measured R_{xy} is close to the instrument limit (0.00001Ω) and the data is quite noisy due to the large carrier concentration and the thickness, an expected negative trend in the R_{xy}-H

plot was observed and the extracted slope supports the carrier concentration at about 5×10^{21} cm^{-3} level, consistent with other measurements.

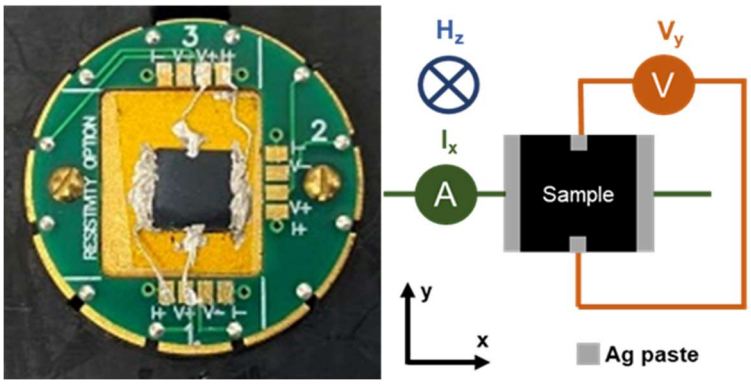

Figure E.28. The setup for Hall effect measurements (left) and the demonstration of the measurement (right).

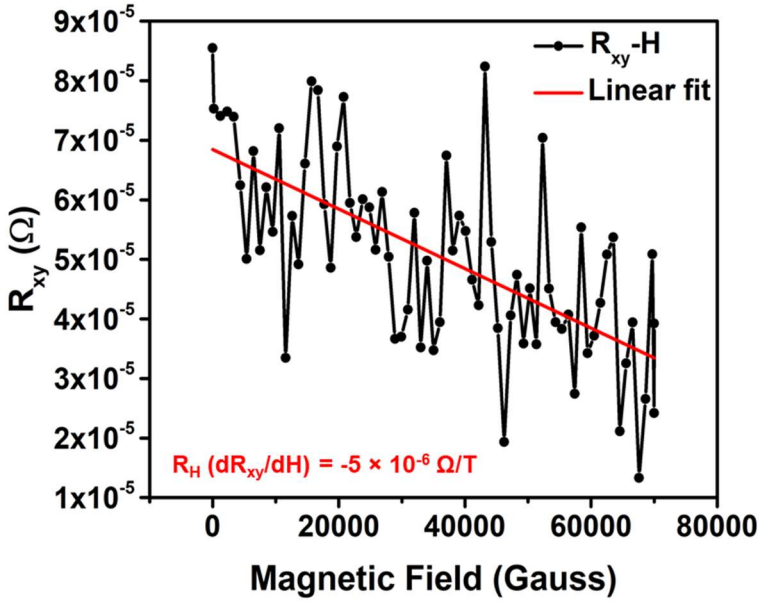

Figure E.29. R_{xy}-H plot and linear fit for Hall coefficient (H_R).

E.5.7 UV-Vis-NIR Diffuse Reflectance Spectrum

UV-Vis-NIR diffuse reflectance spectra were collected on a Varian Cary 5000 spectrophotometer with powder samples loaded in a Praying Mantis air-free diffuse reflectance cell with KCl powder as the non-adsorbing matrix. The Kubelka-Munk conversion of the raw diffuse reflectance spectrum was obtained by applying the formula $F(R) = (1-R)^2/2R$.

E.5.8 UV-Vis-NIR Specular Reflectance Spectra

UV-Vis-NIR specular reflectance spectra (200-2000 nm) were collected on Shimadzu UV-3600 Plus UV-VIS-NIR spectrophotometer with a 5-degree relative specular reflectance accessory. IR specular reflectance spectra (570-8000 cm^{-1}) were collected with 64 scans at a spectral resolution of 4 cm^{-1} on an IR microscope (Hyperion 2000, Bruker Optics Inc., USA) coupled to a Fourier transform infrared (FTIR) spectrometer (Vertex 70, Bruker Optics Inc., USA) with a mid-IR glowbar source. Since the rough surface of the pressed pellet causes non-specular reflectance light loss compared to mirror standards, the experiments were conducted following a reported method[26] based on pressed pellets with a metal-coating. First, a 12 mm pressed pellet of NiTTFtt was coated with 100 nm thick aluminum covering a half of one face and on the other face, 100 nm thick gold was applied in the same way. Second, for UV-NIR reflectance spectra, we measured the relative reflectance of both the sample surface and aluminum-coated surface, separately with respect to the aluminum mirror. Finally, the absolute reflectance spectrum of NiTTFtt was obtained by dividing the sample's reflectance with that of the aluminum-coated surface. This treatment allowed us to exclude the effect of surface roughness due to the similar roughness of the sample surface and the metal-coated surface. For the IR spectrum, the method is similar but instead of aluminum, gold was used as the reference. For both UV-NIR and IR spectra, a large area of the sample surface is targeted, which provides an average response and further helps to minimize the effect of surface roughness.

For the specular reflectance spectrum, the Hagen-Rubens (H-R) approximation for the far IR region was fit based on $R(\omega) \sim 1-\sqrt{\omega}$ relation. A Kramers-Kronig analysis was then performed following a literature procedure.[27, 28] A numerical calculation was used for the reflectance data (570-50000 cm^{-1}).[29] For the extrapolation to zero, the H-R approximation was used for the region

below 570 cm^{-1} to 0 cm^{-1}. To extrapolate the reflectance from 50000 cm^{-1} to infinity, a constant value (~0.06) was used for the 50000-100000 cm^{-1} region, the equation $R(\omega) \propto 0.06\ \omega^{-1.5}$ was used to extrapolate the reflectance from 50000 to 10^6 cm^{-1}, and for the reflectance above 10^6 cm^{-1} (i.e., the free electron region), the equation $R(\omega) \propto \omega^{-3}$ was used.[30]

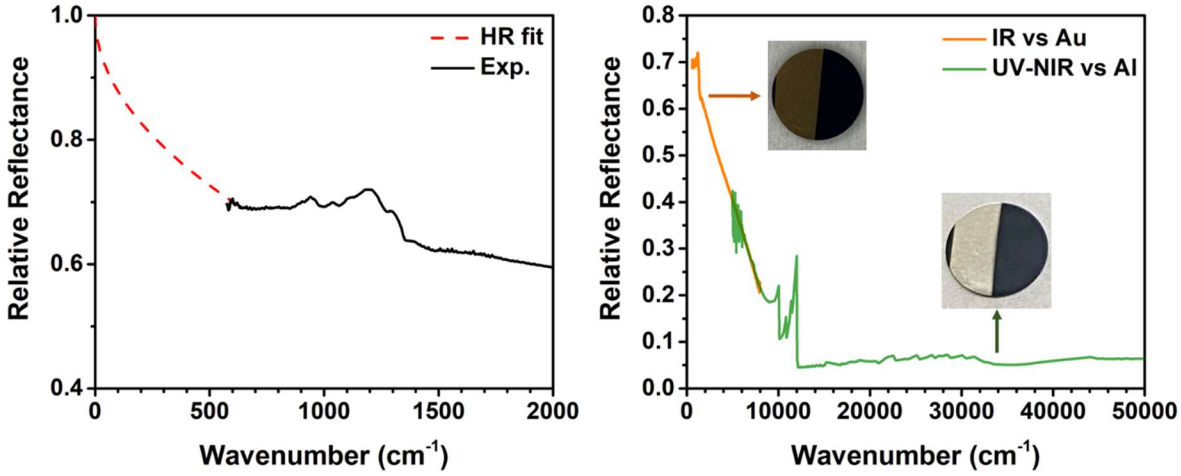

Figure E.30. Specular reflectance spectrum and H-R fit (left) and the specular reflectance collected with two different instruments and references (right).

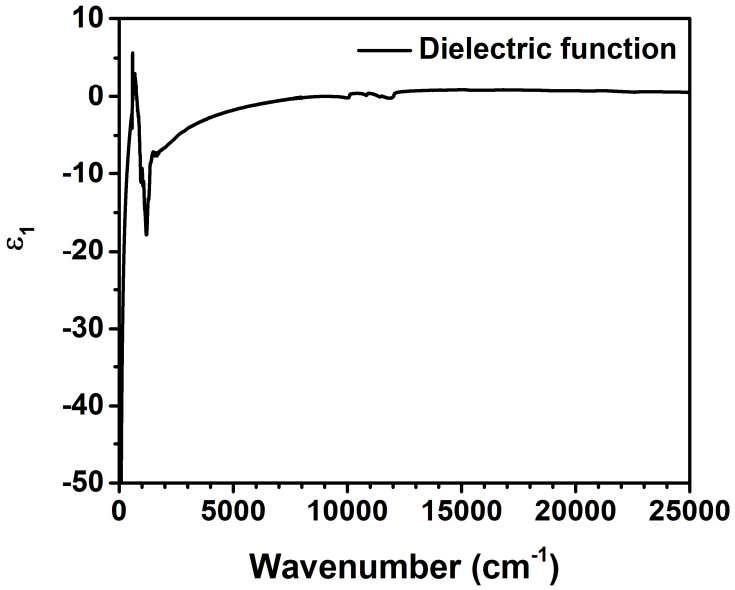

Figure E.31. The real part of the dielectric function, $\varepsilon_1(\omega)$.

E.6 Stability Tests

E.6.1 Thermogravimetric Analysis

Thermogravimetric analysis (TGA) was performed using a TA Instruments Discovery analyzer. Approximately 2 mg of sample was loaded into a pre-tared Pt pan and measured under N_2 or air. Samples were measured from 35 °C to 700 °C using a linear temperature ramp of 10 °C min^{-1}. The decomposition temperature was defined by the one where less than 95% mass is left.

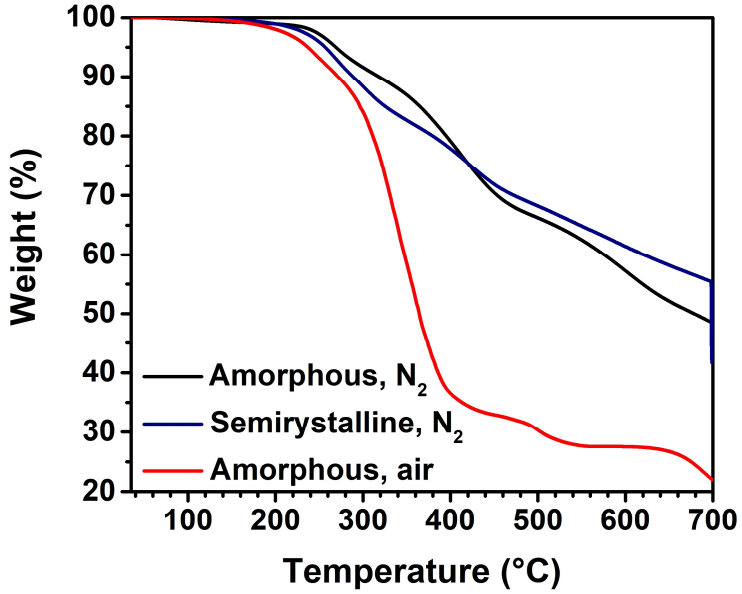

Figure E.32. TGA spectra of amorphous NiTTFtt under N_2 (black) and air (red) and semicrystalline NiTTFtt under N_2 (blue).

E.6.2 PXRD Spectra of Semicrystalline NiTTFtt Before and After Two-weeks of Air-Exposure

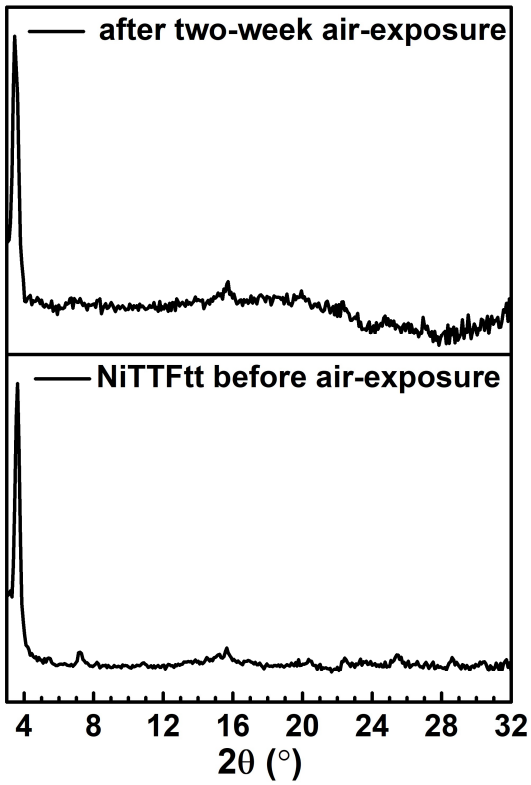

Figure E.33. PXRD spectra of semicrystalline NiTTFtt before and after two-week air-exposure.

E.6.3 High Temperature Variable-Temperature Resistance

A 7 mm pressed pellet (thickness, 162 μm) was symmetrically deposited with four gold nodes on the edges. The heated resistance measurements were carried out in air with a home-made setup as shown in **Figure E.34**. A polyimide flexible heater (PLM-106/10-P, max T=149 °C) was used as the heat source, whose temperature was read and controlled by a temperature controller (Digi-Sense Advanced Temperature Controller, Cole Parmer, the blue K-type thermocouple in the **Figure E.34**). The sample temperature was read by a thermometer (Traceable Thermocouple Thermometer, the yellow K-type thermocouple). The sheet resistances were measured by Semiconductor Device Analyzer (Keysight B1500A) with the van der Pauw method.

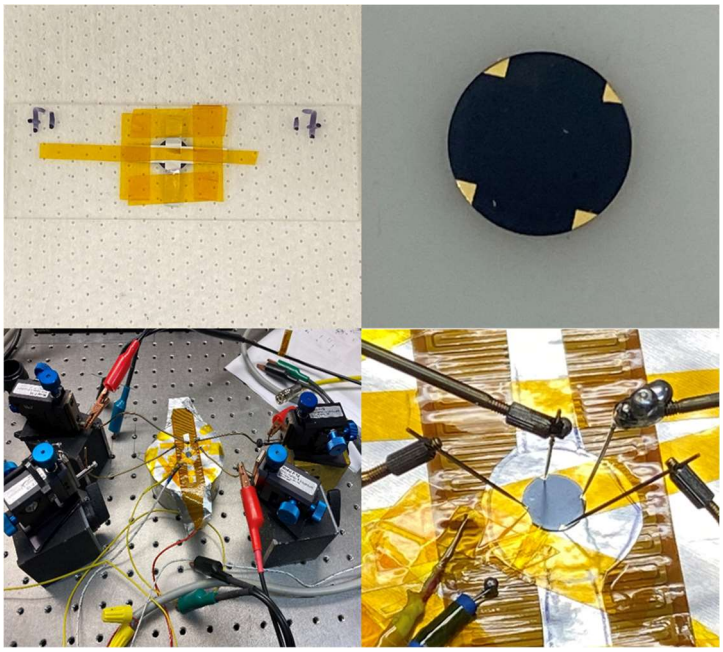

Figure E.34. The demonstration of making gold-deposited pressed pellet for Van Der Pauw measurement (top) and the home-made setup for in-air heated electrical conductivity measurements(bottom).

E.6.4 Long-Term In-Air Resistance Measurements

After the high temperature varied-temperature resistance measurements were done, the same setup and the sample were maintained in air and the resistance at room temperature was examined every 2 days. The conductivity of the pellet can be estimated by R_{sheet} (0.14 Ω) and thickness (162 μm) ($\sigma = 1/(R_{sheet} \times t)$), which is about 450 S/cm consistent with the result of linear four-point probe conductivity measurements in the glovebox (471 S/cm on the cold-pressed pellet, previous section).

E.7 Theoretical Calculation

E.7.1 Band Structure Calculations

In these calculations, we determine the band structure and density of states for the 3D dimer, 3D monomer, and 1D monomer models using Density Functional Theory (DFT) in Quantum espresso.[31, 32] The kinetic energy cutoff of basis plane-wave functions (100 Ry), Marzari-

Vanderbilt-DeVita-Payne cold smearing[33] temperature (0.001 Ry), energy convergence threshold (1e-8 Ry), and k-point sampling were optimized to reduce error in the band structure. All calculations used a PAW pseudopotential with a PBE functional and a nonlinear core correction from PSlibrary.[34, 35] Brillouin zones are generated by the SeeK-path tool,[36, 37] and only relevant points used in the band structure of the primitive cell were included for clarity.

The 2-subunit unit cell geometry predicted by PXRD was used for 3D dimeric model calculations, with k-point sampling using a 5×5×5 Monkhorst-pack grid. Additionally, the dimeric structure was reduced to a monomeric unit cell such that the neighboring chains have the same glide symmetry as the dimeric unit cell using a triclinic box. These 3D monomeric calculations were then performed using k-point sampling using a 9×3×6 Monkhorst-pack grid. Finally, the 3D monomeric unit cell was altered to have side lengths of 50 angstroms (leaving only the chain-axis box length unaltered) to create a quasi-1D unit cell. Calculations on this system were performed using a 9×1×1 Monkhorst-pack grid.

An additional series of calculations were performed on a modified 3D monomeric unit cell, such that the lattice vectors align with the chain, pi-stacking, and plane-stacking axes. Slight variations in pi-stacking lattice vector were chosen such that neighboring chains are shifted along the chain axis relative to each other, to compare to the molecular calculations. Shift lengths of 0.5 angstroms, 1.0 angstroms, and 1.5 angstroms were chosen, each with k-point sampling using a 3×3×9 Monkhorst-pack grid.

The density of states plots for both 3D systems show significant density around the fermi level, indicating that the 3D systems are metallic. By contrast, the 1D monomer shows very little density around the fermi level. Combined with the crossing of bands at the fermi level at the gamma-point, this indicates that the 1D monomer is semimetallic. The packing of chains into a 3D structure

causes a transition from semimetal to a metal. Likewise, the band structures for both 3D systems have several bands crossing the fermi level, further indicating that the 3D system is metallic.

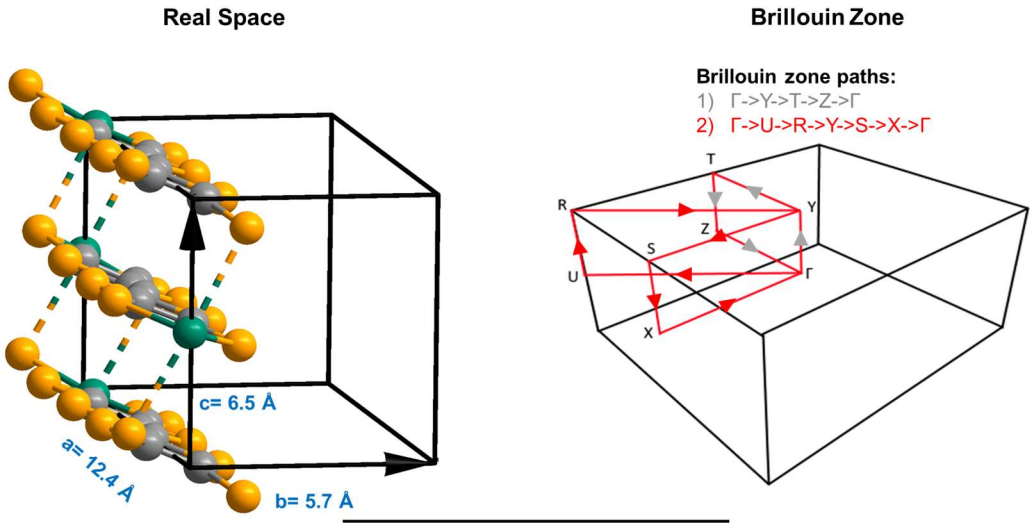

Real Space		1st Brillouin Zone
a axis (longest)	->	Γ-Y (shortest)
b axis (shortest)	->	Γ-X (longest)
c axis	->	Γ-Z

Figure E.35. The real unit of the proposed structure and its Brillouin zone, corresponding to Figure 3B.

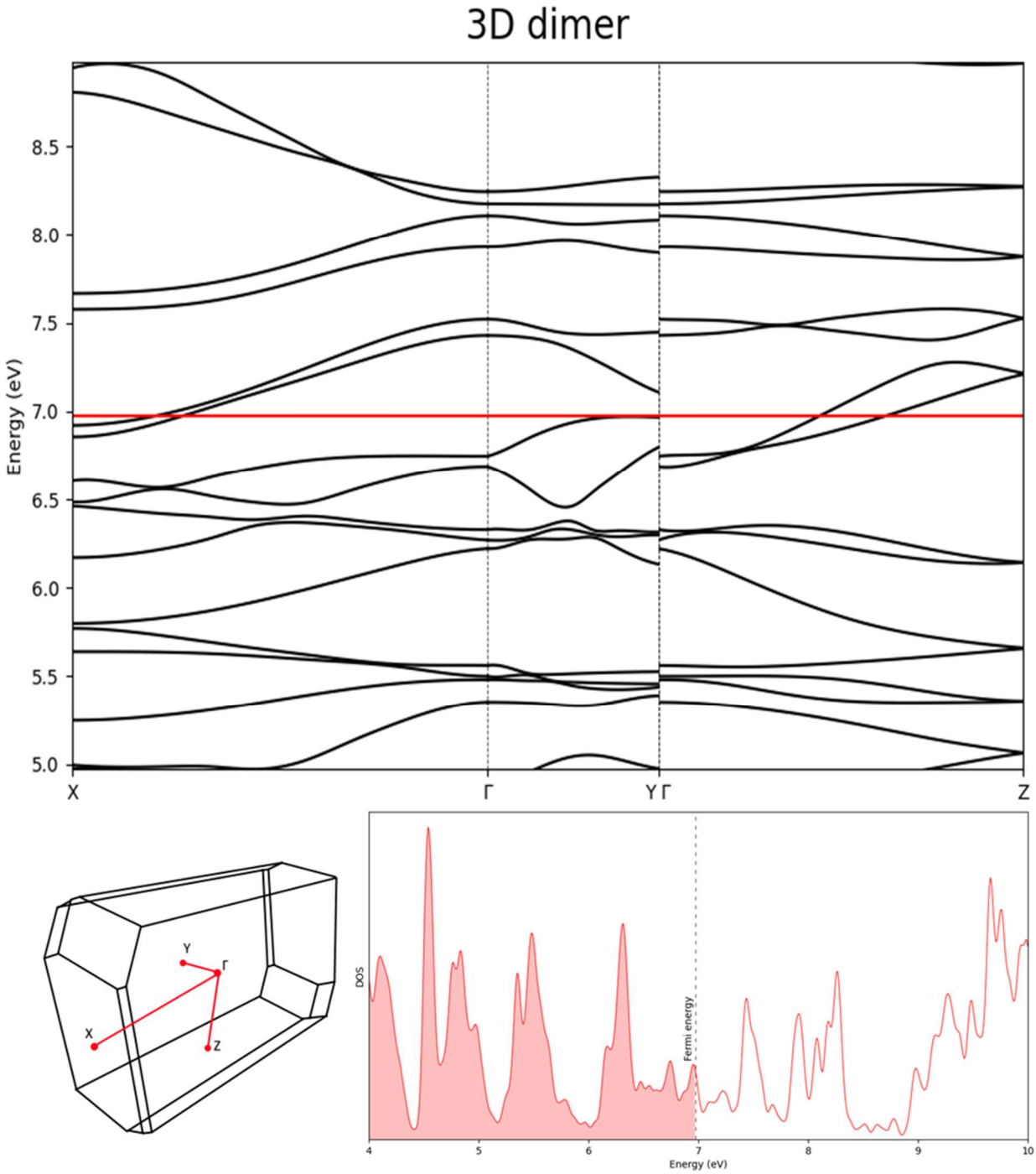

Figure E.36. The band structure and density of states of 3D dimer. This is still the band structure calculation of the proposed structure but with different Brillouin zone paths (only take Γ-x, y, z).

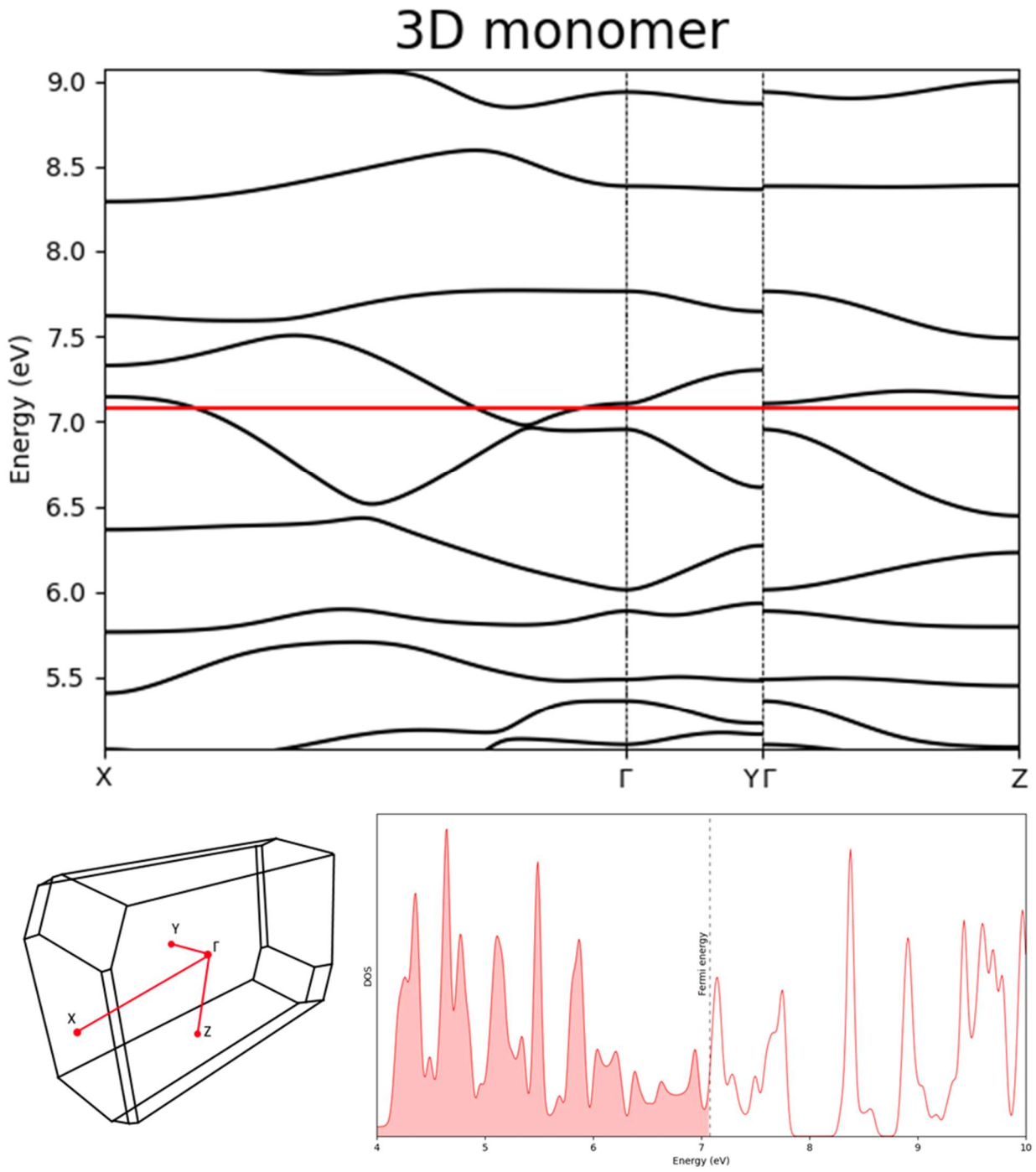

Figure E.37. The band structure and density of states of 3D monomer.

The shifted 3D monomer calculations decrease in energy with increasing shift distance, which agrees with molecular calculations and PXRD predictions indicating that the ground state structure is likely not perfectly aligned. Additionally, the energy only changes by 0.14 kcal/mol over the

shift distances studied, indicating that the potential energy surface for these chain interactions is quite shallow. Due to the shallowness of the potential energy surface, geometries in the physical system can vary quite a lot from the systems studied here, even with relatively low thermal energy, which agrees with the hypothesis that NiTTFtt forms an amorphous solid. However, the fact that all 3D systems studied retain metallic behavior indicates that we can reasonably conclude that many (if not most) possible amorphous geometries support metallic character.

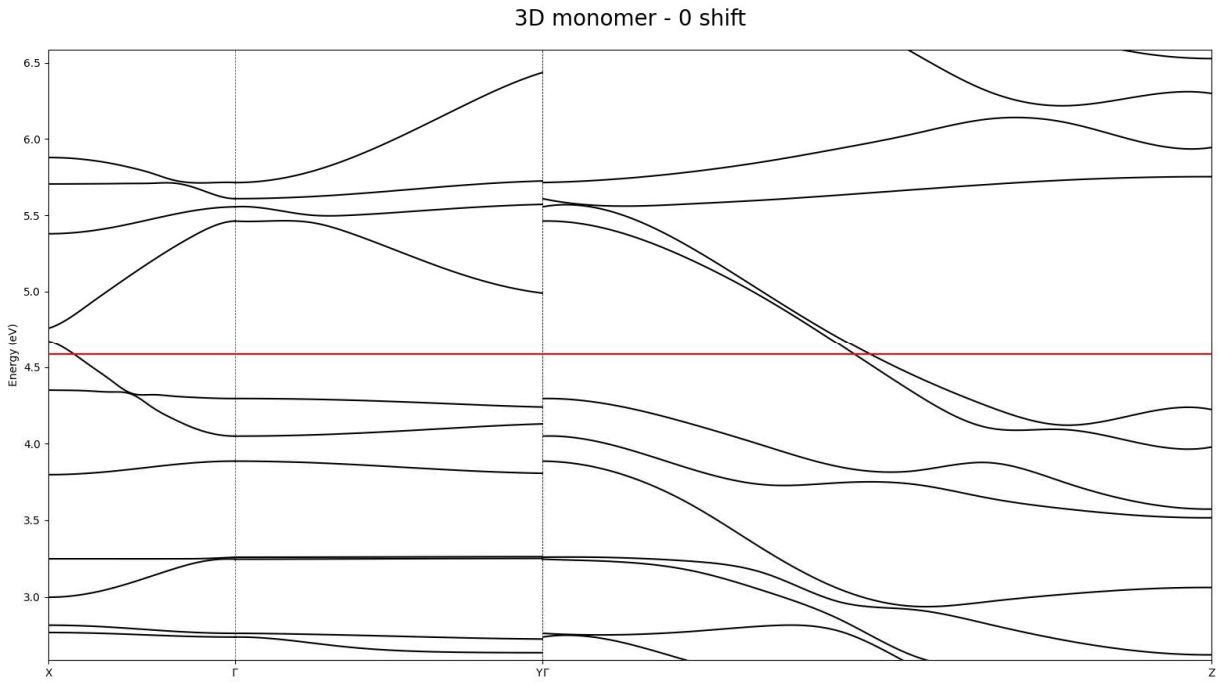

Figure E.38. The band structures of shifted 3D monomer (0 shift).

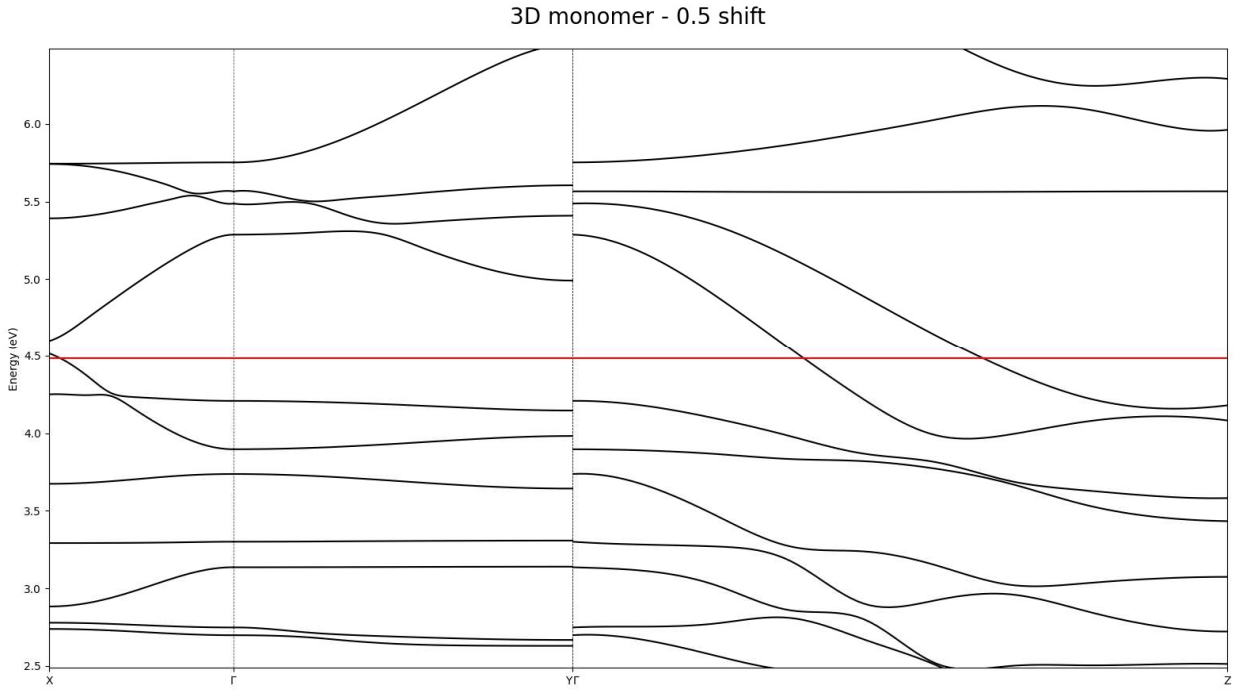

Figure E.39. The band structures of shifted 3D monomer (0.5 shift).

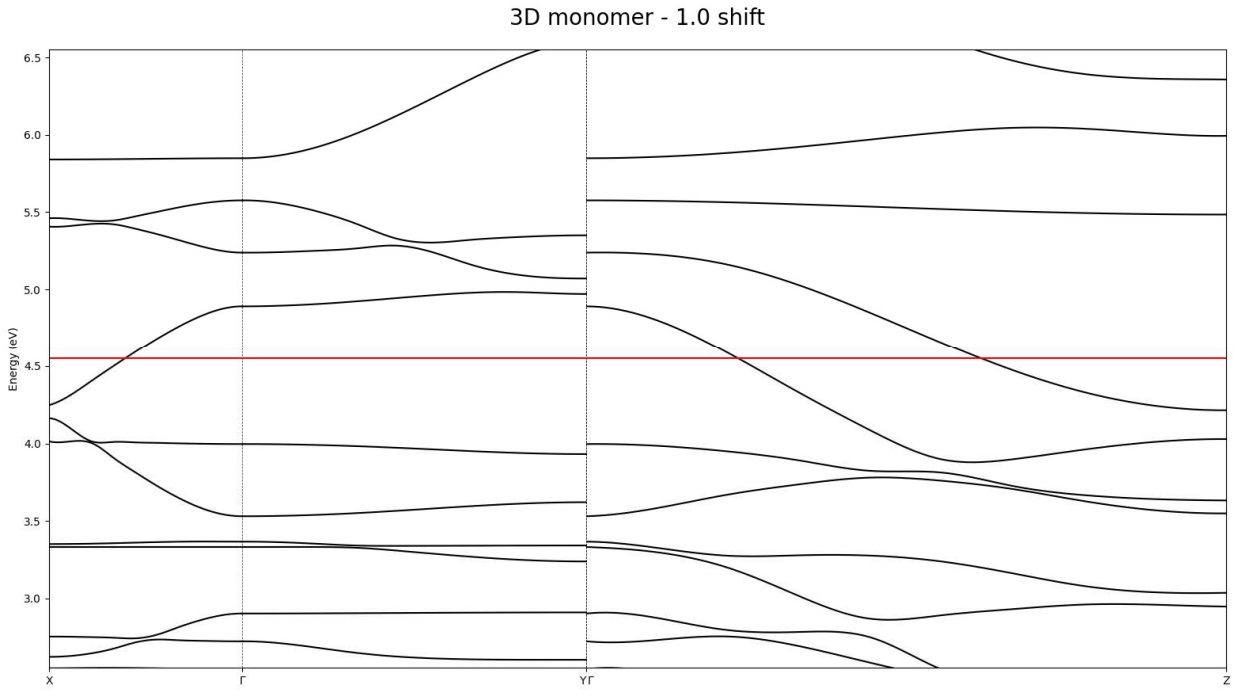

Figure E.40. The band structures of shifted 3D monomer (1.0 shift).

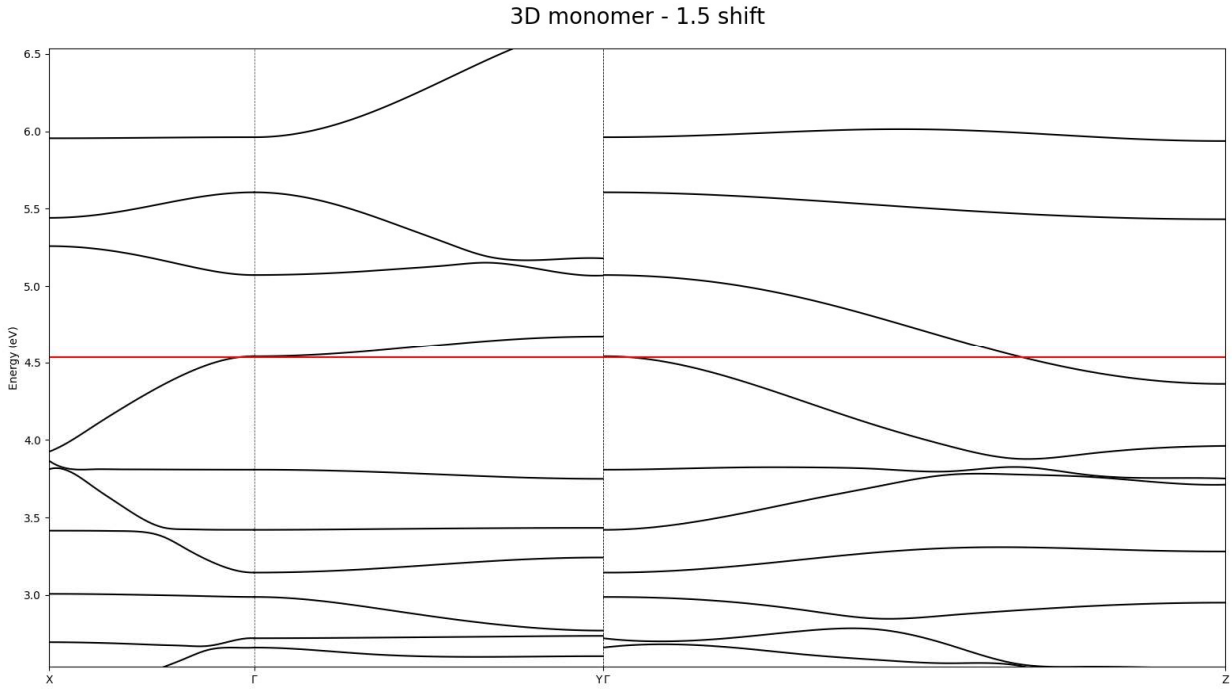

Figure E.41. The band structures of shifted 3D monomer (1.5 shift).

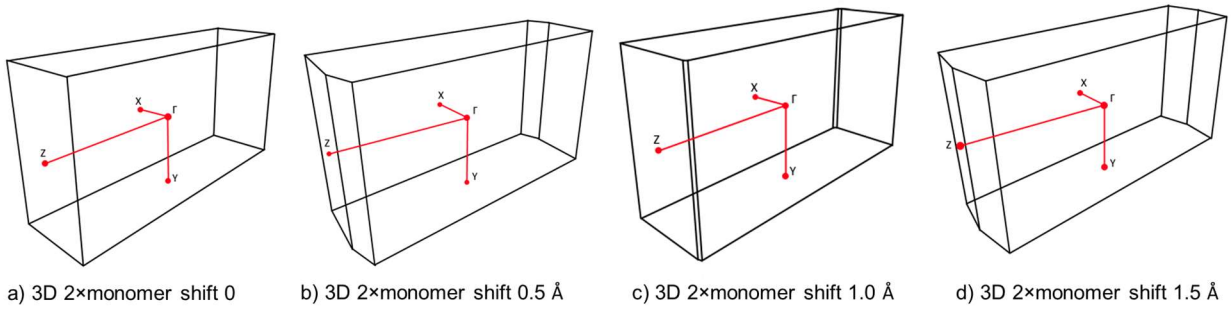

Figure E.42. Brillouin zones of 3D structures of shifted chains.

E.7.2 Molecular Calculations

A bimolecular model was constructed from the NiTTFtt solid structure to emulate the inter-layer interactions present in the amorphous extended structure, with the individual unit displayed in Figure 3C. An inter-layer distance of 3.35Å was chosen based on the average distance measured in the structure. Several calculations were run on the model to investigate the dependence of the electron correlation present in the extended solid based on the orientation of the individual NiTTFtt units. Investigated geometries include: (i) two units symmetrically stacked on top of each other

(*top*), (ii) a 1 Å shift parallel along the central TTF C–C bonds (*para*), (iii) a 1 Å shift perpendicular to the central TTF C–C bonds (*perp*), and (iv) a twist by an angle of 10 degrees over the central TTF CC bonds (*angle*).

The results for B3LYP[38]/6-31G*[39] with the GD3BJ[40] dispersion correction and [20,20] active space variational 2-electron reduced density matrix (V2RDM)[41, 42, 43]/6-31G[44] calculations are displayed in **Table E.4**. DFT calculations show a shallow potential energy surface around the symmetrically aligned structure, with shifts in both the parallel as well as perpendicular directions with respect to the central TTF C–C bonds being favorable, while a 10-degree twist over the on-top aligned TTF C-C bonds is slightly unfavorable. This result agrees with observations made from the X-ray crystal structure of $[(Nidppe)_2TTFtt][BAr^F{}_4]$,[45] which displays both parallel and perpendicular displacements of the individual NiTTFtt units.

To further understand the energetics of the inter-unit displacements, CASSCF calculations were carried out with the V2RDM method and a large active space of 20 electrons distributed in 20 molecular orbitals ([20,20]) with a 6-31G basis set. Similar molecular systems containing $TTFtt^{2+}$ units have previously been shown to exhibit multi-reference correlation in their electronic structure and as such DFT is not sufficient for their description. Indeed, our calculations show that all model systems display multi-reference correlation, with the degree of biradical character exhibited depending on the alignment of the two units. Figure 3C displays the highest occupied natural orbital (HONO) and lowest unoccupied natural orbital (LUNO) and their occupation numbers (NON) for each of the three studied spatial arrangements. The symmetrically aligned *top* structure exhibits the lowest degree of multi-reference character, however, with HONO and LUNO occupations of 1.55 and 0.41, it nonetheless displays a significant amount of strong correlation and biradical character. In this arrangement the HONO and LUNO split into one orbital that is clearly

bonding across the π stack and shows good overlap across the two individual NiTTFtt units, the HONO, and one orbital that is anti-bonding across the π stack and shows no density bridging the two individual units, the LUNO. Both parallel as well as perpendicular displacements of the individual NiTTFtt units result in significant increases in multi-reference correlation. The *para* structure exhibits near-biradical NON of 1.19 and 0.81 for the HONO and LUNO, respectively, and additional significant fractionalization in the HONO-1 and LUNO+1, which display NON of 1.56 and 0.42 as compared to 1.70 and 0.29 in the *top* structure, while the *perp* arrangement shows slightly less significant but still noteworthy changes to the HONO and LUNO occupations with λ_{HONO} = 1.31 λ_{LUNO} = 0.63. In both cases these changes in the NON are accompanied with corresponding changes to the natural orbitals and in both shift arrangements we observe inter-unit

overlap in the LUNO along the π-stacking axis. Lastly, the introduction of a 10-degree twist angle shows no significant changes in the frontier natural orbital occupations and the natural orbital densities. The trends displayed by the NON mirror those of the LUMO-HOMO gaps calculated with DFT; ΔE_{MO} decreases as we shift the NiTTFtt units and fractionalization in the V2RDM HONO and LUNO increases.

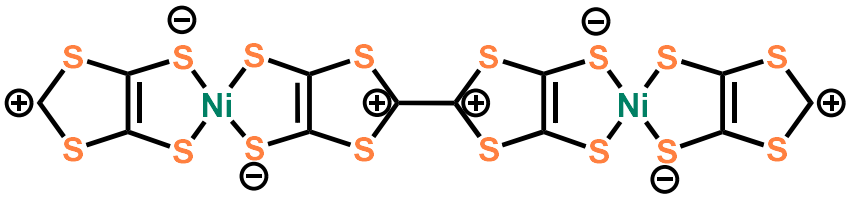

Figure E.43. The molecular fragment of NiTTFtt used for the molecular calcualtions.

Table E.4. Electronic energy and enthalpy differences (in kcal/mol) of the parallel (para), perpendicular (perp) shifted and 10 degree twisted (angle) structures versus the symmetrically aligned (top) structure.

B3LYP/6-31G*	[20,20] V2RDM/6-31G

	ΔE	ΔH	ΔE_{MO}	ΔE	ΔH	E_c	λ_{385}	λ_{386}	λ_{387}	λ_{388}
top			32.88			- 246.43	1.70	1.55	0.41	0.29
para	-6.3	- 3.99	20.88	- 33.43	- 31.64	- 291.03	1.56	1.19	0.84	0.42
perp	-4.8	-3.1	26.87	- 25.5	- 24.9	- 259.33	1.60	1.34	0.63	0.20
angle	0.8	2.0	34.54	- 10.7	-9.5	- 255.60	1.68	1.55	0.44	0.33

ΔE_{MO} denotes the LUMO-HOMO gap in millihartree, E_c denotes the electronic correlation energy, defined as $E_{V2RDM} - E_{HF}$ in millihartree, and λ_N denotes the occupations of the Nth natural orbital.

E.8 References

[1] Holder, C. F.; Schaak, R. E. Tutorial on Powder X-Ray Diffraction for Characterizing Nanoscale Materials. *ACS Nano* **2019**, *13* (7), 7359–7365.

[2] Ravel, B.; Newville, M. ATHENA , ARTEMIS , HEPHAESTUS : Data Analysis for X-Ray Absorption Spectroscopy Using IFEFFIT. *J. Synchrotron Radiat.* **2005**, *12* (4), 537–541.

[3] Rehr, J. J.; Albers, R. C. Theoretical Approaches to X-Ray Absorption Fine Structure. *Rev. Mod. Phys.* **2000**, *72* (3), 621–654.

[4] Toby, B. H.; Von Dreele, R. B. GSAS-II : The Genesis of a Modern Open-Source All Purpose Crystallography Software Package. *J. Appl. Crystallogr.* **2013**, *46* (2), 544–549.

[5] Qiu, X.; Thompson, J. W.; Billinge, S. J. L. PDFgetX2 : A GUI-Driven Program to Obtain the Pair Distribution Function from X-Ray Powder Diffraction Data. *J. Appl. Crystallogr.* **2004**, *37* (4), 678–678.

[6] Petkov, V. Pair Distribution Functions Analysis. *Characterization of Materials*; John Wiley & Sons, Inc.: Hoboken, NJ, USA, 2012; 1361–1372.

[7] *Dassault Systèmes BIOVIA, Material Studio, San Diego: Dassault Systèmes 2017.*

[8] Okano, Y.; Zhou, B.; Tanaka, H.; Adachi, T.; Ohishi, Y.; Takata, M.; Aoyagi, S.; Nishibori, E.; Sakata, M.; Kobayashi, A.; Kobayashi, H. High-Pressure (up to 10.7 GPa) Crystal Structure of Single-Component Molecular Metal [Au(tmdt)$_2$]. *J. Am. Chem. Soc.* **2009**, *131* (20), 7169–7174.

[9] Kobayashi, Y.; Terauchi, T.; Sumi, S.; Matsushita, Y. Carrier Generation and Electronic Properties of a Single-Component Pure Organic Metal. *Nat. Mater.* **2017**, *16* (1), 109–114.

[10] Kobayashi, A.; Fujiwara, E.; Kobayashi, H. Single-Component Molecular Metals with Extended-TTF Dithiolate Ligands. *Chem. Rev.* **2004**, *104* (11), 5243–5264.

[11] Tanaka, H.; Okano, Y.; Kobayashi, H.; Suzuki, W.; Kobayashi, A. A Three-Dimensional Synthetic Metallic Crystal Composed of Single-Component Molecules. *Science.* **2001**, *291* (5502), 285–287.

[12] Giannozzi, P.; Baseggio, O.; Bonfà, P.; Brunato, D.; Car, R.; Carnimeo, I.; Cavazzoni, C.; de Gironcoli, S.; Delugas, P.; Ferrari Ruffino, F.; Ferretti, A.; Marzari, N.; Timrov, I.; Urru, A.; Baroni, S. Quantum ESPRESSO toward the Exascale. *J. Chem. Phys.* **2020**, *152* (15), 154105.

[13] Vogt, T.; Faulmann, C.; Soules, R.; Lecante, P.; Mosset, A.; Castan, P.; Cassoux, P.; Galy, J. A LAXS (Large Angle X-Ray Scattering) and EXAFS (Extended X-Ray Absorption Fine Structure) Investigation of Conductive Amorphous Nickel Tetrathiolato Polymers. *J. Am. Chem. Soc.* **1988**, *110* (6), 1833–1840.

[14] Morrison, C.; Sun, H.; Yao, Y.; Loomis, R. A.; Buhro, W. E. Methods for the ICP-OES Analysis of Semiconductor Materials. *Chem. Mater.* **2020**, *32* (5), 1760–1768.

[15] Lee, K.; Cho, S.; Heum Park, S.; Heeger, A. J.; Lee, C.-W.; Lee, S.-H. Metallic Transport in Polyaniline. *Nature* **2006**, *441* (7089), 65–68.

[16] de Caro, D.; Fraxedas, J.; Faulmann, C.; Malfant, I.; Milon, J.; Lamère, J.-F.; Collière, V.; Valade, L. Metallic Thin Films of TTF[Ni(dmit)$_2$]$_2$ by Electrodeposition on (001)-Oriented Silicon Substrates. *Adv. Mater.* **2004**, *16* (910), 835–838.

[17] Liu, Z.; Liu, T.; Savory, C. N.; Jurado, J. P.; Reparaz, J. S.; Li, J.; Pan, L.; Faul, C. F. J.; Parkin, I. P.; Sankar, G.; Matsuishi, S.; Campoy-Quiles, M.; Scanlon, D. O.; Zwijnenburg, M. A.; Fenwick, O.; Schroeder, B. C. Controlling the Thermoelectric Properties of Organometallic Coordination Polymers via Ligand Design. *Adv. Funct. Mater.* **2020**, *30* (32), 2003106.

[18] Ma, T.; Dong, B. X.; Grocke, G. L.; Strzalka, J.; Patel, S. N. Leveraging Sequential Doping of Semiconducting Polymers to Enable Functionally Graded Materials for Organic Thermoelectrics. *Macromolecules* **2020**, *53* (8), 2882–2892.

[19] D. Schroder, *Semiconductor material and device characterization*, 3rd editionrd ed. Piscataway NJ; Hoboken N.J.: IEEE Press; Wiley, **2006**.

[20] Schmidt, V.; Mensch, P. F. J.; Karg, S. F.; Gotsmann, B.; Das Kanungo, P.; Schmid, H.; Riel, H. Using the Seebeck Coefficient to Determine Charge Carrier Concentration, Mobility, and Relaxation Time in InAs Nanowires. *Appl. Phys. Lett.* **2014**, *104* (1), 012113.

[21] Beretta, D.; Bruno, P.; Lanzani, G.; Caironi, M. Reliable Measurement of the Seebeck Coefficient of Organic and Inorganic Materials between 260 K and 460 K. *Rev. Sci. Instrum.* **2015**, *86* (7), 075104.

[22] Halim, J.; Moon, E. J.; Eklund, P.; Rosen, J.; Barsoum, M. W.; Ouisse, T. Variable Range Hopping and Thermally Activated Transport in Molybdenum-Based MXenes. *Phys. Rev. B* **2018**, *98* (10), 104202.

[23] https://www.lancaster.ac.uk/users/esqn/windsor04/docs/artuno-cg.pdf

[24] Moreira, H.; Yu, Q.; Nadal, B.; Bresson, B.; Rosticher, M.; Lequeux, N.; Zimmers, A.; Aubin, H. Electron Cotunneling Transport in Gold Nanocrystal Arrays. *Phys. Rev. Lett.* **2011**, *107* (17), 176803.

[25] http://www.phys.utk.edu/labs/modphys/Hall%20Effect.pdf.

[26] Jiang, Y.; Oh, I.; Joo, S. H.; Seo, Y.-S.; Lee, S. H.; Seong, W. K.; Kim, Y. J.; Hwang, J.; Kwak, S. K.; Yoo, J.-W.; Ruoff, R. S. Synthesis of a Copper 1,3,5-Triamino-2,4,6-Benzenetriol Metal–Organic Framework. *J. Am. Chem. Soc.* **2020**, *142* (43), 18346–18354.

[27] Czapla, B.; Hanssen, L. M. Direct Method of Extracting Complex Refractive Index from Routine Fourier Transform Infrared Reflectance/Transmittance Measurements. *Reflection, Scattering, and Diffraction from Surfaces VII*; Hanssen, L. M., Ed.; SPIE, 2020; Vol. 1, p 11.

[28] Ng, S. S.; Hassan, Z.; Abu Hassan, H. Kramers–Kronig Analysis Of Infrared Reflectance Spectra With A Single Resonance. *J. Teknol.* **2006**, *44* (1), 67–75.

[29] Ohta, K.; Ishida, H. Comparison among Several Numerical Integration Methods for Kramers-Kronig Transformation. *Appl. Spectrosc.* **1988**, *42* (6), 952–957.

[30] Wooten, F. Optical Properties Measurement Techniques Solar Energy Materials Special Issue. *Sol. Energy Mater.* **1989**, *18* (3–4), 231.

[31] Giannozzi, P.; Baroni, S.; Bonini, N.; Calandra, M.; Car, R.; Cavazzoni, C.; Ceresoli, D.; Chiarotti, G. L.; Cococcioni, M.; Dabo, I.; Dal Corso, A.; de Gironcoli, S.; Fabris, S.; Fratesi, G.; Gebauer, R.; Gerstmann, U.; Gougoussis, C.; Kokalj, A.; Lazzeri, M.; Martin-Samos, L.; Marzari, N.; Mauri, F.; Mazzarello, R.; Paolini, S.; Pasquarello, A.; Paulatto, L.; Sbraccia, C.; Scandolo, S.; Sclauzero, G.; Seitsonen, A. P.; Smogunov, A.; Umari, P.; Wentzcovitch, R. M. QUANTUM ESPRESSO: A Modular and Open-Source Software Project for Quantum Simulations of Materials. *J. Phys. Condens. Matter.* **2009**, 21 (39), 395502.

[32] Giannozzi, P.; Andreussi, O.; Brumme, T.; Bunau, O.; Buongiorno Nardelli, M.; Calandra, M.; Car, R.; Cavazzoni, C.; Ceresoli, D.; Cococcioni, M.; Colonna, N.; Carnimeo, I.; Dal Corso, A.; de Gironcoli, S.; Delugas, P.; DiStasio, R. A.; Ferretti, A.; Floris, A.; Fratesi, G.; Fugallo, G.; Gebauer, R.; Gerstmann, U.; Giustino, F.; Gorni, T.; Jia, J.; Kawamura, M.; Ko, H.-Y.; Kokalj, A.; Küçükbenli, E.; Lazzeri, M.; Marsili, M.; Marzari, N.; Mauri, F.; Nguyen, N. L.; Nguyen, H.-V.; Otero-de-la-Roza, A.; Paulatto, L.; Poncé, S.; Rocca, D.; Sabatini, R.; Santra, B.; Schlipf, M.; Seitsonen, A. P.; Smogunov, A.; Timrov, I.; Thonhauser, T.; Umari, P.; Vast, N.; Wu, X.; Baroni, S. Advanced Capabilities for Materials Modelling with Quantum ESPRESSO. *J. Phys. Condens. Matter* **2017**, *29* (46), 465901.

[33] Marzari, N.; Vanderbilt, D.; De Vita, A.; Payne, M. C. Thermal Contraction and Disordering of the Al(110) Surface. *Phys. Rev. Lett.* **1999**, *82* (16), 3296–3299.

[34] Prandini, G.; Marrazzo, A.; Castelli, I. E.; Mounet, N.; Marzari, N. Precision and Efficiency in Solid-State Pseudopotential Calculations. *npj Comput. Mater.* **2018**, *4* (1), 72.

[35] Lejaeghere, K.; Bihlmayer, G.; Björkman, T.; Blaha, P.; Blügel, S.; Blum, V.; Caliste, D.; Castelli, I. E.; Clark, S. J.; Dal Corso, A.; de Gironcoli, S.; Deutsch, T.; Dewhurst, J. K.; Di Marco, I.; Draxl, C.; Dułak, M.; Eriksson, O.; Flores-Livas, J. A.; Garrity, K. F.; Genovese, L.; Giannozzi, P.; Giantomassi, M.; Goedecker, S.; Gonze, X.; Grånäs, O.; Gross, E. K. U.; Gulans, A.; Gygi, F.; Hamann, D. R.; Hasnip, P. J.; Holzwarth, N. A. W.; Iuşan, D.; Jochym, D. B.; Jollet, F.; Jones, D.; Kresse, G.; Koepernik, K.; Küçükbenli, E.; Kvashnin, Y. O.; Locht, I. L. M.; Lubeck, S.; Marsman,

M.; Marzari, N.; Nitzsche, U.; Nordström, L.; Ozaki, T.; Paulatto, L.; Pickard, C. J.; Poelmans, W.; Probert, M. I. J.; Refson, K.; Richter, M.; Rignanese, G.-M.; Saha, S.; Scheffler, M.; Schlipf, M.; Schwarz, K.; Sharma, S.; Tavazza, F.; Thunström, P.; Tkatchenko, A.; Torrent, M.; Vanderbilt, D.; van Setten, M. J.; Van Speybroeck, V.; Wills, J. M.; Yates, J. R.; Zhang, G.-X.; Cottenier, S. Reproducibility in Density Functional Theory Calculations of Solids. *Science.* **2016**, *351* (6280).

[36] Hinuma, Y.; Pizzi, G.; Kumagai, Y.; Oba, F.; Tanaka, I. Band Structure Diagram Paths Based on Crystallography. *Comput. Mater. Sci.* **2017**, *128*, 140–184.

[37] Togo, A.; Tanaka, I. Spglib: A Software Library for Crystal Symmetry Search. **2018**, 1–11.

[38] Becke D., A. Density-Functional Thermochemistry. III. The Role of Exact Exchange. *The Journal of Chemical Physics.* 1993, 5648–5652.

[39] Francl, M. M.; Pietro, W. J.; Hehre, W. J.; Binkley, J. S.; Gordon, M. S.; DeFrees, D. J.; Pople, J. A. Self-consistent Molecular Orbital Methods. XXIII. A Polarization-type Basis Set for Second-row Elements. *J. Chem. Phys.* **1982**, *77* (7), 3654–3665.

[40] Grimme, S.; Ehrlich, S.; Goerigk, L. Effect of the Damping Function in Dispersion Corrected Density Functional Theory. *J. Comput. Chem.* **2011**, *32* (7), 1456–1465.

[41] Gidofalvi, G.; Mazziotti, D. A. Active-Space Two-Electron Reduced-Density-Matrix Method: Complete Active-Space Calculations without Diagonalization of the N-Electron Hamiltonian. *J. Chem. Phys.* **2008**, *129* (13), 134108.

[42] Mazziotti, D. A. Variational Minimization of Atomic and Molecular Ground-State Energies via the Two-Particle Reduced Density Matrix. *Phys. Rev. A* **2002**, *65* (6), 062511.

[43] Mazziotti, D. A. Large-Scale Semidefinite Programming for Many-Electron Quantum Mechanics. *Phys. Rev. Lett.* **2011**, *106* (8), 083001.

[44] Hehre, W. J.; Ditchfield, R.; Pople, J. A. Self-Consistent Molecular Orbital Methods. XII. Further Extensions of Gaussian-Type Basis Sets for Use in Molecular Orbital Studies of Organic Molecules. *J. Chem. Phys.* **1972**, *56* (5), 2257–2261.

[45] Xie, J.; Boyn, J. N.; Filatov, A. S.; McNeece, A. J.; Mazziotti, D. A.; Anderson, J. S. Redox, Transmetalation, and Stacking Properties of Tetrathiafulvalene-2,3,6,7-Tetrathiolate Bridged Tin, Nickel, and Palladium Compounds. *Chem. Sci.* **2020**, *11* (4), 1066–1078.

Appendix F:Supporting Data for Chapter 7

F.1 Composition Characterizations

F.1.1 Composition summary

Table F.1. Element ratios (Li, S, Ni and Sn) summary based on various technologies.

	LiTHF-NiTTFtt	Li-NiTTFtt	NiTTFtt
Sn/Ni (ICP-MS)	0.03	0.03	0.03
Li/Ni (ICP-MS)	0.85	0.89	<0.01
Li/Ni (ICP-OES)	0.94	0.94	<0.01
S/Ni (XPS)	5.9	5.6	7.7
S/Ni (XRF)	5.1	5.7	7.5
S/Ni (ICP-OES)	5.8 (8:1.4)	5.7 (8:1.4)	8.2
Practical formula	$[Li(THF)_{1.5}]_{1.2}Ni_{0.4}$ $[NiC_6S_8]$	$Li_{1.2}Ni_{0.4}$ $[NiC_6S_8]$	NiC_6S_8

Table F.2. Elemental analyses of C, H, and N.

Materials	Accurate formula	C %	H %	N %
$[Li(THF)_{1.5}]_{1.2}N$	$Li_{1.18}Ni_{1.37}TTFtt(SnBu_2)_{0.04}(THF)_{1.77}$	29.05[b]	2.71	0
$i_{0.4}[NiC_6S_8]$	$C_{13.4}H_{14.88}Li_{1.18}Ni_{1.37}O_{1.77}S_8Sn_{0.04}$ [a]	28.87[c]	2.69	0
$Li_{1.2}Ni_{0.4}$	$Li_{1.18}Ni_{1.37}TTFtt(SnBu_2)_{0.04}$	17.80	0.17	0
$[NiC_6S_8]$	$C_{6.32}H_{0.72}Li_{1.18}Ni_{1.37}S_8Sn_{0.04}$	17.43	0.11	0
NiC_6S_8	$Ni_{0.96}TTFtt(SnBu_2)_{0.04}[BAr^F]_{0.04}$	21.29	0.28	0
	$C_{7.6}H_{1.2}B_{0.04}F_{0.96}Ni_{0.96}S_8Sn_{0.04}$	22.12	0.93	0

a) Grey represents accurate formulars. b) Blue represents theoretical values. c) Red represents experimental values.

F.1.2 Inductively Coupled Plasma- Mass Spectrometry/Optical Emission Spectrometry

Inductively coupled plasma mass spectrometry (ICP-MS) data was obtained with an Agilent 7700x ICP-MS and analyzed using ICP-MS Mass Hunter version B01.03. The samples were diluted in 2% HNO_3 matrix and analyzed with a ^{159}Tb internal standard against a 12-point standard curve over the range from 0.1 to 500 ppb. The correlation was >0.9997 for all analyses of interest. Data collection was performed in Spectrum Mode with five replicates per sample and 100 sweeps per replicate. Solutions for ICP-MS were prepared by digesting 2 mg of material in 1 mL HNO_3 (trace metal grade) solution in a fume hood overnight at room temperature. The solution was diluted with ultrafiltered deionized water for ICP-MS analysis.

An Agilent 700 series spectrometer was used for inductively coupled plasma optical emission spectroscopy (ICP-OES). The sample preparation was referred to the reported procedure[1] to improve the accuracy of Sulfur determination. Solutions for ICP-OES were prepared by digesting 2 mg of materials in 0.5 mL HNO_3 and 0.5 mL H_2O_2 (trace metal grade) solutions in tight-sealed high-density polyethylene (HDPE) centrifuge tubes overnight and then diluted with ultrafiltered deionized water.

F.1.3 X-ray Fluorescence Measurements

X-ray fluorescence (XRF) measurements were performed on pressed pellets with a Rigaku NEX DE VS spectrometer under a He atmosphere.

F.1.4 X-ray and Ultraviolet Photoelectron Spectroscopy

X-ray photoelectron spectra (XPS) were collected with the AXIS Nova spectrometer (Kratos Analytical) equipped with a monochromatic Al Kα X-ray source. The Al anode was powered at

10 mA and 15 kV. The instrument work function was calibrated to give a Au $4f_{7/2}$ metallic gold binding energy of 83.95 eV. The instrument base pressure was ca. 1×10^{-10} Torr. The analysis area size was 0.3×0.7 mm^2. For calibration purposes, the binding energies were referenced to the C 1s peak at 284.8 eV. Survey spectra were collected with a step size of 1 and 160 eV pass energy. Ultraviolet photoelectron spectra (UPS) were collected with the AXIS Nova spectrometer using UV-radiation source. The high-resolution spectra were collected with a pass energy of 40 and a 0.1 eV step size. Pressed pellets were affixed to conductive carbon tape under N_2 before loading into the spectrometer.

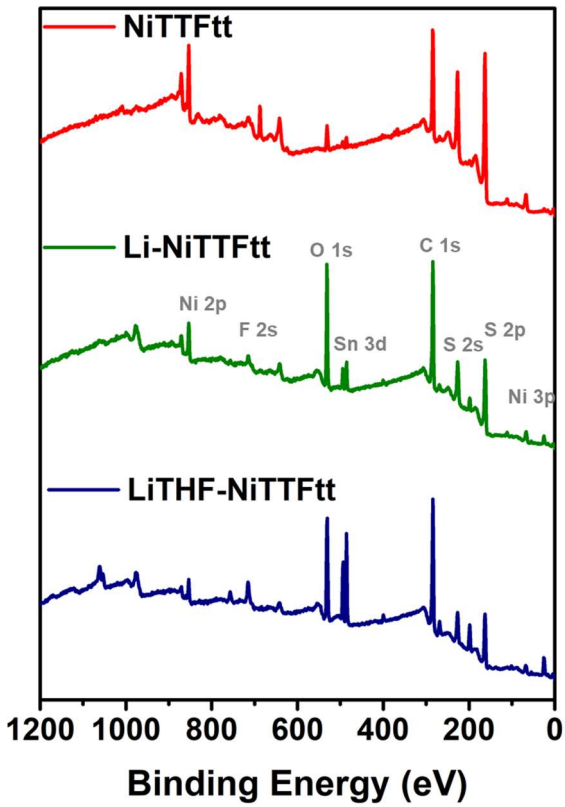

Figure F.1. XPS survey spectra of NiTTFtt (red), Li-NiTTFtt (green), and LiTHF-NiTTFtt (blue).

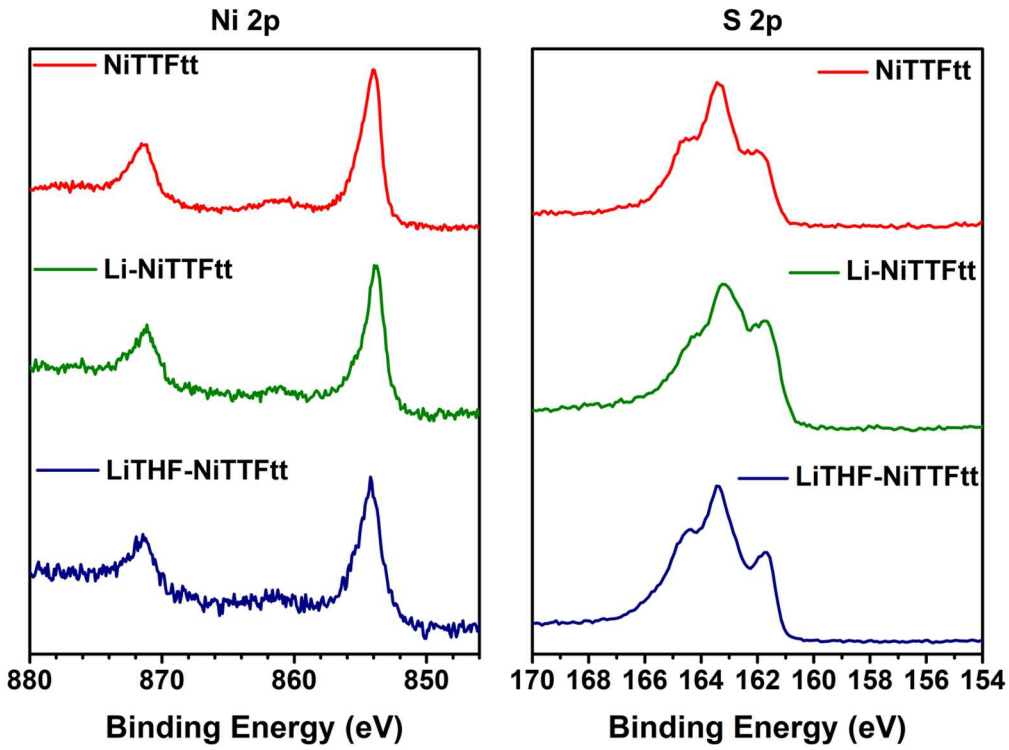

Figure F.2. High-resolution XPS spectra of NiTTFtt (red), Li-NiTTFtt (green), and LiTHF-NiTTFtt (blue).

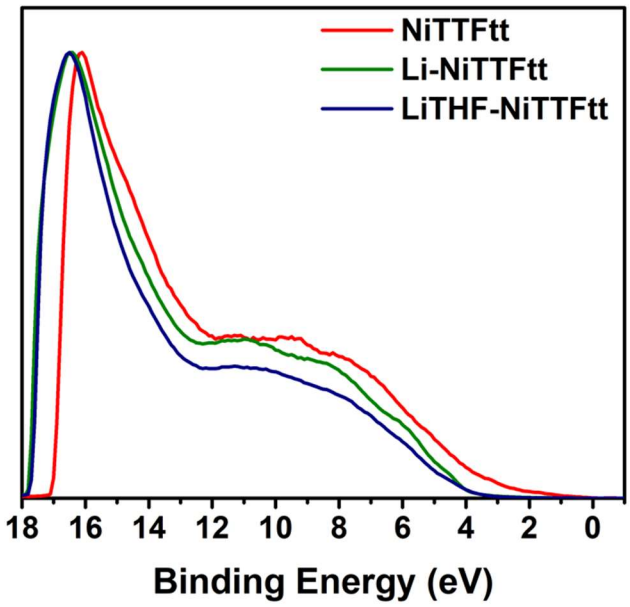

Figure F.3. UPS spectra of NiTTFtt (red), Li-NiTTFtt (green), and LiTHF-NiTTFtt (blue).

F.1.5 X-ray Absorption Spectroscopy

Powder samples of NiTTFtt, LiNiTTFtt and LiTHF-NiTTFtt were prepared by grinding finely with polypropylene as a binder. A Teflon washer (5.3 mm internal diameter) was sealed on one side with Kapton tape and the ground powder was then transferred to the inside of this ring before compacting with a Teflon rod and sealing the remaining face with Kapton tape. X-ray absorption near-edge spectra (XANES) were employed to probe the local environment around Ni. Data were acquired at the Advanced Photon Source at Argonne National Laboratory with a bending magnet source with ring energy at 7.00 GeV. Ni K-edge (8333 eV) data were acquired at the MRCAT 10-BM beam line in transmission. The incident, transmitted, and reference X-ray intensities were monitored using gas ionization chambers. A metallic nickel foil standard was used as a reference for energy calibration and was measured simultaneously with experimental samples. X-ray absorption spectra were collected at room temperature.

Data collected was processed using the Demeter software suite[2] by extracting the EXAFS oscillations $\chi(k)$ as a function of photoelectron wavenumber k. The theoretical paths were generated using FEFF6[3] and the models were done in the conventional way using the fitting program Artemis.

Table F.3. XAS data summary.

	LiTHF-NiTTFtt	Li-NiTTFtt	NiTTFtt
K-Edge energy (eV)[a]	8836.7(4)	8836.9(4)	8837.2(4)
Ni-S bond length (Å)	2.161(6)	2.161(6)	2.177(9)
Ni-C bond length (Å)	3.01(3)	3.01(3)	3.00(3)

a) The K-edge energy was defined as the first inflection point of the edge.

Table F.4. EXAFS fit parameters for Li-NiTTFtt.

Li-NiTTFtt	N	R (Å)	σ^2 (Å^2)	R-factor	Reduced chi-square
Ni-S	4	2.161(6)	0.0033(7)	0.0077	778
Ni-C	4	3.01(3)	0.005(4)		

ΔE_0 = -1(1) eV; S_0^2 = 0.61(6); Independent Points: 9.7; Fitting Range: k: 2.1-12.5 Å^{-1}; R: 1.3-2.8 Å; N, Coordination numbers; R, interatomic distances; σ^2, Debye-Waller factors (the mean-square deviations in interatomic distance). The values in parentheses are the estimated standard deviations; ΔE_0, change in the photoelectron energy; S_0^2, amplitude reduction factor.

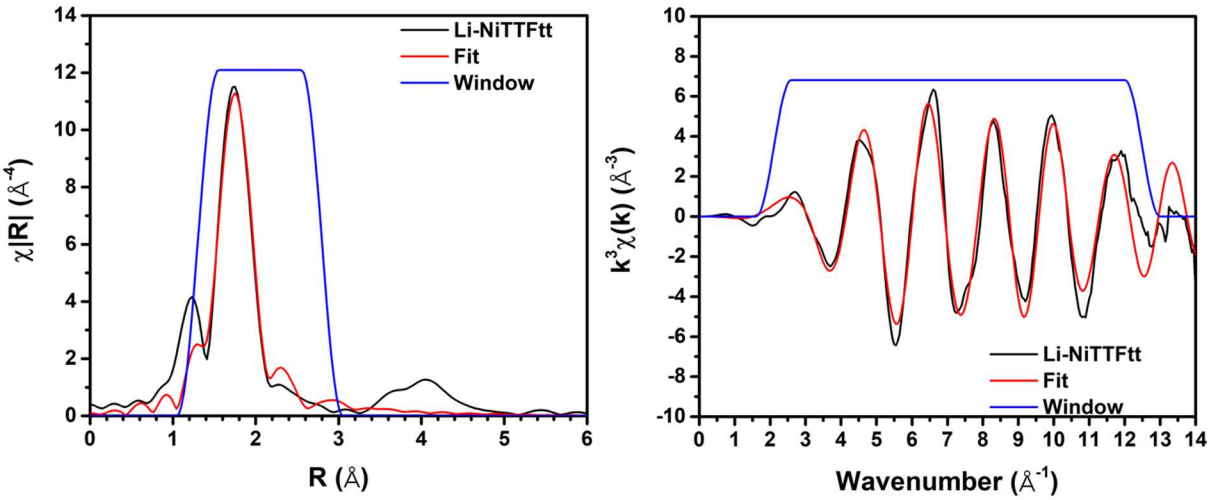

Figure F.4. EXAFS spectra in R-space (left)and k-space (right) of Ni K-edge absorption of Li-NiTTFtt. The experimental data (black), simulated fit (red), and window (blue) are shown.

Table F.5. EXAFS fit parameters for LiTHF-NiTTFtt.

LiTHF-NiTTFtt	N	R (Å)	σ^2 (Å^2)	R-factor	Reduced chi-square
Ni-S	4	2.161(6)	0.0033(7)	0.0077	629
Ni-C	4	3.01(3)	0.005(4)		

ΔE_0 = -1(1) eV; S_0^2 = 0.61(6); Independent Points: 9.7; Fitting Range: k: 2.1-12.5 Å^{-1}; R: 1.3-2.8 Å; N, Coordination numbers; R, interatomic distances; σ^2, Debye-Waller factors (the mean-

square deviations in interatomic distance). The values in parentheses are the estimated standard deviations; ΔE_0, change in the photoelectron energy; S_0^2, amplitude reduction factor.

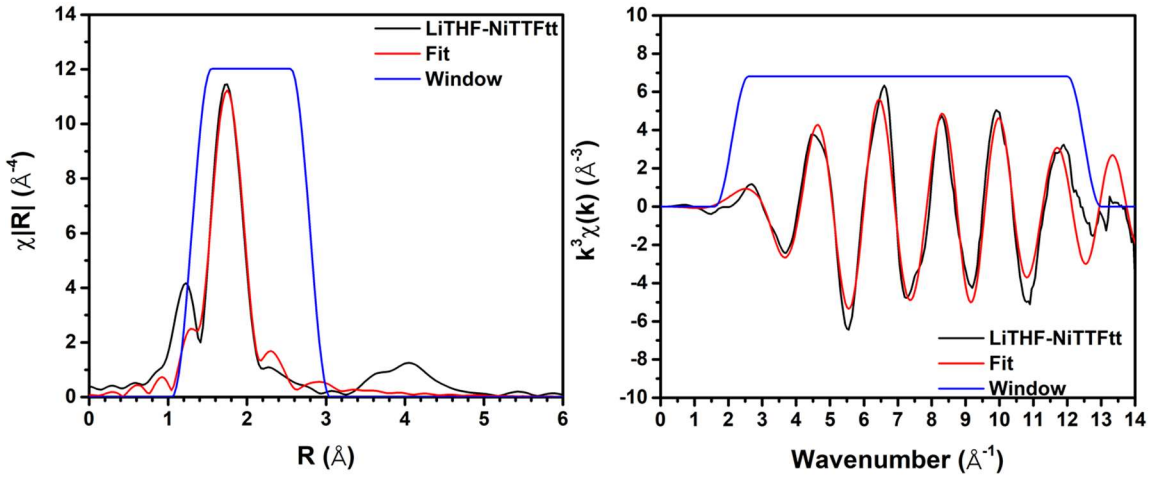

Figure F.5. EXAFS spectra in R-space (left)and k-space (right) of Ni K-edge absorption of Li-NiTTFtt. The experimental data (black), simulated fit (red), and window (blue) are shown.

F.1.6 Infrared Spectroscopy

Infrared spectra were recorded on a Bruker Tensor II FTIR spectrometer with MCT detector operated at 77 K. Data were processed and background corrected with OPUS software (version 7.5). An additional manual correction for scattering was also applied. Samples were prepared under N_2 by grinding solid samples with Nujol, placed between two KBr crystal plates, and measured in air under ambient conditions.

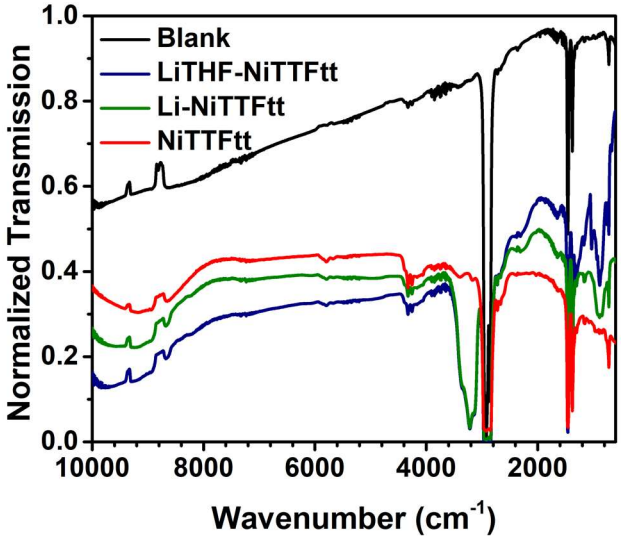

Figure F.6. Infrared transmittance spectra as Nujol mulls in the range of 600-10000 cm-1. All NiTTFtt materials show a broad absorption from 10000 to 7000 cm^{-1}, which are consistent with the diffuse reflectance spectra.

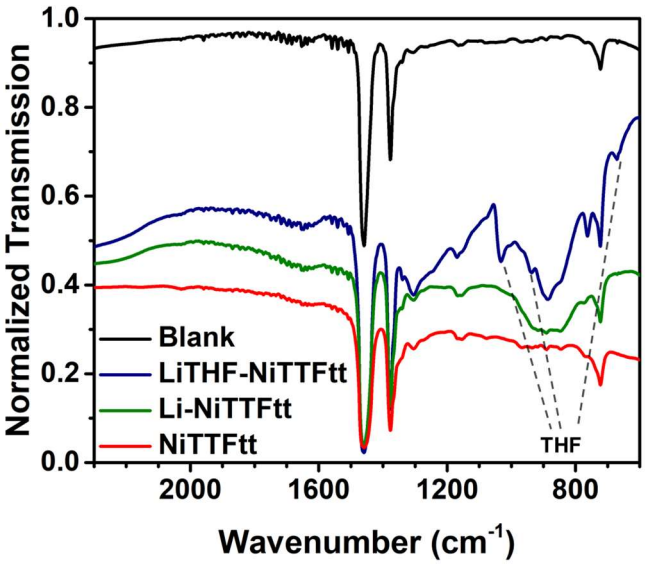

Figure F.7. Infrared transmittance spectra as Nujol mulls in the range of 600-2500 cm-1. The vibration features of THF are only observed in **LiTHF-NiTTFtt**.

F.1.7 Raman Spectroscopy

Raman spectra were obtained with a Horiba LabRamHR Evolution confocal microscope. A Si (111) wafer was used for calibration. The samples of 7 mm round pressed pellets were excited

using a 532 nm light source operating at 5 % of its power and using 100x long path objective and a 600 mm^{-1} grating. For the air-sensitive samples of Li-NiTTFtt and NiTTFtt, the pellets were sealed with additional glass slides and double-layer imaging spacers (Grace Secure Seal, 20 mm DIA × 0.12 mm Depth), shown in **Figure F.8**.

Figure F.8. Demonstration of air-free Raman sample preparation.

F.2 Physical Characterizations

F.2.1 Solid-state CV

Electrochemical experiments for were performed using cyclic voltammetry (CV) on a BASi Epsilon potentiostat/galvanostat. 4 mg fine powder of LiTHF-NiTTFtt was added into 0.05 mL N-methylpyrrolidone (NMP) solution of 10 mg/mL polyvinylidene fluoride (PVDF). After the resulted mixture was violently shaken, few drops were pipetted onto the bottom of a glassy carbon electrode. After the solvent was fairly dried under ambient conditions, the glassy carbon electrode was dried in a vial under vacuum overnight. The mass of materials deposited on the electrode, 1.4 mg, was calculated by subtraction of the mass of the glassy carbon electrode before and after deposition. In addition to the glassy carbon working electrode, a Pt flake and a Ag wire were used

as the counter and reference electrodes, respectively. The reference electrode potential was measured vs. the $FeCp_2^+/FeCp_2$ couple in a separate solution of the relevant electrolyte (with blank glass carbon working electrode instead) to correct for the liquid junction potential. The CV experiments were taken in 0.1 M $LiPF_6$/MeCN at 10 mV/s scan rate. All operations were done in the N_2-filled glovebox.

F.2.2 Room-Temperature Electrical Conductivity and Seebeck Measurements

Electrical conductivity measurements of LiTHF-NiTTFtt and Li-NiTTFtt were performed in a two-contact geometry at room temperature under N_2.

The measurements of Li-NiTTFtt are based on a previously reported setup as the same as NiTTFtt. **Error! Bookmark not defined.**, [4] Gold electrical contacts (75 nm thick) for electronic conductivity (σ) and Seebeck coefficient (α) measurements were deposited onto 8 mm pressed pellets via thermal evaporation through homemade shadow masks. The electronic conductivity was measured in the in-plane direction by using a four-probe geometry with a 0.2 mm spacing between electrodes and electrodes length of 1 mm. The Seebeck coefficient was measured with two 1 mm^2 gold pads, which are either 3 or 1 mm apart. A detailed schematic is shown in the previous report. Four probe conductivity measurements were performed using a custom-designed probe station in an argon glovebox. Voltage and current measurements were performed using a Keithley 2400 source meter and a Keithley 6221 precision current source. A constant current was applied to the outer contacts, and the resultant steady state voltage response was recorded from the two inner contacts. The resistance (R, ohm) of the sample was extracted from the slope of the IV sweep by using Ohm's law (R = V/I). The conductivity σ was then calculated via the following equation (**Equation E.3**):

$$\rho = \frac{V}{I} \frac{\pi t}{\left(\frac{\sinh\left(\frac{t}{s}\right)}{\sinh\left(\frac{t}{2s}\right)}\right)}$$

Where t is the thickness of the sample and s is the separation distance between neighboring probes.

This formula has been previously applied for a thick Si wafer,[5] which is similar to the round pressed pellet. The Seebeck coefficient measurements were performed on the same probe station. Two Peltier elements were placed 5 mm apart to provide the temperature difference ($\Delta T = T_H - T_C$). Two thermocouples were used to collect the hot and cold side temperatures, and two probes were used to measure the corresponding voltage value. A minimal amount of thermally conductive silicone paste was applied to the tips of the thermocouple to ensure good thermal contact between the thermocouple and the gold pads. A delay of 200 s was used for voltage measurements to ensure that a steady-state temperature gradient and voltage were reached. The Seebeck coefficient was calculated from the slope of a linear fit for the ΔV vs ΔT plot. The measurements were taken within an approximate ΔT of ±3 K around 300 K so that the Seebeck coefficient did not change significantly over $T \pm \Delta T$. A series of measurements on Ni foil (0.03 mm, >99.9%) were performed at 25 °C to determine the systematic error. The measured Seebeck coefficient of Ni is −20.3 ± 1.3 μV/K, which matched well with reported values in the literature (−19 μV/K at 25 °C). [6, 7]

While the Seebeck measurements were identical, the electrical conductivity of LiTHF-NiTTFtt was measured by using a two-probe method due to high resistivity. Samples were prepared as pressed pellets clamped between two brass electrodes (4.8 mm diam.) in a plastic sleeve, allowing measurement of the sample thickness with calipers. Linear sweep voltammetry was conducted using a BASi Epsilon potentiostat/galvanostat, with the reference and counter electrode terminals

connected to one electrode and the working electrode terminal to the other. The resulting data were fit to a straight line to obtain the sample resistance.

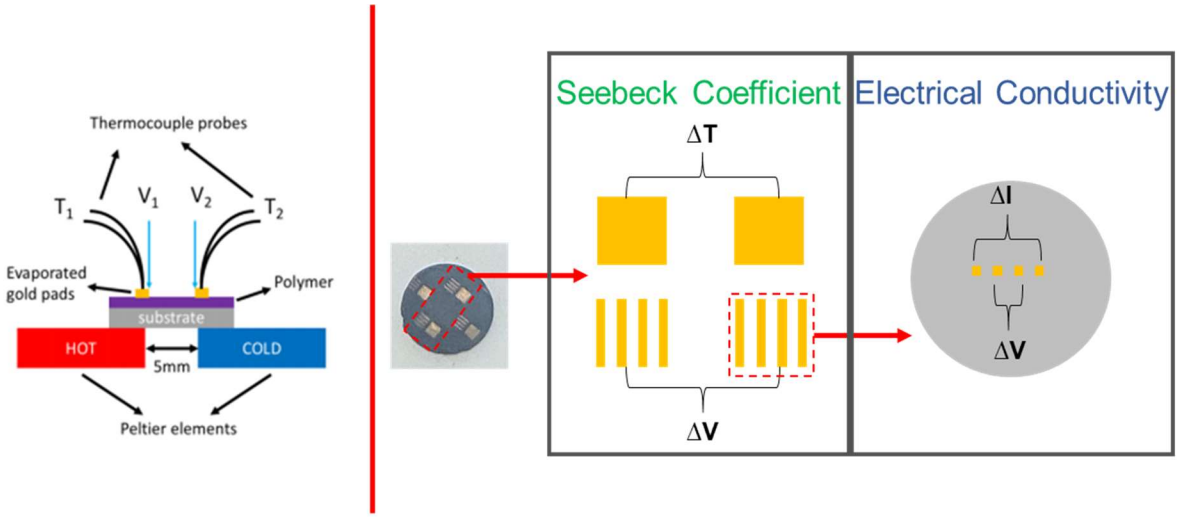

Figure F.9. The schematic for the homemade setup for Seebeck measurements (left) and a demonstration(right) of the gold-deposited 8 mm pressed pellets for the measurements of Seebeck coefficient and electrical conductivity.

F.2.3 Variable-Temperature Electrical Resistance

The as-synthesized powders of Li-NiTTFtt and LiTHF-NiTTFtt was pressed into 6 mm × 6 mm squared pellets and cut into 2 mm × 6 mm slides. The pellet slides were then mounted into the ceramic dual inline package (KYOCERA C-dip 16 pins) and two ends of pellets were connected with gold nodes by conductive silver paste. The variable temperature I–V measurements (two-probe) were carried out in a CRYOSTATION® S50 system (Montana Instruments). For Li-NiTTFtt, the system was first cooled to 40 K and then slowly warmed up to target temperatures at 10 K step to 200 K and then at 20 K step until the sample thermally equilibrated at room temperature (295 K). At each temperature, the system was under vacuum and allowed to stabilize for 10 minutes before I–V profiles were collected from _100 mV to 100 mV. Ohmic I–V profiles were observed for all temperatures from 40 K to 295 K, and a linear fit of the I–V curve was used to get the conductance (G) of the sample. Since the resistance of the LiTHF-NiTTFtt sample

became giant and out of the instrument's measurement range, the conductance was recorded starting from 180 K to 295 K with a15 K step.

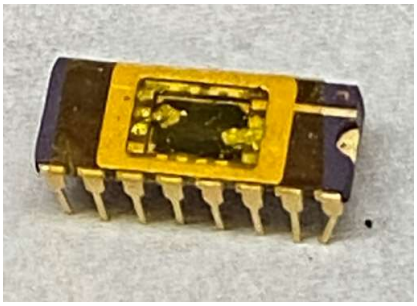

Figure F.10. Demonstration of air-free sample preparation for VT-resistance measurements.

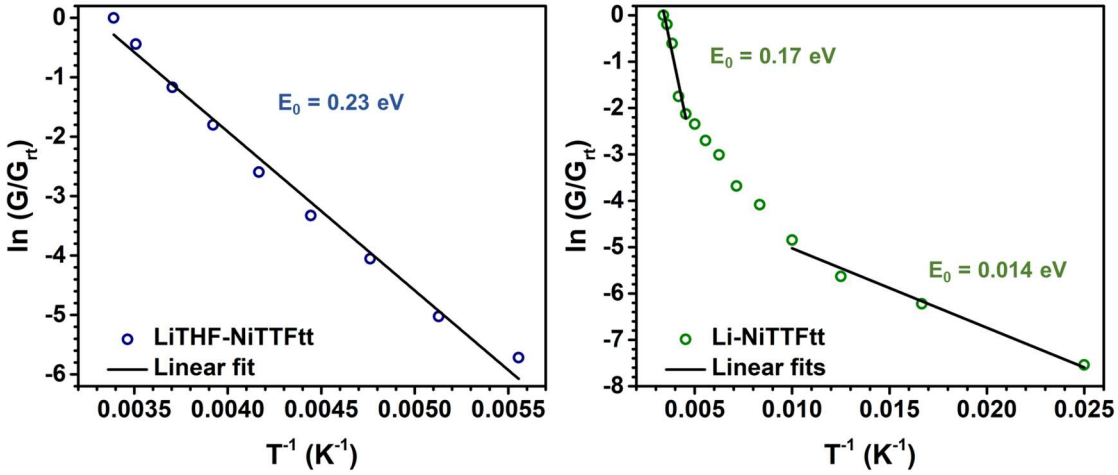

Figure F.11. Arrhenius plots and fits of LiTHF-NiTTFtt (left) and Li-NiTTFtt (right).

F.2.4 UV-Vis-NIR Diffuse Reflectance Spectrum

UV-Vis-NIR diffuse reflectance spectra were collected on a Varian Cary 5000 spectrophotometer with powder samples loaded in a Praying Mantis air-free diffuse reflectance cell with KCl powder as the non-adsorbing matrix. The Kubelka-Munk conversion of the raw diffuse reflectance spectrum was obtained by applying the formula $F(R) = (1-R)^2/2R$.

F.2.5 Thermogravimetric Analysis

Thermogravimetric analysis (TGA) was performed using a TA Instruments Discovery analyzer. Approximately 2 mg of sample was loaded into a pre-tared Pt pan and measured under N_2 or air. Samples were measured from 35 °C to 700 °C using a linear temperature ramp of 10 °C min^{-1}. During loading samples into the pan, samples had to be exposed to the air for about one min. Li-NiTTFtt could be partially oxidized leading to some mass off in the beginning (**Figure F.12**). Therefore, the thermal stability of Li-NiTTFtt was more accurately determined by DSC (**Figure F.13**), during the whole process of which was under N_2.

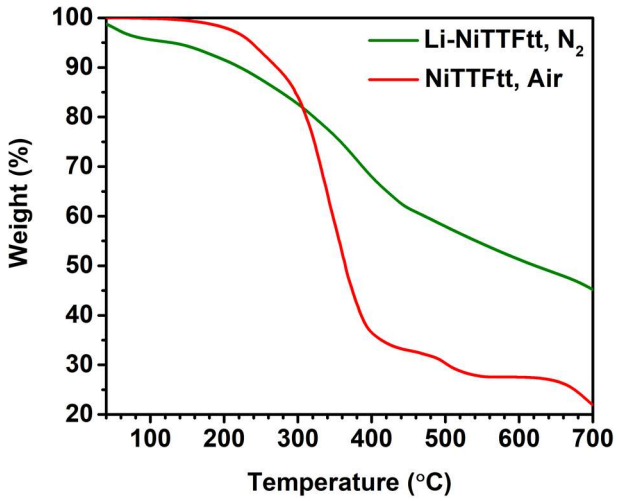

Figure F.12. TGA spectra of NiTTFtt (red) and Li-NiTTFtt (green).

F.2.6 Differential Scanning Calorimeter

Differential Scanning Calorimeter (DSC) for Li-NiTTFtt and NiTTFtt was performed using a TA Instruments Discovery analyzer. Approximately 7 mg of sample was sealed into a Tzero pan with a hermetic lid. The air-sensitive Li-NiTTFtt sample was sealed in the glovebox (the TA press was pumped into the glovebox). Under N_2, the samples were measured in the temperature range of 20-150 °C using a linear temperature ramp of 10 °C min^{-1} over two cycles.

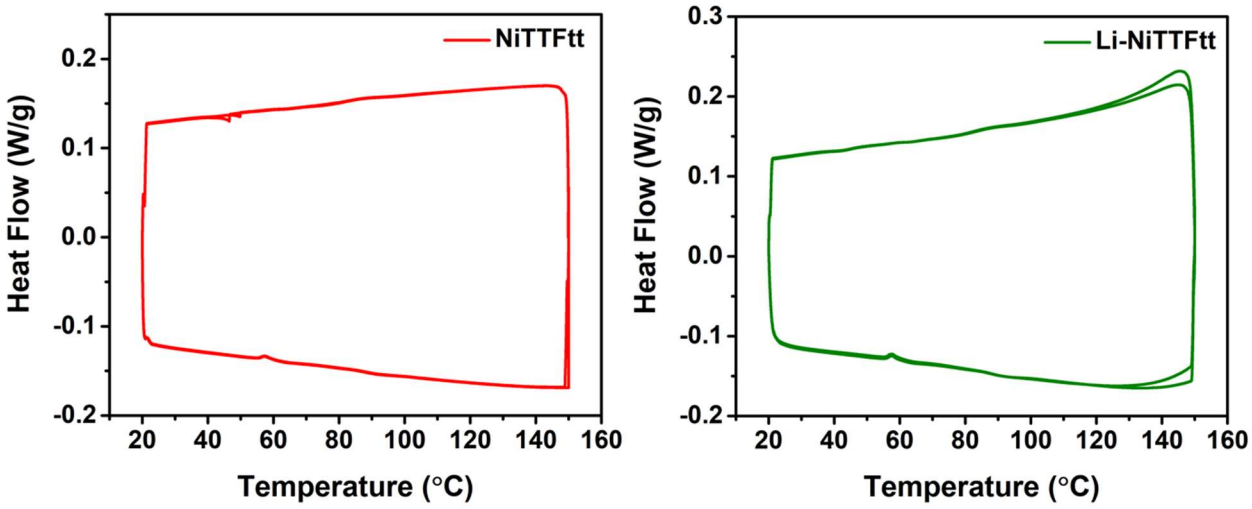

Figure F.13. DSC spectra of NiTTFtt (left) and Li-NiTTFtt (right) in the temperature range of 20-150 °C.

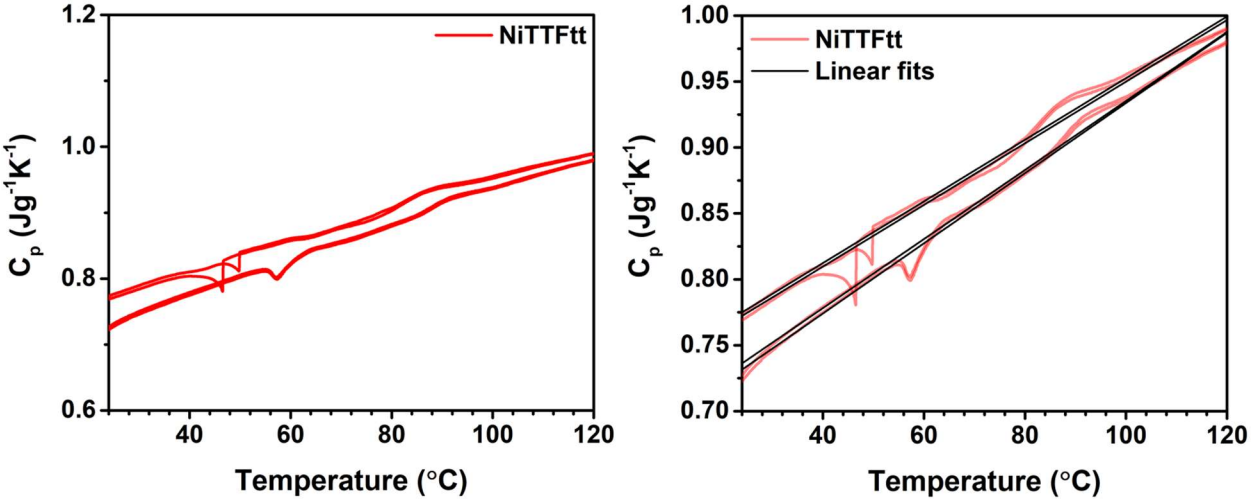

Figure F.14. Temperature-dependent heat capacity of NiTTFtt (left) and corresponding linear fits (right) for the calculation of average Cp over 24-120 °C, the temperature range of which is the condition for PT experiments. The calculated Cp are 0.821. 0.827, 0.905, and 0.904 $Jg^{-1}K^{-1}$ and the average is 0.86 (4) $Jg^{-1}K^{-1}$.

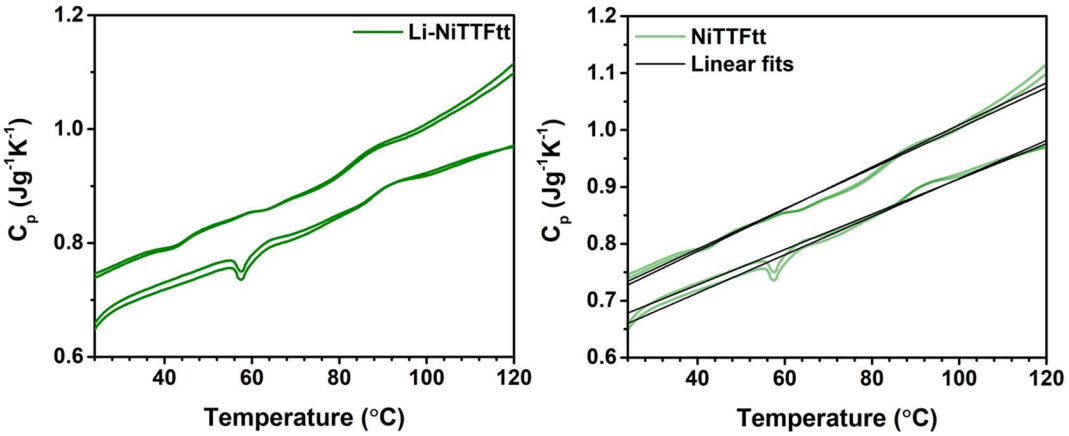

Figure F.15. Temperature-dependent heat capacity of NiTTFtt (left) and corresponding linear fits (right) for the calculation of average Cp over 24-120 °C, the temperature range of which is the condition for PT experiments. The calculated Cp are 0.859. 0.862, 0.887, and 0.884 $Jg^{-1}K^{-1}$ and the average is 0.87 (1) $Jg^{-1}K^{-1}$.

F.2.7 Photo-Current Measurements

The 7 mm round pellets were mounted onto a glass slide and connected to two copper tapes with silver paste and In wires as shown in **Figure F.16**. By connecting the copper tapes with wires to the Echem station, the photocurrent was measured with a BASi Epsilon potentiostat/galvanostat. 850 nm LED (advanced illumination, SL073) was used as the light source (spot size, 33 mm diam.; power density, 93.7 W/m^2).

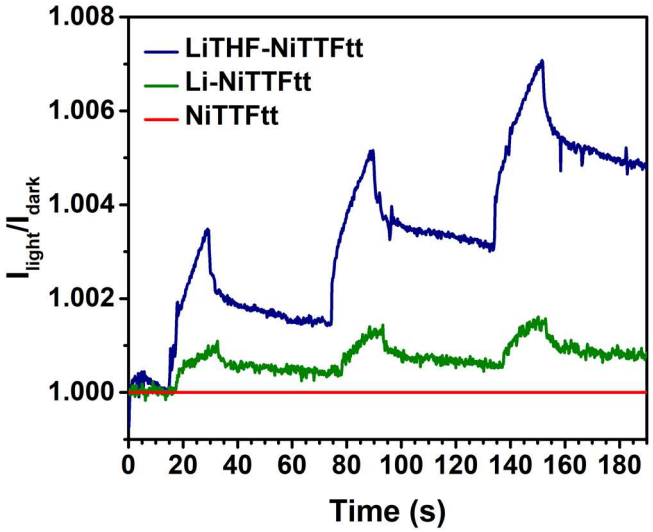

Figure F.16. Photo-current tests of NiTTFtt (red), Li-NiTTFtt (green), and LiTHF-NiTTFtt (blue). The decay time is much longer than the light-on time but the currents in **Li-NiTTFtt** and **LiTHF-NiTTFtt** samples are not reset. Since on-off cycles in PT experiments take almost the same time, these phenomena are not caused by thermal effect.

F.2.8 Photo-Thermal Conversion Measurements

An 8 mm round pellet of **NiTTFtt** (thickness 272 μm) was placed in a white thermal-insulated foam as shown in Figure F.19. The laser source is composed of a laser diode emitting at 808 nm (Thorlabs, L808P500MM) placed in a laser diode mount (Thorlabs, TCLDM9), which is controlled by a driver (TED 200C) and temperature controller (LDC 205C). The IR camera (FLIR, E30bx) was used for temperature monitor. For **Li-NiTTFtt**, the setup is similar with two minor adjustments (Figure F.19): 1) a 7 mm round pellet was used; 2) the measurements were done in a N_2-filled glovebox instead of in-air; 3) while the IR camera was pumped into the glovebox, the laser source was still placed outsides but the light penetrated a quartz window and was reflected on the pellet by adjusting minor. The laser power for both cases were calibrated with a power sensor (Thorlabs, S310C).

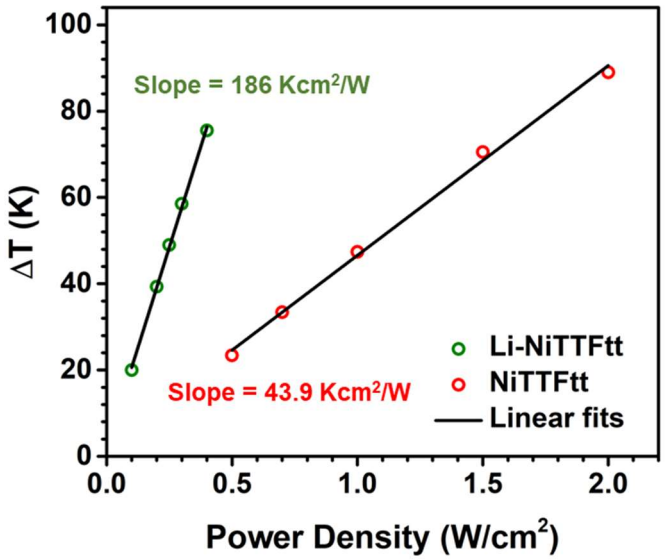

Figure F.17. Photo-thermal conversion of NiTTFtt (red) and Li-NiTTFtt (green) during the PTE experiments (in circuit). Linear relationships between temperature increasements and irradiation power densities. Under the same power density, the temperature rise is small than what is measured in PT condition (without circuit), which is observed in literature too.[8]

F.2.9 Calculation of PT efficiency

The calculation of photothermal conversion efficiency was based on the previous reported method[8, 9, 10] and the details are as follows:

$$\sum_i m_i C_{p_i} \frac{dT}{dt} = Q_L - Q_{ext}$$

Equation F.1

where m_i and $C_{p,i}$ are the mass and heat capacity of system components, and ΔT is the temperature between sample and surroundings.

Q_L is the absorbed light energy and can be determined with the following equation:

$$Q_L = I(1 - 10^{-A_{808}})\eta_{PT}$$

Equation F.2

where I is the laser power; A_{808} is the absorbance of the materials at the wavelength of 808 nm; η_{PT} is the photo-thermal conversion efficiency.

Q_{ext} is the external heat lost into the environment which is nearly proportional to the linear thermal driving force as the proportionality constant, namely

$$Q_{ext} = hS\Delta T$$

Equation F.3

where h is the heat transfer coefficient; S is the surface area of the system.

At the maximum steady-state temperature, T_{max}, the photothermal heat energy input is equal to the external heat loss,

$$\sum_i m_i C_{p_i} \frac{dT}{dt} = Q_L - Q_{ext} = 0$$

namely,

$$Q_L = I(1 - 10^{-A_{808}})\eta_{PT} = Q_{ext} = hS\Delta T_{max}$$

and then,

$$\eta_{PT} = \frac{hS\Delta T_{max}}{I(1 - 10^{-A_{808}})}$$

Equation F.4

In order to get the hS, we focus on the cooling process, during which the laser is off and Q_L is zero, so

$$\sum_i m_i C_{p_i} \frac{dT}{dt} = -Q_{ext} = -hS\Delta T$$

Equation F.5

A dimensionless temperature, θ, is introduced as

$$\theta = \frac{\Delta T}{\Delta T_{max}}$$

, and we substitute it into the last equation (**Equation F.5**) and obtain

$$\frac{d\theta}{dt} = -\frac{hS}{\sum_i m_i C_{p_i}} \theta$$

namely,

$$\frac{d\theta}{\theta} = -\frac{hS}{\sum_i m_i C_{p_i}} dt$$

whose integration formal is

$$\ln\theta = -\frac{hS}{\sum_i m_i C_{p_i}} t$$

Equation F.6

Define $\tau = \frac{\sum_i m_i C_{p_i}}{hS}$,

Thus, $t = -\tau \ln\theta$, and cooling time coefficient, τ, can be determined by the linear fit of t- lnθ curves (**Figure F.18**).

Therefore, $hs = \frac{\sum_i m_i C_{p_i}}{\tau}$ and then we get **Equation 7.1**

$$\eta_{PT} = \frac{hS\Delta T_{max}}{I(1-10^{-A_{808}})} = \frac{\sum_i m_i C_{p_i} \Delta T_{max}}{\tau I(1-10^{-A_{808}})} \geq \frac{mC_p \Delta T_{max}}{\tau I(1-10^{-A_{808}})}$$

Since the samples were laid on a white thermal-insulated foam, which displayed no detectable temperature change during the experiments, here we assume the heat was only reserved in the pellet at the thermal equilibrium.

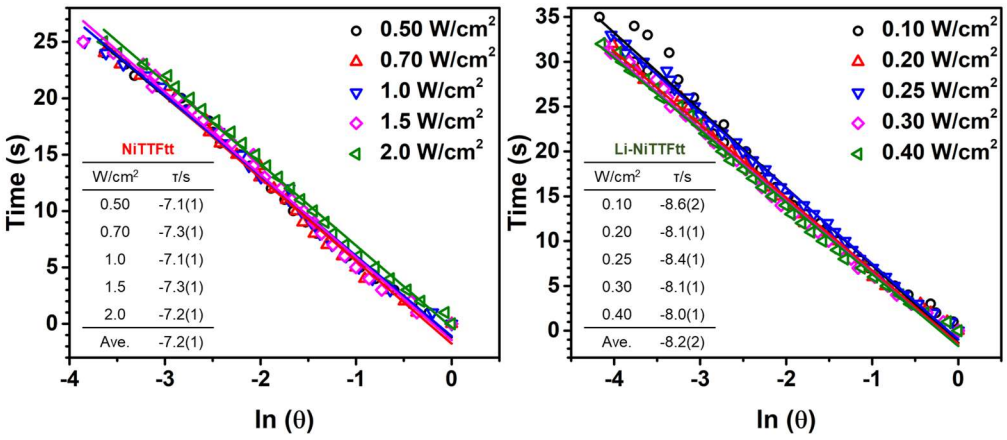

Figure F.18. The time-lnθ linear curves corresponding to the cooling process (laser off) of NiTTFtt (left) and Li-NiTTFtt (right).

Table F.6. Parameters for PT efficiency calculation.

	m (mg)	Cp ($Jg^{-1}K^{-1}$)	k[a] (Kcm^2/W)	τ (s)	S (cm^2)	$1-10^{-A_{808}}$	η_{PT} (%)
NiTTFtt[b]	21	0.87	44	7.2	0.17	0.94	71
Li-NiTTFtt	11	0.86	230	8.2	0.30	0.94[d]	94

a) the slopes of temperature-power density plots (**Figure 7.6**C); b) a 8 mm round pressed pellet and thickness is 271 μm; c) a 7 mm round pressed pellet and thickness is 208 μm; d) assumed to be the same as NiTTFtt. Even assuming 100 % absorption, the efficiency is at least 88 %.

F.2.10 NIR-Seebeck Voltage Measurements

For PTE experiments of Li-NiTTFtt, we used the similar setup in the glovebox but measured the Seebeck voltage with two probes connected to a multimeter (Agilent 34410A, associated with software, Keysight Benchvue) as shown in Figure F.19. While one end was smashed with gold pods (a homemade gold-deposited glass slide), other end of two In wires was connected with the pellet edges along a diametrical dimension by using Ag paste. To avoid the shielding from the Ag paste, the face of the pellet that did not contain Ag paste was exposed to the light.

Figure F.19. Demonstration of the setup for PT and PTE experiments in a N_2-filled glovebox including the thermal insulating foam as the sample holder(left), electrical connects and the IR camera (middle), and the 808 nm laser irradiation through the quartz window from the outsides (right). For PT measurements, the gold probes are lifted avoiding an electrical circuit. The setup for NiTTFtt PT experiments is identical except exposed to the air.

As for NiTTFtt, since we found the Ag paste was degraded in air after heat-up, some gold panels were deposited on the pellet's edge and used for direct connection with probes. In order to create good electric contacts between gold panels and probes, the soft foam substrate was replaced with thermal/electric-insulating Kepton tapes (**Figure F.20**).

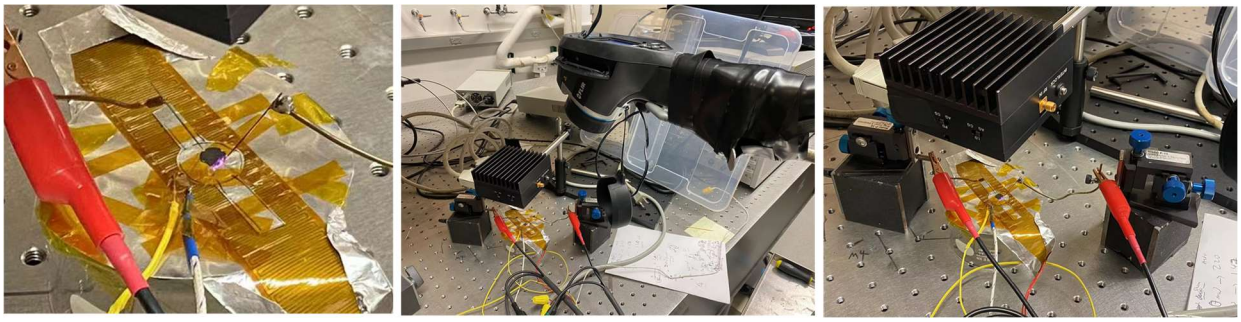

Figure F.20. Demonstration of the setup for PTE experiments of NiTTFtt in air.

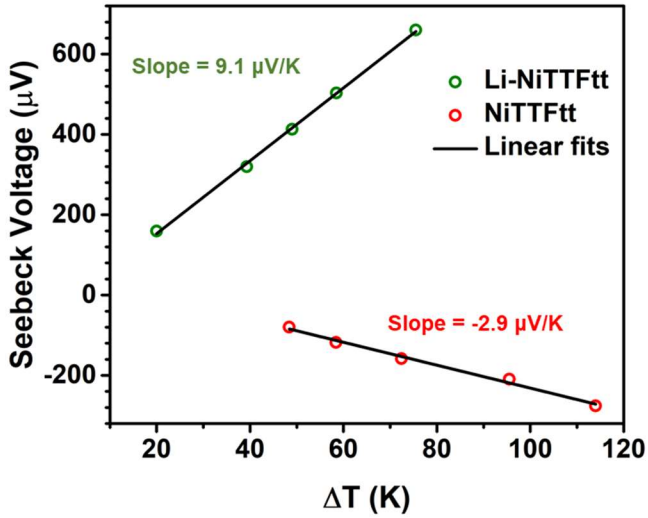

Figure F.21. The plots of Seebeck Voltage to temperature gradients during PTE experiments. The Seebeck coefficients calculated (slope) are consistent with the values obtained with Peltier setup.

F.3 References

[1] Morrison, C.; Sun, H.; Yao, Y.; Loomis, R. A.; Buhro, W. E. Methods for the ICP-OES Analysis of Semiconductor Materials. *Chem. Mater.* **2020**, *32* (5), 1760–1768.

[2] Ravel, B.; Newville, M. ATHENA , ARTEMIS , HEPHAESTUS : Data Analysis for X-Ray Absorption Spectroscopy Using IFEFFIT. *J. Synchrotron Radiat.* **2005**, *12* (4), 537–541.

[3] Rehr, J. J.; Albers, R. C. Theoretical Approaches to X-Ray Absorption Fine Structure. *Rev. Mod. Phys.* **2000**, *72* (3), 621–654.

[4] Ma, T.; Dong, B. X.; Grocke, G. L.; Strzalka, J.; Patel, S. N. Leveraging Sequential Doping of Semiconducting Polymers to Enable Functionally Graded Materials for Organic Thermoelectrics. *Macromolecules* **2020**, *53* (8), 2882–2892.

[5] D. Schroder, *Semiconductor material and device characterization*, 3rd editionrd ed. Piscataway NJ; Hoboken N.J.: IEEE Press; Wiley, **2006**.

[6] Schmidt, V.; Mensch, P. F. J.; Karg, S. F.; Gotsmann, B.; Das Kanungo, P.; Schmid, H.; Riel, H. Using the Seebeck Coefficient to Determine Charge Carrier Concentration, Mobility, and Relaxation Time in InAs Nanowires. *Appl. Phys. Lett.* **2014**, *104* (1), 012113.

[7] Beretta, D.; Bruno, P.; Lanzani, G.; Caironi, M. Reliable Measurement of the Seebeck Coefficient of Organic and Inorganic Materials between 260 K and 460 K. *Rev. Sci. Instrum.* **2015**, *86* (7), 075104.

[8] Kim, B.; Shin, H.; Park, T.; Lim, H.; Kim, E. NIR-Sensitive Poly(3,4-Ethylenedioxyselenophene) Derivatives for Transparent Photo-Thermo-Electric Converters. *Adv. Mater.* **2013**, *25* (38), 5483–5489.

[9] Wang, Y.; Zhu, W.; Du, W.; Liu, X.; Zhang, X.; Dong, H.; Hu, W. Cocrystals Strategy towards Materials for Near-Infrared Photothermal Conversion and Imaging. *Angew. Chemie Int. Ed.* **2018**, *57* (15), 3963–3967.

[10] Paściak, A.; Pilch-Wróbel, A.; Marciniak, Ł.; Schuck, P. J.; Bednarkiewicz, A. Standardization of Methodology of Light-to-Heat Conversion Efficiency Determination for Colloidal Nanoheaters. *ACS Appl. Mater. Interfaces* **2021**, *13* (37), 44556–44567.